

ABOUT THE CONFERENCE

Conference Registration

On-site registration and advance registrant badge pick-up will be located in the lobby of the Penn Stater Conference Center Hotel beginning Tuesday afternoon and continuing through Friday morning during the following hours:

Tuesday, June 23	3 to 5 p.m.
Wednesday, June 24.....	7:30 a.m. to 5 p.m.
Thursday, June 25	7:30 a.m. to 4 p.m.
Friday, June 26.....	7:30 to 10 a.m.

ABOUT THE CONFERENCE LOCATION

Computer / Network Facilities

The Penn Stater Conference Center Hotel has complimentary wireless Internet access throughout the facility. Additionally, there are a limited number of computers available on the first level to check e-mail on a complimentary basis.

Box Lunch Package

A three-day box lunch plan at the Penn Stater Conference Center is available, but must be purchased at the EMC registration desk. The lunches will be available in the exhibition area, located in Presidents Hall 1 & 2. The deadline to purchase tickets is 10 a.m. on Wednesday, June 24.

Residence Hall Dining Hours

Pollock Commons Dining Hall

Breakfast: 7 to 9:30 a.m. Lunch: 11 a.m. to 2 p.m. Dinner: 4:30 to 7:30 p.m.

Special Notes: Breakfast is included for those staying on campus. No refunds will be made for late arrivals, early departures or missed meals.

Additional Dining Options

The Penn Stater Conference Center Hotel offers two excellent dining options, The Gardens Restaurant and Legends Pub. Each serves classic American cuisine with an eclectic flair. For off-campus options, visit www.lionsmenu.com to find local restaurants.

Parking

Parking at the Penn Stater Conference Center Hotel is complimentary. Overnight parking at the campus residence halls is \$7 per day. Parking passes for the residence halls can be purchased at the Pollock Commons desk.

Shuttle

The Penn State residence halls and dining facilities are not located within walking distance to the session meetings rooms at the Penn Stater Conference Center Hotel. A daily shuttle from the Pollock Commons to the Penn Stater will be provided and will operate during normal conference hours.

Messages

A message board will be located near the EMC registration desk on the lobby level of the Penn Stater Conference Center Hotel throughout the conference.

Campus Guide

2009-10

- 103 103 Building, The inset
- 300 300 Building, The H3
- ACA Academic Activities F8
- ACP Academic Projects G8
- AAD Agricultural Administration E6
- ASL Agricultural Analytical Services Lab A8
- AGR Agricultural Arena C12
- AGE Agricultural Engineering E5
- ASI Agricultural Science & Industries E6
- ASM All-Sports Museum D10
- ARC Almqvist Research Center B11
- ALT Althouse Lab F5
- ARL Applied Research Lab (ARL) H2
- ASB Applied Science G1
- ARB Arboretum C6 (complete Summer '10)
- ARM Armsby F5
- ART Arts (Playhouse Theatre) E4
- ACG Arts Cottage F5
- BAG Bag House H3
- BCS Bank of America Career Services F7
- BEM Beam D4
- BVR Beaver Stadium D10
- BDK Beecher-Dock House H8
- BND Benedict House H8
- BFC Bennett Family Center G8
- BCR Berkey Creamery E6
- BTL Biomechanics Teaching Lab E3
- BLB Blue Band B8
- BKS Bookstore G5
- BRL Borland E5
- BKE Boucke F5
- BNR Breazeale Nuclear Reactor G9
- BJC Bryce Jordan Center E9
- BKH Buckhout Lab F5
- BJR Burrowes F4
- BST Bus Station G2
- BUS Business D6
- BUT Butler (Ag Engineering) B11
- BFM Butler Farm B7
- CSQ Calder Square II H4
- CRG Carnegie G4
- CRP Carpenter E3
- CDR CEDAR E4
- CFS Center for Sustainability F12
- CBL Centralized Biological Lab H11
- CMT Central Milk Testing Lab A12
- CPV Centre County-Penn State Visitors Center C12
- CHB Chambers E3
- CHN Chandlee Lab G4
- CEL Chemical Ecology Lab A12
- CHM Chemistry F5
- CUL Coal Utilization Lab G8
- CMP Computer Building E7
- CRN Corn Breeding Lab B11
- DCX Dairy Complex A9
- DVL Davey Lab F5
- DBG Daybridge Child Development Center inset
- DKE Deike G3
- EES Earth-Engineering Sciences G1
- ELR East Area Locker Room F8
- EHP East Campus Heating Plant G12
- EAP East Parking Deck E6
- EIS Eisenhower Auditorium F6
- ECH Eisenhower Chapel E4
- EPD Eisenhower Parking Deck F6
- EEE Electrical Engineering East G3
- EEW Electrical Engineering West G3
- ELT Elliott H3
- ENG Engineering Services G1
- EUN Engineering Units (A-C) H3
- EXE Executive Education E2
- FMD Farms Department B11
- FNK Fenske Lab F5
- FRG Ferguson E5
- FLT Fleet Operations B10
- FDS Food Science E7
- FRD Ford D3
- FRL Forest Resource Lab G9
- FRR Forest Resources D6
- FRM Forum E4
- FRH Fraternity House F3, G3
- FRN Frear North F5
- FRS Frear South F5
- GRD Gardner House H9
- GNS General Stores B10
- GLF Golf Course (White) F1
- GRN Grange G6
- GIP Greenberg (Ice Pavilion) F8
- GYP Gypsy Moth Research Lab A12
- HWL Hallowell G2
- HMD Hammond H3
- HZM HazMat Building A6
- HI Headhouse I E6
- HII Headhouse II E6
- HIII Headhouse III E6

- HHD Health & Human Development H5
- HND Henderson G5
- HNS Henderson South H5
- HNG Henning E6
- HUB Hetzel Union Building (HUB) G5
- HPC High Pressure Combustion Laboratory A7
- HNZ Hintz Family Alumni Center H3
- HLB Holuba Hall F9
- HRS Horse Barn A11
- HSL Hosler G3
- HBS Hostetter (Business Services) B7
- HFS Housing & Food Services B6
- HPD HUB Parking Deck G6
- IHL Ihseng F3
- IST Information Sciences & Technology G2
- IM Intramural D9
- IMF Intramural Fields C8, D8, D9
- JMS James H3
- JFF Jeffrey Field C9
- KTZ Katz C7
- KLR Keller E3
- KRN Kern E3
- LWR Land & Water Research G11
- LFB Lasch Football Building F9
- LDY Laundry B10
- LND Leonhard G1
- LFS Life Sciences F6
- LTL Livestock Testing Lab B12
- LBT Lubert inset
- MNT Maintenance I (Pollock) G8
- MTR Mateer E3
- MRI Materials Research Institute inset
- MRL Materials Research Lab G10
- MCL McAllister G5
- NAT McCoy Natatorium E7
- MTL Meats Lab D11
- MED Medlar Field at Lubrano Park E12
- MRK Merkle A12
- MSC Millennium Science Complex F6 (complete Summer '11)
- MOR Moore E3
- MLR Mueller Lab F5
- MIF Multi-Sport Indoor Facility F10
- MRC Mushroom Research Center A7
- MUS Music E4
- MII Music II E4
- NLI Nittany Lion Inn E2
- NLS Nittany Lion Shrine E3
- NPD Nittany Parking Deck E3
- NLL Noll Lab F2
- OBK Obelisk G4
- OBT Old Botany G4
- OMN Old Main G4
- OSM Osmond Lab F5
- OSW Oswald Tower F4
- OUT Outreach Innovation inset
- PMA Palmer Museum of Art E5
- PRK Park Avenue Building D4
- PSQ Pasquerilla Spiritual Center E4
- PRL Pasture Research Lab E6
- PNL Paterno Library F4
- PTL Pattee Library F4
- PTN Patterson E5
- PVN Pavilion Theatre E5
- PDT Penn State Downtown Theatre Center H4
- PSC Penn Stater Conference Centre Hotel inset
- OPP Physical Plant C10
- PCG Pine Cottage F5
- PLK Pollock G7
- PND Pond Lab F4
- POS Post Office G5
- PWR Power Plant H3
- PRO Procurement Services B7
- RKL Rackley E3
- RBR Reber H3
- REC Recreation (Rec Hall) F2
- RSC Research Center (A,B,C,D) G10
- RSE Research East G9
- RSW Research West G1
- RDH Rider House H3
- RDR Rider H4
- RTR Ritenour F6
- ROB Robeson Cultural Center G5
- SKT Sackett H4
- SVG Salvage Warehouse B7
- STF Sarni Tennis Facility F7
- SHC Schreyer Honors College H6
- SCH Schreyer House B5
- SCB Schwab Auditorium G4
- SHD Shields E8
- SPK Sparks F4
- SCG Spruce Cottage F5
- SDL Steidle G3
- SFB Stuckeman Family Building E5
- STH Student Health Center F7

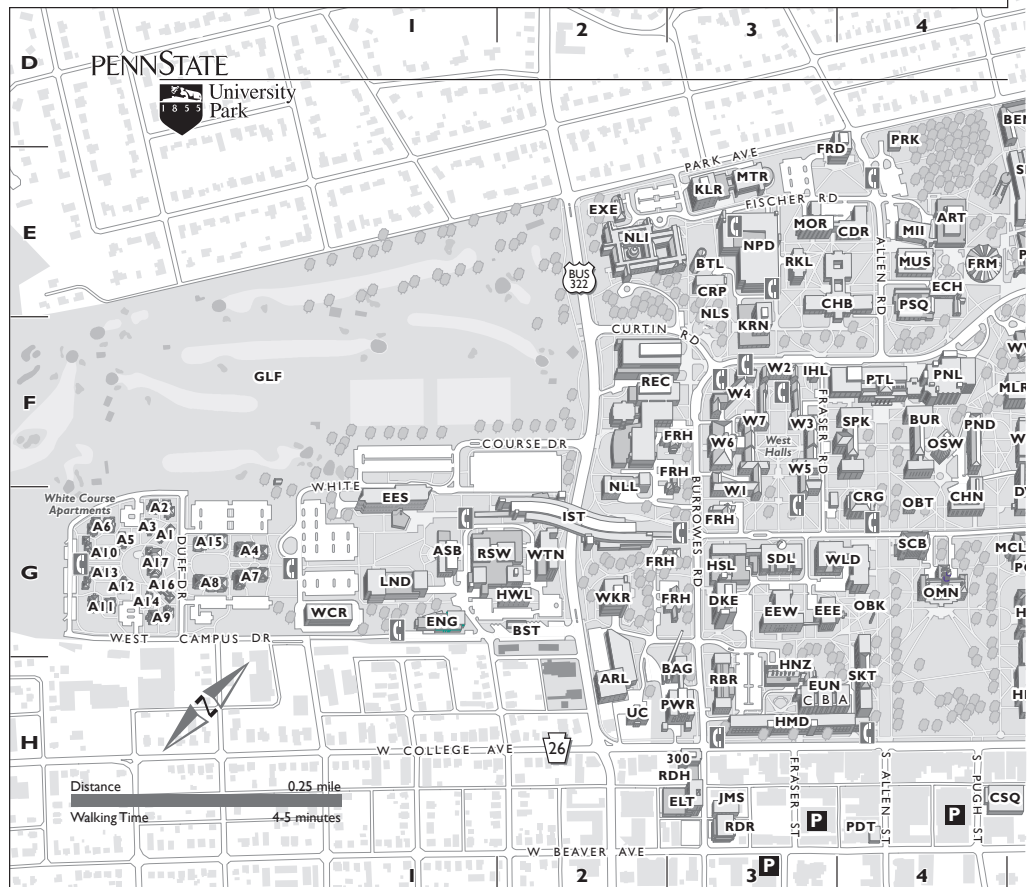
- SWM Swimming Pool (outdoor) F7
- SWI Swine Research G12
- TCH Technology Center inset
- TCM Telecommunications F5
- TNS Tennis F8
- TMS Thomas F6
- TFS Track & Field Stadium F11
- TRN Transportation Research G10
- TRF Turfgrass Museum A8
- TSN Tyson E6
- UC University Club H2
- USI University Support I A7
- USII University Support II A7
- VTC Valentine Turfgrass Res. Cntr. B8
- VIS Visual Arts E5
- WGR Wagner E8
- WKR Walker G2
- WTK Warrick Lab F5
- WTN Water Tunnel (G.Thomas) G2
- WVR Weaver F5
- WCR West Campus Chiller G1
- WHT White G6
- WML Whitmore Lab F5
- WLD Willard G3

East Residence Halls

- E1 Bigler Hall E7
- E2 Brumbaugh Hall D7
- E3 Curtin Hall E7
- E4 Findlay Commons D7
- E5 Fisher Hall D7
- E6 Geary Hall D7
- E7 Hastings Hall D8
- E8 Johnston Commons D7
- E9 McKean Hall D8
- E10 Packer Hall D7
- E11 Pennypacker Hall E8
- E12 Pinchot Hall D7
- E13 Snyder Hall D8
- E14 Sprout Hall D7
- E15 Stone Hall D8
- E16 Stuart Hall D7
- E17 Tener Hall D7

Eastview Terrace

- ET1 Brill Hall G8
- ET2 Curry Hall G8
- ET3 Harris Hall G8
- ET4 Miller Hall H8
- ET5 Nelson Hall H8
- ET6 Panofsky Hall H8
- ET7 Young Hall H7



- Nittany Residence Area**
 NT1 Nittany Apartments **F8**
 NT2 Nittany Community Center **F7**
 NT3 Nittany Hall **G8**

- North Residence Halls**
 N1 Holmes Hall **D5**
 N2 Leete Hall **D5**
 N3 Runkle Hall **D5**
 N4 Warnock Commons **D5**

- Pollock Residence Halls**
 P1 Beaver Hall **G7**
 P2 Hartman Hall **G6**
 P3 Hiester Hall **G7**
 P4 Mifflin Hall **G6**
 P5 Pollock Commons **G7**
 P6 Porter Hall **G7**

- P7 Ritner Hall **G7**
 P8 Shulze Hall **G7**
 P9 Shunk Hall **G7**
 P10 Wolf Hall **G7**

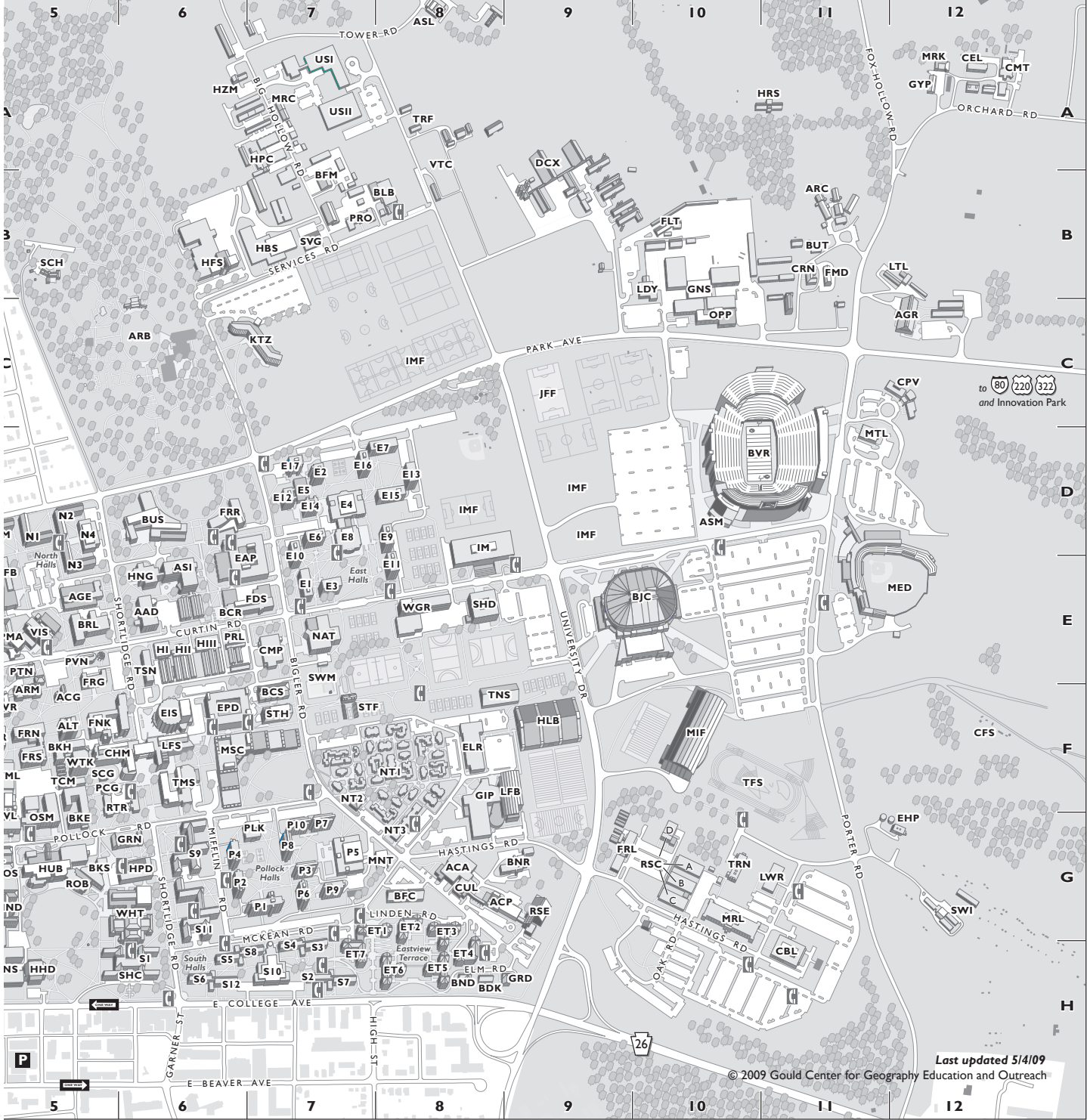
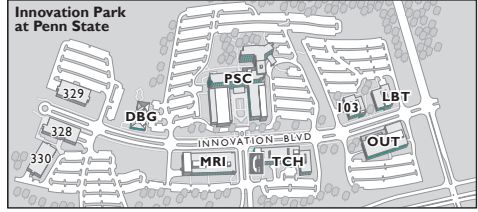
- South Residence Halls**
 S1 Atherton Hall **G6**
 S2 Cooper Hall **H7**
 S3 Cross Hall **H7**
 S4 Ewing Hall **H7**
 S5 Haller Hall **H6**
 S6 Hibbs Hall **H6**
 S7 Hoyt Hall **H7**
 S8 Lyons Hall **H7**
 S9 McElwain Hall **G6**
 S10 Redifer Commons **H7**
 S11 Simmons Hall **G6**
 S12 Stephens Hall **H6**

- West Residence Halls**
 W1 Hamilton Hall **F3**
 W2 Irvin Hall **F3**
 W3 Jordan Hall **F3**
 W4 McKee Hall **F3**
 W5 Thompson Hall **F3**
 W6 Waring Commons **F3**
 W7 Watts Hall **F3**

- White Course Apartments**
 A1 Berreuter Hall **G1**
 A2 Cunningham Hall **G1**
 A3 Donkin Hall **G1**
 A4 Dunham Hall **G1**
 A5 Farrell Hall **G1**
 A6 Ferguson Hall **G1**
 A7 Garban Hall **G1**
 A8 Grubb Hall **G1**

- A9 Haffner Hall **G1**
 A10 Holderman Hall **G1**
 A11 Ikenberry Hall **G1**
 A12 Lovejoy Hall **G1**
 A13 Osborn Hall **G1**

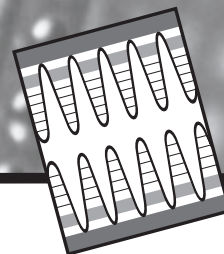
- A14 Palladino Hall **G1**
 A15 Patterson Hall **G1**
 A16 Ray Hall **G1**
 A17 Weston Community Center **G1**



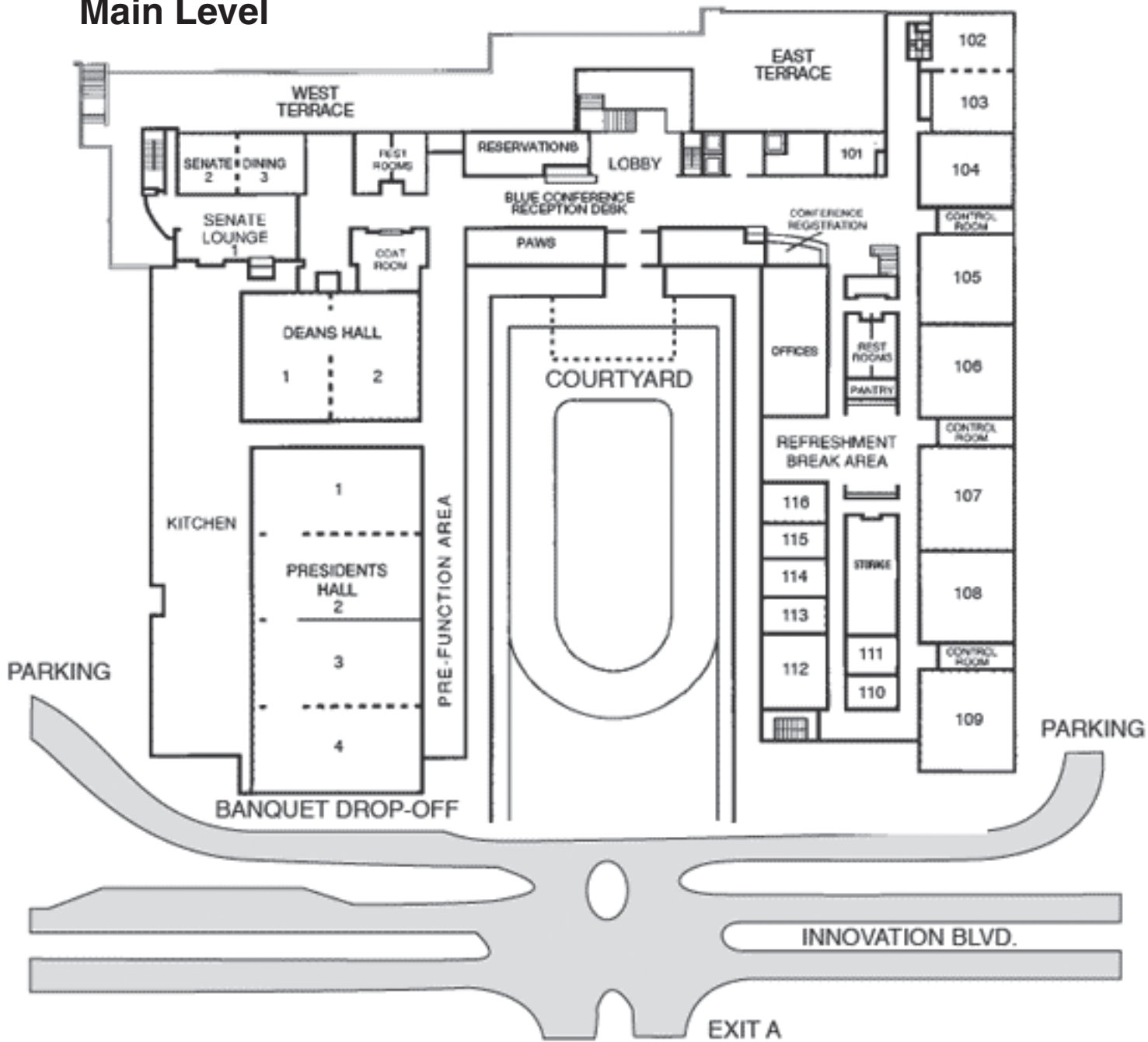
Last updated 5/4/09

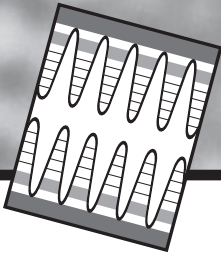
© 2009 Gould Center for Geography Education and Outreach

PENN STATER MAPS



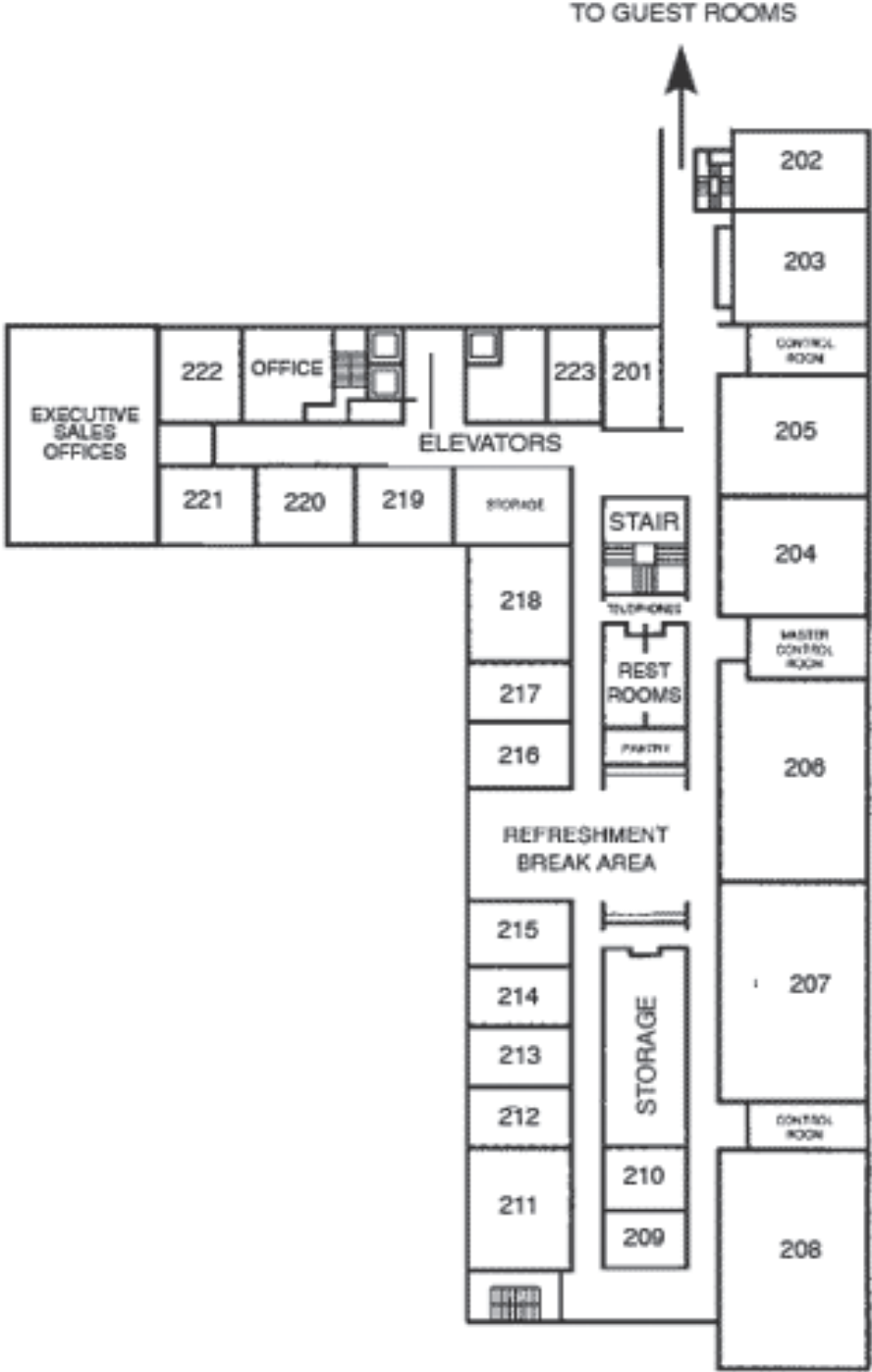
Main Level



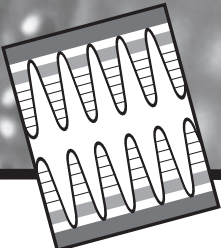


PENN STATER MAPS

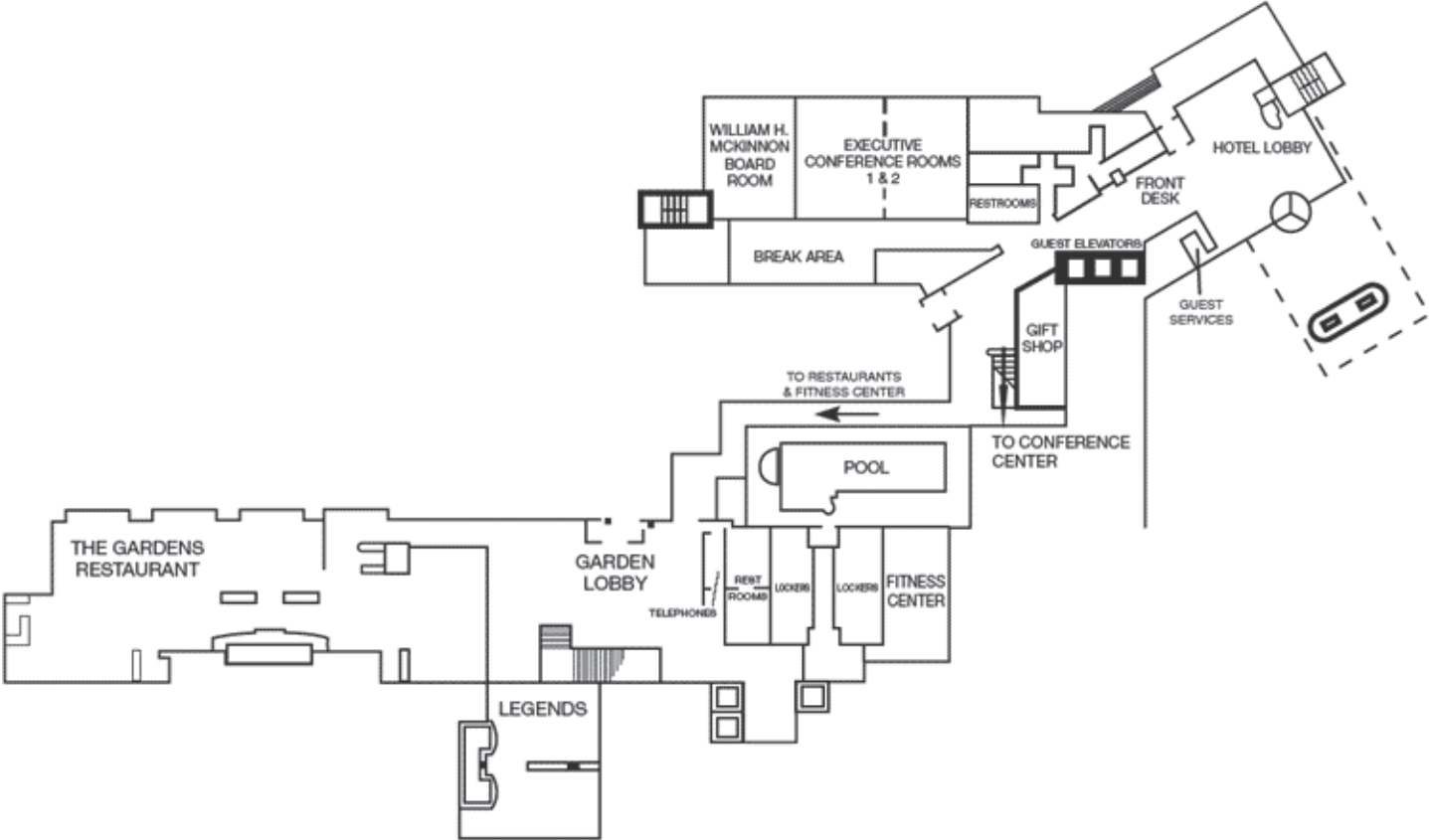
Second Level

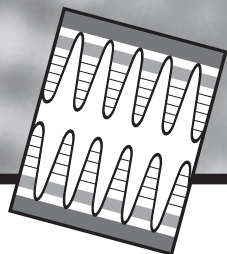


PENN STATER MAPS



Garden Level





NETWORKING & SOCIAL EVENTS

Welcoming Reception

Wednesday, June 24, 6 to 8 p.m.
Penn Stater Conference Center, Presidents Hall 1 & 2

EMC SummerFest

Thursday, June 25, 6:30 to 9 p.m., Presidents Hall
Mingle and celebrate summer during a night of guaranteed fun and surprises.
Tickets include dinner and entertainment and are free to both full conference and student registrants. Guests and one-day registrants pay \$60 or \$25 for children 12 and under. A limited number of tickets are available at the EMC registration desk. Deadline for ticket sales is 5 p.m. on Wednesday, June 24.

Coffee Breaks

Presidents Hall 1 & 2 (Wednesday & Thursday only)
First & second level break areas (Wednesday through Friday)
Coffee, tea, soft drinks and light fare offered each day

Policies



Americans with Disabilities Act

TMS strongly supports the federal Americans with Disabilities Act (ADA) which prohibits discrimination against, and promotes public accessibility for, those with disabilities. In support of and compliance with this Act, we ask that those attendees of EMC requiring specific equipment or services indicate their needs on the enclosed housing form or by contacting the TMS Meeting Services Department at: mtgserv@tms.org

Audio/Video Recording Policy

TMS reserves the rights to any audio and video reproduction of all presentations at every TMS-sponsored meeting. Recording of sessions (audio, video, still photography, etc.) intended for personal use, distribution, publication, or copyright without the express written consent of TMS and the individual authors is strictly prohibited.

Dress

Casual clothing is in order with a sweater or light jacket occasionally needed for the evenings. Layered clothing is recommended for cooler days or in air-conditioned buildings. The average afternoon temperature in late June reaches the middle 80 degrees and the nighttime temperature drops to between 55 and 65 degrees.

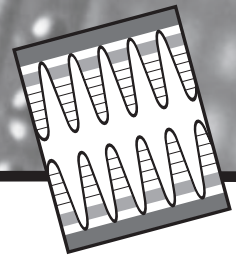
Refund Policy

The deadline for all refunds was June 5, 2009. No refunds are issued at the meeting. All fees and tickets are non-refundable after the June 5, 2009 deadline.

Campus Smoking Policy

Pennsylvania State University prohibits smoking in its buildings, including residence halls. Smoking is permitted in designated areas outside.

EMC EXHIBITION



To complement the engaging technical and networking programs, EMC also features an exhibition of electronic materials technology and related services. This is an opportunity for EMC attendees to meet these providers and acquaint themselves with their capabilities and products.

You are encouraged to visit the exhibits and interact with the participating vendors.

Exhibit Location:

Presidents Hall 1 & 2

Exhibit Dates and Hours:

Wednesday, June 25, 2009 • 10:50 a.m. to 4 p.m. & 6 p.m. to 8 p.m.

Thursday, June 26, 2009 • 10 a.m. to 4 p.m.

PENN STATE IS SERIOUSLY GREEN

“Going green” is not a buzz phrase simply bandied about the Penn State campus. The university takes it seriously. While visiting the exhibit, dining or networking, consider these initiatives launched at Penn State that will sweeten your conference experience:

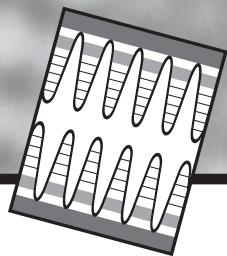
Current ‘GREEN’ Efforts at the Penn Stater & The Nittany Lion Inn

- ‘Recycled’ recycling bins (made from headboards removed during our guestroom renovation)
- Recycling program in front and back of house
- Bulk food for breaks instead of individually wrapped packages (including sugars)
- For disposables, utilize corn-based biodegradable cups, flatware, and ‘to-go’ shells, compostable Eco Hot Cups, and wooden stir sticks for coffee
- Composting efforts for all food waste
- Utilize office paper that is 30% recycled content and bleach free
- Optional terry re-use program for guestrooms
- Recycling bags in guestrooms
- Purchase food from local and PA vendors
- Participation in Penn State’s Waste Cooking Oil to Biodiesel project

ATTENTION STUDENTS!

Become a member of the Material Advantage student program for just \$25 and receive the benefits of four varied materials organizations!

For full details on benefits, including scholarships and awards totaling more than \$600,000, visit www.materialadvantage.org.



AWARDS

John Bardeen Award

Established in 1994, this award recognizes an individual who has made outstanding contributions and is a leader in the electronic materials field.

Citation: For his outstanding and creative contributions to science and technology of silicon carbide and group III nitrides.

2009 Recipient: Robert F. Davis

Carnegie Mellon University

"John Bardeen cast a large shadow of excellence over the materials science and physics communities in terms of his considerable intelligence and his creation of new knowledge. I am pleased that TMS has chosen to recognize his genius with the John Bardeen Award. I am very honored to both be the recipient of this award for 2009 and to join the list of distinguished persons who received this award in prior years."



Nominate Your Colleague for the TMS 2010 John Bardeen Award!

About John Bardeen

John Bardeen's career of theoretical and experimental research set the foundation for the current state of understanding of electronic materials. Two areas in which Bardeen had great impact were the invention and development of the solid-state transistor and the theory that developed greater understanding of superconductivity.

For Award Criteria and Additional Information

Pick up a nomination form at the EMC registration desk, or visit the TMS Web site at www.tms.org/Society/honors.html.

STUDENT BEST PRESENTATION AWARD WINNER

Student awards are given annually by the Electronic Materials Committee for the best presentations by students at the conference. Student papers are judged on both scientific content and presentation at the Electronic Materials Conference. The award will be presented during the plenary session on Wednesday morning, June 24, in the Presidents Hall 3 & 4.

Recipient: J. Renee Pedrazzani

University of Rochester, Institute of Optics

Paper: Virtual Elimination of Surface Leakage Currents in Unpassivated IR Photodetectors

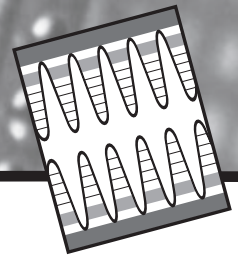
Advisor: Prof. Gary W. Wicks

- ACerS = The American Ceramic Society
- ASM = ASM International
- AIST = Association for Iron & Steel Technology
- TMS = The Minerals, Metals & Materials Society

N MATERIAL™
ADVANTAGE
The Student Program for Materials Science and Engineering

Everything Else Is Immaterial

PROCEEDINGS



EMC does not publish formal conference proceedings; however, the *Journal of Electronic Materials* (*JEM*) encourages both presenters and attendees to submit manuscripts of their work.

EMC is welcoming submissions for two upcoming special issues of the *JEM*.

Group III Nitrides, SiC and ZnO

Deadline: August 1, 2009

Guest editors: Grace Xing, Jamie Phillips, and Robert Stahlbush

Nanowires: Synthesis, Fabrication, and Characterization

Deadline: August 1, 2009

Guest editors: Diana Huffaker, Xinyu Liu, Suneel Kodambaka, and David Janes



Journal of Electronic Materials Manuscript Submission

JEM employs an online manuscript submission and review system. To be considered for publication, authors must submit manuscripts electronically. Detailed submission guidelines are available at the journal's Web site:

www.springer.com/11664, with submissions of manuscripts at: <http://jems.edmgr.com>.

JEM's Editorial Board

Editor

Suzanne E. Mohny, The Pennsylvania State University

Associate Editors

Katayun Barmak, Carnegie Mellon University
Ishwara Bhat, Rensselaer Polytechnic Institute
L.J. Brillson, The Ohio State University
Sinn-wen Chen, National Tsing Hua University
Deborah Chung, University at Buffalo

Kurt G. Eyink, Air Force Research Laboratory
Darrel Frear, Freescale Semiconductor
Rachel S. Goldman, University of Michigan
William C. Mitchel, Air Force Research Laboratory
Alberto Salleo, Stanford University

Robert Stahlbush, Naval Research Lab
Susanne Stemmer, University of California
Michael Tischler, OCIS Technology LLC
Bruce Wessels, Northwestern University
Jihui Yang, GM R&D Center

Editorial Oversight Committee

L.J. Guido, Virginia Polytechnic Institute
J. L. Merz, University of Notre Dame

L. S. Rea, Wright-Patterson Air Force Base
T.D. Sands, Purdue University

X. Zhou, Nanyang Technological
University-Singapore

About JEM

JEM is a monthly archival journal of TMS and the Institute of Electrical and Electronic Engineers (IEEE). Articles are reviewed and selected by peers who serve as voluntary associate and special issue editors. The journal provides a forum for the rapid circulation of original research results. It contains technical papers detailing critical new developments in the field of electronic materials, as well as invited and contributed review articles on topics of current interest. Further questions about content may be directed to the editor, Prof. Suzanne Mohny at mohny@ems.psu.edu

JEM Subscription

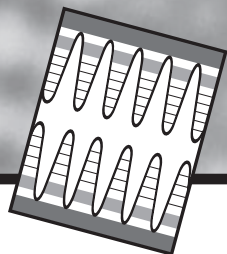
2010 *JEM* issues will include manuscripts of papers presented at 2009 EMC. Individuals may subscribe to *JEM* by contacting Springer, the journal's publisher in North America:

Telephone (800) 777-4643 / E-mail journals-ny@springer.com

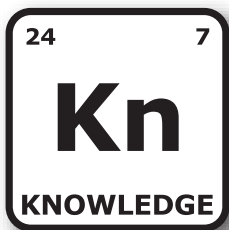
Outside North America:

Telephone (212) 460-1500 or +49 (0) 6221-345-4303 / E-mail subscriptions@springer.com

TMS and IEEE members receive a discount!



PUBLICATIONS



Your Materials Books and More e-Store!

TMS KNOWLEDGE RESOURCE CENTER

<http://knowledge.tms.org>

Stay in the Know with these electronic materials-related publications available from the TMS Knowledge Resource Center

<i>Nitride Semiconductors: Proceedings from the 7th International Conference of Nitride Semiconductors</i>	
Tomas Palacios and Debdeep Jena, guest editors (CD)	(Also available in print) \$100
<i>Wide Bandgap Semiconductor</i>	
Stephen J. Pearton, editor	\$168
<i>MEMS: A Practical Guide to Design, Analysis and Applications</i>	
Jan G. Korvink and Oliver Paul, editors	\$249
<i>Handbook of Silicon Wafer Cleaning Technology, 2nd edition</i>	
Karen Reinhardt and Werner Kern, editors	\$249
<i>Handbook of Semiconductor Silicon Technology</i>	
William C. O'Mara, Robert B. Herring and Lee P. Hunt, authors	\$168
<i>Burn-In Testing: Its Quantification and Optimizations</i>	
D.B. Kececioglu and F-B Sun, authors.....	\$95*
<i>Structural Integrity and Reliability in Electronic Materials</i>	
W.J. Plumbridge, R.J. Matela and A. Westwater, editors.....	\$154**

*TMS member pays \$86

**TMS member pays \$139

Select from 3 convenient ordering options:

WEB

<http://knowledge.tms.org/home.aspx>

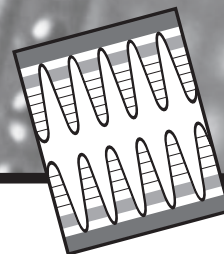
E-MAIL

publications@tms.org

PHONE

724-776-9000, ext. 256 or
800-759-4TMS

CONFERENCE ORGANIZERS



Electronic Materials Committee

OFFICERS:

Robert Biefeld, Chairman
Sandia National Laboratories

Edward Yu, Past-Chairman
University of California, San Diego

Mark Goorsky, Vice-Chairman
University of California, Los Angeles

Christian Wetzel, Treasurer
Rensselaer Polytechnic Institute

Michael Capano, Secretary
Purdue University

Robert Shull, NIST – Gaithersburg, Chair EMPMD

MEMBERS:

Andrew Allerman, *Sandia National Laboratories*
Brian Bennett, *Naval Research Laboratory*
Russell Dupuis, *Georgia Institute of Technology*
Kurt Eyink, *US Air Force*
Rachel Goldman, *University of Michigan*
Doug Hall, *University of Notre Dame*
Jung Han, *Yale University*
Karl Hobart, *Naval Research Laboratory*
Archie Holmes, Jr., *University of Virginia*
Tom Jackson, *The Pennsylvania State University*
Debdeep Jena, *University of Notre Dame*
Kei-May Lau, *Hong Kong University of Science & Technology*
Pat Lenahan, *The Pennsylvania State University*
Maria Losurdo, *Institute of Inorganic Methodologies
and Plasmas, IMIP-CNR*

Suzanne Mohney, *The Pennsylvania State University*
Peter Moran, *Michigan Technological University*
Sarah Olsen, *University of Newcastle-Upon-Tyne*
Jamie Phillips, *University of Michigan*
Steve Ringel, *Ohio State University*
Ben Shanabrook, *Naval Research Laboratory*
Glenn Solomon, *National Institute of Standards and Technology*
Robert Stahlbush, *Naval Research Laboratory*
Alec Talin, *Sandia National Laboratories*
Mike Tischler, *Quanlight*
Christine Wang, *Massachusetts Institute of Technology-
Lincoln Laboratory*
William Wong, *Palo Alto Research Center*
Jerry Woodall, *Purdue University*
Ya-Hong Xie, *University of California, Los Angeles*

INVITED ORGANIZERS FOR THE 2009 EMC CONFERENCE:

The Electronic Materials Conference wishes to thank the following invited organizers for their support and contribution to the technical program presented at this year's conference.

Ganesh Balakrishnan, *University of Mexico*
Seth Bank, *University of Texas at Austin*
Kris Bertness, *National Institute of Standards and Technology*
Leonard Brillson, *The Ohio State University*
Mayank Bulsara, *Massachusetts Institute of Technology*
Michael Chabiny, *University of California, Santa Barbara*
Cindy Colina, *Tyndall National Institute*
Alan Doolittle, *Georgia Institute of Technology*
Michael Dudley, *State University of New York at Stony Brook*
Patrick Fay, *University of Notre Dame*
Randall Feenstra, *Carnegie Mellon University*
Avik Ghosh, *University of Virginia*
Diana Huffaker, *UCLA*
David Janes, *Purdue University*
Suneel Kodambaka, *UCLA*
Thomas Kuech, *University of Wisconsin*

Pat Lenahan, *The Pennsylvania State University*
Xinyu Liu, *University of Notre Dame*
Yicheng Lu, *Rutgers University*
Michael Manfra, *Purdue University*
Thomas Myers, *Texas State University*
David Norton, *University of Florida*
Lisa Porter, *Carnegie Mellon University*
Joan Redwing, *The Pennsylvania State University*
Alberto Salleo, *Stanford University*
Randy Sandhu, *Northrop Grumman*
Susanne Stemmer, *University of California, Santa Barbara*
Kevin Turner, *University of Wisconsin—Madison*
George Wang, *Sandia National Laboratories*
Bruce Wessels, *Northwestern University*
Ping-Show Wong, *UCLA*
Huili (Grace) Xing, *University of Notre Dame*

SESSION LISTING

Wednesday AM June 24, 2009		Wednesday AM June 24, 2009		Wednesday AM June 24, 2009	
EMC Student Awards and Plenary Lectures Room: Presidents Hall III & IV		Session A: Epitaxy Room: 105		Session B: Low Dimensional Structures: Wires and Dots; Dots in Wires Room: 106	
8:20 AM	Welcome and Student Awards	10:00 AM	A1, Optical and Structural Investigations of the Novel Direct Band Gap Material Ga(NAsP) Grown Lattice-Matched on (001) Si SubstrateBernardette Kunert	10:00 AM	B1, (Invited) Reengineering the Optics of Quantum Dots with Mechanical StrainGarnett Bryant
8:30 AM	(Plenary), Electronic Materials Science Challenges in Renewable EnergyRichard King	10:20 AM	A2, (Student) Effects of Mg Doping on the Luminescence Characterization of GaAsN Alloys Grown by MBEKazuyuki Umeno		
9:20 AM	Break	10:40 AM	A3, (Student) Effect of Si-Cap Thickness on Device Performance of Buried Channel Si/Ge _{1-x} C _x /Si DevicesEn-shao Liu	10:40 AM	B2, Nano-Fabrication and Optical Characterization of InAs QDs Pillar Structures Embedded with NiobiumYasuhiro Idutsu
		11:00 AM	A4, (Student) Impact of High-Order Silane Precursors for Silicon Epitaxial Growth on Surface Open SitesKeith Chung	11:00 AM	B3, (Student) Lithography-Free Synthesis of Freestanding Gold Nanoparticle Arrays Encapsulated within Dielectric NanowiresWenchong Hu
		11:20 AM	A5, Photovoltaic-Quality Silicon Epitaxy by Hot-Wire CVD at Glass-Compatible TemperaturesCharles Teplin	11:20 AM	B4, (Student) Effect of Indium Seeding Layer on the Formation and Properties of InN Nanowires on Si by Molecular Beam EpitaxyYi-Lu Chang
		11:40 AM	A6, Structural Characteristics of TaC Films as Buffer Layers for Epitaxy of GaN on SiCTsvetanka Zheleva	11:40 AM	B5, High Efficiency Green Emission from InGaN Wires Measured in 4K-300K RangeVladimir Protasenko

SESSION LISTING

Wednesday AM June 24, 2009		Wednesday AM June 24, 2009		Wednesday AM June 24, 2009	
Session C: Semiconductor Processing Room: 108		Session D: Materials Integration: Wafer Bonding and Engineered Substrates Room: 206		Session E: Organic Thin Film and Crystalline Transistors: Devices, Materials and Processing I Room: 207	
10:00 AM	C1, (Student) Dynamic Study on Formation Processes and Thermal Stability of Nickel Germanides by Using <i>In Situ</i> Transmission Electron MicroscopyJae-Wook Lee	10:00 AM	D1, Unveiling the Complex Evolution of Strain in Nanopatterned Strained Si Membrane Directly on OxideOussama Moutanabbir	10:00 AM	E1, Organic Complementary Inverters and Non-Volatile Memory Elements Based on Ferroelectric Field-Effect Transistors Tse Nga Ng
10:20 AM	C2, Experimental Raman Study and Finite Element Modeling of Strain Distribution in Patterned Device Islands on Strained Silicon-on-Insulator (sSOI) SubstratesDiefeng Gu	10:20 AM	D2, (Student) Cleave Engineered Layer Transfer Substrates with InP Templates for Growth of InGaAs/InAlAs Quantum Well StructuresMonali Joshi	10:20 AM	E2, (Student) Dependence of Charge Injection on Contact Height in Poly(3-Hexylthiophene)-Based Bottom-Contact Field-Effect TransistorsKumar Singh
10:40 AM	C3, (Student) Electronic Passivation of Silicon (100) Surfaces by Organic Layer of 1,10-PhenanthrenequinoneSushobhan Avasthi	10:40 AM	D3, (Student) Surface Chemistry, Electrical Properties, and Passivation-Enhanced Luminescence Achieved Using Dry Sulfur Surface Passivation for Wafer Bonding Applications Mike Jackson	10:40 AM	E3, (Student) Fabrication and Application of Graphene Electrodes and Graphene-Coated Gold Electrodes in Organic Field-Effect TransistorsChen-Guan Lee
11:00 AM	C4, The Role of Atomic Displacements and Vacancy Complexes in Hydrogen Ion-Induced GaN Thin Layer ExfoliationOussama Moutanabbir	11:00 AM	D4, (Student) Effect of Radical Activation for Low Temperature Si to Si Wafer Bonding Ki Yeol Byun	11:00 AM	E4, Compact Model for Sub-Threshold Operation in Polymer Semiconductor Thin Film TransistorsSanjiv Sambandan
11:20 AM	C5, Late News	11:20 AM	D5, (Student) Study of the Formation, Evolution and Dissolution of Interfacial Bonding Defects Based on the Hydrogen Storage and Diffusion MechanismsSebastien Vincent	11:20 AM	E5, Fluoroalkyl Phosphonic Acid Self-Assembled Monolayer Gate Dielectrics to Control the Threshold Voltage in Low-Voltage Organic Thin-Film TransistorsUlrike Kraft
11:40 AM	C6, Late News	11:40 AM	D6, Late News	11:40 AM	E6, Late News

Wednesday AM June 24, 2009		Wednesday PM June 24, 2009		Wednesday PM June 24, 2009	
Session F: III-Nitride: Growth of Electronic Devices Room: 208		Session G: Narrow Bandgap Materials Room: 105		Session I: Quantum Dot Optical Characterizations and Photonic Devices Room: 106	
10:00 AM	F1, (Student) Low-Sheet-Resistance Multiple AlN/GaN Heterojunctions Grown by MBEYu Cao	1:30 PM	G1, Improved Migration-Enhanced Epitaxy for Self-Aligned InGaAs DevicesMark Wistey	1:30 PM	I1, (Student) Lasing of Whispering-Gallery Modes in Asymmetric Waveguide GaInP Micro-Disks with InP Quantum DotsYaya Chu
10:20 AM	F2, (Student) Growth and Characterization of N-Polar GaN/AlGaIn/GaN HEMTs on SiC by Metal Organic Chemical Vapor DepositionDavid Brown	1:50 PM	G2, (Student) Transport Properties of δ -Doped InSb/Al _x In _{1-x} Sb Quantum Well Heterostructures with Varying Subband OccupationOliver Pooley	1:50 PM	I2, (Student) Nanocrystal Laser from Colloidal InP/ZnS Quantum DotsShuai Gao
10:40 AM	F3, (Student) Nanoscale Temperature Distribution, Defect Mapping and Evolution Inside Active AlGaIn/GaN High Electron Mobility TransistorsChung-Han Lin	2:10 PM	G3, Integration of n- and p-Channel InGaSb Quantum Wells for Low-Power Complementary Logic CircuitsBrian Bennett	2:10 PM	I3, Late News
11:00 AM	F4, (Student) The Dominant Gain Limiting Mechanism in Wafer-Fused AlGaAs/GaAs/GaN HBTsChuanxin Lian	2:30 PM	G4, Strain Balanced InAs/InAsSb Superlattices for Mid IR PhotodetectorsDavid Lackner	2:30 PM	I4, (Student) Properties of InAs/GaAs Quantum Rings and Their Application to Terahertz DetectionGuan Huang
11:20 AM	F5, (Student) Ultra-Low Contact Resistance for Self-Aligned HEMT Structures on N-Polar GaN by MBE Regrowth of InGaIn-Based Contact LayersNidhi Nidhi	2:50 PM	G5, (Student) Performance Augmentation of InAs/GaSb Superlattice LWIR Detectors by Surface TreatmentsMaya Narayanan Kutty	2:50 PM	I5, Energy Transfer Pumped Efficient Infrared Colloid Quantum Dot Light Emission DiodesChunfeng Zhang
11:40 AM	F6, (Student) Investigation of Mg Ion-Implanted GaN as Current Blocking Layer in a CAVETSrabanti Chowdhury	3:10 PM	Break	3:10 PM	Break
		Session H: Epitaxy for Devices Room: 105		Session J: Quantum Dot Materials Characterization and Epitaxy Room: 106	
		3:30 PM	H1, (Student) Comparison of Device Performance of Light Emitting Transistors with Zn-Doped and C-Doped BaseYong Huang	3:30 PM	J1, Isotopically Controlled Semiconductor Low Dimensional SystemsOussama Moutanabbir
		3:50 PM	H2, (Student) Annealing Stability of Nanoparticle-Enhanced Tunnel Junctions for High-Efficiency Solar Cells and Mid-Infrared LasersAdam Crook	3:50 PM	J2, (Student) MBE Growth of Highly Tensile Strained Thin Ge LayersYijie Huo
		4:10 PM	H3, AlGaInSb-VECSEL Grown on GaAs Based DBRs for High-Power Emission at 2 μ mThomas Rotter	4:10 PM	J3, (Student) Application of Mist Deposition Process in the Formation of Semiconductor Quantum Nanodot FilmsAditya Kshirsagar
		4:30 PM	H4, Fabrication of Narrow Ridges for High-Performance High-Temperature cw Interband Cascade LasersChulsoo Kim	4:30 PM	J4, Formation of Si-Nanocrystals in SiO ₂ via Ion Implantation and Rapid Thermal ProcessingIain Crowe
		4:50 PM	H5, Late News	4:50 PM	J5, (Student) Deep Level Traps in Single and Multiple InAs/(InGaAs)GaAs Self-Assembled Quantum Dot StructuresTetsuya Asano

SESSION LISTING

Wednesday PM June 24, 2009		Wednesday PM June 24, 2009		Wednesday PM June 24, 2009	
Session K: ZnO Thin Film Transistors Room: 108		Session L: Thermoelectrics and Thermionics Room: Presidents Hall III & IV		Session M: Carbon Based Nanowires and Tubes Room: 206	
1:30 PM	K1, Fabrication and Characterization of Amorphous InGaZnO-Based Thin Film TransistorWantae Lim	1:30 PM	L1, (Student) Scanning Hot Probe Method for Thermoelectric Characterization of Nanostructured Thin-Films: Controlling the Heat Transfer Mechanisms between the Tip and the SampleYanliang Zhang	1:30 PM	M1, (Student) Horizontally Aligned Single-Walled Carbon Nanotubes on Patterned SiO ₂ /Si SubstratesTakaomi Kishimoto
1:50 PM	K2, (Student) Low Temperature Annealing of the Room Temperature Deposited Amorphous InGaZnO4 Thin Film TransistorsYoung Gwang Yoon	1:50 PM	L2, (Student) Thermoelectric Power Characterization of Individual Sb ₂ Se ₃ Single Crystal Nanowires and NanotubesWei Jiang	1:50 PM	M2, (Student) Electromagnetic Shielding Properties of Excimer-Laser-Synthesized-Single-Wall-Carbon Nanotubes/Polyurethane Nanocomposite FilmsBrahim Aissa
2:10 PM	K3, Design and Characterization of ZnO-Based Metal-Semiconductor Field-Effect Transistors on Glass SubstrateHeiko Frenzel	2:10 PM	L3, Self-Supporting Nanowire Arrays Templated in Branched Porous Anodic Alumina for Thermoelectric DevicesHatem Elmatbouly	2:10 PM	M3, Electroluminescence from Electrolyte-Gated Carbon Nanotube ArraysJana Zaumseil
2:30 PM	K4, (Student) Plasma-Enhanced Atomic Layer Deposition ZnO TFTsDevin Mourey	2:30 PM	L4, (Student) Ultrafast Microwave-Stimulated Sculpting and Thermoelectric Properties of Bismuth and Antimony Chalcogenide NanoplatesRutvik Mehta	2:30 PM	M4, Late News
2:50 PM	K5, (Student) Low Temperature Pulsed PECVD ZnO Thin Film TransistorsDalong Zhao	2:50 PM	L5, Nonlinear Electric Transport in Wet-Chemically Synthesized Sb ₂ Se ₃ NanowireC. Karthik	2:50 PM	M5, Late News
3:10 PM	Break	3:10 PM	Break	3:10 PM	Break
3:30 PM	K6, ZnO Field Effect Transistors on Silicon by MOCVDBruce Willner	3:30 PM	L6, Hydrothermal Synthesis of Bi _{0.5} Sb _{1.5} Te ₃ and the Effect of Sintering Temperature on Thermoelectric Characteristics of the Pressed MatsChia-Jyi Liu	Session N: Group IV Nanowires Room: 206	
3:50 PM	K7, (Student) ZnO Field-Effect Transistors with Dual-Gate StructureChan Ho Park	3:50 PM	L7, (Student) Fabrication of p-Type Pb _{0.5} Sn _{0.5} Te Thermoelectric Power Generation Elements by Mechanical AlloyingAaron Lalonde	3:50 PM	N2, 'Bulk' P Doping of Ge Nanowires Reduces ConductivityShixiong Zhang
4:10 PM	K8, (Student) Dual-Gate Operated ZnO Nanowire Field-Effect TransistorsJung-hwan Hyung	4:10 PM	L8, (Student) Alternative Substrates for Metal/Semiconductor Superlattices for Thermionic Energy ConversionJeremy Schroeder	4:10 PM	N3, (Student) Twinning Superlattices: A Correlated Raman and Transmission Electron Microscopy Study on Individual Silicon NanowiresFrancisco Lopez
4:30 PM	K9, Thin Film Encapsulation of Oxide Based Thin Film TransistorsPatrick Goernn	4:30 PM	L9, Cooling Effects of Field Emission from SemiconductorsMoon Chung	4:30 PM	N4, Self-Cleaning Silicon Nanowire Elastomeric CompositesWilliam Wong
4:50 PM	K10, Transparent Photo-Stable Complementary Inverter with Organic-Inorganic Nano-Hybrid DielectricsMin Suk Oh	4:50 PM	L10, Late News	4:50 PM	N5, Late News

Wednesday PM June 24, 2009		Wednesday PM June 24, 2009		Thursday AM June 25, 2009	
Session O: III-Nitride: Optical Devices on Non-Polar Substrates Room: 207		Session Q: III-Nitride: Processing of Electronic Devices Room: 208		Session S: Epitaxy on Si Room: 105	
1:30 PM	O1, (Student) Polarization Study of Yellow Defect Luminescence from Polar and Non-Polar Bulk GaNShi You	1:30 PM	Q1, (Student) Mechanism of Interaction between Hydrogen and the Two Dimensional Electron Gas in AlGaIn/GaN High Electron Mobility TransistorsJason Gu	8:20 AM	S1, (Student) Annihilation Mechanism of Stacking Faults on GaP Layers Grown on Si Substrates within the Critical ThicknessYamane Keisuke
1:50 PM	O2, (Student) MOCVD Growth of True Blue m-Plane GaN Laser DiodesKathryn Kelchner	1:50 PM	Q2, (Student) Surface Passivation and Gate Insulation of AlGaIn/GaN High Electron Mobility Transistors Using in-situ SiNxMarko Tadjer	8:40 AM	S2, (Student) Evolution of Epitaxial (211)Ge on (211)Si Grown by CVDShashidhar Shintri
2:10 PM	O3, (Student) Blue-Green GaInN/GaN Light Emitting Diode on Non-Polar m-Plane Bulk GaNMingwei Zhu	2:10 PM	Q3, Plasma Surface Cleaning of Ultrathin Barrier AlN/GaN Heterostructures for Device FabricationQingling Hang	9:00 AM	S3, Growth of High-Quality Ge on Si through Nanoscale Windows in Thin Chemical Oxide for Multijunction Solar Cells.....Darin Leonhardt
2:30 PM	O4, (Student) Growth and Characterization of High Indium Content m-Plane InGaIn LEDsKathryn Kelchner	2:30 PM	Q4, (Student) Comparison of Plasma-Etching Induced Damage Recovery Treatments on GaN MOS Capacitors and Electrical Performance of Plasma-Etched GaN MOSFETs.....Ke Tang	9:20 AM	S4, Monolithic Integration of Ga(NAsP)/(BGa)(AsP) - Laser Device Structures Lattice-Matched on (001) Silicon SubstrateBernardette Kunert
2:50 PM	O5, (Student) N-Polar (Al, In, Ga)N Grown by Metalorganic Chemical Vapor DepositionQian Sun	2:50 PM	Q5, Influence of NH ₃ in the Surface Passivation Dielectrics on AlGaIn/GaN Heterostructures Grown on a-Plane (11-20) and c-Plane (0001) SapphireSubramaniam Arulkumaran	9:40 AM	S5, (Student) Structural and Optical Properties of Rolled-up InGaAs/GaAs Quantum Dot Microtubes on SiVicknesh Sahnuganathan
3:10 PM	Break	3:10 PM	Break	10:00 AM	Break
Session P: III-Nitride: Growth and Characterization of Non-Polar Materials Room: 207		Session R: III-Nitride: AlGaIn Materials and Devices Room: 208		Session T: Metamorphic and Templated Growth Room: 105	
3:30 PM	P1, (Student) The Origin of Pits and Striations on the Surface of Nonpolar a-Plane GaNChristopher Yerino	3:30 PM	R1, (Student) Surface Characteristics of Single Crystalline, (0001)-Oriented AlN Wafers and Implications for Epitaxial Growth.....Anthony Rice	10:20 AM	T1, (Student) Metamorphic InGaAs and InGaP on GaAs for Multispectral Detector ApplicationsKrishna Swaminathan
3:50 PM	P2, (Student) Nucleation and Evolution in the Two-Step Growth of a-Plane GaN for Improving the Microstructural QualityQian Sun	3:50 PM	R2, Photoluminescence Lifetimes and Internal Quantum Efficiencies of AlGaIn Based 250-nm Light Emitting Diodes from Pseudomorphic Growth on Bulk AlN.....Gregory Garrett	10:40 AM	T2, (Student) Block Copolymer Lithography for Defect Reduction in Epitaxial Growth of Large Lattice-Mismatched MaterialsSmita Jha
4:10 PM	P3, Carrier Lifetime of m-Plane GaNGrace Metcalfe	4:10 PM	R3, Low-Dislocation Density Al _x Ga _{1-x} N Layers for High-Power UV-Visible Light Emitters Using an "in-situ" Silane Treatment.....Qhalid Fareed	11:00 AM	T3, Heteroepitaxial Growth of Single Crystalline-like Films of Ge and Si on Flexible, Polycrystalline SubstratesVenkat Selvamanickam
4:30 PM	P4, (Student) Kinetic Wulff Diagram: Toward Rational Design of Nonpolar and Semipolar GaN HeteroepitaxyChristopher Yerino	4:30 PM	R4, (Student) Growth of AlGaIn and InAlN Ternary Alloys Using Digitally-Alloyed Modulated Precursor Flow Epitaxial Growth.....Suk Choi	11:20 AM	T4, Metalorganic Vapor Phase Epitaxial Growth of (211)B CdTe on (211) Si Substrates Using Ge and ZnTe Interfacial Layers.....Sunil Rao
4:50 PM	P5, 4H-Polytype AlN/AlGaIn MQW Structure Isopolytypically Grown on m-Plane 4H-SiC.....Masahiro Horita	4:50 PM	R5, (Student) Polarization Enhanced p-Type Conductivity in Graded N-Face Al-GaN Slabs.....John Simon	11:40 AM	T5, Low Dislocation Density GaN via Nanowire Templated Lateral Epitaxial Growth (NTLEG).....George Wang
		5:10 PM	R6, MOCVD Growth and Characterization of Mg-Doped AlN-AlGaIn Short-Period SuperlatticesAndrew Allerman		

SESSION LISTING

Thursday AM June 25, 2009		Thursday AM June 25, 2009		Thursday AM June 25, 2009	
Session U: Flexible and Printed Thin-Film Electronics Room: 106		Session V: Oxide Thin-Film Integration I Room: 108		Session W: ZnO Growth Room: Deans Hall I	
8:20 AM	U1, Printable Bottom-Contact Organic Field-Effect TransistorsSeonghoon Lee	8:20 AM	V1, (Student) Atomic-Layer-Deposited HfO ₂ Gate Dielectrics on InP Using Silicon Interface Passivation LayerYen-Ting Chen	8:20 AM	W1, (Student) Properties of In-Doped ZnO Films Grown by Metalorganic Chemical Vapor Deposition on GaN(0001) TemplatesTammy Ben-Yaacov
8:40 AM	U2, (Student) Inkjet Printed Small Molecule Organic Thin Film TransistorsYuanyuan Li	8:40 AM	V2, (Student) Growth of Epitaxial (110) 0.7Pb (Mg _{1/3} Nb _{2/3}) O ₃ - 0.3PbTiO ₃ Thin Films on r-Plane Sapphire Substrates by RF Magnetron SputteringLakshmi Krishna	8:40 AM	W2, (Student) MBE Growth and Characterization of Ag-Doped Zinc Oxide Thin FilmsJessica Chai
9:00 AM	U3, Self Organised Electrodes Using Controlled Coffee Stain Phenomena for High Aspect Ratio Polymer Field Effect Transistors on 3D SubstratesSanjiv Sambandan	9:00 AM	V3, High Quality SrTiO ₃ Thin Films Grown by Hybrid Molecular Beam EpitaxyRoman Engel-Herbert	9:00 AM	W3, (Student) Growth and Characterization of Non-Polar ZnO/ZnMgO Quantum-Wells Synthesized by Pulsed Laser DepositionMei-Hui Liang
9:20 AM	U4, (Student) Printing Silicon from Nanoparticle SuspensionsNoah Jafferis	9:20 AM	V4, (Student) Growth and Microstructure of Homoepitaxial Strontium Titanate Thin Films by Molecular-Beam EpitaxyCharles Brooks	9:20 AM	W4, Ultrasonic Spray Assisted Mist-CVD for the Growth of Crystalline and Amorphous ZnOShizuo Fujita
9:40 AM	U5, High Resolution Patterning by Selective Surface Modification and Dip-Casting for Low-Cost Fully Printed ElectronicsYong-Hoon Kim	9:40 AM	V5, (Student) The Growth and Properties of Sr _{n+1} Ti _n O _{3n+1} Ruddlesden-Popper PhasesChe-Hui Lee	9:40 AM	W5, MOCVD of Zinc Oxide Transparent Conductive OxideBruce Willner
10:00 AM	Break	10:00 AM	Break	10:00 AM	Break
10:20 AM	U6, Towards Low-Noise Flexible ElectronicsOana Jurchescu	10:20 AM	V6, Stabilization of a Very High-k Tetragonal ZrO ₂ Phase by Direct Doping with GermaniumSotiria Galata	10:20 AM	W6, Low Temperature ZnO Growth for Nanotube Fabrication by Atomic Layer DepositionDiefeng Gu
10:40 AM	U7, (Student) Two-Level Stretchable Conductors on Elastomeric SubstratesJoyelle Jones	10:40 AM	V7, (Student) Atomic Layer Deposited HfO ₂ Thin Films on InGaAs/InP: Technology Development and Application in Realization of Memory Diode and Quantum DevicesJie Sun	10:40 AM	W7, (Student) Ag/N/Ag-N Doped ZnO Nanostructures Prepared by Wet-OxidationRuiqun Chen
11:00 AM	U8, A New Method for Integrating Electronics into TextilesThomas Kinkeldei	11:00 AM	V8, (Student) Impact of Growth Process on Native Point Defects and Correlation with Dielectric Properties of Barium Strontium TitanateMitchell Rutkowski	11:00 AM	W8, Photoluminescence Properties of Highly Dispersed ZnO Quantum Dots in Polyvinylpyrrolidone Nanotubes prepared by a Single Capillary ElectrospinningG.L. Yang
11:20 AM	U9, (Student) Mechanical and Thermal Stretching of Fully Encapsulated Elastomeric ConductorsWenzhe Cao	11:20 AM	V9, The Growth and Characterization of Crystalline MgO Films on 6H-SiC by Molecular Beam EpitaxyMatthew Snyder	11:20 AM	W9, (Student) Generalized Theoretical Model for Ferroelectric Properties of BaTiO ₃ , BaTiO ₃ -ZnO, and ZnO-BaTiO ₃ -ZnO Thin FilmsVenkata Voora
11:40 AM	U10, Late News	11:40 AM	V10, (Student) Adsorption-Controlled Growth of Ferromagnetic EuO and the Effect of La DopingAlexander Melville	11:40 AM	W10, (Student) Ferroelectric Thin Film Field-Effect Transistors Based on ZnO/BaTiO ₃ HeterostructuresMatthias Brandt

Thursday AM June 25, 2009		Thursday AM June 25, 2009		Thursday AM June 25, 2009	
Session X: Molecular Electronics: Devices, Materials, and Molecular Electronics and Chem/Bio Sensors Room: Deans Hall II		Session Y: Graphene I Room: 206		Session Z: III-Nitrides: MBE Growth and Intersubband Structures Room: 207	
8:20 AM	X1, (Student) Understanding Molecular Modulation of Semiconductor Band-Bending through Transport Studies on Metal-Molecule-Semiconductor Device JunctionsArchana Bahuguna	8:20 AM	Y1, (Invited) Graphene Synthesis on C-Face and Si-Face 4H-SiCMichael Capano	8:20 AM	Z1, Near-Infrared Intersubband Absorption in MBE-Grown Lattice-Matched InAlN/GaN SuperlatticesOana Malis
8:40 AM	X2, Temperature-Dependent Transport in Gold-Molecule-p+ Si DevicesDavid B. Janes			8:40 AM	Z2, GaN/AlN-Based Nanostructures for Intersubband DevicesEva Monroy
9:00 AM	X3, (Student) Optical and Electronic Multi-Probe Vibrational Spectroscopic Characterization of Molecular Junction Based on Self-Assembled MonolayerMasato Maitani	9:00 AM	Y2, (Student) Uniformity of Epitaxial Graphene Films on Si-Face SiC(0001)Luxmi Luxmi	9:00 AM	Z3, (Student) Growth and Characterization of N-Polar InGaN and InGaN/GaN MQWs by Plasma Assisted Molecular Beam EpitaxySansaptak Dasgupta
9:20 AM	X4, Investigation of Semiconductor-Molecule-Semiconductor Devices: ZnS/MHA/GaAs DevicesDavid B. Janes	9:20 AM	Y3, Effects of SiC Surface Orientation and Temperature on the Quality of Epitaxial GrapheneVirgil Shields	9:20 AM	Z4, Change in Stress Evolution of MBE GaN across Growth Mode RegimesJeremy Acord
9:40 AM	X5, (Student) Passivation of GaAs Surface Using SAM of Redox-Active Ruthenium Based Organic Molecules in a Matrix of Non Redox Active OPE1 MoleculesRand Jean	9:40 AM	Y4, Few-Layer Graphene Formation Mechanisms on 4H-SiC(0001)Michael Bolen	9:40 AM	Z5, (Student) Low Dislocation-Mediated Reverse Bias Leakage in (0001) GaN via Novel High-Temperature MBE GrowthJeremy Law
10:00 AM	Break	10:00 AM	Break	10:00 AM	Break
10:20 AM	X6, (Student) 1.55 Micron Light Emission from Microcavity Light-Emitting Devices with PbSe Colloidal Quantum DotsFan Zhang	10:20 AM	Y5, (Invited) Epitaxial Graphenes on Silicon CarbidePhillip First	Session AA: III-Nitride: MBE Growth Room: 207	
10:40 AM	X7, Microfluidic Biochips for Label-Free Multi-Immunosensors Based on Carbon Nanotube Arrayed MicroelectrodesKenzo Maehashi				
11:00 AM	X8, (Student) Carbon-Derived Nano-Crystalline Diamond Films - Tailoring the Electronic and Bio-Sensing Properties by Nitrogen IncorporationSupil Raina	11:00 AM	Y6, (Student) Three-Dimensional Island Morphology of Graphene on C-Face SiC(000-1)Nishtha Srivastava	10:40 AM	AA2, (Student) Effect of AlN Nucleation on the Heteroepitaxial Growth of N-Face GaN on C-Face SiC by Plasma-Assisted MBE for High Electron Mobility TransistorsMan Hoi Wong
11:20 AM	X9, Late News	11:20 AM	Y7, (Student) AFM Studies of Wrinkles and Ridges on Graphene Grown on the Carbon Face of 4H-SiC (000-1)Gyan Prakash	11:00 AM	AA3, (Student) Analysis of Degenerate p-Type GaN by Metal Modulated EpitaxyElaiissa Trybus
11:40 AM	X10, Late News	11:40 AM	Y8, (Student) STM and XPS Studies of Moiré Superlattices and Ridges on Few-Layer Graphene Grown on 4H-SiC(000-1)Laura Biedermann	11:20 AM	AA4, Near Band-Gap Luminescence of Hexagonal Boron Nitride Grown on Ni(111) Substrate by Plasma-Assisted MBEChiun-Lung Tsai
				11:40 AM	AA5, Late News

SESSION LISTING

Thursday AM June 25, 2009		Thursday PM June 25, 2009		Thursday PM June 25, 2009	
Session BB: III-Nitride: Optical Devices I Room: 208		Session CC: III-V NW - Characterization Room: 106		Session EE: Oxide Thin Film Integration II Room: 108	
8:20 AM	BB1, (Student) Growth and Characterization of GaInN Blue Light-Emitting Diodes with GaInN Quantum BarriersWonseok Lee	1:30 PM	CC1, Surface Recombination in GaN Nanowires before and after Surface TreatmentsJohn Schlager	1:30 PM	EE1, (Student) Thermodynamic Properties and Phase Diagram of Ferroelectric PbTiO ₃ from First-Principles CalculationsZhi-Gang Mei
8:40 AM	BB2, (Student) High Efficiency GaInN-Based Multi-Quantum Wells Grown on High-Crystalline Quality, Freestanding, and Thick GaInN LayerDaisuke Iida	1:50 PM	CC2, Temporal Analysis of Photoconductive Decay in GaN NanowiresNorman Sanford	1:50 PM	EE2, (Student) Cation Dominated Memristive Behavior in Lithium Niobite Thin FilmsWilliam Calley
9:00 AM	BB3, (Student) Design and Characterization of Electrically-Injected InGaN/GaN Photonic Crystal LEDsElizabeth Rangel	2:10 PM	CC3, (Student) Growth, Structural, Optical, and Electrical Characterization of Nitride Nanowires Grown by MBE on Silicon SubstratesKevin Goodman	2:10 PM	EE3, (Student) Impact of the Presence of Sub-Micron Grain Boundaries on the in-Plane Ionic Conductivity of Thin Film Gd-Doped CeO ₂Matthew Swanson
9:20 AM	BB4, (Student) A Monolithic LED Micro-Display on an Active Matrix Substrate by Flip-Chip TechnologyZhaojun Liu	2:30 PM	CC4, (Student) Polarization-Sensitive Two-Color Detectors and Photovoltaic Devices by Solution-Synthesized Quantum-Wire SolidsAmol Singh	2:30 PM	EE4, Effect of Stoichiometry on the Two-Dimensional Electron Gas at the LaAlO ₃ /SrTiO ₃ Interface Grown by MBEMaitri Warusawithana
9:40 AM	BB5, (Student) Fabrication of Moth-Eye Structure on p-GaN Layer of GaN-Based LEDs Using UV Nanoimprint LithographyEun-Ju Hong	2:50 PM	CC5, Late News	2:50 PM	EE5, Structural and Magnetic Properties of Epitaxial EuTiO ₃ Thin Films Grown by Molecular-Beam EpitaxyJune Hyuk Lee
10:00 AM	Break	3:10 PM	Break	3:10 PM	Break
		Session DD: III-V NW - Growth and Processing Room: 106		3:30 PM	EE6, Optical Properties and Structure of Magnetron Sputtered Vanadium Oxide Thin FilmsOrlando Cabarcos
		3:30 PM	DD1, Self-Catalyzed Growth of GaAs Nanopillars on Nanopatterned GaAs, Silicon, and Silicon Dioxide Surfaces by MOCVDPing-Show Wong		
		3:50 PM	DD2, Core-Shell p-n Gallium Nitride NanowireAric Sanders	3:50 PM	EE7, Magnetic and Electric Properties in (SrMnO ₃) _n / (LaMnO ₃) _{2n} SuperlatticesCarolina Adamo
		4:10 PM	DD3, Fabrication of Large Scale GaN Nanowire Vertical Devices in ParallelChristopher Dodson	4:10 PM	EE8, (Student) Dielectric Tensors of High-k <i>Pbnm</i> Perovskites from First PrinciplesSinisa Coh
		4:30 PM	DD4, (Student) Oxygen Plasma Exposure Effects on Indium Oxide Nanowire TransistorsSeongmin Kim	4:30 PM	EE9, Dielectric Tensor of Single Crystals of the Alternative Gate Oxide Candidate LaLuO ₃Tassilo Heeg
		4:50 PM	DD5, (Student) Evidence of Mg Enhanced Desorption of GaNMatthew Brubaker	4:50 PM	EE10, (Student) Atomic Scale Effects of Fluorine in MOS Gate StacksJason Ryan
		5:10 PM	DD6, Late News	5:10 PM	EE11, Late News

Thursday PM June 25 2009		Thursday PM June 25 2009		Thursday PM June 25 2009	
Session FF: ZnO Characterization		Session GG: Organic Thin Film and Crystalline Transistors: Devices, Materials and Processing II		Session HH: Spin-Dependent (or Spintronic) Electronic Materials	
Room: Deans Hall I		Room: Deans Hall II		Room: 105	
1:30 PM	FF1, The Richardson Constant for Schottky Contacts to n-ZnOMartin Allen	1:30 PM	GG1, (Invited) Time-Resolved Electric Force Microscope Studies of Long-Lived Charge Traps in Functionalized Pentacene and Anthradithiophene TransistorsJohn Marohn	1:30 PM	HH1, (Invited) Efficient Room Temperature Spin Filter Based on a Non-Magnetic Semiconductor at Zero Magnetic FieldWeimin Chen
1:50 PM	FF2, Stability of Schottky Barriers on ZnO PLD Thin Films beyond 400 KHolger von Wenckstern				
2:10 PM	FF3, Identification of Native Defects in as-Grown ZnO Single CrystalsIrina Buyanova	2:10 PM	GG2, Controlled p-Doping of Organic Wide Band Gap Materials with Molybdenum TrioxideMichael Kroeger	2:10 PM	HH2, MCD Investigation on Mn Doped CdSe Quantum RibbonsXinyu Liu
2:30 PM	FF4, (Student) Nanoscale Deep Level Defect Mapping and Energetics at ZnO(0001) SurfacesTyler Merz	2:30 PM	GG3, (Student) New Fluorinated Anthradithiophene DerivativesMarsha Loth	2:30 PM	HH3, Multiple Magnetic States in Silicon Carbide Diluted Magnetic SemiconductorsAndrei Los
2:50 PM	FF5, Stoichiometry Dependent Incorporation and Electrical Activity of Zn Interstitials in Homoepitaxial ZnO Thin FilmsAlexander Lajn	2:50 PM	GG4, (Student) Investigations of Charge Transport and Bias Stress in Anisotropic Polythiophene Thin Films Fabricated via Directional CrystallizationLeslie Jimison	2:50 PM	HH4, Late News
3:10 PM	Break	3:10 PM	Break	3:10 PM	Break
3:30 PM	FF6, Defects at Oxygen Plasma Cleaned ZnO Polar SurfacesYufeng Dong	3:30 PM	GG5, (Student) The Effect of Polydispersity on Intermolecular Packing in π -Stacking Conducting Polymer SystemsTomasz Young	3:30 PM	HH5, (Invited) Antiferromagnetic Interlayer Exchange Couplings in $\text{Ga}_{1-x}\text{Mn}_x\text{As}/\text{GaAs}$ Diluted Ferromagnetic Semiconductor MultilayersJae-Ho Chung
3:50 PM	FF7, Atomistic Structure of Dislocations in ZnO Revealed by Opto-TEM and PL SpectroscopyYutaka Ohno	3:50 PM	GG6, Halogen Substitution to Improve Crystal Packing and Performance of Soluble Organic SemiconductorsJohn Anthony		
4:10 PM	FF8, Electrical Characterization of Defect Levels in $\text{Mg}_x\text{Zn}_{1-x}\text{O}$ PLD Thin FilmsHolger von Wenckstern	4:10 PM	GG7, (Student) Transport Anisotropy in Films of Organic n-Type Semiconductor with Controlled in-Plane Grain-Boundary OrientationJonathan Rivnay	4:10 PM	HH6, (Student) Magnetotransport Measurements on $\text{In}_{1-x}\text{Mn}_x\text{Sb}$ Ferromagnetic Semiconductor AlloysNidhi Parashar
4:30 PM	FF9, (Student) Effect of Post-Deposition Processing on ZnO Thin FilmsTingfang Yen	4:30 PM	GG8, Functionalized Tetrafluorotetracenes: Synthesis and Characterization of New Materials for OTFTsAdolphus Jones	4:30 PM	HH7, (Student) Engineering the Interlayer Exchange Interaction between MnAs and (Ga,Mn)AsMark J. Wilson
4:50 PM	FF10, (Student) Characterization of Channel/Dielectric Interfacial Trap States in ZnO-Based Thin-Film Transistors by Spectral Response AnalysisKimoon Lee	4:50 PM	GG9, (Student) Light-Induced Trap Release Probed in Polycrystalline Pentacene Films by Time-Resolved Electric Force MicroscopyJustin Luria	4:50 PM	HH8, Late News
5:10 PM	FF11, Late News	5:10 PM	GG10, Late News	5:10 PM	HH9, Late News

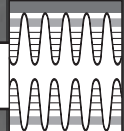
SESSION LISTING

Thursday PM June 25 2009		Thursday PM June 25 2009		Thursday PM June 25 2009	
Session II: Graphene II Room: 206		Session JJ: III-Nitride: Indium Nitride Room: 207		Session LL: III-Nitride: Optical Devices II Room: 208	
1:30 PM	II1, (Invited) Influence of Edges on the Morphology, Electronic Structure and Magnetism in Graphene Sheets and NanoribbonsVivek Shenoy	1:30 PM	JJ1, Multiple Mobility Channel Electron Transport Properties in InN Grown by MBEKejia Wang	1:30 PM	LL1, (Student) Efficiency Limitations of Green GaInN/GaN Light Emitting Devices under High ExcitationWei Zhao
		1:50 PM	JJ2, Auger Recombination and Photoluminescence in Mg-Doped InNSteven Durbin	1:50 PM	LL2, Barrier Effect on Hole Transport and Carrier Distribution in InGaN/GaN Multiple Quantum Well Visible Light-Emitting DiodesJianping Li
2:10 PM	II2, (Student) Thermal Conduction in Graphene and Graphene MultilayersSuchismita Ghosh	2:10 PM	JJ3, (Student) Adducts Formation in MOCVD Growth of InAlN: Growth Pressure DependenceMikiyasu Tanaka	2:10 PM	LL3, Effect of MOCVD Growth Temperature on the Optical and Structural Properties of InGaN Quantum Well StructuresMary Crawford
2:30 PM	II3, (Student) Current Saturation and High-Field Transport in GrapheneTian Fang	2:30 PM	JJ4, (Student) Selective Area Growth of InN Nano-Crystals on Pt-Mask Patterned Sapphire (0001) Substrate by RF-MBEJumpei Kamimura	2:30 PM	LL4, (Student) Device Performance of Fabricated Yellow Emitting GaInN/GaN LED on C-Plane Bulk GaN SubstrateWenting Hou
2:50 PM	II4, (Student) High-Field Characteristics of Top-Gated Epitaxial Graphene Field-Effect TransistorsDavid Shilling	2:50 PM	JJ5, (Student) Pt Catalyst-Assisted Metal-organic Vapor Phase Epitaxy of InNKohei Sasamoto	2:50 PM	LL5, (Student) Well Width Study of InGaN Multiple Quantum Well Structures for Blue-Green Laser DiodesVeit Hoffmann
3:10 PM	Break	3:10 PM	Break	3:10 PM	Break
3:30 PM	II5, (Student) Graphene Field-Effect Transistors Formed on Semi-Insulating 4H-SiCKonishi Keita	Session KK: III-Nitride: Nanostructures Room: 207		Session MM: III-Nitride: MOCVD Growth and Pseudo-Substrates Room: 208	
3:50 PM	II6, Epitaxial Graphene: Predicting Carrier Mobility Using Raman SpectroscopyJoshua Robinson	3:30 PM	KK1, Nanoribbon AlN/GaN HFETs: Towards Enhancement Mode DevicesTom Zimmermann	3:30 PM	MM1, Dislocation Reduction in GaN Epilayers on Sapphire and Silicon Using a Self-Assembled Monolayer of Silica MicrospheresQiming Li
		3:50 PM	KK2, (Student) OMVPE Growth and Characterization of III-Nitride Nanorod LEDsIsaac Wildeson	3:50 PM	MM2, (Student) High Pressure MOVPE Having High-Speed Switching Valves for the Realization of High Quality AlGaIn/GaN at Low TemperatureKentaro Nagamatsu
4:10 PM	II7, (Student) Discrepancies in Calculating Mobility in 2D Graphene and Graphene Nanoribbon FETsKristof Tahy	4:10 PM	KK3, Position Dependent, above and below Band Gap Photoconductivity in GaN Nanowire Photo-Gated FETsAric Sanders	4:10 PM	MM3, Device Applications of GaN Lateral Polarity JunctionsRamón Collazo
4:30 PM	II8, (Student) Epitaxial Graphene Micro-BridgesShriram Shivaraman	4:30 PM	KK4, Control of the Growth Kinetics of GaN(11-22) for the Synthesis of GaN/AlN Nanostructures with Reduced Internal Electric FieldEva Monroy	4:30 PM	MM4, (Student) Realization of Full Wafer Low Dislocation Density Al _{0.25} Ga _{0.75} N on AlN/Sapphire Using Facet-Controlled Epitaxial Lateral OvergrowthKenichiroh Takeda
4:50 PM	II9, Stress and Disorder in Epitaxial Graphene/SiC by Raman SpectroscopyM.V.S. Chandrashekhar	4:50 PM	KK5, Late News	4:50 PM	MM5, Growth of GaN through Confined Epitaxy: Improving Materials, Enabling DevicesJennifer Hite
5:10 PM	II10, Late News	5:10 PM	KK6, Late News	5:10 PM	MM6, Growth Mechanism of AlN/Sapphire Grown by Vapor Phase Epitaxy Using Al and Li ₃ NYoshihiro Kangawa

Friday AM June 26, 2009		Friday AM June 26, 2009		Friday AM June 26, 2009	
Session NN: Contacts to Semiconductor Epilayers and Nanowires Room: 106		Session OO: Nanoscale Characterization Room: 108		Session QQ: Solar Cells - Organic, Hybrid and Inorganic Room: Deans Hall II	
8:20 AM	NN1, (Student) Size Dependence of Nanowires (NWs) on the Formation of Silicide Contacts to Silicon Nanowire Field-Effect Transistors (SiNW FETs)Seung-Yong Lee	8:20 AM	OO1, (Student) Influence of InGaAs Well on the Size and Distribution of InAs/GaAs Quantum DotsVaishno Dasika	8:20 AM	QQ1, Toward Metamorphic Multijunction GaAsP/Si Photovoltaics Grown on Optimized GaP/Si Virtual Substrates Using Anion-Graded GaAs _y P _{1-y} BuffersTyler Grassman
8:40 AM	NN2, (Student) Method for Extracting Schottky Barrier Heights of Contacts to Semiconductor NanowiresNicholas Dellas	8:40 AM	OO2, (Student) Using Scanned Probe Microscopy to Measure Local Electric Field Gradient Fluctuations in PolymersNikolas Hoepker	8:40 AM	QQ2, Growth and Characterization of BaSi ₂ /Si Heterostructure toward Si-Based High-Efficiency Solar CellsYuta Matsumoto
9:00 AM	NN3, (Student) Numerical Simulation of Reduced Contact Resistance via Nanoscale Topography at the Metal/Semiconductor InterfaceBrian Downey	9:00 AM	OO3, Effects of Embedded Dipoles on the Electrical Response of Self-Assembled MonolayersPengpeng Zhang	9:00 AM	QQ3, Etched Silicon Pillar Array Solar CellsHeayoung Yoon
9:20 AM	NN4, (Student) High Doping Effects on the In-Situ and Ex-Situ Ohmic Contacts to n-InGaAsAshish Baraskar	9:20 AM	OO4, Spatially-Resolved Cathodoluminescence Study of III-Nitride NanowiresGeorge Wang	9:20 AM	QQ4, Epitaxial Film Silicon Solar Cells Fabricated by Low-Temperature Hot Wire Chemical Vapor DepositionDavid Young
9:40 AM	NN5, Nanofabrication of Niobium Electrodes for Superconducting Light Emitting DiodesJae-Hoon Huh	9:40 AM	OO5, Combination of Optical Characterization and In Situ Electron MicroscopyMin Gao	9:40 AM	QQ5, Microstructural and Electronic Properties of Thin Film Si:H and Ge:H for Uncooled Microbolometer ApplicationsNikolas Podraza
10:00 AM	Break	10:00 AM	Break	10:00 AM	Break
10:20 AM	NN6, (Student) The Role of Interfacial Oxidation on the Long-Term Stability of Ni-Based Ohmic Contacts to n-Type SiCAriel Virshup	Session PP: Non-Destructive Testing and In-Situ Control Room: 108		10:20 AM	QQ6, Characterizing the Interfacial Composition of Organic Bulk Heterojunction Solar Cells Using Organic Thin-Film Transistor AnaloguesCalvin Chan
		10:20 AM	PP1, Characterization of Planar InAs Thin Films by Transmission Electron Microscopy and Spectroscopic EllipsometryKurt G Eyink		
10:40 AM	NN7, (Student) Ohmic Contacts to Implanted (0001)4H-SiCMingyu Li	10:40 AM	PP2, (Student) Characterization of Near-Surface Electrical Properties of Multi-Crystalline Silicon WafersPatrick Drummond	10:40 AM	QQ7, Material and Device Requirements for Intermediate-Band Solar CellsJamie Phillips
11:00 AM	NN8, Improved n-Type 4H-SiC Schottky Barrier Diodes Using Metal Boride ContactsRani Kummari	11:00 AM	PP3, (Student) 1/f Noise Characterization of Si:H Thin Films for MicrobolometersMyung-Yoon Lee	11:00 AM	QQ8, Newly Developed Acene-Based Organic Semiconductors for Solar Cell ApplicationsZhong Li
11:20 AM	NN9, (Student) Reduction of the Specific Contact Resistance in p-Type GaN-Based Devices via Polarization DopingJacob Melby	11:20 AM	PP4, (Student) Piezoelectric Thin Films for Low Voltage, High Frequency MEMS Transducer ArrayHyunsoo Kim	11:20 AM	QQ9, Investigation of the Photo Response in Blended Organic Photovoltaic Films Using Conductive-Tip Atomic Force MicroscopyBehrang Hamadani
11:40 AM	NN10, Electrical Characteristics of Ti/Al Contacts to N-Polar n-Type GaN for Vertical LEDs.....Tae-Yeon Seong	11:40 AM	PP5, Effect of Applied Pressure on the Electrical Properties of Nano-Deformed Materials.....David Vodnick	11:40 AM	QQ10, Late News
12:00 PM	NN11, (Student) Characterization of Contact Resistance of Al, Ti, and Ni on High-Quality InN Films Grown by RF-MBEShogo Kikuchi	12:00 PM	PP6, (Student) Electronic Properties of Nanostructured PbTe(In) FilmsAlexandr Dobrovolsky	12:00 PM	QQ11, Late News

SESSION LISTING

Friday AM June 26, 2009		Friday AM June 26, 2009		NOTES
Session RR: Silicon Carbide Room: 206		Session SS: III-Nitride: Characterization of Defects Room: 207		
8:20 AM	RR1, (Student) MOS Characteristics of (000-1) 4H-SiCZengjun Chen	8:20 AM	SS1, Quantitative and Depth-Resolved Defect Spectroscopy in InGaN/GaN HeterostructuresAndrew Armstrong	
8:40 AM	RR2, Study of 4H-SiC/SiO ₂ Interface Traps in n-Type Nitrided MOS Capacitors Using Thermally Stimulated Current and Capacitance Voltage MethodsPeter Muzykov	8:40 AM	SS2, (Student) Characterization of Traps in N-Face AlGaIn/GaN Materials and Devices Using Deep Level Optical SpectroscopyTony Homan	
9:00 AM	RR3, (Student) Nucleation Mechanism of Polytype Transformation in 6H and 15R SiC CrystalsYu Zhang	9:00 AM	SS3, (Student) Evidence of a Donor Trap at the Negative Polarization Interface of a Ga-Face GaN / InGaIn / GaN Quantum WellChristopher Schaake	
9:20 AM	RR4, (Student) The Physical Distribution of Defects in 4H SiC MOS StructuresBrad Bittel	9:20 AM	SS4, (Student) Photo-Assisted High-Frequency Capacitance-Voltage Characterization of Interface States Density in Si ₃ N ₄ /GaN Metal-Insulator-Semiconductor InterfacesBrian Swenson	
9:40 AM	RR5, MOCVD HfO ₂ /SiO ₂ Gate Stacks for Improved Reliability in SiC MOSFET'sNick Sbrockey	9:40 AM	SS5, (Student) Elastic Buckling of AlN Ribbons on Elastomeric SubstrateHuichan Seo	
10:00 AM	Break	10:00 AM	Break	
10:20 AM	RR6, On the Driving Force for Shockley Stacking Fault Motion in Hexagonal SiCJoshua Caldwell	Session TT: III-Nitride: Growth and Characterization of Optical Devices Room: 207		
		10:20 AM	TT1, Characterization of Recessed-Gate AlGaIn/GaN HEMTs as a Function of Etch Depth.....Travis Anderson	
10:40 AM	RR7, (Student) Nucleation Mechanism of Dislocation Half-Loop Arrays in 4H-Silicon Carbide Homo-EpitaxyNing Zhang	10:40 AM	TT2, (Student) AlGaIn/GaN HFET Structures Grown on Vicinal Bulk GaNJudith Grenko	
11:00 AM	RR8, (Student) Characterization of 4H-SiC Schottky and p-n Diodes Using Thermally Stimulated CurrentMarko Tadjer	11:00 AM	TT3, (Student) Study of Growth Kinetics and Characterization of AlGaIn Grown by Ammonia-Based Metal-Organic Molecular Beam EpitaxyDaniel Billingsley	
11:20 AM	RR9, (Student) Generation of Dislocations and Precipitates in Heavily Al-Doped 4H-SiC Epitaxial Layers Grown by the Low-Temperature Halo-Carbon MethodHrishikesh Das	11:20 AM	TT4, (Student) Interface Analysis of Ti/Al/Ti/Au Ohmic Contacts with Regrown n+-GaIn Layers Using Molecular Beam EpitaxyHuichan Seo	
11:40 AM	RR10, Late News	11:40 AM	TT5, (Student) Growth and Characterization of Gallium Nitride on Magnesium Calcium OxideAndrew Gerger	
12:00 PM	RR11, Surface Related Defect in 4H SiC SubstratesMary Ellen Zvanut	12:00 PM	TT6, Late News	



EMC Plenary Lecture/Student Awards

Wednesday AM
June 24, 2009

Room: Presidents Hall III & IV
Location: Pennsylvania State University

Session Chair: Mark Goorsky, University of California, Los Angeles

8:20 AM Welcome and Student Awards

8:30 AM

Electronic Materials Science Challenges in Renewable Energy: *Richard King*¹; ¹Spectrolab, Inc.

Electronic materials research can make or break many emerging renewable energy technologies. Photovoltaics represents one of the greatest of these opportunities for electronic materials science to impact the climate change and energy security problems that we face today. Solar electricity generation from photovoltaics has been growing at a rate of over 40% per year for the last decade, with nearly 8 GW of solar cells produced in 2008. Multijunction III-V solar cells, with roughly double the efficiency of conventional flat-plate silicon cells, have a powerful effect on the cost effectiveness of new concentrator photovoltaic (CPV) systems now being deployed around the world, making this technology one of the most viable options for plentiful solar-generated electricity. Multijunction solar cells divide the solar spectrum into smaller slices, delivering experimental efficiencies over 40%, and enabling theoretical efficiency over 60%. This requires access to semiconductor materials with a wide variety of high and low band gaps for the individual subcells, while maintaining long minority-carrier lifetime and high mobility. Subcells with the optimum band gaps can be reached with approaches such as metamorphic growth on lattice-mismatched substrates, integration of group IV, III-V, and II-VI semiconductors, wafer bonding, and other technologies, but with the formidable electronic materials science challenges of managing dislocation nucleation, propagation, and recombination activity, and integration of dissimilar electronic materials. Researchers are bringing their experience on novel electronic materials in telecommunications, computing, imaging, displays, and other areas to a host of important renewable energy technologies: new opportunities in organic-inorganic hybrid photovoltaics and printed thin-film electronics; electrodes and ionic conductors in batteries and fuel cells for electric vehicles; power electronics for DC to AC conversion; thermoelectrics and thermionics; and new applications for carbon nanotubes and other low-dimensional structures for energy conversion and storage, to name a few. This talk will discuss some of the outstanding electronic materials issues in high-efficiency photovoltaics and other green energy technologies. Electronic materials breakthroughs, both fundamental and applied, are key for renewable energy sources to meet a major part of the world's >1.8 TW demand for electric power, and through electric transportation, displace a significant portion of the global >5 TW demand for petroleum.

9:20 AM Break

Session A: Epitaxy

Wednesday AM
June 24, 2009

Room: 105
Location: Pennsylvania State University

Session Chairs: Seth Bank, University of Texas at Austin; Archie Holmes, University of Virginia

10:00 AM

A1, Optical and Structural Investigations of the Novel Direct Band Gap Material Ga(NAsP) Grown Lattice-Matched on (001) Si Substrate: *Bernardette Kunert*¹; Sven Liebich²; Martin Zimprich²; Steffen Zinnkann²; Kerstin Volz²; Wolfgang Stolz²; ¹NAsP III/V GmbH; ²Material Sciences Center and Faculty of Physics

The GaP based dilute nitride Ga(NAsP) reveals a direct electronic band gap for high As concentrations. The incorporation of As into GaP leads also to an

increase in lattice constant but the additional incorporation of a few percentages of N reduces the lattice spacing of the quaternary compound material system Ga(NAsP) again. This lattice re-adjustment allows for a defect-free deposition of Ga(NAsP) onto GaP as well as Si substrates since the lattice-mismatch between GaP and Si is very low (0.36%). At the same time the N induces a strong red-shift of the emission wavelength, which is well known for dilute nitrides. This characteristic band gap bowing leads to a further energy separation between the conduction band minimum at X and Γ in k-space and, therefore, to an even more pronounced direct band structure formation. Efficient luminescence and electrically pumped laser operation of Ga(NAsP) device structures was already demonstrated on GaP substrate, hence, the transfer of the active material system onto Si substrate would open up a completely new field of applications for optoelectronic integrated circuits (OEICs). This paper focuses on the optical and structural properties of Ga(NAsP)-multi quantum well heterostructures (MQWHs) in dependence of the active material composition and the barrier material. Pseudomorphically strained Ga(NAsP)/(BGa)(AsP)-MQWHs were grown by low temperature metal organic vapour phase epitaxy (MOVPE) in a commercial reactor system on (001) GaP and (001) Si substrate. Because of the slightly smaller lattice constant of Si in comparison to GaP, the N content of Ga(NAsP) has to be increased by about 2% for the integration onto Si substrates. The N incorporation behaviour will be compared for the growth on GaP and Si substrates, respectively. Room temperature photoluminescence (PL) investigations show that a post-growth annealing treatment leads to a significant increase in luminescence efficiency. Also the N-content strongly affects the PL intensity and emission wavelength. High-resolution X-ray diffraction (XRD) measurements of MQWHs grown on Si substrates reveal abrupt hetero-interfaces and a high crystal quality. All these results and achievements, already obtained at a very early stage of development for this new class of dilute nitride, underline on one side the successful transfer onto Si substrates and on the other side clearly point to the enormous potential for applications in the field of OEICs.

10:20 AM Student

A2, Effects of Mg Doping on the Luminescence Characterization of GaAsN Alloys Grown by MBE: *Kazuyuki Umeno*¹; Yuzo Furukawa¹; Saburo Mitsuyoshi¹; Noriyuki Urakami¹; Hiroshi Okada¹; Akihiro Wakahara¹; Hiroo Yonezu¹; ¹Toyoashi University of Technology

GaAsN alloy based dilute nitrides have received much attention for novel optoelectronic devices. Impurity doping is an important issue to fabricate pn junction devices and affects the luminescence characterization. However, there are only a few reports about the p-type (In)GaAsN alloys grown by molecular beam epitaxy (MBE), where Be has been used as a p-type dopant. In this work, we have focused attention on Mg as a novel p-type dopant for the MBE growth and have investigated the luminescence characterization of the Mg-doped GaAsN alloys. The GaAsN:Mg samples were grown with a conventional solid-source MBE apparatus. A 0.5- μm -thick GaAs_{0.994}N_{0.006}:Mg layer was grown at 460°C and on a semi-insulating GaAs (001) substrate, after a 0.3- μm -thick undoped GaAs layer was grown at 580°C. For the Mg doping, we used a standard Riber effusion cell filling metallic Mg (6N) and the Mg-cell temperature (MCT) was controlled between 280 and 380°C. Photoluminescence (PL) spectra were measured at 18-300 K by pumping with a 532-nm solid-state laser. Hall effect measurements on the GaAsN:Mg samples were carried out using the van der Pauw method. The hole concentration increases with increase in the MCT; the maximum hole concentration $p = 2 \times 10^{20} \text{ cm}^{-3}$ when the MCT is 380°C. Therefore Mg is a controllable acceptor element for the MBE growth of the GaAsN alloys. The integrated PL intensity drastically increases with increase in the hole concentration up to $p = 9 \times 10^{18} \text{ cm}^{-3}$. For the GaAsN:Mg sample with the hole concentration smaller than $p = 6 \times 10^{18} \text{ cm}^{-3}$, the so-called S-shape behavior is obtained for the temperature dependence of the PL peak photon energy (PPE). On the other hand, no S-shape behavior is observed for the GaAsN:Mg sample with hole concentration larger than $p = 9 \times 10^{19} \text{ cm}^{-3}$; the temperature dependence of the PL PPE can be fitted using the Varshni formula. The S-shape behavior is observed for typically undoped GaAsN alloys and the PL emission at below ~100 K might be originated localized states due to nitrogen clusters. The temperature dependence of the PL PPE obeys the Varshni formula for the GaAsN:Mg sample with $p = 9 \times 10^{19} \text{ cm}^{-3}$. Therefore it is expected that the localized states decrease as

the Mg concentration increases and thus the integrated PL intensity may increase. This is probably because Mg-N bonds are formed during the growth since the Mg atoms can occupy the Ga site. In conclusion, we have demonstrated the Mg doping for the GaAsN alloys and have investigated the luminescence characterization of the Mg-doped GaAsN alloys. Mg has been successfully doped in the GaAsN alloys up to $p=2 \times 10^{20}$. It was clarified that the room-temperature PL intensity of the GaAsN alloys was drastically improved by Mg doping.

10:40 AM Student

A3, Effect of Si-Cap Thickness on Device Performance of Buried Channel Si/Ge_{1-x}C_x/Si Devices: Mustafa Jamil¹; En-shao Liu¹; Fahmida Ferdousi¹; Joseph Donnelly¹; Emanuel Tutuc¹; Luigi Colombo²; Sanjay Banerjee¹; ¹The University of Texas at Austin; ²Texas Instruments Inc.

This work presents the fabrication and characterization of epitaxially grown column IV based quantum well devices. Buried channel Si/Ge_{1-x}C_x/Si p-MOSFETs were fabricated on Si/Ge_{1-x}C_x/Si stacks grown epitaxially in an ultra high vacuum chemical vapor deposition (UHVCVD) system. Ge_{1-x}C_x ($x < 1\%$) layers were chosen for their extremely low threading dislocation density (TDD $\sim 3 \times 10^5/\text{cm}^2$) compared to pure Ge layers grown directly on Si substrates (TDD $\sim 10^7$ - $10^8/\text{cm}^2$). The main focus of this study was to investigate the effects of Si cap thickness and hence the valence band offset on the device performance of Ge_{1-x}C_x based p-MOSFETs. Electrical characterizations were carried out on devices with different Si cap thicknesses (3 to 9 nm) from room temperature down to 77K. The Si cap thickness dependence of the drive current, sub-threshold slope, effective hole mobility, gate leakage current density, $I_{\text{on}}/I_{\text{off}}$ ratio has been investigated at different temperatures. The thickest (9 nm) cap device showed high off-state leakage. However, three orders of magnitude decrease in off-state leakage was observed in the thickest Si-cap device at 77K. A significant parallel conduction has been observed specially in the thicker Si cap devices, which also show degraded sub-threshold slope. The stair-case behavior of the split capacitance-voltage (C-V) characteristics of the buried channel devices has been used to determine the gate bias at which a second sub-band, confined primarily in the lower mobility Si cap layer becomes occupied. The gate-to-channel capacitance-voltage (C_{gc} -V) characteristics measured at 77K are fitted to a theoretical model to assess the valence band off-set. One-dimensional Poisson and Schrödinger equations were solved self-consistently to calculate the valence band offset at the Ge well - Si cap interface. A relatively large hole band-offset (eg. 660 meV for the 7 nm Si cap thickness) and type II band alignment have been observed in our devices. This large valence band offset makes Si cap a promising option for passivating Ge-based high mobility p-MOSFETs. However, the observation that the Si conduction-band (CB) is slightly lower in energy than the Ge_{1-x}C_x CB may explain the degraded behavior of the Si capped Ge based n-MOSFETs to some extent. In summary, this work demonstrates the importance of using optimal cap thickness for Si-capped Ge-based p-MOSFETs.

11:00 AM Student

A4, Impact of High-Order Silane Precursors for Silicon Epitaxial Growth on Surface Open Sites: Keith Chung¹; James Sturm¹; ¹Princeton University

In this abstract we show high-order silanes enable an increase of open surface sites as measured by diborane adsorption. It has been observed that the epitaxial growth rate with increasing silane order (i.e. going from silane to disilane to trisilane [1] and NPS [2]) was increased when compared with conventional silane gas. Previously, we have proposed a "concerted reaction" model to explain the enhancement of the high growth rates with neopentasilane compared with conventional silane [3]. In that work we hypothesize that possible concerted surface reactions allow for epitaxial growth without the need for the creation of open surface sites via hydrogen desorption. We have also observed that the resulting surfaces in epitaxial layers grown with high-order silanes are smoother than those surfaces of epitaxial layers grown with silane, even at higher epitaxial growth rates. It is known that surface hydrogen coverage hinders silicon adatom diffusion and leads to rough surfaces [4] during silicon epitaxy. This implies that the growth surfaces with high-order silanes have reduced hydrogen coverage (i.e. more open sites) during CVD growth. To test this hypothesis, we determine the diborane surface adsorption rate and use this value as a measure of the number of open sites during growth (i.e. the amount of diborane adsorbed is directly proportional to the number of open

sites). Diborane surface adsorption rates were determined for silane, disilane, and neopentasilane from temperatures of 550°C to 700°C. We found that for diborane surface adsorption rate is higher for NPS than for disilane, and the diborane adsorption rate is higher for disilane than for silane when compared at the same temperature, using the same diborane flow rate and growth conditions. This is consistent with our hypothesis that there are more open sites during the growth process with high-order silanes. Furthermore, the silicon adsorption rates were also determined for silane, disilane, and neopentasilane. These silicon adsorption rates are compared with the diborane adsorption rates of the corresponding gas. The ratio of these rates were ~ 12 and the same for all gases and temperatures from 550°C to 700°C. This implies that the boron adsorption mechanism is unrelated to the silicon precursor and dependent on the open site coverage only. [1] P.R. Fischer et. al., ECS Transactions, v3 (2) 2006, pp203-215 [2] J.C. Sturm et. al., ECS Transactions, v 6, n 1, May 2007, pp 429-436 [3] K. H. Chung et. al., Appl. Phys. Lett., v92, March 2008, pp113506-8[4] D. P. Adams et. al., Appl. Phys. Lett., v63 (26) Dec. 1993, pp3571-73

11:20 AM

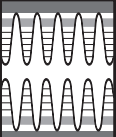
A5, Photovoltaic-Quality Silicon Epitaxy by Hot-Wire CVD at Glass-Compatible Temperatures: Charles Teplin¹; Ina Martin¹; Maxim Shub¹; Robert Reedy¹; Kim Jones¹; Manuel Romero¹; Paul Stradins¹; Howard Branz¹; ¹NREL

Epitaxial crystal silicon films 2- to 10-microns thick on high-quality seed layers on foreign substrates have the potential to approach wafer silicon photovoltaic (PV) efficiencies at thin-film area costs. However, PV applications require that the epitaxy be done at high growth rates and at a temperature compatible with low-cost substrates. Growth of PV-quality epitaxial silicon with these constraints remains a technological challenge. We report dramatic improvements over our previous work [1] in the quality of epitaxial silicon grown by hot-wire chemical vapor deposition (HWCVD) from silane precursor gas. Epitaxial layers up to 40-microns have defect densities of about $2 \times 10^5 \text{ cm}^{-2}$, corresponding to defects separated by more than 20 microns. This should be adequate for film-silicon photovoltaic applications, where layer thickness are expected to remain under 10 microns. Transmission electron microscopy shows that many of the remaining defects originate at the substrate/epitaxy interface, suggesting that further defect reduction is possible with improved surface preparation. Our films are grown at above 100 nm/min, at about 680°C, a temperature compatible with relatively inexpensive substrates such as borosilicate glass. Both n- and p-type epitaxial layers have been grown by mixing small amounts of PH₃ or B₂H₆ into the source SiH₄ gas. Hall measurements show that that majority carrier mobilities in our epitaxial films are close to those obtained on high-quality silicon wafers. Comparison of carrier concentrations determined by Hall measurements and dopant concentrations determined by secondary ion mass spectrometry indicate that all incorporated P dopants contribute electron carriers. Using a simple growth rate model, we have optimized gas utilization and reached an epitaxial deposition rate of 300 nm/min. Initial devices demonstrate the potential of HWCVD epitaxy, but crystalline defects and/or impurities still limit the minority carrier lifetime. TEM, cathodoluminescence, SIMS and local (micron-scale) electron-beam based diffusion length measurements are being used to understand the keys to improved material quality. We will present systematic studies of the epitaxial quality as a function of deposition temperature in the 620-750°C range, as well as initial epitaxial films grown on layer-transferred silicon.[1] Q. Wang et al., J. Appl. Phys. 100, 093520 (2006).

11:40 AM

A6, Structural Characteristics of TaC Films as Buffer Layers for Epitaxy of GaN on SiC: Tsvetanka Zheleva¹; Kevin Kirchner¹; Michael Derenge¹; Kenneth Jones¹; R.D. Vispute²; ¹Army Research Laboratory; ²University of Maryland

Tantalum carbide films have useful functional properties as protective coatings for high-temperature components and diffusion barriers for large scale silicon metallization. Recently we explored the properties of TaC films for Ohmic contacts to silicon carbide (SiC) high-temperature and high-power devices, masks for selective area growth (SAG) for high-temperature, high power devices (SAG as an alternative for ion implantation), encapsulant layers for SiC-based high power devices and buffer layers for lattice mismatch accommodation at GaN/SiC interfaces. The present work examines the potential of using tantalum carbide films as an interfacial buffer layer to accommodate



the lattice mismatch between the SiC substrate and the gallium nitride (GaN) layer, and thus to improve the epitaxy of GaN on TaC/SiC heterostructures. Using the pulsed laser deposition (PLD) technique for growth of TaC on SiC, various growth parameters have been optimized, such as growth temperature, film thickness, substrate orientation and post-growth annealing conditions. The subsequent growth of GaN films was performed by metal organic chemical vapor deposition (MOCVD). The morphology of the TaC and GaN films was analyzed using scanning electron microscopy (SEM) and atomic force microscopy (AFM), and the structure of the films was studied using x-ray diffraction (XRD), transmission electron microscopy (TEM), and high resolution TEM (HRTEM) techniques. Annealing in the range of 1200 to 1600°C does not improve the morphology and the structure of the PLD-grown TaC films on SiC substrates, as studied by SEM and XRD techniques. The structure of the TaC films on the SiC substrate at 1000°C is polycrystalline, although earlier growth experiments revealed larger single crystal grain regions hinting a potential for optimized single crystal growth. At higher growth temperatures of 1100°C and 1200°C the TaC film structure is polycrystalline, as studied with XRD and TEM. TEM analysis indicates that at 1100°C the TaC/SiC interface is diffuse and non-uniform in contrast revealing a tendency for interfacial reaction with SiC. Studies with TEM show that at higher growth temperatures of 1200°C the TaC films react strongly with the SiC top surface and forms an interfacial product, possibly Ta-Si phase. MOCVD deposition of GaN films on TaC/SiC substrate reveal polycrystalline GaN with a rough surface, as shown with XRD and TEM. The growth of TaC on SiC, and the stability of their surfaces and interfaces is discussed in terms of recrystallization kinetics and phase formation based on the ternary Si-C-Ta phase diagram analysis.

a configuration-interaction treatment of the electron-hole coupling. A bend in the nanomechanical structure acts like a DC electric field, inducing Stark-like level shifts. One to ten meV energy shifts are possible. A bend that is symmetric about the QD mimics a vertical electric field which pushes electrons and holes in the same direction, further into the dot or towards the wetting layer, depending on how the bridge is bent. A bend antisymmetric about the QD mimics an in-plane electric field that pushes electrons and holes in opposite directions along the bend. This behavior can be correlated to the bend-induced changes in the local deformation potential. As a consequence, the applied strain can control and reorder the levels of electrons and holes in vertically or laterally coupled dots, thereby inducing crossovers between the coupled dots. Holes and electrons cross between coupled dots at different applied strain, providing control over the direct/indirect character of optical transitions. Hole states can be distorted by twenty percent in the direction of applied strain. This leads to large changes in exciton exchange splitting and the polarized response of bright transitions. This capability should be critical for applications such as entangled photon sources, where the elimination of asymmetric exchange splitting is essential, or cavity-coupled QDs, where control of the exchange induced dark states is needed. The consequences for the quantum optics of quantum dots will be discussed.

10:40 AM

B2, Nano-Fabrication and Optical Characterization of InAs QDs Pillar Structures Embedded with Niobium: *Yasuhiro Idutsu*¹; Makoto Takada²; Saki Ito²; Hiroyasu Sato²; Huh Jae-Hoon³; Daimotsu Kato²; Sotaro Ida²; Hiroataka Sasakura¹; Hidekazu Kumano¹; Ikuo Suemune¹; ¹Hokkaido University, JST-CREST; ²Hokkaido University; ³Hokkaido University, GCOE

Quantum dots (QDs) have been studied for fundamental physics and many applications such as single electron devices and single photon sources. In a conventional planar structure, photon extraction efficiency is very small (~3%) since the refractive index of GaAs (3.4) is much larger than that of air (1). Therefore, it is important to improve the photon extraction efficiency for the highly efficient photon emitters. In this paper, we studied a novel InAs QDs pillar structure embedded with Niobium (Nb). This structure limits the photon emission to the surface and thus high photon extraction is expected. Large enhancement of photoluminescence (PL) up to 40-times was observed from the present embedded pillar structures. InAs QDs were grown on epi-ready (001) semi-insulating GaAs substrates with metal-organic (MO) molecular-beam-epitaxy (MBE) system. After removing the GaAs surface oxides with the simultaneous injection of trisdimethylamino-arsenic at 560°C, 100-nm-thick GaAs buffer layers were grown at 510°C. Then the temperature was decreased to 480°C to grow InAs QDs. 50-nm-thick GaAs cap layer were grown at 450°C. The pillar structures were fabricated as follows. The negative-type electron beam (EB) resists were coated on SiO₂ layers deposited on GaAs surface with chemical vapor deposition (CVD) system. The pillar patterns were drawn with EB lithography system. The SiO₂ and GaAs layer were etched with reactive ion etching (RIE) system and inductively-coupled plasma(ICP)-RIE system using CHF₃ and Cl₂ gas. Pillar structures were embedded with SiO₂ and Nb with vacuum deposition equipment. The pillar samples were pasted on a supporting substrate with Indium. The pillars and deposited metal layers were transferred to the supporting substrate by removing the GaAs substrate of the pillar sample. The removed sample surface was observed with scanning electron microscopy (SEM). The PL measurements were carried out at 4K with the excitation of Ti:Sapphire laser emitting at the wavelength of 850nm. A liquid-nitrogen cooled InGaAs detector was used to measure PL spectra. The transferred pillar structures surrounded by Nb metal were observed by SEM, and the smooth embedded pillar surface was found. Optical properties of the embedded pillar and normal pillar as a reference were studied. Due to a number of QDs involved in one pillar, multiple peak structures were observed for both samples. It should be stressed that more than 10-fold enhancement of PL intensity was observed by the embedded structures. According to the pillar diameter dependence of square root of PL integrated intensity, the embedded pillar shows 6.4-times increase of the gradient to the normal pillar structure, which is equivalent to the 40-times enhancement of the photon extraction efficiency including excitation efficiency. This work is supported by Hokkaido Univ. and Hokkaido Innovation through NanoTechnology Support (HINTS).

Session B: Low Dimensional Structures: Wires and Dots; Dots in Wires

Wednesday AM
June 24, 2009

Room: 106
Location: Pennsylvania State University

Session Chairs: Ping-Show Wong, University of California, Los Angeles; James Merz, University of Notre Dame

10:00 AM Invited

B1, Reengineering the Optics of Quantum Dots with Mechanical Strain: *Garnett Bryant*¹; Natalia Malkova¹; James Sims¹; Michal Zielinski²; W. Jaskolski³; Javier Aizpurua⁴; ¹National Institute of Standards and Technology (NIST); ²Institute of Microstructural Sciences; ³Instytut Fizyki; ⁴Donostia International Physics Center

Semiconductor quantum dots (QD) have attracted great interest due to their potential applications in electronics, optoelectronics, and quantum information. A highly desirable feature for applications in optics is an ability to dynamically control the exciton states in QDs. Dynamical control could be achieved by using externally imposed mechanical strain to reengineer the QD structure and thereby induce or split level degeneracies, polarize optical transitions, induce entanglement, or modify coupling in closely spaced dots, all capabilities needed to use dots in nanodevices and quantum information processing. Interest in nanomechanical devices for low-power computing, energy harvesting and precision sensing has recently developed. Embedded QDs provide an optical interface to such nanomechanical devices. To exploit these hybrid nanomechanical/quantum dot devices, one must understand the coupling between internal strain due to lattice mismatch, externally imposed mechanical strain and the electronic states of self-assembled quantum dots embedded in the nanomechanical device. To identify the effects of mechanical strain, we consider pyramidal InAs QDs embedded in a GaAs nanomechanical bridge. The bridge is bent to simulate an external strain applied to reengineer the QDs. We use atomistic tight-binding theory for the electron and hole states. Relaxation of local strain and imposed strain are both important, so we include them on an equal footing via valence force field theory. Exciton states are determined using

11:00 AM Student

B3, Lithography-Free Synthesis of Freestanding Gold Nanoparticle Arrays Encapsulated within Dielectric Nanowires: *Wenchong Hu*¹; Bangzhi Liu¹; Nicholas Dellas¹; Sarah Eichfeld¹; Pramod Nimmatoori¹; Joan Redwing¹; Suzanne Mohney¹; Theresa Mayer¹; ¹Pennsylvania State University

One-dimensional arrays of noble metal nanoparticles can sustain coupled surface plasmon modes that transport light below the diffraction limit. These structures are typically fabricated on planar substrates by direct write electron-beam lithography or by template directed assembly of solution synthesized metal nanoparticles. This talk will discuss the lithography-free synthesis of one-dimensional (1D) Au nanoparticle arrays encapsulated within freestanding silicon dioxide (SiO₂) nanowires by dry thermal oxidation and vacuum annealing of Au-coated silicon nanowires. The mechanisms responsible for the formation of 1D Au nanoparticle arrays were studied using single crystal silicon nanowires grown by the Au-catalyzed vapor liquid solid technique with diameters ranging from 20 to 50 nm. Following growth, the Au catalyst particles were selectively etched from the nanowire tips, and a 10-nm thick layer of Au was evaporated onto the surface of the nanowires. Control samples were also prepared without the evaporated Au thin film. All of the nanowire samples were thermally oxidized at 700°C for 3 hours by flowing 1L/min ultra-high-purity O₂ in a quartz tube furnace. The silicon nanowires were removed from the substrate by sonication and placed onto a molybdenum grid for in situ vacuum annealing and microstructure analysis using transmission electron microscopy (JEOL 2010 LaB6 TEM). The annealing temperature was increased from 20°C to 1000°C under ultra high vacuum conditions. Additional studies were conducted using a single oxidation step at 850°C for 1 hour to form the Au nanoparticle array in a vacuum tube furnace with a pressure of 5×10^{-7} Torr. The control samples without Au thin film had a uniform 8 to 12 nm thick SiO₂ shell that surrounded the entire length of the nanowire. The resulting oxide thicknesses followed the expected dry oxidation kinetics for cylindrical silicon nanowires. The addition of the Au thin film resulted in a rapid and complete oxidation of the silicon nanowire, which left a solid Au nanowire core surrounded by a SiO₂ shell for the same oxidation conditions. The thickness of oxide shell depended on the starting diameter of the silicon nanowire and varied from 5 to 20 nm. In situ vacuum annealing of these Au-SiO₂ core-shell nanowires showed that the solid Au nanowire core fragmented into an array of Au nanoparticles with uniform diameter and spacing as the temperature was increased beyond 900°C. The ratio of spacing to particle diameter was ~3 independent of particle diameter, which follows the Rayleigh instability for solid cylindrical structures. Similar results were found using the single step oxidation and annealing at 850°C. This new process provides a simple, lithography-free method for producing freestanding 1D metal nanoparticle arrays encapsulated in dielectric nanowires.

11:20 AM Student

B4, Effect of Indium Seeding Layer on the Formation and Properties of InN Nanowires on Si by Molecular Beam Epitaxy: *Yi-Lu Chang*¹; Arya Fatehi¹; Jonathan Guillemette¹; Thomas Szkopek¹; Zetian Mi¹; ¹McGill University

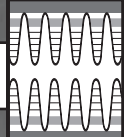
InN nanowires, due to the low bandgap (~0.7 eV), high electronic mobility and low toxicity, have emerged as a promising material for future nanophotonic and nanoelectronic devices. Such nanowires can be epitaxially grown under nitrogen rich conditions without the use of any metal catalyst. However, the resulting InN nanowires generally exhibit tapered morphology, with uncontrolled electrical and optical properties. In this context, we have investigated the molecular beam epitaxial growth and characterization of InN nanowires directly on Si substrates. We have developed a special growth technique, with the use of an in situ indium seeding layer, that enables the achievement of non-tapered InN nanowires on Si with well controlled properties. Such InN nanowires also exhibit bright photoluminescence at 300 K and are relatively free of dislocations and stacking faults. InN nanowires were grown on Si(111) substrates using radio-frequency plasma-assisted MBE under N-rich conditions. A nitrogen flux of 1.6 sccm and a plasma forward power of 325-425 W were used. The indium flux was varied in the range of $0.3 - 1.0 \times 10^{-7}$ Torr. InN nanowires spontaneously formed on Si, GaN or AlN layers generally exhibit tapered morphology as well as a large variation in size. To achieve controlled growth of InN nanowires, we have employed an in situ deposited thin (~2 ML) indium seeding layer on Si prior

to the growth of InN nanowires. The deposited indium forms liquid droplets on the Si surface at elevated temperatures, which are believed to serve as seeds for the initial nucleation of InN nanowires. InN nanowires grown using this special technique exhibit non-tapered morphology, with identical top and bottom sizes. The wires are of wurtzite structure and well separated, with the c-axis oriented vertically to the Si(111) substrate. By varying the thickness of the indium seeding layer as well as growth conditions, InN nanowires with diameters in the range of 20 – 200 nm (or larger), and areal densities from ~ 5 μm⁻² to ~ 500 μm⁻² can be achieved. The structural and optical properties of such non-tapered InN nanowires were also studied using high resolution transmission electron microscopy (TEM) and micro-photoluminescence, respectively. The high resolution TEM studies confirm that InN nanowires on Si are structurally uniform, of single crystal, and relatively free of dislocations and stacking faults. Bright photoluminescence are also measured at room temperature. Detailed characterization and analysis of the temperature-dependent photoluminescence characteristics and transport properties of such high quality, non-tapered InN nanowires will also be presented.

11:40 AM

B5, High Efficiency Green Emission from InGaN Wires Measured in 4K-300K Range: *Vladimir Protasenko*¹; Kevin Goodman¹; Thomas Kosel¹; Huili (Grace) Xing¹; Debdeep Jena¹; ¹University of Notre Dame

Pristine III-V nitride semiconductors provide wide range of direct optical bandgaps (InN, E_g=0.67 eV through GaN E_g=3.4 eV to AlN E_g=6.2 eV), while their (Al, In, Ga)N alloys exhibit continuous tuning of optical properties through the whole near-infrared to deep ultra-violet spectral range. This useful property of nitrides has been already utilized in a variety of applications. For example, In(Ga, Al)N allows have been employed in manufacturing of blue- and green-emitting diodes and UV laser diodes. The growth of In(Ga, Al)N films on Al₂O₃ or Si substrates often results in threading dislocations with surface densities many orders higher than that achieved in growth of, for example, AlGaAs or AlInGaP layers. It is still puzzling phenomenon, but high density of dislocations does not compromise significantly the quantum yield of InGaN or InAlN emission. Nevertheless, finding the ways of reduction of dislocation density and release of strain are important and challenging problems. The growth of wires instead of films might be one of them. One-dimensional geometry of wires provides larger surface area available for efficient termination of threading dislocations, which are usually considered as quenching centers for radiative emission. Here we report the data on the emission of InGaN wires grown by molecular beam epitaxy (MBE) on Si(111) substrates. Indeed, measured at room temperature (RT) ~8% quantum yield (QY) of InGaN wires is almost two orders higher than corresponding QY (0.1%) of films having the same chemical composition. Undoubtedly, it indicates a high chance of success of wires employed in light-emitting diode devices. Under excitation with 325 nm of HeCd laser (3.81 eV, above GaN 3.4 eV bandgap), RT spectra of InGaN wires reveal three bands which we assign to the emission of GaN inclusions (~360 nm) and to InGaN (~400 nm, and ~530 nm). Green emission is the strongest and grows ~10 times when the substrate is cooled down to 4K. Same time, much weaker at room temperature, 400 nm emission grows by ~160 times. In a separate experiment we found that emission spectra of InGaN wires changes considerably when excited with 373 nm beam (3.32 eV, less than GaN 3.4 eV bandgap). Obviously, GaN emission disappears. What is not expected is that ~400 nm emission band becomes strongest in the spectra while green emission diminishes considerably. It hints the emission probably originates from areas having different structural or chemical (or both) compositions. Additional emission lifetime measurements and high resolution TEM images of wires provide support for this model. In a model, which we are going to present, we consider structural and chemical inhomogeneity of InGaN wires as a primary origin for above mentioned optical phenomena.



Session C: Semiconductor Processing

Wednesday AM
June 24, 2009

Room: 108
Location: Pennsylvania State University

Session Chairs: Patrick Fay, University of Notre Dame; Thomas Kuech, University of Wisconsin

10:00 AM Student

C1, Dynamic Study on Formation Processes and Thermal Stability of Nickel Germanides by Using *In Situ* Transmission Electron Microscopy: *Jae-Wook Lee*¹; Kwan-Woo Song¹; Jee-Hwan Bae¹; Min-Ho Park¹; Han-Byul Kang¹; Hyounsub Kim¹; Cheol-Woong Yang¹; ¹Sungkyunkwan University

Ge MOSFET (Metal Oxide Semiconductor Field Effect Transistor) has been considered as one of the promising devices for future high-speed CMOS technology due to high carrier mobility (two times higher for electrons and four times higher for holes as compared to those in Si). Self-aligned silicide (SALICIDE) is essential in current deep-sub micron very-large-scale-integration (VLSI) circuit fabrication to reduce the parasitic resistance. Ni silicide, considered as the material choice for the future nodes, has several advantages over Ti silicide and Co silicide which include: low temperature silicidation, no bridging failure property, small mechanical stress, low silicon consumption, and one step silicidation process. Similarly, Ni shows advantages to form germanide for Ge MOSFET application over other materials. Ni forms metal-germanide at the lowest temperature among the many metal-germanide systems such as those with Ti and Co, and such a low formation temperature is beneficial in preventing the thermodynamic instabilities of the gate dielectric material and dopant deactivation of the doped regions in Ge-based transistors. Although Ni germanide has several advantages as a local interconnect material, its poor thermal stability inhibits its application to deep submicrometer devices. However, it has been reported that the thermal stability of Ni germanide improved slightly through the addition of an alloying element, such as Ta or Zr. In this study, the formation and morphological evolution of metal (Ni, Ni-Ta, Ni-Zr) germanides as a function of temperature was investigated by *in situ* annealing of 15 nm-thick metal/Ge systems in the transmission electron microscope (TEM) with a specimen heating holder. The sheet resistance of the germanides formed in the Ni_{0.9}Ta_{0.1}/Ge system was lower at temperatures above 550°C than the Ni/Ge system. Through the addition of Ta atoms, Ni germanide grain growth was retarded and the surface morphology of the Ni germanide layer improved. An approximately 5 nm-thick Ta-rich layer formed on the top of the germanide layer. Eventually, the agglomeration of Ni germanide was retarded and the thermal stability of the Ni germanide formed from the Ni-Ta alloy became superior to that formed from the pure Ni. The microstructures and chemical compositions of the phases formed by the reaction were examined by HR-TEM and STEM BF/HAADF micrographs, CBED, and STEM/EDS techniques. In addition, the behavior of Ta atoms was identified by EELS elemental mapping and STEM/EDS techniques.

10:20 AM

C2, Experimental Raman Study and Finite Element Modeling of Strain Distribution in Patterned Device Islands on Strained Silicon-on-Insulator (sSOI) Substrates: *Diefeng Gu*¹; Mingyao Zhu²; Falk Naumann³; Matthias Petzold³; Helmut Baumgart¹; ¹Old Dominion University; ²The College of William and Mary; ³Fraunhofer Institute for Mechanics of Materials

It is well established that the strain in sSOI wafers can be maintained during the high temperature processing steps required by CMOS technology if suitable precautions are taken during patterning of the sSOI wafer into device islands. Routinely a rigid capping layer, such as SiO₂ is used to reduce strain relaxation caused by cutting the strained film into small islands. Here, we study the simplest but scientifically relevant case, where in the absence of capping layers or any other precautions, strain relaxation by film patterning and high temperature annealing can be observed. The thermal stability of bi-axial strain is maintained solely by a non-epitaxial bonded interface with the amorphous buried oxide in sSOI after patterning and subsequent high temperature annealing. For this

study, sSOI wafers with various strained-Si layer thicknesses (15, 70 and 100 nm) were fabricated by Smart Cut™ technology. The biaxial tensile strained Si was initially grown on strain-relaxed Si_{0.8}Ge_{0.2} substrates. The sSOI was patterned by electron beam lithography (EBL) using positive resist. After EBL exposure and development of the exposed area, the exposed s-Si was etched by wet-etching. The patterned sSOI device islands have a periodicity range from 3 μm to 1.5 μm. Selective wet etching of s-Si stops at the buried SiO₂ interface and the size of the strained-Si pillars can be controlled by etching time. The atomic force microscopy (AFM) image was used to confirm that all strained-Si at the exposed area has been etched by measuring the etched trench depth. The strain of the patterned sSOI was measured by Raman spectroscopy and the strain values were averaged for several locations throughout the patterned area. Laser power of 0.2 mW was used for the beam to avoid local heating. The plot shows that the strain relaxes significantly for all sSOI after patterning even without high temperature annealing. This result agrees well with the finite element (FE) simulation. However, the strain relaxation is more pronounced for thicker s-Si layers because the thicker s-Si layer has more space to form misfit dislocations that results in strain relaxation. The strain relaxation may be related to the geometry – in a thicker film the upper layer is further removed from the rigid bonded substrate that sustains strain, and it is easier for the top surface to elastically contract, distorting the tall sidewalls. The patterned sSOI wafers were then annealed at high temperatures and the strain relaxation was characterized by Raman spectroscopy. Our FE modeling corroborates the experimental result that most strain relaxation occurs at the edges of the device islands while the corners of the rectangular patterns exhibit the maximum strain relaxation.

10:40 AM Student

C3, Electronic Passivation of Silicon (100) Surfaces by Organic Layer of 1,10-Phenanthrenequinone: *Sushobhan Avasthi*¹; Yabing Qi¹; Jeffrey Schwartz¹; Antoine Kahn¹; James Sturm¹; ¹Princeton University

Recently there has been a great deal of interest in Silicon-Organic heterojunctions for photovoltaic and other device applications. A pre-requirement for such heterojunctions is the electronic passivation of the silicon surface, i.e. energy levels at the silicon surface in the bandgap must be removed. Such states lead to the recombination of minority carriers and prevent the Fermi level from being modulated at the surface. In this work we present the use of the organic molecule 1,10-Phenanthrenequinone (PQ) to passivate the silicon (100) surface. We present two sets of data to support our arguments; Metal-insulator-semiconductor capacitor (MISCAP) high frequency CV curves and spectrum from Ultraviolet Photoelectron (UPS), Inverse Photoelectron and X-ray photoelectron Spectroscopy (XPS). All the PQ depositions were done in a thermal evaporator with a base pressure of 2x10⁻⁷ torr. Prior to deposition the silicon samples were hydrogen-passivated using an RCA clean followed by a HF dip. The thickness of the PQ layer, as measure by a quartz crystal, was 10nm. After a deposition at room temperature the PQ bonds to the silicon surface. In the proposed bonding orientation [1], the p- electron conjugation of PQ is preserved. Metal-insulator-semiconductor capacitors were made to test the ability of PQ to passivate the surface states and thus allow a gate to change the surface band-bending and thus the capacitance. The structures used a hard-baked photoresist, AZ5214, as the insulator and silicon as the semiconductor with and without the PQ passivation. The use of low temperature vacuum bake (95 °C) and lack of any aggressive chemistry during insulator deposition insures that the passivating PQ layer is not altered in any way. Without PQ, the large number of surface states on the silicon made it impossible to change the surface band bending and the capacitance was fixed. With PQ, clear regions of inversion and accumulation were seen at the expected values, showing that PQ was effective at passivating the silicon surface states. Second, we have measured the band alignment of PQ on p+ Silicon from UPS and IPES done in UHV conditions. The bandgap of PQ layer is found to be ~3.18eV. The VB of silicon and HOMO of PQ have a small offset of 0.16eV while the offset between CB of Silicon and LUMO of PQ is 1.9eV. Using XPS to probe the core level of silicon we can measure the band bending due to surface defects in silicon. Our experiments give a band bending of ~0.2 ± 0.1eV. So within the error margin we claim to have no appreciable band bending in the silicon; more evidence that we have a well passivated surface.

11:00 AM

C4, The Role of Atomic Displacements and Vacancy Complexes in Hydrogen Ion-Induced GaN Thin Layer Exfoliation: *Oussama Moutanabbir*¹; Yves Chabal²; Martin Chicoine³; Reinhard Klause-Rehberg⁴; Roland Scholz¹; Oliver Seitz²; Stephan Senz¹; Ulrich Goesele¹; ¹Max Planck Institute of Microstructure Physics; ²Department of Materials Science, University of Texas at Dallas; ³Universite de Montreal; ⁴Martin-Luther-University Halle-Wittenberg

Heteroepitaxial growth of GaN on non-lattice-matched foreign substrates leads unavoidably to the formation of growth-related defects that occur to relax the strain. These growth-related threading dislocations significantly limit the quality of the grown GaN layers with undesirable impact on device performance. High quality GaN bulk substrates can be produced by hydride vapor phase epitaxy growth of thick GaN layers on sapphire and subsequent separation from the sapphire substrate. The current cost of these freestanding GaN wafers is still so high that the concept of transfer of several layers from one wafer to appropriate host substrates is technologically and economically highly attractive. A promising strategy to integrate bulk quality thin layers onto various host materials is ion-cutting process, which is based on direct wafer bonding in combination with hydrogen ion implantation. This work deals with the underlying physics and the role of hydrogen-defect interaction in GaN thin layer splitting. The microstructural evolution of ion implantation-induced damage was investigated by transmission electron microscopy, high resolution x-ray diffraction, positron annihilation spectroscopy, ion channeling, elastic recoil detection, and infrared spectroscopy. A high concentration of void-like nanoscopic structures, nanobubbles, is detected immediately after implantation. Positron annihilation measurements demonstrate that the detected structures are vacancy clusters. The nature of these vacancy clusters was studied by lifetime positron annihilation spectroscopy. FTIR data show that H-defect vibrational spectrum peaks at 3141 cm⁻¹ mode attributed to VGa-H4. A large fraction of H was found to be trapped in higher frequency modes which we associate tentatively to N-H stretch modes in the internal surfaces of nanobubbles. These nanobubbles persist during annealing up to 450 oC. An increase of the strain is observed in this temperature range. This strain relaxes partially above 450 oC following the formation of the platelets which are embryos of the microcracks leading to the formation of the extended internal surfaces.

11:20 AM C5, Late News

11:40 AM C6, Late News

**Session D:
Materials Integration:
Wafer Bonding and Engineered Substrates**

Wednesday AM
June 24, 2009

Room: 206
Location: Pennsylvania State University

Session Chairs: Cindy Colinge, Tyndall National Institute; Kevin Turner, University of Wisconsin, Madison

10:00 AM

D1, Unveiling the Complex Evolution of Strain in Nanopatterned Strained Si Membrane Directly on Oxide: *Oussama Moutanabbir*¹; Manfred Reiche¹; Nikolai Zakharov¹; Angelika Hähnel¹; Wilfried Erfurth¹; Falk Naumann²; Matthias Petzold²; Ulrich Goesele¹; ¹Max Planck Institute of Microstructure Physics; ²Fraunhofer for Mechanics of Materials

Strain is as a key factor for enhancing and tailoring the optical and electronic properties of thin films and nanostructures. In particular, the introduction of strain in the fabrication of Si-based transistors is the subject of increasing interest as one of the promising possibilities to respond to the relentless demand of higher performance ICs. Indeed, recent models suggest that a strained Si lattice can give hole mobilities of up to 4× the unstrained value, and electron mobilities up to 1.8× the unstrained value. In this work, we will describe methods of strain manipulation at the wafer level and the fabrication of ultra

thin strained Si membrane directly on SiO₂. The fabrication is a multi-step process consisting of SiGe heteroepitaxy, growth of lattice mismatch-induced strained Si layer, hydrogen implantation, wafer bonding, and thin layer transfer. In addition, we will address the strain stability during nanoscale patterning, which is a crucial step in the fabrication of strained Si-based devices. Extended ordered arrays of nanostructures with lateral dimensions in the range of 80 to 400 nm were fabricated from the strained Si membrane by combining electron beam lithography and reactive ion etching. High resolution cross-sectional transmission electron microscopy (HRXTEM) and UV micro-Raman spectroscopy were used to evaluate the post-patterning strain in a single nanostructure. In HRXTEM the strain is estimated by measuring the angle between the vertical atomic planes at the edges of a single structure. Both techniques suggest that nanoscale patterning induces a partial relaxation of the strain. The extent of the relaxation was found to depend on the size, geometry, and thickness. Detailed 3D finite-element simulations show that this relaxation implies a complex redistribution of the strain characterized by a highly strained Si/SiO₂ interface. A detailed mechanistic picture of this phenomenon will be discussed. Besides understanding the nanomechanical properties of Si structures, our finding has also implications in the emerging strained silicon-on-insulator technology.

10:20 AM Student

D2, Cleave Engineered Layer Transfer Substrates with InP Templates for Growth of InGaAs/InAlAs Quantum Well Structures: *Monali Joshi*¹; Song Hu¹; Sumiko Hayashi¹; Sara Lu¹; Mark Goorsky¹; ¹University of California, Los Angeles

Cleave Engineered Layer Transfer (CELT) substrates were fabricated via silicon nitride wafer bonding and hydrogen exfoliation techniques. [M. Joshi et. al., ESL 11, 8 (2008)]. The CELT substrate is comprised of a thin (0.3 μm) InP layer bonded to a silicon handle wafer with a 3.3 μm layer of porous silicon (60% porosity) at its surface created by anodic etching, shown in Figure 1. The porous layer is used as a mechanical release layer for transfer of overlying layers after device growth. Nanoindentation results show that the Young's modulus and other mechanical properties can be controllably adjusted as these properties decrease with increasing layer porosity, and our results are in agreement with theoretical modeling. As fabricated, the composite substrate is sufficiently strong to withstand CMP and withstands fracture attempts through the porous layer. Upon annealing at typical device growth temperatures, high resolution x-ray diffraction (HRXRD) measurements of the porous silicon lattice parameter show that the layer undergoes a shift from an initial out-of-plane tensile strain of 0.08% to a compressive strain of -0.14%, as adsorbed species from the anodization process desorb at temperatures > 300°C. [Y. Ogata, et. al. JAP 90, 12 (2001)]. Contrary to previous studies [A. Chelyadinsky, et. al. J. Electrochem. Soc. 144, 4 (1997)], the porous layer in-plane lattice parameter is observed to retain its registry with the substrate throughout annealing. SEM cross-sectional imaging shows the microstructure of the porous silicon layer coarsens during annealing at these temperatures, shown in Figure 3. Nanoindentation measurements of the layers after anneal show a decrease in Young's modulus by approximately 30%. This change in microstructure and corresponding decrease in mechanical properties of the porous silicon layer enables transfer of the template and device layers by fracture through this layer only after growth and device fabrication. InGaAs/InAlAs quantum well structures were grown on the InP-based CELT substrates by metal organic vapor phase epitaxy (MOVPE). [S. Hayashi, et. al. JAP 98, 9 (2005)]. Characterization was carried out by HRXRD, atomic force microscopy, cross-sectional transmission electron microscopy (XTEM) and photoluminescence (PL). Identical quantum well structures were grown on bare InP and characterized for comparison. The PL was comparable for the samples, indicating that the composite substrate does not adversely affect the quality of epitaxial deposition. XTEM imaging is consistent with this observation, as no induced defects were observed in the InP layer or quantum well device layers grown on the CELT substrate. Microstructural changes in the porous layer were observed after growth, however the crystalline-quality of the device and the InP growth template were not compromised.

10:40 AM Student

D3, Surface Chemistry, Electrical Properties, and Passivation-Enhanced Luminescence Achieved Using Dry Sulfur Surface Passivation for Wafer Bonding Applications: *Mike Jackson*¹; *Jeremy Ou-Yang*¹; *Sumiko Hayashi*¹; *Mark Goorsky*¹; ¹University of California, Los Angeles

The properties of III-V interfaces formed by direct wafer bonding are determined by the state of the surfaces prior to contacting and by the reactions that occur within the interface during the post-bonding anneal. III-V surfaces such as GaAs have a native oxide layer which is difficult to completely eliminate at atmospheric pressure by chemical means, such that wafer bonded interfaces can be dominated by the unfavorable mechanical and electronic properties that result. Often, elevated annealing temperatures (>600°C) and large compressive forces must be employed to cause the interfacial oxide layer to break up and form better contact between the III-V layers; yet such harsh processing conditions can be undesirable for processed samples with limited thermal budget. A surface treatment prior to bonding that reduces the inclusion of unfavorable oxides in the interface might improve the bond strength and interface properties, reducing the need for high temperature processing. Such a process is highly desirable for the fabrication of heterogeneous devices such as lattice mismatched multi-junction solar cells. This study investigates the role of sulfur at the interface between direct bonded III-V materials. A method of III-V surface passivation that uses sulfur vapor and ultraviolet illumination under high vacuum has been modified to produce hydrophobic smooth surfaces suitable for bonding. Large area bonding occurs for GaAs/GaAs, InP/InP, and GaAs/InP at room temperature and bulk fracture strength is achieved after annealing GaAs/GaAs at 400°C and InP/InP at 300°C. Large compressive forces are not required during the annealing. XPS measurements of the bonded surface (after splitting with a razor) of a GaAs/GaAs sample annealed to 300°C shows sulfur remaining at the interface. The XPS signals for Ga-oxides and As-oxides are lower for the sample bonded with a chemical oxide-etch plus UV-sulfur exposure than for a sample bonded immediately after oxide etching indicating that the sulfur may inhibit the amount of water or oxygen adsorbed from ambient available to react with the III-V during the bond strengthening anneal to form undesirable oxide. The XPS measurements are consistent with electrical measurements that indicate that the bonded interface shows very good electrical conductivity after bonding at these low temperatures and the results are consistent with photoluminescence measurements which demonstrate that the sulfur coverage improves the passivation and hence reduces band-bending across the interface. The passivation of III-V surfaces with sulfur or sulfide-containing solutions is known to improve the surface electronic properties by the replacement of surface oxide bonds with a thin sulfide; however, our approach demonstrates that evaporation-based techniques provide high quality, conductive interfaces without the use of solutions that can leave residual species at the interface.

11:00 AM Student

D4, Effect of Radical Activation for Low Temperature Si to Si Wafer Bonding: *Ki Yeol Byun*¹; *Isabelle Ferain*¹; *Cindy Colinge*¹; ¹Tyndall National Institute

The simplicity of the direct bonding process has given rise to many materials integration schemes such as hydrophilic silicon to silicon bonding. In the latter case, a wafer surface activation is usually conducted before the bonding operation. It is expected to deliver high bond strength after low anneal temperatures. Activation can be accomplished using wet chemistry, plasma or ultraviolet exposure. In our experiment, <100> oriented p-type Czochralski grown bare silicon wafers with a diameter of 100mm were used. The resistivity of the wafers was 10–20 Ω cm. The activation and bonding were performed in an AML AW04 aligner bonder fitted with an in-situ surface activation tool using radicals (RAD) [1]. Prior to wafer bonding, the wafers were activated by radicals (O₂, Ar, N₂) generated from remote circular plasma which surrounds the wafers (chamber pressure=1mbar, exposure duration=10 minutes). The bonding was carried out following exposure within the AML bonder after the chamber was pumped down to 10-5mbar. After bonding, wafers were annealed for 24 hours first at 200°C and then at 400°C. The annealing was conducted in a convection oven in a nitrogen ambient. Due to the the mesh ring configuration,

ions which escape the plasma ring do not strike the wafer surface with high velocity. The latter has been confirmed by ellipsometry-based measurements showing that there was no significant surface damage after radical exposure of bare Si wafers. Bonded wafers were imaged before and after annealing using an infrared source. The defect density suggests that a long radical exposure using oxygen radicals results in a substantially lower interface defect density. This can possibly be attributed to the creation of a reactive oxide layer during free oxygen radical exposure, which improves the diffusivity of reactants at the Si surface and increases the bond strength. On the other hand, N₂ and Ar radical activation bonding generated a higher interface voids after post-bonding annealing. This suggests that the nature of the radicals used for the activation determines the quality of intrinsic voids and the distribution of the voids. The result is in agreement with the bond strength values extracted from a razor blade test. Due to their large defect density, the samples exposed to nitrogen and argon radicals prior to the bonding exhibit low bond strength values, even after 400°C anneal. This experiment has been conducted in order to investigate the impact of a radical exposure prior to a hydrophilic wafer bonding. Our results point towards a surface reactivity modification after radical exposure, without notable modification of the native oxide thickness. As compared to reference samples, exposure to oxygen radicals results in a significant improvement of the bond strength after a low temperature anneal.

11:20 AM Student

D5, Study of the Formation, Evolution and Dissolution of Interfacial Bonding Defects Based on the Hydrogen Storage and Diffusion Mechanisms: *Sebastien Vincent*¹; *Ionut Radu*¹; *Jean-Daniel Penot*²; *Francois Rieutord*²; ¹SOITEC S.A.; ²CEA-INAC

Silicon wafer bonding is nowadays a mature technology, being widely used for the manufacturing of silicon on insulator and other engineered substrates used in the IC industry. More recently, Si and SiO₂ bonding has attracted interest for other applications such as MEMS and 3D device integration. One of the main criteria to assess the quality of the bonded structure is the realization of defect-free interfaces. The formation of defects at the bonding interface upon post bonding thermal treatments (also called thermal voids) has a direct impact on the quality of the bonded structures. In this paper, the mechanisms of the formation, evolution and dissolution of the thermal voids will be presented and discussed. For this study 8-inch Si (100) wafers have been used to realize Si/SiO₂ bonding structures with different thicknesses of the thermal oxide. Prior to the direct bonding, the wafers were cleaned using standard wet cleaning (SC1 and SC2). After the bonding, the Si/SiO₂ structures were annealed at various temperatures ranging from 200°C to 1000°C for different annealing times. In case of a hydrophilic bonding of a Si wafer to an oxidized silicon wafer (SiO₂), the water monolayers initially trapped at the bonding interface are removed during annealing as observed by Fourier Transformed Infra-Red microscopy (FTIR). In addition, using High Energy X-Ray Reflexion (HEXRR) it has been observed that the adsorbed water diffuses through the native silicon oxide, leading to an oxidation of the Si already upon annealing at 200°C. This oxidation reaction leads to the production of hydrogen which will locate either in the SiO₂ or at the bonding interface. The measurements of hydrogen inside the SiO₂ has been performed using Nuclear Reaction Analysis (NRA) and mass spectrometry. In case of excess hydrogen (above the solubility limit), interface defects will form as observed by Scanning Acoustic Microscopy (SAM). From the experimental results, a model of interface defect formation based on hydrogen solubility in SiO₂ is proposed. Based on this model, the growth of the thermal voids at 400°C and 600°C and their dissolution for annealing temperature above 800°C have been studied. The growth and the dissolution of thermal voids will be discussed based on the mechanism of hydrogen diffusion from the SiO₂ matrix to the defect. The hydrogen diffusion mechanism has been related to the internal pressure of defects, calculated considering the mechanical and elasticity theory.

11:40 AM D6, Late News

Session E:

Organic Thin Film and Crystalline Transistors: Devices, Materials and Processing I

Wednesday AM
June 24, 2009

Room: 207
Location: Pennsylvania State University

Session Chairs: Michael Chabinye, University of California, Santa Barbara; Alberto Salleo, Stanford University

10:00 AM

E1, Organic Complementary Inverters and Non-Volatile Memory Elements Based on Ferroelectric Field-Effect Transistors: *Tse Nga Ng¹; Sanjiv Sambandan¹; Robert Street¹; Rene Lujan¹; Ana-Claudia Arias¹; Chris Newman²; He Yan²; Antonio Facchetti²; ¹Palo Alto Research Center; ²Polyera Inc*

Organic complementary circuits are demonstrated for integration with mechanical sensors to enable the fabrication of health monitoring devices, such as sensor tapes to detect traumatic brain injury. Organic thin-film transistors were fabricated by inkjet patterning with bilayer dielectrics that were compatible with both p- and n-type semiconductors. The inverters showed a typical gain of 8 with VDD at 10V and -3dB cutoff at 150 kHz. Because the charge trapping rates of the complementary semiconductors were different, circuit design parameters were examined to stabilize the inverter gain and noise margin. Since this sensor tape application requires data storage over 1 week, ferroelectric field effect transistors (feFETs) are also developed for use as memory devices. The mobility, threshold voltage, and capacitance of ferroelectric transistors were analyzed to understand mechanisms affecting retention loss. With better understanding of the interfacial effects, memory cell structures are improved to retain 50% of output current over 7 days. Due to the gradual decrease in feFET current, calibration method for extracting the original input voltage is demonstrated. Finally, ferroelectric transistor dimensions will be discussed with regards to improving data retention time.

10:20 AM Student

E2, Dependence of Charge Injection on Contact Height in Poly(3-Hexylthiophene)-Based Bottom-Contact Field-Effect Transistors: *Kumar Singh¹; Tomasz Young¹; Tomasz Kowalewski¹; Richard McCullough¹; Lisa Porter¹; ¹Carnegie Mellon University*

In this study we observed a dependence of charge injection on the contact height in organic field-effect transistors based on poly(3-hexylthiophene) (P3HT) as the active layer and Au bottom contacts. In an earlier study we showed that field-effect mobility (μ) and contact resistance (R_C) are inversely proportional to each other and dependent upon the molecular weight of P3HT in bottom-contact P3HT-based FETs. This interdependence was attributed to the dependence of charge injection on the charge transport through a region of poor nanomorphology in the vicinity of the contacts caused by their geometry (i.e., the step between the surface of the contacts and the channel region). To verify the effect of the contact height, bottom contact FETs were fabricated in two different configurations: a near-planar configuration in which the contacts are recessed in the SiO₂ surface (planar contact structure), and a conventional bottom-contact configuration with a contact height of 50nm (normal contact structure). The channel length (L) was varied from 3 to 40 μm , whereas the channel width was fixed at 250 μm . The contact resistance was measured using the transmission line method. Field-effect mobility values were calculated using both the saturation and linear regions of the I-V characteristics. It was observed that R_C for planar contacts is lower than that for the normal contacts (e.g., at a gate voltage, $V_G = -80\text{V}$, $R_{C(\text{planar})} = 0.5\text{M}\Omega$ and $R_{C(\text{normal})} = 0.6\text{M}\Omega$). When the field-effect mobility values obtained from the saturation region are compared, for small channel lengths (3-10 μm) the mobility in the FETs having planar contacts was higher than the mobility in the FETs with normal contacts (e.g., at $L = 5\mu\text{m}$ and $V_D = -80\text{V}$, $\mu_{\text{planar}} = 0.15\text{cm}^2\text{V}^{-1}\text{s}^{-1}$ and $\mu_{\text{normal}} = 0.1\text{cm}^2\text{V}^{-1}\text{s}^{-1}$). However, for channel lengths greater than 10 μm , the mobility values merged (e.g., at $L = 20\mu\text{m}$, $\mu_{\text{planar}} \approx \mu_{\text{normal}} = 0.06\text{cm}^2\text{V}^{-1}\text{s}^{-1}$). Effective field-effect mobility values obtained from the linear region, corrected for R_C , were found to be 0.11 $\text{cm}^2\text{V}^{-1}\text{s}^{-1}$

s^{-1} for both normal and planar contacts. Our prior and present results indicate that for short-channel FETs the charge injection is controlled by the geometry of the contacts. In a normal contact structure the step between the surface of the contacts and the channel disrupts the self-assembly of the P3HT film resulting in poor morphology in the vicinity of the contacts and hence lower mobility and higher contact resistance. However, for long-channel devices the charge injection becomes limited by the charge conduction through the polymer, and the effect of geometry of the contacts becomes insignificant. We also plan to conduct atomic force microscopy to study the morphology in the vicinity of the contacts and scanning Kelvin potentiometry (SKPM) to observe the potential drop within the channel which will help in direct visualization of charge injection and transport in individual FETs.

10:40 AM Student

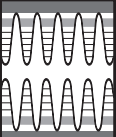
E3, Fabrication and Application of Graphene Electrodes and Graphene-Coated Gold Electrodes in Organic Field-Effect Transistors: *Chen-Guan Lee¹; ¹University of Texas at Austin*

Organic Field-Effect Transistors have been intensively investigated in the last two decades. Compared to their inorganic peers which generally need sophisticated fabrication technologies, organic semiconductors are advantageous due to easy processing and are compatible with flexible substrates. In this study, we report the effects of using graphene electrodes on the characteristics of pentacene field-effect transistors. Graphene electrodes were fabricated by drop casting from a suspension containing reduced graphene oxide, onto a patterned surface possessing regions with a large difference in surface energy. To fabricate a pattern containing regions with a large difference in surface energy, a thermally- oxidized n-type silicon was used as a substrate. A thin layer of hydrophobic CYTOP® (5-nm thick) was spin-coated on the substrate and patterned with photolithography. The solvent for the suspension of reduced graphene oxide platelets is a mixture of DMF (dimethylformamide) and water in a volume ratio of 9:1 (DMF:H₂O). When drop cast on the patterned surface, the colloidal suspension preferentially adhered to the hydrophilic silicon dioxide, which is the electrode region. 'Graphene' electrodes could then be formed through repeated drop casting and air drying. After annealing on a hot plate at 120°C for 20 minutes, pentacene was deposited to a thickness of 250 Å at a deposition rate of 0.1 Å/s. For comparison, standard gold electrodes were fabricated in a parallel process. Results show transistors with the 'graphene' electrodes have similar performance to those with standard gold electrodes, even though the conductivity of the graphene electrodes is more than two orders of magnitude less than that of the gold electrodes. The best results were obtained by combining the Au and graphene. We employed bottom-contact device geometry with recessed source/drain geometry. The reduced graphene oxide platelets attach to the gold electrodes due to differences in surface energy between Au and CYTOP®. Our results show that the field-effect mobility of the devices with the graphene modified electrodes has increased more than a factor of 3 compared to the devices having standard gold electrodes (from 0.04 to 0.13 cm^2/Vs). This result shows that using graphene as an interfacial layer to improve charge injection from contacts will help the performance of organic transistors. We attribute the improved performance of the graphene/Au source/drain electrodes to better charge injection at the graphene/pentacene interface compared to the Au/pentacene interface. We will also report on the effects of interfacial graphene on the characteristics of other organic semiconductor based transistors.

11:00 AM

E4, Compact Model for Sub-Threshold Operation in Polymer Semiconductor Thin Film Transistors: *Sanjiv Sambandan¹; Rene Kist¹; Rene Lujan¹; Tse Ng¹; Ana Arias¹; Robert Street¹; ¹Palo Alto Research Center*

Polymer semiconductor based thin film transistors (TFTs) are of interest for applications in large area electronic systems. Due to the presence of states in the bandgap, these devices experience charge trapping and a threshold voltage shift in time with applied gate bias. Therefore, any transistor operating continuously for a sufficiently long time moves closer to sub-threshold mode operation. Understanding forward sub-threshold current-voltage (IV) characteristics in polymer TFTs is thus of importance. Assuming a p-type device we attempt to develop a compact model of sub-threshold operation in polymer TFTs for the purpose of circuit simulations. There are several key challenges in modeling



the sub-threshold operation of polymer TFTs. 1. In sub-threshold operation the Fermi-level stays within the deep localized states. In materials such as amorphous silicon, the deep states have an exponential distribution in energy with a single or several discrete characteristic voltages. Typically polymer semiconductors have deep states with the characteristic voltage being a continuous function of energy, which leads to distributions close to a Gaussian. This feature needs to be modeled. 2. The deposition of polymer semiconductors is typically via spin coating or ink jet printing where the control over the thickness of semiconductor is weak. The thickness is therefore unknown. If the Debye length of the deep states is greater than the thickness there exists a non zero electric field at the back interface of the device thereby affecting IV characteristics. On the other hand if the semiconductor is very thick, we have conduction mechanisms in the bulk which are strongly dependent on the source-drain bias. These mechanisms have a Poole-Frenkel (P-F) like behavior and the model must be able to account for this. 3. Due to the large number of states, the metal-semiconductor contact barrier will probably not be strongly dependent on the metal work function. The injection current at the contacts is a nonlinear function of the electric field and will have to be modeled since its influence on the sub-threshold current is significant. The above features are achieved as follows. Firstly, the effective capacitance of the deep states is made a function of the applied gate-source bias. Using extractable parameters, we can thus identify the deep-state distribution with energy. Secondly, the model includes transport mechanism of carriers in localized states, namely, variable range hopping of carriers and polarons both of which have a P-F behavior. P-F behavior is also observed in space charge limited current due to extended state transport. All these mechanisms result in a loss of saturation of the output characteristics. Finally, the effect of contact barrier is modeled with extractable parameters.

11:20 AM

E5, Fluoroalkyl Phosphonic Acid Self-Assembled Monolayer Gate Dielectrics to Control the Threshold Voltage in Low-Voltage Organic Thin-Film Transistors: *Ulrike Kraft*¹; *Ute Zschieschang*¹; *Frederik Ante*¹; *Claudia Kamella*¹; *Konstantin Amsharov*¹; *Edwin Weber*²; *Martin Jansen*¹; *Klaus Kern*¹; *Hagen Klauk*¹; ¹Max Planck Institute for Solid State Research; ²TU Bergakademie Freiberg

For many applications of organic thin-film transistors (TFTs), high-capacitance gate dielectrics that can be processed at low temperature are of interest. Several approaches exist, including vapor-deposited metal oxides [TSE, 515, 3132], ultra-thin polymers [APL, 88, 173507], self-assembled nanodielectrics [PNAS, 102, 4678], and thin hybrid dielectrics based on alkyl phosphonic acid self-assembled monolayers (SAM) on plasma-oxidized aluminum gate electrodes [Langmuir, 24, 1665]. None of these approaches, however, provides systematic and reproducible control of the threshold voltage. To allow the threshold voltage of low-voltage organic TFTs to be controlled systematically, we have synthesized a fluoroalkyl phosphonic acid for SAMs with electron-withdrawing character on plasma-oxidized aluminum gates. The fluoroalkyl phosphonic acid was synthesized in a two-step reaction. First, fluoroalkyl-diethyl ester was obtained by a Michaelis-Arbuzov reaction of 1 iodo-1H,1H,2H,2H-perfluorododecane and triethylphosphite, both purchased commercially and reacted at 150°C for one day. The main byproduct, ethyl iodide, was distilled off continuously during the reaction to avoid unwanted side reactions, and excessive triethylphosphite was then eliminated by vacuum distillation. In the second step, the ester was hydrolyzed in hydrochloric acid, yielding (3,3,4,4,5,5,6,6,7,7,8,8,9,9,10,10,11,11,12,12,12-heneicosafuorododecyl)-phosphonic acid. The product was purified by recrystallization in methanol. Low-voltage organic TFTs using the synthesized fluoroalkyl phosphonic acid as an electron-withdrawing gate dielectric were prepared on a doped silicon substrate. A 20 nm thick aluminum gate electrode was deposited by evaporation, followed by a brief oxygen plasma to create a ~3 nm thick aluminum oxide. The substrate was then immersed in a 2 propanol solution of the fluoroalkyl phosphonic acid, allowing a densely packed molecular monolayer to self-assemble on the oxidized aluminum gate. The total thickness of the AlO_x / SAM gate dielectric is about 5 nm, providing a capacitance of 880 nF/cm². Static contact angles on the fluoroalkyl SAMs are about 122° and systematically larger than on alkyl SAMs (~110°). For the semiconductor, a 30 nm thick pentacene film was deposited in vacuum. TFTs were completed by

evaporating gold source and drain contacts through a shadow mask. Owing to the small thickness and large capacitance of the gate dielectric, the TFTs operate with voltages of about 3 V. Carrier mobility (0.6 cm²/Vs) and on/off current ratio (10⁵) are similar to those of pentacene TFTs with alkyl phosphonic acid SAM. Compared with the TFTs with alkyl phosphonic acid SAM, however, the threshold voltage of the TFTs with fluoroalkyl SAM is shifted by more than 1 V towards more positive values. This substantial difference in threshold voltage is a direct consequence of the electron-withdrawing character of the fluoroalkyl SAM. Therefore, the use of fluoroalkyl phosphonic acids in self-assembled monolayer gate dielectrics provides a powerful method to systematically control the threshold voltage of low-voltage organic TFTs.

11:40 AM E6, Late News

Session F: III-Nitride: Growth of Electronic Devices

Wednesday AM
June 24, 2009

Room: 208
Location: Pennsylvania State University

Session Chair: Michael Manfra, Purdue University

10:00 AM Student

F1, Low-Sheet-Resistance Multiple AlN/GaN Heterojunctions Grown by MBE: *Yu Cao*¹; *Huili Xing*¹; *Debdeep Jena*¹; ¹University of Notre Dame

It has been proved that the single AlN/GaN heterojunctions are capable to provide low sheet resistance down to 150 O/sq for FETs engineering. FETs fabricated with this structure have shown current density more than 2.3 A/mm with the transconductance up to 480 mS/mm. These results have shown that AlN/GaN heterojunctions are promising to push the performance of GaN HEMTs into a new level which the traditional AlGaN/GaN HEMTs are not able to reach. In this work, we show that by growing multiple pseudomorphic AlN/GaN heterojunctions, 2DEGs are formed at the multiple interfaces between AlN and GaN. These 2DEGs are parallel to each other. By taking the advantage of these multiple 2DEGs, the in-plane sheet resistance can be further lowered. We studied the transport and structural properties of such multiple AlN/GaN heterojunctions grown by MBE. All growths were performed under metal rich conditions at a RF Nitrogen plasma power of 275 W. The epitaxial AlN layer thickness was varied from 0.75-4.5nm with the GaN thickness varying from 2.9-58nm in each period. The sample structures were studied by X-ray diffraction measurement and the measured data were fitted to simulations. AFM measurements showed very smooth morphologies with atomic steps around dislocation surface terminations, with a RMS roughness of ~0.3nm for 2X2 micron scans. 2DEGs were observed in Hall-effect measurements. In the structure with 3 periods of 2.6 nm AlN and 30 nm GaN heterojunctions, a total sheet charge density of 6.32x10¹³ cm⁻² was found with the mobility of 520 cm²/Vs. This sheet charge density is about triple that in single AlN/GaN heterojunctions where the AlN cap is 2.6 nm. However, in more cases we found the sheet charge density does not always scale with the thickness of AlN or the number of periods. In the structure consisting 9 period AlN/GaN heterojunction structures, where AlN is 4.2 nm and GaN is 58 nm in each period, the sheet charge density is achieved at 1.08x10¹⁴ cm⁻² with the mobility to be 1567 cm²/Vs, whereas in single AlN/GaN heterojunctions, the sheet charge density is as high as 3.5x10¹³ cm⁻². Inspecting the band diagram of such multiple heterojunctions, we find the valence band of GaN can reach the Fermi level. The existence of holes makes the Hall result not scale with AlN barrier thickness and the number of periods. Nevertheless, the combination of these conductive channels provides the sheet resistance as low as 37 O/sq at room temperature, which is impossible to be achieved with single heterojunctions. The high 2DEG mobilities and the very low sheet resistance observed point towards the fact that high-quality epitaxial AlN/GaN multilayers were successfully grown, open the window for a number of new possible applications.

10:20 AM Student

F2, Growth and Characterization of N-Polar GaN/AlGaIn/GaN HEMTs on SiC by Metal Organic Chemical Vapor Deposition: *David Brown*¹; *Stacia Keller*¹; *Rongming Chu*¹; *Steven DenBaars*¹; *Umesh Mishra*¹; ¹University of California at Santa Barbara

GaN-based High Electron Mobility Transistors (HEMTs) have shown excellent promise in microwave and millimeter-wave power electronics. To date, most reports have focused on Ga-polar devices, primarily due to the relative ease of growth of GaN crystals along this orientation. Growth along the N-polar direction, however, would enable the development of novel device structures due to reversal of polarization charges at heterointerfaces. Such structures have been successfully grown by molecular beam epitaxy. In the past, the investigation of N-polar films by metal organic chemical vapor deposition (MOCVD) was hampered due to difficulties in their growth, often leading to rough surfaces caused by the formation of hexagonal hillocks. Recent developments have made heteroepitaxy of smooth GaN films on misoriented sapphire and SiC substrates possible. In this study, N-polar HEMTs grown on misoriented 4H-SiC substrates by MOCVD were fabricated. The electrical characteristics of the devices, including IV curves, leakage currents, transfer characteristics, and S-parameters were measured. The performance of the measured devices was comparable to typical Ga-polar devices. The device structure investigated consisted of a $\text{Al}_{0.25}\text{Ga}_{0.75}\text{N}$ barrier, a 25 nm GaN channel, and a 5 nm Si_xN_y gate insulator grown on a GaN buffer, which was all grown on a misoriented SiC substrate. A channel sheet charge density of $6.6 \times 10^{12} \text{ cm}^{-2}$ and a mobility of $1370 \text{ cm}^2\text{V}^{-1}\text{s}^{-1}$ were obtained with a Hall measurement at room temperature. The resistance of the alloyed Ti/Al/Ni/Au ohmic metal stack was 0.48 $\Omega\text{-mm}$. The device shows a pinch-off voltage of -6 volts and a peak transconductance (g_m) of 135 mS/mm. At the knee voltage, the device had a current of approximately 0.55 A/mm at a gate voltage of 0 V. The measured buffer leakage current was 1 mA/mm at a drain bias of approximately 290 volts. Two-terminal gate leakage is less than 0.1 $\mu\text{A/mm}$ at drain voltages less than 30 V. For a three terminal breakdown measurement, the breakdown voltage, defined as the voltage where the drain current reaches 1 mA/mm, is in excess of 150 volts for a gate bias 2 V below pinch-off. Current and power gain cutoff frequencies were 17 GHz and 33 GHz respectively for a gate length of 0.7 μm . To the best of our knowledge, this is the first report of N-polar GaN HEMTs on SiC grown by MOCVD.

10:40 AM Student

F3, Nanoscale Temperature Distribution, Defect Mapping and Evolution Inside Active AlGaIn/GaN High Electron Mobility Transistors: *Chung-Han Lin*¹; *T. Merz*²; *D. Douthett*²; *M. Hetzer*²; *Jungwoo Joh*³; *Jesús del Alamo*³; *U. Mishra*⁴; *L. Brillson*⁴; ¹Department of Electrical and Computer Engineering, The Ohio State University; ²Department of Physics, The Ohio State University; ³Microsystems Technology Laboratories, Massachusetts Institute of Technology (MIT); ⁴Departments of Electrical and Computer Engineering and Materials, University of California-Santa Barbara

Because of its inherent material properties, GaN-based high electron mobility transistors (HEMTs) are very suitable for high power operation. However, under these conditions, Joule heating and high electric fields inside the device may generate defects that adversely affect device properties. In this study, we use depth-resolved cathodoluminescence spectroscopy (DRCLS), atomic force microscopy (AFM) and Kelvin probe force microscopy (KPFM) to investigate the temperature distribution and defect generation inside state-of-the-art AlGaIn/GaN-based HEMTs on a scale of tens of nanometers. Using DRCLS to monitor temperature-dependent near band edge (NBE) energies during actual device operation, we found continuous and significant temperature increases from drain to gate over the $\sim 600 \text{ nm}$ gate - drain spacing even under low power operation. DRCLS also provided maps across the HEMT's source-gate-drain regions of NBE emission intensities, which decrease with the formation of deep level defects. Indeed, such maps reveal inhomogeneous NBE darkening inside the channels and under the gates that may be sites of recombination-induced defect heating. KPFM maps indicate a correlation between higher surface potential and darkened regions. Furthermore CL spectra versus position inside channels and along/under gates reveal deep level "yellow band" (YB) (i.e., Ga vacancy-related) and "blue band" (BB) emissions which increase over 12 hours

device operation. According to the DRCLS signal from both the "channel" and "under gate", we found the defect generation after 12 hours operation of the GaN-based HEMTs. The averaged YB/NBE ratio vs. position shows that YB under the gate on the drain side increases by 3.5x compared with $\sim 2.2x$ under the gate on the source side (~ 2.2 times) and very little in the channel region. Furthermore, YB emission exhibits much larger changes than BB with operation and location, indicating a link between this defect and device degradation. Thus DRCLS with $\sim 50 \text{ nm}$ spatial resolution laterally and tens of nm vertically provides detailed correlations between temperature under actual state-of-the-art device operation, defect distribution and specific defect evolution laterally and depth-wise with device operation. The results obtained with this combination of techniques can be used to reveal and in principle predict physical mechanisms of AlGaIn/GaN HEMT degradation under realistic conditions.

11:00 AM Student

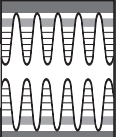
F4, The Dominant Gain Limiting Mechanism in Wafer-Fused AlGaAs/GaAs/GaN HBTs: *Chuanxin Lian*¹; *Huili Xing*¹; ¹University of Notre Dame

(Al)GaN materials have established themselves in high speed and high power applications, owing to their large band gap energies and high anticipated electron saturation velocity. Unlike the rapid development of AlGaIn/GaN high electron mobility transistors, that of AlGaIn/GaN heterojunction bipolar transistors (HBTs) has been greatly impeded by the highly resistive p-GaN material. A proposed solution is to utilize AlGaAs/GaAs heterostructures as the emitter-base and keep GaN as the collector to make use of the unity emitter injection efficiency, large base transport factor of AlGaAs/GaAs, and high breakdown field of GaN. Unfortunately, the large lattice mismatch between GaAs and GaN makes it very difficult to grow high quality GaAs on GaN. Instead, direct wafer fusion has been utilized to heterogeneously integrate AlGaAs/GaAs and GaN for HBT fabrication, and encouraging device performance ($\beta \sim 20$ and $f_T \sim 2.6 \text{ GHz}$) has been achieved demonstrating the feasibility of using wafer fusion to form active device regions. Compared to as-grown AlGaAs/GaAs/GaN HBTs, however, fused AlGaAs/GaAs/GaN HBTs exhibit severe gain degradation. Understanding the electron transport mechanisms that govern the device operation is essential to obtain insight into gain limiting factors for subsequent device design and fusion process optimization. For this purpose, temperature dependent I-Vs have been measured on both fused and as-grown HBTs. It was found that β of the as-grown HBTs increased first followed by decreasing, while that of the fused HBTs decreased monotonically, with decreasing temperature. Effects of high temperature annealing on the β -T relationship in the fused HBTs were ruled out by temperature dependent study on the as-grown HBTs annealed at conditions similar to those employed in the fusion process. Instead, an energy barrier was possibly formed at the base-collector junction by an interfacial disordered material at the fused GaAs/GaN interface revealed by TEM. Electrons need to pass through this barrier by thermionic emission and/or phonon-assisted tunneling, leading to increasing electron transmission rates with increasing temperature. It was also noted that the fused HBTs exhibit large output conductance at the forward active regime in the common-emitter I-Vs. Hall effect measurements on the p-GaAs base of the same fused sample revealed a hole density as high as $6 \times 10^{18} \text{ cm}^{-3}$, indicating that the observed small apparent Early voltage was unlikely due to the depletion region extended into the base. On the other hand, the base-collector junction energy barrier could be lowered by higher collector bias, resulting in large output conductance. Furthermore, the fused HBTs have much smaller gain than the as-grown HBTs annealed at similar conditions and show negligible gain dependence on the base thickness. All these observations suggest that the bonded GaAs/GaN interface is most probably the dominant factor limiting current gain in the fused AlGaAs/GaAs/GaN HBTs.

11:20 AM Student

F5, Ultra-Low Contact Resistance for Self-Aligned HEMT Structures on N-Polar GaN by MBE Regrowth of InGaIn-Based Contact Layers: *Nidhi Nidhi*¹; *Sansaptak Dasgupta*¹; *Man Hoi Wong*¹; *Uttam Singiseti*¹; *Mark Wistey*¹; *Mark Rodwell*¹; *James Speck*¹; *Umesh Mishra*¹; ¹University of California Santa Barbara

AlGaIn/GaN based HEMTs have been of interest to the semiconductor community because of their high breakdown voltage, high sheet carrier density, and the high saturation velocity of GaN. The N-polar orientation of



GaN-based HEMTs are particularly suited for ultra-high speed applications because of several advantages associated with them as compared to Ga-polar, such as lower contact resistance, better electron confinement, low gate leakage, low dispersion devices and enhancement mode operation. In this paper, we demonstrate a pathway towards designing a self-aligned structure to achieve ultra-high speed performance from N-polar GaN HEMTs. The devices use a gate-first methodology with regrown access regions similar to those reported for InGaAs channel MOSFETs, to achieve very high aspect ratio with low access resistance. Refractory W gate metal is used such that the gate metal stack can withstand MBE regrowth temperatures. The gate metal stripes are covered with SiO₂ cap and sidewalls to avoid contaminating the MBE chamber. Contact layers consisting of InGaN graded from 1% In to higher In compositions (preferably InN) are regrown to achieve ultra-low Ohmic contact resistance. All MBE regrowths were done on MOCVD GaN templates on sapphire with W gates fabricated on them. InN regrowth was first investigated to study growth morphology and contact resistance from metal to regrown InN. Regrowth was done at various temperatures (570°C, 525°C, 475°C). Non-alloyed contact resistance from metal to InN was measured to be 2-5 Ω-μm. Due to uniform surface morphology, 475°C is chosen as an optimum temperature for regrowth of InN. Regrowth on graded InGaN doped with 1×10¹⁹ cm⁻³ Si was then investigated for various temperatures (610°C, 550°C, 475°C). The ending In composition was found to increase from 26% to 43%. The contact resistance from metal to graded InGaN was observed to increase with In composition which is contrary to the expected trend. It is believed that this could be a result of defects in the regrown films grown at lower temperatures or change in surface pinning position with varying In compositions. However, a relatively low contact resistance of 120 Ω-μm was obtained for InGaN regrown at 610°C. To further decrease the contact resistance, a graded InGaN layer (1-26%) capped with 10nm of InN was regrown at 610°C on a N-polar HEMT structure on SiC. The contact resistance to the 2DEG using this contact layer was measured to be 60 Ω-μm. This is the lowest reported contact resistance to an AlGaIn/GaN HEMT structure. It can be projected that lower contact resistances could be obtained by grading to higher In composition InGaN with InN cap. To conclude, with the gate-first and regrown access regions technique for making self aligned N-polar HEMTs, very high frequency performance can be achieved.

11:40 AM Student

F6, Investigation of Mg Ion-Implanted GaN as Current Blocking Layer in a CAVET: *Srabanti Chowdhury*¹; Brian Swenson¹; Stacia Keller¹; Umesh Mishra¹; ¹University of California-Santa Barbara

We present promising performance of Mg implanted GaN as current blocking layer (CBL) used in a CAVET (Current Aperture Vertical Electron Transistor). A CAVET is a vertical device with source and gate on top and a current aperture that allows current to flow vertically down from the source to the drain. CBL is designed to block current flowing vertically through any other path but the aperture. For CAVETs to acquire high break down voltages, it is necessary to have good CBL that has low leakage. Mg-ion implanted GaN can be used for the purpose. In the present work, the current blocking capability of Mg-ion implanted GaN has been studied with different ion-implantation energy (E_{imp}) using controlled experiments. A simple structure comprising of n⁺GaN/n-GaN/CBL/n⁺GaN was used for the study. 500nm of n-GaN on thick n⁺GaN layer was grown in MOCVD on a 2 inch sapphire wafer. The wafer was cleaved into quarters and implanted with Mg-ion at energies 80keV, 100keV, 120keV and 140keV respectively, keeping the dose constant at 1e15/cm². The four implanted samples implanted at different E_{imp} were cleaved into two halves. Each half was used as the control sample. Control samples were treated with UV-Ozone for 1 hour and treated with HF for 30 seconds, right before growing the n⁺GaN/n-GaN on top of the ion-implanted layer. The other halves at different energies were treated with H₂SO₄ followed by DI water rinse. The samples were next treated with HCl:DI (1:3) mixture. The samples were treated with UV-Ozone and HF identical to the control samples and immediately transferred to MOCVD chamber where the top n⁺GaN/n-GaN were grown using identical conditions. Diode-like structures with a top and bottom Ti/Au contacts were fabricated on these samples. The results shown here are measured on a diode with 250 × 250 μm² area. From the results we observe that with increasing energies the leakage

current increased for both the series, with and without acid treatment (H₂SO₄ followed by HCl). For a given energy, device which was treated with acid prior to the regrowth of the top n⁺ GaN/n-GaN layers showed significant reduction in leakage current compared to the control sample. A leakage current as low as 10mA/cm² was measured from an acid treated sample with Mg implanted at energy of 80keV. The capacitance measured with frequency ranging from 100 kHz to 10 MHz showed a steady value of 0.03 μF/cm². The devices could block a maximum voltage of 35V, which corresponds to breakdown electric field of over 3MV/cm. In conclusion current blocking capability of Mg-ion implanted GaN was studied for four different E_{imp} , with surface treated with acid prior to regrowth. This work is funded by Toyota Motor Corporation, Japan

Session G: Narrow Bandgap Materials

Wednesday PM
June 24, 2009

Room: 105
Location: Pennsylvania State University

Session Chair: Ganesh Balakrishnan, University of New Mexico

1:30 PM

G1, Improved Migration-Enhanced Epitaxy for Self-Aligned InGaAs Devices: *Mark Wistey*¹; Uttam Singiseti¹; Ashish Baraskar¹; Greg Burek¹; Arthur Gossard²; Mark Rodwell¹; ¹University of California, Santa Barbara, ECE Department; ²University of California, Santa Barbara, Materials Department

Parasitic contact and access resistances limit the bandwidth of high speed electronic and optoelectronic devices. Molecular beam epitaxy can provide very highly doped layers and in-situ Mo deposition for low resistance contacts. But regrowth of contacts next to a finished device often results in undesirable gaps. On the other hand, self-aligned contacts provide the shortest electrical path from external contacts to a device, and they require no critical lithography. In this study, we examine regrowth of n⁺⁺ InGaAs for self-aligned contacts next to SiO₂ gate structures as a function of temperature, V/III ratio, and pulsed deposition. Growth is challenging because Si doping above 5E19/cm³ is required for contact resistances below 1E-8 Ω-cm², but this produces either extremely rough films or gaps near the gate, depending on temperature. On the other hand, a modification of migration-enhanced epitaxy (MEE) at high temperature with continuous arsenic flux produced smooth films. Single monolayers of Group III atoms were deposited with a flux ratio V/III~3, separated by a 15 sec soak under a 2-5E-6 torr As₂ flux. At temperatures below 520°C, significant crosshatching occurred near the gate, which we attribute to preferential migration of In from the SiO₂ to the substrate, resulting in compressive strain and relaxation. Growth at 540-560°C does not show significant relaxation roughening in SEM. Indium evaporation at these temperatures requires 10-34% additional indium to maintain lattice-matched conditions. In contrast to Shen's results on InAs (Shen JCG 1995), we find that increasing substrate temperature leads to [111] faceted growth rather than a uniform "rising tide." Growth at 540°C with alternating 4x2 - 3x1 - 4x2 RHEED patterns produced films which were both smooth in the far field and showed no apparent gap near the gate. High levels of silicon doping (8E19/cm³) initially raised two concerns. First, Si concentrations are well above the solid solubility limit in InGaAs. MEE provides increased time for relaxation processes to occur during growth, and the high temperatures tend to drive toward thermodynamic limits. Second, Si is only a donor when sitting on a Group III lattice site, but MEE creates Group III-rich surfaces. However, electron concentrations as measured by Hall were virtually identical whether the Si was provided simultaneously with Group III atoms or in the middle of the As soak. It appears that Si preferentially takes surface Group III sites even on an arsenic-poor surface. Using these self-aligned regrowth techniques, we have fabricated the first III-V MOSFETs with self-aligned regrowth of source-drain contacts. These techniques will enable lateral scaling of future III-V MOSFETs and HEMTs to tens of nanometers.

1:50 PM Student

G2, Transport Properties of δ -Doped InSb/Al_{1-x}In_xSb Quantum Well Heterostructures with Varying Subband Occupation: *Oliver Pooley*¹; Adam Gilbertson²; Louise Buckle³; Stuart Coomber³; Martin Emeny³; Mike Fearn³; Phil Buckle³; Lesley Cohen²; Tim Ashley³; ¹University of Manchester; ²Imperial College; ³Qinetiq

Electronic transport in remotely doped heterostructures is a subject of great interest in the fields of high-speed electronics (high electron mobility transistors – HEMTs) and ballistic mesoscopic devices. In devices where ballistic transport is a requirement, it is necessary to optimise both the carrier mobility and concentration in the two-dimensional electron gas (2DEG). High quality growth of InSb-based heterostructures is presented. Due to the large lattice mismatch between InSb and its alloy AlInSb, growth is challenging. However, when compared to the more common III-V compounds such as GaAs, InSb offers several advantages - the lowest bulk electron effective mass and narrowest band gap of any (III-V) semiconductor (0.014m_e and 170meV at room temperature), a large dielectric constant (16.8ε₀) and a large Landé g-factor (~-51). We present variable temperature Hall measurements on 30nm δ -doped InSb/Al_{1-x}In_xSb quantum well heterostructures, with different well to dopant separation and top cap thickness. Data are presented between 4.5K and 300K. Carrier modulation is achieved by application of bias to a top metal gate. At 4.5K (300K) samples have carrier densities that range from $2.0 \times 10^{11} \text{cm}^{-2}$ ($3.4 \times 10^{11} \text{cm}^{-2}$) to $2.5 \times 10^{12} \text{cm}^{-2}$ ($2.8 \times 10^{12} \text{cm}^{-2}$) and mobilities from 48 000cm²/Vs (20 000cm²/Vs) to 256 000cm²/Vs (47 500cm²/Vs). Based on these results, heterostructures are modelled using a self-consistent Schrodinger-Poisson approach. It is shown that within the set of samples available there is both single and multiple subband occupancy. Mobilities are explained within a model based on the relaxation time approximation. From this model, we conclude that low temperature mobilities are limited by remote ionised impurity (RII) scattering and high temperature mobilities are dominated by phonon scattering. The change in mobilities between samples with differing heterostructure designs but with similar carrier concentrations is accounted for by this model. In order to fully understand the mobilities in samples with identical designs but different doping, it is necessary to understand the significance of single and multiple subband occupancy. We also demonstrate a change in the transport properties (reduction in carrier concentration, increase in mobility) due to the ex situ deposition of dielectric (SiO₂) films of varying thicknesses directly onto the surface. These films are shown to fundamentally alter the relationship between carrier concentration and mobility at both low and high temperature.

2:10 PM

G3, Integration of n- and p-Channel InGaSb Quantum Wells for Low-Power Complementary Logic Circuits: *Brian Bennett*¹; James Champain¹; J. Boos¹; Mario Ancona¹; Nicolas Papanicolaou¹; ¹Naval Research Laboratory

Antimonide-based compound semiconductors have been exploited for low-power, high-frequency, n-channel FETs. LNAs operating at 10-100 GHz consume 3-10 times less power than comparable InP- or GaAs-based circuits. For digital applications, a key to low-power operation is circuits using complementary n- and p-channel FETs. Recently, we demonstrated strain enhancement of hole mobilities in GaSb and InGaSb quantum wells, with room-temperature values reaching 1300-1500 cm²/V-s.² These quantum wells were used in p-channel FETs.³ Intel/Qinetiq examined InSb-channel FETs with mobilities of 1200 cm²/V-s and f_T's as high as 140 GHz for a 40 nm gate length.⁴ The current work focuses on identifying a suitable n-channel FET and integrating the n- and p-FETs into a single heterostructure. An n-channel partner for the p-FETs needs to have: a sufficient conduction-band offset for electron confinement, a similar lattice constant, and enhancement-mode performance. Based upon the calculated band structure, it may be appropriate to use the same antimonide material for the n- and p-channels. We grew modulation-doped GaSb/AlGaSb and InGaSb/AlGaSb heterostructures. The structures are p-type in the absence of intentional doping. Nominally sufficient levels of Te-doping result in highly-resistive structures. We are able to achieve n-type doping by using extremely high levels of Te doping; activation efficiencies are only about 3%. Other groups also reported extremely high n-type doping for GaSb⁵ and InGaSb⁶ n-FETs. We speculate that a high density of deep traps exists in either the well or barrier. For GaSb and In_{0.2}Ga_{0.8}Sb quantum wells, we achieved room-temperature mobilities as high as 7000-9000 cm²/V-s. We designed a structure in which a single In_{0.2}Ga_{0.8}Sb layer serves as

both the n- and p-channels. It was grown by MBE on GaAs, and consisted of a relaxed 1.5 μm buffer layer of Al_{0.8}Ga_{0.2}Sb, followed by 10- nm In_{0.2}Ga_{0.8}Sb, 10-nm Al_{0.8}Ga_{0.2}Sb, 5-nm In_{0.2}Al_{0.8}Sb, Te-delta-doping, 6-nm Al_{0.8}Ga_{0.2}Sb(Te), 3-nm Al_{0.8}Ga_{0.2}Sb, 4-nm In_{0.2}Al_{0.8}Sb, and 2-nm InAs. The In_xGa_{1-x}Sb channel is in biaxial compression, with a 1% strain. As-grown, the structure was n-type with an electron mobility of 4000 cm²/V-s. After removal of a portion of the upper barrier, the dominant carrier switched to holes, with a mobility near 850 cm²/V-s. Previous research in this area used separate channels for the n- and p-FETs, with hole mobilities less than 300 cm²/V-s. The next steps will be to fabricate enhancement-mode n- and p-FETs from the same structure and incorporate a suitable oxide. ¹B.R. Bennett et al., SSE 49, 1875 (2005). ²B.R. Bennett et al., APL 91, 042104 (2007); JCG 311, 47 (2008). ³J.B. Boos et al., Electr. Lett. 43, 834 (2007). ⁴M. Radasavljevic et al., IEDM Tech. Dig., 727 (2008). ⁵X. Li et al., SSE 41, 1853 (1997). ⁶G. Delhaye et al., JAP 104, 066105 (2008).

2:30 PM

G4, Strain Balanced InAs/InAsSb Superlattices for Mid IR Photodetectors:

*David Lackner*¹; Tom Cherng¹; Oliver Pitts¹; Michael Steger¹; Michael Thewalt¹; Simon Watkins¹; ¹Simon Fraser University

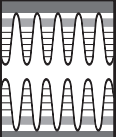
InAs_{0.91}Sb_{0.09} lattice-matched to GaSb has received steady attention in the past few years for optical detectors in the 3-5 micron range. Attempts to increase the detection wavelength by increasing the Sb mole fraction have been hindered by the lack of lattice-matched substrates. In this work we report the growth of strain balanced InAs/InAsSb superlattice structures lattice-matched to GaSb for potential application in photodetectors beyond 5 microns. The strain balanced method permits the incorporation of larger Sb mole fractions in the Sb layers, considerably extending the absorption cutoff. For equal InAs and InAsSb layer thicknesses, strain balance is achieved at an Sb mole fraction of 0.18. Calculations based on accepted band bowing parameters for InAsSb, including strain effects, predict a 77K bandgap wavelength of over 5 microns for the lattice-matched structure. We have grown a series of InAs/InAsSb strain compensated superlattices with equal layer thicknesses of 20 nm. The layer structures were grown by organometallic vapor phase epitaxy. Structural quality was investigated in detail by high resolution XRD, TEM, STEM, and EDS. We report the observation of PL emission as a function of Sb content in the InAsSb wells. A 4.2K emission wavelength of 5.0 microns is observed for an Sb mole fraction of 0.15 in the InAsSb layers. PL emission is at least 60 meV lower than expected compared with simple calculations based on accepted bowing and strain parameters. While this could be interpreted as evidence for type II band alignment between InAs and InAsSb, we do not see the usual blue shift as a function of excitation intensity normally seen in type II material combinations. It is more likely that the reduced emission energy is due to compositional fluctuations in the InAsSb. These structures will be eventually incorporated in pin heterojunction photodiodes, however narrow gap materials such as InAsSb suffer from large thermal diffusion currents, especially near room temperature. One solution is to use a heterojunction structure in which the InAsSb is bounded by a wider gap layer. Our approach has been to use an Al-free compound semiconductor more compatible with OMVPE, such as InPSb. Here, we report on the electrical properties of p-InP_{0.7}Sb_{0.3}/i-InAsSb/n-GaSb heterojunction diode structures. The data indicate a large improvement in diode properties relative to p-InAsSb/n-InAsSb homojunction structures grown on GaSb. Ideality factors of 1.76 and 5.7 were observed at 292 and 77K respectively, and R₀A values as high as 172 and 3051 Ohm-cm² were observed at 292 and 77K respectively. An additional complication with this material combination is the potential formation of a rectifying junction at the i-InAsSb/n-GaSb interface. At high GaSb doping conditions (>>10¹⁷ cm⁻³) we show that this junction becomes Ohmic due to tunneling.

2:50 PM Student

G5, Performance Augmentation of InAs/GaSb Superlattice LWIR Detectors by Surface Treatments: *Maya Narayanan Kutty*¹; Elena Plis¹; Arazhou Khoshakhlagh¹; Stephen Myers¹; Nutan Gautam¹; Sanjay Krishna¹;

¹University of New Mexico

Infrared detectors operating in the long wave infrared (LWIR) regime (12–32μm) are widely used for missile detection and tracking, medical diagnostics and treatment, and surveillance. The current commercial detector technologies



available for this wavelength range are Mercury-Cadmium-Telluride (MCT) and quantum well infrared (QWIP) detectors. There are problems in the epitaxial growth of mercury-based compounds which limit manufacturing yield for MCT large area focal plane arrays (FPAs). QWIPs have larger dark currents and lower quantum efficiency compared to the interband devices. Over the past two decades, InAs/ (In, Ga) Sb strained layer superlattices (SLSs) have been investigated as an attractive alternative technology to the present-day IR detection systems. The effective bandgap of the SLS can be tuned by modifying the individual material thickness. SLS technology combines advantages of normal incidence absorption, low tunneling currents, compositional uniformity over a large area and commercial availability of low defect density substrates. Moreover SLS-based devices are predicted to have enhanced carrier lifetimes due to suppressed Auger recombination processes. Present-day fabrication of SLS based detectors involves definition of the physical dimensions of the device, which results in the exposure of its sidewalls. Generally GaSb and its alloys possess poor reproducibility of surface characteristics due to non-optimized etch processes. Best sidewall-profiles are usually obtained by plasma assisted isotropic etch processing which damages the surface, leading to excessive surface leakage currents. We believe by optimization of etching procedures we can improve the performance of LWIR SLS devices significantly while maintaining a good sidewall profile. For our initial experiments, we have investigated various chemical etchants on (100) 525 μm thick Te doped ($n\sim 5\times 10^{17}\text{cm}^{-3}$) GaSb substrates. The HCl: H₂O₂: H₂O solution gave us the optimal surface morphology and etching rate. The next set of experiments will compare the performances of single pixel molecular beam epitaxially (MBE) grown SLS detector ($\lambda_{\text{cutoff}}\sim 12\mu\text{m}$) which are fabricated using three methods, namely, plasma assisted etch only, previously optimized chemical etch and combinations of both. The absorbing region of the detector was formed by 16ML InAs/6MLGaSb with imposed InSb interfaces. The aim of our work is to bridge the surface characteristics with device stability and reproducibility of performance. The correlation between conditions of the etching processes and improved signal to noise ratio of the studied device will be presented.

3:10 PM Break

Session H: Epitaxy for Devices

Wednesday PM Room: 105
June 24, 2009 Location: Pennsylvania State University

Session Chair: Brian Bennett, Naval Research Laboratory

3:30 PM Student

H1, Comparison of Device Performance of Light Emitting Transistors with Zn-Doped and C-Doped Base: *Yong Huang*¹; Jae Hyun Ryou¹; Forest Dixon²; Milton Feng²; Nick Holonyak²; Russell Dupuis¹; ¹Georgia Institute of Technology; ²The University of Illinois at Urbana-Champaign

Light emitting transistors (LETs) operating at around 1.55 μm were investigated using InP/InAlGaAs material system grown by metalorganic chemical vapor deposition (MOCVD). Device epitaxial structures were achieved by incorporating InGaAs quantum wells (QWs) in the base region of the N-InP/p-InAlGaAs/N-InAlAs heterojunction bipolar transistors (HBTs), and both current gain and long-wavelength light emission were obtained. It was found that control of the p-type doping profile in the base layer is one of the key factors that dictate the performance characteristics of long wavelength LETs. Epitaxial growth of the devices was carried out between 600°C and 650°C at a reactor chamber pressure of 100 Torr. Both Zn and C were used as the p-type dopant in this study. A typical NpN LET structure consists of (from the bottom to the top) a Si-doped InP subcollector, an undoped In_{0.52}Al_{0.48}As collector, an undoped In_{0.53}(Al_{0.25}Ga_{1-x})_{0.47}As grading layer with x_{Al} from 1 to 0.25, a Zn- or C-doped In_{0.53}(Al_{0.25}Ga_{0.75})_{0.47}As base/active region with an undoped compressively-strained In_{0.58}Ga_{0.42}As QW embedded in the middle of the base layer, an InP:Si emitter and an emitter contact. The devices were fabricated using

standard optical lithography and wet chemical etching to form an emitter and base mesa. AuGe/Ni/Au was used as the emitter and collector ohmic contacts and Au/Zn/Au as the base contact. Secondary ion mass spectrometry (SIMS) shows that in the LET with Zn-doped base Zn diffuses into both emitter and the adjacent graded collector, while in the C-doped LET, C stays in place and forms abrupt junctions. The turn-on voltages are 0.89 V and 0.78 V for the Zn-doped LET and the C-doped LET, respectively, indicating the presence of a potential spike at emitter-base junction due to Zn diffusion. In addition, Zn diffusion into the undoped QW region degrades the optical quality by creating non-radiative recombination centers, which is confirmed by the electroluminescence (EL) peak power for both devices. The C-doped SQW LET exhibits much higher light output owing to the intact active layer. C-doped LETs have a higher emitter injection efficiency and luminescence efficiency, but it is not granted without a problem. Whereas Zn will inevitably diffuse into active region and plague the QW, Zn can be contained only in the base region through proper engineering of growth conditions. It was found that Zn-doped LET has a much higher current gain. The diffusion-suppressed Zn-doped LET has a DC current gain of 45 in sharp contrast to the low current gain of about 0.25 in the C-doped LET. Short minority carrier lifetime in C-doped materials is considered to account for the low gain, which is possibly due to the low growth temperature and low V/III ratio used during C-doping.

3:50 PM Student

H2, Annealing Stability of Nanoparticle-Enhanced Tunnel Junctions for High-Efficiency Solar Cells and Mid-Infrared Lasers: *Adam Crook*¹; Hari Nair¹; Karun Vijayraghavan¹; Mark Wistey²; Jeremy Zimmerman³; Joshua Zide⁴; Arthur Gossard²; Seth Bank¹; ¹University of Texas at Austin; ²University of California, Santa Barbara; ³University of Michigan; ⁴University of Delaware

Low-loss tunnel junctions are essential for a number of devices and applications, particularly interconnecting the junctions of solar cells and minimizing electrical/optical losses in vertical-cavity surface-emitting lasers (VCSELs). They are particularly attractive for longer wavelength lasers because performance fundamentally degrades due to increasing p-type free carrier absorption (FCA). We have recently proposed tunnel junctions as an attractive approach for realizing high-efficiency mid-infrared diode lasers in the $\sim 3\text{-}5\ \mu\text{m}$ range for chemical/biological sensing and laser-based countermeasures. We investigate the stability of ErAs nanoparticle-enhanced tunnel junctions to post-growth thermal annealing. This thermal stability is essential for dilute-nitride devices including lasers and future 4-junction solar cells. One issue with traditional tunnel junctions is obtaining high active n-type carrier concentrations. For example, Si-doped GaAs is practically limited to a free electron concentration of $\sim 5\times 10^{18}\ \text{cm}^{-3}$, especially if the sample is subjected to post-growth annealing, as is necessary for dilute-nitride materials. Dopants such as Tellurium can produce higher active concentrations, but are undesirable because of their high diffusivity and vapor pressure that can corrupt doping profiles and background carrier concentrations, degrading device performance. Therefore, traditional tunnel junctions are incompatible with GaInNAs(Sb)-based devices, such as 4-junction solar cells and dilute-nitride lasers. Most rare earth mononictides (e.g. ErAs and ErSb) are rocksalt semimetals that may be embedded as epitaxial nanoparticles within a III-V matrix. Inclusion of these nanoparticles at the tunnel junction interface provides additional states that allow tunneling to occur via a two-step process, effectively halving the tunneling distance for each step, dramatically increasing tunnel currents. Indeed, we observed a 10⁵x enhancement in tunneling current, under both forward and reverse bias, with the introduction of 1.2 monolayers of ErAs ($\sim 30\%$ surface coverage of nanoparticles ~ 4 MLs in height). This dramatic tunneling enhancement significantly reduces the amount of n- and p-doping required for an efficient tunnel junction. The reduction of the acceptor doping substantially reduces p-type FCA losses for high-efficiency lasers and also allows low-loss tunnel junctions for solar cells, despite the limited ($\sim 5\times 10^{18}\ \text{cm}^{-3}$) n-doping. While ErAs nanoparticles are thermodynamically stable embedded within GaAs, the robustness of these tunnel junctions to thermal annealing has not yet been studied. We will present a systematic study of nanoparticle-enhanced tunnel junctions, comparing unannealed devices with those that have been subjected to rapid thermal annealing that is consistent with the optimal post-

growth annealing required for dilute-nitride devices. One key issue is whether the shaping of nanoparticles into rods or pyramids, which can further enhance tunneling currents by $\sim 5\text{-}7\times$, is stable under annealing.

4:10 PM

H3, AlGaInSb-VECSEL Grown on GaAs Based DBRs for High-Power Emission at 2 μm : *Thomas Rotter*¹; Ganesh Balakrishnan²; Diana Huffaker¹; Jerome Moloney³; Joerg Hader³; Mike Yarborough³; ¹University of California, Los Angeles; ²University of New Mexico; ³University of Arizona

This presentation focuses on the growth of a high power optically pumped VECSEL structure operating at 2 μm with a GaInSb QW ($a_0 = 6.09 \text{ \AA}$) based active region on GaAs/AlGaAs distributed Bragg reflectors (DBR) ($a_0 = 5.65 \text{ \AA}$). The reason for using a GaAs based DBR is its superior heat conductivity and reduced absorption at the laser wavelength in comparison with GaSb based DBRs, which is expected to make higher VECSEL output powers possible. The growth of the GaSb based active region on GaAs is facilitated by an interfacial misfit (IMF) dislocation array, which relaxes the strain due to the lattice mismatch at the GaSb/GaAs interface. It eliminates the need for a thick metamorphic buffer to bridge the lattice mismatch between GaAs and GaSb, and thereby provides the opportunity to take advantage of the long wavelength emission from GaSb based active regions in conjunction with a mature DBR technology based on AlGaAs/GaAs. We will provide a detailed analysis of the IMF growth mode and the quality of the III-Sb material grown upon it using TEM, XRD and surface morphology characterization. The III-Sb based VECSEL active region is grown by MBE on an MOCVD grown DBR consisting of 25 pairs of 149nm GaAs / 172 nm Al_{0.95}Ga_{0.05}As. Its reflectivity maximum of 99.5 % is centered at 2 μm . The surface roughness as measured by AFM is 0.3 nm RMS, which is slightly higher than the typical 0.2 nm of an epi ready GaAs substrate. There are two main technical challenges related to the MBE growth of the VECSELS. First, the IMF based growth of III-Sb on GaAs leads to differences in strain and relaxation of the epilayer as compared to growth on GaSb substrates. This influences the optical emission from the III-Sb active region, since it depends on the compressive strain in the quantum wells. It requires an independent development of the active region, grown on GaAs. Second, the transfer of the IMF growth technology from growth on GaAs substrates to growth on the MOCVD grown AlGaAs/GaAs DBR is nontrivial. At a pumpwavelength of 1064nm (Nd:YAG laser) pulsed operation was shown using the VECSEL chip without advanced cooling technology and cw operation has been achieved using a SiC heatspreader bonded to the VECSEL surface. Pulsed operation with 1 μs pulses and 330 Hz repetition rate showed output powers between 8W (at threshold) and 200W. These results were achieved with the VECSEL chip as grown mounted on a heatsink at 15°C, using an output coupler with 10cm radius of curvature and 98% and 96% reflectance.

4:30 PM

H4, Fabrication of Narrow Ridges for High-Performance High-Temperature cw Interband Cascade Lasers: *Chulsoo Kim*¹; Mijin Kim¹; William Bewley¹; J. Lindle¹; Chadwick Canedy¹; J. Abell¹; Igor Vurgaftman¹; Jerry Meyer¹; ¹Naval Research Laboratory

Cw room-temperature operation of interband cascade lasers (ICLs) was recently achieved by means of careful optimization of the doping profiles and stage number. A narrow-ridge electroplated ICL emitting at $\lambda = 3.75 \mu\text{m}$ lased cw up to a maximum temperature of $T_{\text{max}} = 319 \text{ K}$ and produced 13 mW of cw power at 300 K and 40 mW at 275 K. Furthermore, an ICL emitting at 3.3 μm operated cw up to 334 K, which is the highest operating temperature for any semiconductor laser in the 3.0-4.6 μm spectral range. Further improvements in the ICL performance may be obtained once the processing of the narrow-ridge waveguides is optimized. Owing to very anisotropic conductivities in the superlattice claddings and the active region of the ICL, significant current spreading can occur unless ridge waveguides are defined by etching through the active region of the devices. For the present test, two similar 5-stage ICL structures were grown by MBE. Ridges with 9 μm width were defined by photolithography followed by reactive-ion etching of a Si₃N₄ etch mask. The ridge was etched through the active region to a depth of 4.8 μm using Cl-based inductively-coupled plasma (ICP) etching machine. The two samples were etched at different ICP powers, (a) 2000 W and (d) 1000 W. The SEM

micrographs of the final devices are shown in Fig. 1. The reduced ICP power results in less steep sidewalls, and less damage from radical ions is expected. After the ICP etching, four different wet etching conditions were applied to the samples, (b) and (c) for the first sample shown in (a) and (e) and (f) for the second sample shown in (d). The structures were etched in a phosphoric-acid base etchant in order to remove some of the damage from the ICP etching, and the cleaning process was carried out typically within 5 minutes of the plasma-enhanced chemical vapor deposition of the Si₃N₄ film. As shown in Fig. 1, the relatively-thick AlSb injection barriers in each stage were selectively undercut with different etch depths, (b) 127.6 nm, (c) 67.7 nm, (e) 31.6 nm, and (f) 16.2 nm respectively, due to the preferential etching by phosphoric acid. The ratio of the cw threshold current density j_{th} for the narrow-ridge devices to that for 150- μm -wide broad-area lasers at 78 K is shown in Fig. 2. The value of j_{th} is clearly negatively impacted by the undercut. Fig. 3 plots the increase in j_{th} (78 K) as the ridge is made narrower, which underscores the importance of the processing optimization for making single-lateral mode devices. The room-temperature j_{th} for the previously developed etch and the one employed in Fig. 1(f) are shown in Fig. 4.

4:50 PM H5, Late News

Session I: Quantum Dot Optical Characterizations and Photonic Devices

Wednesday PM
June 24, 2009

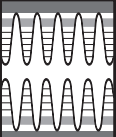
Room: 106
Location: Pennsylvania State University

Session Chairs: Garnett Bryant, National Institute of Standards and Technology (NIST); James Merz, University of Notre Dame

1:30 PM Student

I1, Lasing of Whispering-Gallery Modes in Asymmetric Waveguide GaInP Micro-Disks with InP Quantum Dots: *Yaya Chu*¹; A. Mintairov¹; Y. He¹; J. Merz¹; N. Kalyuzhnyy²; V. Lantratov²; S. Mintairov²; ¹University of Notre Dame; ²Ioffe Physical Technical Institute

Whispering-gallery-mode (WGM) semiconductor microdisk (MD) resonators with embedded quantum dots (QDs) are interesting for the realization of low threshold lasers and for solid-state cavity quantum electrodynamics (CQED) experiments, as was demonstrated using InGaAs/GaAs [1-3], GaAs/AlGaAs [4] CdSe/ZnSe [5] and Ge/Si [6] QD materials. In the present paper we report for the first time the fabrication and lasing properties of WGM GaInP MDs with InP QDs, which has the advantage of large dot sizes ($\sim 100 \text{ nm}$), small dot density ($5 \times 10^9 \text{ cm}^{-2}$) and emission wavelengths near the $\sim 750 \text{ nm}$ spectral range [7], which is not available for other material systems. GaInP MDs (radius $R = 1\text{-}4 \text{ \AA}956 \text{ mm}$) with InP QDs were fabricated on Si or GaAs substrates by using either a wafer bonding (WB) [8] or a wet oxidation (WO) technique [9]. Sharp lines related to $\text{TE}_{m,l}$ and $\text{TM}_{m,l}$ ($m = 28\text{-}10$, $l = 1, 2$) WGMs have been identified in the photoluminescence spectra of these MDs. Near-field optical scanning microscopy measurements reveal that between one and five InP QDs are coupled to WGMs in these MDs. A lasing threshold power of 6.956W was measured for a $\text{TE}_{21,1}$ mode in a WO MD having radius $R = 2 \text{ \AA}956 \text{ m}$ and quality factor $Q = 5 \times 10^3$. Lasing from a few (or even a single) dot was manifested by the absence of a decrease in the line-width of the mode near the threshold. The Purcell factor P_F [10] was calculated to be 63.4, which corresponds to a spontaneous emission rate of $\gamma_{46} = 0.91$ [11] and which is in excellent agreement with the experimental value 0.9 obtained from an emission versus excitation intensity curves [12]. We believe that this is the first observation of room-temperature CW optically-pumped lasing in InP QD MDs. [1]. H. Cao, et al., Appl. Phys. Lett. 76, 3519 (2000); [2] P. Michler, et al., Appl. Phys. Lett. 77, 184 (2000); [3] A. Kiraz, et al., Appl. Phys. Lett. 78, 3932 (2001). [4]. E. Peter, et al., Phys. Rev. Lett. 95, 067401 (2005) [5] J. Renner, et al., Appl. Phys. Lett. 89, 231104 (2006) [6]. J. S. Xia, et al., Appl. Phys. Lett. 91, 011104 (2007). [7] D. A. Vinokurov, et al., Semiconductors, Vol. 35 (2), pp. 235-237 (2001) [8]. Y. Chu, et al., Phys.



Lett. A (in press) [9]. S. A. Blokhin, et al., Phys. of Semiconductor Devices 40, 476 (2005). [10] J. M. Gérard and B. Gayral, J. J. Lightwave Technol. 17, 2089 (1999) [11] G. S. Solomon, et al., Phys. Rev. Lett. 86, 3903 (2001)[12]. G. Björk, et al., IEEE J. Quantum Electronics 27, 2386 (1991).

1:50 PM Student

I2, Nanocrystal Laser from Colloidal InP/ZnS Quantum Dots: *Shuai Gao*¹; Chunfeng Zhang¹; ¹Pennsylvania State University

Colloidal semiconductor nanocrystal quantum dots (NQDs) have emerged as a new family of optical gain media featuring high efficiency, broad wavelength coverage, temperature insensitivity and low lasing threshold. Amplified spontaneous emission (ASE) and lasing from Cd(S,Se,Te)-based NQDs have been realized with a variety of photonic structures including microrings, microspheres, photonic crystals, and distributed feedback resonators. Nevertheless, the toxicity of cadmium will hinder most of their applications due to the environmental concerns. To this end we have investigated ASE and lasing properties of InP NQDs as a new family of cadmium-free nanocrystalline gain medium. In the present study, we modified the existing synthetic technique to grow InP/ZnS NQDs as a new family of cadmium-free nanocrystalline gain medium: InP cores were synthesized in a non-coordinating solvent by injecting P(TMS)₃ to the In(Ac)₃ in the presence of fatty acid precursors. By employing fatty amine precursors, the temperature of InP nucleation has been altered significant from the early reported values. The technique of successive ion layer adhesion and reaction (SILAR) method was applied to synthesize ZnS shells by consecutively injecting, to the reaction solution, zinc and sulfur precursors at precisely determined doses. By controlling the NQD size, the emission can be tuned continuously from 530nm to 700nm upon the variation of the amount of the fatty acid in the reaction solution. The quantum yield of the as prepared InP/ZnS QDs was measured to be as high as =50%. We have observed, for the first time, amplified spontaneous emission and optical gain in close-packed InP/ZnS NQD films upon UV excitation. Moreover, the optical gain profile of InP/ZnS NQDs was matched to the second order feedback of holographic polymer-dispersed liquid crystal (H-PDLC) gratings, leading to the very first demonstration of an optical pumped, nanocrystal laser based on InP/ZnS NQDs. The output color can be selected by tailoring the size of InP/ZnS nanocrystals and the grating periodicity.

2:10 PM I3, Late News

2:30 PM Student

I4, Properties of InAs/GaAs Quantum Rings and Their Application to Terahertz Detection: *Guan Huang*¹; Wei Guo¹; Pallab Bhattacharya¹; Gamin Ariyawansa²; A. G. U. Perera²; ¹University of Michigan; ²Georgia State University

Semiconductor quantum rings are interesting nanostructures whose electronic and optical properties can be of interest for a variety of applications. In the present study, we have investigated the formation and electronic properties of the quantum rings and those of THz Quantum Ring Intersubband Detectors (QRIDs) designed and fabricated with QR active regions. An ensemble of QRs was formed as follows. Self organized InAs QDs were first grown by MBE on GaAs at 530°C. A pair of GaAs/AlAs capping layers with thickness 10/10 Å was then deposited at the same temperature to partially cover the QDs, after which the substrate temperature was ramped up by 30°C. During this annealing process, the center uncovered area of the QD evaporated and diffused outward to form the rings. After the QR formation, an 8nm GaAs capping layer was deposited at the annealing temperature and followed by 3 min annealing at 600°C. In the detector heterostructures, the QRs were doped n-type with Si at an estimated doping level of 1.5-2 electrons per ring. The areal density of the QRs is estimated to be 10¹⁰cm⁻² from AFM measurements. At 300K, photoluminescence measurements show a peak at 1.1 μm. The electron energy levels of the quantum rings were calculated by the effective mass technique. Three electron states at 161, 60 and 39meV below the GaAs band edge and several hole states are found to be present. Capacitance-voltage measurements were made to determine the spectral position of the bound electron and hole levels in the quantum rings. The Schottky barrier heterostructures were grown with a single buried QR layer, n- or p-type back contact layers (for the measurement

of electron and hole energy levels, respectively) and a tunnel barrier layer. The measured capacitance-voltage characteristics were analyzed and the energy position of the electron and hole ground states agree extremely well with the theoretically calculated values. The terahertz detector heterostructures with top and bottom n-contacts were designed, grown and fabricated for surface-normal top illumination. 15 QR layers were incorporated in the active region. The measured dark current densities at a bias of -1V are 5×10⁻⁵, 4.7×10⁻² and 3.5×10⁻¹A/cm² at 4.2, 80 and 300K, respectively. Normal incidence spectral response measurements in the range of 7-120K reveal three response peaks at ~6.5 THz (48μm), 10THz (30μm) and 12.5THz (25μm) upto 80K. The spectral extent of the first response peak extends to ~3THz. The intersubband transition energies are in excellent agreement with the calculated electron energy levels in the QRs. The calibrated responsivity values are ~23 mA/W and 37mA/W for the 6.5 and 10THz response at 80K. The specific detectivity D* is measured to be 1.4×10⁹ at 80K for the 6.5THz response. Work supported by AFOSR and NSF.

2:50 PM

I5, Energy Transfer Pumped Efficient Infrared Colloid Quantum Dot Light Emission Diodes: *Chunfeng Zhang*¹; Ting Zhu¹; Shuai Gao¹; Jian Xu¹; ¹Pennsylvania State University

Semiconductor nanocrystals quantum dots (NQDs) have been regarded as excellent phosphors for next generation's light emitting devices due to their high photoluminescence efficiency, color tunability, temperature insensitivity, and robust stability. NQD light emitting diodes (LEDs) with emission wavelength range from blue to infrared have been made in last few years. These LEDs show potentials in upgrading some of today's photonic technique. For instance, the visible CdSe NQD LEDs can be used for displaying and lighting, and the PbS/PbSe NQD LEDs can be designed for telecommunication since the infrared (IR) emission light (1200~1600 nm) covers the most important communication wavelengths. Nevertheless, due to the difficulty of high density current injection, efficiencies of these LEDs with the conventional designs are limited. In this work, we report our recent design of IR NQD LEDs with two-order higher efficiency based on resonant energy transfer (ET) pumping. In this design, the active layer was chosen to be hybrid composite of polymer (MEH-PPV) and PbSe NQDs. Förster type ET process is in charge of energy injection from polymer to NQDs since emission band of polymer locates in the absorption band of NQDs. Well-passivated PbSe NQDs were synthesized based on the noncoordinating solvent technique with size monitored by visible/IR absorption spectroscopy. By over-night stirring, the blending of PbSe NQDs in MEH-PPV solution was realized via linking coated ligands to polymer. Prior to the devices, we tested the ET processes in the composite by photoluminescence excitation (PLE) spectra and time-resolved PL spectroscopy. PLE spectra were recorded with emission wavelength fixed at the NQD emission range. In the well-prepared polymer/NQD composites, a significant peak at the maximum of polymer absorption can be observed. Typically, in the composites with efficient ET, excitation efficiency ratio at 510 nm (polymer absorption peak) is over 20 to that at 400 nm (polymer absorption valley). Dynamical characterization on the ET was based on time-resolved PL study of the polymer emission. Efficient ET from polymer to NQD increase the relaxation rate. In our test, a 30% wt NQD doping typically leads the lifetime reduction from ~340 ps to ~150 ps. Estimated by the measured data, ~60% of the harvested energy by polymer will transfer to PbSe NQDs. To characterize the performance of new designed devices, we compared it with LEDs based on the conventional layer by layer design. At the same current density, the electroluminescence intensity is over 100 times higher and the maximum output is over 200 times higher in the new designed hybrid LEDs.

3:10 PM Break

Session J:

Quantum Dot Materials Characterization and Epitaxy

Wednesday PM
June 24, 2009

Room: 106
Location: Pennsylvania State University

Session Chairs: Ben Shanabrook, Naval Research Laboratory; Diana Huffaker, University of California, Los Angeles

3:30 PM

J1, Isotopically Controlled Semiconductor Low Dimensional Systems: *Oussama Moutanabbir*¹; ¹Max Planck Institute of Microstructure Physics

Over the last two decades, the availability of silicon and germanium enriched isotopes impacted our understanding of subtle physical properties of bulk materials and thin films. It is well established now that the isotopic composition affects several properties, such as phonon energies, band structure, and lattice constant. Large isotopic effects were also reported for thermal conductivity. More subtle nuclear spin-related isotopic effects have led to the development of new concepts in solid-state quantum information and spintronics. Simultaneously to the progress in semiconductor stable isotope research, the study of phenomena and manipulation of matter on the nanoscale has attracted a great deal of attention motivated by the novel functionalities achievable by exploiting the size-related properties. Enormous efforts have been put to develop new nanofabrication processes. In this work, we propose to manipulate the isotopic composition of Si and Ge-based nanosystems. In the first part of this presentation, the atomic transport during the strain-driven self-assembly of Ge/Si nanocrystals will be addressed. By using ⁷⁰Ge and ⁷⁶Ge enriched isotopes, we developed a method to highlight subtle mechanisms in the growth of strained Ge/Si nanostructures via Stranski-Krastanov mode. This growth process is characterized by a transition from a strained metastable 2D layer to 3D islanding to relieve the compressive strain due to lattice mismatch between Si and Ge. Here we used ⁷⁶Ge to grow the 2D layer and the transition to 3D nanodots was insured by a ⁷⁰Ge beam. Based on this 2-isotope growth, we were able to distinguish between the atoms originating from the metastable 2D layer and those from the direct beam during the growth of strained Ge/Si nanodots. Micro-Raman spectroscopy was used to study the nanodot Ge-Ge and Si-Ge intrinsic optical phonon modes. Within the harmonic approximation, the frequencies of these modes allow the quantification of the surface mass transport during the nucleation and growth. At a deposition temperature of 620 °C, we found that at the early stage of the growth more than 85% of Ge atoms in nanodot originate from the strained metastable 2D layer. This shows that the atoms in the 2D migrate easily to the growing nanodots compared to the atoms from the direct beam. A detailed model of the atomic processes in the strain-mediated self-assembly will be presented. In the second part, we will demonstrate that the manipulation of the isotopic composition in low dimensional Si structures creates new opportunities to explore fundamental science and improve our understanding of the physical properties of Si-based nanosystems. Acknowledgment: Heartfelt thanks are extended to S. Miyamoto, K. M. Itoh (Keio University), S. Senz, Z. Zhang, U. Goesele (Max Planck Institute of Microstructure Physics), and E. E. Haller (UC Berkeley)

3:50 PM Student

J2, MBE Growth of Highly Tensile Strained Thin Ge Layers: *Yijie Huo*¹; Hai Lin¹; Yiwen Rong¹; Theodore Kamins²; James Harris¹; ¹Stanford University; ²Hewlett-Packard Laboratories

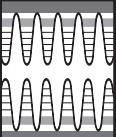
In the past few years, germanium has become an important optoelectronic material due to its nearly direct band gap properties and their advantages. In theory, tensile strained Ge has much higher electron and hole mobilities than bulk Ge. Furthermore, with about 1.4% biaxial tensile strain, Ge becomes a direct band gap material enabling numerous optoelectronic applications in the group IV material system. Liu et al. used the thermal expansion coefficient difference between Ge and Si to achieve 0.3% tensile strained Ge layer. Recently, Bai et al. have grown up to 1.37% tensile strained Ge on top of InGaAs buffer layers by metal-organic chemical vapor deposition. Ge quantum dots were formed if higher strain was applied. In this paper, we report Ge growth on InGaAs buffer

layers by molecular beam epitaxy (MBE), which is strained as high as 2% and has the potential to become a direct band gap semiconductor. All of the samples studied in this work were grown on (100) semi-insulating GaAs wafers. First, one or two layers of step-graded, lattice relaxed InGaAs buffer layers were grown in a III-V MBE system. High temperature anneals were performed after each InGaAs layer growth to reduce the threading dislocation density. After transferring the wafer to a group IV MBE chamber under ultra high vacuum (~10⁻⁹ Torr), a thin layer of 10 nm Ge was coherently grown at a 1 nm/min growth rate. Clear 2x4 and 2x2 surface reconstruction RHEED patterns were observed after InGaAs and Ge growths, respectively. Finally, an InGaAs cap layer was grown to eliminate the surface states of Ge. The 10 nm tensile strained Ge layer between In_{0.3}Ga_{0.7}As layers is clearly illustrated in the SEM image. The cracks in the top cap layer are due to anti-phase domain formation. The AFM image shows the RMS surface roughness is 0.58 nm within a 1x1 μm region. X-ray diffraction (XRD) and Raman scattering were carried out to measure the Ge layer strain. XRD (004) rocking scan and reciprocal mapping were used to determine the in-plane lattice constant of InGaAs buffer layers. From XRD measurement, the strain of Ge layer can be calculated under the assumption that the 10 nm Ge layer is 100% coherent with the buffer layer. Raman spectra were recorded at room temperature in a backscattering geometry. The Ge signal peak red-shift corresponds to tensile strain. The strains of Ge are calculated by both methods and are in good agreement with theory. The Ge layer with as high as 2% tensile strain is achieved in this study. According to our knowledge, this is the highest tensile strained Ge reported so far. Additional characterization and results will be presented.

4:10 PM Student

J3, Application of Mist Deposition Process in the Formation of Semiconductor Quantum Nanodot Films: *Aditya Kshirsagar*¹; S. Ramani¹; K. Shanmugasundaram²; T. Zhu¹; K. Sridhara¹; S. Gao¹; Q. Zhang¹; S. Mohney¹; J. Xu¹; J. Ruzyllo¹; ¹Pennsylvania State University; ²Intel Corp.

Semiconductor quantum dots (NQDs) have gained significant interest due to their utility for quantum confinement, allowing novel optoelectronic and electronic devices. Typically, the deposition of quantum dot films has been done by suspending them in solvent and then spin-coating the resulting colloidal solution on the substrate followed by thermal curing. The limitations of this approach include, among others, inadequate control over nanodot films in the single nm thickness regime and incompatibility of spin-on processes with oddly shaped and/or flexible substrates. Moreover, there are problems in pattern definition in the case of spin-on processes. Mist deposition technology offers an attractive alternative to current methods of thin film formation, which use colloidal solution precursors including spin-on. The principle of mist deposition is to convert the liquid source material into a fine mist with droplet size on the order of 0.25 micron, which is then carried into the deposition chamber in a pressurized stream of N₂ gas, and the droplets are allowed to coalesce on the substrate at room temperature. This forms a uniform film of liquid on the substrate, which can be thermally treated to burn off solvent and leave a thin film of solid on the surface. The effectiveness of mist deposition has been demonstrated earlier in various applications including deposition of high-k dielectrics, organic semiconductors and photoresist. There has been exploratory research regarding the use of mist deposition in the fabrication of quantum dots based LEDs. In this report selected aspects of the process of formation of semiconductor quantum nanodot films by mist deposition are explored. The precursor used in this experiment was CdSe quantum dots (average size 5.5 nm) mixed with toluene at varied concentrations. In the later stage of this study Si nanodots (average size 5 nm) suspended in toluene were also used. Both blanket deposition of CdSe nanodot films as well as films patterned using mechanical masks were carried out. As substrates, Si wafers as well as glass plates and flexible substrates were used. TEM images showing an ultra-thin film formed by CdSe NQDs sandwiched between polymer of Si and glue have been obtained. Fluorescence intensity studies of the CdSe nanodot film patterned using square mechanical masks were carried out. The AFM characterization was employed to monitor changes of the NQD film surface morphology as a function of mask size and deposition time. Using mist deposition, CdSe NQDs were used to fabricate red LEDs and their emission spectrum was obtained.



Overall, the results of this study confirm the potential of mist deposition in the fabrication of NQD films. In the full account of this work, a range of additional results confirming this conclusion will be discussed.

4:30 PM

J4, Formation of Si-Nanocrystals in SiO₂ via Ion Implantation and Rapid Thermal Processing: *Iain Crowe*¹; Andrew Knights²; Matthew Halsall¹; Uschi Bangert¹; Russel Gwilliam³; Reza Kalilikashiban¹; Paul Coleman⁴; ¹University of Manchester; ²McMaster University; ³Surrey Ion Beam Centre; ⁴University of Bath

Silicon nanocrystal (Si-nc) based material systems have already been proposed as candidates for increased efficiency photo-voltaic cells after the recent observation of Multiple Exciton Generation (MEG) [1]. The observation of a tunable room temperature visible luminescence band means that they are also being proposed as novel complimentary nano-phosphors in solid state display and lighting technologies [2, 3]. Reports of optical gain [4, 5] and the compatibility with CMOS processing will make them a very attractive light source for enhanced integrated chip functionality as computing makes the transition to photonics. By using techniques such as ion beam implantation and rapid thermal processing (RTP), improvements in the control over Si-nc size and density can be realized, whilst extending the characterization 'tool-kit' to include complimentary photoluminescence (PL) and positron annihilation spectroscopy (PAS) techniques ought to lead to a wider understanding of the defect types and the role they play in the non-radiative de-excitation of carriers. In this contribution we describe the results of a recent study of the evolution of Si-nc's in thermally grown SiO₂ via ion beam implantation and RTP. We present evidence for the formation of crystalline silicon inclusions, ~2nm in diameter that exhibit efficient room temperature (RT) luminescence around 1.6eV (750 - 800nm) for annealing times as short as ~1s at 1100°C. Their presence is confirmed by measurement of the relatively long PL lifetime, which increased from 30 to 50µs with increasing annealing time from 1 to 100s at 1100°C. Further, we correlate the PL dynamics from the Si-nc ensemble with data obtained using PAS, which we believe provides evidence of defect removal with increasing anneal time, specifically the removal of vacancy-type structural defects at the Si-nc/SiO₂ interface.

4:50 PM Student

J5, Deep Level Traps in Single and Multiple InAs/(InGaAs)/GaAs Self-Assembled Quantum Dot Structures: *Tetsuya Asano*¹; Zhaoqiang Fang²; Anupam Madhukar¹; ¹University of Southern California; ²Wright State University

Since the discovery of strain-driven coherent three-dimensional island formation, self-assembled quantum dots (SAQDs) have been widely studied for scientific interest and device applications owing to their unique properties arising from three-dimensionally confined electronic structures. After nearly two decades of studies on such a highly strained (2-7% lattice mismatch) material structures, minimal densities (<~10⁷/cm²) of extended-defects in single and multiple SAQD structures have been achieved. By contrast, studies on point defects in SAQD structures are very limited. Point defects can create deep levels that can trap and/or scatter carriers, ultimately limiting the performance of SAQD devices. In this presentation, we discuss how deep levels affect the characteristics of quantum dot infrared detectors (QDIPs). Results of deep level transient spectroscopy (DLTS) and secondary ion mass spectroscopy (SIMS) are discussed which reveal that different types of deep levels are present in different layers of the typical SAQD structures. Our previous studies of temperature-dependent dark currents in QDIPs revealed that in 20-period of [2.1ML InAs/20ML InGaAs/GaAs] undoped multiple SAQD (MQD) structures sandwiched by n-doped contact layers, the built-in potential created in the undoped MQD region can become as high as ~ 730 meV under zero applied bias[1]. Such a high built-in potential compared with the electron binding energy in SAQDs (~225 meV) indicates that electrons are trapped in other deeper levels as well, reducing the free carrier density in SAQDs and degrading the device performance. To uncover the characteristics of these deep traps, we performed DLTS measurements on single 2.1 ML InAs SAQD layer capped with 20 ML InGaAs QW embedded in n-doped GaAs and control samples. DLTS spectra were studied at three different combinations of reverse bias and filling pulse

bias to probe the deep levels characteristic of the three different layers: (a) GaAs layer below SAQD layer grown under optimum MBE condition at 600°C. (b) the region across SAQD layer, and (c) GaAs layer above the SAQD layer grown by low-temperature MBE at 500°C. In the overgrown GaAs layer, deep levels with a binding energy ~0.44eV are found with a density of ~2×10¹⁵ /cm³, which can be attributed to native defect-related traps[2]. This highlights the need to improve the quality of overgrown capping layers that are per-force grown at low temperatures. This work was supported by US AFOSR and AFRL. [1] T. Asano et. al., J. Appl. Phys. 104, 113115 (2008).[2] D. C. Look et. al., J. Appl. Phys. 76, 1029 (1994).

Session K: ZnO Thin Film Transistors

Wednesday PM
June 24, 2009

Room: 108
Location: Pennsylvania State University

Session Chairs: Thomas Jackson, Pennsylvania State University; David Norton, University of Florida

1:30 PM

K1, Fabrication and Characterization of Amorphous InGaZnO-Based Thin Film Transistors: *Wantae Lim*¹; Erica Douglas¹; S. Kim¹; David Norton¹; Steve Pearton¹; Fan Ren¹; H. Shen¹; W. Chang¹; ¹University of Florida

We report on the fabrication and characterization of amorphous (a-) InGaZnO-based thin film transistors (TFTs) on glass and flexible substrates. The resistivity of InGaZnO channel layer deposited by RF magnetron sputtering at room temperature was ~ 1 Ω.cm, which can be controlled by changing oxygen partial pressure during the deposition process. The InGaZnO TFTs operated in enhancement mode and showed low operating voltages in the range of 0.5-2.5 V, drain current on-to-off ratios of ~ 10⁵, sub-threshold gate-voltage swing of 0.25-0.5 V/decade-1, and high saturation mobilities of 5-12 cm².V⁻¹.s⁻¹. The device characteristics exhibited small shifts during 1000 hours aging time at room temperature. The results demonstrate that a-InGaZnO films are an appropriate channel material for transparent electronics and display applications.

1:50 PM Student

K2, Low Temperature Annealing of the Room Temperature Deposited Amorphous InGaZnO4 Thin Film Transistors: *Young Gwang Yoon*¹; Jae-Hyung Jang¹; ¹GIST

Amorphous oxide semiconductors (AOS) have recently been actively investigated for thin film transistors in the application area of display devices such as backplane of active matrix organic light emitting diodes (AMOLED) and active matrix liquid crystal display (AMLCD). The optical and electronic properties of AOS materials have superior compared to amorphous silicon counterpart that is conventionally used for current display devices in terms of light transparency in the visible spectrum and the higher field effect mobility. InGaZnO4 (IGZO) thin film is one of the most promising AOS materials, which can be processed in low temperature with highly uniform electrical properties. There also have been literatures reporting the effect of post-annealing on the performance of IGZO thin films deposited by various methods. The post-annealing process increased carrier concentration in channel and improve the interface between the channel and source/drain in a view of decreasing of the barrier related with the contact of materials with different workfunctions. However, the annealing temperature stayed quite high above 300°C. In this study, rapid thermal annealing was carried out at low temperatures at 200°C on the thin film transistors consisting of 85-nm-thick IGZO channel deposited by rf magnetron sputtering at room temperature. IGZO TFTs with W/L ratio of 500/20µm , 800/20µm were fabricated by conventional bottom gate configuration. PECVD grown silicon nitride was used as gate dielectric material. The fabrication processes include photolithography and wet etching of IGZO by diluted HF(100:1), reactive ion etching of silicon nitride, Ti/Au(200nm/300nm) metallization for source and drain contacts. Growth temperature of IGZO is detected from reference sample with a real time monitoring in the growth

chamber. The temperature on the sample increased due to the ion bombardment, but the growth temperature was below 65°C. As-fabricated IGZO TFTs have on-off current ratio of 2×10^3 and saturation mobility of 0.1 cm²/Vs and threshold voltage of 14V. When the low temperature post-annealing process was carried out, the performance of the IGZO TFTs were dramatically improved. IGZO TFTs undergone the post-annealing at 200°C for 20min have on-off current ratio of 1.5×10^6 and saturation mobility of 2.7 cm²/Vs and threshold voltage of 4.2 V. By the effect of the post-annealing process at 200°C, the field effect mobility and on-off current ratio have been improved more than an order of magnitude, and the threshold voltage was also reduced. The sub-threshold slope improved after the annealing indicates the improved oxide-semiconductor interfaces. In conclusion, the temperatures of all the fabrication processes including the sputtering and annealing were kept below 200°C, and the TFTs exhibited quite good electrical characteristics. The detailed electrical characteristics of the devices and the material characteristics of IGZO will also be discussed in the presentation. This work is supported by the SEAHERO program under Grant 07SeaHeroB01-03.

2:10 PM

K3, Design and Characterization of ZnO-Based Metal-Semiconductor Field-Effect Transistors on Glass Substrate: *Heiko Frenzel*¹; Michael Lorenz¹; Alexander Lajn¹; Holger von Wenckstern¹; Holger Hochmuth¹; Gisela Biehne¹; Marius Grundmann¹; ¹Universität Leipzig

We report on the fabrication of metal-semiconductor field-effect transistors (MESFETs) by reactive dc-sputtering of Ag as Schottky-gate contact on ZnO thin-film channels grown by pulsed-laser deposition (PLD) on quartz glass substrates. ZnO-based MESFETs on sapphire substrates with excellent characteristics have been reported in [1]. However, for large area applications in transparent electronics, the use of cheap glass substrates is mandatory. The non-epitaxial growth leads to a higher density of structural defects. The 20 – 30 nm thin ZnO channel layer is highly textured. It is c-axis-oriented but exhibits twists and tilts of the grains in plane. The n-type doping is adjusted by the Al-content in the PLD targets. Using 0.01% or 0.001% aluminium, results in a doping concentration in the range between $1E+16$ and $1E+18$ cm⁻³. MESFETs were processed by means of standard photolithography techniques. After etching ZnO mesas as channel, the source and drain contacts were deposited by dc-sputtering of Au and the Schottky gate-contacts were fabricated by reactive dc-sputtering of Ag in an oxygen/argon-atmosphere. Subsequently, an Au-capping-layer was sputtered on the Ag for passivation. The source-drain I-V output characteristics and transfer characteristics of the presented MESFETs show n-type behaviour. Depending on the growth conditions, comprising the oxygen partial pressure and the channel thickness, the FETs can be tailored normally-on or -off. In the case of the normally-off MESFETs, the source-drain current is tuneable over 6 decades in a gate-voltage range of only 1 V with an off-voltage of 0 V. They exhibit very low off-currents in the picoampere range corresponding to the reverse leakage current of the Ag Schottky diodes. The forward bias voltage is limited to the Schottky diode's built-in voltage, where the depletion layer is reduced to zero. As typical for MESFETs, higher forward voltages lead to higher currents through the gate and early breakdown. Channel mobilities were extracted from the transfer characteristic and reached values up to 1.4 cm²/Vs which are respectable for polycrystalline ZnO on amorphous glass substrate. This work is supported by Deutsche Forschungsgemeinschaft within the framework of Sonderforschungsbereich 762 "Functionality of Oxidic Interfaces" and the Graduate School "Leipzig School of Natural Sciences - BuildMoNa". [1]H. Frenzel, A. Lajn, M. Brandt, H. von Wenckstern, G. Biehne, H. Hochmuth, M. Lorenz, and M. Grundmann, Appl. Phys. Lett. 92, 192108, 2008

2:30 PM Student

K4, Plasma-Enhanced Atomic Layer Deposition ZnO TFTs: *Devin Mourey*¹; Dalong Zhao¹; David Saint John¹; Nikolas Podraza¹; Thomas Jackson¹; ¹Pennsylvania State University

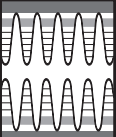
We have used a novel plasma-enhanced atomic layer deposition (PEALD) process to deposit ZnO thin films at 200°C. PEALD of ZnO has been previously demonstrated using a metal organic zinc source and high-reactivity reactants such as O₂ and H₂O [1]. In this work, we use low-reactivity reactants, either

CO₂ or N₂O, and a plasma to generate the reactive species needed for reaction. This approach allows for a simplified PEALD process where the low-reactivity reactant can be used to generate the reactive oxygen species, but also purge the byproducts of both steps. In addition, PEALD provides the uniformity of an ALD process, with the ability to add substantial energy from the plasma, which may be important in controlling the free carrier concentration, doping, and for low-temperature deposition. ZnO or Al₂O₃ films are deposited layer-by-layer by first providing a pulse of a metal precursor, diethylzinc (DEZ) for ZnO or trimethylaluminum (TMA) for Al₂O₃, purging the excess precursor with the low-reactivity reactant, and then pulsing the RF plasma to react the absorbed zinc or aluminum precursor. The process is repeated to deposit thin films. From X-ray diffraction and transmission electron microscopy (TEM), we find 30 nm thick ZnO films from CO₂ and N₂O to be (002) textured with ~10-20 nm columnar grains. Undoped ZnO PEALD thin films from CO₂ and N₂O form high resistivity layers and enhancement mode thin film transistors (TFTs). This is substantially different from most reports of conventional ALD ZnO with water or oxygen, where undoped films typically have low resistivity and form depletion mode devices, requiring the addition of a compensating dopant to form high resistivity films.[2] The film growth characteristics for ZnO films deposited by PEALD from CO₂ and N₂O are different resulting in substantial differences in film structure as well and TFT performance. TFTs were fabricated by depositing 37 nm of PEALD Al₂O₃ on glass with a chromium layer deposited by ion beam sputtering. Devices with 30 nm thick PEALD ZnO layers deposited from CO₂ had a field-effect mobility of 10-12 cm²/Vs and threshold voltage of ~ 7 V. Devices fabricated with 30 nm thick PEALD ZnO layers deposited from N₂O exhibited field-effect mobility of 22-25 cm²/Vs and threshold voltage of ~ 7.5 V. Differences pertaining to thin film growth and interfacial effects are examined as the cause of this substantial device mobility difference. In particular, microstructural information from cross sectional TEM and optical property variations observed from spectroscopic ellipsometry show distinct differences between films grown using N₂O and CO₂, which may explain the differences in electrical performance. [1] S-H. K. Park, et al. *Electrochemical and Solid-State Letters*. 9(10) G299-G310 (2006). [2] S. J. Lim, et al. *Applied Physics Letters*. 91, 183517 (2007).

2:50 PM Student

K5, Low Temperature Pulsed PECVD ZnO Thin Film Transistors: *Dalong Zhao*¹; Devin Mourey¹; Thomas Jackson¹; ¹Pennsylvania State University

ZnO-based thin film transistors (TFTs) are potentially higher performance and improved stability replacements for amorphous silicon TFTs in large-area displays. A variety of techniques have been used to deposit ZnO thin films, including metal organic chemical vapor deposition (MOCVD), sputtering, pulsed laser deposition (PLD), and atomic layer deposition (ALD). Plasma-enhanced chemical vapor deposition (PECVD) is the current technique used to deposit silicon nitride and amorphous silicon in large-area displays, however, it is difficult to grow high-quality interfaces between ZnO and dielectric materials by PECVD. [1] Pulsed PECVD has been reported for many materials, with improvement in film quality for some. [2] We have used pulsed PECVD to fabricate ZnO films at low temperature (200°C) from diethyl zinc (DEZ) and nitrous oxide (N₂O). The weak reactant N₂O was used instead of oxygen to minimize premature reactions which can result in non-uniform deposition. In pulsed PECVD the reactants are supplied continuously and an RF plasma is periodically pulsed to deposit thin films. The reaction byproducts generated by plasma are typically fully purged before next plasma step. Short plasma pulse times can be important to minimize deposition from species desorbed from the chamber walls during the plasma pulse. It has been reported that pulsed plasma deposition of ZnO results in improvement in film quality and device performance. Optical properties by spectroscopic ellipsometry show a denser film from pulsed PECVD compared to PECVD and TFTs fabricated using pulsed PECVD ZnO thin films also have higher field-effect mobility. In this work, pulsed PECVD ZnO TFTs were fabricated using a bottom-gate structure. 100 nm thick Cr was deposited by ion beam sputtering on glass as a blanket gate layer followed by 35 nm of plasma-enhanced atomic layer deposition (PEALD) Al₂O₃ as dielectric [3], and 10 nm undoped ZnO by pulsed PECVD. The ZnO was patterned by wet etching in dilute HCl, and titanium source and drain



electrodes were deposited by sputtering and patterned by lift-off. 20 μm channel length TFTs had field effect mobility $>15 \text{ cm}^2/\text{V}\cdot\text{s}$, threshold voltage of 6.6 V, subthreshold slope of $\sim 370 \text{ mV}/\text{dec}$, and a current on/off ratio $>10^8$. Pulsed PECVD plasma deposition is a promising approach for depositing high quality thin films of ZnO at low temperature. [1] J. Sun, D. Mourey, D. Zhao, and T. N. Jackson. *Journal of Electronic Materials*, Vol. 37, No. 5, 2008 [2] M. T. Seman, D. N. Richards, P. C. Rowlette, and et al, *J. Vac. Sci. Technol. A* 26, 1213 (2008).[3] D. Mourey, J. Sun, D.Zhao, and T. N. Jackosn. "Plasma-enhanced atomic layer deposition ZnO TFTs." 5th International Workshop on Zinc Oxide and Related Materials. Ypsilanti Mi, 2008.

3:10 PM Break

3:30 PM

K6, ZnO Field Effect Transistors on Silicon by MOCVD: *Bruce Willner*¹; Shangzhu Sun¹; Gary Tompa¹; ¹Structured Materials Industries, Inc.

Zinc oxide (ZnO) is an attractive material for high-speed high power transistor fabrication. ZnO has a wide bandgap of 3.37eV and an exciton binding energy of 59 meV. Furthermore, ZnO has been found to have a high breakdown field of $5 \times 10^6 \text{ V}/\text{cm}$, slightly higher than GaN and SiC, the materials that currently dominate the high performance power transistor field. ZnO also exhibits a carrier saturation velocity higher than SiC or GaN. Metal organic chemical vapor deposition (MOCVD) is an ideal tool to produce these materials, providing high quality material, and allowing well controlled deposition of more complex layer structures through parameter control. A MOCVD tool, designed specifically for ZnO deposition, was used to deposit high quality ZnO films for device fabrication. MOCVD is a highly scalable production technique which can provide uniform, pin-hole-free deposition over large areas. A chamber for ZnO deposition on up to 19 2" wafer has been built. ZnO deposition with thickness variation of under 3% across an 8" diameter substrate have been achieved. The material and fabrication costs for ZnO are estimated to be approximately 1/8 that of GaN or SiC. Very recent developments have shown that, properly fabricated, ZnO material and device parameters can meet the requirements to produce a high power device. Intrinsic n-type ZnO was deposited over a thermal silicon dioxide dielectric layer on a silicon wafer. MOCVD ZnO films were deposited at temperatures between 400°C and 600°C using oxygen and metalorganic zinc sources. 500Å thick films demonstrated 1.5×10^3 to $7 \times 10^3 \text{ } \Omega/\text{sq}$. sheet resistance, or, approximately, 1×10^{-2} to $4 \times 10^{-2} \text{ } \Omega/\text{sq}$ resistivity. The structure was processed into a field effect transistor with a lateral channel design. The current-voltage characteristics of three fabricated ZnO MOSFET devices showing good transistor action and very good on/off ratios. Devices exhibit a saturation field effect mobility of greater than $20 \text{ cm}^2/\text{V}\cdot\text{s}$. Saturation current densities of greater than 100 mA/mm was also achieved.

3:50 PM Student

K7, ZnO Field-Effect Transistors with Dual-Gate Structure: *Chan Ho Park*¹; Kimoon Lee¹; Min Suk Oh¹; Seongil Im¹; Byoung Hoon Lee²; Myung Mo Sung²; ¹Yonsei University; ²Hanyang University

Dual-gate field effect transistors (DG-FET) in Si-based technology have been proposed to overcome short-channel effect and to extend Si complementary metal-oxide-semiconductor technology into the sub-100 nm scaling. We realized that if the gates could be operated independently, the phenomena of electrostatic gate coupling give rise to an interesting mode of transistor operation. However, the fabrication of the FET with dual-gate structure should overcome difficulties in making the top channel properties matched to those of bottom channel. We fabricated ZnO-based dual gate thin-film transistors (TFTs) with 20 nm-thick Al_2O_3 for both top and bottom dielectrics, which were deposited by atomic layer deposition on glass substrates at 200 °C. As characterized with single gate (SG), dual gate (DG), and ground plane (GP) modes, our ZnO-TFTs well operated under 5 V. DG-mode TFT showed a field mobility of $0.4 \text{ cm}^2/\text{V}\cdot\text{s}$, high saturation current of 6 μA and on/off current ratio of $\sim 10^6$ while SG- and GP-mode TFTs showed similar value of mobility but with lower current. Using DG- and GP-mode, NOR gate operation was well demonstrated. Whether top or bottom gate is biased for sweep, our TFT almost symmetrically operates under a low voltage of 5 V. The threshold voltage of our DG TFT was systematically controlled from 0.5 to 2.0 V by varying counter gate input from +5 to -2 V.

4:10 PM Student

K8, Dual-Gate Operated ZnO Nanowire Field-Effect Transistors: *Jung-hwan Hyung*¹; Dong-joo Kim¹; Duk-il Suh²; Sang-kwon Lee¹; ¹Chonbuk National University, Korea; ²Gwangju Institute of Science and Technology

1-dimensional nanowires (NWs) are especially attractive building-blocks for nanoscale electronic and photonic devices application because of their unusual physical and chemical properties [1]. Recently, zinc oxide NW (ZnONW) field-effect transistors (FETs) are fabricated with a bottom-gate in three-probe FET structure [2,3]. Most previously reported indicated that ZnONW FETs with a back-gate had less electrical performances (such as conductivities, on-off current ratio etc.) because the surface of ZnONW is strongly affected by chemical adsorption [4]. To prevent this chemical adsorption in the ZnONW surface and to enhance the device performance, ZnONW FETs should be passivated. Moreover, the ZnONW need to fabricate with top-gate geometry. Recently, Chang et al. studied a $\text{SiO}_2/\text{Si}_3\text{N}_4$ passivation layers to fabricate the device and showed that the device performance was highly improved [5].

In this letter, we investigate on the fabrication and electrical characteristics of passivated ZnONW FETs with a both bottom-gate and top-gate geometry in FET structure. The FETs with a top-gate geometry exhibited clear n-channel enhancement mode (E-mode) behavior. We found that the current on-off ratio (I_{on}/I_{off}) and transconductance with a top-gate structure were estimated to be ~ 50 and ~ 10 times higher than those with bottom-gate geometry. REFERENCE [1]J. T. Hu, T. W. Odom, and C. M. Lieber, *Acc. Chem. Res.* 32, 435 (1999). [2]J. Goldberger, D. J. Sirbully, M. Law, and P. Yang, *J. Phys. Chem. B* 109, 9 (2005) [3]H. W. Ra, K. S. Choi, C. W. Ok, S. Y. Jo, K. H. Bai, and Y. H. Im, *Appl. Phys. Lett.* 93, 033112 (2008). [4]A. F. Kohan, G. Ceder, D. Morgan, and C. G. Van de Walle, *Phys. Rev. B* 61, 22 (2000). [5]P. C. Chang, Z. Fan, and C. J. Chien, *Appl. Phys. Lett.* 89, 133113 (2006).

4:30 PM

K9, Thin Film Encapsulation of Oxide Based Thin Film Transistors: *Patrick Goerrn*¹; Thomas Riedl²; Wolfgang Kowalsky²; ¹Princeton University; ²Technical University of Braunschweig

Thin film transistors (TFTs) with a transparent amorphous oxide semiconductor (TAOS) channel combine the excellent uniformity of amorphous devices with a high saturation field effect mobility, one order of magnitude larger than that of TFTs based on amorphous silicon (a-Si:H). Moreover, they are transparent in the visible part of the spectrum. Thus TAOS based TFTs enable the realization of applications beyond reach for a-Si:H such as active matrix bottom-emitting organic light emitting diode (OLED) displays with high filling factors or even entirely transparent active matrix displays. Transparent thin-film-transistors (TFTs) with a channel semiconductor based on the zinc tin oxide (ZTO) system deposited by plasma assisted pulsed laser deposition (PAPLD) are presented. The mobility of these devices is higher than $10 \text{ cm}^2/\text{V}\cdot\text{s}$ and the threshold voltage is the range of 0 V. We already demonstrated fully transparent OLED pixels by integrating transparent OLEDs on top of these transparent TFTs and, very recently, the realization of the first transparent active matrix OLED pixel drivers with ZTO channels. The circuits are highly transparent in the visible part of the spectrum and suitable for see-through AM OLED displays with brightness levels of 2000 cd/m² at 100 Hz refresh rate and full-HD resolution. PAPLD ZTO TFTs are extremely stable versus bias/current stress, which is very important for active matrix OLED applications. The devices have been subject to electrical stress via $V_{gs}=10\text{V}$ and a $V_{ds}=10 \text{ V}$ leading to a drain-source current of 188 μA . In optimized TFTs with a composition of $[\text{Zn}]:[\text{Sn}] = 36:64$ the relative change of the saturated field effect mobility was less than 1% and the threshold voltage shift was about 320 mV after 1000 hours of operation. In this study, we describe the effect of thin film encapsulation on transparent PAPLD ZTO TFTs. We find that chemisorption or desorption of oxygen are the underlying physical processes. We apply three different methods to desorb oxygen from the channel surface: thermally activated desorption in vacuum; light induced desorption; and chemical reaction with the strongly reducing agent trimethyl aluminium (TMA) during atomic layer deposition (ALD) thin film encapsulation. In vacuum an overall change of the threshold of less than 1 V within 500 h is found. ALD encapsulation shifts the threshold by about 2V. Based on a detailed understanding of the interaction of the TFT channels with

oxygen the low oxygen sensitivity of PAPLD grown ZTO TFTs is attributed to an optimized oxidation during the deposition, enabled by the highly energetic PLD plasma and the application of oxygen radicals supplied by an additional oxygen plasma source. Essentially, a two-step encapsulation process is proposed that enables the application of high-performance ALD grown permeation barriers for active matrix OLED displays using metal-oxide driving electronics.

4:50 PM

K10, Transparent Photo-Stable Complementary Inverter with Organic-Inorganic Nano-Hybrid Dielectrics: *Min Suk Oh*¹; Sung Kyu Park¹; Yong Hoon Kim¹; Jeong In Han¹; Kimoon Lee²; Kwang Hyun Lee²; Sung Hoon Cha²; Byoung Hoon Lee³; Myung Mo Sung³; Seongil Im²; ¹Korea Electronics Technology Institute; ²Yonsei University; ³Hanyang University

“Transparent” electronics has been one of the key terminologies forecasting the ubiquitous technology era. Several researchers have thus extensively developed transparent oxide-based thin-film transistors (TFTs) on glass and plastic substrates although in general high voltage operating devices have been mainly studied considering transparent display drivers. However, low voltage operating oxide TFTs with transparent electrodes are very necessary if we are aiming at logic circuit applications, for which transparent complementary or one-type channel inverters are required. The most effective and low power consuming inverter should be a form of complementary p-channel and n-channel transistors but real application of those complementary TFT inverters also requires electrical- and even photo-stabilities. Since p-type oxide TFTs have not been developed yet, we previously adopted organic pentacene TFTs for the p-channel while ZnO TFTs were chosen for n-channel on sputter-deposited AlOx film. As a result, decent inverting behavior was achieved but some electrical gate instability was unavoidable at the ZnO/AlOx channel interface. Here, considering such gate instability issues we have designed a unique transparent complementary TFT (CTFTs) inverter structure with top n-ZnO channel and bottom p-pentacene channel based on 12 nm-thin nano-oxide/self assembled monolayer laminated dielectric, which has a large dielectric strength comparable to that of thin film amorphous Al₂O₃. Our transparent CTFT inverter well operate under 3 V, demonstrating a maximum voltage gain of ~20, good electrical and even photoelectric stabilities. The device transmittance was over 60 % and this type of transparent inverter has never been reported, to the best of our limited knowledge.

Session L: Thermoelectrics and Thermionics

Wednesday PM
June 24, 2009

Room: Presidents Hall III & IV
Location: Pennsylvania State University

Session Chairs: Mayank Bulsara, Massachusetts Institute of Technology; Timothy Sands, Purdue University

1:30 PM Student

L1, Scanning Hot Probe Method for Thermoelectric Characterization of Nanostructured Thin-Films: Controlling the Heat Transfer Mechanisms between the Tip and the Sample: *Yanliang Zhang*¹; Eduardo Castillo¹; Claudiu Hapenciuc¹; Theodorian Borca-Tasciuc¹; ¹Rensselaer Polytechnic Institute

This work discusses a scanning hot probe method that provides the simultaneous measurement of thermal conductivity and Seebeck coefficient of thin-film structures with a spatial resolution of several microns. The commercially available hot probe is made from a wire shaped as a cantilever beam. The tip area of the wire was etched to uncover the Pt-Rh core which is 5 microns in diameter and 200 microns long. A micromirror mounted on the cantilever is used to control the probe-sample distance by deflecting the feedback laser beams. The probe is electrically heated using AC power from a function generator with the frequency chosen such that the AC temperature rise of the tip is negligible. The DC temperature rise of the probe generates a DC temperature gradient and a DC Seebeck voltage drop across the sample when the heated probe is in contact with the sample's surface. The average temperature rise of

the probe is determined using joule heating thermometry. This work focuses on discussing the contribution of the heat transfer mechanisms between the tip and the surface. The thermoelectric properties of the film have been extracted using a heat transfer model that involves all the major heat transfer mechanisms in the system. Through experimental validation that air conduction is shown to be typically the dominant thermal transport mechanism in the contact region, the heat conduction radius and contact thermal resistance- the two essential unknown parameters in the model are assumed to be uniform in various samples. Calibrations were performed on two different bulk samples with known thermal conductivities so that the two parameters can be obtained based on the model analysis, which left the thermal conductivity of thin-films the only unknown for the measurements done on the thin-film samples. The importance of the water layer heat transfer, supported by experiments performed on hydrophilic and hydrophobic surfaces, is discussed in this work and techniques to eliminate this contribution are developed. The Seebeck coefficient can be determined from the dependence of the Seebeck voltage on the temperature gradient developed across the film, while the highest film temperature at the tip is calculated by a refined model which involves the non-uniform temperature distribution along the length of probe. Experiments performed on thermoelectric samples will be presented and discussed.

1:50 PM Student

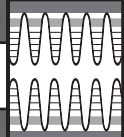
L2, Thermoelectric Power Characterization of Individual Sb₂Se₃ Single Crystal Nanowires and Nanotubes: *Wei Jiang*¹; C. Karthik¹; R. Mehta¹; G. Ramanath¹; T. Borca-Tasciuc¹; ¹Rensselaer Polytechnic Institute

In this paper we will report the Seebeck coefficient characterization of nanorods and nanotubes of Sb₂Se₃. Nanorods and nanotubes (40 to 100 nm in diameter and 5-6 micron length) of Sb₂Se₃ were synthesized via a rapid microwave route and were dispersed on a Si/SiO₂ substrate. The Seebeck coefficient of individual Sb₂Se₃ nanotubes/nanorods will be measured with nanofabricated devices which consist of one heater to provide the temperature gradient and two sets of thermometers to sense the temperature gradient and measure the thermoelectric voltage. The electrode configuration also allows for electrical conductivity measurements of the nanostructure. Test devices have been fabricated by a three-step electron beam lithography technique followed by metal evaporation and lift-off process. Preliminary results obtained with the first generation device show a linear increase in the Seebeck voltage measured across a nanotube as a function of the power dissipated into the heater. This result demonstrates that a temperature gradient large enough to generate a significant Seebeck voltage across the nanotube could be generated by the device current configuration. Experiments with second generation devices are ongoing. Temperature dependent measurements will be carried out in a cryostat in the range from 80K to 300K. Simultaneous electrical conductivity measurements will be performed with the same test structure. The measured properties will be linked to the electrical properties and the structure of the Sb₂Se₃ nanostructures.

2:10 PM

L3, Self-Supporting Nanowire Arrays Templated in Branched Porous Anodic Alumina for Thermoelectric Devices: *Hatem Elmatbouly*¹; Timothy Sands¹; Kalapi Biswas¹; ¹Purdue University

Arrays of thermoelectric nanowires templated in porous anodic alumina (PAA) have potential for enhanced performance relative to bulk materials in micro-Peltier coolers and waste heat generators. The nanowire topology offers the advantages of crystallographic texture control, suppression of lattice thermal conductivity through boundary scattering of phonons, elastic relaxation of misfit strain and opportunities for tailoring the radial electric field through vapor or liquid-phase modification of the exposed nanowire surfaces. A significant challenge, however, is the template material, which can serve as a thermal shunt. The template can be selectively etched, but must be replaced with a lower thermal conductivity material to prevent the nanowires from collapsing. By replacing the porous anodic alumina (PAA) template (~1.2 W/m-K) with SU-8 epoxy (~0.2 W/m-K), we have demonstrated a reduction in the thermal conduction of the matrix by a factor of about five, reducing the parasitic contribution of the matrix to about 5% of the total thermal conductivity. However, the degradation temperature of SU-8 (~380°C) limits the utility of this



approach, especially for the higher operating temperatures (300-550°C) needed for thermoelectric generators designed to run off waste heat from automotive exhaust, industrial processes or combustion for portable power devices. In the work described here, a method for creating a branched PAA (B-PAA) template is demonstrated. The process utilizes localized self-heating to destabilize the planar anodization front, yielding branched and interconnected pores that grow at a rate of about 300 microns per hour. The resulting template consists of primary pores separated by ~ 5 microns, from which secondary pores emanate. The secondary pores from adjacent cells intersect to create an interconnected pore network. Electrochemical deposition of thermoelectric materials, including Bi₂Te₃, PbTe and related alloys into the B-PAA, followed by selective etching of the B-PAA yields self-supporting nanowire arrays with thicknesses up to about 200 microns, thereby eliminating the thermal shunt through the template. By retaining vertical electrical continuity, lateral structural stability, and nanoscale wire dimensions with an array thickness that exceeds 100 microns, these self-supporting nanowires arrays are compatible with device designs that permit the large temperature differences (>100°C) that are needed for efficient power generation. This work was supported by a grant from the Office of Naval Research (N000140610641).

2:30 PM Student

L4, Ultrafast Microwave-Stimulated Sculpting and Thermoelectric Properties of Bismuth and Antimony Chalcogenide Nanoplates: *Rutvik Mehta¹; C. Karthik¹; B. Singh¹; Y. Zhang¹; E. Castillo¹; W. Jiang¹; N. Ravishankar¹; T. Borca-Tasciuc¹; G. Ramanath¹; ¹Rensselaer Polytechnic Institute*

Nanostructured forms of V-VI semiconductors are attractive for realizing high figure of merit thermoelectrics for novel applications such as harvesting electrical power from heat, and solid state refrigeration of hot-spots in nanodevices. Doping nanostructured V-VI semiconductors is essential to optimize properties to realize high ZT materials. Although many wet-chemical and templating techniques have been devised over the last several years to synthesize chalcogenide nanostructures with shape and/or size control, these approaches are limited by lack of scalability, poor crystal quality, template removal issues and absence of methods for doping. Here, we report the rapid (< ~ 2 minutes) scalable solvothermal synthesis of 5-20-nm-thick hexagonal shaped nanoplates of sulfur doped, Bi₂Te₃, Bi₂Se₃, and Sb₂Te₃ by microwave-stimulation. We further demonstrate the induction or suppression of branching by manipulating the surfactant concentration, which acts as both a shape-mediating agent as well as for dopant delivery. Such nanostructures pave the way for combining thermoelectric cooling with high-surface area heat spreading for solid-state refrigeration and power generation applications. We synthesized the nanoplates by exposing a mixture of trioctylphosphine, pentanediol with the bismuth and tellurium precursors and thioglycolic acid to 2.4 GHz microwave radiation. The nanoplate edge lengths are tunable between 100 nm to 1 micron by adjusting the microwave dose, which, however, has negligible effect on the nanoplate thickness. Electron microscopy and diffraction analyses reveal that each nanoplate is a rhombohedral single crystal with a R-3m structure that grows in a layer-by-layer fashion. The smallest layer step within each nanoplate is ~1 nm, reminiscent of the basic building block with the atomic layers within a unit cell. X-ray photoelectron spectroscopy and infrared spectroscopy reveal the lack of an oxide layer due to surface passivation by thioglycolic acid acting as molecular capping agents. Core level XPS spectra of sulfur from the nanoplates also reveal sulfur bonding with bismuth and selenium, indicating strong presence of sulfur near the nanoplate surface. We were able to controllably induce platelet branching by adjusting the thioglycolic acid concentration, underscoring the importance of the capping agent in nanostructure shape selection. Thermoelectric property characterization of the annealed films of the nanoplates reveal Seebeck coefficient with opposite signs from the bulk counterparts, consistent with sulfur doping, showing the ability to tune carrier concentration of the nanostructures. We also present thermoelectric property characterization of bulk nanocomposite pellets fabricated from the nanoplates. Finally, we will present the electrical and thermoelectric responses measured from test structures with electrically contacted individual nanoplatelets, and discuss the effects of thickness, edge length and branching in the context of theoretically predicted figures of merit for these structures.

2:50 PM

L5, Nonlinear Electric Transport in Wet-Chemically Synthesized Sb₂Se₃ Nanowire: *C. Karthik¹; Rutvik Mehta¹; Wei Jiang¹; Ganapathiraman Ramanath¹; Theodorian Borca-Tasciuc¹;* ¹Rensselaer Polytechnic Institute

Chalcogenide semiconductor nanowires and nanorods have been the subject of extensive research as building blocks for a variety of electronic, photonic and biomedical applications, especially in the thermoelectric and memory switching arena. In this paper we report the electrical characteristics of chemically synthesized nanorods of a wide band gap (E_a ~1eV) semiconductor, Sb₂Se₃. Nanorods (80 to 100 nm in diameter and 5-6 micron length) of Sb₂Se₃ were synthesized via a rapid microwave route. Nanorods were dispersed on a Si/SiO₂ substrate and the gold electrode contacts were fabricated in a four-probe configuration using e-beam lithography. The I-V characteristics were measured in the range of 150–310 K. While at low applied voltages the measured I-V curves show an Ohmic behavior, at higher voltages the I-V characteristics are strongly nonlinear. Around a critical threshold voltage V_{th}, the current increases drastically and the voltage snaps back towards lower voltages and the slope of the I-V curves becomes negative (Negative Differential Resistance, NDR). With the increase in the ambient temperature, the threshold voltage V_{th} shifts towards lower voltages. The experiments showed that the I-V trace is completely reversible without any significant hysteresis. The S-shaped I-V characteristics, where the sample goes from a high resistance state to a low resistance state known as “threshold switching” has been observed before in amorphous chalcogenide semiconductors including nanowires. Semiconductors exhibit this behavior, provided that a carrier generation driven by field and carrier concentration competes with a strong Shockley–Hall–Read (SHR) recombination via localized states. Amorphous chalcogenides are ideal systems to exhibit this behavior with their high level of defects which leads to the high concentration of donor as well as acceptor trap states. We report this behavior in a crystalline semiconductor nanowire which has not been observed before. The main reason responsible for the observed nonlinear transport in the present case might be the high surface area leading to the presence of high concentration of surface defect states. The surface states dominated transport was confirmed in our case through ambient dependent conductivity measurements (in vacuum vs air). The present results are relevant for applications of Sb₂Se₃ nanowires in the thermoelectric and memory-switching fields.

3:10 PM Break

3:30 PM

L6, Hydrothermal Synthesis of Bi_{0.5}Sb_{1.5}Te₃ and the Effect of Sintering Temperature on Thermoelectric Characteristics of the Pressed Mats: *Chia-Jyi Liu¹; Gao-Jih Liu Liu¹;* ¹National Changhua University of Education

Thermoelectric materials are considered as one of the energy and environment-friendly materials due to the Seebeck and Peltier effects. The former effect produces electrical power, and the latter effect provides cooling capability without using coolants. Bismuth alloys show the highest dimensionless figure of merit ZT around room-temperature and are one of the most commercialized thermoelectric materials. Turning the currently best thermoelectric materials into nanostructure might help improve thermoelectric figure of merit by increasing the thermoelectric power as a result of an enhanced density of states and by reducing thermal conductivity as a result of an increased phonon scattering. In this study, we synthesize Bi_{0.5}Sb_{1.5}Te₃ powders using hydrothermal methods. The resulting powders are characterized by powder x-ray diffraction, scanning electron microscopy, transmission electron microscopy, atomic force microscopy, and energy dispersive x-ray spectroscopy (EDX). The hydrothermally prepared Bi_{0.5}Sb_{1.5}Te₃ powders exhibit hexagonal platelets in shape. The hexagonal platelets have various sizes with the dimension of 200-1500 nm in edge and 30-50 nm in thickness. EDX results indicate the atomic ratio of Bi:Sb:Te = 1:3.2:5.9, which is close to the starting material with atomic ratio of Bi:Sb:Te = 1:3:6. The growth mechanism of nanoplatelets appears to be different from the sheet-rod growth mechanism of Bi₂Te₃ [1-2] since there is no Te rod observed in the sample. Measurements of electrical resistivity, thermoelectric power, thermal conductivity, and Hall effect are carried out on the pressed pellets sintered at various temperatures between 300 and 380°C in an evacuated ampoule. It is found that electrical resistivity increases with sintering temperature. However,

the sample sintered at 340°C shows the maximum thermoelectric power at all temperatures. Room-temperature Hall measurements indicate that the charge carrier is of p-type for all the samples. The hole concentration correlates well with the thermoelectric power. Samples with smaller hole concentration leads to larger thermoelectric power. At 295 K, electrical resistivity, thermoelectric power, and thermal conductivity of the hydrothermally-prepared Bi_{0.5}Sb_{1.5}Te₃ sintered at 340°C are 6.4 mΩ-cm, 273 μV/K, and 0.37 W/m K, respectively. The resulting power factor and dimensionless figure of merit are 11.6 μW/cm-K² and 0.93, respectively. The power factor is much smaller than the typical value of 40 μW/cm K² due to its lower carrier concentration of 7.31x10¹⁸ cm⁻³ as compared to the optimal value of 10¹⁹ cm⁻³. However, the thermal conductivity is relatively small with κ = 0.37 W/m K, which shows significant reduction of thermal conductivity and hence enhances the thermoelectric performance. [1] Yuan Deng, Chang-Wei Cui, Ni-La Zhang, Tian-Hao Ji, Qing-Lin Yang, Lin Guo, J. Solid State Chem. 179, 1575 (2006).[2] Chia-Jyi Liu, Gao-Jih Liu, Chun-Wei Tsao, Yu-Feng Lu, Li-Shin Chang, Proceedings ICT'07, 26th International Conference on Thermoelectrics, IEEE.

3:50 PM Student

L7, Fabrication of p-Type Pb_{0.5}Sn_{0.5}Te Thermoelectric Power Generation Elements by Mechanical Alloying: *Aaron Lalonde*¹; Lakshmi Krishna¹; Peter Moran¹; ¹Michigan Technological University

The potential of Pb_xSn_{1-x}Te-based alloys formed from a melt as highly efficient p-type thermoelectric elements for power generation modules designed to operate at temperatures between ~ 200-450°C has been demonstrated in the literature. The emerging consensus is that nano-scale compositional and structural variations resulting from small additions of AgSbTe₂ or modifying the preparation method results in material with unusually high thermoelectric functionality. Mechanical alloying is an alternative to melt-alloying that can engender non-equilibrium nano-scale compositional and structural features in alloys. Although it is clear that Pb_xSn_{1-x}Te can be made by mechanically alloying powders of Pb, Sn, and Te, the literature lacks an assessment of whether Pb_xSn_{1-x}Te with sufficiently large and reproducible carrier concentrations, mobilities, and Seebeck coefficients that are stable at temperatures of ~450°C can be fabricated by consolidating mechanically alloyed material into thermoelectric elements. This work addresses that need. The approach taken is to first determine the kinetics of mechanically alloying Pb_{0.5}Sn_{0.5}Te (with 5% AgSbTe₂) from 99.9% pure elemental powders using a vibratory "SPEX" mill. Twelve hours of milling is shown to result in completely alloyed material with an ~50nm grain size. Methods for consolidating the powder to minimize oxide contamination that would otherwise preclude thermoelectric functionality are then developed. Finally the average value and standard deviation in carrier concentration, mobility, and Seebeck coefficient are measured, both before and after exposure to 450°C for 50hrs, for a set of three Pb_{0.5}Sn_{0.5}Te (without AgSbTe₂) thermoelectric elements fabricated independently. Solid p-type Pb_{0.5}Sn_{0.5}Te elements with appropriate and reproducible carrier concentrations, mobilities and Seebeck coefficients can be obtained despite the use of starting materials that are only 99.9% pure and the potential for oxidation inherent in the fabrication process. In particular, room temperature carrier concentrations of 4.19x10¹⁹ cm⁻³ (σ=3%) and mobilities of 252 cm²V⁻¹s⁻¹ (σ=7%) are observed for the three samples. Exposure to 450°C for 50hrs decreases the room temperature carrier concentration to 3.21x10¹⁹ cm⁻³ (σ=4%), while increasing the mobility to 321 cm²V⁻¹s⁻¹ (σ=4%). The room temperature conductivity does not significantly change upon exposure to the elevated temperature (1653 Ω⁻¹cm⁻¹, σ=8%). The voltage developed across the material when exposed to a large temperature gradient (430-315°C) yields a Seebeck coefficient of 223 μV°C⁻¹. These results are on par with or better than highly functional Pb_xSn_{1-x}Te and AgSbTe₂-Pb_xSn_{1-x}Te thermoelectric material made by melt alloying [1-3]. Careful definition of a reducing atmosphere in the pre-consolidation environment is shown to be critical. The pertinent length scales implied by the electrical transport data will be discussed in the framework of the material's microstructure and the temperature dependence of electrical conductivity, Seebeck coefficient, and thermal conductivity.

4:10 PM Student

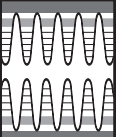
L8, Alternative Substrates for Metal/Semiconductor Superlattices for Thermionic Energy Conversion: *Jeremy Schroeder*¹; Polina Burmistrova¹; Robert Wortman¹; Timothy Sands¹; ¹Purdue University

Thermionic carrier transport in metal/semiconductor superlattices is a promising energy conversion approach based on nanocomposite materials.¹ Despite the poor thermoelectric properties of the individual metal and semiconductor layers, metal/semiconductor superlattices are expected to enhance the power factor (S²σ) through energy barrier filtering while suppressing thermal conductivity (κ) via interface scattering of phonons. Superlattice structures from three materials systems (ZrN/ScN, (Zr,W)N/ScN, and HfN/ScN) were deposited on three substrates (MgO, Al₂O₃, and Si) to examine the viability of substrates other than MgO for thermionic-based energy conversion devices. Silicon is of particular interest due to its low cost, scalability, and ease of processing. The ZrN/ScN materials system was investigated due to previous work that demonstrated a Schottky barrier height of 280 meV, a value that modeling suggests may yield ZT values exceeding 2.5 at temperatures of ~1000K.² The (Zr,W)N/ScN materials system is of interest due to a reported reduction in thermal conductivity (1.8 W/m-K) compared to unalloyed ZrN/ScN (5 W/m-K).³ Finally, the HfN/ScN materials system is currently being explored for further thermal conductivity reduction based on hafnium's higher atomic mass. Superlattices (1 μm) of varying periods were deposited on 100-MgO, 0001-Al₂O₃, and 100-Si substrates by reactive DC magnetron sputtering in a high vacuum deposition system (10⁻⁸ Torr base pressure). First, 300nm metal buffer layers (ZrN or HfN) were deposited to accommodate lattice strain due to lattice mismatch between the substrate and metal layer. Then, superlattices were sputtered from Zr, W, Hf, and Sc targets at 200W power in an Ar(4scm)/N₂(6scm) ambient at 5mTorr with a substrate temperature of 850°C. The resulting film orientation, texture, and microstructure were characterized by high resolution x-ray diffraction (HRXRD), field emission scanning electron microscopy (FESEM), and transmission electron microscopy (TEM). All three materials systems showed similar behavior, but the results on HfN-based structures are highlighted here. HfN/ScN superlattices exhibited strong 100-texture on all three substrates with 200-HfN rocking curve full-width-at-half-maximum (FWHM) values of 3.1°(MgO), 3.2°(Al₂O₃), and 9.9°(Si). Asymmetric phi scans revealed an epitaxial relationship on MgO: HfN{100}<010> || MgO{100}<010> while superlattices on sapphire exhibited multivariant epitaxial growth: HfN{100}<110> || Al₂O₃{0001}<100>. Superlattices on silicon showed uniaxial texture and TEM revealed a columnar grain structure with superlattices within the grains. In addition, FESEM revealed nanoscale interface roughness that may assist in cross-plane thermionic transport by relaxing the requirement for conservation of lateral momentum.¹ Interestingly, HfN/ScN superlattice structures on silicon did not exhibit any film cracking whereas the ZrN-based materials systems all exhibited cracking on silicon. Therefore, silicon remains a viable alternative substrate for HfN-based superlattices. However, future characterization of the thermal conductivity (κ) and power factor (S²σ) will ultimately reveal if HfN/ScN is suitable for thermionic-based energy conversion devices that operate at high temperatures (600-1000°C).

4:30 PM

L9, Cooling Effects of Field Emission from Semiconductors: *Moon Chung*¹; Alexander Mayer²; Brock Weiss³; Nicholas Miskovsky³; Paul Cutler³; ¹University of Ulsan; ²Universitaires Notre-Dame de la Paix; ³Pennsylvania State University

A thermoelectric device attracts much attention owing to its eco-friendly and small-sized properties. It generates the electric current in the presence of heat and, reversely, gives out heat in the presence of current flow. However, the Peltier device still exhibits poor efficiency. Field emission which is tunneling under strong electric field also gives rise to cooling. It is known the metallic cathode is heated at low temperatures and cooled at relatively high temperatures. This dual character changes to be one-way in semiconductor cathodes. The semiconductor cathode has been found to yield only cooling at all temperatures by the recent theoretical work of authors. This implies that there is a lot of feasibility for a new type of solid state cooler if an appropriate semiconductor is



found. In the conference, we will present the theoretical work for field emission from semiconductors Si and GaN. We first calculate the energy exchange $\Delta\epsilon$ (i.e. the energy loss of the cathode) which is defined as the difference between the average energies of field and replacement electrons. If $\Delta\epsilon > 0$, the cathode loses heat via field emission of electron and is cooled. A formal theory is developed to describe the replacement process of the injected charge carriers to compensate the field emission. It leads to analytic expressions for $\Delta\epsilon$, which exhibit the dependence on field, temperature, and doping concentration in a parametric form. The analytic and numeric results reveal the important feature that $\Delta\epsilon$ is positive for all temperatures. For Si, we obtained $\Delta\epsilon \sim 0.1$ eV at a realistic configuration. This implies that field emission always give rise to considerable cooling for a semiconductor emitter. When Joule heating is included, there is still a net cooling for a wide range of emitted current density j . For a sample of resistivity ρ and length L , the Joule heating rate is given by $\rho L j^2$ (Watts/cm²). The cooling contribution due to field emission is given by the energy loss per electron times the total number of electron emitted to vacuum. Thus the cooling rate is $\Delta\epsilon j/e$ (Watts/cm²), where e is the electronic charge. It is surprisingly found that a net cooling is produced. The cooling rate is also found to be controlled by the doping concentration. The obtained results for Si and GaN will be presented to show possibility of the field emission solid state cooler with high efficiency.

4:50 PM L10, Late News

Session M: Carbon Based Nanowires and Tubes

Wednesday PM
June 24, 2009

Room: 206
Location: Pennsylvania State University

Session Chairs: Ya-Hong Xie, University of California, Los Angeles; Suneel Kodambaka, University of California, Los Angeles (UCLA)

1:30 PM Student

M1, Horizontally Aligned Single-Walled Carbon Nanotubes on Patterned SiO₂/Si Substrates: *Takaomi Kishimoto*¹; Shin Iwasaki¹; Yasuhide Ohno¹; Kenzo Maehashi¹; Koichi Inoue¹; Kazuhiko Matsumoto¹; ¹Osaka University

Single-walled carbon nanotubes (SWNTs) are one of the promising materials for fabrication of nanoscale devices such as field-effect transistors due to their unique mechanical, chemical and electrical properties. Generally, the growth direction of SWNTs is difficult to be controlled on SiO₂/Si substrates. Recently, SWNTs were aligned to a specific crystallographic direction on sapphire or single-crystal quartz substrates. However, direction control of SWNTs on SiO₂/Si substrates is still demanded for fabrication of nanodevices. In this study, we demonstrated aligned SWNTs on patterned SiO₂/Si substrates with groove and terrace structures, which were fabricated using the electron-beam (EB) lithography and reactive ion etching (RIE) techniques. The lines were patterned using the EB lithography. SiO₂ was etched by RIE technique to form groove and terrace structures with the height of 40 nm. The width of the grooves and the terraces were estimated to be 140 and 60 nm, respectively. The 0.5-nm-thick Co catalyst was patterned on the patterned substrates. SWNTs were synthesized by chemical vapor deposition. The SWNTs on the patterned substrates were observed by scanning electron microscopy. The SWNTs were aligned on the patterned SiO₂/Si substrates while SWNTs grown on the plane SiO₂ substrates were meandering in random direction. Most of SWNTs on the patterned substrates were grown astride a few groove and terrace structures. The growth direction of the SWNTs was parallel to the groove and terrace structures. From the SEM images, it dominates to fix the SWNTs on the edge of the terraces. To clear the growth mechanism, the van der Waals force between SWNTs and patterned SiO₂ substrates was calculated. Using groove and terrace structures, the direction of the force lines concentrates on the edge of the terraces. As a result, the density of the van der Waals force line on the edges of the terraces becomes much higher than that on the edge of the grooves. Therefore, the SWNTs will be preferentially grown along the edge of the terraces. This result

was consistent with the SEM images. This method will be promising to control the directions of SWNTs on SiO₂/Si substrates.

1:50 PM Student

M2, Electromagnetic Shielding Properties of Excimer-Laser-Synthesized-Single-Wall-Carbon Nanotubes/Polyurethane Nanocomposite Films: *Brahim Aissa*¹; M.A. Habib¹; L.L. Laberge²; T.A. Denidni¹; D. Therriault²; My Ali El Khakani¹; ¹Institut National de la Recherche Scientifique; ²Ecole Polytechnique de Montreal

We report on the successful fabrication of nanocomposite films consisting of an appropriate mixture of single wall carbon nanotubes (SWCNTs) and reinforced curable resin polyurethane (PU). These SWCNTs/PU nanocomposite films were directly prepared on glass substrate by means of a relatively simple and efficient solvent casting method. The SWCNTs were first synthesized by means of the UV laser ablation of a Co/Ni-doped graphite target, physico-chemically purified, and adequately dispersed into the thermoset PU polymer matrix by means of an ultrasonic treatment in dichloromethane followed by a high-shear mixing step using a 3-roll mill. The as-grown and purified nanotubes were systematically characterized by various techniques, including microRaman, x-ray photoelectron spectroscopy (XPS), and thermogravimetric analysis (TGA). Transmission electron microscopy observations revealed that the laser-synthesized-SWCNTs generally self-assemble into bundles featuring a very high aspect ratio (≈ 103), with diameters in the nm range and length reaching few micrometers. Following their purification, some of the SWCNTs were found to have carboxyl groups attached to their surface, as derived from XPS analyses. The electrical properties of the developed SWCNTs/PU nanocomposite films were investigated as a function of their SWCNTs content (i.e.; loading). It is found that the electrical conductivity of the SWCNTs/PU films increases by more than 106 when the SWCNTs loading is increased from 0.1 to 5 wt. %. On the other hand, the electromagnetic shielding attenuation (ESA) performance of the SWCNTs/PU nanocomposite films was also characterized in the super high frequency band, ranging from 7 to 12 GHz, using the coaxial transmission line method. A deep ESA band, centered around 9 GHz, was systematically measured for the SWCNTs/PU nanocomposite films. The attenuation was as high as $[-30]$ dB for the nanocomposite films containing SWCNTs loadings of 2.5 wt. % and above. The high aspect ratio of our SWCNTs is shown to enable electrical percolation within the nanocomposite at relatively low nanotube loading. By comparing the electrical conductivity of the films, on one hand, and their ESA performance, on the other hand, a direct correlation is established between their conduction level and their electromagnetic shielding capacity. Indeed, both physical properties were found to scale similarly with the SWCNTs loading of the nanocomposite films.

2:10 PM

M3, Electroluminescence from Electrolyte-Gated Carbon Nanotube Arrays: *Jana Zaumseil*¹; Xinning Ho²; Jeffrey Guest¹; John Rogers²; Gary Wiederrecht¹; ¹Argonne National Laboratory; ²University of Illinois at Urbana-Champaign

Light emission from semiconducting single-walled carbon nanotubes (SWNT) has been intensely studied over the past few years. Near-infrared luminescence results from exciton recombination and its wavelength is mainly determined by the nanotube diameter and chirality vector (m,n). As a quasi-one-dimensional material, the surrounding medium of carbon nanotubes also has a strong influence on their emission wavelength, peak width and quantum yield. For example, the photoluminescence yield of suspended nanotubes is significantly higher than when they are in contact with a substrate. Successful implementation of carbon nanotubes in optoelectronic devices requires an understanding of the underlying physical processes that affect charge transport and exciton recombination. Previously, electroluminescence from carbon nanotubes was demonstrated for ambipolar single nanotube and random network field-effect transistors using SiO₂ or Al₂O₃ as a gate dielectric. Here we demonstrate near-infrared electroluminescence from carbon nanotube field-effect transistors that are gated via a polymer electrolyte or ionic liquid. Due to the high effective capacitance of up to 50 $\mu\text{F}/\text{cm}^2$, electrolyte gating achieves large carrier densities at low gate voltages with minimal current hysteresis. Efficient injection of holes and electrons leads to ambipolar device characteristics and light-emission where

holes and electrons meet and recombine radiatively. We use aligned, high density arrays of carbon nanotubes, which enable spatial and spectral resolution of electroluminescence from an ensemble of nanotubes with various diameters and chiralities simultaneously without quenching by metallic nanotubes or energy transfer to nanotubes with smaller bandgaps, which occurs in random networks. We find that the unusual environment of an electrolyte with high mobile ion concentrations does not excessively quench electroluminescence from carbon nanotubes.

2:30 PM M4, Late News

2:50 PM M5, Late News

3:10 PM Break

Session N: Group IV Nanowires

Wednesday PM
June 24, 2009

Room: 206
Location: Pennsylvania State University

Session Chairs: Ya-Hong Xie, University of California, Los Angeles; Suneel Kodambaka, University of California, Los Angeles (UCLA)

3:30 PM Student

N1, Growth of Silicon Nanostructures Synthesized by Au-Catalyzed Chemical Vapor Deposition: *Tae-Hong Kim*¹; Seung-Yong Lee¹; Dong-Joo Kim¹; Sang-Kwon Lee¹; ¹Chonbuk National University

One dimensional silicon nanostructures have recently become of interest for potential applications in various areas such as optics, electronics, solar cell, thermo-electronics, and chemical sensors. These nanostructures have been synthesized with various methods such as chemical vapor deposition (CVD), solution, and laser ablation using vapor-liquid-solution (VLS) mechanism. The quantum effects in the electronics and optical properties of the nanodevices are strongly related to nanostructure's dimensions. Therefore, the controllability of the dimension and alignment of the nanostructures such as nanowires (NWs) and nanorods (NRs) is highly required to employ them as elements of nanodevices. In this study, we investigate the morphology of silicon nanowires (SiNWs) grown on Si substrate by nanoscale Au-catalyzed chemical vapor deposition. The initial nucleation of the SiNWs from the Au-Si islands is examined while varying island sizes. We also investigate the variation of the morphology and dimension of the SiNWs under the different condition of growth pressures, temperatures, and duration. In particular, preferential growth directions of the nanowires were identified for Si (001) and (111) substrates. The Au-Si islands were formed by Au thin-film (1.4-4 nm) deposition at room temperature followed annealing at 700°C for 10 min. The Au thin-film was employed as liquid-droplet catalysis during the growth. The SiNWs were grown by exposing the substrates with Au-Si islands to a mixture of gasses SiH₄ with and without carrier gas (H₂). The growth temperatures and the pressures were to be 700~900°C and 6~15 Torr, respectively. We observed that the silicon nanostructures was to be root-like, worm-like, and tapered with a growth condition. The SiNWs are about 40~200 nm in diameter and 4~15 μm in length. The SiNWs grown on Si (001) substrate were randomly grown while most of the SiNWs on Si (111) substrate were vertically grown along the <111> direction. Our results indicated that the pressure highly affects on the growth direction of SiNWs on Si (111) substrate. Structural characterization of a large number of SiNWs shows that SiNWs were synthesized at a total pressure of ~6.6 Torr with a preferable growth direction of <111> direction while the SiNWs under the growth pressure of ~2.6 Torr were grown along <112>.

3:50 PM

N2, 'Bulk' P Doping of Ge Nanowires Reduces Conductivity: *Shixiong Zhang*¹; Danny Perea¹; Eric Hemesath¹; Lincoln Lauhon¹; ¹Northwestern University

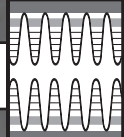
One dimensional semiconductor nanowires are being intensively investigated due to potential applications in nanoelectronics and optoelectronics.¹ While

much effort has focused on silicon nanowires, germanium has a higher electron and hole mobility, so higher performance is expected and has been demonstrated for p-type Ge nanowire based field effect transistors.² However, the intrinsic behavior of nominally phosphorus doped Ge nanowires³ has raised some questions regarding the relative influence of surface states, dopants, and unintentional impurities in establishing the majority carrier concentration in Ge nanowires. We have, for the first time, quantified the doping level of Au catalyzed P-doped Ge nanowires⁴ and compared doping and unintentional impurity levels with the electrical properties of the nanowires. Ge nanowires were synthesized by chemical vapor deposition employing vapor-liquid-solid (VLS) growth mechanism. Four probe measurements were used to determine the temperature dependent nanowire resistivity, and gate measurements were employed to determine the carrier type and mobility. Surprisingly, we find that the introducing of phosphorus reduces the conductivity of Ge nanowires. The gate measurements show that the undoped Ge nanowires have p-type characteristics while the P: Ge have intrinsic characteristics. The temperature dependence of resistivity of both wires shows an activated behavior near room temperature, and the activation energy extracted from the plots does not correspond to any potential impurity levels in Ge. To exclude the general concern that the use of metal catalyst in VLS growth introduces electrically active impurities in significant concentrations, we employed atom probe tomography to determine the distribution and concentration of bulk impurities in Ge nanowires. We found no evidence of Au acceptors (concentration below 10¹⁷ cm⁻³) in nominally undoped Ge nanowires, and the concentration of phosphorous in P: Ge nanowires is as high as 2×10¹⁸ cm⁻³. We conclude that this concentration of P is insufficient to overcome the effect of surface states on hole accumulation. Wet chemical passivation was used to temporarily reduce the surface state density of the undoped Ge nanowires, which reduced conductivity of the nanowire, confirming the contribution of surface states to the conductivity. A quantitative model of the relative influence of surface states, dopants, and bulk impurities on conductivity will be presented. ¹Lieber, C. M. MRS Bulletin 2003, 28, (7), 486-491. ²Wang, D. W.; Wang, Q.; Javey, A.; Tu, R.; Dai, H. J.; Kim, H.; McIntyre, P. C.; Krishnamohan, T.; Saraswat, K. C. Applied Physics Letters 2003, 83, (12), 2432-2434. ³E. Tutuc et al. Appl. Phys. Lett. 89, 263101 (2006). ⁴Lauhon et al, Nature Nanotechnology, in press.

4:10 PM Student

N3, Twinning Superlattices: A Correlated Raman and Transmission Electron Microscopy Study on Individual Silicon Nanowires: *Francisco Lopez*¹; Eric Hemesath¹; Lincoln Lauhon¹; ¹Northwestern University

Silicon nanowires are of interest as highly scaled components of new electronic and electromechanical device technologies. Nanowires can be synthesized by conventional chemical vapor deposition processes and devices can be fabricated using standard processing techniques, facilitating integration with current technologies that nanowires may enhance. The mechanical characteristics of nanowires may be particularly compelling, as they can be grown as perfect defect-free single crystals, but planar defects in the form of lamellar twins are also known to occur for nanowires with certain crystallographic orientations. Here we present a detailed investigation of ordered twin defects in single silicon nanowires using correlated transmission electron microscopy (TEM) and Raman spectroscopy. Raman spectra from ~20 nm nanowires reveal that planar faults are often not randomly distributed, but exhibit local order resulting in twinning superlattice domains. When such domains extend across the entire nanowire, new phases distinct from the diamond cubic result. These structures have distinct electronic and vibrational properties, including different band gap and valence band energies. More specifically, we find that the 3C, 2H, and 9R polytypes of silicon may co-exist within a single growth sample and within a single nanowire, and that the Raman spectra for these polytypes can be explained using simple Brillouin zone-folding arguments. Previously, ensemble Raman spectroscopy measurements have been used by other workers to claim that hexagonal and diamond cubic Si nanowires grow simultaneously, and that nanowire growth conditions are responsible for new phases of silicon. We find that the situation is more complex, as multiple phases are observed within a single nanowire, as well as variations in phase along the nanowire. These new phases are best understood as arrays of planar defects with varying defect



densities. Planar defects are sometimes associated with changes in nanowire crystallographic axis during growth, and changes in the defect structure can be mapped by Raman spectral imaging. We find that Raman spectroscopy is sensitive down to the single twin level in small nanowires, as well as to the periodicity of the twinning. The relevance of this finding is underscored by the recent reports of Au atom trapping in such defects for silicon nanowires grown with Au catalyst particles. On a more detailed level, polarization-dependent Raman studies enable us to differentiate between nanowires of pure phases and those having mixed or random planar fault distribution. We will clarify some inconsistencies in the literature regarding peaks positions, widths, and relative intensities of the Raman spectrum of 2H Si, and discuss the newly discovered 9R nanowire polytype.

4:30 PM

N4, Self-Cleaning Silicon Nanowire Elastomeric Composites: *William Wong¹; Tse-Nga Ng¹; Rene Lujan¹; Palo Alto Research Center*

The texturing of surfaces has been demonstrated to modify surface energies in order to create self-cleaning surfaces. These superhydrophobic surfaces are typically created using processes that directly modify the surface of interest. Many approaches exist to form textured surfaces ranging from selective etching of nano-scale features to depositing self-assembled monolayers. The surfaces created are usually fixed onto the processed surface and limits the materials choices that can create these self-cleaning structures. We have investigated the use of nanowire embedded composites for surface energy modification, creating super-hydrophobic conditions (contact angles greater than 150°) on elastomeric films. The films can be removed from its process wafer and laminated onto a different substrate, creating a self-cleaning surface by selective layer transfer. A bottom-up approach to fabricating super-hydrophobic surfaces using Si nanowires (SiNWs) embedded in polydimethylsiloxane (PDMS) will be presented. A dense network of SiNWs having ordered (vertically oriented) and disordered structures was first synthesized on Si (111) substrates by chemical-vapor deposition. The as-grown SiNW network, having a nanowire length of ~ 30 microns, was found to be hydrophilic with a water contact angle of ~ 5°. A composite SiNW/PDMS layer (of ~ 20 micron thickness), with the ordered SiNWs protruding out from the PDMS surface, was created by drop-casting the PDMS onto the SiNW surface. A resulting water contact angle of 150° was measured on the composite layer surface, greater than the contact angle of ~80° on bare PDMS. Results for free-standing SiNW/PDMS composite layers and applications towards nanocomposite laminates will be presented. Finally, the effect on the thermal conductivity of the embedded SiNWs on the composite materials will be explored and discussed.

4:50 PM N5, Late News

emitted from and propagated in the bulk of polar and non-polar GaN substrates. PL spectroscopy was performed in surface emission and edge emission configurations using a HeCd (15 mW) CW-laser and the YL was analyzed by a polarizer and dispersed by a spectrometer and detected by a charge coupled device array. The top surface emission of polar c-plane and non-polar m-plane and a-plane samples is analyzed first. For the polar GaN, the YL (peak 560 nm), no intensity difference is found for polarization along the a-axis (E//A) and along the m-axis (E//M). However, for the non-polar m-plane sample (peak 526 nm), the ratio of E//A to E//C is 0.68. For the a-plane sample (peak 530 nm) the ratio of E//M to E//C is 0.60. It is known that non-polar GaN based LEDs show partially polarized quantum-well emission in the direction perpendicular to the c-axis due to the splitting of the valence band structure, however the different polarization properties of the YL indicate that the defect center might also reflect the hexagonal band structure, which may reveal further details of the defect. Beyond this surface emission study, we find additional information from the edge emission, e.g., from the m-plane and a-plane edges of the c-plane bulk sample. In this, the laser excitation point on the sample is scanned from the edge of the sample to the center. Emission from the (1-100) plane (m-plane) shows an intensity ratio E//A to E//C that varies from 0.81 to 0.89 as the excitation moves from 1 mm to the edge to 5 mm. For the edge-emission from the (11-20) plane (a-plane), the ratio of E//M to E//C changes from 0.71 to 0.81 along the same spot variation. The decreasing degree of polarization as the light propagating longer in the sample indicates that the different intensity between polarization parallel and perpendicular to the c-axis observed from the edge is not induced by the transmission through the surface (Fresnel effect). It rather suggests that any imperfections of the sample induce a light scattering towards the stronger polarization direction. Its relevant light scattering length was determined in this way and compared to theoretical results. This work was supported by a DOE/NETL Solid-State Lighting Contract of Directed Research under DE-FC26-06NT42860.

1:50 PM Student

O2, MOCVD Growth of True Blue m-Plane GaN Laser Diodes: *Kathryn Kelchner¹; University of California, Santa Barbara*

(Al,Ga,In)N materials have proven useful for laser diode applications from near-UV into the visible range since their first demonstration in 1995. Significant progress has been made in growth, design and fabrication techniques to reduce lasing threshold, increase output power, and improve device lifetimes. Unlike traditional c-plane (Al,Ga,In)N heterostructures, nonpolar m-plane (1-100) orientated quantum wells lack built-in polarization induced electric fields, preventing quantum confined Stark effect (QCSE) and therefore increasing radiative recombination efficiency. Since its first demonstration at 405nm in 2007, m-plane GaN laser diodes have shown potential for improved laser characteristics. The advantage of nonpolar GaN based laser diodes is expected to be even greater in blue and green spectral range. This work is focused on the growth and fabrication of m-plane GaN laser diodes emitting in the true-blue spectrum, 450nm through 460nm. One of the biggest challenges for growing longer wavelengths devices on m-plane GaN is incorporating high indium containing InGaN alloys in the multiple quantum wells (MQWs). This study required extensive growth optimizations of MQW active region for emission in the true blue range. All growths were carried out by atmospheric pressure metal organic chemical vapor deposition (MOCVD) on low defect density free-standing m-plane substrates. Samples were characterized by optical microscope, X-ray diffraction, and secondary ion-mass spectroscopy. Optical properties were tested with photoluminescence (PL) and electroluminescence, and electrical properties with transmission-line measurement (TLM). Results show indium incorporation, as well as the structural and optical quality of the MQWs, depend greatly on growth temperature, growth rate, precursor and carrier gas flows, and thickness of QWs. InGaN characterization growths show peak wavelengths up to 490nm with room temperature PL, and indium content up to 28%. Waveguide and band-diagram modeling were employed in the design of full laser diode structures. Initial laser growths consisted of n-type GaN followed by n-AlGaIn cladding, n-GaN waveguiding layer, four period InGaIn/GaN MQWs, thin p-AlGaIn electron blocking layer, p-GaN waveguiding layer, p-AlGaIn cladding, and p-GaN and p++GaIn contact layers. The sample was then processed into

Session O:

III-Nitride: Optical Devices on Non-Polar Substrates

Wednesday PM
June 24, 2009

Room: 207
Location: Pennsylvania State University

Session Chair: Jung Han, Yale University

1:30 PM Student

O1, Polarization Study of Yellow Defect Luminescence from Polar and Non-Polar Bulk GaN: *Shi You¹; Yong Xia¹; Yufeng Li¹; Theeradetch Detchprohm¹; Christian Wetzel¹; Future Chip Constellation, Rensselaer Polytechnic Institute*

High quality bulk GaN material is the optimum substrate for the homoepitaxy of light emitting diodes (LEDs) and laser diodes. However, the material still suffers from many structural and point defects. The availability of bulk GaN substrates oriented along several crystallographic axes affords an excellent opportunity of the well-known defect-related yellow luminescence (YL) band observed in photo-luminescence (PL), centered at approximately 2.2–2.3 eV. Here we present a study of the light polarization properties of the YL, both, as

broad-area laser bars parallel to the c-axis, with mesas and facets defined by dry-etching. Pulsed testing was done on unpackaged and uncoated facets at room temperature. Electrical and optical measurements of these initial laser diodes showed threshold current density (J_{th}) as low as 6kA/cm², with threshold voltage of 10V. The spectrum shows clear stimulated emission at a wavelength of 437nm with FWHM of less than 2nm. Further improvements are expected with optimized growth conditions and fabrication of ridge structures with cleaved facets and facet coating. Details of the growth, design, fabrication and characterization of blue m-plane laser diodes would be presented at the conference.

2:10 PM Student

O3, Blue-Green GaInN/GaN Light Emitting Diode on Non-Polar m-Plane Bulk GaN: *Mingwei Zhu*¹; Theeradetch Detchprohm¹; Shi You¹; Wei Zhao¹; Wenting Hou¹; Yufeng Li¹; Yong Xia¹; Liang Zhao¹; Stephanie Tomasulo¹; Tanya Paskova²; Edward Preble²; Drew Hanser²; Christian Wetzel¹; ¹Rensselaer Polytechnic Institute; ²Kyma Technologies, Inc.

High performance blue light emitting diodes (LEDs), employing GaInN/GaN heterostructures have been commercialized on polar c-axis oriented substrates in spite of the presence of large spontaneous and piezoelectric polarization in their active regions. The polarization-induced electric field could lead to a longer emission wavelength and lower radiative recombination efficiency due to the spatial separation of electron and hole wave functions. This problem magnifies for green light emitters, which experience a stronger electric field due to the larger InN fraction in their quantum wells (QWs). Growth along non-polar directions, such as a-axis and m-axis, thus offers great potential to achieve better device performance for longer wavelength light emitters. Non-polar GaN can be grown on foreign substrates, such as γ -LiAlO₂ and r-plane sapphire. However, the epitaxial film still suffers from high density of extended defects, which are believed to act as nonradiative recombination centers and degrade device performance. With the recent advancement of hydride vapor phase epitaxy technology, non-polar low-defect-density substrates become available when sliced from c-plane-grown bulk GaN. It provides an ideal candidate to achieve high efficiency LED with long emission wavelength. Here we report a 494-nm blue-green LED grown on such low-defect-density m-plane GaN substrate. The full device was deposited by metalorganic vapor phase epitaxy. The smooth active region consisted of 8 pairs of GaInN/GaN QWs sandwiched between 2- μ m n-GaN and 0.2- μ m p-GaN. When collecting from the backside of the wafer, it delivers a light output power of 2.1 mW at an injection current of 100 mA, where its external quantum efficiency reaches the maximum. The m-plane LED experiences a much smaller wavelength blue shift with increased current compared to c-plane LEDs in the same wavelength range. Under CW operation, its peak wavelength blue shifts by 2 nm when current increases from 2 to 100 mA, followed by red shift at higher current. For c-plane LEDs, the blue shift could be as large as 5 to 7 nm. Their wavelengths continue to decrease until heating plays a major role, resulting in a red shift. From X-ray diffraction measurement, we find that a much higher InN fraction is required for m-plane QWs to emit light of same color as c-plane. The indium composition in this m-plane LED is about 23% while c-plane ones contain merely 10%. This further confirms the absence of polarization field along the m-axis. Our optical measurement also suggests that the light emitting from the top surface of m-plane LED is highly polarized. A polarization ratio $(I_{E/a} - I_{E/c}) / (I_{E/a} + I_{E/c})$ of 0.52 was found at an injection current of 20 mA. This work was supported by a DOE/NETL Solid-State Lighting Contract of Directed Research under DE-FC26-06NT42860.

2:30 PM Student

O4, Growth and Characterization of High Indium Content m-Plane InGaN LEDs: You-Da Lin¹; Arpan Chakraborty²; Hsun Chih Kuo¹; Stuart Brinkley¹; James Speck²; Steven DenBaars²; Shuji Nakamura²; *Kathryn Kelchner*¹; ¹ECE Department, University of California, Santa Barbara; ²Materials Department, University of California, Santa Barbara

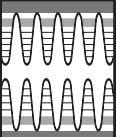
Nonpolar group-III-nitride optoelectronic device have drawn much attention recently. Charge separation due to spontaneous and piezoelectric polarization inherent to the wurtzite structure has adverse effects on the performance of commercially available c-plane oriented III-nitride devices. Despite recent

reports on short-wavelength m-plane InGaN/GaN LED performances,¹⁾ there are very few reports on growth and properties of high In content m-plane InGaN LEDs. Long wavelength nonpolar devices have huge potential for closing the green-gap. In this study, we have done a comprehensive investigation on the growth and characterization of m-plane LEDs with high In containing InGaN alloys. The LED structures were heteroepitaxially grown on m-plane GaN substrates (supplied by MCC) by atmospheric-pressure metal-organic chemical vapor deposition. The device structure consisted of a 4 μ m Si-doped n-type GaN layer, followed by the active region consisting of un-doped In_xGaN_{1-y} barriers and In_xGa_{1-x}N well. For fixed In content in the wells and the barriers, the well width was varied from 2 nm to 4 nm, and the barrier width from 7.5 to 25 nm. The number of period was varied from 1 to 5. The effect of the interrupt time between the well and the barrier was also investigated. A Mg-doped AlGaIn electron blocking layer was grown after the active region, followed by a 200 nm p-type GaN layer. The as-grown samples were investigated by RT photoluminescence (PL) and DC and pulsed electroluminescence (EL) measurements. Indium composition in the wells and the barriers were determined by high-resolution x-ray diffraction. For the same In content, it was observed that the EL and PL emission wavelength increased with the increasing well width and eventually the wavelength rolled-off for 4 nm thick well. This can be explained by the quantum confinement effect. However, significant drop in the output power was observed for well width exceeding 3 nm. This could be explained by reduced recombination efficiencies at longer wavelength. For the barrier series, the output power increased with the increase in the barrier width. For all the samples that were tested, there was minimal difference in the EL and PL emission wavelength. Furthermore, almost no blue shift in the emission wavelength was observed for drive currents ranging between 5-300 mA, under pulsed operation. This suggests the absence of polarization field inside the MQWs. The LEDs were packaged into conventional lamp and the nature of polarization was studied. The details of epitaxial growth, fabrication, packaging and characterization would be presented at the conference. This work was partly supported by the Solid State Lighting and Energy Center (SSLEC) at UCSB.1)K. C. Kim et al., Appl. Phys. Lett. 91, 181120 (2007).

2:50 PM Student

O5, N-Polar (Al, In, Ga)N Grown by Metalorganic Chemical Vapor Deposition: *Qian Sun*¹; Yu Zhang¹; Tsung Shine Ko¹; Benjamin Leung¹; Christopher Yerino¹; In-Hwan Lee¹; Jung Han¹; Hyunjin Kim²; Arto Nurmikko²; ¹Yale University; ²Brown University

With the well-established properties and limitations of Ga-polar (0001) III-Nitride, there has been an increasing interest in exploring alternative crystallographic planes including non-polar and semi-polar directions. N-polar (000-1) offers a diametrically different atomic configuration from its Ga-polar counterpart in surface stoichiometry and atomistic configuration, allowing an access to kinetic epitaxy space and new applications that are not normally attainable on Ga-polar surface. The investigation of N-polar III-Nitride, nevertheless, remains at an embryonic stage. In this paper, we present a study on the issues related to the low-temperature (LT) GaN buffer, the effect of high-temperature (HT) growth parameters on GaN morphology and microstructure, as well as the opportunities and challenges of N-polar (Al, In)GaN heterostructure. All the samples were grown by MOCVD on c-plane sapphire with the N-polarity confirmed by both TEM CBED and KOH solution etching. After a quick review of the effect of sapphire nitridation and the N-polar GaN growth evolution, we will examine the necessity of a LT-GaN buffer, and the influence of growth temperature and thermal annealing of LT-GaN buffer. For the HT growth of N-polar GaN, it is found that a high T, a reduced reactor pressure P, and a low V/III ratio are normally required to obtain a smooth N-polar GaN surface (free of hexagonal hillock). N-polar GaN reported to date often exhibits a steep increase in the full-width at half-maximum (FWHM) of x-ray rocking curve (XRC) as the diffraction plane is inclined from basal to pyramidal, and to prismatic planes. Under various growth conditions, however, our N-polar GaN shows a great tunability in the slope of the FWHM-Chi plots, from a steep increase to a nearly invariant or even a shallow decrease. The correlation between the microstructure variation and the change of surface morphology implies an interplay between the crystallites misalignment and



the nucleation/evolution dynamics. Although N-polar InGa_N growth appears to incorporate In more readily than Ga-polar InGa_N, it is consistently observed that N-polar InGa_N QWs give a much weaker luminescence with a broad (often white) spectrum than Ga-polar QWs. In an attempt to unveil the origin of this poor optical performance, we studied N-polar InGa_N epilayer grown on N-polar GaN template. In the x-ray 2 θ / ω scans, a strong phase separation peak is often detected at the low-angle side of the InGa_N main diffraction and gets more pronounced as the growth rate increases or the growth T decreases. The XRC of the phase separation peak is 3-4 times broader than that of the main peak. There may be a high density of stacking faults (or cubic phase) formed during the N-polar InGa_N growth (typically at a LT), which will be verified by TEM.

3:10 PM Break

Session P: III-Nitride: Growth and Characterization of Non-Polar Materials

Wednesday PM
June 24, 2009

Room: 207
Location: Pennsylvania State University

Session Chair: Jung Han, Yale University

3:30 PM Student

P1, The Origin of Pits and Striations on the Surface of Nonpolar a-Plane GaN: *Christopher Yerino*¹; Qian Sun¹; Tsung-Shine Ko¹; In-Hwan Lee¹; Jung Han¹; ¹Yale University

In the development of nonpolar GaN growth on sapphire, morphological imperfection in the form of pits and striations is one of the most inhibiting issues for device applications. Such features have been attributed vaguely to the anisotropy of nonpolar surfaces. This work intends to provide a qualitative model regarding major steps in morphological evolution responsible for the formation of surface defects. While the heteroepitaxial process on a-plane GaN resembles the islanding-coalescing dynamics commonly observed on c-plane GaN, the lack of crystallographic symmetry in surface kinetics of a-GaN dramatically complicates the geometry in morphological evolution. The origin of a-GaN morphological defects is deduced from growth interruptions combined with the coalescence behavior of SAG islands. A-plane GaN was grown on r-plane sapphire by a standard MOCVD process using an AlN buffer, GaN growth temperature around 1050°C, 60-300 mbar pressure, and V/III of 190-1600. Growth interruptions were studied by SEM for several stages of the coalescence process. For SAG experiments, SiO₂ was patterned with a grid of circular openings onto a-GaN epilayers. The initial formation of SAG islands (using the above conditions) provided measurement of facet growth rates on convex island geometry. Extended SAG growths were performed up to the time the islands coalesced, when new surfaces emerged with concave geometries and faster growth rates. Consideration of both convex and concave growth fronts enables satisfactory explanation of morphological evolution during islanding and coalescing stages, respectively, and can be broadly applied to other heteroepitaxial systems. Features in the planar growth interruptions are well correlated with the observed SAG islanding and coalescence. SAG islands bear relatively slow {000-1}, {0001}, {10-11}, {10-10} and {11-20} facets, producing an elongated, "space-shuttle" shape where the aspect ratio is a function of growth conditions and underlying heterogeneous surface. Depending on their relative positions, a-plane islands upon contact (the onset of coalescence) will create concave growth fronts along c-, m-, and pyramidal axes. The nature of concave growth fronts requires a set of faster planes to arise, including {11-22}, {10-1-2}, and {20-21} which are saddle points on the kinetic Wulff plot. During planar growth, the c-axis elongation of islands influences the initial coalescence by forming networks of voids and ridges roughly along [0001]. Points of contact between ridges form pyramidal {11-22} and {10-1-2} planes that "zip up" the elongated grooves along Ga-polar and N-polar directions, respectively. The commonly observed pentagonal or

heptagonal pits form once the oppositely-facing pyramidal planes meet. As the pyramidal planes advance along and fill these grooves, they leave behind much shallower V-shape grooves, bounded by slightly off-axis a-planes at local growth rate maxima, forming what are known as striations.

3:50 PM Student

P2, Nucleation and Evolution in the Two-Step Growth of a-Plane GaN for Improving the Microstructural Quality: *Qian Sun*¹; Tsung Shine Ko¹; Christopher Yerino¹; Yu Zhang¹; In-Hwan Lee¹; Jung Han¹; Bo Hyun Kong²; Hyung Koun Cho²; ¹Yale University; ²Sungkyunkwan University

Many groups have reported that the conventional growth condition for c-plane GaN (c-GaN) does not work for a-plane GaN (a-GaN) heteroepitaxy, but often yields a rough surface with many pits. A reduced pressure P and a low V/III ratio are commonly found effective in eliminating the surface pits for a-GaN; however, a-GaN epilayers prepared under such conditions always contain a very high density of structural defects and give very broad on-axis (11-20) x-ray rocking curves (XRCs) with a high anisotropy along the in-plane m- and c-axes. In contrast, a high V/III ratio and an increased P seem to produce rough a-GaN but with much narrower XRCs, implying an improved microstructural quality. These two observations lead to the consideration of a two-step growth scheme, with a nucleation step favoring the structural quality followed by rapid island coalescence to attain smooth surface morphology. All a-GaN samples were grown on nominally on-axis r-sapphire with a 60-nm-thick AlN buffer (deposited at 1150 °C). For the baseline (sample A), 2- μ m-thick a-GaN was grown in one step on the AlN buffer at 1050 °C, 60 mbar and a V/III ratio of 187. In situ optical reflectance of sample A exhibits instant oscillations, an indicator of quasi-two-dimensional growth mode. With the insertion of a nucleation step under an increased V/III (187-2162) and/or P (60-300 mbar), the a-GaN growth surface becomes increasingly rough. Once the growth is switched to the second-step condition (sample A condition), the reflectance is quickly recovered through an enhanced lateral growth, resulting in a pit-free surface. Compared to c-GaN, nonpolar a-GaN contains much more complicated structural defects, including screw, edge, and mixed type threading dislocations (TDs), and stacking faults (SFs) bounded by partial dislocations (PDs). To obtain a full picture of the a-GaN microstructure, we carried out a comprehensive XRC study for both on-axis and off-axis planes spanning over a sufficiently large azimuthal and polar angular space. The full-widths at half-maximum (FWHM) of a-GaN XRCs have been reduced from (0.25 θ , 0.56 θ) for the on-axis (11-20) XRCs along the c- and m-axes and (0.61 θ , 0.67 θ) for the off-axis (-2110) and (11-24) to (0.17 θ , 0.21 θ) and (0.29 θ , 0.32 θ) with a minimum anisotropy, respectively. Moreover, a modified Williamson-Hall x-ray analysis on the 30 θ -inclined m-plane (n0-n0) (n = 1, 2, and 3) shows a substantial increase in the c-axis lateral coherent length from 19 to 60 nm, which is roughly inversely proportional to the density of basal-plane SFs. TEM observations also confirmed a significant reduction of defect density in the two-step grown a-GaN, as compared to sample A (one-step growth). The improvement of microstructural quality is further supported by a record electron mobility of 190 cm²/V-sec with a 2DEG density of 1.5 x 10¹³cm⁻² in a-plane AlGa_N/GaN HFET.

4:10 PM

P3, Carrier Lifetime of m-Plane GaN: *Grace Metcalfe*¹; Paul Shen¹; Michael Wraback¹; Asako Hirai²; Erin Young²; James Speck²; ¹US Army Research Laboratory; ²University of California, Santa Barbara

The development of nonpolar or semipolar III-nitride materials has advanced significantly, partly as a means to eliminate strong internal polarization-related electric fields characteristic in c-plane oriented III-nitride heterostructures. Because of the difficulty in growing high quality nonpolar or semipolar III-nitride material, little is known about the carrier dynamics in these materials as it relates to defects such as stacking faults. Recently, stacking fault (SF)-free m-plane (10-10) GaN free-standing substrates have been grown by Mitsubishi Chemical Co., Ltd. In this paper, we present carrier lifetime studies on SF-free and various SF density m-plane GaN samples using femtosecond time-resolved reflectivity. The SF-free m-plane GaN substrate is ~330 μ m-thick and was cut from c-plane oriented bulk GaN grown by HVPE. The other m-plane GaN samples grown by HVPE, MOCVD, and NH₃-MBE on an m-plane SiC substrate have a SF density of 3 X 10⁵ cm⁻¹, 1 X 10⁶ cm⁻¹, and 3 X 10⁶ cm⁻¹,

respectively. The experiments were performed with a pump center wavelength varying between 355 nm to 365 nm, and a probe center wavelength below the bandgap. The photo-excited carriers created by the pump pulse cause a bleaching of the probe absorption, and thereby an initial negative change in reflectivity, $\Delta R/R$. The subsequent decay of $\Delta R/R$ primarily characterizes the decay of carriers from the conduction band either through radiative recombination or trapping and non-radiative recombination. In general, the GaN samples with SFs demonstrate shorter carrier lifetimes with increasing SF density (with the decay time at 355 nm pump wavelength being about 450 ps, 30 ps, 5 ps, and 10 ps for SF densities of 0 cm^{-2} , $3 \times 10^5 \text{ cm}^{-2}$, $1 \times 10^6 \text{ cm}^{-2}$, and $3 \times 10^6 \text{ cm}^{-2}$, respectively), suggesting that the SFs act as traps/recombination centers, thereby reducing the carrier lifetimes in the bands. However, the MOCVD-grown GaN film shows a faster decay time (~ 5 ps) than that of the higher SF-density sample, suggesting the MOCVD-grown sample has other traps or deep levels which play a large role in the carrier dynamics. The time-resolved measurements from the SF-free substrate show both a large-amplitude slow and small-amplitude fast exponential decay. We attribute the fast decay, which is ~ 25 ps at 355 nm pump wavelength and increases with longer wavelength, to surface recombination effects. As the pump wavelength becomes longer, the fast decay signal decreases in amplitude due to increasing absorption depth and decreased absorption at the surface. The slow decay signal provides a measure of the dominant carrier decay time in the bulk, which is determined to be ~ 450 ps for the SF-free substrate.

4:30 PM Student

P4, Kinetic Wulff Diagram: Toward Rational Design of Nonpolar and Semipolar GaN Heteroepitaxy: *Christopher Yerino*¹; Qian Sun¹; Tsung-Shine Ko¹; Benjamin Leung¹; In-Hwan Lee¹; Jung Han¹; ¹Yale University

The material research of GaN has undergone rapid expansion from exclusively Ga-polar, c-axis growth into diverse crystallographic orientations. There have been impressive reports regarding lighting emitting devices built on m-, a-, and semipolar planes. The opportunities presented by the multiplicity of orientations are accompanied by a daunting challenge of optimizing heteroepitaxial process along each individual axis, where progress has been made largely by an empirical, knob-turning exercise. Mesoscopic crystal growth phenomena are governed by minimization of energy (surface tension and strain), which was first analyzed mathematically by Wulff. The so-called "kinetic Wulff diagram" (growth velocity versus surface orientation) has shown sufficiency in predicting the shape evolution under non-equilibrium conditions. To lay down the foundation of the Wulff principle toward understanding and controlling nonpolar and semipolar growth, we present a detailed mapping of kinetic Wulff plots through a novel and quantitative measurement technique, differential selective area growth ($\Delta R/R$ -SAG). Our study explores a wide range of growth conditions (40-300 mbar, 1000-1100 °C, and V/III: 20-4000) on polar, nonpolar, and semipolar epilayers, so growth axes spanning the entire crystallographic sphere can be produced. SAG was carried out similar to conventional epitaxial lateral overgrowth experiments using silicon dioxide as the inert mask. Samples employed in this study include Ga-polar c-plane GaN, m-plane GaN on 4H SiC, a-plane GaN on r-plane sapphire, N-polar GaN on sapphire, and semipolar (11-22) GaN on m-sapphire. These samples were adjacently arranged under nominally identical MOCVD growth environment. The use of mask patterns with annular window openings facilitates the measurement of all facets relevant to heteroepitaxial dynamics including slow, stable facets on the outer ring (Wulff plot minima, e.g. (1-101)) and faster, metastable facets (Wulff plot saddle points, e.g. (11-22)) delineating the inner voids. In addition to (0001), (1-101), (1-100), and (11-22) planes commonly seen on c-plane SAG islands, we observed (11-20), (000-1), (10-1-2), and (20-2-1) facets from mesas grown on a-, m-, semipolar, and/or N-polar planes. A lower growth pressure or V/III ratio makes the Wulff diagram more symmetric in the basal plane, while elongating the islands on the c-axis. An increase in reactor pressure or V/III ratio truncates the islands along [0001] and accelerates (11-20), widening their basal-plane diameter and height. Beyond scientific interest, we seek to correlate Wulff plots with heteroepitaxy, including island growth and coalescence dynamics. The application of Wulff plots to tailor island shapes and control morphological evolution, particularly on semipolar (11-22) orientations, will be presented to validate our model. Last we will report the exploitation of morphactants to

actively control and manipulate growth kinetics during MOCVD heteroepitaxy, accessing new kinetic pathways unavailable by conventional parameters.

4:50 PM

P5, 4H-Polytype AlN/AlGaN MQW Structure Isopolytypically Grown on m-Plane 4H-SiC: *Masahiro Horita*¹; Tsunenobu Kimoto¹; Jun Suda¹; ¹Kyoto University

AlN and related alloys with a nonpolar growth direction have attracted much attention for high-efficient deep ultraviolet light-emitting devices due to the elimination of the unfavorable effects of built-in electric fields in heterostructures. We have reported that the high-quality 4H-polytype AlN can be grown on 4H-SiC (11-20) *a*-plane and (1-100) *m*-plane by molecular-beam epitaxy. The densities of stacking faults and threading dislocations of grown layer are $2 \times 10^6 \text{ cm}^{-2}$ and $8 \times 10^7 \text{ cm}^{-2}$, respectively. In order to apply the high-quality 4H-AlN to light-emitting devices, it is important to realize quantum well structures. In this paper, growth and characterization of AlGaN and AlN/AlGaN multiple quantum well (MQW) structure on nonpolar 4H-SiC are presented. In order to obtain the AlGaN for QW active layers, AlGaN growth was performed on 4H-SiC both nonpolar *a*- and *m*-plane with various Al/Ga flux ratio. From reflection high-energy electron diffraction, it was found that the AlGaN layers have 4H-polytype in both nonpolar faces. In *m*-plane growth, $\text{Al}_{0.9}\text{Ga}_{0.1}\text{N}$ (Ga composition $x = 0.1$) was obtained at the Ga flux ratio ($F_{\text{Ga}}/(F_{\text{Ga}}+F_{\text{Al}})$) of 0.35 while negligibly small Ga composition was observed in AlGaN *a*-plane growth. It should be noted that the small Ga incorporation was also observed in *a*-plane growth of wurtzite (2H) AlGaN. We believe that the low Ga incorporation for *a*-plane is general phenomena for high-Al content AlGaN. At the present time, we conclude that the *m*-plane is more favorable for AlGaN growth than the *a*-plane from the viewpoint of composition controllability. Growth of AlN/Al_{0.9}Ga_{0.1}N MQW structure on *m*-plane 4H-SiC was carried out. The MQW structure consisted of AlN template layer (50 nm), 10 pairs of AlN (15 nm)/Al_{0.9}Ga_{0.1}N (4 nm) MQW layer, and AlN cap layer (130 nm) in order of growth. TEM observation of MQW structure revealed that (1) the 4H-polytype was maintained in the whole of MQW structure and that (2) additional generation of extended defects was not observed at the AlN/AlGaN interface. In low-temperature cathodoluminescence (CL) measurements of the MQW structure, a band edge emission peak was observed at the energy of 5.40 eV (230 nm). The blueshift of the band edge peak was not observed with increasing excitation power density, suggesting that the MQW structure is free from the built-in electric field due to the polarization. These results demonstrate the feasibility of high efficient light-emitting devices with 4H-polytype AlN and related alloys.

Session Q:

III-Nitride: Processing of Electronic Devices

Wednesday PM
June 24, 2009

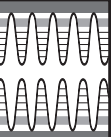
Room: 208
Location: Pennsylvania State University

Session Chair: Michael Manfra, Purdue University

1:30 PM Student

Q1, Mechanism of Interaction between Hydrogen and the Two Dimensional Electron Gas in AlGaIn/GaN High Electron Mobility Transistors: *Jason Gu*¹; Jacob Melby¹; Mahak Khandelwal¹; Robert Davis¹; Yuh-Renn Wu²; ¹Carnegie Mellon University; ²National Taiwan University

The mechanism of electrical response in the Al_xGa_{1-x}In_xN/GaN high electron mobility transistor (HEMT) upon exposure to hydrogen in the presence of a catalyst is not completely understood. In this research, experiments have been conducted to understand the physio-chemical processes that cause the change in the electronic properties of the two-dimensional electron gas (2DEG) within the HEMT device. Thin film heterostructures containing 60 nm Al_{0.2}Ga_{0.8}N/1.5 μm GaN/100 nm AlN were grown on SiC(0001) substrates using metalorganic vapor phase epitaxy. Schottky diodes were fabricated using Ti as the ohmic contact and Pt as the catalyst/Schottky contact. Capacitance-voltage (CV) curves were acquired in both pure nitrogen and 0.375, 0.750, 1.500, 3.125,



6.250, and 12.5 vol.% of H₂. A marked change in the capacitance of the device was observed upon exposure to all amounts of H₂; complete saturation in these curves was not observed at any concentration. The 2DEG carrier densities in the devices exposed to nitrogen and all H₂/N₂ mixtures were determined via CV measurements to be 4.71x10¹² electrons/cm² and 5.51x10¹² electrons/cm², respectively. Saturation of the carrier density with respect to H₂ concentration was observed at 2 vol.% H₂ in N₂. Interface state passivation and hydrogen dipole formation are proposed to occur simultaneously after hydrogen is introduced. Interface state passivation was examined using a Schrödinger-Poisson solver. The simulations modeled heterostructures with ionized donor states located between 1.0 and 1.7 eV below the conduction band edge (CBE), measured by Spencer and Koley, and 0.6 eV below the CBE, predicted by Segev and Van der Walle. The donor states of lowest energy were removed/filled in order to model the passivation of these states. The 2DEG carrier density without passivation was predicted to be 4.62x10¹² electrons/cm². As the states are passivated, the Fermi and charge neutrality levels shift toward the CBE due to the filling of the states located between 1.0 and 1.7 eV below the CBE. The calculated 2DEG carrier density increased to 5.68x10¹² electrons/cm², corresponding to Fermi level pinning at 0.6 eV below the CBE. Further reduction of the interface state density does not cause further increase in the 2DEG carrier density, corresponding to the saturation region of the observed 2DEG carrier density. The good agreement between the measured and predicted changes in the 2DEG carrier density support the interface state passivation mechanism. The lack of saturation in the capacitive response despite the saturation of the response in charge density is due to the formation of hydrogen dipoles. These dipoles cause a parallel shift in the capacitance voltage curve, thereby allowing higher capacitances at a constant voltage.

1:50 PM Student

Q2, Surface Passivation and Gate Insulation of AlGaIn/GaN High Electron Mobility Transistors Using in-situ SiNx: Marko Tadjer¹; Travis Anderson²; Michael Mastro²; Karl Hobart²; Yoosuf Picard²; Fritz Kub²; Charles Eddy, Jr.²; ¹University of Maryland; ²Naval Research Laboratory

High breakdown field, high 2DEG mobility, and low on resistance have resulted in promising power switching applications for AlGaIn/GaN based high electron mobility transistors (HEMTs). Currently, one of the main performance limiting factors has been the passivation of the device surface. This has been traditionally done using PECVD SiNx, however, an approach using in-situ grown SiNx has been demonstrated by Germain et al. to result in increased drain current density and transconductance [1]. By avoiding exposure of the AlGaIn surface to atmosphere, in-situ SiNx passivates surface states, reduces frequency dispersion, and improves overall device reliability. This paper compares AlGaIn/GaN HEMT devices fabricated with no passivation, PECVD SiNx passivation, and in-situ SiNx passivation by means of electrical and optical characterization. Device fabrication was performed on non-intentionally doped 25 nm Al(0.25)Ga(0.75)N / 2 μm GaN, grown by MOCVD on sapphire or n+ 4H-SiC substrates. A 100 nm deep mesa isolation trench was etched using a Cl₂-based ICP process, and a Ti/Al/Ni/Au Ohmic metal stack was evaporated and annealed for 30 sec at 950 °C. Following Ni/Au Schottky gate deposition, the sample was diced in two pieces, where subsequently 100 nm PECVD SiNx was deposited as a passivation layer on one half. The in-situ SiNx on the third AlGaIn/GaN sample was grown using a 0.5 % SiH₄ and N₂ atmosphere at 1050 °C and 50 Torr pressure, resulting in about 2 nm/min SiNx growth rate. The Ni/Au metal stack on that sample acted as an MIS gate. A SiNx thickness of about 30 nm was observed by transmission electron microscopy (TEM), and confirmed using high frequency (100 kHz) capacitance-voltage measurements. The measured accumulation capacitance was about 38.6 nF/cm² using a SiNx dielectric constant of 7.5. Measurements from depletion to accumulation resulted in a flatband voltage of -0.14 V, with hysteresis of 0.52 V at the reverse sweep direction, corresponding to 10.4 nC/cm² negative charge in the SiNx layer. Electroluminescence (EL) characterization using a LN₂ cooled CCD camera was performed on all three samples [2]. Improved surface passivation resulting from the in-situ SiNx layer was demonstrated by obtaining EL images of devices biased in forward blocking mode. No luminescence was observed from the gate-drain region of an in-situ passivated HEMT up to 400 V drain bias,

whereas using PECVD SiNx passivation resulted in luminescence proportional to the drain bias. [1] M. Germain et al., Mat. Res. Soc. Symp. Proc., vol. 831, pp. E6.7.1, 2005. [2] J. D. Caldwell, R. E. Stahlbush, O. J. Glembocki, K. X. Liu, and K. D. Hobart, J. Vac. Sci. Technol. B 24, 4 (2006).

2:10 PM

Q3, Plasma Surface Cleaning of Ultrathin Barrier AlN/GaN Heterostructures for Device Fabrication: Qingling Hang¹; Yu Cao¹; Tom Zimmermann¹; Debdeep Jena¹; Huili (Grace) Xing¹; ¹University of Notre Dame

The wide band gap and high electron saturation velocity of GaN make it suitable for high-power and high-speed devices. Recently ultrathin barrier (~ 4 nm) AlN/GaN heterostructures [1,2] have emerged as attractive options for ultrascaled GaN-based FETs to achieve operation speed higher than 300 GHz. High densities of 2-dimensional electron gases (> 2 x 10¹³ cm⁻²) can be obtained utilizing a few nanometer thick AlN barrier and its polarization properties. O₂ plasma is generally used to remove photoresist residues with a minimal effect on the 2DEG properties in conventional AlGaIn/GaN HEMTs. However, this O₂ plasma descum process needs to be reevaluated for ultrascaled devices with critical dimensions of nanometers. In this study, we applied a series of plasma surface cleaning conditions on as-grown and oxide-coated AlN/GaN heterostructures. The 2DEG density and mobility were monitored as an excellent indicator for possible plasma damages. The AlN/GaN samples were all grown by plasma assisted molecular beam epitaxy. The AlN barrier thickness is about 4 nm. The as-grown samples show a charge density of ~ 3x10¹³ cm⁻² and mobility > 1000 cm²/Vs. In the first experiment reactive ion etching (RIE) was used for the O₂ plasma treatment on as-grown samples. It was found that the 2DEG sheet resistance increased by a factor of 20 after 20 seconds' etching using a power as low as 50W and a pressure of 10mTorr. The sheet resistance stayed about the same with increasing etching time. The Hall effect measurements showed that this sheet resistance increase is a result of decrease in both 2DEG density and mobility upon the plasma treatment. For the second sample milder O₂ plasma was employed using inductively coupled plasma RIE (ICP-RIE). Upon 20 seconds' treatment the 2DEG density dropped slightly but the mobility decreased by a factor of 2. With increasing etching time the sheet resistance saturates about 4 times of its original value. CF₄ was also used to study the plasma damage, which was found to be smaller using similar plasma conditions. To protect the 2DEG, 3 nm Al₂O₃ or HfO₂ film was deposited by atomic layer deposition (ALD) on the AlN surface. Upon HfO₂ deposition both the 2DEG density and mobility increased slightly, while upon Al₂O₃ deposition the 2DEG density slightly increased and mobility slightly decreased. Both oxide layers was found to help mitigate the plasma damage, especially the ALD Al₂O₃ is effective in maintaining the 2DEG properties in a rather broad range of O₂ plasma powers. It demonstrates that a 3 nm ALD Al₂O₃ coating is adequate to minimize damages to the underlying 2DEG during plasma surface cleaning. [1] Y. Cao et al, Appl. Phys. Lett. 90, 182112 (2007). [2] T. Zimmermann et al. IEEE Electron Dev. Lett., 29, 661 (2008)

2:30 PM Student

Q4, Comparison of Plasma-Etching Induced Damage Recovery Treatments on GaN MOS Capacitors and Electrical Performance of Plasma-Etched GaN MOSFETs: Ke Tang¹; T. Chow¹; ¹Rensselaer Polytechnic Institute

Gallium Nitride (GaN) have generated a lot of interest for high-temperature and high-power devices because of its wide band gaps and large critical electrical field. In these device fabrications, plasma-etching is a very useful step in changing surface morphology, such as creating mesas, trenches and recessed gate regions. However, these dry etch induced damages in the near surface regions can deteriorate the electrical properties of the devices. Recently, different effective recovery methods were reported including N₂ plasma, KOH or NaOH wet etch and TMAH wet etch treatments. In this paper, we compared the effects of these treatments on plasma-etched GaN surfaces by evaluating the electrical characteristics of MOS capacitors and evaluated the effectiveness of the treatments by characterizing the electrical characteristics of GaN MOSFETs. Six pieces of samples from the same 2" UID GaN/Sapphire were prepared for MOS capacitors. After initial solvent and RTA cleans, these samples were dry etched by Chlorine based plasma and followed by different post-dry-etch treatments as listed in table I. The rest fabrication steps are the

same as described in reference 3. C-V curves were swept from accumulation to deep depletion between 100Hz to 1MHz for all six capacitors. Comparing to the control sample T0, all the wet etch treated samples (T1-T4) have similar negative shifted flatband voltages, while T5 (N₂ plasma) has the most negative flatband voltage. Among all the plasma etched and treated capacitors, T3 (15min. TMAH) has the smallest C-V dispersion. G- ω measurements were also conducted to extract the interface state density D_{it} of these differently treated capacitors. It shows that all of these three post-dry-etch treatments result in small D_{it}, with T3 (15min. TMAH) giving the lowest value, indicating they are all effective in restoring the MOS interface qualities, and the longer time 15min. of TMAH is the best. GaN MOSFETs were also fabricated to evaluate the post-dry-etch treatments effect. The process condition of capacitor T4 was picked to be conducted on the sample surface before gate oxide deposition, while the other one is un-etched as a controlling sample. The similar output IV characteristics and temperature dependence of field-effect mobility of these two MOSFETs indicating the hydroxide wet etch treatment is really effective in recovering the GaN/SiO₂ interface quality. In summary, we have compared the most popular GaN dry etch recovery methods on both GaN MOS capacitors and FETs. It turns out that hydroxide wet etch especially TMAH is the best post-dry-etch treatment in terms of both flatband voltage and interface state density.

2:50 PM

Q5, Influence of NH₃ in the Surface Passivation Dielectrics on AlGaIn/GaN Heterostructures Grown on a-Plane (11-20) and c-Plane (0001) Sapphire: *Subramaniam Arulkumaran*¹; Ng Geok Ing¹; Susai Lawrence Selvaraj²; Takashi Egawa²; ¹Nanyang Technological University; ²Nagoya Institute of Technology

Surface passivation has been found to reduce current slump and microwave power degradation of AlGaIn/GaN high-electron-mobility transistors (HEMTs). Recently, the enhancement of sheet carrier density (n_s) was observed on both a-plane and c-plane sapphire grown AlGaIn/GaN heterostructures (HSs) by plasma enhanced chemical vapor deposition (PECVD) grown SiN with NH₃ (NH₃-SiN) passivation [1]. No reports on the passivation of a-plane sapphire grown AlGaIn/GaN HSs by SiON and SiN deposited without NH₃ (NH₃-free-SiN). In this work, we report for the first time the passivation-induced changes in the transport properties of AlGaIn/GaN HSs on non-polar and polar (0001) sapphire by NH₃-SiN, NH₃-free-SiN and Silicon Oxynitride (SiON). Hall effect measurements as a function of temperature (80 to 400 K) were carried out before and after 120 nm of dielectric layer passivation. The enhancement of n_s was observed on the c-plane sapphire grown AlGaIn/GaN HSs after SiN and SiON passivation. However, no considerable n_s increase was observed after NH₃-free-SiN. The a-plane sapphire grown AlGaIn/GaN HSs exhibited n_s increase (20%) and decrease (80%) after NH₃-SiN and NH₃-free-SiN passivation, respectively. No considerable increase of n_s was observed after SiON passivation. The increase and decrease of μ_{H} for a-plane and c-plane sapphire grown AlGaIn/GaN HSs were observed by NH₃-free SiN passivation, respectively. This is due to the change of piezoelectric effect in the AlGaIn/GaN HSs by the passivation of highly packed density of Si and N in NH₃-free-SiN. The product of n_s μ_{H} decreases for both c-plane and a-plane sapphire grown AlGaIn/GaN HSs after NH₃-free-SiN passivation. However, the product of n_s μ_{H} increases for both c-plane and a-plane sapphire grown AlGaIn/GaN HSs after SiN (NH₃) and SiON passivation. The incorporation of H₂ in SiN and the film stress to the HSs play a major role in the enhancement of n_s and n_s μ_{H} . The SiON, NH₃-SiN and NH₃-free-SiN passivation induced changes in the non-polar and polar (0001) sapphire grown AlGaIn/GaN HSs are useful results for the design of high-frequency and high-power AlGaIn/GaN HEMTs.[1] S. Arulkumar, S.L. Selvaraj, T. Egawa and G.I. Ng, Appl. Phys. Lett., 92, (2008), 092116, 1-3.

3:10 PM Break

Session R: III-Nitride: AlGaIn Materials and Devices

Wednesday PM
June 24, 2009

Room: 208
Location: Pennsylvania State University

Session Chairs: Alan Doolittle, Georgia Institute of Technology; Randall Feenstra, Carnegie Mellon University

3:30 PM Student

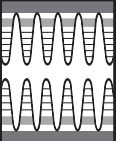
R1, Surface Characteristics of Single Crystalline, (0001)-Oriented AlN Wafers and Implications for Epitaxial Growth: *Anthony Rice*¹; Ramon Collazo¹; Rafael Dalmau²; James Tweedie¹; Seiji Mita¹; Zlatko Sitar¹; ¹North Carolina State University; ²HexaTech, Inc.

(0001)-oriented, Al-polar AlN wafers were processed from single crystalline AlN boules grown by physical vapor transport (PVT). Chemical and thermal surface treatments were conducted on mechanically polished (MP) and chemo-mechanically polished (CMP) wafers to assess their suitability as substrates and to determine a surface conditioning process for homoepitaxial growth of AlN thin films. MP surfaces analyzed by AFM exhibited low roughness (~0.5 nm RMS) and polishing scratches, while CMP surfaces were smoother (~0.1 nm RMS roughness) and scratch-free, possibly indicating that work-damage introduced during mechanical polishing steps was removed during chemo-mechanical polishing. MP substrates annealed at 1600°C in N₂ roughened due to preferential evaporation at work-damaged scratches. Similar thermal treatment of CMP substrates produced uniform surface steps with terrace height of ~3 nm and terrace width of ~30 nm. While no additional scratches were produced on thermally treated CMP substrates, protrusions with ~10 nm radius were observed at kink sites (site density ~10⁸ cm⁻²). XPS analysis of MP and CMP substrates indicated the presence of a native oxide layer composed of mixed aluminum oxide/hydroxide species, while the oxide layer of thermally treated substrates had stoichiometry closer to Al₂O₃ due to dehydration of hydroxides at high temperature. Additional surface treatments, consisting of wet chemistry and thermal annealing under NH₃ atmosphere, were performed on various as-polished and high-temperature treated substrates to determine the influence on surface morphology and composition. Wet chemical treatment in acidic solutions reduced the oxygen surface molar fraction relative to as-polished substrates, while the surface stoichiometry shifted toward an aluminum hydroxide component. Annealing of substrates at 1250°C under 60 Torr NH₃ converted the hydroxide surface to AlN. Epitaxial AlN thin films were grown on treated substrates by metal-organic chemical vapor deposition (MOCVD) utilizing several processing conditions. Results on epilayer growth on MP, CMP, and treated surfaces will be presented, and implications for AlN homoepitaxy will be discussed.

3:50 PM

R2, Photoluminescence Lifetimes and Internal Quantum Efficiencies of AlGaIn Based 250-nm Light Emitting Diodes from Pseudomorphic Growth on Bulk AlN: *Gregory Garrett*¹; Hongen Shen¹; Michael Wraback¹; James Grandusky²; Shawn Gibb²; Leo Schowalter²; ¹US Army Research Laboratory; ²Crystal IS, Inc.

The recent development of the pseudomorphic growth of AlGaIn layers on high quality bulk AlN substrates with etch pit densities less than 10⁴ cm⁻² has reduced the importance of threading dislocations on luminescence efficiency and focused attention more on point defects due to the propensity of Al to getter impurities. We present time-resolved photoluminescence (PL) studies on two samples of this new class of material for deep ultraviolet light emitting diodes (DUV-LEDs), comparing carrier recombination rates with measured PL efficiencies. The samples studied are AlGaIn multi-quantum well LED structures grown by metalorganic chemical vapor deposition (MOCVD) with the p-GaN layer omitted to allow optical excitation. The thickness of the pseudomorphic, MOCVD grown, 70% Al, AlGaIn base layer was 10 times greater than that expected from a Matthews and Blakeslee model. While nominally the same structures, one sample emitted at 247 nm (S247) and another emitted at 253



nm (S253). Time-resolved PL was taken using a 150-fs pulsed laser centered at 235 nm and at a fluence ranging from ~ 86 nJ/cm² (*low*) to ~ 51 μ J/cm² (*high*). The internal quantum efficiency (IQE) was estimated by comparing the temperature dependent data at 13K, where non-radiative processes are assumed saturated, with that at 300K. It was found that S247 had an IQE of 44 and 60% at the *low* and *high* excitations, while S253 had an IQE of 11 and 27%. The corresponding 13 and 300K PL lifetimes were ~ 518 ps and ~ 312 ps for S247 at both fluences, while S253 showed power dependent lifetimes of 877 to 600 ps at 13K and 120 to 176 ps at 300K for *low* to *high* excitation. The relatively short and intensity independent low-temperature PL lifetime in the high IQE S247 sample is indicative of its high quality, as localization associated with alloy or interface fluctuations would lead to the longer and intensity dependent PL lifetime observed in S255. Moreover, the weak temperature dependence of the PL lifetime in S247 is correlated with that of the radiative lifetime, perhaps due to the larger exciton binding energy in these higher Al content quantum wells. Finally, the long room-temperature nonradiative lifetime and its weak intensity dependence (566 to 760 ps) in S247 suggest a much smaller density of point defects relative to that in S255, for which the nonradiative lifetime varies from 135 to 242 ps. These results indicate that despite low dislocation densities in both samples control of point defects, interface and alloys fluctuations remain essential to development of high performance devices.

4:10 PM

R3, Low-Dislocation Density Al_xGa_{1-x}N Layers for High-Power UV-Visible Light Emitters Using an “in-situ” Silane Treatment: *Ohalid Fareed*¹; Joseph Dion¹; Jiawei Li¹; Bin Zhang¹; Asif Khan¹; ¹University of South Carolina

Research interest in the III-Nitride ultraviolet (UV) and visible light emission devices has significantly increased over the past few years. To increase the light emission efficiency of III-N UV-visible light emitters requires the deposition of high quality low-defect density layers of AlGa_xN ($x \sim 0$ to 0.5) over substrates such as sapphire. The heteroepitaxy of AlGa_xN over sapphire using conventional metal organic chemical vapor deposition (MOCVD) leads a large number (10^8 - 10^{10} cm⁻²) of threading dislocations. These high defect densities lead to decreased emission efficiency and a lifetime reduction especially for the UV LEDs with UV-B emission. Lateral overgrowth of AlGa_xN has been reported by various groups including ours. However, this approach needs additional lithography/etching steps which adds complexity and cost to the fabrication process. In this paper, we present a novel “in-situ” SiH₄ treatment method to reduce the dislocation densities in Al_xGa_{1-x}N layers. For the first time we have extended the Al-composition range to well over 30%. The Al_xGa_{1-x}N ($x \sim 0$ to 0.5) layers were grown over sapphire using low-pressure by metal organic chemical vapor deposition (MOCVD) after the deposition of a high-quality AlN buffer layer. A new pulsed MOCVD approach was used for the deposition of this AlN buffer layer. The in-situ SiH₄ treatment was carried out during the MOCVD growth of the AlGa_xN layer. Our procedure resulted in Al_xGa_{1-x}N layers ($x \sim 0$ to 0.5) with (TD) densities from 6.3×10^7 cm⁻² to 3×10^8 cm⁻². These dislocation densities were measured by wet-etching/atomic force microscopy (AFM) and confirmed using transmission electron microscopy (TEM) images. Thus by the in-situ treatment, we succeeded in reducing the TD densities in Al_{0.35}Ga_{0.65}N layers by about 1-2 orders of magnitudes. The crystalline quality of the AlGa_xN overgrown layers was studied by high-resolution x-ray-diffraction (HR-XRD) rocking curves for the symmetric and the asymmetric measurements. Room-temperature photoluminescence (RT-PL) intensity for the SiH₄ treated layers increased by about a factor of 50. Carrier lifetimes increased from 89 ps to 3.63 ns. We also carried out a study to determine the mechanism responsible for the defect reduction. In this paper details of our experimental work and the results of our study will be discussed in detail.

4:30 PM Student

R4, Growth of AlGa_xN and InAlN Ternary Alloys Using Digitally-Alloyed Modulated Precursor Flow Epitaxial Growth: *Suk Choi*¹; Hee Jin Kim¹; Jae-Hyun Ryou¹; Russell Dupuis¹; ¹Georgia Institute of Technology

Al-bearing III-nitride semiconductor materials are essential for the development of high-frequency and high-power electronic devices and optoelectronic devices operating in the ultraviolet spectral region due to their wide bandgap and unique electronic characteristics. Especially, InAlN alloys are attracting

much attention, due to their lattice matching capability to GaN substrates or buffer layers and large variations of bandgap energy which can be potentially used for the fabrication of advanced electronic and optoelectronic devices. The epitaxial growth of these alloys with various aluminum (Al) compositions with atomically smooth surface and excellent crystalline quality is very important for the realization of high performance devices. However, limited surface adatom mobility of Al and homogeneous reactions leading to adduct formation hampers the growth of high-quality layers by metalorganic chemical vapor deposition (MOCVD). Growth in very high temperature with minimum V/III ratio was suggested, but the incorporation of gallium (Ga) or indium (In) in the epitaxial layer drastically decreases in this growth condition, making the alloy composition control very difficult. Modulated precursor flow epitaxial growth (MPEG) was previously proposed as an alternative growth method to achieve high quality AlN and AlGa_xN layers. However, MPEG is not very effective in controlling composition in the growth of ternary alloys such as AlGa_xN and InAlN, mainly due to the large sticking coefficient differences between Al and other group III adatoms. In this paper, we report the growth of high quality AlGa_xN and InAlN alloys by using digitally-alloyed MPEG (DA-MPEG) and their characterization. Epitaxial layers of DA-MPEG Al_xGa_{1-x}N layers were grown on AlN and GaN template by low-pressure MOCVD at 1060°C and a chamber pressure of 75 Torr. A period of DA-MPEG AlGa_xN consists of an AlN sub-layer grown by MPEG and conventionally-grown Al_yGa_{1-y}N sub-layer. For the MPEG of AlN, TMAI was introduced to the reactor chamber, followed by 90 seconds of NH₃ flow. Then, atomic monolayer of Al_yGa_{1-y}N sub-layer was deposited by flowing TMAI and TMGa together with NH₃. By controlling the composition of Al_yGa_{1-y}N sub-layer, we can control the overall composition of DA-MPEG Al_xGa_{1-x}N layer. From the HR-XRD ω -2 θ scans for the symmetric (002) diffraction of DA-MPEG Al_xGa_{1-x}N layer, the overall alloy composition was determined to be $x \sim 0.81$, ~ 0.66 , and ~ 0.56 , indicating controllability of Al composition. Surface morphology observed by AFM shows smooth surface with well developed step flow and root mean square (RMS) roughness below 2 nm in all scan areas. This value is comparable or better than conventionally grown AlGa_xN layer which is grown at higher temperature. The growth and characterization of InAlN alloys by DA-MPEG scheme will be also presented.

4:50 PM Student

R5, Polarization Enhanced p-Type Conductivity in Graded N-Face AlGa_xN Slabs: *John Simon*¹; Vladimir Protasenko¹; Chuanxin Lian¹; Huili Xing¹; Debdeep Jena¹; ¹University of Notre Dame

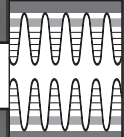
The development of nitride based UV optical devices has been limited due to the difficulties in growth and processing of high conductivity p-type and n-type layers of high Al composition AlGa_xN. High acceptor activation energies of Mg dopants, combined with low mobilities of holes in nitrides result in low conductive p-type layers, limiting the optical and high frequency performance of any bipolar device. By using the polarization charges found in nitride semiconductors it is possible to controllably enhance the conductivity, both for n- and p-type layers. By choosing the correct grading direction, it is possible to generate slabs of positive or negative fixed polarization charges, which act as donor or acceptor like impurities respectively. These charges do not need to be thermally ionized and therefore can allow for enhanced temperature-independent electrical conductivity. In this work we report in the enhancement of the p-type conductivity in graded AlGa_xN layers grown by plasma assisted molecular beam epitaxy (RF-MBE). Samples consisted Mg doped AlGa_xN layers in which the Al composition was graded from 0 to 30% over 85 nm, grown on top of commercially available semi-insulating N-face GaN substrates. A substrate temperature of 600°C and a growth rate of 150 nm/hr were used, and samples were doped with a Mg acceptor concentration of $\sim 5.6 \times 10^{18}$ cm⁻³. The samples were capped with a heavily doped p-type layer for improved ohmic contacts. A control Mg doped GaN sample was grown under the same growth conditions for comparison. These samples were processed into van-der Pauw patterns by etching down to the semi-insulating substrate in a C₁₂ plasma with an RIE etcher. As deposited Ni/Au metal layers were used for ohmic contacts and deposited in an electron beam evaporator. Temperature dependent Hall-effect measurements were performed on the samples from room-temperature down to 100K. The bulk doped GaN sample had a room temperature hole concentration

of $8 \times 10^{17} \text{ cm}^{-3}$ and exhibited carrier freeze out as temperatures was lowered from room temperature. Room temperature hole concentrations of $2.4 \times 10^{18} \text{ cm}^{-3}$ and resistivities of $0.55 \text{ } \Omega\text{cm}$ were obtained in the graded AlGaIn slabs. This resulted in a 3x enhancement in the hole concentration at room temperature as compared to the bulk doped GaN sample. Virtually no carrier freeze out was observed in the graded AlGaIn structures at lower temperatures. An effective acceptor activation energy of $\sim 9 \text{ meV}$ was extracted for the graded AlGaIn sample. The technique we demonstrate here is an effective way to produce both p and n-type layers in applications where both types of doping is challenging, such as deep UV optoelectronic devices that require large Al composition AlGaIn layers.

5:10 PM

R6, MOCVD Growth and Characterization of Mg-Doped AlN-AlGaIn Short-Period Superlattices: *Andrew Allerman*¹; *Mary Crawford*¹; *Mary Miller*¹; *Stephen Lee*¹; ¹Sandia National Laboratories

A p-type, optically transparent cladding material is needed to realize laser diodes with deep-UV emission near 280 nm, which is a wavelength useful for biological agent detection. However, achieving p-type conductivity in $\text{Al}_x\text{Ga}_{1-x}\text{N}$ alloys with Al mole fractions exceeding 0.50 has been elusive due to the large acceptor ionization energies. We report on the growth and characterization of Mg-doped, short-period superlattice (Mg-SPSL) structures that reproducibly exhibit p-type resistivities of 7-9 ohm-cm at room temperature ($p_0 = 4 \times 10^{17} \text{ cm}^{-3}$, $\mu = 2 \text{ cm}^2/\text{V/s}$). These structures have an optical transparency similar to random-alloy AlGaIn epilayers with an Al mole fraction of 0.57-0.59. Our work follows that reported by Nikishin et. al. in 2005 where gas-phase molecular beam epitaxy was used to achieve p-type conductivity in Mg-SPSL structures consisting of AlN and $\text{Al}_{0.08}\text{Ga}_{0.92}\text{N}$ epilayers. They reported a resistivity of 6 ohm-cm in a Mg-SPSL structure that had an effective band gap of 5.1 eV, equivalent to that of an $\text{Al}_{0.72}\text{Ga}_{0.28}\text{N}$ random-alloy epilayer. In this work, we employed metal-organic chemical vapor deposition (MOCVD) to grow Mg-doped $\text{AlN-Al}_{0.23}\text{Ga}_{0.77}\text{N}$ SPSL structures using conventional precursors and ammonia. Initially, growth conditions at 75 Torr were developed that yielded p-type $\text{Al}_{0.23}\text{Ga}_{0.77}\text{N}$ epilayers with a resistivity of 2.1 ohm-cm ($p_0 = 9.1 \times 10^{17} \text{ cm}^{-3}$, $\mu = 3.3 \text{ cm}^2/\text{V/s}$). Subsequently, Mg-SPSL structures with periods ranging from 10-26 Å and individual layers ranging from 5-16 Å were grown on previously prepared AlN-on-sapphire templates. All structures were subject to a 900°C Mg-activation anneal in N_2 for 5 minutes. X-ray diffraction (XRD), optical transmission and reflectance, and Hall effect measurements were used to characterize the Mg-SPSL structures. Good agreement was found between the intended Al composition of the target structure and measurements by XRD and reflectance. For example, the average Al composition for a Mg-SPSL structure with 10 Å barriers and 10 Å wells is calculated to be 0.61, while measurements made by XRD yielded an average Al composition 0.61, and reflectance measurements indicated an Al composition between 0.59-0.63. The SPSL period determined by XRD was 18 Å. Satellite peaks in XRD spectra from Mg-SPSL structures showed reduced sharpness compared to undoped or Si-doped SPSL structures suggesting that the presence of Mg during growth alters the growing surface and the interfaces of the epilayers. The impact of SL period, duty cycle, and growth conditions on resistivity and optical transmission will be presented. Ultimately we achieved a p-type resistivity of 6 ohm-cm in a Mg-SPSL structure with an effective Al composition of 0.74. This work was partially funded through the DARPA Semiconductor AlGaIn Injection Laser program (Dr. H. Temkin, program manager). Sandia is a multiprogram laboratory operated by Sandia Corporation, a Lockheed Martin Company, for the United States Department of Energy's National Nuclear Security Administration under contract DE-AC04-94AL85000.



Session S: Epitaxy on Si

Thursday AM
June 25, 2009

Room: 105
Location: Pennsylvania State University

Session Chairs: L. Ralph Dawson, University of New Mexico; Jerry Woodall, Purdue University

8:20 AM Student

S1, Annihilation Mechanism of Stacking Faults on GaP Layers Grown on Si Substrates within the Critical Thickness: *Yamane Keisuke*¹; Tsuyoshi Kawai¹; Yuzo Furukawa¹; Akihiro Wakahara¹; Hiroshi Okada¹; Hiroo Yonezu¹; ¹Toyohashi University of Technology

A high quality GaP/Si heteroepitaxial growth within the critical thickness is one of the key technologies for the realization of a Si-based monolithic optoelectronic integrated circuit. In this layer, generation of stacking faults, anti-phase domains (APDs) and the melt-back etching between Ga and Si are the significant problems. Although a large number of trials have been performed for these difficulties, few reports have been focused on GaP layers whose thickness is below the critical value. We have already achieved a pit-free and APD-free GaP layer on Si within the critical thickness. However, stacking faults could not completely be suppressed. In this work, we could remarkably reduce the stacking faults density with post growth annealing. Moreover, new evidence of the annihilation mechanism was found by cross-sectional transmission electron microscopy (X-TEM). GaP layers were grown on Si (100) substrates misoriented by 4° toward [011] by using a solid source molecular beam epitaxy (MBE) apparatus. 20-nm-thick GaP layers were grown at 440 °C by MBE. After the growth, substrate temperature was increased to 700°C or 730°C and immediately decreased to 440°C. Then, a 30-nm-thick GaP layer was grown by MBE to ease TEM observation. In order to clarify the annealing effect, a 50-nm-thick GaP layer was grown on the Si substrate by MBE without the annealing. Finally we applied the 730°C annealing to the pit-free and APD-free GaP layer grown by migration enhanced epitaxy. The APDs were self-annihilated below the critical thickness and no misfit dislocations were observed in all samples. The stacking faults density was decreased with increasing the annealing temperature. We have already confirmed that 20-nm-thick GaP layers were completely desorbed at around 750°C and no annealing effect was obtained. In the case of without the annealing, it is worth noting that the most stacking faults propagated from the GaP/Si interface to the GaP surface. This stacking fault is referred to as the SF-A hereafter. In the case of the 700°C annealing, in contrast, several stacking faults propagated from the middle of the annealed GaP layer. This one is referred to as the SF-B hereafter. These results suggest that the SF-B was in the middle of the annihilation process. Generally, stacking faults were thought to be surrounded by the two partial dislocations. During the annealing, the climb motion of these partial dislocations could be enhanced and the area of the stacking faults was decreased. Therefore, the stacking faults density was remarkably reduced at higher annealing temperature. Finally we applied the 730°C annealing to the pit-free and APD-free GaP layer with low stacking faults density. As a result, no stacking faults were observed and very smooth surface with root-mean square surface roughness of less than 0.2 nm was obtained.

8:40 AM Student

S2, Evolution of Epitaxial (211)Ge on (211)Si Grown by CVD: *Shashidhar Shintri*¹; Sunil Rao¹; Ishwara Bhat¹; Priyalal Wijewarnasuriya²; ¹Rensselaer Polytechnic Institute; ²Army Research Laboratory

Heteroepitaxy of Ge on Si has gained immense technological importance for a range of electronic and photonic devices, including next generation metal oxide semiconductor field effect transistors (MOSFETs), since Ge exhibits much higher mobility values than Si. The motivation for the current work arises from the need for having a high quality interfacial layer of chemical vapor deposition (CVD) grown Ge for the growth of CdTe on (211)Si used in infrared focal planar arrays. For the MBE growth of II-VI material HgCdTe, (211)B

CdTe or (211)B CdTe grown on (211)Si substrates are used. We have initiated work on the growth of (211)B CdTe on (211)Si substrates using MOVPE. Prior to the growth of CdTe, a thin interfacial layer of Ge is grown on (211)Si substrate. Use of this interfacial layer has been shown to produce much higher quality CdTe on Si than the layers grown without this interfacial layer. Hence optimization of this Ge layer on (211)Si is necessary to improve the CdTe layer quality further. A systematic study of Ge nucleation and subsequent epitaxy on (211)Si is carried out using GeH₄ (1% in H₂) as the reactant source. The growth is carried out for similar coverages in the temperature range of 400-800°C. Two types of Si substrates are used for the present study. One where Si wafers are cleaned by the standard RCA method but with an HF dip as the final step which creates a hydrogen passivation on Si (type A) and the other where after the RCA clean, a thin oxide (~1.5 nm) is deliberately grown on Si (type B). The use of intentionally grown oxide on Si is motivated by an earlier study that shows the presence of thin oxide actually improves the Ge layer quality. The Ge islands grown on these two different types of substrates at different temperature conditions are studied by AFM and TEM. The evolution of Ge islands on Si shows distinct variation between the two types of substrates analyzed. The islands have a hexagonal footprint and appear to elongate along the <111> direction parallel to the step edges on the (211) surface for the H terminated Si surface where as dome shaped islands without distinct facets appear on the oxidized Si surface. The formation of a flat epilayer is also delayed in the case of oxide grown on Si. The possibility of lateral growth of Ge on the oxide layer for type B substrates is verified by TEM. The samples grown with different growth conditions are also annealed to study the possible change in morphology of the islands. Finally the quality of the thicker grown Ge epilayers is studied by XRD and AFM.

9:00 AM

S3, Growth of High-Quality Ge on Si through Nanoscale Windows in Thin Chemical Oxide for Multijunction Solar Cells: *Darin Leonhardt*¹; Josephine Sheng¹; Jeffrey Cederberg²; Malcolm Carroll²; Sang Han¹; ¹University of New Mexico; ²Sandia National Laboratories

Multijunction solar cells based on III-V materials have now exceeded 40% efficiency, but still remain expensive for terrestrial applications. In an effort to reduce their cost, we have scaled up a process to produce low threading dislocation density Ge films on 2-inch-diameter offcut silicon substrates. The process first requires the formation of a 2 nm thick chemical oxide on the Si surface by immersion in a Pirhana solution (3 parts H₂SO₄ to 1 part 30 wt% H₂O₂). Exposure of this surface to a flux of Ge atoms using molecular beam epitaxy produces 3-7 nm diameter openings in the oxide. Ge islands preferentially nucleate inside the openings, grow, and coalesce into a continuous film. Cross-sectional transmission electron microscopy (TEM) of the resulting Ge films is used to examine the interface and film quality. The TEM images reveal that the Ge films contain a large number of stacking faults near the Ge-Si interface that mostly terminate within 100 nm from the interface. The stacking fault density reaching the film surface is estimated at 10⁷/cm². It is believed that the stacking faults form during the island coalescence stage of growth. However, threading dislocations are absent within the resolution of the TEM. After growth, the surface of the Ge films have a root-mean-square (RMS) roughness of 30 nm as measured with atomic force microscopy (AFM). To prepare the films for GaAs growth, we developed a slurry-free process to polish the Ge films. The polishing solution consists of 1 part 30 wt% H₂O₂ to 50 parts DI water. Post polishing AFM shows that the resulting films have below 1 nm RMS, but that the surface contains roughly 3x10⁷/cm² slightly raised and elongated protrusions. It is believed that these protrusions are due to groups of stacking faults that intersect the film surface as seen in the TEM. Lastly, the Ge surface is cleaned and passivated in oxygen plasma before GaAs growth. Growth of GaAs is done using metal organic chemical vapor deposition on a GaAs, offcut Ge, and our engineered Ge/Si substrates for comparison. Growth of GaAs on the Ge/Si sample has an RMS roughness of 36 nm and shows the same raised protrusions as the Ge surface. Photoluminescence of all three samples shows that the Ge/Si sample has an intensity that is one fourth that of GaAs grown on GaAs and offcut Ge substrates.

9:20 AM

S4, Monolithic Integration of Ga(NAsP)/(BGa)(AsP) - Laser Device Structures Lattice-Matched on (001) Silicon Substrate: *Bernardette Kunert*¹; Sven Liebich²; Steffen Zinnkann²; Rafael Fritz²; Igor Neméth²; Jens Ohlmann²; Kerstin Volz²; Wolfgang Stolz²; ¹NAsP III/V GmbH; ²Material Sciences Center and Faculty of Physics

The low lattice mismatch between GaP and Si offers an immense advantage over standard III/V semiconductors for the epitaxial deposition on Si substrates because the incorporation of a few percentages of Nitrogen (N) or Boron (B) decreases the lattice constant of Ga(NP) and (BGa)P respectively towards the one of Si. This III/V lattice adjustment allows for the growth of several micrometer thick III/V layers on Si substrate without the formation of any dislocation defects. In contrary to GaP the novel dilute nitride Ga(NAsP) reveals a direct electronic band structure due to its high As content. Optical gain in line with electrically pumped laser operation has been demonstrated with device structures based on GaP substrates. Therefore, the monolithic growth of this novel GaP based material system on Si substrates would opens up a completely new field of optoelectronic functionalities for Si microelectronics. In this study we present the successful transfer of the active material system Ga(NAsP) on (001) Si substrate. Pseudomorphically strained Ga(NAsP)/(BGa)(AsP)-multi quantum well heterostructures (MQWHs) were grown by low temperature metal organic vapour phase epitaxy (MOVPE) in a commercial reactor system on (001) Si substrates. In addition whole laser device structures were realised. No indication for dislocation formation was found in the III/V film by applying high-resolution X-ray diffraction (XRD) and transmission electron microscopy (TEM). The complete integration scenario can be divided into three parts as will be discussed: The Si buffer growth and Si surface treatment to achieve a double-stepped surface, the nucleation of the first GaP layers without defects such as stacking faults or twins and finally the growth of the active device structure. Due to the difference in the thermal expansion coefficients of III/V compound semiconductors and Si, the relaxation-free integration of whole device structures requires a precise strain-management taking also the applied growth temperatures into account. The design and selection of materials of the first laser structures will be discussed with the focus on strain management as well as material properties.

9:40 AM Student

S5, Structural and Optical Properties of Rolled-up InGaAs/GaAs Quantum Dot Microtubes on Si: *Vicknesh Sahnuganathan*¹; Feng Li¹; Arya Fatehi¹; Zetian Mi¹; ¹McGill University

Recently, significant progress has been made in the development of III-V semiconductor lasers on Si, as well as the monolithic integration with Si-based waveguide devices. However, their practical applications have been limited, to a large extent, by the generation and propagation of dislocations, due to the large lattice and thermal mismatches between III-V materials and Si. In this context, we have performed a detailed investigation of the structural and optical properties of free-standing InGaAs/GaAs quantum dot (QD) microtubes grown and transferred on Si, which can be designed as highly reliable nanoscale lasers and phased laser arrays. We have achieved, for the first time, free-standing InGaAs/GaAs QD microtubes on Si that are nearly free of dislocations. We have further demonstrated coherent emission from such microtubes, with wavelengths in the range of 1.1 – 1.3 μm . InGaAs/GaAs QD heterostructures were first grown on a 50 nm AlAs layer on GaAs or Si substrates by molecular beam epitaxy. The heterostructure consists of a 20 nm In_{0.18}Ga_{0.82}As and 30 nm GaAs layer as well as two In_{0.5}Ga_{0.5}As QD layers embedded in the GaAs matrix. Free-standing QD microtubes are formed by selective etching the underlying AlAs sacrificial layer of a U-shaped mesa and the resulting self-rolling of the InGaAs/GaAs bilayer, due to strain relaxation. The presence of a sinusoidal corrugation at the inner edge of the U-shaped mesa can lead to microtubes with an engineered geometry. The tube diameter is determined by the InGaAs/GaAs bilayer thickness and compositions, while the tube wall thickness is directly related to the etching time, or the number of revolutions. Such microtubes can be formed directly on Si or transferred on Si substrates using a newly developed substrate-on-substrate transfer technique. From detailed transmission electron microscopy studies, it was confirmed that InGaAs/GaAs

QD microtubes transferred on Si are structurally uniform and relatively free of dislocations. Emission characteristics of InGaAs/GaAs QD microtubes were studied using micro-photoluminescence measurements. The measured emission spectrum at a pump power of 32 μW is characterized by six groups of sharp optical resonant modes, with the dominant modes of each group spaced apart by approximately 20.5 meV. Additionally, associated with each azimuthal mode is a group of at least five spectral eigenmodes, separated by 3 – 4 meV, which are directly related to light localization along the tube axis due to the presence of surface corrugations. Detailed studies of the structural and optical properties of such free-standing QD microtubes, as well as the achievement of nanoscale microtube lasers on Si will be presented.

10:00 AM Break

Session T: Metamorphic and Templated Growth

Thursday AM
June 25, 2009

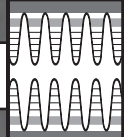
Room: 105
Location: Pennsylvania State University

Session Chairs: Steven Ringel, Ohio State University; Christine Wang, Massachusetts Institute of Technology, Lincoln Laboratory

10:20 AM Student

T1, Metamorphic InGaAs and InGaP on GaAs for Multispectral Detector Applications: *Krishna Swaminathan*¹; Tyler Grassman¹; Qilin Gu¹; Tony Homan¹; Steven Ringel¹; ¹The Ohio State University

III-V semiconductors with lattice constants between GaAs and InP have many important applications, including photovoltaics and photodetectors, due to the richness of bandgaps available. However, the vast majority of these materials are inaccessible in typical growth regimes due to the constraint of lattice-matching to conventional substrates. On the other hand, substrate engineering via compositionally-graded buffers can be used to accommodate the large lattice misfit necessary to reach the desired lattice constants, while minimizing threading dislocation density, allowing for the growth of high-quality, relaxed, lattice-mismatched materials, leading to a tunable materials platform. In this work, we investigate the properties of metamorphic In_{0.14}Ga_{0.86}As and In_{0.61}Ga_{0.39}P p-i-n photodetector structures grown on GaAs substrates using In_xGa_{1-x}As step graded buffers of interest for monolithically integrated multispectral visible/infrared detector applications. 3-step compositionally-graded In_xGa_{1-x}As buffers with overall thicknesses of 1.5 μm and an average grading rate of 0.67% misfit/ μm were grown using MBE. Composition, misfit, and relaxation for the graded buffer and subsequent device layers were determined via high-resolution triple axis x-ray diffraction (TA-XRD) reciprocal space maps, which showed strong and distinct diffraction peaks for each layer, with no significant mosaic spread. The presence of a small residual strain in the final In_xGa_{1-x}As buffer layer was accounted for by growing a lattice-matched step-back layer, producing a high-quality In_{0.14}Ga_{0.86}As virtual substrate that ensures exact unstrained, lattice-matching of the subsequent device layers. This In_{0.14}Ga_{0.86}As metamorphic virtual substrate was then utilized to grow lattice-matched In_{0.14}Ga_{0.86}As and In_{0.61}Ga_{0.39}P p-i-n detector structures, with bandgaps (cut-off wavelengths) of 1.2 eV (1020 nm) and 1.7 eV (725 nm), respectively. J-V measurements show excellent forward bias characteristics and extremely low, voltage-independent dark current densities (reverse bias) of $< 1 \times 10^{-7} \text{Acm}^{-2}$ for In_{0.14}Ga_{0.86}As and $< 1 \times 10^{-8} \text{Acm}^{-2}$ for In_{0.61}Ga_{0.39}P at 300K. Deep level transient spectroscopy (DLTS) measurements performed on the detector structures revealed very low trap concentrations (in the undoped layers) of $< 4 \times 10^{12} \text{cm}^{-3}$ for In_{0.14}Ga_{0.86}As and $< 1 \times 10^{14} \text{cm}^{-3}$ for In_{0.61}Ga_{0.39}P, which compares favorably with that of n-GaAs ($8 \times 10^{12} \text{cm}^{-3}$) and n-In_{0.49}Ga_{0.51}P lattice matched to GaAs ($3 \times 10^{14} \text{cm}^{-3}$), respectively, and indicates the metamorphic buffer, in spite of a residual dislocation density, does not contribute an increase in electronic bandgap states, critical for low noise, high sensitivity photodetector applications. The minimal XRD mosaic spread, low dark current densities and low trap concentrations indicate very high material quality, with low threading dislocation densities,



as a result of the optimal graded buffer design. Additional characterization, including cross-sectional and plan-view TEM are in progress. We will report here the growth and characterization of these high-quality $\text{In}_{0.14}\text{Ga}_{0.86}\text{As}$ and $\text{In}_{0.61}\text{Ga}_{0.39}\text{P}$ metamorphic materials and single-cell detector structures, as well as progress toward fabrication of vertically integrated, metamorphic dual-spectrum InGaP/InGaAs .

10:40 AM Student

T2, Block Copolymer Lithography for Defect Reduction in Epitaxial Growth of Large Lattice-Mismatched Materials: *Smita Jha*¹; Thomas Kuech²; Susan Babcock³; Luke Mawst⁴; ¹Department of Chemistry, University of Wisconsin-Madison; ²Department of Chemical and Biological Engineering, University of Wisconsin-Madison; ³Department of Materials Science and Engineering, University of Wisconsin-Madison; ⁴Department of Electrical and Computer Engineering, University of Wisconsin-Madison

The introduction of defects during the growth of large lattice mismatched III-V materials typically occurs through the injection of 60° dislocations from the surface of the film or islands once a critical thickness or size has been reached. The threading segments from these surface-nucleated dislocations lead to electrically active states which deteriorate device performance. Strain relaxation at the earliest stages of growth, wherein 90° dislocation are still capable of climb from the film surface or from the edge, allows for the development of misfit arrays without the addition of threading segment of the growing island. Intentional patterning has been effective in the past for the formation and strain relief of small islands on lattice-mismatched substrates as long as the patterns grown are on a lateral length scale which is on the order of the diffusion length. Nanoscale patterning to force this length scale can be achieved by directed self assembly of block copolymers on a full wafer at 20 nm length scales. We have employed cylinder-forming diblock copolymer based nano-lithography (BCL) followed by MOVPE growth for defect reduction in heteroepitaxial materials. The 20 nm SiO_2/GaAs substrate was initially pretreated with hydroxy-terminated random polystyrene-polymethylmethacrylate (PS-r-PMMA) copolymer brush material. After the forming of the 'brush' layer, the cylinder-forming PS-b-PMMA was spin-coated onto the wafer. The coated wafer was annealed at 190°C under vacuum to induce the morphology consisting of PMMA cylinders oriented perpendicular to the surface of the substrate. The vertically-oriented PMMA cylinders were removed by acetic acid development after UV irradiation. The removal of the PMMA cylinders generates a well-defined pattern consisting of ~20nm holes on ~40 nm centers over the entire wafer surface. This pattern was transferred to the underlying SiO_2 by RIE. GaSb (8% lattice mismatch) films were subsequently grown using triethylgallium and triethylantimony on patterned as well as non-patterned GaAs (100) substrates. The GaSb growths on non-patterned GaAs substrates have large islands whereas the films grown on patterned substrates are smooth. High resolution x-ray diffraction was used to assess the defect density in the grown films. Initial results on 250 nm thick GaSb film grown on patterned GaAs substrate indicate a sharp reduction in the rocking curve peak with a GaSb (004) FWHM of ~ 453" compared to the corresponding film grown on non-patterned GaAs of ~ 1070". Growth of 750 nm thick films exhibited further reductions to 232". The growth on the patterned substrate is much smoother and nominally specular. The effects of growth temperature and annealing will be discussed. These initial results indicate that the use of BCL-based nanopatterning could be developed into a general approach for defect reduction in large lattice mismatched material combinations.

11:00 AM

T3, Heteroepitaxial Growth of Single Crystalline-like Films of Ge and Si on Flexible, Polycrystalline Substrates: *Venkat Selvamani*¹; ¹University of Houston

Single crystalline films of Ge and Si are desired for several applications where grain boundaries, especially those of high-angle type are deleterious to product performance. However, it is very expensive and in several cases, near impossible to fabricate single crystalline films over large areas or long lengths. A specific example is photovoltaics where cells based on III-V semiconductors have exhibited efficiencies of about 40%, but have found only limited use because of their cost, primarily driven by the high cost of single crystal substrates. On the other end of the spectrum, thin film solar cells offer

advantage of low-cost fabrication, but have not yielded the higher efficiencies of single crystalline cells. Hence, achievement of single crystalline III-V and Si thin film photovoltaics on polycrystalline substrates concomitantly with a low density of defects can be game-changing in the photovoltaic research arena by combining high efficiency with low cost. We are working towards this goal by developing single crystalline-like films of Ge and Si on flexible, polycrystalline substrates. The first enabler that we use is a biaxially-textured template made by ion beam assisted deposition (IBAD). IBAD has been very successfully developed and used for high quality, epitaxial high temperature superconductor (HTS) thin film for electric power transmission in single piece lengths of more than a kilometer. In the IBAD process, materials with rock-salt structures such as MgO are deposited on amorphous layers on polycrystalline substrates, with simultaneous ion beam bombardment. Under appropriate conditions, within a first few nanometers of the film, a good degree of biaxial texture is achieved. The degree of biaxial texture can be improved to about 2 - 3 degrees grain to grain misorientation over the entire film by hetero-epitaxial film deposition atop the IBAD layer. Very superior electrical performance is attained when HTS films are grown epitaxially on IBAD templates in spite of the lattice mismatch and small grain sizes, mainly because misfit dislocations caused by lattice mismatch are actually beneficial for pinning of flux lines and grain boundaries less than 5 degrees misorientation are not harmful. When IBAD templates are directly applied to fabricate epitaxial Ge and Si thin films however, misfit dislocations caused by any lattice mismatch are expected to be deleterious to their properties. Hence, in addition to the first enabler, namely biaxially-textured IBAD templates, we are working on another type of enabler to grow Ge and Si through heteroepitaxy with minimal defects. Graded buffer layers to reduce the lattice mismatch as well as and large-grain thin films of Si/Ge/Si-Ge to reduce grain boundaries are also included in our approach. Progress made in growth of heteroepitaxial single crystal-like Ge and Si films on flexible, polycrystalline substrates will be discussed in this presentation.

11:20 AM

T4, Metalorganic Vapor Phase Epitaxial Growth of (211)B CdTe on (211) Si Substrates Using Ge and ZnTe Interfacial Layers: *Sunil Rao*¹; Shashidhar Shintiri¹; Ishwara Bhat¹; Randolph Jacobs²; ¹Rensselaer Polytechnic Institute; ²US Army NVESD

(211)B CdTe is the preferred buffer layer for epitaxial growth of device quality HgCdTe films on Si substrates. Molecular beam epitaxy (MBE) has been used to obtain high quality (211)B CdTe films on (211)Si substrates[1][2]. The 19% lattice-mismatch between CdTe and Si has limited the threading dislocation (TD) density in the state-of-the-art MBE grown material to the mid-10⁵cm⁻² range. The higher growth temperatures (>400°C) and techniques like epitaxial lateral overgrowth (ELOG) used during metal organic vapor phase epitaxy (MOVPE) could help in further reducing the TD density. One of the challenges in MOVPE is to maintain the Si surface clean and oxide free before growth. A previous study [3] has used a high temperature (800-900°C) pre-growth annealing of the Si substrates (in the presence of GaAs wafers to create As overpressure). We have used an alternative approach; a thin Ge film is grown before the CdTe growth. The precursor GeH_4 has been shown to be effective in removing native oxides during MOVPE of (100) CdTe on Si [4]. A two-step growth process has been found to be essential to obtain good surface morphology of the Ge films on (211) Si substrate, initial nucleation at 500°C followed by growth at higher temperature (650°C) to increase the growth rate. The substrates were then cooled down to the CdTe growth temperatures in presence of As. It was observed that the films grown without this As exposure had high twinning content and were (211)A CdTe while the films grown with As exposure were (211)B CdTe. The grown (211)B CdTe films displayed a rough surface morphology. A thin ZnTe film (100-200nm thick) between the Ge and CdTe layers has been used to alleviate this problem. Further studies on improving the quality of CdTe by using cyclic annealing will be conducted and reported at the conference. This is the first report of successful growth of (211)B CdTe directly on (211)Si using MOCVD. This work was partially supported by US Army STTR contract W911NF-07-C-0105 through Agiltron Inc. (Dr. Matthew Erdtmann) and US ARMY Phase I STTR contract W911NF-07-C-0085 through Brimrose Corp. [1] A. Million et. al., J. Cryst. Growth, 159,

76 (1996). [2] Rujirawat S. et. al., Appl. Phys. Lett., 71 (13), 1810 (1997). [3] M. Niraula et. al., J. Elec. Mater., 35, 1257 (2006).[4] W. Wang et. al., J. Elec. Mater., 24, 451 (1995).

11:40 AM

T5, Low Dislocation Density GaN via Nanowire Templated Lateral Epitaxial Growth (NTLEG): *George Wang*¹; *Qiming Li*¹; *Yong Lin*¹; *J. Randall Creighton*¹; ¹Sandia National Laboratories

We present here a novel application of vertically aligned GaN nanowire arrays as 3D strain-compliant templates for the lateral growth and coalescence of high quality GaN films on lattice-mismatched sapphire. In contrast to current epitaxial lateral overgrowth techniques used to reduce dislocation densities, this approach, referred to here as "nanowire templated lateral epitaxial growth" (NTLEG), requires no growth interruption or costly patterning. Using metal-catalyzed MOCVD, we have achieved the growth of highly aligned and dense arrays of single crystalline GaN nanowires uniformly on unpatterned 2-inch diameter sapphire. Surprisingly, the nanowire density and the degree of alignment were found to be highly sensitive to changes in the Ni catalyst film thickness below 1 nm, a regime rarely explored in catalyzed nanowire growth. For submonolayer Ni films, the formation of high-density and ultra-small Ni islands with a narrow size distribution is attributed to the high activation energy for Ni diffusion on sapphire, which in turn leads to high-density and highly aligned GaN nanowires. From these nanowire arrays, we have been able to demonstrate fully coalesced, nonpolar a-plane GaN NTLEG films. TEM analysis reveals that the films have dislocation densities roughly 50 times lower than a-plane GaN films grown using standard nucleation layers. We also performed a finite element analysis of the strain distribution at the nanowire/substrate interface. The model shows that the strain decays to zero at a distance away from the substrate of one half the lateral dimension of the nanowire. This demonstrates the theoretical basis for strain relief in the NTLEG film, which is distant from the highly localized strain field at the nanowire/sapphire junction. Sandia is a multiprogram laboratory operated by Sandia Corporation, a Lockheed Martin Company, for the United States Department of Energy under contract DE-AC04-94AL85000. This work is supported by DOE EERE/NETL.

8:40 AM Student

U2, Inkjet Printed Small Molecule Organic Thin Film Transistors: *Yuanyuan Li*¹; *Devin Mourey*¹; *Sankar Subramanian*²; *John Anthony*²; *Thomas Jackson*¹; ¹Pennsylvania State University; ²University of Kentucky

Solution based organic semiconductors have been widely investigated for their potential in low cost flexible electronics. The p-type organic semiconductors triethylsilylethynyl anthradithiophene (TES ADT) and 5,11-Bis(triethylsilylethynyl) anthradithiophene (diF-TESADT) have been shown to exhibit high field effect mobilities in organic thin film transistors (OTFT) fabricated using spin or drop casting.[12] However, there is inherently a large amount of material waste in spin casting and subsequent patterning of organic thin films may not be simple. We report here organic thin film transistors using TES-ADT or diF-TES-ADT deposited by inkjet printing. For this work we used a Dimatix 2831 piezoelectric drop-on-demand inkjet printer with slightly modified printhead cartridges to allow small amounts of printing material to be conveniently used. The OTFTs for this work used a simple structure with gold source and drain electrodes photolithographically defined on a 210 nm thick thermally grown silicon dioxide gate dielectric layer on a heavily doped n-type silicon wafer. A 2 wt% solution of TES-ADT in toluene was printed with substrate and printhead temperature of 28 °C and a drop spacing of 40 μm. 16 V, 3.6μs pulses were used for piezoelectric drive and resulted in stable jetting at a frequency of 5kHz. TES-ADT OTFTs fabricated with these conditions and 10μm channel length had a field-effect mobility of ~0.025 cm²/V□s and near zero threshold voltage. It has previously been reported that spin cast diF-TES ADT forms a different crystal microstructure on pentafluorobenzeneethiol (PFBT) treated Au and untreated regions.[3] For diF-TES-ADT inkjet printing we used a 1 wt% solution in chlorobenzene and print parameters similar to those used for TES-ADT. diF-TES-ADT was printed as either single drops or multiple drops onto gold source and drain electrodes treated with PFBT. diF-TES-ADT OTFTs fabricated with 10 μm channel length had field-effect mobility of ~0.05 cm²/V□s and threshold voltage of ~1 - 2 V. Despite the modest mobility, printed structures on PFBT-treated surfaces typically show large grains, similar to spin cast films, suggesting other issues may limit mobility in these devices.

9:00 AM

U3, Self Organised Electrodes Using Controlled Coffee Stain Phenomena for High Aspect Ratio Polymer Field Effect Transistors on 3D Substrates: *Sanjiv Sambandan*¹; *Ana Arias*¹; *William Wong*¹; *Robert Street*¹; ¹Palo Alto Research Center

An important advantage of polymer electronics is the possibility of solution processed electronics and therefore the use of fluid mechanic concepts to achieve novel fabrication techniques. An interesting feature of a drying droplet of a nano-particle colloidal solution of is the coffee stain effect. If the contact angle of the droplet is less than 90deg, and the ambient conditions encourage droplet drying, the droplet has a maximum evaporation rate at the boundary. Due to temperature and hence surface tension gradients, there results an effective flow of nanoparticles to the boundary. When the droplet completely dries out, we are left with a ring like stain of nanoparticles which decreases in concentration from the periphery inwards. One can think of a scenario where this phenomenon could be used for electrode deposition using silver nano particle-water colloids. However, it is important to achieve deposition patterns which are of geometries different from concentric rings eg. parallel lines. In order to achieve this we dip a hydrophilic substrate called the control plate, (of any geometry) in a puddle of nanoparticles colloid present on the sample substrate. The capillary force between the control plate and nanoparticles solution leads to lateral force on the colloidal puddle. On the other hand the pinning of the fluid boundary leads to coffee stain formation. Both these forces lead to periodic stain formation with fine spatial separation between consecutive stains. The control substrate can also be moved up and down at a constant or variable velocity to control the line separation. If the sample substrate is 3dimensional, one can achieve patterning without any change in setup. Important variables that affect the printed pattern: a.) Surface tension between solution and control plate – can be controlled by modifying plate surface, temperature – Affects the distance of separation between the patterned lines. b.) Surface tension between solution and substrate – Important - can be controlled by modifying substrate, temperature

Session U:

Flexible and Printed Thin-Film Electronics

Thursday AM
June 25, 2009

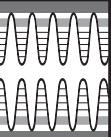
Room: 106
Location: Pennsylvania State University

Session Chairs: William Wong, Palo Alto Research Center; Michael Chabinye, University of California, Santa Barbara

8:20 AM

U1, Printable Bottom-Contact Organic Field-Effect Transistors: *Seonghoon Lee*¹; *Jung-Pyo Hong*¹; ¹Seoul National University

We have developed a simple and innovative solution-based crystal growth method to fabricate bottom-contact well-oriented crystalline organic field effect transistors (OFETs); the method involves the direct growth of crystals by employing a modified drop-cast method and using a micropipette similar to an ink-jet printing process. A two-liquid system (xylene-water system) is considered and dozens of TIPS pentacene crystals are directly self-organized and grown on an active channel region in the highest-mobility direction via the isothermal evaporation of the solvent in the two-liquid system. The obtained TIPS pentacene crystals transistors with PFTP-Ag electrodes exhibit a p-type mobility of 0.30 cm²/V*s in the saturation region and a large current on/off ratio of 4 x 10⁸. These are practical OFET values. Our innovative method for directly growing organic crystals on patterned channel regions by utilizing a micropipette and the hydrophobic-hydrophilic interaction between the two constituents of the two-liquid system similar to an ink-jet printing process, is expected to be suitable for the fabrication of low-cost and mass-producible printable electronic devices.



– Pinning is essential for line formation, depinning is essential for parallel line formation. Thus the solvent must pin to the substrate while the solute must not. c.) Temperature – Controls rate of evaporation and therefore the rate of solute deposition d.) Vapor Pressure – Controls rate of evaporation (control environment volume) e.) Solute – Its molecular packing density controls features of the coffee stain. Solute must not pin/stick to the substrate surface with a force greater than surface tension with the control plate. Gaps of about 1-5micron spacing were obtained with silver-water colloids.

9:20 AM Student

U4, Printing Silicon from Nanoparticle Suspensions: *Noah Jafferis*¹; James Sturm¹; ¹Princeton Institute for the Science and Technology of Materials (PRISM) and Department of Electrical Engineering, Princeton University

While both amorphous silicon and organic semiconductors have maximum FET mobilities on the order of 1 cm²/V·s, some organic materials may be printed in patterned form from a wet solution. Such an additive patterned process would avoid the need for photolithography and etching of blanket layers, and waste less material. Thus the goal of this project is to develop an approach to print silicon. Unlike earlier work where a liquid polysilane was first printed and then converted to silicon by annealing, our approach is to print silicon directly from a suspension of Si-nanoparticles. This will avoid the necessity of any post-deposition processing, such as high temperature annealing or laser crystallization. Single-crystal silicon nanoparticles ranging from 1 nm to 4 nms have successfully been produced by electrochemical wet etching of single-crystal silicon to form porous silicon, and then creating a nanoparticle suspension in acetone or other solvents (such as water) by ultrasonic agitation of the wafer in the chosen solvent. Acetone was used because it is readily available and evaporates quickly. Luminescence measurements and direct TEM imaging were used to determine the size distribution and verify the crystallinity of the particles. Production of nanoparticles was maximal (10¹⁶ particles / hour·cm²) for etching current densities of 2 to 10 mA/cm². Sufficient quantities of these particles have been produced to enable the deposition of thin-films on the order of 100 nm thick from a single droplet. The films were characterized by electron microscopy, energy dispersive X-ray spectroscopy, secondary ion mass spectroscopy, and AFM. Under the proper conditions, continuous films can be produced over the entire area (~0.25cm²) of the deposited droplet, with little variation in the thickness. The intrinsic roughness was ~3 nm RMS. Porosity of the deposited films was measured, by weighing, to be ~50-90%. It was found that using acetone as the solvent resulted in high carbon content in the film, but low oxygen content (carbon ~10at.%, oxygen ~1at.%). Using water instead did reduce the carbon content and greatly increased the oxygen content (carbon <1at.%, oxygen >30at.%). The number of hydrogen atoms was nearly the same as that of silicon, which is consistent with the idea that the silicon bonds on the nanoparticles' surfaces are primarily hydrogen-terminated. For the acetone-prepared films, the number of oxygen atoms corresponded to a maximum of 1 or 2 oxygen atoms per Si-nanoparticle. The films have been shown to be chemically and physically stable – They can withstand common solvents, photoresist developer, chrome etch, etc., and they can be patterned using a typical dry silicon etch, but at a reduced etch rate of ~10-20 nm/min compared with ~50-100 nm/min for nc-Si. The films have dark conductivities of ~10⁻⁸ Ω⁻¹·cm⁻¹, comparable to that of intrinsic nanocrystalline silicon.

9:40 AM

U5, High Resolution Patterning by Selective Surface Modification and Dip-Casting for Low-Cost Fully Printed Electronics: *Yong-Hoon Kim*¹; Sung Kyu Park¹; Min-Koo Han²; Jeong-In Han¹; ¹Korea Electronics Technology Institute; ²Seoul National University

Recently, direct printing technologies are becoming more important in the field of electronic devices due to their fast, easy, and low-cost manufacturing. Several approaches, such as, nano-scale imprinting, soft-lithography, self-formation, ink-jet printing, and barrier-like structure with photoresist layer have been introduced and showed promising results. However, there still remains several problems in applying these technologies to low-cost roll-to-roll processes due to the process complexity and necessity of conventional photolithography process. In this report, we demonstrate simple and easy fabrication process for building fine patterned metal electrodes and organic semiconductors which can

be easily adopted to roll-to-roll process. This process includes surface patterning of self-assembled monolayer (SAM) by non-relief lithography and simple dip-casting process. By employing these processes, fast and cost effective manufacturing is possible, as well as high resolution patterning of various materials. For the patterning of Ag electrodes for source and drain, hydrophobic octadecyltrichlorosilane (OTS) was formed over the thermally oxidized silicon dioxide by dipping. Then, deep UV (DUV) radiation was performed through a quartz photomask to generate SAM patterns. The 185 nm exposure results in rapid removal of the OTS SAM layer which has been confirmed by water contact angle measurements. After OTS patterning, the samples were dipped into Ag nano-ink which includes nano-particles with an average diameter of 10 ~ 20 nm and pulled out to form the source and drain electrodes. The printing quality or the channel length of a transistor was significantly affected by the withdrawal speed of the sample and also the viscosity of the Ag nano-ink. By optimizing the dip-casting parameters, channel lengths of 5 ~ 10 μm were easily achieved. Also, to achieve high molecular ordering and fine patterning of organic semiconductors, another DUV exposure was performed with quartz mask, resulting in a new barrier structure for confining organic solution. Finally, TIPS-pentacene from 2 wt% chlorobenzene solution was ink-jetted over the pre-patterned barrier-like structure and the dropped TIPS-pentacene ink was automatically confined within the patterned OTS area. With patterned Ag source-drain electrodes and TIPS pentacene, field-effect mobility of about 0.03 ~ 0.06 cm²/V·s, on/off current ratios >10⁶, and subthreshold slope <0.7 volt/decade, which are similar to that of OTFTs from ink-jet printed semiconductors and photolithographically patterned electrodes.

10:00 AM Break

10:20 AM

U6, Towards Low-Noise Flexible Electronics: *Oana Jurchescu*¹; Hao Xiong¹; Devin Mourey²; Dalong Zhao²; Jie Sun²; Marsha Loth³; Curt Richter¹; John Anthony³; Thomas Jackson²; David Gundlach¹; ¹National Institute of Standards and Technology; ²Pennsylvania State University; ³University of Kentucky

The fabrication of large-area, light-weight, low-cost flexible electronics on plastic substrates limits the processing temperatures and consequently the materials that can be incorporated in devices. Most conventional semiconductor devices require high deposition temperatures, and thus are incompatible with plastic substrates. Organic semiconductors and ZnO can overcome this limitation and are particularly attractive due to their low production cost. We present current-voltage (I-V) and low frequency noise (1/f) measurements on thin film transistors (TFTs) fabricated with these two classes of materials and discuss the effect of the current fluctuations in the device stability. TFTs were fabricated on heavily-doped silicon wafers with a thermally grown silicon dioxide which serves as the gate dielectric. Organic TFTs were made by using an inverted-coplanar geometry, having photolithographically defined source and drain contacts. For this study, thin films of fluorinated 5,11-bis(triethylsilyl ethynyl) anthradithiophene were spin-cast from solution to form the active layer. We demonstrate for the case of organic TFTs that the electrical characteristics and noise spectra are strongly influenced by the structural defects. The moderate mobility of the organic TFTs (0.1 to 0.5 cm²/V·s for this study) limit the applications that can be supported to only low-frequency circuit operation. The Hooge parameter for this set of devices was of order 1 to 10, similar to that reported previously for pentacene TFTs employing an inverted-coplanar geometry. ZnO TFTs were made by using an inverted-staggered geometry, where the source and drain contacts are deposited and patterned on top of the ZnO active layer and are opposite the field-accumulated channel. Importantly, we show that the high mobility (1 to 10 cm²/V·s) and low Hooge parameter (10⁻³ to 10⁻²) make ZnO TFTs a promising technology for meeting the demands of superior performance for future electronic devices.

10:40 AM Student

U7, Two-Level Stretchable Conductors on Elastomeric Substrates: *Joyelle Jones*¹; Oliver Graudejus¹; Wenzhe Cao¹; Sigurd Wagner¹; ¹Princeton University

We fabricated two layers of encapsulated stretchable conductors on poly dimethyl siloxane (PDMS). The first conducting layer contained 5 mm long,

1 mm wide, 75 nm thick Au lines (with 3 nm of Cr for adhesion) patterned by photolithography on a PDMS substrate and then encapsulated by photopatternable silicone (PPS) (Dow Corning WL 5150). Openings in the PPS were patterned by photolithography to enable electrical connections to the underlying metal layer. The second conducting layer contained Au lines of the aforementioned dimensions patterned by photolithography on the PPS and then encapsulated by a second PPS layer. The electrical resistance of the layered encapsulated conductors was measured as the structure was stretched by 30%. Both metal layers remained electrically conducting and a continuous electrical connection was maintained between the two layers. We will discuss our fabrication methods and present the electrical performance of the multi-layered structure.

11:00 AM

U8, A New Method for Integrating Electronics into Textiles: *Thomas Kinkeldei¹; Kuniyunde Cherenack¹; Gerhard Troester¹; ¹Swiss Federal Institute of Technology*

Currently, electronics are mostly integrated into textiles (1) by using commercial ICs which provide a large range of electronic functions but alter the textile properties or (2) by weaving or sewing threads with limited functionality such as metallic and optical fibers into the textile. Our aim is to develop an unobtrusive method to integrate high-performance electronic devices like sensors or transistors into clothing. As substrate we use a flexible Kapton foil, because its good resistance against high temperatures and chemicals. We build up the devices using micro-fabrication techniques, cutting the foil into fibers and weaving them into a textile. In this paper we discuss our method of fabricating and weaving foil fibers. We investigated several methods of cutting a substrate of 75 μm thickness, into fibers: a laser, a waterjet cutter, a dicing saw and a cutting plotter. We compared the various cutting methods with regard to edge quality and minimum fiber width achieved. The smallest fibers that we cut were $\sim 50 \mu\text{m}$ wide using a dice-cutter. The cutting-alignment error between the blade and the edge of a metallized test pattern is less than 10 μm . SEM pictures of cut fibers show clean edges without tearing or cracking. The mechanical properties like tensile strength and elongation of bare and metallized fibers of varying widths were compared to standard textile yarns (CA 02776 220, conductive magnet wire with diameter 0.25 mm and PYSS11717x2 a coated nylon yarn). We chose a 500 μm -wide Kapton stripe in our final design since fibers of this width have a mechanical strength of 9.4 N, what is comparable to the textile fibers used in our weaving process. We experimented with weaving these fibers into a textile using an industrial band-weaving machine. Our results show that the weaving process does not damage the stripe edge, or metal structures patterned on the stripe surface. In addition, the textile properties like comfort and flexibility are unaffected by the integrated Kapton fibers. This approach shows that it is possible to use the advantages of micro processing on large-area substrates for manufacturing textile integratable electronic fibres.

11:20 AM Student

U9, Mechanical and Thermal Stretching of Fully Encapsulated Elastomeric Conductors: *Wenzhe Cao¹; Oliver Graudejus¹; Joyelle Jones¹; Sigurd Wagner¹; ¹Princeton University*

We have been developing elastically stretchable microelectrode arrays (SMEAs) for application to the study of traumatic brain injury. The basic structure is an elastomeric membrane substrate on which thin-film gold conductors are patterned and then encapsulated with a photopatternable elastomer. We make the substrate of poly dimethyl siloxane (PDMS) and the encapsulation of photopatternable silicone (PPS). We anticipate other applications of similar elastically stretchable devices in biomedicine, conformable electronic surfaces, and comfortable electronic textiles. The silicones of the substrate (PDMS) and the encapsulation (PPS) are versatile materials by virtue of their unique combination of properties, which include optically transparency, electrically insulation, mechanical properties of rubber, and biocompatibility. Fully encapsulated thin-film gold electrodes can remain conducting up to more than 80% tensile strain. PDMS also has special thermal properties — large thermal expansion and poor heat conduction. Its coefficient of thermal expansion (CTE) of $\sim 300 \text{ ppm}/176\text{C}$ is more than 20 times larger than of the gold conductors, 14 $\text{ppm}/176\text{C}$. Therefore varying the temperature of the SMEA can produce a

large tensile or compressive strain in the gold conductor, and causes substantial change in its electrical resistance. To explore the thermal response we fabricated thin-film gold conductors with the following process sequence: 1) preparation by spin-coating on glass substrates followed by thermal curing of 0.3 mm thick membranes of polydimethyl siloxane; 2) electron-beam evaporation of a 1.5 nm titanium adhesion layer and of 75 nm gold conductor; 3) patterning of the metal stack by photolithography and wet etch; 5) electron beam evaporation of a top adhesion layer of Ti; 6) encapsulation of the lines with photopatternable silicone (PPS); and 7) opening of contact vias in the PPS encapsulation layer, to expose contacts to the gold conductors. First we measured the electrical resistance of the encapsulated, 50-micrometer wide and 5-mm long lines under uniaxial mechanical strain. Under a protocol of stepwise 0.1% tensile strain increment every 3 seconds, the resistance is very nearly linear with strain up to 30% strain, and cycles between ~ 100 Ohms when fully relaxed and ~ 500 Ohms at 30% strain. Then we measured the resistance of the same sample under thermal stretch. The sample was heated from room temperature to 180/176C at the rate of 300/176C/hour. Its electrical resistance increased with the temperature nearly linearly. The resistance at the peak temperature was 38% higher than at room temperature; upon cooling and heating it cycles reproducibly. We will describe the structure and fabrication of the encapsulated lines, present their resistance change during cyclic mechanical stretching and thermal expansion, and discuss their potential as temperature sensor.

11:40 AM U10, Late News

Session V: Oxide Thin Film Integration I

Thursday AM
June 25, 2009

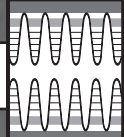
Room: 108
Location: Pennsylvania State University

Session Chairs: Patrick Lenahan, Pennsylvania State University; Susanne Stemmer, University of California, Santa Barbara

8:20 AM Student

V1, Atomic-Layer-Deposited HfO₂ Gate Dielectrics on InP Using Silicon Interface Passivation Layer: *Yen-Ting Chen¹; Han Zhao¹; Jung Hwan Yum¹; Yanzhen Wang¹; Jack C. Lee¹; ¹The University of Texas at Austin*

The mainly challenge for III-V based MOSFETs is the absence of stable dielectrics, forming good interface quality with III-V substrate. Thus, passivation techniques, such as using Si interface passivation layer (IPL) have been reported recently [1-2]. These previous work primarily focused on Ga-based III-V substrates. In this letter, we have applied ALD HfO₂ gate stack with Si IPL on InP substrates. MOSCAPs were fabricated on n-type InP (100) wafer. The surface native oxides were removed with the 1% dilute HF solution, followed by 20% (NH₄)₂Sx dip [3], resulting in a clean S-passivated InP surface. Then, a thin layer of $\sim 10 \text{ \AA}$ silicon was deposited by dc magnetron sputtering in Ar ambient at 400°C, followed by ex situ ALD 51 \AA HfO₂ deposition using tetrakis (dimethyl-amino) hafnium [Hf(NMe₂)₄] and H₂O as the precursors at 200°C. For comparison, MOSCAPs having 70 \AA HfO₂ as a gate dielectric without Si IPL were fabricated. These two samples have similar EOT of $\sim 18 \text{ \AA}$ and $\sim 17.4 \text{ \AA}$, respectively. The post-deposition annealing (PDA) was performed at 500°C for 1min in N₂ ambient, then PVD TaN was used for gate electrode. After gate patterning, AuGe/Ni/Au alloy was deposited for the backside contact. The samples were then annealed at 420°C for 20sec in N₂. MOSFETs fabrication procedures for gate-last processes are described in Table I. The schematic vertical device structure of the TaN/HfO₂/Si IPL/InP MOSFET is shown in Fig. 1. MOSCAPs with and without Si IPL show similar hysteresis (0.24V vs 0.28V, Fig. 2-3). The samples without Si IPL reveal poor frequency dispersion as large as 15.3% from 1MHz to 10KHz, while the 10 \AA Si IPL /51 \AA HfO₂ stacked gate dielectric illustrates a much smaller frequency dispersion of 6.42% [Fig. 4 and Fig. 5]. In Fig. 6, the maximum transconductance of 10 \AA Si IPL /51 \AA HfO₂ stacked gate dielectric (2.3 ms/mm) is more than 3 \times higher than the G_m value (0.647 ms/mm) of single 70 \AA HfO₂ gate dielectric. The subthreshold swing



also improves from 136.7mV/dec to 102.8mV/dec by using Si IPL. MOSFETs with Si IPL show much higher current driver capability (Fig. 7). The maximum driver current under $V_d = 2V$ and $V_g - V_t = 1.2V$ for the gate dielectric with and without Si IPL are 6.7 mA/mm and 1.53 mA/mm, respectively. Fig. 8 presents the gate leakage current of MOSFETs. The gate leakage current density reduces from $3.94 \times 10^{-2} A/cm^2$ to $1.32 \times 10^{-3} A/cm^2$ at $V_g = 1V$ by employing Si IPL. In conclusion, we present InP MOSCAPs and MOSFETs using Si IPL and ALD HfO₂ dielectrics. Under similar EOT, the MOSCAPs with Si IPL show better interface quality indicated by frequency dispersion behavior. Consequently, higher transconductance and drive current density, lower SS and gate leakage current were realized for MOSFETs.

8:40 AM Student

V2, Growth of Epitaxial (110) 0.7Pb (Mg_{1/3}Nb_{2/3}) O₃ - 0.3PbTiO₃ Thin Films on r-Plane Sapphire Substrates by RF Magnetron Sputtering: Lakshmi Krishna¹; Madhana Sunder¹; Peter Moran¹; ¹Michigan Technological University

Developing methods to grow epitaxial Pb(Mg_{1/3}Nb_{2/3})O₃-0.3PbTiO₃ (PMN-PT) thin films on commercially available large area substrates is necessary if their unusual dielectric properties are to be fully leveraged in device applications. The major issues in achieving growth of epitaxial PMN-PT perovskite thin films on commercial substrates are (1) the formation of the undesirable PMN-PT pyrochlore phase and (2) film-substrate lattice mismatch. In this work, we investigate the direct growth of epitaxial (110) perovskite PMN-PT thin films on commercially available r-plane (102) Sapphire substrates. We demonstrate that epitaxial (110) PMN-PT thin films can be deposited on r-plane (102) Sapphire substrates using RF magnetron sputtering through a two step deposition process. We report on how this growth technique effectively suppresses the undesirable pyrochlore phase. Specifically we have found that a 30 nm thick amorphous PMN-PT seed layer deposited at 250°C and subsequently subjected to rapid thermal anneal (RTA) at 850°C results in the formation of a (110) perovskite PMN-PT template, that can be used for subsequent growth of 300 nm thick epitaxial (110) perovskite PMN-PT films. This low temperature template is shown to be critical for suppressing the pyrochlore phase. The epitaxial (110) PMN-PT thin films grown by this method exhibit a comparatively narrow X-ray rocking curve full width at half maximum (FWHM) of 0.1°. We analyze the crystallography of the in-plane epitaxial relationship observed between the cubic PMN-PT and hexagonal Al₂O₃ in terms of the unusually large mismatch of crystal structure and atomic spacing that would normally be expected to preclude epitaxial growth.

9:00 AM

V3, High Quality SrTiO₃ Thin Films Grown by Hybrid Molecular Beam Epitaxy: Roman Engel-Herbert¹; Bharat Jalan¹; Susanne Stemmer¹; ¹University of California, Santa Barbara

Much work in oxide thin films has focused on solution-based methods, sputtering or pulsed laser deposition. However, low energetic, high-purity techniques such as molecular beam epitaxy (MBE) are required to decrease the intrinsic defect concentrations in these films. Titanates with the perovskite and related structures are among the most important complex oxides, exhibiting properties as diverse as ferroelectricity, superconductivity and strongly-correlated Mott-Hubbard-type insulator characteristics. Oxide MBE growth of cation and oxygen stoichiometric titanates has, however, proved challenging. Furthermore, the low vapor pressure of Ti severely limits growth rates and film thicknesses from effusion cells. Reported growth rates are no better than 1 nm/min. Here, we report on a new method for the growth of TiO₂ and SrTiO₃ films by MBE that is capable of high growth rates and produces stoichiometric films with extremely high structural quality. In particular, we use a metal organic source for Ti. This source has orders of magnitude higher vapor pressure than solid Ti. A solid source is used for strontium and a rf oxygen plasma source is used to supply oxygen. We demonstrate the growth of epitaxial (101) rutile TiO₂ films on (012) sapphire substrates at temperatures between 485 and 725° C. Growth rates were as high as 125 nm/hr. Without any additional source of oxygen, the growth rate exhibited two distinctly different (Arrhenius-type) growth regimes as a function of temperature, whereas in the presence of an oxygen plasma the growth rate became independent of temperature. Reflection

high-energy electron diffraction (RHEED), which showed layer-by-layer growth in the initial stages of film growth, microstructures, surface morphology and electrical characteristics will be reported as a function of growth parameters. Films grown with an oxygen plasma were insulating while those without were semiconducting. We demonstrate epitaxial growth of single crystalline SrTiO₃ (001) films on (001) SrTiO₃ and (001) (La_{0.3}Sr_{0.7})(Al_{0.65}Ta_{0.35})O₃ substrates, respectively. RHEED oscillations showed layer-by-layer growth on both the substrates. The full width half maxima of x-ray diffraction rocking curves were similar to that of the substrates, i.e. 34 arcsec on LSAT. The film surfaces were nearly ideal with root mean square surface roughness values of less than 0.1 nm. We will present a detailed growth study as a function of substrate temperature, TTIP and Sr fluxes and oxygen pressure and relate the growth parameters to films' stoichiometry. We will compare the electrical and dielectric properties of the films to those grown by sputtering.

9:20 AM Student

V4, Growth and Microstructure of Homoepitaxial Strontium Titanate Thin Films by Molecular-Beam Epitaxy: Charles Brooks¹; Lena Fitting Kourkoutis²; Tassilo Heeg²; Jürgen Schubert³; David Muller²; Darrell Schlom²; ¹The Pennsylvania State University; ²Cornell University; ³Research Centre Jülich

We report the structural properties of homoepitaxial (100) SrTiO₃ films grown by reactive molecular-beam epitaxy (MBE). The lattice spacing and x-ray diffraction (XRD) rocking curves of stoichiometric MBE-grown SrTiO₃ films are indistinguishable from the underlying SrTiO₃ substrates. Off-stoichiometry for both strontium-rich and strontium-poor compositions (i.e., Sr_{1-x}TiO_{3+d} films with -0.2 < x < 0.2) results in lattice expansion with significant changes to the shuttered reflection high-energy electron diffraction oscillations, XRD, and film microstructure. The dependence of lattice spacing on non-stoichiometry is significantly smaller for MBE-grown films than for homoepitaxial (100) Sr_{1-x}TiO_{3+d} films prepared by pulsed-laser deposition or sputtering. Film microstructure was studied by scanning transmission electron microscopy (STEM). A film set was also grown by codeposition to study the effect of source shuttering during growth.

9:40 AM Student

V5, The Growth and Properties of Sr_{n+1}Ti_nO_{3n+1} Ruddlesden-Popper Phases: Che-Hui Lee¹; Xiaoxing Xi¹; Darrell Schlom²; Wei Tian¹; Nathan Orloff³; Nik Podraza¹; ¹Pennsylvania State University; ²Cornell University; ³University of Maryland

The Sr_{n+1}Ti_nO_{3n+1} Ruddlesden-Popper (RP) homologous series is of particular interest because its n=∞ member SrTiO₃ has a wide range of applications in electronic devices. Therefore, the investigation of other members in this homologous series is a promising path for searching new materials with improved properties. In this study we explore the dielectric and optical properties of the Sr_{n+1}Ti_nO_{3n+1} RP homologous series, as well as the effects of strain on the films. Sr_{n+1}Ti_nO_{3n+1} (n=1-5) RP series thin films have been grown on (001) (LaAlO₃)_{0.3}(Sr_{0.25}Al_{0.25}Ta_{0.5}O₃)_{0.7} (LSAT) and (110) DyScO₃ substrates by reactive molecular beam epitaxy. (001)LSAT substrates have a lattice constant which is close to the whole RP series of films, providing from 0.4% to 0.9% of compressive strain for n=1 to n=5. On the other hand, (110) DyScO₃ substrates provide 1.5% to 1.0% of tensile strain for n=1 to n=5. A precise stoichiometry and absolute monolayer doses within 1% error are achieved by monitoring reflection high-energy electron diffraction intensity oscillations. X-ray diffraction reveals that the whole series of samples are phase-pure and commensurate to the substrates. For the samples grown on LSAT, the frequency-dependent relative permittivity as a function of temperature and dc electric field is explored by using interdigitated capacitors and coplanar waveguides. The in-plane relative permittivities (ε₁₁) of the n=1,2,3 members are 42±3, 54±3, and 77±2, respectively, at room temperature, and independent of frequency. At low temperatures, ε₁₁ increases and the n=3 member shows electric field tunability. The optical properties of the samples are studied using ex situ spectroscopic ellipsometry. The optical band gap decrease monotonically from 3.48 eV (n=1) to 3.14 eV (n=∞) with increasing n. For the samples grown on DyScO₃, we investigate the material property changes induced by epitaxial strain. The Sr_{n+1}Ti_nO_{3n+1} (n=1-5) RP series does not

show ferroelectricity at room temperature. However, previous work has shown that when imposing a modest strain, the $n=\infty$ member of the RP series, SrTiO₃, becomes ferroelectric even at room temperature. Therefore the $n=1-5$ members of the Sr_{*n-1*}Ti_{*n*}O_{3*n+1*} RP series are potential ferroelectrics in their strain state.

10:00 AM Break

10:20 AM

V6, Stabilization of a Very High-k Tetragonal ZrO₂ Phase by Direct Doping with Germanium: Athanasios Dimoulas¹; Dimitra Tsoutsou¹; *Sotiria Galata*¹; Georgia Mavrou¹; Yerassimos Panayiotatos¹; Georgios Apostolopoulos¹; ¹NCSR Demokritos

Very high-k dielectrics ($k \gg 20$) are needed for next generation aggressively scaled transistors. One route is to stabilize higher-k tetragonal phase in ZrO₂ and/or HfO₂. This offers the advantage of high-k (30-40) without reducing band offsets which is beneficial for gate leakage. First principle calculations predict that small ionic radius Ge (and Si) at moderate doping levels (12%) are the most efficient in stabilizing the t-ZrO₂. Recently we reported the stabilization of the tetragonal ZrO₂ phase in ZrO₂/GeO₂/Ge gate stacks due to an unintentional finite GeO₂ decomposition during the growth process. In this work, we show that by directly (intentionally) doping the ZrO₂ with Ge, a high-k tetragonal phase can be stabilized at very low Ge concentration (a few at. %) and very low growth temperatures (~250-360°C). This phase remains stable after annealing in N₂ up to 1050°C. ZrO₂ and Ge-doped ZrO₂ films were prepared by atomic oxygen beam deposition on SiON/pSi. Both types of substrates are chemically stable upon ZrO₂ deposition. The Ge was incorporated by co-evaporation during the ZrO₂ growth. The Ge atomic fraction x ($x = \text{Ge}/[\text{Ge} + \text{Zr}]$) was estimated by Rutherford back scattering (RBS). Film thickness (nominal ~20 nm) was estimated by x-ray reflectivity (XRR). From XRD measurements, it can be inferred that at very low temperatures (150°C and below) the films are amorphous, while at the highest temperature of about 530°C, the film is a mixture on monoclinic and tetragonal phases. A pure tetragonal phase is obtained at intermediate temperature of 225 and 360°C. The t-ZrO₂ phase is stabilized with Ge concentrations x as small as 1.3 at % while at large $x \sim 32$ at % the film is mostly amorphous. As x increases, the tetragonality ratio $2c/\text{sqrt}(2)a$ increases reaching a maximum value of about 2.043 for $x \sim 6.5$ at %. From capacitor C-V measurements, the dielectric permittivity k can be estimated. The k -value increases with increasing x up to a maximum of ~38 for $x \sim 6.5$ at %. This is attributed to the increase of tetragonality as observed by GIXRD. In conclusion, intentional doping of Ge into ZrO₂ at low (optimum) deposition temperatures (225°C) leads to a k value enhancement which could be beneficial for device scaling. A maximum k value of 37.7 can be obtained when Ge concentration is about 6.5 at. %. According to experimental evidence, this enhancement is correlated with the stabilization of the tetragonal ZrO₂ phase upon doping. The Ge-doped ZrO₂ films retain their tetragonal structure after high temperature annealing.

10:40 AM Student

V7, Atomic Layer Deposited HfO₂ Thin Films on InGaAs/InP: Technology Development and Application in Realization of Memory Diode and Quantum Devices: *Jie Sun*¹; Marcus Larsson¹; Ivan Maximov¹; H. Q. Xu¹; ¹Lund University

InGaAs/InP semiconductor heterostructure has interesting electron transport properties, such as small electron effective mass, high electron mobility, large effective g -factor, and strong spin-orbit coupling strength. HfO₂ is a high- κ dielectric material with large band offset to semiconductors and, thus, is used to improve the gating efficiency and reduce the gate leakage in state-of-the-art silicon technology. However, little is known on the properties of HfO₂ on InP-based semiconductors. In this work, we grow ~30 nm HfO₂ by atomic layer deposition (ALD) with precursors Hf[N(CH₃)₂]₄ and H₂O on modulation doped In_{0.75}Ga_{0.25}As/InP two-dimensional electron gas (2DEG) at 100°C. Annealed Au/Ge ohmic contact is made in the 2DEG layer. A metal-HfO₂-semiconductor diode is fabricated by thermal evaporation of 50 nm Ti/Au metal layer onto the HfO₂ film. As-made diode shows current rectification behavior, and large hysteresis is observed in the I-V curve. We ascribe that effect to the Fermi level pinning at trapping states of the interface between HfO₂ and

InGaAs/InP. The hysteresis effect, however, can be used to realize a memory diode, where the current is manipulated between a high state and a low state. The HfO₂ film on InGaAs/InP has a breakdown field of more than 4 MV/cm and under normal device operation conditions, the gate leakage current density is in the order of 10^{-8} - 10^{-7} A/cm². The excellent dielectric properties can be used to realize gate-defined quantum dot devices. The Schottky barrier of metal/InP is typically less than 0.5 eV, making it difficult to do gating due to the large gate leakage. The problem is solved by incorporating HfO₂ as the gate dielectric. We grow HfO₂ at 100°C, and thus patterning by lift-off is possible. Therefore, although the HfO₂/InP interface is instable, the electrical connection between the interface layer and the gates or the ohmic contacts is avoided. In this way, double dot devices are realized by lithographically patterned gates, which deplete the 2DEG below by applying negative voltages. Transport properties of the double dot are measured at low temperature and the charge stability diagram is studied. Two quantum point contacts (QPCs) are also fabricated as integrated charge sensors. The event which adds or removes a single electron of the dot will change the electrostatic potential in the nearby QPC. By measuring the conductance of the QPC one can sense the location of the charge in the double dot. In summary, the properties of the ALD-HfO₂ on InGaAs/InP are carefully studied. The developed technology opens a new gateway to fabricate quantum devices in InGaAs/InP through gating.

11:00 AM Student

V8, Impact of Growth Process on Native Point Defects and Correlation with Dielectric Properties of Barium Strontium Titanate: *Mitchell Rutkowski*¹; J. Zhang¹; D. R. Douth¹; L.M.B. Alldredge²; W. Chang²; S. W. Kirchofer²; L. J. Brillson¹; ¹The Ohio State University; ²Naval Research Laboratories

Ferroelectric materials have wide applications in electronics because of their very high and tunable dielectric constant. In particular, they find important applications in RF communications as voltage-controlled oscillators, tunable filters, and phase shifters. However, to perform effectively at high frequencies, it is critical to minimize dielectric loss ($\tan \delta$). Thus studies of Ba_{0.5}Sr_{0.5}TiO₃ (BST) for tunable microwave devices show enormous variations in dielectric constant as well as a strong dependence on lattice distortions and growth method. We have observed that the strain states of films deposited by RF sputter deposition or pulsed laser deposition (PLD) vary with oxygen pressure, with sputtered films changing from tensile to compressive to tensile strain while PLD films go from compressive to tensile strain with increasing oxygen pressure. The in-plane dielectric constant and tunability of these films increase as in-plane strain becomes more tensile, and then decrease as a spontaneous polarization is induced. Thus dielectric properties depend on both strain and oxygen content. We have now used depth-resolved cathodoluminescence spectroscopy (DRCLS) to probe the defects associated with these growth processes and found correlations between growth methods, dielectric properties, and specific defect concentrations. We measured DRCLS spectra from ~1 μm Ba_{0.5}Sr_{0.5}TiO₃ films deposited by PLD either directly on (100) MgO or doped 1% with W and deposited on a randomly oriented BST buffer on (100) MgO. These display high defect emissions (normalized to the band gap) corresponding to 1.6 eV Ti³⁺, 2.0 oxygen vacancy (VO), and 2.55 eV VO complex defects in the strained BST/MgO film versus 2-3x lower defects in the strain-relieved, doped BST/buffer/MgO film. Indeed, in the latter film, VO complexes are no longer present and an intrinsic self-trapped exciton emerges. Both showed relatively uniform features in depth and across their surfaces. Furthermore, the higher defect densities correlate with a higher $\tan \delta$ of 1.9×10^{-2} vs. 7.3×10^{-3} for the BST/MgO vs. BST/buffer/MgO films, respectively. A series of ~300 nm Ba_{0.5}Sr_{0.5}TiO₃ films deposited by RF sputtering showed in-plane dielectric loss, ϵ , and tunability increasing as (i) in-plane strain changes from compressive to tensile and (ii) Ti³⁺ increasing and VO decreasing. Overall, dielectric loss and native point defects are strongly correlated in PLD-deposited Ba_{0.5}Sr_{0.5}TiO₃ films. Lattice relaxation suppresses Ti³⁺ but increases oxygen vacancies in RF sputtered Ba_{0.5}Sr_{0.5}TiO₃. These results highlight the importance of engineering lower native point defects in complex oxides to advance their use in ferroelectric and ferromagnetic applications.

11:20 AM

V9, The Growth and Characterization of Crystalline MgO Films on 6H-SiC by Molecular Beam Epitaxy: *Matthew Snyder*¹; Mark Fanton¹; David Rearick¹; Jeremy Acord¹; Joshua Robinson¹; Xiaojun Weng²; ¹Pennsylvania State University Electro-Optics Center; ²Pennsylvania State University Materials Research Institute

The next generation of high-power, high-frequency devices will require the successful integration of a functional oxide layer with a wide-gap semiconductor device on a single chip. The first step in this process involves integration of the oxide layer with a suitable substrate such as 6H-SiC. Functional perovskite oxides such as BaTiO₃ and SrTiO₃ have large mismatches with SiC, necessitating an interfacial “buffer” layer between the oxide and substrate. MgO is one buffer layer candidate and has a (111):(100) lattice mismatch with SiC of ~3.2%, and a mismatch of ~5.4% with (111):(111) oriented BaTiO₃. MgO is also stable at high temperatures. MgO has been deposited on SiC in the past, but at low temperatures (<150°C), and only in very thin layers. This study attempts to optimize the growth of MgO on 6H-SiC. We investigated the growth of crystalline MgO deposited on the Si-face of (100)-oriented 6H-SiC substrates by molecular beam epitaxy (MBE) in order to determine ideal conditions for the deposition of an MgO buffer layer. The films were monitored in-situ by a RHEED system, and characterized after growth by X-ray diffraction (XRD), atomic force microscopy (AFM), and transmission electron microscopy (TEM). MgO crystalline orientation, crystal quality and film morphology on 6H-SiC were explored over a range of deposition temperatures and ozone flow rates. Two modes of film growth were observed in our study: Stranski-Krastanov and Volmer-Weber. Stranski-Krastanov (layer-plus-island) growth occurred at higher ozone flow rates and resulted in the highest-quality films, while films deposited at lower ozone fluxes grew as grainy, misoriented films in the Volmer-Weber (island) mode. There is also a correlation between deposition temperature and film quality; films grown at higher temperatures (up to 350°C) were generally of higher quality than those grown at lower temperatures. The highest-quality MgO film on SiC was deposited at 350°C with a background ozone pressure of 1.7x10⁻⁵ Torr, and resulted in a (111)-oriented Stranski-Krastanov film with a rocking curve full-width half-maximum of 0.21°. The surface of these MgO films were confirmed under AFM to have a generally terraced pattern (due to SiC terraces) with some basal-plane (100) faceting along the (111) MgO terraces. The MgO/SiC interface was investigated by TEM and was found to be atomically sharp, with no sign of oxidation visible in the SiC substrate.

11:40 AM Student

V10, Adsorption-Controlled Growth of Ferromagnetic EuO and the Effect of La Doping: *Alexander Melville*¹; ¹Pennsylvania State University

Europium Oxide (EuO) has attracted significant interest as a ferromagnetic half-metal insulator, and as a compound that exhibits nearly 100% spin-polarization. In the past, thin film EuO was fabricated by flux-matching the Eu flux and the oxygen flux. However, this is problematic because Eu easily overoxidizes (to form Eu₃O₄ and Eu₂O₃) in the presence of too much oxygen and oxygen-deficient EuO forms Eu_{1-x}O. In this paper, we fabricate thin film EuO using adsorption-controlled growth via molecular-beam epitaxy. Adsorption-controlled growth is achieved with a substrate temperature that is high enough to prevent the adsorption of Eu metal onto the surface. In this way, only oxidized Eu (EuO) can form on the substrate surface. By supplying an overpressure of Eu metal ($J_{Eu} = 1.1 \times 10^{14}$ atoms/(cm²·s)), film growth is limited by the available oxygen, which prevents higher oxidation since there is less oxygen than europium. We used orthorhombic (110) YAlO₃ (YAO) substrates with a ~2% lattice mismatch in tensile strain. YAO was chosen despite the lattice mismatch because yttria-stabilized zirconia (which has no mismatch with EuO) over-oxidizes the interface. The (001)-oriented films were grown at a substrate temperature (T_{sub}) of 590°C with oxygen partial pressures (P_{O_2}) ranging from 2.5x10⁻¹⁰ torr to 1x10⁻⁸ torr. The oxygen flux becomes greater than the Eu flux (based on higher Eu oxidation states seen in X-ray diffraction) when $P_{O_2} > 2 \times 10^{-9}$ torr. We then grew a thickness series of samples using $P_{O_2} = 1 \times 10^{-9}$ torr to determine epitaxial quality of adsorption-controlled growth and to measure the critical thickness. The critical thickness (the onset of film relaxation) was determined to be 382±25Å by comparing the full width at half

maximum (FWHM) of the rocking curves. Relaxation of the thin films as a function of thickness can be seen in broadening rocking curves. Commensurate films have rocking curves as narrow as the substrate. The films we grew are commensurate and have higher epitaxial quality than previously reported, with 34 arcseconds (0.0097°) the narrowest FWHM achieved, even under epitaxial tensile strain. We then doped the EuO with 5% La to monitor its effects on electric and magnetic properties. A temperature series ($T_{sub} = 420^\circ\text{C} - 640^\circ\text{C}$) of 5% La³⁺-doped EuO was grown under the previous conditions, with a target thickness of 35 nm, below the critical thickness. The Curie temperature ($T_C = 100^\circ\text{C}$) and charge carrier density both increased at low growth temperatures ($T_{sub} < 470^\circ\text{C}$), but returned to the undoped levels at high growth temperatures, indicating temperature-dependant dopant behavior.

Session W: ZnO Growth

Thursday AM
June 25, 2009

Room: Deans Hall I
Location: Pennsylvania State University

Session Chairs: Jamie Phillips, University of Michigan; Yicheng Lu, Rutgers University

8:20 AM Student

W1, Properties of In-Doped ZnO Films Grown by Metalorganic Chemical Vapor Deposition on GaN(0001) Templates: *Tammy Ben-Yaacov*¹; Tommy Ive¹; Chris Van de Walle¹; Umesh Mishra¹; James Speck¹; Steven DenBaars¹; ¹University of California, Santa Barbara

ZnO has many unique electrical, piezoelectric, and optical properties which make it an applicable material to optoelectronic devices. Consequently, there is a widespread effort towards epitaxial growth of high quality, single crystal ZnO thin films, and much work on controlling the electrical properties of these films. For ZnO to be used for optoelectronic applications, it is necessary to control the n-type conductivity of ZnO films, while simultaneously achieving good surface morphology and crystal quality. This is a major challenge, as undoped ZnO almost always exhibits n-type conductivity, and the introduction of dopants has a strong impact on the film morphology and crystal quality. In this study, we present the properties of 0.5µm-thick In-doped ZnO(0001) films grown by MOCVD on semi-insulating GaN/Al₂O₃ templates. An undoped ZnO buffer layer was deposited at 450°C with a reactor pressure of 50 torr before the temperature was increased to 950°C for the high temperature deposition of the ZnO epitaxial layer. At 950°C, a thin unintentionally doped (UID) ZnO layer was deposited first, and then In was introduced for the growth of a thicker ZnO: In layer. The VI/II ratio was 550 and 11000 for the buffer layer and the high temperature epitaxial layer, respectively. The TMIn flows ranged from 3 sccm to 50 sccm. The growth rate was 2.2 Å/s. We compared the electrical properties, film morphology, and crystal quality of In-doped films to a comparable undoped film to clearly see the effects of the In doping. Carrier concentration, mobility, and sheet resistance were evaluated by Hall measurements. All In-doped films had carrier concentrations significantly greater than the undoped sample, as the range for In-doped samples was 7.7x10¹⁸-1.8x10¹⁹ cm⁻³, as compared to 5.4x10¹⁷ cm⁻³ for the undoped sample. A minimum sheet resistance of 184 Ω/sq was achieved, which is significantly lower than 3100 Ω/sq measured for the undoped sample. For low In flows, the electron concentration increased as the dopant flow increased, in good agreement with the In concentration measured by SIMS. The highest electron concentration (1.8x10¹⁹ cm⁻³) was realized for the sample grown with 5 sccm TMIn. When the In concentration was increased beyond this point, the measured electron concentration decreased, which may indicate that much of the In was not incorporated as a simple shallow donor. The samples with higher In concentration were “overdoped,” i.e., the In concentration was so high that the material quality began to degrade. The crystal quality was assessed by recording the FWHM of XRD ω-scans across the symmetric (0002) reflection. The ZnO:In films have good crystal quality, as the sample grown with 3 sccm TMIn had a narrow FWHM of 0.136° (489

arcsec), and the quality of the ZnO:In films decreased slightly with increasing TMIn flow.

8:40 AM Student

W2, MBE Growth and Characterization of Ag-Doped Zinc Oxide Thin Films: *Jessica Chai*¹; Robert Burke¹; Rueben Mendelsberg¹; Roger Reeves¹; John Kennedy²; Holger Wenckstern³; Marius Grundmann³; Kevin Doyle⁴; Tom Myers⁴; Steve Durbin¹; ¹University of Canterbury; ²GNS Science; ³Universität Leipzig; ⁴Texas State University

In recent years, ZnO has garnered interest for UV light-emitting diodes (LEDs) and lasers, an area currently dominated by group III nitrides, arsenides, and phosphides. It is believed that one day ZnO will compete with the current technology; however it will be necessary to overcome the hurdle of producing high-conductivity p-type ZnO first. A multitude of studies have been carried out concerning p-type doping of ZnO but with minimal success. Doping with group V elements has exposed issues concerning the formation of point defects such as Zn interstitials and O vacancies. Group I elements have also been explored, but they have been found to act as donors due to their tendency to form interstitials because of their small ionic radii. More recently, Yan et al. have evaluated the suitability of Group IB dopants as a means of resolving these problems and have found that Cu, Ag, and Au may suppress the formation of O vacancies and Zn interstitials, under certain growth conditions. In this study, the potential of Ag as a p-type dopant for ZnO has been investigated by plasma-assisted molecular beam epitaxy (PAMBE). The Ag-doped ZnO epilayers were grown on (0001) sapphire substrates over a substrate temperature range of 400-800°C. The doping concentration was varied from 0.004-0.4% by adjusting the Ag flux between 4×10^9 and 4×10^{11} atoms/cm²s. Rutherford backscattering spectroscopy (RBS), Hall effect measurements, reflection high-energy electron diffraction (RHEED), low temperature photoluminescence (PL), deep level transient spectroscopy (DLTS), and thermal admittance spectroscopy (TAS) were all utilized to investigate the electrical, optical, and structural properties of the as-grown ZnO films. In these studies, RBS revealed that 94% of Ag incorporated substitutionally on Zn sites at a doping concentration of 0.04% and a substrate temperature of 600°C, and relatively less Ag successfully incorporated substitutionally at higher doping concentrations. Through RHEED analysis, the films were observed to remain single crystalline above substrate temperatures of 600°C as long as the doping concentration remained below 0.04%. Hall effect measurements indicated that the films were n-type with a slight reduction in the carrier concentration at higher doping levels, and samples grown at a substrate temperature of 600°C were found to consistently possess the lowest carrier concentrations. Low temperature PL was dominated by the presence of donor-bound excitons and red-shifted with increasing doping concentration due to the incorporation of Ag substitutionally within the lattice. Evidence exists to suggest that Ag effectively suppressed the defect band of ZnO when grown under O-rich conditions. Finally, DLTS and TAS measurements indicated the possible existence of a deep acceptor level at 319 meV which is associated with Ag and corresponds well with the theoretical level calculated by Yan et al.

9:00 AM Student

W3, Growth and Characterization of Non-Polar ZnO/ ZnMgO Quantum-Wells Synthesized by Pulsed Laser Deposition: *Mei-Hui Liang*¹; Yen-Teng Ho¹; Wei-Lin Wang¹; Yi-Sen Shih¹; Li Chang¹; ¹Department of Materials Science and Engineering, National Chiao Tung University, Hsinchu, Taiwan

For device applications, The use of non-polar ZnO surfaces is of particular interest since QW structures can be grown without a reduction of the exciton binding energies as demonstrated in non-polar GaN layers. In this work, we have studied the growth of ZnO/ Zn_{0.8}Mg_{0.2}O quantum-wells on r-plane sapphires. In addition to the growth characteristics, the microstructure and optical properties of ZnO/ Zn_{0.8}Mg_{0.2}O QW structure with different well widths are also reported. The QW structures consisted of a ZnO well layer sandwiched between ZnMgO barrier layers. (11 0) Zn_{0.8}Mg_{0.2}O and a-plane ZnO epilayers were grown by pulsed-laser deposition (PLD) with various well widths. The smallest thickness of ZnO-layer and ZnMgO-layer is 1.8 nm and 2.3nm, respectively. A KrF excimer laser with $\lambda=248$ nm was used for PLD deposition of ZnO and ZnMgO films. The time duration of the laser pulse was 25 ns, power density was 1-2 J/cm², and the pulse frequency was 3 Hz. The

base pressure in the growth chamber was 1×10^{-8} Torr. The oxygen flow was introduced to the chamber in which the oxygen partial pressure was kept at 1.4×10^{-2} Torr. The substrate temperature was varied in the range of 650-800°C. The growth process was monitored in situ by reflection high-energy electron diffraction (RHEED). The surface morphology was examined by atomic-force microscopy using a DI3100-AFM microscope. High-resolution X-ray diffraction measurements were carried out using a Bede D1 diffractometer in the triple-axis mode. Photoluminescence (PL) spectra were acquired using a continuous He-Cd ($\lambda=325$ nm) laser as the excitation source. Microstructural characterization was carried out using cross-sectional transmission electron microscopy (TEM) with X-ray energy-dispersive spectroscopy (EDS) for the measurements of chemical compositions. TEM in Fig. 1 clearly shows multilayer structure of ZnO and Zn_{0.8}Mg_{0.2}O films. The epitaxy relationship between ZnO and r-sapphire is known to be // and [0001]ZnO// . Photoluminescence measurement revealed the confinement effect on emission peaks by a blueshift with reduction in the thickness of the ZnO well layer. As shown in Fig. 2, the emission peak is at 3.512 eV for well of 1.8 nm, whereas it is at 3.388 eV for width of 5.6 nm. The x-ray rocking curves, RHEED patterns, and AFM (Fig. 3) demonstrate anisotropic growth of ZnO and ZnMgO with smooth surface in stripe morphology. References: 1. B. P. Zhang, N. T. Binh, K. Wakatsuki, C. Y. Liu, and Y. Segawa, N. Usami Appl. Phys. Lett., 86, 032105 (2005).

9:20 AM

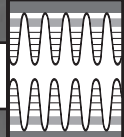
W4, Ultrasonic Spray Assisted Mist-CVD for the Growth of Crystalline and Amorphous ZnO: Hiroyuki Nishinaka¹; Yudai Kamada¹; Naoki Kameyama¹; Kentaro Kaneko¹; *Shizuo Fujita*¹; ¹Kyoto University

We show the unique and promising potential of ultrasonic spray assisted mist-chemical vapor deposition (CVD) as an inexpensive, safe and environmental-friendly large-area growth method for high-quality crystalline and amorphous ZnO thin films. In this technique liquid solutions of source materials are used as precursors. They are ultrasonically atomized and the mist particles formed are transferred to the reaction area with the carrier gas[1,2]. In this way, the mist sources can substitute for vaporized sources of toxic and/or dangerous metalorganics. This technique, therefore, can possess excellent controllability for source supply comparable to metalorganic-CVD (MOCVD). The growth can be done even under the open air, allowing low-cost and large-area growth with applying a linear-source nozzle[1]. Using zinc acetate or acetylacetonato as a precursor for Zn with changing the substrate materials and temperatures, (i) transparent and smooth c-axis oriented ZnO thin films were grown on glass substrates, (ii) ZnO films were grown at the substrate temperature lower than 200°C, (iii) single-crystalline ZnO on sapphire attained the mobility of 90 cm²/Vs, which was reasonably high compared to various ZnO thin films grown by MOCVD, and (iv) two-dimensional step-flow growth, which had been difficult by MOCVD, was achieved by homoepitaxial layers on ZnO substrates. Doping and alloy layers were successfully achieved by adding the required source precursors in the source solution. The results showed as followed; (i) Al-doped ZnO on glass attained low resistivity of the order of $10^{-4} \Omega\text{cm}$, which was a standard for certain applications as a transparent conducting oxide, (ii) single crystalline (0001)-oriented wurtzite Zn_{1-x}Mg_xO thin films were prepared between $x=0$ and 0.3 without phase segregation of rocksalt structure. This growth technique has also been applied to other oxide thin films such as Al₂O₃, Ga₂O₃, Fe₂O₃, and their alloys. The mist-CVD method is not only low-cost and environmental-friendly but also superior to the existing CVD methods for the growth of oxide thin films. [1] Y. Kamada et al., Jpn. J. App. Phys. 45 (2006) L857.[2] H. Nishinaka and S. Fujita, J. Cryst. Growth, 310 (2008)5007.

9:40 AM

W5, MOCVD of Zinc Oxide Transparent Conductive Oxide: *Bruce Willner*¹; Shangzhu Sun¹; Gary Tompa¹; ¹Structured Materials Industries, Inc.

Zinc Oxide (ZnO) and its alloys are wide bandgap semiconductors that can serve very effectively as transparent contact layers on electronic and optoelectronic devices such as solar cells and LEDs. ZnO has a wide bandgap and strong exciton bonding energy, a high field effect mobility, low cost deposition and substrates, and compatibility with many other materials, especially oxides. ZnO films have very high transparency at visible and UV wavelengths, good lattice match to GaN and good high temperature stability. High conductivity transparent ZnO



can be produced by doping with Al, In, or Ga. Despite degenerate doping, 2 at.% or more, the material crystalline quality, as shown by photoluminescence and other characterizations, and optical transparency remains very good. The alloying of ZnO with magnesium or cadmium oxide provides the ability to tune the energy bandgap and index of refraction without a large change in the lattice constant. One approach to delivering these materials is metal-organic chemical vapor deposition (MOCVD), which can produce high quality films of varied and well-controlled composition, uniformly over large areas. MOCVD deposited ZnO demonstrates significantly higher material quality than sputtered ZnO, and at much lower cost than MBE. We have optimized a reactor design with a high rotation speed susceptor, performance scaled from 2" to 16" diameter deposition planes and with modeling scaled to greater diameters for single and multi-layer ZnO structures. MOCVD offers greater composition control to the deposited layers, including the ability to vary the composition during deposition. Doping densities lower than 10^{15} cm^{-3} and as high as 10^{22} cm^{-3} are possible, allowing precise control of the electrical and optical properties of the material. CVD and MOCVD processes are readily scalable to large volume production, and CVD provides good step coverage, which cannot be achieved with physical vapor deposition methods. The characteristics of the films produced are observed using XRD, XRF, Hall, optical, and other techniques. Deposited film structures exhibit pin-hole-free, smooth morphology and can be tuned to exhibit amorphous, polycrystalline and single crystalline films at temperatures from 300°C to 1000°C. We demonstrate 3% thickness uniformity across an 8" wafer. High quality, conductive films can be produced below 500°C. MOCVD-grown conductive ZnO films on a glass substrate grown at 420°C with Ga-doping in mid 10^{21} cm^{-3} show a cutoff wavelength of 375 nm, matching the ZnO bandgap, and high transparency.

10:00 AM Break

10:20 AM

W6, Low Temperature ZnO Growth for Nanotube Fabrication by Atomic Layer Deposition: *Diefeng Gu*¹; Kanda Tapily¹; Yao Yao²; Pragya Shrestha¹; Helmut Baumgart¹; ¹Old Dominion University; ²University of Virginia

Zinc oxide (ZnO) thin films were obtained by the atomic layer deposition (ALD) method using diethyl zinc (DEZn) and water precursors. A good linearity between ZnO film thickness and ALD cycles was observed at various temperatures. The ALD growth window of ZnO ranges from 100 °C to 160 °C under the other optimized processing parameters. Inside the ALD window ZnO growth rate of 2.2 Å/cycles was achieved on Si surface at 150 °C through a good linear fitting [1]. The surface morphology and roughness of ZnO film was characterized by atomic force microscopy (AFM). The AFM results showed that the surface roughness of ZnO is a function of film thickness and deposition temperature. At low deposition temperature, the surface roughness increases as the film thickness increases. At high deposition temperature, however, the surface roughness decreases as the film thickness increases. A higher surface roughness was observed after annealing at 600 °C in N₂ for 10 min. The ZnO film grown on Si wafer at 160 °C has polycrystalline structure obtained from X-ray diffraction (XRD) and cross sectional transmission electron microscopy (XTEM). An interfacial layer was observed between ZnO and Si for a 50 nm thick ZnO film. ZnO was deposited into anodic aluminum oxide (AAO) pores with an aspect ratio of 300 (pore diameter: 200 nm, depth: 60 μm) by ALD [2]. A conformal and complete ZnO coating inside the AAO pores was achieved by extended exposure time for the precursors during deposition. Energy-dispersive spectroscopy (EDS) was used to characterize the distribution of ZnO in the nanopores. ZnO nanotubes or nanorods have been obtained after removing the AAO template depending on the ZnO film thickness. [1] E. Guziewicz, I. A. Kowalik, M. Godlewski, K. Kopalko, V. Osinniy, A. Wójcik, S. Yatsunenko, E. Lusakowska, W. Paszkowicz, and M. Guziewicz, *J. Appl. Phys.* 103, 033515 (2008).[2] C.-J. Yang, S.-M. Wang, S.-W. Liang, Y.-H. Chang, and C. Chen, *Appl. Phys. Lett.* 90, 033104 (2007).

10:40 AM Student

W7, Ag/N/Ag-N Doped ZnO Nanostructures Prepared by Wet-Oxidation: *Ruiqun Chen*¹; Wei Gao¹; ¹University of Auckland

The synthesis and applications of Zinc oxide (ZnO) nanostructures were intensively studied worldwide, not only because of its unique optical/electrical properties, but also due to its vast range of nanostructures. We investigated a rarely studied method - wet oxidation - to produce single crystal ZnO nanowires/belts. Comparing to other well-studied vapor phase processes, wet-oxidation has the advantages such as low facility requirement, good adhesion between nanowires and substrates, which is useful for the applications such as Dye Solar cell. However, doping was hard to be realized due to the limitation of Zn precursor microstructure. In this paper, we report the development of doping method for the wet-oxidation to produce p-type ZnO nanostructures. P-type conductivity was resulted from Ag/N/Ag-N doping. Ag was doped to Zn thin films before wet oxidation by Magnetron Sputtering, while N doping was achieved by introducing NH₃ into wet-oxidation atmosphere. The SEM study showed the Ag-doping did not eliminate the layer structure of Zn precursor particle, and therefore, the ZnO nanostructures can still grow out from those nucleation sites. High resolution transmission electron microscopy (HRTEM), cathodoluminescence (CL)/ photoluminescence (PL) measurement and electrical measurement were used to examine the effects of the Ag, N doping on the electrical and optical properties of ZnO nanostructures. In HRTEM study, layers pattern of lattice distortion caused by Ag was observed at the root of Ag doped ZnO nanobelts, and the Ag concentration gradient along the nanobelt growing direction gave an insight of Ag oxidation/diffusion mechanism in this process. When comparing to the undoped ZnO, CL measurements showed that Ag doping increased the UV emission and red-shifted the UV peak wavelength for 10 nm, which is corresponding to the Ag acceptor site in the energy band. Low-temperature PL analysis confirmed the CL results, and gave detailed information of the Ag/N/Ag-N doped ZnO band structure, and finally the p-type conductivity was confirmed by electrical measurement.

11:00 AM

W8, Photoluminescence Properties of Highly Dispersed ZnO Quantum Dots in Polyvinylpyrrolidone Nanotubes Prepared by a Single Capillary Electrospinning: *Y.C. Liu*¹; *X.H. Li*¹; *C.L. Shao*¹; *X.Y. Chu*¹; *C.H. Wang*¹; *G.L. Yang*²; ¹Centre for Advanced Optoelectronic Functional Materials Research, Key Laboratory of UV Light-Emitting Materials and Technology, Ministry of Education, Northeast Normal University; ²Department of Physics, Drexel University

Low dimensional ZnO nano-composite materials have attracted great attentions due to their promising applications in nano-scale electronic or optical devices, catalysts, biomaterials, sensors, and so forth. However, ZnO nanoparticles embedded in electrospun polymer nanotubes are rarely reported. In this work, ZnO quantum dots (QDs) had been highly dispersed into PVP nanotube walls, where the PVP molecules not only decreased the interactions among the dispersed ZnO QDs, but also passivated the surface defects of ZnO QDs. The scanning electron microscopy and transmission electron microscopy images illustrate that the composite nanotubes are tubular structures with ZnO QDs filled in the nanobube walls separately. PL and resonant Raman spectra indicate that the composites exhibit narrower band edge emissions and less laser thermal effects due to the well dispersion of ZnO QDs in the nanotube walls and the passivation of PVP molecules on the surface defects of ZnO QDs. As the diameters of ZnO QDs is 3~5 nm, a strong confinement is more applicable here. The temperature-dependent PL spectra of the composite nanotubes exhibits blue shifted band gap, enlarged exciton binding energy and less exciton-LO phonon interaction due to the quantum confinement effects. The blue shift of PL peak position is contributed by the confinement-induced blue shift of the electronic levels and the red shift from the increased coulomb interaction energy. As the blue shift increases as $1/R^2$ (R is the diameter of QDs) while the red shift increases as $1/R$, the blue shift will dominates the lowest exciton energy for the ZnO QDs. Thus, the PL peak was blue shifted. On the other hand, due to the increased coulomb interaction energy, the distance between electron and hole is decreased. As a result, the exciton binding energy is increased. Moreover, as the exciton Bohr radius is compressed, the polarization of excitons becomes weak.

Thus, LO replicas of ZnO QDs which reflect the exciton-LO phonon coupling strength are much weaker than that of ZnO powders.

11:20 AM Student

W9, Generalized Theoretical Model for Ferroelectric Properties of BaTiO₃, BaTiO₃-ZnO, and ZnO-BaTiO₃-ZnO Thin Films: Venkata Voora¹; T. Hofmann¹; M. Brandt²; M. Lorenz²; M. Grundmann²; N. Ashkenov²; M. Schubert¹; ¹Department of Electrical Engineering, and Nebraska Center for Materials and Nanoscience, University of Nebraska-Lincoln; ²Institut für Experimentelle Physik II, Universität Leipzig

Heterojunctions composed of wurtzite-structure ZnO and perovskite-structure BaTiO₃ are interesting because of the coupling between the switchable spontaneous polarization of the BaTiO₃ and non-switchable spontaneous polarization of ZnO [1, 2]. BaTiO₃, ZnO-BaTiO₃, and ZnO-BaTiO₃-ZnO structures were deposited by pulsed laser deposition on (001) silicon substrates using a rotatable multi-target holder. Subsequently polarization hysteresis properties were investigated in order to study the spontaneous polarization exchange coupling behavior. Depending on the polarity of the applied bias the heterostructures reveal strong reversible resistive and capacitive switching behavior, and hysteresis due to the ferroelectric polarization. Temperature dependent measurements reveal complete disappearance of the hysteresis at the paraelectric phase transition, which is further corroborated by electro-optic Raman and ellipsometry measurements. From these investigations we conclude that BaTiO₃ ferroelectricity is the driving cause of the hysteresis, instead of trap charges injected through the interfaces [3, 4]. Depletion layer formation in ZnO is the origin of the highly resistive behavior for DC currents, and which can be controlled by the ferroelectric polarization in the BaTiO₃ layer. We develop a generalized physical model to analyze the Sawyer-Tower response of our experimental structures. Our model accounts for the depletion charges, the non-switchable spontaneous polarization of ZnO, and the switchable spontaneous polarization of BaTiO₃. The model data are in excellent agreement with the measured voltage dependent polarization hysteresis responses of the heterostructures. Furthermore, the influence of physical model parameters on the ZnO-BaTiO₃ and ZnO-BaTiO₃-ZnO characteristics will be presented. References: [1]. M. Schubert, N. Ashkenov, T. Hofmann, H. Hochmuth, M. Lorenz, M. Grundmann, and G. Wagner, *Ann. Phys.* 13, 61 (2004). [2]. V. M. Voora, T. Hofmann, M. Brandt, M. Lorenz, M. Grundmann, and M. Schubert *Phys. Stat. Sol. (c)* 5, 1328 (2008). [3]. B. N. Mbenkum, N. Ashkenov, M. Schubert, M. Lorenz, H. Hochmuth, D. Michel, M. Grundmann, and G. Wagner, *Appl. Phys. Lett.* 86, 091904 (2005). [4]. N. Ashkenov, M. Schubert, E. Twardowski, H. V. Wenckstern, B. N. Mbenkum, H. Hochmuth, M. Lorenz, W. Grill, and M. Grundmann, *Thin Solid Films* 486, 153 (2005).

11:40 AM Student

W10, Ferroelectric Thin Film Field-Effect Transistors Based on ZnO/BaTiO₃ Heterostructures: Matthias Brandt¹; Heiko Frenzel¹; Holger Hochmuth¹; Michael Lorenz¹; Marius Grundmann¹; ¹Universitaet Leipzig

Both ZnO and BaTiO₃ (BTO) are transparent oxide materials. While BTO is a perovskite and shows ferroelectric switching of the electrical polarization at room temperature, ZnO crystallizes in the wurtzite structure and therefore has a fixed spontaneous polarization. Further, ZnO is a semiconductor and is very easily doped n-type, while BTO is an insulating ferroelectric at room temperature. The combination of both materials results in a coupling of the polarizations, which leads to an asymmetry in the ferroelectric hysteresis of the BTO. The free carrier concentration in the ZnO is influenced by the sign and magnitude of the polarization in the BTO. Recently, a model has been developed in order to describe that coupling in ZnO/BTO heterostructures, and the effects on the free charge carriers in the ZnO. Further, metal-semiconductor field effect transistors have been demonstrated in the ZnO system. The ability to control the free carrier concentration in the ZnO by the polarization of the BTO can be used to develop ZnO/BTO heterojunction ferroelectric field effect transistors, forming non-volatile memory elements. We have grown epitaxial BTO/ZnO heterostructures by pulsed laser deposition on lattice matched SrTiO₃:Nb substrates and on SrRuO₃ buffered SrTiO₃ substrates. Epitaxial growth of the BTO layer has been confirmed by X-ray diffraction and transmission electron microscopy. The electrical properties of simple ZnO/BTO heterostructures have

been investigated by current-voltage and capacitance-voltage measurements, showing that the BTO layer is highly insulating ($I < 10^{-11}$ A/cm²). The structures were processed into field effect transistors, and their output and transfer properties have been studied. The structures were normally on, and currents of up to 10 μ A were achieved which could be controlled over at least 6 orders of magnitude by the applied gate voltage. The dielectric constant of the BTO could be determined to be 197. The channel mobility has been calculated, and reached values of up to 0.27 cm²/Vs, which is in range of the mobility reported for ZnO metal-insulator-FETs. A clear dependence of the source-drain current on the previously applied gate field has been observed, and was reproducible in repeated switching cycles, showing the suitability of the structure as a memory device. Current ratios of up to 1000 could be achieved between the two possible polarization states. The dependence of the device performance on the growth conditions, especially the BTO thickness and ZnO dopant concentration has been studied. Long time transfer characterization measurements have been carried out, in order to study possible device degradation.

Session X:

Molecular Electronics: Devices, Materials, and Molecular Electronics and Chem/Bio Sensors

Thursday AM
June 25, 2009

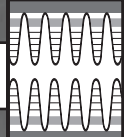
Room: Deans Hall II
Location: Pennsylvania State University

Session Chair: Avik Ghosh, University of Virginia

8:20 AM Student

X1, Understanding Molecular Modulation of Semiconductor Band-Bending through Transport Studies on Metal-Molecule-Semiconductor Device Junctions: Archana Bahuguna¹; Fernanda Alanis-Camacho¹; Avik Ghosh¹; Nathan Swami¹; ¹University of Virginia

An understanding of the effects of molecular adsorption on the modulation of semiconductor band-bending is of great significance for the characterization of electronic coupling in a variety of device paradigms such as contacts for molecular electronics, [1], probing the passivation of semiconductor surface states, [2], and probing signal transduction for sensor schemes based on the controlled introduction of surface charge using molecular dipoles on self-assembled monolayers (SAMs) on semiconductor substrates. [3]. The fitting of experimental transport data at metal-molecule-semiconductor junctions to models on electronic coupling, [4], can enable the extraction of significant device parameters that can eventually guide the development of novel chemistries and device structures that are based on modulated semiconductor band bending. Much of the prior model fits to transport data do not account for tunnel barrier shape, asymmetry of the Schottky device junctions and dipoles at the molecule-semiconductor interface. In this study, the Non-equilibrium Green's Function (NEGF) formalism was used to examine electronic transport and band bending at metal - molecule - semiconductor device junctions, and correlate transport characteristics to experimental I-V data. COOH-terminated SAMs of varying length (SH-CnCOOH, n=7, 10, 15) were deposited on patterned areas (7 μ m) on GaAs (001) substrates; and copper complexation and electroless deposition methods were used to ensure the deposition top metal contacts, without any penetration into the underlying SAM layer [5]. In this manner, the molecular device length was varied from 0.7 nm to 2 nm, and substrate doping was varied from n+ doping (1018/cm³) to p+ doping (1019/cm³). Based on this, the effects of varying SAM length, substrate doping, and molecular dipole on voltage division were determined by fitting the model to the experimental I-V characteristics, to enunciate the role of the tunnel barrier shape, semiconductor band bending, depletion width and surface charge on transport. [1] Lodha S, Carpenter P, Janes DB, *J. Appl. Phys.* 2006, 99. [2] Y. Liu, H. Yu, *J. Phys. Chem. B* 2003, 107, 7803-7811. [3] Ashkenasy, G.; Cahen, D.; Cohen, R.; Shanzer, A.; Vilan, A. *Acc. Chem. Res.* 2002, 35, 121. [4] Neshor G., Vilan A., Hwang J., Cohen H., Cahen D., Amy. F., Chan C., Hwan H., Kahn A., *J. Phys. Chem. B*



2006, 110, 14363-14371.[5] Camacho-Alanis F., Wu L., Zangari G., Swami N. Journal of Mat Chem. (2008), 18, 5459-5467. DOI/10.1039/b800001a.

8:40 AM

X2, Temperature-Dependent Transport in Gold-Molecule-p+ Si Devices:

Adina Scott¹; David Janes¹; ¹Purdue University

Recently, there has been considerable interest in developing molecular electronic systems for sensing, nanoelectronic, and memory applications. Advances in fabrication techniques and measurement capabilities have resulted in a wealth of data on molecular conductance. Much of the work that has been done to date has utilized metal electrodes, however this has posed significant problems for device stability, integration with existing technologies, and interpretation of results. These problems can be addressed by replacing one of the metal electrodes with silicon (Si). A variety of molecular layers can be covalently bound to Si surfaces, leading to chemically stable junctions. In-situ spectroscopic characterization can be utilized to verify the integrity of the resulting structures. Moreover, it has been proposed theoretically and demonstrated experimentally using scanning tunneling spectroscopy that novel behavior such as negative differential resistance can be achieved due to the interplay between molecular electronic orbitals and the bandstructure of degenerately doped silicon. In spite of these promising experimental and theoretical results, much of the experimental work on integrated metal/molecule/semiconductor devices has utilized lightly-doped semiconductors or structures where there is a large built-in potential. Such devices exhibit significant rectification and Schottky diode-like behavior at low biases, suggesting that the semiconductor contact is dominating the transport behavior. By utilizing a system in which there is little or no semiconductor barrier, it is possible to tune the devices into regimes where the molecular layer is the limiting conduction barrier even at low biases. This presentation will describe devices which achieve this condition by employing a p+ Si substrate and a Au top electrode, providing little band offset. Such devices are of great interest since significant changes in device transport can be achieved by modifying the molecular layer. The use of degenerately-doped Si allows for measurement of temperature-dependent properties since the carriers in the semiconductor do not freeze out. In the present study, electron transport through gold/molecule/p+ Si devices is measured for various molecular layers at various temperatures. Transport mechanisms will be discussed based on considering the voltage and temperature-dependent electronic properties. The physics of carrier transport in such systems can be analyzed considering the Si bandstructure and molecular orbital energies as well as non-idealities such as surface states. Measured electronic transport properties are correlated with spectroscopic data suggesting that molecular vibronic properties play an important role in tunneling transport under certain conditions.

9:00 AM Student

X3, Optical and Electronic Multi-Probe Vibrational Spectroscopic Characterization of Molecular Junction Based on Self-Assembled Monolayer:

Masato Maitani¹; Heayoung Yoon¹; Orlando Cabarcos¹; Theresa Mayer¹; David Allara¹; ¹Pennsylvania State University

Metal-molecule-metal (M3) junction structure has been used to study electronic characteristics of molecules for application to the electronic material. Since it is difficult to access to molecules embedded in junction, deconvolution of electronic characteristics of molecules from other factors, such as contamination, metal-originated characteristics, or other unpredictable feature, has been a large challenge. Here, we propose a reliable M3 junction structure, crossed-wire (CW) junction, capable of multi-lateral assembly with high yield and also optical and electronic multi-probe vibrational spectroscopic characterizations, surface enhanced Raman spectroscopy (SERS) and inelastic electron tunneling spectroscopy (IETS), to directly study switching molecules embedded in M3 structure. The CW junction is prepared by the electric-field assisted alignment of Au nano wire (diameter: ~220nm) on oligoanilinthiolate (OAn) SAM assembled on Au bottom nano wire (width: ~100nm and 1µm). OAn CW junction displays switching characteristics with high and low conductance state as previously reported. IETS spectra of the high and low conductance state of OAn CW junction reveal distinct spectra with high / low conductance state under temperature controlled condition (~4K). Surface Plasmon enhanced Raman spectroscopy (SERS) is capable to study real-time

spectroscopic characteristics in high and low conductance state of CW junction. The spectra from OAn SAM in CW junction show similar spectra to that from bare OAn SAM on SERS active surface. The intense spectra observed only at the intersection of wires clearly indicates that the spectra contain information mainly from molecules in the junction. Finite difference time domain (FDTD) calculation reveals the enhanced EM field confined in the junction proves small amount of molecules in the nano-size junction area. Time dependant SERS measurement indicates the intense spectral fluctuation of OAn CW junction (width:~100nm) but SERS active substrate. This fluctuation can be attributed to the orientational fluctuation of bent OAn molecule. This fluctuation was predicted by density functional theory calculation of OAn molecule in which different stable orientations exist with small variation of energy. Nevertheless, averaged spectra within ~100sec displayed similar spectra to the one from SERS active substrate. Therefore, OAn molecule has stable orientation in the low conductance state, although the molecule always change orientation slightly in ambient temperature. High conductance state also exhibited the intense spectral fluctuation. The averaged spectra, however, show different vibrational modes from low conductance state. And moreover, these spectra are consistent to the IETS spectra. According to these results, we discuss the switching model of OAn CW junction in the presentation.

9:20 AM

X4, Investigation of Semiconductor-Molecule-Semiconductor Devices:

ZnS/MHA/GaAs Devices: Patrick Carpenter¹; Peng Lu²; David Janes¹; Amy Walker²; ¹Purdue University; ²Washington University in St. Louis

There have been many studies of the electrical properties of metal-molecule-metal structures (MMM) and metal-molecule-semiconductor (MMS) structures. MMS devices are of particular interest because the substrates used to fabricate these devices are technologically relevant and covalent molecule-semiconductor bonds can be formed. Electrical properties of these devices can be manipulated by varying dopant densities, electrostatic properties, and surface properties of the semiconducting contact. Even though there has been a considerable amount of progress made on these devices, there are still many challenges that need to be overcome, particularly related to depositing the metal without penetrating through the molecular layer. Semiconductor-molecule-semiconductor (SMS) devices could eliminate these problems, and allow enhanced functionality through tuning composition/doping of both contacts. Semiconductors, such as ZnS, are of particular interest because its wide band gap and structural properties can be utilized for photovoltaic and optical applications. In the current study we have fabricated ZnS/Mercaptohexadecanoic Acid (MHA)/GaAs devices for electrical and structural characterization. Using standard photolithography techniques, we patterned p⁻-GaAs (N_A = 1 x 10¹⁹ cm⁻³) and n⁻-GaAs (N_D = 1 x 10¹⁸ cm⁻³) substrates for MHA molecular deposition. Using a previously published chemical bath deposition (CBD) procedure, ZnS was deposited on the monolayer. Scanning Electron Microscopy (SEM) images were taken of the samples in order to study the morphology of the ZnS layer. Preliminary studies indicate that the density of the ZnS increases as device area decreases. Using standard electrical probing techniques, current-voltage data was obtained from ZnS/MHA/GaAs devices. The preliminary data shows that both the p⁻-GaAs and n⁻-GaAs devices show a change in conductivity from their respective control samples. Current densities in the p⁻-GaAs devices are higher than in the n⁻-GaAs devices. Rectification is also observed in one direction for the p⁻-GaAs devices and in the opposite direction for the n⁻-GaAs devices. Further work is being performed to determine the doping of the deposited ZnS and the band lineups between the ZnS and the GaAs substrates.

9:40 AM Student

X5, Passivation of GaAs Surface Using SAM of Redox-Active Ruthenium Based Organic Molecules in a Matrix of Non Redox Active OPE1 Molecules:

Rand Jean¹; Dmitry Zemlianov¹; Bin Xi¹; Tong Ren¹; David Janes¹; ¹Purdue University

Recent investigations have spurred interest in the use of organic molecules to complement and maybe replace modern day semiconductor electronics. The use of redox-active molecules is particularly intriguing due to the possibility of obtaining high density memory as well as low power and fast switching devices. Previous studies have indicated that in some metal/molecule/metal

THURSDAY AM

configurations, specifically those with redox-active molecules, the molecular density of states offer the most significant current conduction path since their molecular levels are close to contact Fermi levels and thus can be reached through modest bias voltages. This property makes such molecules attractive candidates for device engineering. In the past, redox-active molecules have been investigated while being anchored to metallic surfaces (usually Au) using self assembly techniques. In this study, redox-active molecules were covalently bonded to semiconducting (GaAs) surfaces; this structure can have the added flexibility and versatility of semiconductors in addition to the aforementioned benefits of the easily accessed redox-active molecular density of states. Also the molecule of interest, diruthenium (III) tetra-2-anilinoipyridinate-2-(Trimethylsilyl) ethyl-4'-(ethynyl) phenyl Sulfide ("Ru complex"), has net spin charge, thus opening the possibility for spintronics based applications. The Ru complex molecules were embedded in a matrix of shorter aromatic 2-(Trimethylsilyl) ethyl-4'-(ethynyl) phenyl sulfide ("OPE1") molecules. Unlike most investigations which use alkanethiols to passivate surfaces and surround the redox-active molecule of interest, the aromatic OPE1 molecules can also passivate the GaAs surface, forming SAMs with little defects and thus provide a suitable supporting under-layer for the Ru complex. The motivation for the use of the OPE1 includes the morphological similarity between the OPE1 molecule and the anchor end of the Ru complex. Molecular deposition included solution-based self assembly of the OPE1, followed by deposition of the Ru complex molecule using similar techniques. The OPE1 deposition was monitored over a 42 hour time period. The gradual growth, saturation and slight decline of the OPE1 SAM have been characterized using single wave ellipsometry (SWE) and x-ray photoemission spectroscopy (XPS), and an optimal time for molecular deposition, corresponding to the period of least surface oxidation and greatest molecular height, was subsequently obtained. Cyclic voltammetry (CV) data qualitatively describes the surface coverage of the OPE1 using bare GaAs and ODT as extremities in coverage. Lastly using FTIR, the evolution of the Ru complex insertion was monitored; it is shown that the number of Ru complex molecules can be easily manipulated to a certain saturation limit by varying the Ru complex deposition time.

10:00 AM Break

10:20 AM Student

X6, 1.55 Micron Light Emission from Microcavity Light-Emitting Devices with PbSe Colloidal Quantum Dots: *Fan Zhang*¹; *Lai Wei*¹; *Ting Zhu*¹; *Shuai Gao*¹; *Chunfeng Zhang*¹; *Jian Xu*¹; *Brian Downey*¹; *Suzanne Mohney*¹; ¹Pennsylvania State University

Semiconductor colloidal quantum dots (QDs) are nanoparticles that smaller in size than the diameter of a Bohr exciton in a bulk crystal of the same material. The development of low-cost solution-based synthesis of well-characterized QD samples has generated a new material set for the next-generation light-emitting devices. Particularly, PbSe QD-based light emitting devices (LEDs) which operate at wavelength of ~1.55 micron are greatly favored for a wide range of applications in telecommunication, high-speed circuits and systems due to their compact size, silicon substrate compatibility and high internal quantum efficiency (>80%) of PbSe QDs within the near infra-red (NIR) regime. However, a potential problem for cavity-free PbSe QD LEDs is that they often have broad emission bands (~140nm), while many abovementioned applications require LEDs operated at a much narrower full-width-at-half-maximum (FWHM) bandwidth. A possible solution is to modify the emission properties of PbSe QDs by embedding them inside microcavity structures. The confinement applied by the microcavity will alter the optical mode density within it, and spatially and spectrally redistribute the emission output, resulting in significant improvement in light output directionality and purification of colors. In this conference, we report the design, fabrication and characterization of the optical-pumped PbSe QD microcavity devices, in which the QDs were sandwiched between a TiO₂/SiO₂ Bragg interference mirror and a metallic mirror in order to modify the spectral and directional properties of their emission. The photoluminescence (PL) spectrum of a reference thin-film PbSe QD sample exhibits a maximum at the wavelength of 1.51 micron and a FWHM of 139nm. In contrast, a narrow band emission is observed for the microcavity device with a FWHM of 12nm, which is 11.6 times less than that of the reference sample. In addition, the peak

wavelength of the PL emission from the cavity-coupled QDs is red-detuned from the free-space luminescence maximum by 48nm. This detuning is in good agreement with the measured difference between the free-space luminescence maximum and the resonance wavelength of the microcavity, as revealed by a spectral hole in the reflectance spectrum of the microcavity for the normal incidence. The spontaneous emission from PbSe QDs in the microcavity device is also enhanced with respect to free-space luminescence, in directions normal to the cavity axis. The emission pattern of the cavity output was recorded where the relative intensity of the light at the peak emission wavelength is graphed as the function of the azimuthal angle, representing the directionality of light emission from the QDs in the cavity. The measured angular dependence can be fitted well to a Gaussian function with a FWHM of ~9° for the resonance wavelength.

10:40 AM

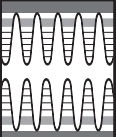
X7, Microfluidic Biochips for Label-Free Multi-Immunosensors Based on Carbon Nanotube Arrayed Microelectrodes: *Kenzo Maehashi*¹; *Yuichi Tsujita*¹; *Kazuhiko Matsumoto*¹; ¹Osaka University

We fabricated microfluidic and label-free multi-immunosensors by the integration of carbon nanotube (CNT)-arrayed electrodes and microchannels with pneumatic micropumps. Recently, micro total analysis system (micro-TAS) has attracted attention in many fields. It has great advantages of consuming only a very small amount of reagents for analysis and of markedly reducing analysis time. The development of microfluidic systems makes a large contribution toward fabrication of micro-TAS. Furthermore, micro-TAS requires small and highly sensitive biosensors. We have already fabricated label-free amperometric biosensors using carbon nanotubes (CNTs) and microfluidic CNT sensors. CNTs have the high ability to promote electron-transfer reactions in electrochemical measurements because of a very large specific surface of them. In this abstract, we fabricated microfluidic and label-free immunosensors based on CNT microelectrodes. In the chips, we controlled the flows of four reagents and electrochemically detected two kinds of cancer markers; prostate-specific antigen (PSA) and human chorionic gonadotropin (hCG). In the microfluidic systems, four kinds of sample solutions were transported from each liquid inlet into microchannels using six pneumatic micropumps. There are three channels on the chip, and each channel has four CNT, one platinum and one Ag/AgCl electrodes. One channel contains two inlets and two pneumatic micropumps made of poly(dimethylsiloxane) (PDMS). The pneumatic micropump consisted of three PDMS layers; an air layer, an intermediate membrane and a liquid layer. It can inject 7.8 nL of the liquid per one cycle. Using these pumps, four CNT electrodes in upper channel were modified with PSA antibodies on the chip. Simultaneously, CNT electrodes in middle channel were modified with hCG antibodies using another pumps. In the chip, 10 ng/mL PSA in 50 mM phosphate buffer solution (PBS) and 10 ng/mL hCG in PBS were introduced into CNT electrodes and were incubated. Then, they were detected by differential pulse voltammetry after the electrodes were washed by PBS. After introduction of 10 ng/mL PSA and 10 ng/mL hCG, the electrochemical signals increased, which indicates that antigen-antibody complexes were formed on CNT electrodes. Therefore, two kinds of proteins were simultaneously detected in the microfluidic chip. We fabricated the microfluidic and label-free immunosensors based on CNT microelectrodes. Using our chips, the flows of four reagents were controlled, and two kinds of cancer markers, PSA and hCG, were detected simultaneously. Microfluidic CNT biochips with pneumatic micropumps are one of the promising platforms for highly sensitive and multi-biosensors of various biomolecules.

11:00 AM Student

X8, Carbon-Derived Nanocrystalline Diamond Films - Tailoring the Electronic and Bio-Sensing Properties by Nitrogen Incorporation: *Supil Raina*¹; *Weng Kang*¹; *Jim Davidson*¹; ¹Vanderbilt University

Carbon-derived nanocrystalline diamond films are promising materials for field emission devices, microelectrodes, and NEMS applications due to the material properties such as chemically inert, mechanically hard, and bio compatible. We have reported on nanodiamond film for field emission devices¹ and chemical sensing.² In this work, we tailor the electronic and bio-sensing properties of nanodiamond films by in situ nitrogen incorporation. Various



levels of nitrogen-incorporated nanocrystalline diamond films were grown in a MPECVD machine using H₂/CH₄/N₂ gases, keeping the H₂/CH₄ ratio (9:1) constant and increasing the N₂ flow rate for 15sccm, 30sccm, 60sccm and 90sccm labeled as film S0, S1, S2, and S3. SEM study shows complete and conformal nanodiamond coverage for all films with surface morphology changes from a distinct 'ridge' like to a more 'cauliflower' like nano-structures as the N₂ flow rates increased. Raman spectra show characteristic peaks at 1332 cm⁻¹ attributed to sp³ carbon (diamond) and a shoulder at 1140cm⁻¹, common signature of nanocrystalline phase. The sp² carbon (graphite) peak appears at 1586cm⁻¹ but shifts towards lower wave numbers with higher N₂ flow rates. XPS C1s spectra indicated presence of carbon-nitrogen bonding in addition to the sp³ and sp² hybridized carbon-carbon bonds. The peaks fit at 284.6eV and 285.4eV, contributed by sp² C-C and sp³ C-C hybridized bonds. The sp³ peak intensity decreases (while the sp² increases) with increased N₂ flow rate. The peaks locate at 286.5eV and 287.5eV correspond to C-N and C₃N₄, respectively, and both of these peaks consistently increase in intensity with increased N₂ flow rate. Cyclic voltammograms were used for characterizing the electrochemical and bio-sensing properties. The background scan at 100mV/s in 0.1M PBS at physiologic pH 7.4 revealed a working potential window of ~3.0 V for all the films. However, films S0 and S1 show distinctly different and better sensitivity for detection of dopamine as compared to S2 and S3. Films S0 and S1 showed very well defined redox peaks detectable due to dopamine/o-quinone redox reactions. Films S2 and S3 were also able to detect presence of dopamine but with poor peak definition and wide peak-peak separation, exhibiting sluggish reaction kinetics and the peak definition was completely lost at 1mM DA and at scan rates greater than 50mV/s. The findings demonstrate that a controlled amount of nitrogen incorporation in nanodiamond film (S0 and S1) is vital to maintain superior bio-sensing behavior, however, higher N₂ inclusion (S2 and S3) degrades the sensing response due to change in surface morphology and increase in CN and C₃N₄ bonds. ¹K. Subramanian, W. P. Kang, and J. L. Davidson, IEEE Electron Device Letters, 29 (2008) 1259-1261. ²S. Raina, W. P. Kang, J. L. Davidson, Diam. and Rel. Mat., 17 (2008) 896-899.

11:20 AM X9, Late News

11:40 AM X10, Late News

Session Y: Graphene I

Thursday AM
June 25, 2009

Room: 206
Location: Pennsylvania State University

Session Chairs: Randall Feenstra, Carnegie Mellon University; Rajinder Sandhu, Northrop Grumman Space Technology

8:20 AM Invited

Y1, Graphene Synthesis on C-Face and Si-Face 4H-SiC: *Michael Capano*¹; M. L. Bolen¹; B. Biedermann²; G. Prakash²; R. G. Reifenberger²; Y.Q Wu¹; P. D. Ye¹; ¹Purdue University, School of Electrical and Computer Engineering and Birck Nanotechnology Center; ²Purdue University, Birck Nanotechnology Center and Department of Physics

The emergence of graphene as a serious candidate material for high-frequency and digital electronic applications has stimulated intense research on this material. Three major technical hurdles must be surmounted before graphene devices can become commercially viable. These include synthesis of low-defect, uniformly-thick graphene on a suitable substrate, the ability to induce a finite bandgap, and fabrication of dielectric layers compatible with graphene device technology. All are daunting obstacles, but steady progress continues to be realized in all three areas. This presentation will examine the synthesis of graphene by sublimation of silicon carbide (SiC) in a chemical vapor deposition (CVD) environment. The presentation will begin with a brief overview of sublimation in a ultra-high vacuum (UHV) environment, followed by an explanation of how a CVD environment can be applied to form graphene.

Characteristics of graphene on the C-face and Si-face of 4H-SiC will then be presented. On the C-face, continuous layers are achieved at temperatures around 1475-1500°C, depending on hold time. Below this temperature, scanning probe microscopy (SPM) provides evidence that sublimation is initiated from step edges and from defect sites on 4H-SiC terraces. Above 1475°C, numerous artifacts appear in continuous graphene layers, including wrinkles and ridges. The formation of wrinkles and ridges is shown to result from a difference in the coefficients of thermal expansion for SiC and graphene. Wrinkles exist in thin graphene layers formed at temperatures close to 1500°C. At higher temperatures, wrinkles are not present, presumably due to the increased mechanical stiffness of thicker graphene layers. On the Si-face, self-limited graphene layers are observed to have a finger structure, with continuous layers forming at about 1500°C. Graphene fingers are seen to initially form along high-symmetry crystallographic planes in SiC. Comparisons between graphene formed on Si-face SiC and step-free SiC mesas reveal very similar graphene morphology, indicating that surface steps are not essential for Si sublimation for the SiC surface. Additional topics to be presented are the procedures for achieving graphene on step-free SiC surfaces, preliminary graphene synthesis experiments on silicon substrates, and device characteristics that have exhibited electron mobilities exceeding 5000 cm²/Vs in graphene on SiC.

9:00 AM Student

Y2, Uniformity of Epitaxial Graphene Films on Si-Face SiC(0001): *Luxmi Luxmi*¹; Nishtha Srivastava¹; Patrick Fisher¹; Randall Feenstra¹; Jakub Kedzierski²; Yugang Sun³; ¹Carnegie Mellon University; ²Massachusetts Institute of Technology (MIT), Lincoln Laboratory; ³Center for Nanoscale Materials, Argonne National Laboratory

Epitaxial graphene is grown on a SiC substrate by silicon sublimation in a high vacuum chamber. The substrate is first hydrogen etched at 1600°C and then graphitized in situ using a graphite strip heater arrangement.¹ Development of graphene films with overall flat morphology is observed by atomic force microscopy (AFM), low-energy electron diffraction and Raman spectroscopy, and the films are found to have field-effect mobilities exceeding 4000 cm²/Vs at room temperature. The graphene thickness is measured using both Auger electron spectroscopy and low energy electron microscopy (LEEM). A number of morphological features are found to interrupt the flat, uniform morphology of the graphene, including: surface pits, step bunches, and an apparent "secondary" graphitic surface phase. The pits have been previously studied and are believed to arise from the formation of the 6√3 "buffer layer" at the graphene/SiC interface.² The step bunches on the surface originate from steps arising from unintentional miscut of the surface, which at sufficiently high temperature are found to form bunches. Using LEEM, the thickness of the graphene is measured locally across the surface, and it is found that the presence of the step bunches lead to thicker graphene films in their vicinity. Finally, the apparent secondary phase of graphene is observed as locally rough regions in the surface morphology. At low graphene formation temperature these regions can extend substantially over the entire surface, but at higher formation temperatures the regions shrink in size, until they produce only a faint finger-like pattern in the morphology as seen by AFM. Below the secondary phase, well-ordered graphene is still observed to be present, as imaged by LEEM. We tentatively interpret the secondary phase as arising from excess carbon present on top of the surface (as opposed to at the graphene/SiC interface, where it would form well-ordered graphene). The work at CMU was supported by NSF, at MIT by DARPA, and at ANL by DOE. Opinions are those of the authors and are not necessarily endorsed by the funding sources. ¹Luxmi et al., J. Electron. Mater. (2009), <http://dx.doi.org/10.1007/s11664-008-0584-3>. ²J. B. Hannon et al., Phys. Rev. B 77, 241404 (2008).

9:20 AM

Y3, Effects of SiC Surface Orientation and Temperature on the Quality of Epitaxial Graphene: *Virgil Shields*¹; M.V.S. Chandrashekar¹; Shiram Shivaraman¹; Michael Spencer¹; ¹Cornell University

An investigation of the epitaxial growth by thermal decomposition of graphene on on-axis SiC substrates has been conducted. Graphene was grown on both the carbon (C) and silicon (Si) faces in a face-up and face-down orientation with relation to the heater filament in a graphite covered, oven-like

configuration in a cold wall reactor. Surface characteristics were examined by Raman spectroscopy and AFM over a range of temperatures from 1300 to 1450°C after 60 minutes of exposure in a less than 10^{-5} torr vacuum. Raman results indicate disorder characteristics, represented by I_D/I_G , down to <0.02 over a 1 cm^2 wafer surface at the higher temperatures. Growth results on both faces indicate decreasing stress and I_D/I_G with temperature for all orientations. The I_D/I_G ratios in all orientations tend toward values <0.02 at 1450°C. The corresponding surface stress in the epitaxial layers, as indicated by the G-peak positions for the face-up and face-down orientations, differ for the C and Si faces as a function of temperature. The Si face-down orientation displays less red-shifting in G-peak position with increasing temperature than both face-up orientations and the C face-down orientation. This observation indicates greater surface stress for the Si face-down orientation and at the same time a very low degree of disorder as measured by the I_D/I_G values. In contrast, both C face orientations tend towards similar levels of stress relief at higher temperatures. The C face-up orientation also displays more stress relief at lower temperatures than any other configuration. AFM examination of the face-down orientations indicated a much different morphology than the face-up orientations. A significant difference in morphology was also noted between the Si and C faces in the downward and upward direction. The SiC steps were observed to be more apparent through the graphene layer on the Si face than on the C face in the downward orientation throughout the temperature regime examined. The face-up orientations, in contrast, displayed pit-like features on the Si face and large domain-like features on the C face. Surface morphologies on the face-up surfaces obscured any steps in the SiC surface throughout the temperature regime examined, even though the I_D/I_G values decreased to very low values. This observation implied the presence of a thicker, although well-ordered, graphene-like layer on the face-up surfaces. The results of this study suggest, that although increased stress relief with temperature occurs in the epitaxial graphene layer for all orientations of the surface, the Si face-down orientation (in opposition to the temperature gradient) can result in a better combination of low disorder ratio, I_D/I_G , and smooth surface morphology. In addition, results indicate that a very low I_D/I_G can be achieved on either SiC face in any of the orientations examined at higher temperatures.

9:40 AM

Y4, Few-Layer Graphene Formation Mechanisms on 4H-SiC(0001): Michael Bolen¹; Sara Harrison¹; Michael Capano¹; ¹Purdue University

Research on graphene has exploded in the past few years given the profound possibilities it possesses to revolutionize the semiconductor industry. There are many techniques being explored to create a reproducible and uniform graphene layer for electronic devices, one of which is through the sublimation of silicon carbide. The creation of graphite through this method has been known for over 30 years, but the formation mechanisms at the microscopic level have not been thoroughly explored. In this study, growth temperature and growth time are independently varied to determine their effects on graphene formation on 4H-SiC(0001). The graphene is created under high-vacuum conditions using a CVD system. Ex-situ atomic force microscopy (AFM) and scanning tunneling microscopy (STM) are used to probe the graphitized Si-face surface. Height and phase data gathered from AFM depict how graphene spreads over the nominally on-axis 4H-SiC(0001) surface. Data from STM is used to confirm the presence of graphene and corroborate the AFM data. In the first set of experiments, the growth hold time is fixed at 10 minutes while the growth temperature is varied between 1400°C and 1600°C. The second set of experiments keeps the growth temperature constant at 1475°C and varies the growth hold time between 0 and 60 minutes. All growth runs are performed on virgin 4H-SiC(0001) pieces that have been cut from a single, larger wafer. No substrate piece is reused for a growth. It is found that both time and temperature can be used to control the spread of graphene across the 4H-SiC(0001) surface. Both experiment sets exhibit the same graphene formation mechanism. An unequal erosion rate of SiC terraces leads to macroscopic step bunching of unit cell height multiples along the $\{11\bar{2}0\}$ planes. Eroding step edges leave behind finger structures that initially form perpendicular to the erosion direction. Additionally, pit formation is seen on the terrace faces. Hexagonal and triangular pits form along well-defined crystallographic planes and provide

further insight into graphene formation mechanisms. With increasing time, or temperature, the finger structures disappear leaving behind a continuous film of few-layer graphene.

10:00 AM Break

10:20 AM Invited

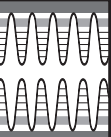
Y5, Epitaxial Graphenes on Silicon Carbide: Phillip First¹; ¹Georgia Institute of Technology

The structure and properties of epitaxial graphene on SiC(0001) and SiC(000-1) surfaces is reviewed, with an emphasis on results obtained via scanning tunneling microscopy (STM) and spectroscopy (STS). We use these techniques to gain an atom-resolved view of the influence of defects (natural and artificially-induced) on transport properties. While scattering from point defects generally degrades the mobility of the material, the electron standing-wave patterns from such scattering can be exploited to measure the momentum-resolved electronic band structure. The overall structure of graphene grown on SiC(0001) (the Si-terminated face) and SiC(000-1) (the C-terminated face) is very different, and sensitive to growth conditions. Multilayer graphene grown on SiC(000-1) in an induction furnace has a novel layer stacking where rotational stacking faults occur throughout the multilayer. Cryogenic (4.3K) tunneling spectroscopy of the magneto-electronic structure of the top graphene layer in C-face multilayer epitaxial graphene shows oscillations in the tunnel differential conductance as a function of magnetic field. Analogous to Shubnikov – de Haas oscillations (SdHO) in magneto-resistance, These “tunneling magneto-conductance oscillations” (TMCO) provide a sensitive measure of the k-space area of a constant energy contour where the energy is determined by the tunnel bias (both filled and empty states can be accessed). The high-resolution band structure $E(k)$ determined from these measurements is perfectly described by a linear Dirac-fermion dispersion with a characteristic velocity of $1.07 \times 10^6 \text{ m/s}$. The energy resolution of the TMCO method is comparable to photoemission experiments at cryogenic temperatures, but the momentum resolution is several times better. Unlike SdHO, which are restricted to the Fermi energy, TMCO requires no electrostatic gate to determine $E(k)$, which makes the technique potentially applicable to a wide range of materials. The stacking faults found throughout multilayer epitaxial graphene have the effect of decoupling the electronic properties of the layers. We show by direct spectroscopy (tunnel differential conductance versus sample bias) that the Landau levels (quantized cyclotron orbits in a magnetic field) are exactly those predicted for ideal graphene. These surprising results, and related data from IR transmission, indicate that multilayer epitaxial graphene well-approximates a stack of decoupled graphene sheets. Consequently, it is an interesting candidate for applications in electronics and electromagnetics. Supported by NSF, NRI-INDEX, and the W. M. Keck Foundation. Work performed in collaboration with G. M. Rutter, J. Hass, D. L. Miller, K. D. Kubista, N. Sharma, D. B. Torrance, M. Ruan, N. Guisinger, W. A. de Heer, E. H. Conrad, J. N. Crain, and J. A. Stroscio.

11:00 AM Student

Y6, Three-Dimensional Island Morphology of Graphene on C-Face SiC(000-1): Nishtha Srivastava¹; Luxmi Luxmi¹; Patrick Fisher¹; Randall Feenstra¹; Jakub Kedzierski²; Yugang Sun³; ¹Carnegie Mellon University; ²Massachusetts Institute of Technology (MIT), Lincoln Laboratory; ³Center for Nanoscale Materials, Argonne National Laboratory

Graphene formation on SiC(000-1) surface (the so-called C-face of the crystal) by annealing in vacuum is reported. The substrates are first H-etched at 1500°C for removing the polishing damage, and then are annealed in vacuum, with base pressure of 10^{-8} Torr, at temperatures ranging from 1100°C to 1400°C for 20 min. Both the H-etching and the graphitization are carried out in the same chamber that employs a graphite strip for heating the substrates.¹ The resulting films are characterized using atomic force microscopy, spatially resolved Auger electron spectroscopy, low energy electron diffraction, Raman spectroscopy, and electrical measurements. Morphology of these films is compared with the graphene films grown on the SiC(0001) surface (the Si-face). It is found that graphene forms as 3-dimensional islands on the C-face, whereas it forms in a 2-dimensional manner on the Si-face. We believe that this difference occurs because of differing interface structures between the graphene and the SiC in the



two cases. Importantly, the graphene is found to be *thinner* in the areas on top of the islands, consistent with a model in which sublimating Si atoms originate from the interface (and hence thicker graphene implies more material loss). At higher temperatures, thicker films are formed, and the morphology appears relatively flat, although strain-induced ripples are observed. Electron diffraction indicates rotational disorder in the graphene, with $\pm 15^\circ$ -oriented spots observed in addition to the known $\pm 2.2^\circ$ -spots.² These graphene films on the C-face are of high quality, with field-effect mobilities exceeding 4000 cm²/Vs at room temperature. The effect of unintentional carbon surface contamination on the quality of the graphene film morphology is also discussed. The work at CMU was supported by NSF, at MIT by DARPA, and at ANL by DOE. Opinions are those of the authors and are not necessarily endorsed by the funding sources. ¹Luxmi et al., *J. Electron. Mater.* (2009), <http://dx.doi.org/10.1007/s11664-008-0584-3>. ²J. Hass et al., *Phys. Rev. Lett.* 100, 125504 (2008).

11:20 AM Student

Y7, AFM Studies of Wrinkles and Ridges on Graphene Grown on the Carbon Face of 4H-SiC (000-1): *Gyan Prakash*¹; Michael Bolen¹; Michael Capano¹; Dmitri Zemlyanov¹; Ronald Reifengerger¹; ¹Purdue University

After heating 4H-SiC (000-1) substrates to temperatures 1475°C < T < 1600°C under vacuum conditions, AFM and XPS studies were performed to characterize the growth of few-layer graphene (FLG) material. The XPS data are used to infer the thickness of the FLG that coats the carbon face of the SiC substrate. The AFM images show that for all temperatures studied, the FLG exhibits a dense mesh of ridges, producing a network of smooth planes bounded by well-defined ridge-like surface features. The smooth planes are often wrinkled, bearing a resemblance to the surface of crumpled paper. From the AFM images, the ridge-like network contributes an additional surface area that can be estimated from the dimensions of the ridges. We find that the additional surface area is comparable with the calculated change in area due to the difference in thermal contraction between a SiC substrate and the FLG overlayer. We conclude that the origin of the ridge-like network is the 2D compressive stress generated by cooling. To better understand the structural stability of the ridges and wrinkles, a series of experiments have been performed to systematically push against them using the AFM probe-tip. The ridges can be moved laterally by a few hundred nanometers and leave behind a debris field that marks their original position. On the other hand, wrinkles move from one location to another, often leaving no discernible signature behind. These observations lead us to believe that the wrinkles are due to buckling of only the top graphene layers, whereas ridges are made from buckled graphene that span many atomic layers. We have also performed studies of the aging of FLG grown at 1525°C. When the FLG surface is studied within a few weeks after growth, the surface is found to be smooth apart from the well-defined ridge-like surface features. When the same sample was scanned ~7 months later, rough patches were observed to decorate the entire surface. Many of these patches were clustered around the ridge-like surface features, suggesting that the ridges may contribute to the roughening of the FLG surface over time.

11:40 AM Student

Y8, STM and XPS Studies of Moiré Superlattices and Ridges on Few-Layer Graphene Grown on 4H-SiC(000-1): *Laura Biedermann*¹; Michael Bolen¹; Michael Capano¹; Dmitri Zemlyanov¹; Ronald Reifengerger¹; ¹Purdue University

Few-layer epitaxial graphene (FLG) was grown on the C-face of silicon carbide (4H-SiC) by heating SiC samples to high temperatures (1450 – 1600°C) in vacuum, as described in Ref. [1]. Surface Si atoms sublime from SiC at high temperature, leaving a carbon-rich surface that reconstructs to form graphene sheets. While many regions of pristine FLG were observed, the nature of the FLG growth can cause two key defects in the C-face samples: graphene ridges and Moiré superlattices. Scanning tunneling microscopy (STM) and x-ray photoemission spectroscopy (XPS) were used to characterize the FLG. To confirm the presence of graphene and to estimate the thickness of the graphene layers, systematic angle-resolved XPS studies were performed. XPS spectra of the FLG showed peaks attributed to the sp² hybridized C-C bonds as well as a shake-up satellite peak, which is a hallmark of aromatic and graphitic systems. From these XPS studies, we estimate the average FLG thickness to be 1.8 ±

0.1 nm for FLG grown at 1475°C and 2.4 ± 0.2 nm for FLG grown at 1500°C. Furthermore, at temperatures below 1475°C, continuous FLG did not form.¹ Since SiC has a larger coefficient of thermal expansion than graphite, when the FLG sample cools from the growth temperature, the contraction of the SiC substrate causes graphene ridges to form. The height of these ridges increases with the graphene layer thickness. STM scans of the ridge morphology are used to confirm the XPS thickness estimate. Moiré superlattices are found near ~20% of ridges. These Moiré regions are never found in the middle of pristine (Bernal stacked) graphene, indicating their origin is closely associated with ridge formation. The compressive stress developed during ridge upheaval causes a rotation in the top layer(s) of the FLG, resulting in the Moiré patterns.¹ The Moiré superlattice is not topographic in origin; the superlattice only appears in STM scans because the rotation of the graphene layers produces a modulation in the density of electron states (DOS). Campanera et al. calculate a factor of two modulation in the DOS across a Moiré superlattice.² STM measurements of I(V) across the superlattice are consistent with this factor of two. The presence of superlattices has important consequences on electronic device development since the additional periodicity in the Moiré region will support narrow minibands in the electronic band structure. ¹L. B. Biedermann, M. L. Bolen, M. A. Capano, D. Zemlyanov, and R. G. Reifengerger, *Phys. Rev. B* (in press). ²J. M. Campanera, G. Savini, I. Suarez-Martinez, and M. I. Heggie, *Phys. Rev. B* 75, 235449 (2007).

Session Z:

III-Nitride: MBE Growth and Intersubband Structures

Thursday AM
June 25, 2009

Room: 207
Location: Pennsylvania State University

Session Chair: Thomas Myers, Texas State University

8:20 AM

Z1, Near-Infrared Intersubband Absorption in MBE-Grown Lattice-Matched InAlN/GaN Superlattices: *Oana Malis*¹; C. Edmunds²; M. Manfra³; D. Sivco³; R. Molnar⁴; ¹Purdue University; ²Binghamton University; ³Alcatel-Lucent; ⁴Massachusetts Institute of Technology (MIT), Lincoln Laboratory

Extensive research in recent years on intersubband transitions in semiconductor heterostructures has resulted in numerous fundamental discoveries and technological device applications. Nitride materials are promising for intersubband light modulation, emission, and detection in the currently inaccessible 1.5-3 μm and 15-70 μm infrared ranges. The conduction band offset between GaN and Al-containing alloys can exceed 1 eV, therefore allowing intersubband energy spacing in the near-infrared range. Intersubband absorption and luminescence around 1.5 μm from GaN/AlGaIn heterostructures has already been reported. However, research efforts have, so far, been hampered by difficulties related to the quality of the materials. The material issues are due in part to the lack of native nitride substrates. Heteroepitaxy of GaN on sapphire typically results in high dislocation density that makes vertical charge transport difficult. Moreover, most of the studies reported in the literature employ high Al-composition AlGaIn alloys. The lattice mismatch between GaN and AlGaIn limits the total thickness of the structures that can be grown before the material relaxes by introducing dislocations and cracks. To eliminate the difficulties involved in growing strain-compensated materials and theoretically calculating their band structure, it is preferable to develop a process for the growth of lattice-matched nitrides. Moreover, the large conduction band offset and lack of piezoelectric effect of the lattice-matched nitrides make them ideally suited for near-infrared optoelectronic applications. In this work we focus on lattice-matched InAlN/GaN heterostructures. The lattice-matched nitride materials have been less investigated due to the challenges in growing high-quality In-containing nitrides. Photo-induced intersubband absorption in InAlN/GaN superlattices grown by metal-organic vapor phase epitaxy has been reported but no detail study of the absorption peak position and width on quantum well width has been performed. We have performed a detail investigation of

intersubband absorption in lattice-matched InAlN/GaN superlattices grown at low temperatures by MBE on thick GaN templates grown by HVPE. X-ray diffraction analysis of the samples indicates that the quality of the material is similar to the best reported In-free nitride heterostructures. Strong intersubband absorption features were observed at room temperature in the technologically important near-infrared range (2.3-2.9 μm). The low limit of the range represents the shortest wavelength ever reported for the lattice-matched nitride heterostructures. The experimental results are in agreement with calculations of the transition energies using a conduction band offset of 1 eV and a spontaneous polarization of 3 MV/cm. Our results prove the potential of the lattice-matched nitrides for quantum devices based on intersubband transitions and pave the way towards light emitters and detectors for spectroscopic applications based on AlInN/GaN system.

8:40 AM

Z2, GaN/AlN-Based Nanostructures for Intersubband Devices: Prem Kandaswamy¹; Lise Lahourcade¹; Alexander Wirthmüller¹; Catherine Bougerol¹; Eva Monroy¹; Houssaine Machhadani²; S. Sakr²; Maria Tchernycheva²; François Julien²; Alon Vardi³; Gad Bahir³; ¹CEA-Grenoble; ²Université Paris-Sud; ³Technion

The extension of intersubband (ISB) optoelectronics towards the near infrared spectral region is interesting for the development of ultrafast photonic devices for optical telecommunication networks, as well as for application in a variety of chemical and biological sensors. Thanks to their large conduction band offset (~1.8 eV for the GaN/AlN system) and subpicosecond ISB scattering rates, III-nitride heterostructures are excellent candidates for high-speed unipolar devices relying on the quantum confinement of electrons. A specific advantage of III-nitrides is their extremely short ISB absorption recovery times (~200 fs) due to the strong Fröhlich interaction in these materials, which opens the way for devices operating in the 0.1-1 Tbit/s bit-rate regime. Furthermore, the remote lateral valleys lie very high in energy (>2 eV above the gamma valley), which is a key feature to achieve ISB lasing. In this talk, we will present the latest achievements in terms of molecular-beam epitaxial growth and characterization of ultra-thin single GaN/AlN QW superlattices for the fabrication of unipolar devices. We will discuss the effect of various growth and design parameters on the device performance. Particularly, we address the influence of surfactants, growth temperature and growth interruptions, and the effect of the substrate and the strain distribution in the active region. Best interface results were achieved at a relatively low substrate temperature, using a Ga excess as a surfactant during the growth of AlN barriers. Under these conditions, the samples present a flat surface morphology with sharp interfaces at the atomic layer scale. However, a commonly observed feature is the presence of monolayer thickness fluctuations that results in multi-peak absorption and emission spectra. We will analyze how these fluctuations relate to dislocations and structural defects. The influence of the buffer and cap layers on the electronic profile and ISB absorption properties will be also analyzed. Additionally, in order to better understand the influence of the electric field on the ISB properties, we will present a comparison of standard (0001)-oriented GaN/AlN QW structures with semipolar (11-22)-oriented samples. The reduction of the internal electric field in semipolar QWs results in a red shift of the ISB absorption line in comparison with similar (0001)-oriented QWs. Finally, as an application example, we will examine the performance of the first prototypes of nitride-based quantum cascade detectors.

9:00 AM Student

Z3, Growth and Characterization of N-Polar InGaN and InGaN/GaN MQWs by Plasma Assisted Molecular Beam Epitaxy: Sansaptak Dasgupta¹; Nikholas Toledo¹; Hisashi Masui²; James Speck²; Steve Denbaars²; Umesh Mishra¹; ¹ECE Department, University of California, Santa Barbara; ²Materials Department, University of California, Santa Barbara

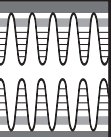
In the past the majority of Group III nitride devices have been fabricated using (Al,Ga,In) nitride epitaxial layers grown in the +c direction. Recently N-polar nitrides (growth direction 000-1) have been epitaxially grown by both MBE and MOCVD, and allows new areas of device design due to the presence of piezoelectric fields in the opposite direction. In this paper we report on growth studies of high In composition N-polar InGaN films and InGaN/GaN MQWs by plasma MBE and to the best of our knowledge this is the first report

on characterization and growth details of high composition N-polar InGaN films grown by PAMBE. The N-polar InGaN films were grown on N-polar free standing GaN substrates from Lumilog. 100 – 150 nm thick InGaN films were grown at constant Ga flux and varying growth temperatures to obtain InGaN films of different composition, grown in a group III rich regime. The as-grown films were characterized in-situ by RHEED, and ex-situ by atomic force microscopy (AFM), X-ray diffraction (HRXRD) and PL-measurements. Reciprocal Space maps of the reflection were studied to ascertain the strain state of the as-grown InGaN films. InGaN/GaN MQWs were studied by growing 5 periods of 7.5 nm Si-doped GaN as the barrier layer and 2.5 nm of $\text{In}_x\text{Ga}_{1-x}\text{N}$ as the well. In the end, p-i-n diodes, were epitaxially grown and exhibited good diode characteristics. HRXRD ω -2 θ scans were done to determine the In-incorporation in the films. With lower temperatures, greater incorporation of In is obtained, however as noticed for the film ($\text{In}_{0.38}\text{Ga}_{0.62}\text{N}$) grown at 520°C we start observing faint signs of phase segregation, as evident by a broadened peak in the XRD scan. The suppression of phase segregation in InGaN films with high In composition (>35%) is being investigated by modified growth techniques. Room temperature PL measurements on the 100 nm InGaN films of varying composition showed enhanced room temperature optical PL corresponding to the band gap emission of the InGaN films. AFM scans of the as-grown InGaN films showed smooth surfaces and atomic steps are observed for films with In composition < 20%. The RMS roughness of the films with In composition of 9%, 19%, 27% are roughly 0.6 nm, 1.3nm and 2.1 nm respectively. InGaN/GaN MQWs were studied by HRXRD and PL measurements. p-i-n diodes consisting of p-doped GaN, UID $\text{In}_{0.12}\text{Ga}_{0.88}\text{N}$, and n-doped GaN were epitaxially grown. These p-i-n diodes exhibited good diode characteristics and a turn-on voltage of around 2.1 V. To summarize, high quality N-polar InGaN films with high In composition and InGaN/GaN MQWs have been grown by PAMBE and characterized. This is a first step to the realization of N-polar optical devices and solar cells.

9:20 AM

Z4, Change in Stress Evolution of MBE GaN across Growth Mode Regimes: Jeremy Acord¹; David Rearick¹; Xiaojun Weng¹; Joshua Robinson¹; Mark Fanton¹; Joan Redwing¹; David Snyder¹; ¹Pennsylvania State University

High electron mobility transistor (HEMT) structures grown by Molecular Beam Epitaxy (MBE) have been extensively researched due to their high power performance and desired use in device and sensor applications. Growth of these devices with a low resultant stress at room temperature in the GaN buffer layer offers increased performance and reliability by optimizing the strain induced piezoelectric polarization in the AlGaIn channel layer while minimizing film cracking. By developing growth processes aimed at controlling the stress in the GaN buffer layer, the stress in the AlGaIn barrier layer can be optimized to promote better performance. The change in growth mode as a function of temperature and Ga to N flux ratio has been previously documented. While the GaN MBE growth mode evolution is known, the effect of growth mode on film stress in these layers is not. This study employed *in-situ* optical substrate curvature and growth rate measurements to investigate the effect of varying the Ga / N flux ratio and substrate temperature on growth stress evolution during deposition of GaN by radio frequency (RF)-plasma assisted MBE. Commercial high-purity semi-insulating 4H-SiC substrates were degreased in solvents, and then etched in a 25% HF/de-ionized water solution to remove any native oxide present on the SiC surface. AlN nucleation layers were grown at 850°C, followed by a GaN buffer layer grown at temperature ranging from 650°C - 700°C. At 650°C with constant Ga-flux (3.0 E-7 Torr, beam equivalent pressure), increasing nitrogen flow through the RF-plasma source from 0.6 sccm (Ga-rich, sample A) to 2.1 sccm (N-rich, sample B) corresponded to a change in the steady-state incremental growth stress from 0.81 GPa compressive to 1.79 GPa tensile. The surface roughness (Ra) of sample A was 0.62 nm, while sample B was 14 nm, indicating a change from the 2D to 3D growth mode, accompanied by an increase in the (0002) rocking curve width from 440'' to 1630''. At an increased stage temperature of 700°C (constant N-flux), decreasing the Ga flux from 7.0 E-7 Torr to 3.5 E-7 Torr (beam equivalent pressure) again changed the growth mode from 2D to 3D, while the steady-state compressive incremental growth stress decreased from 0.85 GPa to 0.13 GPa. The surface roughness increased



from 0.72 nm to 19 nm, while notably the rocking curve width decreased from 380" to 220". This study demonstrates that GaN buffer layers can be grown at controlled stress values while maintaining desired crystal quality and surface morphology. The stress evolution will be discussed in terms of dislocation and film microstructural evolution.

9:40 AM Student

Z5, Low Dislocation-Mediated Reverse Bias Leakage in (0001) GaN via Novel High-Temperature MBE Growth: *Jeremy Law*¹; Gregor Koblmüller²; Feng Wu²; James Speck²; Edward Yu¹; ¹University of California, San Diego; ²University of California, Santa Barbara

Group III-nitride semiconductor materials and devices are eminent candidates for a broad range of electronic and optoelectronic device applications. Recently, progress has been made in molecular-beam epitaxy (MBE) growth of (0001) GaN under N-rich conditions at temperatures above the thermal decomposition regime (>750 °C). These conditions yielded 2D layer-by-layer growth, low surface roughness (< 1 nm RMS roughness), and high electron mobilities (in excess of 1100 cm²/V s for light doping at 300 K) [1]. The local electronic properties of GaN grown under these conditions are yet unexplored. MBE was used to grow Si-doped (low-to-mid 10¹⁶ cm⁻³) GaN on commercially available Lumilog GaN substrates with dislocation densities of approximately 5×10⁸ cm⁻². All samples were grown around 780 °C at constant nitrogen flux of 5.0 nm/min with gallium fluxes ranging from 3.8 to 14 nm/min. None of the samples showed spiral hillocks as typical in low-temperature grown MBE-GaN layers [2]; however, all showed smooth morphology with shallow surface pits. We performed conductive atomic force microscopy (CAFM) where a conductive diamond-coated tip acts as a Schottky contact. A positive bias was applied to an Ohmic contact establishing a reverse bias while the current through the tip was measured with a current amplifier and simultaneously recorded with the topography. Analysis of the CAFM images suggests that there is a narrow band of fluxes near Ga/N>1 where pure screw threading dislocations (already present in the underlying templates and extending into the GaN MBE material) are not conducting. Samples with fluxes of 14 nm/min show poor surface morphology with surface roughness ~ 3 nm RMS, but reduced densities of leakage paths. Samples with Ga fluxes of 7, 6.5, and 5.5 showed excellent morphologies with roughness less than 1 nm RMS and no reverse bias leakage at the highest level of sensitivity of our measurement technique. N-rich samples also showed excellent surface morphologies with roughness approximately 1.5 nm RMS, but increased reverse bias leakage. As the Ga-flux was further decreased under N-rich conditions, the density of reverse bias leakage paths increased. This result is in contrast to prior results at lower growth temperatures that suggested that Ga-rich growth yields higher mobility due to good surface morphology but high reverse bias leakage due to conductive dislocation paths, and that N-rich growth yields lower carrier mobility pursuant to poor surface morphology but low reverse bias leakage [3]. These observations could have substantial implications for the design and expected performance of III-nitride based semiconductor devices. [1] G. Koblmüller, et al., *Appl. Phys. Lett.* 91, 221905 (2007). [2] B. Heying, et al., *J. Appl. Phys.* 85, 6470 (1999). [3] J. W. P. Hsu et al., *Appl. Phys. Lett.* 78, 3980 (2001).

10:00 AM Break

Session AA: III-Nitride: MBE Growth

Thursday AM
June 25, 2009

Room: 207
Location: Pennsylvania State University

Session Chair: Thomas Myers, Texas State University

10:20 AM Student

AA1, Enhancement of Breakdown Voltage Using Selective-Area Growth by Plasma-Assisted Molecular Beam Epitaxy: *Liang Pang*¹; Hui-Chan Seo¹; Patrick Chapman¹; Kyekyoon Kim¹; ¹University of Illinois at Urbana-Champaign

GaN-based materials have been extensively studied for optoelectronic and electronic devices. To realize high-performing devices, low-resistance ohmic contacts and high breakdown voltage are critical. Ion implantation is generally used to achieve low contact resistance. However, high energy radiation is required for high doping, resulting in radiation damage at the surface and in the doped region. These damages can cause severe current leakage. Selective area growth (SAG) is an alternative approach that can avoid ionic and surface damage. We previously reported on the metal-semiconductor field-effect transistors (MESFETs) fabricated by SAG using plasma-assisted molecular beam epitaxy (PAMBE). The SAG technique enabled selective growth of a heavily doped n⁺-GaN layer (1.0E19 cm⁻³) only at the source and drain regions, giving rise to an extremely low contact resistivity (1.8E-8 Ω-cm²), as well as much higher peak current than those without SAG. SAG could also produce a much higher breakdown voltage. Breakdown voltage is heavily dependent on the surface conditions, especially at the drain area, because electrons are trapped from the gate to the surface states and the electric field is concentrated at the drain edge. Compared to ion implantation, SAG effectively avoids the surface damage, leading to substantial breakdown voltage enhancement. In this study, we extend the same SAG technique to high electron mobility transistors (HEMTs) and examine the advantages of SAG over ion implantation. Samples used in this study consisted of four Al_{0.3}Ga_{0.7}N(30nm)/GaN(2μm) templates. Two of the templates were grown by MOCVD on silicon substrate, a substrate that is rarely studied. The other two are on the commonly used sapphire substrate. For each substrate, one sample went through silicon implantation under the condition of 80keV energy and 5E12/cm² dose. The other one was treated via SAG by growing a 60-nm-thick n⁺-GaN layer using PAMBE and subsequently removing poly-GaN and SiO₂ mask by a molten KOH solution. Alloyed ohmic metals of Ti/Al/Ti/Au were deposited on n⁺-GaN for the Ohmic contact, and Ni/Au metals for the Schottky gate. The gate length, width, source-to-drain and source-to-gate distances were 2μm, 100μm, 6μm, and 4μm, respectively. Contact resistance measurements by transmission line method (TLM) showed that SAG provides 2-4 times smaller contact resistivity than implantation, as well as higher peak current. The breakdown voltage measurement will be conducted, with much higher breakdown voltages expected for samples via SAG. The impact of different substrates on the performance of HEMTs will also be described.

10:40 AM Student

AA2, Effect of AlN Nucleation on the Heteroepitaxial Growth of N-Face GaN on C-Face SiC by Plasma-Assisted MBE for High Electron Mobility Transistors: *Man Hoi Wong*¹; Yi Pei¹; James Speck¹; Umesh Mishra¹; ¹University of California Santa Barbara

N-face GaN enables new high electron mobility transistor (HEMT) designs with low contact resistance and strong back-barrier. Their growths require foreign substrates such as C-face SiC due to the absence of semi-insulating native N-face GaN substrates. Therefore, nucleation layers (NLs) are needed to improve the GaN crystalline quality, and growth techniques such as two-step GaN buffers were developed to reduce dislocations. This work systematically correlates the structural and electrical properties of N-face GaN grown by plasma-assisted MBE on C-face SiC to AlN nucleation conditions, culminating in an N-face HEMT with decent large signal RF performance. The importance

of AlN nucleation for achieving high purity, semi-insulating GaN buffers was investigated using samples grown with different NLs (GaN vs. AlN; metal-rich vs. N-rich). SIMS profiles showed that N-rich AlN nucleation was essential for suppressing Si and C diffusion from the substrate into the buffer. This result is consistent with Ga-face growth on Si-face SiC. The impact of the AlN-NL on the structural quality of GaN was examined using x-ray rocking curves on 600-nm-thick GaN buffers (where the first 100nm was optional 'step-one' intermediate GaN) grown on 50-nm-thick N-rich AlN-NLs. Higher AlN growth temperatures reduced the full-width-at-half-maximum (FWHM) of the off-axis (20-2-1) rocking curve, indicating a lower edge-type TD density. AFM images indicated that lower nucleation temperatures resulted in finer and denser AlN grains, which led to more edge-type TDs generated from the coalescence of the smaller GaN nuclei. At a fixed AlN nucleation temperature, doubling the total GaN thickness effectively reduced the FWHM(20-2-1) with insignificant impact on the FWHM(000-2), suggesting that the GaN contained a high fraction of inclined mixed-TDs which reacted with each other (annihilation or fusion), and that reducing the screw-type TDs might be energetically or kinetically unfavorable. Independent of the Ga-flux used for the step-one GaN, the two-step buffer reduced edge-type TDs through enhanced dislocation reactions while simultaneously introducing more screw-type TDs. By recovering the morphology of the 3D AlN-NL platform with a higher Al flux (Al/N~1) prior to starting GaN growth, the tilt mosaic was improved to a level comparable to that without a step-one GaN, while the advantages of a two-step buffer were preserved. N-face HEMTs fabricated on the insulating GaN buffers showed room temperature 2DEG density and mobility of $7 \times 10^{12} \text{cm}^{-2}$ and $1200 \text{cm}^2/\text{Vs}$, respectively. The buffer breakdown voltage at 1mA/mm of buffer leakage was 160V. The maximum drain current was $0.5\text{-}0.6 \text{A/mm}$ at $V_{\text{GS}}=1\text{V}$ for a gate length of $0.7 \mu\text{m}$. Biased in class-AB, power measurements at 4GHz with $V_{\text{DS}}=40\text{V}$ yielded a transducer gain of 12.7dB and a continuous-wave output-power density of 8.1W/mm with an associated power-added efficiency of 54%. The performance is comparable to Ga-face MBE HEMTs without discrete field-plates.

11:00 AM Student

AA3, Analysis of Degenerate p-Type GaN by Metal Modulated Epitaxy: *Elaiissa Trybus*¹; Walter Henderson¹; Gon Namkoong²; Jaime Freitas³; Alan Doolittle¹; ¹Georgia Institute of Technology; ²Old Dominion University; ³Naval Research Laboratory

Recently, Metal Modulation Epitaxy (MME) was introduced as a new growth technique wherein only the metal fluxes (Al, Ga, In, Si, and Mg) are modulated in a short periodic fashion in a plasma-assisted MBE system, while maintaining a continuous nitrogen plasma flux. This led to dramatic improvements in grain size and demonstrated hole concentrations in excess of $4.5 \times 10^{18} \text{cm}^{-3}$ for Mg-doped GaN grown on c-plane sapphire. Herein, we report the use and characterization of degenerately doped p-GaN with hole concentrations as high as $4.3 \times 10^{19} \text{cm}^{-3}$ grown by MME. GaN growth has a well documented surface phase diagram for a range of growth conditions with three distinct growth regimes: Ga-droplet formation, N-rich, and an intermediate regime. Predominately, growth is conducted in Ga-droplet or intermediate regime where a constant metal bilayer prevents the formation of pit threading dislocations. The MME approach, when applied to higher temperatures or in a predominantly droplet rich regime, results in atomically smooth surfaces normally only found when growing in the Ga-droplet regime. However, MME does not allow droplets to accumulate, making it viable for devices that traditionally depend on smooth droplet free interfaces. The influence of growth regimes on hole concentrations will be discussed. In this study a series of GaN Mg-doped samples were grown in a Riber 32 system. The substrate was maintained at 500 and 600 C and the MME modulation scheme consisted of a 50% duty cycle. Because of the low substrate temperature, there is no intermediate regime and by modulating the Ga and Mg shutters, the growth oscillates between the Ga-droplet regime and N-rich regime, allowing Mg incorporation on the proper Ga substitutional site, minimizing compensating N-vacancies and limiting faceting normally associated with N-rich growth. Room temperature photoluminescence (PL) results of the highest hole concentration samples at 500 and 600 C found that the peak intensity of the 600 C sample was 11.5x larger than the 500 C and

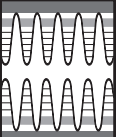
had a peak shift to larger energy. This is consistent with larger incorporation/activation of Mg-acceptors and the possible reduction of the acceptor energy and Fermi-level due to the Mott-Insulator transition. Therefore, the higher deposition temperature results in high Mg incorporation and improved film quality and results in the first known report of degenerately doped p-type GaN.

11:20 AM

AA4, Near Band-Gap Luminescence of Hexagonal Boron Nitride Grown on Ni(111) Substrate by Plasma-Assisted MBE: *Chiun-Lung Tsai*¹; Yasuyuki Kobayashi¹; Tetsuya Akasaka¹; Mokoto Kasu¹; ¹NTT Basic Research Laboratories

Hexagonal boron nitride (*h*-BN), known for its wide band gap in the deep ultraviolet (DUV) region and the exceptionally strong excitonic effect expected owing to its anisotropic structure, is considered to have potential for optoelectronic applications. Despite of many efforts, the electronic and optical properties of bulk *h*-BN largely remain unknown. Near band-gap optical properties play a key role in understanding the electronic structure and energy-transfer mechanism of *h*-BN. In this work, we examined the near band-gap luminescence characteristics of (0001) *h*-BN grown on single-crystal Ni(111) substrate by nitrogen plasma-assisted molecular beam epitaxy (PAMBE). The growth was carried out at a relatively low temperature (900°C) with nitrogen pressure of 1.5×10^{-5} Torr and RF power of 300 W. High-purity elemental boron (99.9999%) was evaporated with an electron-beam gun. A set of four samples with the thickness of 100 nm grown at the rate of 34, 84, 132, and 216 nm/hr, respectively, was used to explore the relationship between the crystal quality and optical properties with the growth rate. The (0002) and (0004) *h*-BN peaks in the (0001) symmetrical $2\theta/\omega$ XRD of sample C and the streaky and sharp (1×1) RHEED pattern in the inset taken along the ω and azimuth, respectively, verify a single-crystal *h*-BN layer with an atomically smooth surface. For sample C, the room-temperature (RT) PL spectrum obtained with ArF excimer laser excitation (wavelength = 193 nm) reveals two emission bands. The broad band centering at 3.54 eV is generally agreed to be impurity-related luminescence, but its actual origin needs further investigation. The other peak at 5.39 eV is attributed to near band-gap emission. The integrated RT PL intensity ratios of 5.39- to 3.54-eV luminescence for these four samples indicate that sample C has the highest ratio. In addition, sample C exhibits the narrowest FWHM of *h*-BN (0002) peak in X-ray diffraction, indicating that the optical and structural properties strongly depend on the growth rate. The possible reason is that the III/V growth ratio for sample C approaches the stoichiometric condition, which could greatly help reduce N-vacancies and defects in *h*-BN. In the temperature-dependent PL spectrum of sample C taken from 10 to 300 K, the near band-gap emission band can be resolved into two individual peaks at 5.3 and 5.5 eV by the Lorentzian fit. The relationship of the integrated PL intensities versus $1000/T$ for the two emissions follows the thermal activation process given by $I(T) = I_0 / (1 + C \cdot \exp(-E_a/k_B T))$. From the least square fit of the experimental data in dashed curves, we extracted the activation energy E_a to be 79.25 and 26.57 meV for the 5.3- and 5.5-eV emission, respectively. The former is tentatively assigned to DAP (donor-acceptor pair) emission, and the latter to bound-excitonic emission.

11:40 AM AA5, Late News



Session BB: III-Nitride: Optical Devices I

Thursday AM
June 25, 2009

Room: 208
Location: Pennsylvania State University

Session Chair: Christian Wetzel, Rensselaer Polytechnic Institute

8:20 AM Student

BB1, Growth and Characterization of GaInN Blue Light-Emitting Diodes with GaInN Quantum Barriers: *Wonseok Lee*¹; *Min-Ho Kim*¹; *Di Zhu*¹; *Ahmed Noemaun*¹; *E. Fred Schubert*¹; *Jong Kyu Kim*¹; ¹Rensselaer Polytechnic Institute

III-nitride-based high-brightness light-emitting diodes (LEDs) operating at visible wavelengths were made possible by the development of metal-organic vapor-phase epitaxy (MOVPE) growth techniques for high-quality AlGaInN materials. The performance of GaN-based LEDs grown on c-plane sapphire substrates strongly depends on the internal electric field induced by spontaneous and piezoelectric polarization in the quantum well (QW) active region. It was reported that the strong polarization-induced electric field causes reduced internal efficiency, quantum-confined Stark effect (QCSE), and electron leakage out of the active region at high drive currents which is responsible for the efficiency droop. Instead of conventional GaN quantum barriers (QBs), the polarization-matched quaternary AlGaInN QBs have been suggested to reduce, or even eliminate the efficiency droop enabled by independent control over interface polarization charges as well as bandgap. However, it is difficult to grow high quality AlGaInN QBs with high aluminum (Al) and indium (In) compositions that are required for complete matching of polarization charges with GaInN QWs. In this study, we demonstrate GaInN based multiple quantum well (MQW) LEDs grown on c-plane sapphire substrate with single-layered GaInN QBs and multi-layered GaInN/GaN QBs for reduced polarization mismatch with GaInN quantum wells, as well as for an additional confinement of carriers in the active region. In comparison with GaInN LEDs with conventional GaN QBs, the GaInN/GaN LEDs show much less blueshift of the peak wavelength with increasing injection current, a lower forward voltage, and a smaller diode ideality factor. Especially, the LEDs with multi-layered GaInN/GaN QBs show a remarkable reduction of efficiency droop. In addition, we investigate the density of pits related to the formation of V-defects in the MQW structure which act as a path for reverse leakage current. The GaInN/GaN MQW structure has much less pit density than GaInN/GaN MQW structure, resulting in two orders lower reverse leakage current at -5 V. We believe that these promising results for the GaInN/GaN LEDs are attributed to the reduced polarization-induced electric field and reduced strain in the MQW active region.

8:40 AM Student

BB2, High Efficiency GaInN-Based Multi-Quantum Wells Grown on High-Crystalline Quality, Freestanding, and Thick GaInN Layer: *Daisuke Iida*¹; *Ryota Senda*¹; *Tetsuya Matsubara*¹; *Motoaki Iwaya*¹; *Satoshi Kamiyama*¹; *Hiroshi Amano*¹; *Isamu Akasaki*¹; ¹Meijo University

There have been many reports on LEDs grown in nonpolar planes, such as the a-plane and m-plane, and in semipolar planes; thus, the problem of the large internal electric field can be solved in principle. However, the problem of the generation of misfit dislocations cannot be overcome because of the large lattice mismatch between the GaN and the GaInN active layer even though nonpolar- and semipolar-plane heterostructures can be fabricated. To reduce the lattice mismatch between the template and the active layer, a thick GaInN ternary alloy layer with a low defect density is one of the most promising candidates for realizing high-efficiency green LEDs and LDs. In a previous study, we grew thick GaInN epitaxial films on GaN templates having different crystal orientations: c-plane, a-plane, and m-plane. The reciprocal space mapping (RSM) of asymmetrical X-ray diffraction (XRD) showed that 1.1- μm -thick Ga_{0.95}In_{0.05}N was coherently grown on m-plane GaN, while GaInN layers grown on a-plane and c-plane GaN exhibited partial relaxation. A 700-nm-thick m-plane Ga_{0.95}In_{0.05}N film with a threading dislocation density of

approximately $1 \times 10^8 \text{ cm}^{-2}$ can be successfully grown on a GaN template using a grooved underlying layer. However, with increasing thickness and/or InN molar fraction of the GaInN layer, plastic relaxation in m-plane GaInN/GaN heterostructures by the generation of misfit dislocations and increased surface roughness were observed. Control of the stress and crystalline quality in GaInN is essential for realizing high-performance green LEDs and LDs. We also succeeded in growing a high quality thick GaInN film on a grooved m-plane GaN template with grooves along the $\langle 0001 \rangle$ direction. The photoluminescence (PL) peak intensity from grooved area of the GaInN film was approximately six times higher than that from the terraced area at room temperature. In this report, we fabricated GaInN-based multiple-QWs (MQWs) on high-crystalline-quality thick GaInN grown on a grooved m-plane GaN template. We also characterized the differences between GaInN-based MQWs on a GaN template and on thick, completely relaxed, and high-crystalline-quality GaInN. The wavelength of the PL peak from the active layer was approximately 535 nm. The PL peak intensity of GaInN-based MQWs grown on thick GaInN layer was approximately 3.0 times higher than that of grown on GaN. We conclude that the PL efficiency obtained from the GaInN/GaN MQWs is dependent not only on the threading dislocation density but also on the lattice mismatch between the GaInN well layer and the underlying layer.

9:00 AM Student

BB3, Design and Characterization of Electrically-Injected InGaN/GaN Photonic Crystal LEDs: *Elizabeth Rangel*¹; *Elison Matioli*¹; *Claude Weisbuch*¹; *James Speck*¹; *Evelyn Hu*¹; ¹University of California, Santa Barbara

Photonic crystal patterning has been investigated as a means to achieve high light extraction efficiency, directional far-field emission patterns, and increased radiance in InGaN/GaN LEDs. However, photonic crystal patterning poses unique challenges for electrical injection in broad-area devices. In particular, the topographical variation of the photonic crystal and the possibility of etch-induced damage introduce additional considerations for the placement of electrical contacts. In this work, current spreading and series resistance are investigated in conjunction with light extraction efficiency for two types of photonic crystal LED architectures. One set of devices employs the concept of spatially separated current injection and light extraction regions, with a centralized metal contact located outside of the photonic crystal. A second set of devices utilizes spatially coincident injection and extraction, with a photonic-crystal patterned indium tin oxide (ITO) current-spreading contact. Triangular-lattice photonic crystals were fabricated with lattice constants of 200nm, 224nm, 248nm and 272nm. The broad-area $800 \times 800 \mu\text{m}^2$ LED dies were covered by $760 \times 760 \mu\text{m}^2$ photonic crystals. As in our previous work, the epitaxial LED structures used here included a low-index AlGaIn cladding layer below the MQW active region in order to enhance the interaction of guided modes with the shallow photonic crystal. Transparent ITO contacts were deposited by RF magnetron sputtering and exhibited sheet resistances on the order of $10 \Omega/\text{square}$ with transmittance as high as 98% at $\lambda = 470\text{nm}$. Reactive ion etching with $\text{CH}_4/\text{H}_2/\text{Ar}$ gas chemistry and a SiO_2 hard mask was used to form the nanoscale photonic crystals in ITO. High pattern fidelity and near-vertical sidewalls were obtained via this fabrication process. In all cases, angle-resolved electroluminescence spectra exhibited distinct bands corresponding to waveguided modes extracted by the photonic crystal. Heavily modified far-field patterns displaying enhanced radiance in the vertical direction were obtained, and the directionality of the emission pattern was seen to correlate with the periodicity of the photonic crystal in a controllable manner. Additionally, anisotropic light extraction along the six-fold symmetric GM directions of the photonic crystal was observed for lattice constants deviating far from $\lambda/2$. At optimum lattice constants, photonic crystal LEDs with centralized contacts exhibited enhancements in vertical emission as high as 2.7x over unpatterned devices. Incorporation of ITO contacts was seen to lead to reduced series resistance and drive voltage. In addition, it was found that a 1.5x enhancement in backside output power could be obtained by patterning only the ITO contacts, minimizing the possibility of etch damage to the underlying p-type GaN. Finally, the emission intensity as a function of distance from the point of current injection was used to estimate the extraction length of the photonic crystal.

9:20 AM Student

BB4, A Monolithic LED Micro-Display on an Active Matrix Substrate by Flip-Chip Technology: *Zhaojun Liu¹; Ka Ming Wong¹; Chak Wah Tang¹; Kei May Lau¹;* ¹The Hong Kong University of Science and Technology

LED array displays made with individually packaged devices have been widely used for various applications. In recent years, different techniques are exploited to fabricate monolithic passive addressable LED arrays [1][2][3][4]. The array dimensions and pixel brightness in conventional passive addressable LED arrays were limited by the loading effect in the same row or column. Therefore, a new addressing scheme with newly developed fabrication technologies is needed to improve the operating effectiveness of monolithic LED arrays. In this paper, we report the design and fabrication of an 8×8 active matrix light emitting diode (AMLED) array. The AMLED array was composed of 8×8 pixels, each of which has dimension of 300 μm×300 μm² and a 50 μm pitch. A standard multiple quantum well (MQW) blue LED wafer grown on a sapphire substrate was used for fabrication of the LED micro array. Silicon dioxide (SiO₂) masks were used for Inductively Coupled Plasma (ICP) etching. The LED layers were etched down to the sapphire substrate. Rows of the array were defined and isolated in this step. SiO₂ mask and ICP were used again to define the mesa structure of each LED pixel. A thin Ni/Au (5/5nm) current spreading layer was deposited onto the p-GaN layer by e-beam evaporation, followed by annealing in an atmospheric ambient at 570°C for 5 minute. Then, a Ti/Al/Ti/Au (30/120/10/30nm) multi-metal layer was evaporated to form the electrodes and as a reflective layer on the p-electrodes simultaneously. Finally, SiO₂ passivation was applied onto the LED wafer. Openings in the SiO₂ were defined and Ni/Au (500/30nm) contact pads were formed in the openings for flip-chip bonding. The active matrix (AM) panel which consists of 8×8 driving circuits was fabricated using standard complementary metal-oxide-silicon (CMOS) process. Each driving circuit has one capacitor and two PMOS transistors (1C2T) so as to control the current flowing through each pixel. After the CMOS process, a TiW/Cu (30/500nm) seed layer was deposited by sputtering and patterned. A thick Cu layer (8 μm) and solder layer (22μm) was plated by electro-plating. After reflow in an annealing furnace, solder bumps were formed into ball shape. The LED micro array was thinned and diced before flipping onto the AM panel. We have demonstrated a monolithic high-resolution active matrix programmed LED micro display by flip-chip technology. The display has the advantages of high brightness, good luminance uniformity and individual controllability. This work shows that integration of GaN-based LEDs with the mature Si manufacturing technology is viable and different lighting systems on a chip can be developed using similar technology.

9:40 AM Student

BB5, Fabrication of Moth-Eye Structure on p-GaN Layer of GaN-Based LEDs Using UV Nanoimprint Lithography: *Eun-Ju Hong¹; Kyeong-Jae Byeon¹; Hyoungwon Park¹; Jaeyeon Hwang¹; Heon Lee¹;* ¹Korea University

Group III nitride based light-emitting diodes have attracted considerable attention as a solid-state lighting because of their highly energy conversion efficiency, long life-time and eco-friendly nature. However, the external quantum efficiency of InGaN-based LEDs is limited by total internal reflection (TIR) at the boundaries between the GaN layers and outer air. In this study, a moth-eye structure was formed on a p-GaN top cladding layer of the GaN-based LEDs in order to improve the light extraction efficiency by reducing total internal reflection. Pseudo moth-eye structure was fabricated onto the p-GaN surface using UV imprinting and inductively coupled plasma (ICP) etching processes. A Nickel template with a moth-eye structure, fabricated by laser interference lithography and electroforming, was used as a master stamp and PVC based polymer mold was replicated using a hot embossing process at a pressure of 30atm for a heating time of 20 minutes and used as an imprint stamp. Prior to imprinting, the surface of the replicated PVC mold was coated with a silane-based hydrophobic self-assembled monolayer (SAM) for easier detachment of mold. After imprinting, the p-GaN top cladding layer was etched by an ICP etching process using SiCl₄/Ar based plasma for a 1 minute. Finally, approximately 100nm high moth-eye patterns were formed on the p-GaN top cladding layer of the LED sample. The effect of the moth-eye pattern was examined by measuring the contact angle of a de-ionized water droplet and

the transmittance of the LED sample with the moth-eye structure. The light extraction efficiency of the LED device with moth-eye structures was verified with photoluminescence (PL) using a 325nm wavelength He-Cd laser. The PL intensity of the moth-eye patterned sample was 5 times higher than the un-patterned reference sample and this implies that the light extraction efficiency was improved by the moth-eye structure on p-GaN layer.

Session CC: III-V NW - Characterization

Thursday PM
June 25, 2009

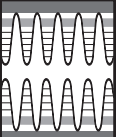
Room: 106
Location: Pennsylvania State University

Session Chairs: David Janes, Purdue University; Kris Bertness, National Institute of Standards and Technology

1:30 PM

CC1, Surface Recombination in GaN Nanowires before and after Surface Treatments: *John Schlager¹; Alexana Roshko¹; Kris Bertness¹; Norman Sanford¹; Aric Sanders¹; Albert Davydov¹; Denis Tsetkov¹;* ¹National Institute of Standards and Technology (NIST)

The properties of surfaces and interfaces have been crucial to the performance of semiconductor devices since the invention of the transistor and earlier. GaN nanowires grown by plasma-assisted molecular beam epitaxy (PAMBE) have been demonstrated to be defect-free via x-ray, photoluminescence (PL), and time-resolved PL (TRPL) measurements. Although TRPL uncovers a variety of excitonic processes and recombination mechanisms at different temperatures ($T = 5 \text{ K} - 300\text{K}$) in these nanowires, at room-temperature surface recombination dominates. Reminiscent of measurements used by the semiconductor industry on confinement test structures of different active volumes, TRPL measurements on GaN nanowires with varying diameters can yield the surface recombination velocity (SRV), a key parameter in evaluating the importance of nonradiative surface recombination. A high SRV, for example, can preclude the efficient operation of a nanowire laser, where radiative recombination is the preferred route for photo- or electrically generated carriers. The SRV is not a fixed attribute of the material surface but can depend on injection level (excitation intensity), temperature, and doping level. It is important to measure SRV under conditions of the ultimate application of interest. We have used TRPL measurements to determine SRV for doped, undoped, alumina-coated, and chemically treated nanowires. Also, nanowires exposed to a combination of air and UV light revealed an increase in SRV. The straightforward determination of SRV in the nanowires is made possible by a combination of factors. One is the predominance of nonradiative recombination at room temperature. Second, the wire diameters are on the order of or smaller than the diffusion lengths in GaN. These properties give the simple linear dependence of PL decay time on nanowire diameter [$\tau \sim d/(4 \text{ SRV})$]. Silicon-doped ($N_d \sim 6 \times 10^{17} \text{ cm}^{-3}$) and unintentionally doped ($N_d \sim 3.5 \times 10^{15} \text{ cm}^{-3}$) nanowires of different diameters (100 nm – 1200 nm) were dispersed on fused silica substrates and field-emission scanning electron microscopy (FESEM) was used to determine wire diameters and exclude doubled wires. Room-temperature TRPL measurements revealed the SRV values to be $9 \times 10^3 \text{ cm/s}$ and $\sim 8 \times 10^3 \text{ cm/s}$ for the doped and undoped samples respectively. Both wires were also conformally coated with alumina via atomic layer deposition after an HCl acid etch. Subsequent TRPL measurements yielded new SRV values of $3 \times 10^4 \text{ cm/s}$ (doped) and $1.3 \times 10^4 \text{ cm/s}$ (undoped). Finally, doped wires were chemically treated with an alcoholic solution of ammonium sulfide after an acid etch. These wires showed little or no change in SRV. New surface treatments (such as conformal coating of the nanowires with HVPE AlN) are planned to possibly reduce SRV for improved optoelectronic device applications. Data from these and other experiments will be presented.



1:50 PM

CC2, Temporal Analysis of Photoconductive Decay in GaN Nanowires: *Norman Sanford*¹; Lorelle Mansfield¹; Kris Bertness¹; Paul Blanchard¹; John Schlager¹; Christopher Dodson¹; Aric Sanders¹; Benjamin Klein¹; ¹National Institute of Standards and Technology (NIST)

Nanowires fabricated in GaN are envisioned for photonics, electronics, sensors, and NEMS. The large surface area to volume ratios warrant better understanding of nanowire surface phenomena. Our c-axis oriented nanowires were grown by nitrogen plasma assisted molecular beam epitaxy, exhibited hexagonal cross sections, and were remarkably free of defects and strain. Details appear elsewhere [1–4]. We studied transient photoconductivity (in air at room temperature) of nanowires exhibiting unintentional n-type conductivity (batch 1), and wires doped n-type with Si (batch 2). Two-terminal test structures were fabricated with individual nanowires placed variously on fused quartz or oxidized Si substrates with ohmic contacts made to the wire ends. Electrode gaps and wire diameters were typically 3–5 micrometers and 100–500 nanometers, respectively. The wire conductivity is proportional to the cross sectional area of the non-depleted neutral region. The dominant photoconductivity mechanism arises from photogenerated holes drifting to the surface, screening the depletion field, and reducing the surface band bending. The resulting increased diameter of the neutral region yields increased conductivity. With illumination ceased conductivity falls as equilibrium is restored by thermionic emission of conduction electrons from the neutral region surmounting the surface barrier and recombining with holes trapped on the surface. Charge neutrality between the surface and the depletion region allows mapping the time decay of the surface hole population to the diameter of the neutral region as manifest by the time decay of wire conductivity. We fit photoconductive transients to a rate equation model using free carrier concentration N and surface capture cross section S as fitting parameters. A detailed description is submitted elsewhere [5]. The fitted values for N ranged from 4–6E16 cm⁻³ for batch 1, and 4–7E17 cm⁻³ for batch 2. The dark surface band bending was estimated in the range of 0.2–0.3 V for batch 1 and 0.3–0.5 V for batch 2. The major sources of error were estimates of wire diameter and the degree to which UV exposure would produce a flatband condition. The fitted values of S ranged roughly from 1E-23 cm² to 1E-21 cm² which is consistent with photoconductive decay requiring several days to complete in some cases. Elevated temperatures (in air) reveal accelerated photoconductive decay. Progress with variable temperature studies performed under vacuum will be presented at the meeting. References: [1] Bertness, et al., *J. Crystal Growth* 287, 522 (2006); [2] Schlager, et al, *J. Appl. Phys.* 103, 124309 (2008); [3] Blanchard, et al., *IEEE Trans. Nanotech.* 7, 760 (2008); [4] Tanner, et al., *Appl. Phys. Lett.* 91, 203117 (2007); [5] Sanford, et al., submitted to *J. of Appl. Phys.*

2:10 PM Student

CC3, Growth, Structural, Optical, and Electrical Characterization of Nitride Nanowires Grown by MBE on Silicon Substrates: *Kevin Goodman*¹; Vladimir Protasenko¹; John Simon¹; Thomas Kosel¹; Debdeep Jena¹; ¹University of Notre Dame

Catalyst-free Molecular Beam Epitaxial (MBE) growth of Nitride nanowires on Silicon substrates is being researched as a possible route to optoelectronic devices integrated with Silicon. Successful growths of GaN, In_xGa_{1-x}N ($x \sim 40\%$), and GaN/AlN heterostructures have been accomplished under N₂ rich conditions on Silicon 111 substrates using methods used for the growth of GaN nanowire by Kikuchi et al. [*JJAP.* 43, 12A (2004) L1524]. TEM studies indicate growth along the c-axis (Figure 1). In HRTEM images, the nanowires appear defect-free throughout their lengths. Optical characterization reveals quantum efficiencies of 2% and 8% for GaN and InGaN wires respectively. This is an 80% increase from published numbers on thin film InGaN with a 40% Indium concentration. The increase is attributed to the low number of defects in the wires yielding no recombination centers for carriers in the band gap. I-V data from single InGaN nanowires with diameters on the order of 80 nm patterned with Electron Beam Lithography show current densities exceeding several kA/cm², as is necessary for successful electroluminescence. Successful tunneling current flow between p-type (111) Silicon substrates and InGaN nanowires grown directly on the substrates has been accomplished (Figure 2).

The current flow is attributed to hole tunneling from the heavily p-type doped Si (111) substrate into the InGaN nanowires through a thin, ~ 2 nm, Silicon Nitride layer which grows on the Silicon inside the Nitrogen rich growth chamber at high temperatures. This method is perhaps a gateway to introduce hole currents in Nitride materials which by themselves have proven difficult to dope p-type. The current-voltage characteristics indicate that successful hole injection into the InGaN nanowires has been achieved, the first step towards achieving electroluminescence in the green spectral window with nanowires grown directly on Silicon.

2:30 PM Student

CC4, Polarization-Sensitive Two-Color Detectors and Photovoltaic Devices by Solution-Synthesized Quantum-Wire Solids: *Amol Singh*¹; Rachel Thompson¹; Vladimir Protasenko¹; Ken Kuno¹; Huili Xing¹; Debdeep Jena¹; ¹University of Notre Dame

Quantum-wires (QWs) are semiconducting nanostructures that show unique electrical and optical properties due to size confinement in two dimensions. The third dimension along the longitudinal direction provides superior charge carrier transport as opposed to quantum-dots. The high aspect ratio imparts strong sensing abilities to quantum-wires. Our quantum-wires are grown by the solution-Liquid-Solid (SLS) a solution growth technique. It is low cost, provides surface passivation by surfactants, solubility and compatibility with various substrates. These attributes makes them suitable for bottom-up device fabrication approach on virtually any substrate with CMOS compatible processing. Two-color photo-detectors have been fabricated using such solution-synthesized CdS ($E_g = 2.42\text{eV}$) and CdSe ($E_g = 1.75\text{eV}$) quantum-wire solids (2D network of quantum-wires). The devices consist of 200x500 micron blocks of CdS and CdSe quantum-wire solids separated by 10 micron gaps. Titanium and gold were evaporated for interdigitated metal contacts. The blocks of quantum-wire solids were fabricated by semiconductors, lithography and liftoff. The as-grown quantum-wires are intrinsic as evident from temperature-dependent transport properties. This makes them suitable for photo-detection applications since it results in low dark current with > 1000 times light (illumination intensity of 540 mW/cm²) to dark current ratio under a voltage bias (5–40 Volts) for both CdS and CdSe quantum-wire solids. The band gaps of CdS and CdSe demarcate three windows in the optical spectrum A , B and C , where $A < E_g^{CdSe} < B < E_g^{CdS} < C$. Blue lies in C , red and yellow in B and were distinctly detected by the QW-based two-color detectors. The photocurrent action spectrum shows band edges of CdS and CdSe the semiconducting component of two-color detectors. In addition to being multispectral, the photodetectors are also found to be polarization sensitive. CdS (CdSe) quantum-wire photodetectors exhibit a photocurrent anisotropy of 16 (17)%. Quantum-wire solids can detect photons even without the application of a voltage bias if they are turned photovoltaic (PV) by asymmetric metal contacts with different work-functions. CdSe quantum-wire solid PV detectors were fabricated with Al ($\phi = 4.26\text{eV}$) and Pt ($\phi = 5.64\text{eV}$) contacts which provide the necessary built-in potential to render the QW solid photovoltaic. In one such device a short circuit current (I_{sc}) of ~ 1.1 nA and an open circuit voltage (V_{oc}) of 140 mV was observed under ~ 5 times AM 1.5-G. The fill factor for this device was $\sim 29\%$. The photocurrent action spectrum of I_{sc} was similar to one with voltage bias and shows the distinct band edge of CdSe. The I_{sc} is also polarization sensitive, with a photocurrent anisotropy of $\sim 9\%$. In conclusion, multispectral polarization-sensitive photovoltaic detectors are demonstrated using solution-synthesized semiconducting quantum-wire solids. The facile synthesis and portability to virtually any substrate indicate that these photovoltaic detectors are very attractive for future optoelectronic applications.

2:50 PM CC5, Late News

3:10 PM Break

THURSDAY
PM

Session DD: III-V NW - Growth and Processing

Thursday PM
June 25, 2009

Room: 106
Location: Pennsylvania State University

Session Chairs: David Janes, Purdue University; Kris Bertness, National Institute of Standards and Technology

3:30 PM

DD1, Self-Catalyzed Growth of GaAs Nanopillars on Nanopatterned GaAs, Silicon, and Silicon Dioxide Surfaces by MOCVD: *Ping-Show Wong*¹; Baolai Liang¹; Diana Huffaker¹; ¹University of California, Los Angeles

Nanowires provide a bottom-up approach for semiconductor fabrication to serve as building blocks for nano-sized structures and devices with designed dimensions and properties at desired locations. We report successful formation of GaAs nanopillars on nanopatterned GaAs, silicon, and SiO₂ surfaces by MOCVD in the self-catalyzed growth mode, an attractive alternative to the other two growth techniques described below. Majority of nanowires are formed in the vapor-liquid-solid growth mode, where metal particles (usually Au) serve as catalysts. Wide choices of material combinations are available for nanowires and substrates even when they are highly lattice mismatched, and the nanowire growth temperature is generally lower than the comparable epitaxial growth. A different approach is to grow nanopillars on nanopatterned substrates in the catalyst-free growth mode. Vertically aligned, highly faceted nanopillar arrays with high aspect ratio and density are available on designed patterns through electron beam lithography. The catalyst-free growth mode avoids possible reactor contamination and introduction of deep level traps through the incorporation of Au catalytical particles, and offers possibility for abrupt axial heterojunction interfaces and simpler integration platform through lateral overgrowth. Compared to these two methods, the self-catalyzed growth of GaAs nanopillars, where Ga droplets, formed in-situ, are used to catalyze subsequent nanopillar growth, combines favorable features of the other two methods, providing flexibility for material systems, nanopillar placement, growth conditions, and being free from hassles of foreign metal particles. We have demonstrated that, through the control of growth conditions, Ga droplets preferentially form only within pattern openings or also on the masking SiO₂ surface. Spherical Ga catalytical particles are observed atop vertically aligned, highly faceted, and downward tapered GaAs nanopillar bodies grown out of openings of nanopatterned GaAs (111)B and Si (111) substrates. On the other hand, nanopillars grown from Ga droplets atop SiO₂ surface are not aligned, seem to point to random directions, and are not as faceted. Phenomenon similar to Ostwald ripening is observed, where Ga droplets that grow into nanopillars expand in diameter at the expense of neighboring droplets, which become smaller in size or turn into clusters. The TEM and EDS are employed to study the crystalline structure and composition of these nanopillars. Stacking faults are observed along the growth direction, and are believed to result from the formation of rotational twins due to random perturbation in growth conditions in the course of nanopillar growth session. Room-temperature and low-temperature photoluminescence of these nanopillars are characterized and studied. Electrical properties including carrier dynamics are analyzed through two schemes: direct probing of attached nanopillars through an Au-coated STM tip, and planar placement of dispersed nanopillars with patterned metal contacts.

3:50 PM

DD2, Core-Shell p-n Gallium Nitride Nanowires: *Aric Sanders*¹; Kris Bertness¹; Paul Blanchard¹; Albert Davydov¹; Christopher Dodson¹; Lorelle Mansfield¹; Norman Sanford¹; John Schlager¹; Dennis Tsvetkov¹; Abhishek Monteyed¹; ¹National Institute of Standards and Technology (NIST)

Gallium Nitride's combination of chemical robustness, high direct bandgap, and tunable bandgap (through inclusion of Al or In) make it almost ideal for high power light-emitting diode (LED) applications. However, between the lack of lattice matched substrates and the tendency for high defect densities, the

realization of high-powered, inexpensive LEDs in the UV and blue has been delayed. We have previously demonstrated the growth of high-quality, low defect density Gallium Nitride nanowires on Si (111) substrates using catalyst-free, plasma-assisted molecular beam epitaxy (PAMBE)[1]. However, having high-quality material on inexpensive substrates is not sufficient. High hole concentrations are required to produce light from electron-hole recombination. Mg is the acceptor atom of choice for achieving high hole concentrations in GaN. Ideally, a light-emitting diode would contain an abrupt junction between p-type and n-type GaN. The incorporation of Mg via PAMBE is known to be problematic, so we have turned to Hydride Vapor Phase Epitaxy (HVPE) for the growth of p-type material. The HVPE growth was performed on the PAMBE grown nanowires, effectively using them as a lattice-matched substrate. This created an abrupt junction between the underlying n-type core and the p-type shell. Several over-growths of wires showed easily discernible contrast between the two regions in scanning electron micrographs. In order to ascertain if these shells were in fact p-type, several tests were performed. First, photoluminescence on wires after HVPE overgrowth revealed the appearance of features at energies of approximately 2.9 eV. Similar features have been linked to Mg incorporation. In addition, several electrical measurements were conducted to determine the nature of the overgrown material. Highly insulating nanowires were coated with Mg:GaN using HVPE. When these wires were tested they showed conducting behavior, indicating that the shell material was conducting. Next, wires fabricated into devices often showed a weak electroluminescence due to tunneling of minority carriers into the nanowire from the metal contacts. A high bias voltage (20-35 V) was required to observe this effect, and it was observable on a small fraction of the total devices fabricated. If the wire was known to be n-type, then the minority carrier (holes) tunneled from the metal contact with higher potential. This has been observed for many wires with n-type FET behavior, and appears as a dim glow from the wire close to the higher potential contact. The opposite metal contact should be the origin of tunneling electrons, and contacts to the shells on the nanowire clearly showed the wire glowing close to the contact with lower potential. In conclusion, n-type nanowire cores have been successfully overcoated with p-type HVPE grown GaN.

4:10 PM

DD3, Fabrication of Large Scale GaN Nanowire Vertical Devices in Parallel: *Christopher Dodson*¹; Grant Aivazian¹; Aric Sanders¹; Paul Blanchard¹; John Schlager¹; Kris Bertness¹; ¹National Institute of Standards and Technology

Processing nanowires on their native growth substrates allows for the fabrication of large scale devices in parallel, such as solar cells, LEDs, or surround-gate field effect transistors. In this particular study, we utilized GaN nanowires grown on an AlN buffer layer on top of a Si(111) wafer. By applying an insulating layer of spin-on-glass (SOG), we were able to fabricate simple two-terminal devices directly on the growth substrate. The tips of the nanowires were contacted with metal contacts, 20nm Ti and 200nm Al for contacting to n-type GaN or 40nm Ni and ~120nm Au for contact to p-type GaN, deposited via electron beam evaporation. The Si substrate was initially contacted with conductive silver epoxy; however, it was determined that this method contributed to the non-linearity of the current-voltage (I-V) curves. A contact study was performed to determine the optimal surface treatment, metal layers, and annealing conditions for ohmic contact formation. This study found that the proper surface treatment was to first subject the silicon to a CF₄:Ar plasma etch to remove any SiO₂ or SiN_x that may have accumulated during growth or storage of the wafer sample. Following the surface treatment, deposition of a titanium and aluminum stack, 20nm Ti capped with 200nm Al, and subsequent annealing of the sample produced an ohmic contact with a contact resistance of 1.6×10^{-5} Ohms·cm². Using this new contact recipe, we fabricated devices from n-type GaN nanowires that were overcoated with a p-type GaN layer prior to the application of SOG. These devices still produced a non-linear shape in the I-V curves and this could be due, in part, to carbon incorporation during the silicon contact deposition or to the Si-GaN hetero junction. Electroluminescence (EL) was observed from this sample while it was under both forward and reverse bias. Under either bias, the EL is consistent with minority carrier injection through non-ohmic contacts. The EL under forward bias could also be a result of recombination at the p-n junction.

4:30 PM Student

DD4, Oxygen Plasma Exposure Effects on Indium Oxide Nanowire Transistors: *Seongmin Kim*¹; Collin Delker¹; Pochiang Chen²; Chongwu Zhou²; Sanghyun Ju³; David Janes¹; ¹Purdue University; ²University of Southern California, Los Angeles; ³Kyonggi University

Wide-band gap oxide nanowires, such as ZnO, In₂O₃ and SnO₂, are attractive for transistor applications, since they can provide high on-currents and large on/off ratios. In order to move toward future commercial nano-electronics, it is still necessary to improve and stabilize the characteristics of nanowire devices and to understand the mechanisms responsible for the current-voltage relationships. Nanowire transistors with channel lengths around one micron have often been analyzed using a long-channel MOSFET model, including the formulas used to extract channel mobility. However, several aspects of the device performance are not well explained by this model, including an early onset of current saturation and high apparent mobilities. Understanding how to realize contacts suitable for high performance devices, and the role of contacts in the current saturation, threshold voltage and apparent mobility, is important for optimizing device performance and projecting scaling with channel length. In this study, the effects of oxygen plasma exposure on i) the nanowire channel and ii) the source/drain contact areas are studied for In₂O₃ nanowire transistors (d ~ 20 nm; Eg ~3.4 eV). In the first case, the nanowire region between pre-formed source/drain metal contacts was exposed to an oxygen plasma ambient and current-voltage characteristics of two-terminal nanowire devices before and after oxygen plasma doping are observed. After oxygen plasma doping for 30 sec and 60 sec, the conductivity of nanowire is dramatically increased. This control experiment suggests that oxygen plasma exposure can result in high n-type doping in the nanowire. In the second case, following passivation of the nanowire channels, contact windows were opened and subsequently exposed to the oxygen plasma. The doping level was varied by adjusting the exposure times (30 sec and 60 sec) of the devices to oxygen plasma with fixed plasma power and oxygen gas flow rate. Following the plasma exposure, metal contacts are deposited and patterned, in order to realize back-gated In₂O₃ nanowire transistors. The electrical properties of nanowire transistors with and without 60 sec oxygen plasma doping were examined. Following oxygen plasma doping, an In₂O₃ nanowire transistor shows an improved subthreshold slope, a significantly increase in on current and a 13X increase in transconductance, corresponding to a comparable increase in apparent mobility. The average on-current for six single In₂O₃ nanowire transistor devices increased from ~ 0.5 μ A to 2 μ A at V_{ds} = 0.5 V and V_{gs} = 4.0 V following oxygen plasma exposure. The increases in on current and apparent mobility is consistent with achieving n+ doping in the contact regions. The results can be understood in terms of the properties of the metal/semiconductor contact, which can be described by a thermionic-field emission model.

4:50 PM Student

DD5, Evidence of Mg Enhanced Desorption of GaN: Lorelle Mansfield¹; Kris Bertness¹; Todd Harvey¹; Norman Sanford¹; *Matthew Brubaker*¹; ¹National Institute of Standards and Technology

We have observed that gallium nitride near the substrate desorbs more readily when magnesium is present during GaN nanowire growth by plasma-assisted molecular-beam epitaxy (PA-MBE). This leads to nanowire morphology that is undesirable for device fabrication. The nanowires have thin base regions and much larger, coalesced tips. The GaN nanowires were grown with a two step process. Substrates for the growth were Si(111) wafers with a buffer layer of aluminum nitride grown by plasma-assisted molecular-beam epitaxy. The first step in the growth process entailed a lower temperature, between 635°C and 750°C, gallium nitride film grown with gallium from a solid-source effusion cell and a nitrogen plasma source. In the second step, the substrate temperature was increased to between 760°C and 800°C to start the nanowire growth. Some of the samples were also doped with magnesium during the nanowire growth step. The nanowire samples were cooled in the presence of nitrogen until the thermocouple near the substrate reached 200°C. Field-emission scanning electron microscopy (FESEM) was performed on cleaved samples to reveal the cross-sectional structure. Nanowires that were not doped had more uniform diameters than the magnesium doped nanowires. The original GaN matrix layer

remained in the undoped samples, although it was not as dense as expected. In the Mg-doped samples, the GaN matrix layer totally decomposed. The nanowires were also tapered and plan-view images showed that they had coalesced tips. It appears that the GaN desorption was enhanced by the presence of magnesium during nanowire growth. We postulate that the Mg enhances desorption due to the formation of magnesium nitride (Mg₃N₂). Mg₃N₂ is a compound which has a melting temperature of 800°C and a boiling point of 700°C in vacuum. Magnesium may attack the GaN film and bind with the nitrogen to form Mg₃N₂, which immediately boils away from the hot surface of the film. Excess gallium is then available to move up the nanowires and enhance the coalescence of the nanowire tips. Suggestions for limiting the Mg₃N₂ formation and improving the GaN:Mg nanowire morphology will be discussed.

5:10 PM DD6, Late News

Session EE: Oxide Thin Film Integration II

Thursday PM
June 25, 2009

Room: 108
Location: Pennsylvania State University

Session Chairs: Peter Moran, Michigan Technological University; Patrick Lenahan, Pennsylvania State University

1:30 PM Student

EE1, Thermodynamic Properties and Phase Diagram of Ferroelectric PbTiO₃ from First-Principles Calculations: *Zhi-Gang Mei*¹; ShunLi Shang¹; Yi Wang¹; Clive A. Randall¹; Zi-Kui Liu¹; ¹Pennsylvania State University

PbTiO₃-based perovskites have attracted tremendous interest as modern piezoelectric materials, which are widely used in medical imaging, acoustic sensors and transducers, actuators, etc. The pure PbTiO₃ has been known to have a ferroelectric tetragonal to paraelectric cubic phase transition with increased temperature or pressure. Since its discovery it has been extensively studied by both experiment and theory. However, the temperature-pressure phase diagram remains scarcely investigated. The negative thermal expansion coefficient (NTE) from 300 to 763 K is still poorly understood. In this study, we investigated the thermodynamic properties of the tetragonal phase using a combined first-principles calculations and quasi-harmonic approximation. The 0 K total energies were calculated using the density functional theory (DFT) within the generalized gradient approximation (GGA). The contribution to the free energy from the lattice vibration was calculated using phonon densities of states (DOSs) or Debye-Grüneisen model. With the deduced Helmholtz free energy (F), the linear thermal expansion coefficient (α), bulk modulus (B), specific heat capacity at constant pressure (CP), enthalpy (H), and entropy (S) of the tetragonal phase as a function of temperature (T) were calculated and compared with the experimental data. Using the current quasi-harmonic approximation, the calculated thermal expansion coefficient (TEC) of a single phase is always positive, thus the NTE of the tetragonal-PbTiO₃ cannot be correctly reproduced. From the statistical point of view, every state in the temperature and pressure phase space should be a mixture of both tetragonal and cubic phases. The free energy at each state can be evaluated using partition function. The fraction of the cubic phase increases with increasing temperature at zero pressure. Since the cubic phase has a smaller unit cell volume that the tetragonal phase, the calculated TEC becomes negative as temperature approaches transition temperature. Since the phonon spectra are unstable for the cubic phase, we cannot evaluate the vibrational free energy (F_{vib}) using the phonon DOS. Instead, Debye-Grüneisen model can be utilized to calculate the free energy. Then the Gibbs free energy (G) can be obtained by considering the pressure effect. Comparison of the Gibbs free energy as a function of pressure and temperature allows us to identify the phase transformation line between the tetragonal and cubic phases. Our predicted temperature-pressure phase diagram agrees qualitatively well with the experimental data. Our calculations show that the cubic phase can be stable at both low and high pressure regions at low temperatures, which agrees with the 0 K calculations of the phase stability by

Kornev et al. It was also found that the configurational mixing entropy (Sconf) of the cubic phase has an important effect on the transition temperature at ambient pressure.

1:50 PM Student

EE2, Cation Dominated Memristive Behavior in Lithium Niobite Thin Films: *William Calley*¹; Walter Henderson¹; Alexander Carver¹; Hang Chen¹; William Doolittle¹; ¹The Georgia Institute of Technology

Lithium Niobite (LiNbO₂) is a Lithium Niobate (LiNbO₃) sub-oxide produced in an oxide MBE system due to low oxygen partial pressure. Single crystal LiNbO₂ is grown on c-axis SiC and Sapphire. The structure of LiNbO₂, a lithium-intercalated niobium sub-oxide, is ideal for lithium ion drift devices due to the ease of intercalation–de-intercalation of lithium throughout the material which, when removed from the material, provides an abundance of lithium vacancies producing p-type material. LiNbO₂ is a 2.0 eV semiconductor with near perfect absorption characteristics, consistent with a well behaved “classic semiconductor” parabolic energy band and has structural quality that rivals well developed semiconductors. LiNbO₂ is naturally n-type when vacuum deposited presumably due to oxygen vacancies. LiNbO₂ can be converted to p-type by de-intercalation. LiNbO₂ has demonstrated n-type conductivity as high as 1700 S/cm and p-type conductivity as high as 2100 S/cm—the highest p-type conductivity reported in an oxide. An n-type LiNbO₂ memristor, starting at low resistance, exhibited an increase in resistance of 200% under constant bias. Additionally, the switching behavior is cation (Li) dominated as opposed to all other ionic switching devices which are anion dominated (mostly O-vacancies). Upon removal of the bias, resistance is stable at the high value for at least 24 hours—the longest idle time tested to date—until a reverse field is applied. The primary charge carriers in LiNbO₂ memristors—electrons resulting from oxygen vacancies—are evenly distributed throughout the film as is lithium. When bias is applied, lithium beneath the positive contact drifts away. The vacancies left by lithium result in charge compensation beneath the positive contact forming a high resistivity region. As constant bias is applied, the resistance increases as the lithium beneath the contact is depleted. When the bias is reversed, a sharp drop in resistance is seen as lithium returns to depleted region; the resistance then increases as lithium is depleted under the other contact. Strukov’s memristor appears to demonstrate an increase of ~700% in resistance based on publications. Similar tests on LiNbO₂ memristors demonstrate substantially smaller changes, approximately 12%, contact separations in the present LiNbO₂ test structures vary between tens and hundreds of microns whereas Strukov uses a contact separation between 3-30 nm. Strukov predicts a reduction of memristive effects by ~106 times for micron scale separations. However, LiNbO₂ still demonstrates memristance due to the higher mobility of lithium ions versus the oxygen vacancy with mobilities of 1E-10 cm²V⁻¹s⁻¹ used in Strukov’s modeling. Lithium diffusion in a similar system, LiCoO₂, has been reported to be ~5E-9 cm²s⁻¹ yielding a mobility of ~1.9E-7 cm²V⁻¹s⁻¹. The 106 scaling factor applied to the LiNbO₂ structure shows potential for equal or greater memristive performance. Specifically, high speed memristive switching appears viable using LiNbO₂.

2:10 PM Student

EE3, Impact of the Presence of Sub-Micron Grain Boundaries on the in-Plane Ionic Conductivity of Thin Film Gd-Doped CeO₂: *Matthew Swanson*¹; Natee Tangtrakam¹; Madhana Sunder¹; Peter Moran¹; ¹Michigan Technological University

The ionic conductivity of Gadolinium doped Ceria (GDC) thin films at temperatures between 400-700°C is of interest due to the application of the material as an electrolyte in low temperature Solid Oxide Fuel Cells (SOFCs). A review of the published literature makes clear that the method in which the film is fabricated has a large impact on the observed conductivity. There are, however, conflicting reports as to the effects of submicron grain boundaries on the conductivity of the GDC film in this temperature regime. Literature assertions^[1-3] suggest that the presence of submicron grain boundaries enhance the conductivities observed in some polycrystalline GDC films. The published literature, however, lacks a direct comparison of the conductivity observed in films fabricated by essentially identical methods, but differing only in the presence or absence of submicron grain boundaries (single crystal films). This

work addresses the need for such a comparison. The approach taken in this work is to first develop methods to fabricate GDC single-crystal and sub-micron-grain polycrystalline GDC films on Al₂O₃ substrates by RF magnetron sputtering from essentially identical growth conditions, and then to compare their conductivities. The method by which ~300nm thick single crystal epitaxial GDC films can be grown under the same conditions as ~300nm submicron-grained polycrystalline films (grain size ~80nm) on an Al₂O₃ substrate is described. It is demonstrated that the presence of a thin (~30nm), annealed, un-doped Ceria template prior to initiating GDC growth promotes single-crystal GDC epitaxy on Al₂O₃ substrates. Data on the conductivity versus temperature measurements between 400-700°C using the Van der Pauw geometry is reported for both the single crystal and sub-micron grained polycrystalline GDC films on Al₂O₃ substrates. These data are analyzed to extract the differences in carrier concentration and carrier mobility between single-crystal and sub-micron grained polycrystalline GDC films. Analysis of these data clearly demonstrates that the boundaries separating ~80nm diameter sub-micron grains degrade the conductivity of GDC films in the temperature regime between 400-700°C. Comparison to literature data reveals that the conductivities of the single-crystal GDC films in this temperature regime are within the same range as data from films that claim enhancement from the presence of sub-micron grains. Though the presence of sub-micron grains in the GDC film does not change the mobile charge carrier concentration by more than ~5%, the mobility of the charge carriers are significantly reduced, leading to a ~4x reduction in the conductivity at the high end of the temperature range, and more than an order of magnitude reduction at the lower temperatures. These results are interpreted in the framework of developing a predictive model of how changing the grain size would likely impact GDC thin film conductivity.

2:30 PM

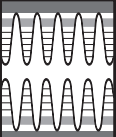
EE4, Effect of Stoichiometry on the Two-Dimensional Electron Gas at the LaAlO₃/SrTiO₃ Interface Grown by MBE: *Maitri Warusawithana*¹; C. Brooks¹; S. Thiel²; M. Zheng³; B. Mulcahy³; N. Reyren⁴; A. Cavaglia⁴; S. Gariglio⁴; J.-M. Triscone⁴; J. Eckstein³; J. Mannhart²; D. Schlom¹; ¹Pennsylvania State University; ²University of Augsburg; ³University of Illinois, Urbana - Champaign; ⁴University of Geneva

The discovery of a quasi 2-dimensional electron gas (q2-DEG) at the interface between SrTiO₃ and LaAlO₃ has enabled a number of exciting developments. So far this q2-DEG has been observed only in films grown by pulsed-laser deposition, which raised a question as to whether this manifestation has a connection with defects that result from the dynamics of the growth scheme employed. We find that a q2-DEG can be obtained between the LaAlO₃ and SrTiO₃ interface using the more gentle growth technique, molecular-beam epitaxy, and that control of the stoichiometry of the LaAlO₃ layer is key to its existence. Small changes in the composition of the LaAlO₃ layer affect the conductivity at the heterointerface. Our experiment effectively rules out oxygen vacancies in SrTiO₃ due to insufficiently oxidizing conditions during film growth as a possible mechanism for the observed conductivity of these samples. A very low sheet carrier density of ~4×10¹² carriers/cm² at 4 K was observed, which also supports the lack of oxygen vacancies compared to the higher sheet carrier densities (~10¹⁶ carriers/cm²) observed in samples grown under poor oxidation conditions. With appropriate stoichiometry the electron gas transitions into a superconducting state below ~200 mK. These findings of the importance of the LaAlO₃ composition on the ability to obtain a q2-DEG and its conductivity when grown by molecular-beam epitaxy open up interesting possibilities. Future directions of fundamental and applied interest including strained interfaces between other oxide phases, modulation doping through artificially layered structures, and the realization of such a q2-DEG on silicon, will be discussed.

2:50 PM

EE5, Structural and Magnetic Properties of Epitaxial EuTiO₃ Thin Films Grown by Molecular-Beam Epitaxy: *June Hyuk Lee*¹; Xiangling Ke¹; Lena Fitting Kourkoutis²; Tassilo Heeg¹; Martin Roeckerath³; Craig Fennie²; Jürgen Schubert³; David Müller²; Peter Schiffer¹; Darrell Schlom²; ¹Pennsylvania State University; ²Cornell University; ³Forschungszentrum Jülich GmbH

EuTiO₃ shares many similarities to SrTiO₃. These perovskite titanates are quantum paraelectrics and crystallize in a cubic structure with a lattice parameter



of 3.905 Å at room temperature. In contrast to the diamagnetic nature of SrTiO₃, bulk EuTiO₃ exhibits antiferromagnetic order at 5 K due to the existence of localized 4f moments on the Eu²⁺ site. This perovskite has been also predicted to be simultaneously ferromagnetic and ferroelectric at sufficiently high values of biaxial compression by Fennie and Rabe.¹ We have grown epitaxial EuTiO₃ thin films on (001) SrTiO₃ and (100) (La_{0.29}Sr_{0.71})(Al_{0.65}Ta_{0.35})O₃ by reactive molecular-beam epitaxy (MBE). Europium and titanium were codeposited onto the substrate under an oxygen background partial pressure of 3.3×10⁻⁸ Torr at a substrate temperature of 650 °C. X-ray diffraction (XRD) reveals phase-pure, epitaxial (001)-oriented EuTiO₃ thin films with ω rocking curve full width at half maximum values as narrow as 22 arc sec, which is close to that of the underlying substrates. Rutherford backscattering spectrometry (RBS) confirms a stoichiometric composition within the 5% measurement accuracy. Scanning transmission electron microscope (STEM) reveals the epitaxial heterostructure with an atomically abrupt interface between the film and the substrate. Contrary to prior reports of ferromagnetic behavior in PLD-grown EuTiO₃,² our stoichiometric EuTiO₃ thin films order antiferromagnetically at 5.5 K and saturation magnetizations are 6.7 ± 0.5 Bohr magnetons (μ_B) per europium atom. The lattice constant dependence on film composition and its effect on ferromagnetic properties will be discussed. ¹C. J. Fennie and K. M. Rabe, Phys. Rev. Lett. 97, 267602 (2006). ²K. Kugimiya, K. Fujita, K. Tanaka, and K. Hirao, J. Magn. Magn. Mater. 310, 2268 (2007).

3:10 PM Break

3:30 PM

EE6, Optical Properties and Structure of Magnetron Sputtered Vanadium Oxide Thin Films: *Orlando Cabarcos*¹; *Bryan Gauntt*¹; *Nikolas Podraza*¹; *Elizabeth Dickey*¹; *David Allara*¹; *Mark Horn*¹; ¹Pennsylvania State University

Vanadium oxide (VOx) thin films have been used for the last twenty years as the imaging material in uncooled infrared imaging devices. The important material properties for this application are a high thermal coefficient of resistance (TCR), controllable resistivity, low electrical noise and process compatibility with standard IC fabrication. However, vanadium can adopt many different oxidation states, yielding a number of stable metal oxides, which can lead to difficulties in reliable and consistent device fabrication. In this work, VOx thin films were fabricated via pulsed-DC magnetron sputtering in an argon and oxygen atmosphere under variable total pressure and oxygen-to-argon ratio (oxygen partial pressure, pO₂) deposition conditions in order to investigate the variability in desired material properties. The resulting vanadium oxide thin films were characterized using a number of complementary techniques including, Rutherford backscattering spectroscopy (RBS), transmission electron microscopy (TEM), electron energy loss spectroscopy (EELS), glancing incidence X-ray diffraction (GIXRD), spectroscopic ellipsometry (SE), and micro-Raman spectroscopy. The wide variety of techniques were used to establish the roles deposition parameters play in the final structure and composition of each film, as well as to determine the resulting effects of these characteristics on the electronic transport and optical properties. Electrical resistivity was calculated from I-V curves acquired from 2–point–probe measurements and thicknesses were measured using spectroscopic ellipsometry. TEM was used to determine film crystallinity and phase identification on a local scale. GIXRD was used to ensure localized measurements from the TEM were representative of the entire film. A transition from nano-crystalline to amorphous growth was observed with increasing oxygen-to-argon ratio. In all samples, the only crystalline phase observed was cubic vanadium oxide with the sodium chloride structure. Though bulk cubic VOx is limited to a maximum of x= 1.3, thin film nano-crystalline VOx with x=2 was observed in the present work. Increased oxygen content correlated with an increase in the film disorder as well as an increase in the film resistivity, which varied over seven orders of magnitude from ~10⁻³ to 10⁴ Ω-cm. The transition from nano-crystalline to amorphous growth and the increase in film resistivity with increasing disorder also correlated with observed changes in the Raman spectra and the complex dielectric function spectra (epsilon = epsilon₁ + epsilon₂) extracted from SE. Additionally, the temperature coefficient of resistance was found to increase with increasing oxygen content from -0.1 to -3.5 %/K. There appears to be a direct correlation between film disorder, resistivity, and TCR. This correlation

may be exploited to engineer materials with the optimum TCR for a given film resistivity. By utilizing these complementary techniques, correlations between changes in the microstructure, composition, optical properties and electronic transport properties have been established.

3:50 PM

EE7, Magnetic and Electric Properties in (SrMnO₃)_n / (LaMnO₃)_{2n} Superlattices: *Carolina Adamo*¹; *Carmela Aruta*²; *Xianglin Ke*³; *Valentina Bisogno*⁴; *Nik Brookes*⁴; *Julius Cezar*⁴; *Pasquale Orgiani*⁵; *Peter Schiffer*³; *Giacomo Ghiringhelli*⁶; *Luigi Maritato*⁵; *Darrell Schlom*¹; ¹Cornell University; ²CNR-INFM Coherentia, Dip. di Scienze Fisiche, Università di Napoli “Federico II”; ³Pennsylvania State University; ⁴European Synchrotron Radiation Facility; ⁵CNR-INFM Coherentia and Dip. di Matematica ed Informatica; ⁶CNR-INFM Coherentia and Dip. di Fisica, Politecnico di Milano

Interesting phases with new electronic and magnetic properties at the interface between insulating oxides have been largely reported.¹ Recently, fascinating phenomena were observed to occur at the interface between the antiferromagnetic insulators, LaMnO₃ and SrMnO₃.²⁻³ In this framework, we report the magnetic and electric properties of epitaxial (SrMnO₃)_n / (LaMnO₃)_{2n} superlattices, where n denotes the pseudocubic unit cells comprising the thickness of SrMnO₃ layer. In particular, we fabricated (SrMnO₃)_n / (LaMnO₃)_{2n} superlattices with different values of n (n=1, 2, 3, 4, 5, 6, 8, 16). We find for small n (n<2) the superlattices behave like the ferromagnetic conductor La_{0.7}Sr_{0.3}MnO₃. As n increases, the saturation magnetization and transition temperature decreases and the superlattices become more insulating. We attribute the induced large magnetization and high conductivity of the superlattices to charge transfer at (SrMnO₃) / (LaMnO₃) interface over a distance of a few unit cells. In order to better understand the magnetic and electronic modifications induced at the interfaces we have measured linear and circular magnetic dichroism in the Mn L_{2,3} absorption spectra of x-rays on (SrMnO₃)_n/(LaMnO₃)_{2n} superlattices with n=1, 5, 8. Whereas the interfacial MnO₂ doped planes show a redistribution of the charge carriers in the eg(x₂-y₂) orbitals, in the thicker layers the eg(3z₂-r₂) are preferentially occupied. The orbital occupation is coupled in a non-trivial way to the diverse ferromagnetic (FM) and antiferromagnetic (AF) anisotropies. In particular we find that, for n>5, the interfacial FM phase does not homogeneously extend in the whole superlattice but it is overwhelmed by the AF bulk phase stabilized by the eg(3z₂-r₂) orbitals. This orbital occupation might optimize the conduction between the FM regions via the AF thick layers, as shown by recent theoretical calculations.⁴ ¹M. Basletic, J.-L. Maurice, C. Carretero, G. Herranz, O. Copie, M. Bibes, E. Jacquet, K. Bouzehouane, S. Fusil, and A. Barthelemy, Nat. Mater. 7, 621 (2008). ²T. Koida, M. Lippmaa, T. Fukumara, K. Itaka, Y. Matsumoto, M. Kawasaki, and H. Koinuma, Phys. Rev. B 66, 144418 (2002). ³Hiroyuki Yamada, M. Kawasaki, T. Lottermoser, T. Arima, and Y. Tokura, Appl. Phys. Lett. 89, 052506 (2006). ⁴S. Dong, R. Yu, S. Yunoki, G. Alvarez, J.-M. Liu and E. Dagotto, Phys. Rev. B 78, 201102(R) (2008).

4:10 PM Student

EE8, Dielectric Tensors of High-k Pbnm Perovskites from First Principles: *Sinisa Coh*¹; *David Vanderbilt*¹; ¹Rutgers University

The electrical thickness of SiO₂ gate insulators in MOSFET's has been scaled down by a factor of 0.7 in each new generation of devices, but that trend has slowed down after the 130 nm generation. Recently, the replacement of SiO₂ with HfO₂-based compounds allowed this trend to continue along its original path and was realized in the current generation of devices manufactured in 45 nm technology. Among the materials under consideration for next-generation high-k dielectrics in MOSFET and other microelectronic devices are several perovskites having orthorhombic space group Pbnm. Among these are LaLuO₃, SrBO₃ (B = Zr, Hf), AScO₃ (A = La, Pr, Nd, Sm, Gd, Tb, Dy), and LaB_{1/2}B'_{1/2}O₃ (B = Ca, Mg and B' = Zr, Hf) (with lower symmetry), which are all compatible with growth on silicon and can have more desirable properties than HfO₂, see Ref. [1]. Using first-principles DFT methods with ultrasoft pseudopotentials and GGA energy functionals, we computed the dielectric tensors, structural properties, and phonon spectra of these materials. All of these structures can be constructed from the cubic perovskite structure by rotating octahedra according to the (a-a-c*) Glazer-notation pattern. On top of these rotations, there are also

displacements of A-site ions. The rotation ($a\text{-}a\text{-}c'$) can be decomposed into two steps: an ($a\text{-}a\text{-}0$) pattern of rotation by angle θ_x , followed by an ($00c'$) pattern by θ_z , in that order. For each structure we estimated the rotation angles θ_x and θ_z by fitting oxygen Wyckoff coordinates and unit-cell ratios to a model in which the octahedra rotate perfectly rigidly. Going across the series of rare-earth scandates, the ionic radii of the rare-earth atom gets smaller, which is reflected in the fact that the rotation angles become larger. At the beginning of the series, for $A = \text{La}$, $\theta_x = 15.2^\circ$, $\theta_z = 10.1^\circ$, while for $A = \text{Dy}$, $\theta_x = 20.2^\circ$ and $\theta_z = 15.1^\circ$. Furthermore, the unit-cell volumes and displacements of A-site ions from ideal cubic positions are also almost linearly increasing with rotation angles. Across the series of rare-earth scandates, ϵ_{xx} and ϵ_{yy} are very slowly decreasing. Average values² are: $\epsilon_{xx} = 30.4$ and $\epsilon_{yy} = 25.5$. On the other hand, ϵ_{zz} increases non-linearly from $\epsilon_{zz} = 28.0$ for $A = \text{La}$ up to $\epsilon_{zz} = 40.8$ for $A = \text{Dy}$. SrZrO_3 and SrHfO_3 show much smaller anisotropies, most probably due to smaller values of rotation angles. Finally, we investigate the possibility of increasing the dielectric tensors of these materials even further by forcing them into the rhombohedral ($a\text{-}a\text{-}a'$) structure. We also report the IR-active modes in all of these structures and analyze trends. (1) D. G. Schlom, S. Guha, S. Datta, MRS Bull. 33, 1017 (2008). (2) Pending final choice of consistent set of pseudopotentials. We expect trends to remain similar.)

4:30 PM

EE9, Dielectric Tensor of Single Crystals of the Alternative Gate Oxide Candidate LaLuO₃: *Tassilo Heeg*¹; Klaus Wiedenmann²; Martin Roeckerath³; Sinisa Coh⁴; David Vanderbilt⁴; Darrell Schlom¹; ¹Cornell University; ²Universität Augsburg; ³Research Centre Jülich; ⁴Rutgers, The State University of New Jersey

In the ongoing search for Si-compatible high- and higher- K dielectrics, LaLuO₃ is being studied as a possible candidate material^{1,2,3} because of its predicted stability in contact with silicon⁴, high optical bandgap (5.6 eV),⁵ and its high, but not fully established K value.⁴ These existing studies on amorphous and crystalline thin films of LaLuO₃ have observed a significant variation in the dielectric constant of LaLuO₃, ranging from 17 to 45. To put these values into context and to distinguish between intrinsic material properties and the influence of the specific thin film fabrication route, we have investigated the dielectric properties of bulk LaLuO₃ experimentally as well as theoretically using density functional theory. Single crystals of the congruently melting composition, La_{0.94}Lu_{1.06}O₃, were grown using the floating-zone technique. Subsequently, slices were cut from these crystals. Since the crystals were rather small (around 5 mm diameter) and heavily cracked, the slices were cut in such orientation that the slices were free of cracks and as big as possible, generally resulting in a random crystallographic orientation. Laue- and four-circle x-ray diffraction were employed to determine the orientation of each piece to enable the full dielectric constant tensor (K_{ij}) of LaLuO₃ to be established. Pt electrodes were deposited onto the slices to form parallel plate capacitors and K of each slice was determined using an HP4284A precision LCR meter. Due to the orthorhombic symmetry of La_{0.94}Lu_{1.06}O₃ (Pbnm, #62), its dielectric tensor has three non-zero components. Using a least-square fitting approach, these components were determined from the measured values. K_{ij} of LaLuO₃ varies as a function of direction from a minimum of 25 ± 3 to a maximum of 47 ± 3 making LaLuO₃ the highest K alternative gate dielectric material known that is Si-compatible with high bandgap. (1) J.M.J. Lopes, M. Roeckerath, T. Heeg, E. Rije, J. Schubert, S. Mantl, V.V. Afanas'ev, S. Shamuilia, A. Stesmans, Y. Jia, D.G. Schlom, Appl. Phys. Lett. 89, 222902 (2006). (2) J.M.J. Lopes, M. Roeckerath, T. Heeg, J. Schubert, S. Mantl, Y. Jia, D.G. Schlom, Microel. Eng. 84, 1890 (2007). (3) J. Schubert, O. Trithaveesak, W. Zander, M. Roeckerath, T. Heeg, H.Y. Chen, C.L. Jia, P. Meuffels, Y. Jia, D.G. Schlom, Appl. Phys. A 90, 577 (2008). (4) D.G. Schlom, J.H. Haeni, MRS Bull. 27, 198 (2002). (5) K.L. Ovanesyan, A.G. Petrosyan, G.O. Shirinyan, C. Pedrini, L. Zhang, Opt. Mater. 10, 291 (1998).

4:50 PM Student

EE10, Atomic Scale Effects of Fluorine in MOS Gate Stacks: *Jason Ryan*¹; Patrick Lenahan¹; Anand Krishnan²; Srikanth Krishnan²; Jason Campbell³; ¹Pennsylvania State University; ²Texas Instruments; ³National Institute of Standards and Technology (NIST)

Recent work has shown that the negative bias temperature instability (NBTI) can be significantly suppressed by incorporating fluorine in the gate oxide

of SiO₂ pMOSFETs.¹ Other studies also suggest that fluorine incorporation may help reduce hot carrier damage and improve radiation hardness.^{2,3} This is consistent with suggestions that fluorine may passivate Si/SiO₂ interface dangling bond defects (P_b centers) more effectively than hydrogen.³ Despite these observations, the atomic-scale role of fluorine is not understood. We employ spin dependent recombination (SDR) and gated diode current measurements (DC-IV) to investigate the atomic-scale role of fluorine. Comparisons are made between conventional "pure" SiO₂ devices, fluorinated SiO₂ devices, and more complex fluorinated high- k based memory devices. Our results suggest that fluorine effectively passivates Si/SiO₂ P_{b0} center precursors, but much less effectively passivates Si/SiO₂ P_{b1} center precursors. Pre- and post- NBTI stress DC-IV measurements on pure SiO₂ and fluorinated SiO₂ pMOSFETs with identical geometry clearly indicate fluorine's effectiveness in suppressing NBTI. SDR measurements on pure SiO₂ MOSFETs clearly demonstrate the dominating NBTI induced defects are P_{b0} and P_{b1} centers.⁴ (P_{b0} and P_{b1} centers are simple Si/SiO₂ interface silicon dangling bond defects and are responsible for many MOS instability problems.) SDR measurements on NBTI stressed fluorinated SiO₂ devices suggest P_{b1} like center generation and an absence of P_{b0} generation. These results suggest that fluorine effectively passivates P_{b0} center precursors but much less effectively passivates P_{b1} center precursors. Additional SDR measurements on fluorinated high- k based memory structures reveal that the defects observed (possibly P_{b1} like) are not identical to those commonly observed in conventional Si/SiO₂. Much broader SDR spectra (observed in both fluorinated SiO₂ and high- k devices with the magnetic field parallel to the (100) normal) suggest the presence of nearby fluorine. (Fluorine has a spin $\frac{1}{2}$ magnetic moment which would broaden or split the spectrum.) The magnetic field orientation dependence of these defects also suggests that they are coupled to fluorine. Rotating the magnetic field perpendicular to the (100) normal splits the spectrum into two lines, suggesting the presence of spin $\frac{1}{2}$ nuclei. Since P_{b0} and P_{b1} defects have significantly different densities of states⁵, our results may be useful in modeling fluorinated oxide device response. Our results also provide a fundamental explanation for fluorine's ineffectiveness at reducing NBTI in nitrided oxide devices; NBTI is dominated by different defects in nitrided oxide devices.⁴ (1) T.B. Hook et al., IEEE Trans. Electron Devices, 48, 1346, 2001. (2) E.F. da Silva et al., IEEE Trans. Nucl. Sci., 34, 1190, 1987. (3) J. Wright et al., IEEE Trans. Electron Devices, 36, 879, 1989. (4) J.P. Campbell et al., IEEE Trans. Dev. Mater. Reliab., 7, 540, 2007. (5) P.M. Lenahan et al., J. Vac. Sci. Technol., B, 16, 2134, 1998.

5:10 PM EE11, Late News

Session FF: ZnO Characterization

Thursday PM
June 25, 2009

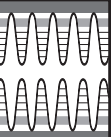
Room: Deans Hall I
Location: Pennsylvania State University

Session Chair: Leonard Brillson, Ohio State University

1:30 PM

FF1, The Richardson Constant for Schottky Contacts to n-ZnO: *Martin Allen*¹; Steven Durbin¹; Karthik Sarpatwari²; Osama Awadelkarim²; Suzanne Mohney²; ¹University of Canterbury; ²The Pennsylvania State University

The Richardson constant (A^*) is a fundamental parameter that describes the transport (via thermionic emission) of carriers across a rectifying metal-semiconductor (Schottky) junction. Crucially, the barrier height (ϕ_b) of a Schottky contact can only be extracted from current-voltage (I - V) measurements by first assuming a value for A^* . The usual approach is to use the semiconductor effective electron mass to derive a theoretical A^* . Crowell and Sze¹ have also proposed a number of additional corrections due to phonon scattering and quantum mechanical reflections. Given the role of A^* in modeling the current conduction across Schottky interfaces, an experimental determination of A^* is important for the design and characterization of devices such as diodes, photodiodes and metal semiconductor field effect transistors. This is particularly



relevant for ZnO, a wide band gap semiconductor with considerable potential for high temperature, radiation resistant, power electronics applications. Experimental A^* values can be extracted from the temperature dependence of the saturation current density, provided the current transport is dominated by the thermionic emission of carriers across a single, homogeneous barrier. Previous attempts to measure an experimental A^* value for ZnO have resulted in values some 1-2 orders magnitude lower than the theoretical prediction^{2,4}. Significantly these reports have all involved Schottky contacts with relatively high ideality factors (η). High values of η are traditionally associated with lateral variations in contact homogeneity and additional transport processes besides pure thermionic emission over a single barrier. In this paper we have employed two approaches to improve on this situation: firstly, we have performed temperature dependent $I-V$ measurements on highly rectifying oxidized iridium Schottky contacts, fabricated using a new methodology⁵, with ideality factors approaching the image-force-controlled limit for ideal laterally homogeneous contacts; and secondly, we have developed a new theoretical method, based on a relationship between the effective values of A^* and $\phi_{b,eff}$, to account for the effects of barrier height inhomogeneity on experimentally determined values of A^* . Using both of these approaches we were able, for the first time, to obtain excellent agreement between the experimental and theoretical values of A^* for ZnO. Furthermore, the same theoretical approach can be used to explain the poor agreement between experimental and theoretical values of A^* in a number of other semiconductor systems. ¹Crowell and Sze, *Solid-State Electron.* 9, 1035 (1966). ²Sheng *et. al.*, *Appl. Phys. Lett.* 80, 2132 (2002). ³von Wenckstern *et. al.*, *Appl. Phys. Lett.* 88, 092102 (2006). ⁴Gür *et. al.*, *J. Phys. Condens. Matter* 19, 196206 (2007). ⁵Allen *et. al.*, *Appl. Phys. Lett.*, in press.

1:50 PM

FF2, Stability of Schottky Barriers on ZnO PLD Thin Films beyond 400 K: Holger von Wenckstern¹; Stefan Müller¹; Matthias Schmidt¹; Matthias Brandt¹; Alexander Lajn¹; Florian Schmidt¹; Michael Lorenz¹; Marius Grundmann¹; ¹Universität Leipzig

We report a concise electrical study of reactively sputtered Ag, Au, Pd, and Pt Schottky barriers on ZnO thin films in the temperature range from 20 K to 600 K. The effective barrier heights $\phi_{b,eff}$ have similar temperature dependencies for all metals and can be modelled taking lateral fluctuations of the barrier potential into account. For temperatures lower than 200 K, the consideration of a single Gaussian broadened barrier is not sufficient; here, two different mean barrier potentials are necessary for an adequate description of $\phi_{b,eff}(T)$. The strongly different area fraction of the two barriers makes the higher of the two barriers (labelled $\phi_{b,m}$ from now on) dominant for $T > 200$ K. We used pulsed-laser deposition to grow a 200 nm thick degenerately doped ZnO:Al layer, serving as ohmic back contact, on a 2 inch a-plane sapphire wafer. On top of the ZnO:Al layer, a 1 μ m thick nominally undoped ZnO layer was deposited at an oxygen partial pressure of 0.02 mbar and a temperature of 650°C. The Schottky barriers were realized by reactive sputtering of the respective metal at a pressure of 0.02 mbar, shadow masks were used to define circular contact with areas between 4×10^{-4} and 5×10^{-3} cm². The temperature dependence of the effective barrier height and the ideality factor showed that for temperatures higher than 200 K ($1/T = 5 \times 10^{-3}$ K⁻¹) the effective barrier heights depend linear on the reciprocal temperature implying that a single barrier model is sufficient to describe current transport. Within this model the mean barrier heights have been determined to be about 1.05 eV, 1 eV, 1.2 eV, and 1.3 eV for Ag, Au, Pd and Pt, respectively. For temperatures lower than 200 K the consideration of a single barrier is not sufficient as particularly evident from the temperature dependence of the ideality factor. Here, we have to account for second barrier being with 0.1 to about 0.25 eV considerably lower than the determined mean barrier heights. This and the small area fraction of the low barrier regions indicate that these are caused by sub-micrometer scale patches. The Schottky barriers are stable up to about 420 K. For higher temperatures they start to degrade and for temperatures higher than about 450 K rectification breaks down. Within this contribution we will discuss strategies to increase the operating temperatures of our diodes clearly above 450 K. One ansatz is the passivation of the ZnO surface using insulators such as Al₂O₃ or HfO₂. Besides the characterization of the Schottky barrier by current-voltage and capacitance-voltage measurements, we employed thermal

admittance spectroscopy, deep level transient spectroscopy (DLTS) and Laplace DLTS to study selected defects contained in the thin films.

2:10 PM

FF3, Identification of Native Defects in as-Grown ZnO Single Crystals: X. J. Wang¹; L. Vlasenko¹; S. J. Pearton²; W. M. Chen¹; Irina Buyanova¹; ¹Linköping University; ²University of Florida

ZnO is currently attracting increasing attention as a key material for a wide variety of electronic and optoelectronic applications. Optical, electrical, and magnetic properties of ZnO are believed to be strongly influenced by native defects, such as oxygen and Zn vacancies. However, unambiguous experimental evidence confirming the formation of these defects in as-grown ZnO as well as evaluations of defect densities is currently sparse. The purpose of the present work is, by combining electron paramagnetic resonance (EPR) and optically detected magnetic resonance (ODMR) spectroscopies, to perform comprehensive defect characterization of as-grown bulk ZnO available commercially. Based on the performed ODMR and EPR measurements, defect formation is found to strongly depend on the employed growth techniques. Specifically, Zn vacancies (V_{Zn}), oxygen vacancies (V_O) and effective mass (EM) donor centers of unknown origin are identified as the main grown-in defects in the bulk ZnO grown from melt. Based on the intensities of the EPR signals, the estimated defect concentrations are $\sim 10^{14}$ cm⁻³ and $\sim (5-8) \times 10^{14}$ cm⁻³ for the positively charged V_{O}^+ and negatively charged V_{Zn}^- centers, respectively. On the other hand, neither V_{O}^- nor V_{Zn} were found in the hydrothermally grown ZnO, where only EPR signals related to the Li acceptor and the EM donor are present. Information regarding thermal stability of the intrinsic defects in ZnO was obtained from thermal annealing experiments. The V_{O}^+ centers are annealed out at 500 °C, as was also observed in electron-irradiated ZnO. This implies that the monitored annealing process is inherent to these defects. On the other hand, the Zn vacancies are found to be thermally stable up to 700 °C. At higher temperatures, the corresponding EPR and ODMR signals are replaced by that of the Li_{Zn} acceptors, possibly due to the thermally activated diffusion of interstitial Li atoms and their annihilation with V_{Zn}^- . This implies strong effects of contamination by residual impurities on the thermal annealing of V_{Zn}^- . Moreover, since annealing temperatures for both vacancy defects are found to be relatively low, the rate of material growth and the speed of cooling processes after the growth can significantly affect the concentrations of these defects in different as-grown ZnO materials due to the effect of partial annealing during the process. We also like to note that, whereas both vacancies were detected in the EPR measurements, only Zn vacancies were observed in the ODMR experiments. This possibly indicates a more important role of the latter in carrier recombination.

2:30 PM Student

FF4, Nanoscale Deep Level Defect Mapping and Energetics at ZnO(0001) Surfaces: Tyler Merz¹; Dan Doutt¹; Leonard Brillson¹; ¹The Ohio State University

ZnO has attracted considerable attention over the past few years for its potential device applications in opto- and microelectronics, yet the understanding and control of electrical contacts to ZnO remain considerable challenges. The diversity of reported electrical contact features reflects the impact of extrinsic factors such as native point defects, impurities, and chemical reactions near ZnO-metal interfaces. Recently, we demonstrated that nanoscale surface asperities on the bare ZnO surface can have high densities of trapped charge that contribute to band bending and free carrier recombination.[1] This work showed a direct correlation between surface morphology, e.g., rms roughness, and recombination velocity of free carriers within the outer few tens of nanometers. Depth-resolved cathodoluminescence spectroscopy (DRCLS) displayed optical emissions from transitions into and out of deep level defects localized within the same near-surface region. We have now used a nanoscale spatially-resolved form of surface photovoltage spectroscopy (SPS) to measure these deep level trap transitions, their energy level positions within the band gap, and their variation across different ZnO surfaces. These spectra reveal multiple defect levels distributed across the band gap. In particular, we now can identify the Zn vacancy energy level position situated 2.1 eV below the conduction band. SPS/ AFM/ KPFM measurements reveal that such defects concentrate

inhomogeneously across the surface and are evident at step edges, crater rims, and other low-coordination sites at the ZnO surface. We adapted a Park Systems XE-70AFM/KPFM to permit spatial imaging and spectral scanning with the Kelvin probe, using a fiber-optically coupled IR-UV light source and monochromator to obtain SPS. The onset of filling or unfilling transitions at a given threshold photon energy causes contact potential difference (cpd) changes between probe tip and ZnO surface, with the cpd vs. hv sign indicating whether photons fill or deplete surface traps. Thus optical transitions that deplete a surface trap of electrons reduce the band bending and the surface work function. Filling transitions produce more band bending and increased work function. Surface regions with smooth (rms roughness < 0.5 nm) exhibit little or no sub-band gap response, whereas stepped regions display: (i) filling transitions at $E_v+0.7, 2.35,$ and 2.65 eV and (ii) unfilling transitions at $E_c-2.1$ eV. Depth-resolved CLS emission at 2.1 eV can be directly correlated with Zn vacancies. Determination of the Zn vacancy energy level within the ZnO band gap permits an assessment of theoretical energy calculations. More generally, identification of specific defects and energy levels with particular surface morphological features provides a new tool to understand ZnO surface states and Schottky barrier formation. I. D.R. Douth, H.L. Mosbacher, G. Cantwell, J. Zhang, J.J. Song, and L.J. Brillson, "Impact of near-surface defects and morphology on ZnO luminescence," *Appl. Phys. Lett.* 94, 042111 (2009).

2:50 PM

FF5, Stoichiometry Dependent Incorporation and Electrical Activity of Zn Interstitials in Homoepitaxial ZnO Thin Films: *Alexander Lajn*¹; H. von Wenckstern¹; G. Benndorf¹; C. Dietrich¹; M. Brandt¹; G. Biehne¹; H. Hochmuth¹; M. Lorenz¹; M. Grundmann¹; ¹Universität Leipzig

We find that the incorporation and the electrical activity of Zn interstitials in homoepitaxial ZnO thin films depend on the stoichiometry of the film, which is tuned during growth by the oxygen partial pressure. Four ZnO thin films ($d \sim 1$ 956nm) were grown by pulsed-laser deposition at 650°C on Crystec (000-1)-ZnO substrates at oxygen partial pressures of 0.1 mbar, 0.016 mbar, 0.002 mbar and 0.0003 mbar, respectively. Atomic force microscopy revealed for all samples a high morphological quality. The surfaces exhibit atomically flat terraces with bi-layer steps of height $c/2$. X-ray diffraction measurements (XRD) showed that all samples grow lattice matched. However, the c -lattice constant is in tendency larger for lower oxygen partial pressures as indicated by a shift of the ZnO (0002) reflection towards lower angles. Therefore only the two films grown at the highest pressure are unstrained. Photoluminescence spectra at $T = 4$ K stem from the thin film and substantiate the trend observed in the XRD measurements. The two thin films grown at the two lowest pressures exhibit a higher band gap than the two unstrained films as indicated by the change of the spectral position of the transition I_{6a} . In particular the sample with the highest c -lattice constant shows the largest shift of the band gap. Besides the c -lattice constant and the band gap, the relative intensities of the I_{6a} and the I_{3a} transitions depend on the oxygen partial pressure. This confirms the change of stoichiometry for the different growth conditions; it does, however, not simply follow the trends observed for the c -lattice constant and the band gap. The intensity ratio of the transitions I_{6a} and I_{3a} is maximal for the sample grown at 0.016 mbar. Further the free exciton transition is only observed for this sample. From this we conclude that for this sample the deviation from the ideal stoichiometric ratio is least. Generally the separation of the electrical properties of the ZnO substrate and the ZnO thin films is nontrivial. By means of thermal admittance spectroscopy we control the depth of the probing volume by the applied dc bias. The reproducible formation of rectifying contacts on homoepitaxial thin films permitted us to characterize the defect level parameters of the homoepitaxial thin films. In contrast to the photoluminescence result the zinc interstitial is only observed for the films grown at the two lowest pressures. This implies that the Fermi level is below the level of the zinc interstitial for the samples grown at the two highest pressures and is explained by an increased compensation. In summary we present a comprehensive and consistent study correlating morphological, structural, optical and electrical properties of homoepitaxial zinc oxide thin films.

3:10 PM Break

3:30 PM

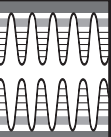
FF6, Defects at Oxygen Plasma Cleaned ZnO Polar Surfaces: *Yufeng Dong*¹; Z.-Q. Fang²; David C. Look²; D. R. Douth¹; R. Adur¹; M. J. Hetzer¹; Leonard J. Brillson¹; ¹Ohio State University; ²Wright State University

ZnO with its large band gap and exciton binding energy has numerous applications and has attracted intensive investigations. Despite the long research history and the number of studies on ZnO, many fundamental issues remain unresolved. The difficulty to dope p-type ZnO has been attributed to the compensation of native defects. Oxygen vacancies (V_{O}), Zn interstitials and hydrogen have been suggested as the origin of native donors in ZnO, while Zn vacancies (V_{Zn}) were considered as an acceptor. Our previous studies on ZnO surfaces and interfaces have revealed the important role of polarity, surface adsorbates, near surface native defects, and thermally induced interface chemical interactions, on the electrical and optical properties of single crystal ZnO and related devices.[1] However, the origin of deep level emissions, the role of native defects and their correlation with optical and electrical properties are still subjects of controversy. In particular, there are few studies on the polarity dependence of such native defects and their correlation with ZnO physical properties. We used depth-resolved cathodoluminescence spectroscopy (DRCLS), IV and CV measurements, AFM, SIMS, and deep level transient spectroscopy (DLTS) to probe the physical properties of surface and near surface defects at (0001) Zn- and (000-1) O- polar surfaces of remote oxygen plasma (ROP) cleaned ZnO. ROP provides a means to remove surface adsorbates, subsurface hydrogen, and native point defects. However, continued ROP produces striking polarity-dependent effects on both native defect concentrations and sub-surface carrier concentrations. It decreases 2.5 eV green emission on both faces but extended ROP generates a new surface 2.1 eV defect emission on the Zn face. Our previous CL study on metal-oxygen interface reactions revealed the correlation of 2.5 eV emission with VO, while our most recent study combining DRCLS and positron annihilation spectroscopy (PAS) related 2.1 eV emission with V_{Zn} . [2] With the introduction of 2.1 eV emission on the Zn face after ROP, the corresponding surface carrier profile and E3 trap profile were decreased. Clearly, the generation of V_{Zn} on the Zn face acts as compensating acceptors, resulting in lower near-surface electron concentration and higher Schottky barriers. No impurity-related polarity-dependence was found by SIMS and we attribute the polarity-related differences to native defects. We conclude that ROP cleans both polar surfaces but extended ROP of the Zn-face generates new V_{Zn} which results in significant optical and electrical polarity-dependences. Our findings demonstrate the importance of polar effects and ROP on forming surface and near-surface defects that control the physical properties of ZnO. In particular, the role of Zn vacancies may provide insight into methods of compensating n-type donors in order to achieve p-type doping. (1. Y. Dong et al., *APL* 93, 072111 (2008). 2. Y. Dong, A. Yu. Kuznetsov, and L. J. Brillson, unpublished.)

3:50 PM

FF7, Atomistic Structure of Dislocations in ZnO Revealed by Opto-TEM and PL Spectroscopy: *Yutaka Ohno*¹; Toshinori Taishi¹; Ichiro Yonenaga¹; Katsushi Fujii¹; Hiroki Goto¹; Takafumi Yao¹; ¹Tohoku University

Defects inducing long-range strain fields, as dislocations, are of considerable importance in semiconductor electronics, since they are frequently introduced during crystal growth and device fabrication, and affect the electronic properties of semiconductor devices. Recently, ZnO is expected for UV light-emitting devices and is supposed that dislocations are more easily introduced than GaN and SiC. However, the nature of the electronic properties of dislocations in ZnO has not been fully elucidated. This paper reports photoluminescence (PL) and optical measurements in a transmission electron microscope (opto-TEM) study of the dislocations in ZnO freshly induced by plastic deformation. Wurtzite ZnO bulk single-crystals were compressively deformed at elevated temperatures 923 - 1123 K to introduce an arbitrary number (typically 10^9 - 10^{10} cm⁻²) of fresh dislocations with the Burgers vector of $a/3\langle 1120 \rangle$. Deformed specimens showed excitonic PL light emission with photon energies of 3.100 and 3.345 eV, as well as their LO phonon replicas at 11 K, and the light intensities increased with increasing dislocation density. The activation energy for a thermal quenching of the 3.100 or 3.345 eV emission band, which corresponds to the depth of



the localized energy level associated with the emission band, was estimated to be 0.3 or 0.05 eV, respectively. The origin of the energy levels was proposed as point defect complexes involving mixed dislocations. The introduction of the dislocations at the elevated temperatures above 923 K did not influence the intensities of the emission bands except the dislocation-related emission bands. TEM under light illumination and CL spectroscopy combined with light illumination revealed that a screw dislocation, presumably acting as non-radiative recombination center, glides under the illumination of a monochromatic light with photon energy above 2.36-2.48 eV, at temperature of 110 K. Since the threshold energy was lower than the band gap energy (about 3.38 eV at 110 K), the glides would take place due to an electron-hole recombination [4] at a defect level of 0.90-1.02 eV depth. When screw dislocations glided, the intensity of the green and yellow emission, which is associated with vacancies, increased. Since the introduction of vacancies by the irradiation of 80-keV electrons for TEM could be negligible, the recombination activity around screw dislocations would be modified by the dislocation glide. One possible explanation is that, a screw dislocation converts into a mixed dislocation acting as radiative recombination center, or that acting as non-radiative recombination center with low recombination activity in comparison with the screw dislocation.

4:10 PM

FF8, Electrical Characterization of Defect Levels in $Mg_xZn_{1-x}O$ PLD Thin Films: *Holger von Wenckstern*¹; Kerstin Brachwitz¹; Matthias Schmidt¹; Florian Schmidt¹; Stefan Müller¹; Christoph Dietrich¹; Jan Zippel¹; Martin Ellguth¹; Michael Lorenz¹; Marius Grundmann¹; ¹Universität Leipzig

We investigated the formation and the energy position of defect levels with respect to the conduction band minimum E_c of $Mg_xZn_{1-x}O$ thin films in dependence on x . The alloying of ZnO by Mg leads to an increase of the band gap, therefore $Mg_xZn_{1-x}O$ layers are commonly used as barrier material for ZnO quantum wells. The electronic properties of $Mg_xZn_{1-x}O$ have been studied in detail for a wide range of compositions mainly using low temperature luminescence measurements [1]. In contrast electrical properties of $Mg_xZn_{1-x}O$ thin films, like the dependence of the thermal activation energy E_t of effective mass donors and deep levels or of the barrier height of Schottky contacts on the magnesium content were not investigated systematically up to now.
 We present a detailed and comprehensive investigation of $Mg_xZn_{1-x}O$ thin films for $0 < x < 0.5$. All samples were grown heteroepitaxially on a-plane sapphire substrates by pulsed-laser deposition. Selected samples were annealed ex-situ for two hours in 700 mbar oxygen at 500°C, 700°C, and 900°C, respectively. The samples were investigated by X-ray diffraction, atomic force microscopy, cathodoluminescence and photoluminescence (PL). The magnesium content in the thin films was determined by using PL and Rutherford backscattering spectroscopy, respectively. Schottky contacts were realized by reactive de-sputtering of Pd [1]. As ohmic contact we used a degenerately doped ZnO:Al layer deposited prior to the $Mg_xZn_{1-x}O$ layer allowing a front-to-back contact geometry [2]. This ensures a low series resistance of the resulting Schottky diodes allowing space charge spectroscopic methods with test frequencies of 1 MHz and above. The Pd/ $Mg_xZn_{1-x}O$ Schottky diodes were characterized at room temperature by current-voltage measurements, capacitance-voltage and admittance spectroscopy in dependence on x and the annealing. Further, we applied thermal admittance spectroscopy, deep level transient spectroscopy (DLTS) and for selected samples Laplace DLTS. Typical DLTS and admittance results show that the thermal activation energy of the E3 defect increases from 300 meV for $x=0$ to about 405 meV for $x=0.09$. We further observed a decrease of the defect emission rates τ_n with increasing annealing temperature. [1] A. Müller, G. Benndorf, S. Heitsch, C. Sturm, M. Grundmann, *Solid State Comm.* 148, 570 (2008). [2] A. Lajn, H. von Wenckstern, Z. Zhang, C. Czekalla, G. Biehne, J. Lenzner, H. Hochmuth, M. Lorenz, M. Grundmann, S. Künzel, C. Vogt, R. Deneke, *J. Vac. Sci. Technol.*, in press. [3] Holger von Wenckstern, Gisela Biehne, R. Abdel Rahman, Holger Hochmuth, Michael Lorenz, and Marius Grundmann, *Appl. Phys. Lett.* 88, 092102 (2006).

4:30 PM Student

FF9, Effect of Post-Deposition Processing on ZnO Thin Films: *Tingfang Yen*¹; Michal DiNezza¹; Alan Haungs¹; Sung Jin Kim¹; Alexander Cartwright¹; Wayne Anderson¹; ¹SUNY-Buffalo

Zinc oxide thin films are useful for several applications including optical coatings and ultraviolet photodetectors. We have explored the effects of post-deposition processing on ZnO thin films deposited by MOCVD or by RF magnetron sputtering. The processing can be a detriment or an enhancement to ultimate applications. Photoluminescence (PL) data were taken for MOCVD-deposited films with processing by oxygen plasma¹, by H₂O₂ surface treatment² (to improve Schottky contact), and rapid thermal anneal (RTA) (to improve electronic properties). RTA gave a reduced FWHM signal as an improved response whereas the other treatments increased the defect PL signal. RF magnetron deposition was conducted in a gas atmosphere of nitrogen, oxygen and argon on an unheated substrate. RTA and ion implantation followed by RTA gave increased conductivity and the latter increased Hall effect mobility from 1.7 to 9.5 cm²/V.s. Metal-semiconductor-metal (MSM) photodetectors were fabricated from RF magnetron-sputtered films using Au or Yb/Au metals with a grid pattern having 2 μm spacing and 6 μm metal width. Nitrogen ion implantation treatment followed by RTA gave the lowest dark current, highest ratio of photo to dark current and highest responsivity of 2.7 A/W using a quartz-halogen illumination. Samples with the ZnO just annealed gave the highest dark and photo-currents. Current transport mechanisms were examined using semi-log and log-log plots. Most films exhibited two primary conduction mechanisms following I~V^m. From 4-8 volts, m= 4.1-4.9 indicating space charge limited current with multiple trapping levels whereas the higher voltage region gave m<1 indicating a more ohmic type behavior where photo-IV curves are nearly horizontal as collection of photo-carriers is nearly complete. The non-annealed ZnO film showed only the one mechanism with m<1 in photo-IV over the entire voltage range indicating excellent carrier collection due to a high built-in electric field, and m~1 in dark-IV suggesting the presence of either the space charge limited current (SCLC) in the velocity saturation regime or tunneling. Response to a fempto-second pulse gave rise and fall times in the range of 12-29 ns for the 4 cases under study. Ion implanted and tube furnace annealed cases gave the lowest rise and fall times. References: 1. H. von Wenckstern, G. Biehne, R. A. Rahman, H. Hochmuth, M. Lorenz, and M. Grundmann, *Applied Physics Letters* 88, 3 (2006). 2. R. Schifano, E. V. Monakhov, U. Grossner, and B. G. Svensson, *Applied Physics Letters* 91, 3 (2007).

4:50 PM Student

FF10, Characterization of Channel/Dielectric Interfacial Trap States in ZnO-Based Thin-Film Transistors by Spectral Response Analysis: *Kimoon Lee*¹; Min Suk Oh²; Gyubaek Lee¹; Chan Ho Park¹; Seongil Im¹; Chi-Sun Hwang³; Sang-Hee Park³; ¹Yonsei University; ²Korea Electronics Technology Institute (KETI); ³Electronics and Telecommunications Research Institute (ETRI)

Oxide-based thin-film transistors (TFTs) have attracted much attention over the last several years because of their great potential toward display drivers and even future electronics integrated on glass. To understand and improve the electrical characteristics of such a device, it is essential to clarify the defect states especially on the channel/dielectric interface, but techniques to characterize that have been rarely reported yet. Now, the authors report on the novel method for characterization of interfacial trap states with ZnO-based TFTs by spectral response analysis. To fabricate the transparent ZnO-based TFTs, an ITO glass was used for the substrate. After source/drain patterning of ITO by wet etching, ZnO semiconductor film was deposited by means of plasma-enhanced atomic layer deposition (PEALD) at the temperature of 200 oC. A 9 nm-thin Al₂O₃ was initially deposited on ZnO channel as a protection layer and the first gate insulator as well by means of ALD with water vapor and trimethylaluminum (TMA) precursor at 200 oC. The ZnO channel with the initial thin Al₂O₃ dielectric was patterned at once by wet etching using diluted HF solution. Then a 159 nm-thick Al₂O₃ was deposited over the active layer with thin first dielectric as second gate insulator at the temperature of 150 oC by means of ALD using TMA and water. The transparent gate electrode consisting of ZnO/Ag/ZnO (sheet resistance of ~4 ohm/square) was deposited with thickness

of 100 nm, followed by patterning with wet etching. When we measure the transfer characteristics of our ZnO-TFT in dark, we can observe the good electrical performance ($\mu\text{sat} \sim 4 \text{ cm}^2/\text{Vs}$, on/off current ratio $\sim 10^7$, and $V_{\text{th}} \sim 0 \text{ V}$) without any observable gate bias-induced hysteresis behavior. However, with an intense monochromatic illumination ($> 10^{16} \text{ photons cm}^{-2}\text{sec}^{-1}$) on the device, the V_{th} starts to shift negatively because the electrons trapped at the ZnO/dielectric interface are released by the optical illuminations. When the illumination energy corresponds to or overcomes the trap level, thus the V_{th} shift as large as the number of density of state (DOS). (Detailed mechanism and analysis will be shown in the meeting.) From these spectral response characteristics of ZnO-TFT, we can clarify and quantify simultaneously the origin of interfacial states on ZnO channel/Al₂O₃ dielectric interface: Oxygen vacancy (Vo), Zn anti-site (Zno), and Oxygen interstitial (Oi) which can be exited from the level of ~ 1.2 , ~ 1.5 , and $\sim 1.76 \text{ eV}$ below the conduction band level with a density of $\sim 1.25 \times 10^{13}$, $\sim 1.31 \times 10^{13}$, and $\sim 1.17 \times 10^{13} \text{ eV}^{-1}\text{cm}^{-2}$, respectively. As a result, we conclude that this methodology of photo-electric spectral analysis is one of novel techniques to measure the characteristics of channel/dielectric interface traps in most of TFTs that expose their channel/dielectric interface to light in device structure.

5:10 PM FF11, Late News

Session GG:

Organic Thin Film and Crystalline Transistors: Devices, Materials and Processing II

Thursday PM
June 25, 2009

Room: Deans Hall II
Location: Pennsylvania State University

Session Chairs: Michael Chabynyc, University of California, Santa Barbara; Alberto Salleo, Stanford University

1:30 PM Invited

GG1, Time-Resolved Electric Force Microscope Studies of Long-Lived Charge Traps in Functionalized Pentacene and Anthradithiophene Transistors: Michael Jaquith¹; Justin Luria¹; John Anthony²; *John Marohn*¹; ¹Cornell University; ²University of Kentucky

We have used time-resolved electric force microscopy to study charge trapping in two pentacene derivatives that have gained considerable attention in thin-film transistor applications – 6,13-bis(tri-isopropylsilyl)ethynyl pentacene (TIPS pentacene) and triethylsilyl ethynyl anthradithiophene (TES ADT). We believe these studies are the first time that long-lived charge traps have been directly imaged in films of either of these molecules. The spatial distribution of long-lived trapped charge was examined in TIPS pentacene, for transistors prepared by four different solution-deposition techniques. The trapped charge distribution is markedly different in the four samples, establishing that charge trapping in this material is at least as sensitive to morphology as is mobility. The rate of trap formation in TIPS pentacene depends strongly on the initial free hole concentration, consistent with the view that charge traps in this material should not be viewed as static defect states but as states that are slowly created by reactions of free holes at a localized defect. In one TIPS pentacene sample, the rate of formation and steady-state concentration of trapped charge was found to be independent of the initial free hole concentration, allowing us to estimate the concentration of the impurity giving rise to the trapped charge. Taken together, our data suggests that the chemical reaction of an inhomogeneously-distributed impurity is a likely source of the long-lived charge traps seen in our TIPS pentacene transistors. Transistors of functionalized anthradithiophene were also prepared, by spin casting and solvent annealing. Transistors made from TES ADT showed evidence of grain boundary trapping. Previous studies have examined the stability of photoexcited TIPS pentacene and TES ADT, leaving the stability of cation radicals (e.g., free holes) in thin films of these compounds largely unaddressed. Our finding that in both materials, regions can be found which exhibit essentially no long-lived traps, indicates that cations of the two materials are not inherently prone to trapping and degradation in an

unilluminated film. We find that electrons can be injected from untreated gold electrodes into both materials, and in both materials we observe a finite electron mobility.

2:10 PM

GG2, Controlled p-Doping of Organic Wide Band Gap Materials with Molybdenum Trioxide: *Michael Kroeger*¹; Sami Hamwi²; Jens Meyer²; Thomas Riedl²; Wolfgang Kowalsky²; Antoine Kahn¹; ¹Princeton University; ²Technische Universität Braunschweig

P-doping of organic large band gap materials with molybdenum trioxide is demonstrated. Organic electronic devices are often limited in device performance due to low intrinsic charge carrier densities and high charge injection barriers at the electrode interfaces. It was already shown, that electrochemical doping of molecular or polymeric thin films is a suitable strategy to overcome these limitations. [1] For certain applications, materials with a large band gap are favorable or even necessary. In these applications carbazole-based molecules like 4,4'-Bis(N-carbazolyl)-1,1'-biphenyl (CBP) were employed. So far, p-doping of these materials was rather inefficient due to their high ionization energy (CBP: 6.2 eV), resulting in a need for high doping concentrations and an only insignificant increase of the electrical conductivity upon p-doping with F4-TCNQ. [2] The electronic structure of MoO₃ thin films exhibits extremely low-lying energy levels, giving an electron affinity (EA) of 6.7 eV and IE of 9.7 eV. Electron transfer from the highest occupied molecular orbital (HOMO) CBP to the acceptor state of MoO₃ is therefore likely. When studying the electronic structure of MoO₃-doped CBP thin films via UPS, a rapid shift of the Fermi level towards the HOMO states becomes visible. This shift is attributed to an increase of excess hole carriers. For doping concentrations higher than 2 mol%, Fermi level pinning occurs at about 500 meV above the HOMO edge. I-V measurements on single-carrier devices confirm a dramatic increase in conductivity upon p-doping. The conductivity increase shows a significant smaller slope for doping concentrations higher than 2 mol%. By correlating UPS results and I-V measurements, we explain our experimental results by modeling the density of states (DOS) as a Gaussian distribution, leading to a significant tail states density above the HOMO edge. Depopulation of these tail states leads to the observed Fermi pinning. [1]K. Walzer, B. Maennig, M. Pfeiffer, K. Leo, Chemical Reviews 2007, 107, 1233.[2]J. Meyer, S. Hamwi, S. Schmale, W. T., H. H. Johannes, T. Riedl, W. Kowalsky, Journal of Materials Chemistry 2009.

2:30 PM Student

GG3, New Fluorinated Anthradithiophene Derivatives: *Marsha Loth*¹; Sean Parkin¹; John Anthony¹; Marina Feric²; Oana Jurchescu²; David Gundlach²; Thomas Jackson³; ¹University of Kentucky; ²National Institute of Standards and Technology; ³Pennsylvania State University

Solution processability is one of the key advantages to organic thin film transistors (TFTs). Our group has previously published the synthesis of the stable fluorinated acene 2,8-Difluoro-5,12-bis(triethylsilyl)ethynyl anthradithiophene (F TES ADT) in a mixture of syn and anti conformations. Although isomeric mixtures are purported to yield low-mobility thin films, these heteroacenes have shown thin film mobilities as high as 1.5 cm²/Vs as well as the ability to self-pattern based on rapid film formation. Poor reproducibility and low scalability in the original synthesis method, a result of low fluorination yields, led us to consider alternative approaches to this material. Fluorination in particular is improved by our new method, significantly reducing the cost to produce the material. As a result of the improved synthesis, new fluorinated ADT derivatives were synthesized which allow us to explore further applications such as solar cells by changing the crystalline packing. These derivatives were also made to improve processability while still retaining the desired interactions for transistors. Single crystal and thin film transistor studies will further elucidate the affect of the alkyl silyl substituents. Work is also in progress to synthesize the isomerically pure anti isomer of this heteroacene, to determine the effect of isomeric purity on film formation and overall device performance.

2:50 PM Student

GG4, Investigations of Charge Transport and Bias Stress in Anisotropic Polythiophene Thin Films Fabricated via Directional Crystallization: *Leslie Jimison*¹; Michael Toney²; Ian McCulloch³; Martin Heeney⁴; Alberto Salleo¹; ¹Stanford University; ²Stanford Synchrotron Radiation Laboratory; ³Imperial College of London; ⁴Queen Mary University of London

Recent developments in the performance of organic semiconductors are proving that these materials have the potential to make a significant impact in the field of macroelectronics. Fabrication of large area devices such as transistor arrays for display backplanes, light emitting diode arrays, and large area photovoltaic cells benefit from the possibility of solution processing and patterning on flexible substrates. As organic semiconductors approach commercialization, there is a need to better understand the relationship between charge transport and microstructure, in particular, to identify the inherent bottlenecks to charge transport. We have used a means of controlling the orientation and size of crystallites in the plane of the substrate to produce films with well-known grain-boundary types. As a result we are able to explore the relationship between trap density within grain boundaries and charge transport. Regioregular poly-3-hexylthiophene (P3HT) is the material under investigation. We have fabricated anisotropic films on glass and silicon substrates via directional solidification, using 1,3,5-trichlorobenzene first as a solvent and then as a substrate for epitaxy. This technique enables us to create films consisting of large (mm²) domains of uniform extinction under crossed polarizers, suggesting long-range orientation of the polymer chain axis. Film microstructure was characterized at the Stanford Synchrotron Radiation Laboratory (SSRL). X-ray diffraction experiments confirm the unique in-plane and out-of-plane texture of the polymer films. Atomic force microscopy reveals a lamellar microstructure within the polymer films. Charge transport in the directionally crystallized films was characterized using thin film transistors with the oriented film as the active layer. Devices were made with different relative orientations between the channel and the polymer film. Transport measurements as a function of charge density and temperature for different orientations of the film confirm mobility anisotropy but no activation energy anisotropy. Furthermore, we investigate room temperature bias stress by measuring the decay of drain current under constant stress, as well as the recovery of the device on the release of stress. Initial results suggest that bias stress behavior is dependent on device orientation. Because these films are anisotropic with respect to the type of grain boundary present, dependence of bias stress on device orientation strongly suggests that bias stress in semicrystalline organic thin films is dependent on the microstructure at the grain boundaries.

3:10 PM Break

3:30 PM Student

GG5, The Effect of Polydispersity on Intermolecular Packing in π -Stacking Conducting Polymer Systems: *Tomasz Young*¹; Rui Zhang¹; Jessica Cooper¹; Courtney Balliet¹; Richard McCullough¹; Tomasz Kowalewski¹; ¹Carnegie Mellon University

Regioregular poly(3-hexylthiophene) (rr-P3HT) has been extensively studied since it was first synthesized. The conjugated structure of rr-P3HT backbone and the overlap of π orbitals of adjacent chains facilitate efficient charge transport with hole mobility as high as $\mu = 0.1 \text{ cm}^2/(\text{V}\cdot\text{s})$. Recent progress in the controlled synthesis of rr-P3HT opened the way to the synthesis of narrow polydispersity materials, which, in turn, were demonstrated to form highly uniform nanofibrillar structures, with the width of the nanofibrils directly correlated with the polymer chain length. Moreover, charge carrier mobility in nanofibrillar rr-P3HT has been shown to increase exponentially with the nanofibril width. In this presentation we will demonstrate that, in addition to being dependent on the polymer chain length, nanofibril width can be strongly affected by the polymer chain end groups and by the presence of low-molecular weight additives. Highly uniform thin films of rr-P3HT films were fabricated with the aid of custom-built deposition chamber allowing one to control the key film deposition conditions such as solvent evaporation rate, temperature and humidity. Such prepared films were then characterized through the combination of phase contrast atomic force microscopy (AFM) and grazing incidence small angle x-ray scattering (GISAXS). In all cases

AFM images revealed the presence of uniform, elongated, locally parallel nanofibrils extending over the length of tens of micrometers. GISAXS patterns revealed the presence of distinct scattering peaks, position of which was in a good agreement with the position of the maxima in two-dimensional Fourier transforms of AFM images, corresponding to the nanofibril widths. Remarkably, the average fibril widths determined from AFM images and GISAXS patterns varied by as much as $\pm 20\%$ with the chemical modification of rr-P3HT chain ends. Systematic nanofibril width variation of the similar magnitude was also observed upon introduction of certain low molecular weight additives. Based on these observations, we propose that the strong phase contrast observed in AFM images is rooted in more pronounced energy dissipation in less-densely packed (or quasi-amorphous) interfibrillar regions in comparison with more crystalline cores. Such difference in packing density can be also used to explain the origin of scattering peaks in GISAXS patterns. We will present the model explaining how chain-end modification and/or introduction of additives can affect the intermolecular interactions in the boundary regions, changing the effective nanofibril width. Possible impact of these effects on the performance of rr-P3HT based devices will be also discussed.

3:50 PM

GG6, Halogen Substitution to Improve Crystal Packing and Performance of Soluble Organic Semiconductors: *John Anthony*¹; Balaji Purushothaman¹; Ying Shu¹; Sankar Subramanian¹; Thomas Jackson²; Sung Kyu Park²; David Gundlach³; Oana Jurchescu³; Marina Feric³; ¹University of Kentucky; ²Pennsylvania State University; ³National Institute of Standards and Technology (NIST)

Our work on the solubilization of chromophores for organic electronic applications has found application in both carbocyclic and heterocyclic linearly-fused hydrocarbons, and has led to the development of structure-property relationships for the design of materials for both thin-film transistors and photovoltaic devices. Critical to these relationships is the link between backbone substitution and crystal packing, which yields control over intermolecular electronic coupling and thin-film morphology of the materials. Using our functionalization strategies, we have been able to design high-performance transistor materials from both pentacene and anthradithiophene chromophores. However, there are still numerous issues to address for the commercial viability of organic semiconductors. Bulk properties such as film morphology and crystallization rate are important to control for high-throughput processing methods. Molecular issues such as HOMO or LUMO energies are important for tuning electrode interfaces and improving semiconductor stability. The most straightforward approach to tuning properties of these crystal-engineered acenes relies on the addition of further functionality. However, great care must be taken to insure these new substituents do not detrimentally disrupt the carefully engineered crystal packing of the materials. Thus, the added groups must be quite small, with significant influence on electronic properties at low loadings. We have chosen halogen substituents to fulfill these requirements for a number of reasons. In general, the halogen substituents are small (certainly smaller than the simplest organic substituent, the methyl group). Their high electronegativity generally yields significant shifts in HOMO and LUMO energy, typically without significantly affecting the HOMO-LUMO gap. More importantly, halogens serve as solid-state synthons, where halogen-bonding or halogen-halogen interactions can be used to subtly alter crystal packing, to increase crystallization speed, or to enhance interactions with treated substrates. This presentation will cover a number of case studies on the effect of partial halogenation on the device application of linearly-fused soluble aromatic compounds. In the case of smaller acenes, halogenation leads to dramatic improvement in π -stacking interactions, leading to high stability molecules with reasonable performance in spin-cast organic transistors. The next higher homologs of acenes - the pentacenes and anthradithiophene, require only minimal halogen substitution to improve processing characteristics. Fluorinated anthradithiophene yields high-performance transistors, while brominated and chlorinated derivatives show significantly decreased performance. Trends in the corresponding dihalo pentacenes will also be presented. Hexacenes, the next higher acene class, are typically so unstable that very little is known of their thin-film or semiconducting properties. We have found that the strategic addition of halogen substituents to these systems increases stability to the point

that they can be studied in thin-film form. Our latest findings on this new class of semiconductor chromophore will be presented.

4:10 PM Student

GG7, Transport Anisotropy in Films of Organic n-Type Semiconductor with Controlled in-Plane Grain-Boundary Orientation: *Jonathan Rivnay*¹; Leslie Jimison¹; Michael Toney²; Antonio Facchetti³; Alberto Salleo¹; ¹Stanford University; ²Stanford Synchrotron Radiation Laboratory; ³Polyera Corporation

Solution processable small molecule organic semiconductors have gained interest due to their potential low cost processing and field effect mobilities nearing that of their vapor deposited, non-soluble counterparts. Unfortunately, pristine films of soluble small molecules suffer from poor thin-film transistor device-to-device reproducibility (mobility, V_T and stability) due to the existence of grain-boundaries that are not uniformly distributed throughout the film. The effect of grain boundaries in thin films of small molecule semiconductors is relatively large compared to that of semicrystalline polymer devices for two reasons: the grain size is often on the order of the channel length preventing averaging effects and boundary regions between grains are more abrupt. Indeed, in semicrystalline polymer films, a single chain can bridge two or more adjacent crystallites, facilitating transport through amorphous-like regions/grain boundaries. Research should thus focus on understanding of the relationship between microstructure and charge transport in order to design devices that do not necessarily eliminate grain boundaries, but limit their penalty on electrical performance, while also allowing for lower device-to-device variability. To this end, in this work we use anisotropic films of the n-type small molecule *N,N'*-bis(*n*-octyl)-(1,7&1,6)-dicyanoperylene-3,4:9,10-bis(dicarboximide), (PDI8-CN₂) to explore the effect of grain boundaries on field effect mobility, and understand their implication in charge transport in thin films. In-plane orientation and morphology are characterized with x-ray diffraction and polarized light microscopy. Thin film transistors (TFTs) were made to probe transport as a function temperature across two types of grain-boundaries that are formed. These PDI8-CN₂-based TFTs exhibit a mobility anisotropy of 72 depending on the relative orientation of the grains with the current flow. Parallel devices, with charge transport parallel to the film growth direction show room temperature mobilities near ~ 0.01 cm²/Vs ($E_A=120$ meV), near that of isotropic solution cast films. Perpendicular devices, on the other hand, show low mobilities of $\sim 10^{-4}$ cm²/Vs ($E_A=300-600$ meV). The difference between the two orientations is much larger than the anisotropy associated with single crystal transport. Though the exact nature of grain boundaries in the orthogonal direction are not well understood we postulate that they are host to large energetic barriers owing to high angle grain boundaries, where molecules in adjacent grains are greatly misoriented.

4:30 PM

GG8, Functionalized Tetrafluorotetracenes: Synthesis and Characterization of New Materials for OTFTs: *Adolphus Jones*¹; Oana Jurchescu²; Marina Feric²; David Gundlach²; John Anthony¹; ¹University of Kentucky; ²National Institute of Standards and Technology

Significant effort has been directed towards organic electronic materials which are easily purified, simply processed, and yield high-performance devices. The acene family, in particular functionalized pentacenes, has demonstrated considerable success achieving those goals. Silylethynyl-functionalized pentacenes have shown high field-effect mobility in transistors, and reasonable performance in organic photovoltaic devices. As part of our further exploration of acenes for organic electronics, we have developed a functionalization strategy for a lower acene homolog, tetracene. Organic field effect transistors have been developed using tri-alkyl-silylethynyl tetrafluorotetracenes. Trimethylsilyl, triethylsilyl, triisopropyl, and tri-*n*-propylsilyl acetylenes were added to tetrafluoroquinone to give the desired molecules. All molecules show 2-D π stacking in the solid state, as expected from fluorinated acenes. The electronic properties of the molecules were also characterized electrochemically with band gaps of ~ 2.3 eV. Bottom contact TFT devices were produced via spin-casting onto gold source and drain electrodes. The triethylsilyl derivative gave the best results having a field effect mobility of 0.042 cm²/Vs.

4:50 PM Student

GG9, Light-Induced Trap Release Probed in Polycrystalline Pentacene Films by Time-Resolved Electric Force Microscopy: *Justin Luria*¹; John Marohn¹; Michael Jaquith¹; ¹Cornell University

Pentacene is a leading candidate for many organic electronics applications, yet even in this comparatively well studied material, charge trapping is poorly understood. Northrup and Chabincyc [1] have considered defects in bulk pentacene that could be created by reactions of hydrogenated and oxygenated pentacene with holes. In single crystal pentacene, D.V. Lang *et al.* [2] have used space-charge-limited current measurement to identify a trap in pentacene that is tentatively consistent with one of the defect candidates of Northrup and Chabincyc. Yet Lang's defect showed a number of puzzling behaviors, including that trapping could be quickly reversed by application of light. Jaquith *et al.* [3] have studied defect formation in thin-film transistors of polycrystalline pentacene. They find a trap formation rate that is dependent on hole concentration, consistent with traps forming by chemical reaction. Yet Jaquith *et al.*'s spatial distribution of traps is highly inhomogeneous, implying that trapping cannot be explained as due to a uniformly-distributed chemical impurity, as in the model of Northrup and Chabincyc. We have developed a general approach to illuminating samples (from above) in an electric force microscope using a fiber-optic cable. We will describe our efforts at using variable-wavelength light to clear traps in polycrystalline pentacene transistors and to follow the trap clearing with high spatial resolution using electric force microscopy. [1] J.E Northrup and M.L. Chabincyc, *Phys. Rev. B* **68**, 041202 (2003). [2] D.V. Lang, *et al.*, *Phys. Rev. Lett.* **93**, 076601 (2004). [3] M.J. Jaquith, E.M. Muller, and J.A. Marohn, *J. Phys. Chem. B* **111**, 7711 (2007).

5:10 PM GG10, Late News

Session HH:

Spin-Dependent (or Spintronic) Electronic Materials

Thursday PM
June 25, 2009

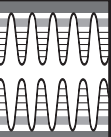
Room: 105
Location: Pennsylvania State University

Session Chairs: Xinyu Liu, University of Notre Dame; Bruce Wessels, Northwestern University

1:30 PM Invited

HH1, Efficient Room Temperature Spin Filter Based on a Non-Magnetic Semiconductor at Zero Magnetic Field: X. Wang¹; I. Buyanova¹; F. Zhao²; D. Lagarde²; A. Balocchi²; X. Marie²; C. Tu³; J. Harmand⁴; *Weimin Chen*¹; ¹Linkoping University; ²University of Toulouse; ³University of California; ⁴LPN

Generating electron spin polarization and coherence at room temperature is one of the most important as well as the most challenging issues for future spintronics and spin-based quantum information technology, which remains unresolved and has attracted intense global research efforts during recent years. Many approaches have been attempted with a varying degree of success. Spin filtering has been demonstrated by employing ferromagnetic metals, diluted magnetic semiconductors, quantum point contacts, quantum dots, carbon-nanotubes and multiferroics, etc., though so far unfortunately mostly with a limited efficiency and primarily at a low temperature or under applied magnetic fields. Here, we present and demonstrate a new approach for an efficient spin filter by defect-engineering of a non-magnetic semiconductor. Such a spin filter is shown to be capable of generating $>40\%$ electron spin polarization at room temperature without requiring external magnetic fields. We provide direct experimental proof for the exact physical mechanism leading to the observed spin filtering effect, i.e. an electron spin-polarized defect, such as a Ga self-interstitial in dilute nitride Ga(In)NAs, can effectively deplete conduction electrons with an opposite spin orientation and can thus turn the non-magnetic semiconductor into an efficient spin filter. The identification of the spin-filtering defects is unambiguously established by their unique spin-resonance signatures derived from the hyperfine interaction between the localized unpaired electron



spin and nuclear spins ($I=3/2$) of the Ga atom with two naturally abundant isotopes ^{69}Ga and ^{71}Ga . We demonstrate how the spin-filtering effects can be engineered by varying the concentration of the responsible defects, which can be achieved during the growth or by post-growth treatments. We also illustrate another attractive feature of this new approach - the spin direction of such spin filters is not fixed in real space but can easily be switched at will by orienting electron spins of the spin-filtering defect at a preferred direction. The present work has thus demonstrated the potential of such a defect-engineered, switchable spin filter as an attractive alternative to generate, amplify and detect electron spin polarization at room temperature without a magnetic material or external magnetic field, i.e. under the conditions desirable for practical device applications [1]. [1] X.J. Wang, I.A. Buyanova, F. Zhao, D. Lagarde, A. Balocchi, X. Marie, C.W. Tu, J.C. Harmand and W.M. Chen, *Nature Materials* (2009) in press.

2:10 PM

HH2, MCD Investigation on Mn Doped CdSe Quantum Ribbons: Xinyu Liu¹; Shaoping Shen¹; Kritsanu Tivakornasithorn¹; Jacek Furdyna¹; Margaret Dobrowolska¹; Jung Ho Yu²; Jin Joo²; Dong Won Lee²; Jae Sung Son²; Taeghwan Hyeon²; Jiwon Park²; Young-Woon Kim²; ¹University of Notre Dame; ²Seoul National University

Diluted magnetic semiconductors (DMS) are known for their strong magneto-optical effects induced by the *sp-d* exchange interaction between band electrons and magnetic (e.g., Mn) ions. During the past two decades, the preparation and characterization of DMS materials on the nanometer scale has grown rapidly, motivated by the fact that these novel structures provide not only new physics due to the quantum confinement but also a new method to fabricate exciting spintronic devices. In this work we discuss the properties of a series of CdSe:Mn nanoribbons synthesized via colloidal chemical route. Transmission electron microscope (TEM) images show that the CdSe:Mn²⁺ quantum ribbons have a highly anisotropic morphology with a uniform thickness of 1.4 nm, with widths ranging from 10 nm to 60 nm, and lengths of a few μm . The growth of these nano-ribbons occurred in the [0001] direction of the wurtzite structure, and the ribbons tend to be stacked into bundle-like aggregates parallel to the ribbon width held together by van der Waals forces. Magnetic circular dichroism (MCD) studies were used for investigating the Zeeman splitting in these one-dimensional (1D) quantum-confined DMS nanostructures. In all samples investigated a strong MCD signal was found at about 2.9 eV, which corresponds to the $1S_0-1S_0$ transition of the electronic absorption spectrum, indicating that the Zeeman splitting of the exciton occurs due to the strong *sp-d* exchange between the CdSe nanoribbon host and the incorporated Mn²⁺ ions. All MCD signals depend on the magnetic field and obey a modified Brillouin function. The Zeeman splitting energy ΔE calculated from the MCD signal increases as the Mn concentration increases, which clearly demonstrates that Mn²⁺ ions are indeed present in the CdSe nanoribbons. Additionally, the experimental results suggest the sign of the parameter of the *s-d* exchange interaction α in these nanoribbons is inverted (i.e., negative) due to an admixture of the valence band wave functions to the conduction band wave functions. We note that such modification of the exchange interaction is expected to be strong in small-size DMS-based quantum nanostructures. The negative sign of the exchange constant α leads to drastic changes in optical properties of these nano-ribbons: the ground exciton state in this case has the spin of +2 and is optically inactive.

2:30 PM

HH3, Multiple Magnetic States in Silicon Carbide Diluted Magnetic Semiconductors: Andrei Los¹; Victor Los²; Andrei Timoshevskii²; ¹Freescale Semiconductor Inc. and ISS. Ltd; ²Institute of Magnetism, National Academy of Science of Ukraine

Possibility to manipulate the electron spin has long been investigated as a foundation for future extremely low power amplifying devices, polarized light emitting diodes, highly sensitive magnetic field sensors, high density 3D magnetic memories, etc. Diluted magnetic semiconductors (DMS) are a class of materials where several percent of semiconductor host atoms are replaced by transition metal impurity. These materials possessing both semiconducting and ferromagnetic properties are expected to bring spin-electronic functionality to mainstream semiconductor technology. A world-wide search for DMS with

ferromagnetic ordering temperatures above room temperature is in progress and SiC, a semiconductor material with many unique properties, is considered a promising candidate for spintronics applications. We present results of a systematic study of magnetic states of first row transition metal impurities in SiC host, which were obtained using a highly accurate ab initio FLAPW calculation technique. We analyze the details of magnetic moments formation and of their change with the unit cell volume, as well as of the host lattice reconstruction due to impurity substitution. We also study the particulars of exchange interactions for different TM impurities and provide estimates of the magnetic ordering temperatures of SiC DMS. In particular, we show that transition metal impurities can exist in both magnetic and nonmagnetic states in SiC host matrix. For some impurities such as Cr, Mn, and Fe the magnetic state can be realized at an equilibrium lattice volume and it is separated by an energy gap from the nonmagnetic state, while for the other like Ni and Co magnetic moments are close to zero in equilibrium lattice and increase while the lattice is expanded. At zero temperature, the magnetic solution is energetically favorable in Cr- and Mn-doped SiC, while for Fe doping the nonmagnetic solution is favored. The energy gap between ferromagnetic and nonmagnetic solutions varies from impurity to impurity, being comparable to thermal energy at room temperature for Mn and Fe, and somewhat larger for Cr. We argue that at a nonzero temperature the relationship between the solutions can change due to the free energy entropy term. Furthermore, we speculate that a mix of the magnetic and nonmagnetic states is possible, which would change the average magnetic moment of the system and self-consistently its magnetic order. Impurity substitution leads to a significant host SiC lattice reconstruction in all cases except when Mn and Fe are in their nonmagnetic states, in which case the atomic positions are very close to those in pure SiC. It was found that Fe atoms in their magnetic state order antiferromagnetically, while Cr and Mn prefer ferromagnetic ordering. The values of magnetic moments, magnetic moment ordering strength and range vary significantly across the range of impurities studied.

2:50 PM HH4, Late News

3:10 PM Break

3:30 PM Invited

HH5, Antiferromagnetic Interlayer Exchange Couplings in Ga_{1-x}Mn_xAs/GaAs Diluted Ferromagnetic Semiconductor Multilayers: Jae-Ho Chung¹; Sun Jae Chung¹; Sanghoon Lee¹; Brian Kirby²; Julie Borchers²; Yong-Jin Cho³; Xinyu Liu³; Jacek Furdyna³; ¹Korea University; ²National Institute of Standards and Technology; ³University of Notre Dame

The spintronics technology requires materials that allow simultaneous control of the charge and the spin degrees of freedom. Recent efforts dedicated in search of such materials have led to the successful fabrication of artificial ferromagnetic semiconductor GaMnAs, where doping of magnetic Mn²⁺ ions into insulating GaAs results in robust ferromagnetism and semiconducting property at the same time. In order to realize useful devices from magnetic semiconductors, however, it is important to be able to control not only the magnetic properties of individual layers but also interactions between them. Until now, the interaction between ferromagnetic GaMnAs layers across nonmagnetic GaAs spacers was explicitly observed to be ferromagnetic only. Since the RKKY interaction in metallic magnetic multilayers is known to produce exchange oscillations between ferromagnetic and antiferromagnetic (AFM) as a function of layer thickness, AFM interlayer exchange coupling has been expected to be attainable also in semiconductor-based multilayers by enhancing carrier concentrations in the spacers. To test this idea, we have fabricated GaMnAs-based multilayers with different carrier concentrations in the spacers. Molecular beam epitaxy was used to deposit 10 periods of Ga_{0.97}Mn_{0.03}As/GaAs on GaAs (001) substrates. In one of the samples, the nonmagnetic GaAs spacers were doped with Be at the concentration of $1.2 \times 10^{20} \text{ cm}^{-3}$. The SQUID magnetometry indicated that the temperature dependence of the magnetization is quite different when the spacers are doped with Be. While the magnetization of the undoped sample is similar to that of single layers showing ferromagnetic behavior, the Be-doped sample shows substantially suppressed net magnetization at low fields. At high fields, however, the magnitude of the magnetization is similar between the two

samples. These behaviors are consistent with the presence of antiferromagnetic and ferromagnetic interlayer exchange couplings in the Be-doped and the undoped samples, respectively. We used polarized neutron reflectivity to directly confirm the nature of the interlayer exchange couplings. In the case of the Be-doped sample, the polarized neutron reflectivity measured below the Curie temperature of $\text{Ga}_{0.97}\text{Mn}_{0.03}\text{As}$ reveals a characteristic splitting at the wave vector corresponding to twice the multilayer period, indicating that the coupling between the ferromagnetic layers are AFM. When the applied field is increased to above the saturation field, this AFM coupling is suppressed and a splitting is observed at the ferromagnetic Bragg peak. When the applied field is subsequently reduced to below the coercive field, the AFM splitting is not recovered at 6 K due to strong uniaxial anisotropy, but is fully recovered at 30 K. This behavior is not observed when the spacers are undoped, and only the ferromagnetic alignment is observed instead. This observation strongly suggests that the AFM interlayer exchange coupling is mediated by charge carriers introduced via Be doping.

4:10 PM Student

HH6, Magnetotransport Measurements on $\text{In}_{1-x}\text{Mn}_x\text{Sb}$ Ferromagnetic Semiconductor Alloys: *Nidhi Parashar*¹; *Nikhil Rangaraju*¹; *Bruce Wessels*¹; ¹Northwestern University

Manganese doped III-V semiconductors are being developed for spin electronics for electrical control of spin transport. While efforts have been focused on GaMnAs, other alloy systems are being investigated for the realization of ferromagnetic semiconductors with Curie temperatures above 295 K. Of special interest are single phase, magnetic, epitaxial $\text{In}_{1-x}\text{Mn}_x\text{Sb}$ alloy films grown by metalorganic vapor phase epitaxy which exhibit room temperature ferromagnetism. However, in order to be used for semiconductor spintronic devices, the presence of carrier-mediated ferromagnetism should be demonstrated. From anomalous Hall effect measurements the nature of ferromagnetism can be determined. Magnetoresistance and Hall measurements of $\text{In}_{1-x}\text{Mn}_x\text{Sb}$ magnetic semiconductor thin films were investigated for temperatures from 1.4 to 300 K and magnetic fields up to 18 T. Films were found to be p-type, with carrier concentration of $\sim 10^{19} \text{ cm}^{-3}$. The Hall resistivity (ρ_{xy}) of a ferromagnetic semiconductor is observed to contain two distinct contributions. The Hall resistivity ρ_{xy} is given by: $\rho_{xy} = R_o(p)B + R_A(\rho_{xx})M$ where, $R_o(p)$ is the ordinary Hall coefficient, $R_A(\rho_{xx})$ is the anomalous Hall coefficient, B is the magnetic field and M is the magnetization. In present study, the Hall resistivity (ρ_{xy}) for $\text{In}_{0.65}\text{Mn}_{0.035}\text{Sb}$ film has a non-linear dependence on magnetic field measured between 4 - 298 K. The anomalous Hall effect and well-resolved hysteresis loops in the Hall resistivity versus magnetic field were observed at room temperature, confirming the carrier-mediated ferromagnetic behavior of the films. In contrast to an earlier study, the magnitude of hysteresis decreased for temperature < 6 K. This unique behavior observed in ρ_{xy} is attributed to the change in sign of magnetoresistance, ρ_{xx} , in the films for $T < 6$ K. The films exhibited a positive magnetoresistance at high temperatures and high fields, whereas for low temperatures and small fields a negative magnetoresistance is observed. The dependence of Hall resistivity on alloy concentration will also be presented.

4:30 PM Student

HH7, Engineering the Interlayer Exchange Interaction between MnAs and (Ga,Mn)As: *Mark Wilson*¹; *Meng Zhu*¹; *Roberto Myers*²; *David Awschalom*²; *Peter Schiffer*¹; *Nitin Samarth*¹; ¹Pennsylvania State University; ²University of California-Santa Barbara

Controlling the exchange interaction between adjoining magnetic layers in metallic systems has allowed for the development of devices such as spin valves and magnetic tunnel junctions. There have also been attempts to control the exchange interaction in ferromagnetic semiconductors, most notably (Ga,Mn)As. For example, successful exchange biasing of (Ga,Mn)As has been shown using both an antiferromagnetic insulator (MnO) [1] and a ferromagnetic metal (MnAs) [2]. The metallic nature of the latter has allowed the fabrication and study of vertical spin transport devices such as spin valves [2] and magnetic tunnel junctions [3]. In such devices, it is essential to understand the parameters that effect the exchange interaction. Here, we report a systematic study of the exchange interaction between the soft ferromagnetic semiconductor (Ga,Mn)As

and the harder ferromagnetic metal MnAs. (Ga,Mn)As and MnAs have a large difference in both their anisotropy constants and Curie temperatures, allowing for manipulation of exchange parameters. All the heterostructures in the study were grown by low-temperature molecular-beam epitaxy on GaAs wafers. We vary all the relevant parameters, including: (Ga,Mn)As thickness, MnAs thickness and Mn concentration. In addition to the bilayer samples, we also grew a series of trilayer structures with a non-magnetic spacer layer and we studied the exchange interaction as a function of spacer layer. We find some evidence that the exchange interaction between the two magnetic layers is hole mediated by changing the doping level of the spacer layer. When capping (Ga,Mn)As with MnAs, we find an annealing-like effect that enhances the Curie temperature. We have developed a simple model that agrees well with experimental observations. This exchange model assumes that the (Ga,Mn)As spins near the interface are aligned with the harder MnAs. As the distance from the MnAs increase, the (Ga,Mn)As rotate in an exchange spring like fashion before eventually aligning with the bulk (Ga,Mn)As. Unlike in a pure exchange spring model, this leads to a quasi-reversible hysteresis loop that changes both as a function of field and (Ga,Mn)As thickness. Supported by ONR-MURI. 1. K. F. Eid et al. Appl. Phys. Lett. 85, 1556 (2004). 2. M. Zhu et al., Appl. Phys. Lett. 91, 192503 (2007). 3. M. Zhu et al., Phys. Rev. B 78, 195307 (2008).

4:50 PM HH8, Late News

5:10 PM HH9, Late News

Session II: Graphene II

Thursday PM
June 25, 2009

Room: 206
Location: Pennsylvania State University

Session Chairs: Debdeep Jena, University of Notre Dame; Suneel Kodambaka, University of California, Los Angeles (UCLA)

1:30 PM Invited

III, Influence of Edges on the Morphology, Electronic Structure and Magnetism in Graphene Sheets and Nanoribbons: *Vivek Shenoy*¹; ¹Brown University

Graphene, an atomic layer of carbon atoms arranged in a honeycomb lattice, is actively being pursued as a material for next-generation electronics because of the high mobility of charge carriers and the potential to control their density by applying a gate voltage. Depending on the type of edge termination, the bonding configuration of atoms located at the edges of graphene sheets can be considerably different from an atom in the periodic honeycomb lattice. Recently we have shown that intrinsic stresses arising from the presence of edges^{1,2} can lead to ripples in freestanding graphene sheets even in the absence of any thermal effects. Compressive edge stresses along zigzag and armchair edges of the sheet cause out-of-plane warping to attain several degenerate mode shapes. We have also demonstrated that edge stresses can lead to twisting and scrolling of nanoribbons as seen in experiments. The effect of these deformation modes on the electronic and magnetic properties will be discussed. Our results underscore the importance of accounting for edge stresses in thermal theories and electronic structure calculations for freestanding graphene sheets. ¹V. B. Shenoy, C. D. Reddy, A. Ramasubramaniam, and Y.-W. Zhang, Physical Review Letters, 101, 245501 (2008). ²C. D. Reddy, A. Ramasubramaniam, V. B. Shenoy, and Y.-W. Zhang, Applied Physics Letters, 94, 101904 (2009).

2:10 PM Student

I12, Thermal Conduction in Graphene and Graphene Multilayers: *Suchsmita Ghosh*¹; Irene Calizo¹; Evgenii P. Pokatilov¹; Denis Nika¹; Desalegne Teweldebrhan¹; Alexander A. Balandin¹; Wenzhong Bao²; Feng Miao²; Chun Ning Lau²; ¹Department of Electrical Engineering and Materials Science and Engineering Program, University of California Riverside; ²Department of Physics and Astronomy, University of California Riverside

In nanometer scale CMOS designs and beyond-CMOS architectures thermal management is crucial for achieving high performance and reliability of circuits. One approach for solving the self-heating problem is finding materials with superior thermal conductivity, which can be integrated with Si circuits for hot-spot removal. Graphene has already revealed unique electronic and optical properties. Our group, for the first time, has shown experimentally that graphene is an excellent heat conductor. This, coupled with graphene's flat geometry and ability for functioning in Si-based devices make graphene very promising material for heat removal from nanoelectronic circuits. Micro-Raman spectroscopy based approach was used as a unique method for measuring the thermal conductivity of graphene flakes suspended across trenches in Si wafers and attached to heat sinks. Laser light was focused in the middle of the suspended portion of the flake and the amount of laser power dissipated in graphene and corresponding local temperature rise were determined from the integrated intensity and spectral position of graphene's Raman G mode. Our measurements revealed that the single-layer graphene has an extremely high room-temperature thermal conductivity exceeding ~3080 W/mK. Extending our work we investigated thermal conduction in graphene multilayers and examined the transition to the limiting case of the basal planes of graphite. The in-plane room-temperature thermal conductivity of high-quality graphite is about 2000 W/mK (although higher values have been also reported for some types of graphite). We improved our experimental technique by utilizing the metal heat sinks instead of graphitic as in the initial experiments. The preliminary results obtained for graphene flakes with n=2, 3, and 4 atomic layers suggest that the thermal conductivity reduces with the increasing number of layers. The thermal conductivity values are in the range between the maximum, achieved for a single layer graphene, and the data for the basal plane of high-quality bulk graphite. We also investigated the thermal conductivity theoretically. The phonon dispersion for all polarizations and crystallographic directions in graphene lattice was obtained using the valence-force field method. The three-phonon Umklapp processes were treated using an accurate phonon dispersion and Brillouin zone, and accounting for all phonon relaxation channels allowed by the momentum and energy conservation laws. It was found that the near room-temperature thermal conductivity of single layer graphene is in the range close to the experimental values. Owing to the long phonon mean free path the graphene edges produce strong effect on thermal conductivity even at room temperature. The work in Balandin group was supported, in part, by DARPA – SRC Focus Center Research Program (FCRP) through its Functional Engineered Nano Architectonics (FENA) center and Interconnect Focus Center (IFC).

2:30 PM Student

I13, Current Saturation and High-Field Transport in Graphene: *Tian Fang*¹; Aniruddha Konar¹; Kristof Tahy¹; Xiangning Luo¹; Huili Xing¹; Debdeep Jena¹; ¹University of Notre Dame

Low-field transport properties of graphene have been extensively investigated. The high mobility of carriers and capacitive gate modulation indicate the suitability of the inherently 2-D material for various device applications. One such application is high-speed RF devices such as multipliers, mixers, and low-noise amplifiers. A property that is desirable for many such applications is a high current drive with current saturation at high electric fields. This feature has not been investigated in detail. We present a combined experimental and theoretical study of current saturation and high-field transport in graphene. We experimentally measure saturation currents in monolayer graphene sheets. The saturation current densities are in the 1 - 2 A/mm range for 2D carrier concentrations in the $\sim 3 \times 10^{12}/\text{cm}^2$ range. This is also the saturation current drive prior to burnout, indicating the current carrying capacity of graphene. These current densities are 2X higher than previous reports [Nature Nano. , 3, 654

(2008)] of saturation currents. In order to explain the intrinsic saturated current drive in 2D graphene, we develop an analytical model based on optical phonon backscattering of carriers. The high electric field that causes current saturation deforms the Fermi circle to two circles with constant energy surfaces that differ by one optical phonon energy. This distribution of carriers results in a saturation current density that varies as the square root of the 2D carrier concentration. A constant saturation velocity model would then be the slope – it evaluates to $v_{\text{sat}} \sim 5.7e7$ cm/s, roughly half the Fermi velocity of graphene. However, the predicted current densities are much higher than what are experimentally measured. An ensemble Monte-Carlo simulation that properly accounts for the inherent degeneracy is developed. The velocity-field curves from the simulation may be fit to a conventional form of velocity saturation, but both the mobility and the saturation velocity have to be made carrier concentration dependent. This points towards the fact that a constant saturation velocity is not attained in graphene and the physics of carrier transport is different. The Monte-Carlo results predict a velocity saturation model (saturation current linearly proportional to carrier concentration) if hot-phonons are neglected. Upon the inclusion of non-equilibrium hot-phonons, the saturation current density closely matches that calculated by the simpler ad-hoc model. The saturation current becomes proportional to the square root of the carrier concentration, and the magnitudes are in close agreement with experimental data. In conclusion, we have experimentally measured saturation current densities in the 1 – 2 A/mm range in graphene, which makes it attractive for RF applications. The saturation mechanism is based on optical phonon emission and the current density is limited by the presence of hot-phonons. The model developed here will be useful for the design of graphene-based devices.

2:50 PM Student

I14, High-Field Characteristics of Top-Gated Epitaxial Graphene Field-Effect Transistors: *David Shilling*¹; Kristof Tahy¹; Xiangning Luo¹; Huili (Grace) Xing¹; Debdeep Jena¹; Luxmi Luxmi²; Randall Feenstra²; ¹University of Notre Dame; ²Carnegie Mellon University

Due to its two-dimensional nature, interest in graphene semiconductor devices is very strong. Saturating field-effect transistor (FET) curves have been recently reported for transistors based on exfoliated single-layer graphene. Epitaxial graphene FETs on SiC have been reported recently with low-field performance characteristics. Here we report transistor characteristics for few-layers epitaxial graphene FETs. We report moderate (~3x) gate modulation and a tendency towards drain current saturation at high drain bias conditions. We compare the performance of these devices with predictions made by a long channel FET model. The graphene layers were prepared on the Si-face of a SiC wafer by first hydrogen etching in vacuum environment at 1570 C, followed by graphitization at 1710 C. The C:Si ratio on the surface was estimated to be ~15. FETs were fabricated with a top-gate structure. The gate oxide was Al₂O₃, and the oxide thickness was 15 nm. We observed empirically that smaller W/L ratios produced better device performance. Therefore, an uncommonly small width-to-length ratio was used. Several FETs were tested at room temperature, and measurements were performed at atmospheric conditions, in vacuum, and in a nitrogen environment. No significant dependence on atmospheric conditions was observed, though the device size had a strong effect on the device characteristics. This can be expected from the inhomogeneity of coverage of graphene on the surface. For large-area devices, we were able to modulate the drain current by 3X or more by varying the gate-source voltage. Saturating characteristics have not been reported in epitaxially grown graphene device. For constant gate-source voltage, increasing the drain-source voltage produced saturating transistor curves, especially for high gate-source bias. By investigating the drain current modulation with the gate voltage at fixed drain biases, we extracted the field-effect mobilities. At high carrier concentrations far from the Dirac point, where this extraction of the mobility is trustworthy, numbers in the range of ~ 1000 cm²/Vs were measured. Another characteristic was the degradation of the mobility at very high carrier concentrations, which is possibly due to the vertical modulation of the electron wavefunction by high vertical electric fields due to the gate. The measured device characteristics can be understood using a simple long-channel FET model with mobilities in the range of 1000 – 2000 cm²/Vs and saturation velocities in the range of 5x10⁷ cm/

s. The large modulation of drain current and the saturating behavior hold much promise for FET applications of epitaxial graphene in the future.

3:10 PM Break

3:30 PM Student

II5, Graphene Field-Effect Transistors Formed on Semi-Insulating 4H-SiC: *Konishi Keita*¹; *Yoh Kanji*¹; *Hibino Hiroki*²; ¹Hokkaido University/Research Center for Integrated Quantum Electronics; ²NTT Basic Research Laboratories

Recently, keen attention is directed to single layer graphene whose transport is described as relativistic Dirac fermion with zero effective mass^{[1][2]}. Room temperature mobility of 200,000cm²/Vs is reported^[3] for samples of graphene sheet printed from graphite chip. Unlike carbon nanotube, graphene devices have greater potential of integration because they can be selectively formed on SiC substrates^[4]. Here we report the fabrication and electrical characterization of thin graphite films formed on 4H-SiC substrate. The polished Si-face Semi-insulating 4H-SiC wafer is initially H₂ etched at 1370°C. After H₂ etching, we leak nitrogen into chamber and remove H₂ remaining behind with it. Then thin graphite films is formed in vacuum by the decomposition of the surface followed by the synthesis of graphite films with substrate temperature of 1,500°C and base pressure of about 1Pa for 10 minutes. We discovered that can control the formation of graphite films on SiC by regulating a parameter of temperature and pressure to form graphite films. The thin graphite films formation can be verified by AFM and Low-Energy Electron Diffraction (LEED)/ Low-Energy Emission Microscope (LEEM) measurements^[5]. The LEEM was used to investigate the reflectivity from this processed sample. As a result, that 1-3 layers graphene was formed was observed. FET structure was defined by using conventional photolithography. Ti/Au layer was used as Ohmic contact and gate electrode. Silicon dioxide (2000Å) was used as a gate oxide between the top gate electrode and graphene channel. Saturation of drain current behavior was not observed. Current modulation of 40% by gate voltage was observed at room temperature. In addition, we observed ambipolar conduction characteristics peculiar to graphene. The Hall measurements revealed carrier concentration of 2.46x10¹²/cm² and mobility of 530cm²/Vs at room temperature, respectively. The Ohmic contact resistance and the sheet resistance of the graphene were 2500Ω and 4000Ω, respectively. The ON/OFF ratios more than 100 were provided in helium temperature. This suggests an existence of a finite band gap. Details of backpressure-dependence on graphene characteristics will be given. ^[1]K. S. Novoselov et al, Nature 438, pp.197-200 (2005); ^[2]Y. Zhang et al, Nature 438, pp.201-204 (2005); ^[3]S. V. Morozov et al, Phys. Rev. Lett. 100, 016602 (2008); ^[4]C. Berger et al, J. Phys. Chem B, 108, 19912 (2004); ^[5]H. Hibino et al, Phys. Rev. B 77, 075413 (2008).

3:50 PM

II6, Epitaxial Graphene: Predicting Carrier Mobility Using Raman Spectroscopy: *Joshua Robinson*¹; *Maxwell Wetherington*¹; *Randal Cavlero*¹; *Mark Fanton*¹; *Eric Frantz*¹; *David Snyder*¹; *Joseph Tedesco*²; *Brenda Van Mill*²; *Paul Campbell*²; *Glenn Jernigan*²; *Rachel Myers-Ward*²; *Charles Eddy*²; *D. Gaskill*²; ¹Pennsylvania State University; ²Naval Research Laboratory

Realization of graphene electronics on the production scale requires the development of large area graphene with the ability to rapidly characterize the material's structural and electronic quality. Currently, the most promising route for large area graphene, suitable for standard device fabrication techniques, is the sublimation of silicon from silicon carbide (SiC) at elevated temperatures (>1200 C). Multiple techniques have proven useful for layer thickness measurements, but to date Raman spectroscopy provides the simplest means to rapidly identify layer thickness and strain uniformity of mono- and bi-layer graphene under ambient conditions. Our work reveals unexpectedly large variation in Raman shift resulting from graphene strain inhomogeneity, which is shown to be correlated with physical topography by coupling Raman spectroscopy with atomic force microscopy. Graphene strain can vary over a distance shorter than 300nm, and may be uniform only over roughly 1 μm. Additionally, We have examined epitaxial graphene with mobility values of 25 – 18,100 cm²/Vs, and show that Raman topography is a vital tool for rapid identification of high mobility material. The Hall mobility of epitaxial graphene on the Si-face of SiC is not only highly dependent on thickness uniformity, but

also on mono-layer strain uniformity. It is not until the thickness and strain domain widths, as measured in Raman topography, are of the same length scale as the device active region that one is able to achieve mobility values higher than 1000 cm²/Vs. In addition, high mobility epitaxial graphene grown on the C-face of SiC is dependent on graphene layer stacking.

4:10 PM Student

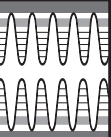
II7, Discrepancies in Calculating Mobility in 2D Graphene and Graphene Nanoribbon FETs: *Kristof Tahy*¹; *Debdeep Jena*¹; *Huili Xing*¹; ¹University of Notre Dame

The electronic properties of graphene, such as high charge carrier concentrations and mobilities, make it a promising candidate for next-generation nanoelectronic devices. Mobilities as high as 200 000 cm²/Vs for suspended graphene, 15 000 cm²/Vs for exfoliated and 5 000 cm²/Vs for epitaxial graphene has been reported. It is well known that mobility is a function of carrier concentration in graphene and such high mobility values can be obtained at very low carrier concentrations only. Another source of vagueness is the method of mobility extraction from measurements. We will propose the limitation and reliability of widely used mobility calculation methods discussing the main variable parameters of the models. Using the equation for the drift current $J = \mu F n e$ one can extract the mobility specifically for a simple 2D graphene field effect transistor geometry: $\mu_{CON} = \sigma / (en) = I_{DS} L / (V_{DS} W en) = I_{DS} L / (V_{DS} W C_{OX} V_{GS})$, where e is the electron charge and n is the 2D carrier concentration. This definition of the mobility is inversely proportional to carrier concentration therefore it gives extremely high mobility values for low carrier concentrations. This can be called conductance based mobility (μ_{CON}). However we can define the field effect mobility (μ_{FE}) as the change in the sheet conductivity of graphene due to carrier density modulation Δn is $\Delta \sigma = \Delta n e \mu$. The expression can be modified to the form: $\mu_{FE} = g L / (V_{DS} W C_{OX})$, where $g = dI_{DS} / dV_{GS}$ is the transconductance. This method will not provide extreme high mobility at low carrier concentration. Just the contrary, the derivative tends to be zero if n is low and as a result the mobility will go to zero as well. By comparing the result of the two calculation method for the same measurement data we can conclude that satisfactory matching can be observed at $n > 10^{12}$ cm⁻² carrier density. However by analyzing many devices we can conclude that the value μ_{CON} is about twice as much than μ_{FE} even at high carrier densities. It can be shown that the two method would give equivalent result in the limiting case when the gate dependence of the source-drain current is linear, which is theoretically true for graphene. Both mobility calculation formulas are inversely proportional to the oxide capacitance. While they follow the same dependence more accurate capacitance calculation will not give a better match of the methods. On the other hand it is important to know its limitations in case of nanoribbons. Applying infinite parallel plate (2D) approximation for wider than 1 μm graphene sheets to calculate the capacitance seems to be appropriate. Below that limit we can use models developed for nanowires or simulation. The model used for nanowires has been found inaccurate for graphene compared to the finite element method simulation. Both technique results orders of magnitude higher capacitances what one can obtain using the parallel plate approximation. Recalculating the mobility using simulated capacitance results much lower values.

4:30 PM Student

II8, Epitaxial Graphene Micro-Bridges: *Shriram Shivaraman*¹; *Xun Yu*¹; *Robert Barton*¹; *Jonathan Alden*¹; *Lihong Herman*¹; *M.V.S. Chandrashekar*¹; *Jiwoong Park*¹; *Jeevak Parpia*¹; *Harold Craighead*¹; *Paul McEuen*¹; *Michael Spencer*¹; ¹Cornell University

This work reports on micron-sized free-standing epitaxial graphene bridges produced from graphene grown on silicon carbide.¹ Experiments have been conducted to probe the mechanical properties of these sheets. Graphene was grown epitaxially on silicon carbide by heating the substrate under high vacuum at ~ 1400°C. The produced films were characterized by Raman spectroscopy to confirm their graphitic nature. The films showed the characteristic G and 2D peaks. A disorder-related D peak was also seen. In order to study the intrinsic nature of epitaxial graphene, it is necessary to isolate graphene from the substrate. For silicon carbide, this is a challenge because of the chemically resistant nature of the material. Dry etching techniques which are usually used for patterning silicon carbide are not useful because the plasmas involved would etch away the



graphene. Thus, a wet etch process is needed. We use potassium hydroxide for etching SiC following the procedure of Kato et al.² Gold contact pads are first evaporated on graphene. The graphene is then photolithographically using an oxygen plasma etch. The final step is the wet etch using potassium hydroxide. The undercut caused by the isotropic wet etching process releases the graphene sheets from the substrate. The sheets were actuated optically using a laser and the fundamental modes of vibration were recorded using optical interferometry. The devices had fundamental modes at ~ 45 MHz with Q factors > 300. The tension extracted from the devices using the geometry of a doubly-clamped beam is in the range of 10^{-6} N. A mechanical pushing experiment was also conducted on the sheets using an atomic force microscope tip. The tension values extracted from these measurements compared favorably with the value extracted from optical actuation. The origin of tension in the devices is under investigation. ¹Shriram Shivaraman et al, submitted to Nano Letters (2009). ²Masashi Kato et al, Jpn. J. Appl. Phys., 42, pp. 4233-4236 (2003).

4:50 PM

II9, Stress and Disorder in Epitaxial Graphene/SiC by Raman Spectroscopy: *M.V.S. Chandrashekar*¹; Virgil Shields¹; Shriram Shivaraman¹; Michael Spencer¹; ¹Cornell University

We present a detailed Raman study of few layer epitaxial graphene/graphite grown on 4H and 6H SiC by thermal decomposition in 2 different growth systems, cold and hot wall. Certain general features in the spectra unify observations for films grown in the different reactors. As epitaxial graphene becomes more disordered, owing to changes in growth conditions, there are changes that occur in the Raman spectrum that give information about the grain size, strain, orientation and overall quality of the films, which we call the disorder trajectory. We focus primarily on the disorder trajectory of the well known graphite G-peak (~1580cm⁻¹) and disorder D-peak (~1350cm⁻¹). The ratio of the intensity of the 2 peaks ID/IG, varies between 0 for ideal graphene/graphite and ~2 for nanocrystalline graphite. This ratio allows determination of distance between defects, or the crystal coherence length.¹ The disorder trajectory of epitaxial graphene/graphite displays two clear branches, one at ID/IG<0.2, which we refer to as the “stress branch” and another at ID/IG>0.4, which we refer to as the “disorder branch”. These two branches are linked by transitional samples with 0.2<ID/IG<0.4, that display certain characteristics of both branches. For samples in the stress branch, termed “graphene like” the G-peak is blue-shifted (up to ~17cm⁻¹) with respect to free-standing graphite, clearly indicating built in compressive stress. There is an increase in disorder as a function of stress in the films, although they remain well oriented. We observe an increase in the stress as a function of surface energy (i.e. substrate orientation), with stress varying from <1GPa for on-axis C-face to >4GPa for 8o off-axis Si-face. These observations indicate that the films interact with the substrate. Films in the disorder branch are much less stressed, not well oriented with the SiC substrate, and are largely disordered. They are not “graphene-like”. Furthermore, there is a slight increasing blueshift with disorder, as has been observed in nanocrystalline graphite. The D-peak redshifts owing to curvature present in the increasingly disordered graphite. The emergence of the out of plane mode at ~2950cm⁻¹ supports this interpretation. The stress relief transitioning from the stress branch into the disorder branch suggests that the relief can occur through disorder. In summary, we have characterized epitaxial graphene films grown on SiC in various growth systems by Raman spectroscopy. Metrics have been presented that can be used to qualify grown films as being “graphene-like”. We find that one source of stress is substrate orientation. We also identify one possible mechanism of stress relief in graphene, which is through disorder.

5:10 PM III10, Late News

Session JJ: III-Nitride: Indium Nitride

Thursday PM
June 25, 2009

Room: 207
Location: Pennsylvania State University

Session Chair: George Wang, Sandia National Laboratories

1:30 PM

JJ1, Multiple Mobility Channel Electron Transport Properties in InN Grown by MBE: *Kejia Wang*¹; Yu Cao¹; Shaoping Shen¹; Zhiguo Ge¹; Malgorzata Dobrowolska-Furdyna¹; Debdeep Jena¹; ¹University of Notre Dame

InN has attracted extensive research interests due to its unique properties and possible applications in optical and electronic devices. The band gap energy of InN is ~ 0.65 eV, which extends the wavelength range of III-V nitride semiconductors into infrared region. The high electron mobility and high saturation velocity make InN a favorable material for highspeed transistors. High quality InN epitaxial film has been grown by molecular beam epitaxy (MBE). Due to the large lattice mismatch between InN and underlying substrates (such as GaN, AlN and sapphire), a high density of defects including dislocations and vacancies was observed in InN. Electron mobility of InN over 1000 cm²/Vs at room temperature has been reported. Early work shows that ionized impurity scattering and charged dislocation scattering are the dominant scattering mechanisms that limit the electron mobility. Quantitative mobility spectrum analysis (QMSA) has been widely used to determine the transport property of different carrier species. So far no one has studied the effect of a spatially varying dislocation density on the electron mobility in InN, and how this can be related to mobility spectrum obtained by QMSA. At University of Notre Dame, InN film has been grown on GaN substrate using MBE with Indium effusion cell and Nitrogen plasma source. Surface morphology was monitored by in-situ RHEED and later characterized by AFM. Smooth and coalesced surface was obtained. Structural qualities are characterized by X-ray diffraction and Transmission Electron Microscope. The as-grown InN is found to have a wurtzite structure, same as the GaN substrate. Narrow peak broadens in InN and high-resolution TEM images verify the high quality of InN epitaxial films. Optical measurements including absorption spectrum and photoluminescence spectroscopy showed that the band gap energy of InN was around 0.65 eV. In this letter, we report the study of transport properties of InN grown by MBE. Using magnetic field dependent Hall effect measurement and QMSA, the concentrations and mobilities of two electron species, associated with the bulk and the surface accumulation layer, were extracted. The mobilities of electrons in the bulk of InN were found to be in the range from 1300 cm²/Vs to 2500 cm²/Vs at room temperature. Taking into account an exponential decay of dislocation density with the InN film thickness, a model was established to describe the position dependence of electron concentration and mobility in the InN film along the growth direction. Calculations show that the electron mobility is dominated by charged dislocation scattering near the growth interface, and then limited by ionized impurity scattering as the film grows thicker. In addition, the calculated electron mobility spectrum is in a good agreement with experimental data from QMSA.

1:50 PM

JJ2, Auger Recombination and Photoluminescence in Mg-Doped InN: Chito Kendrick¹; Maurice Cheung²; Alexander Cartwright²; Young Wook Song¹; Roger Reeves¹; Timothy Veal³; Philip King³; *Steven Durbini*¹; Christopher McConville³; ¹University of Canterbury; ²University at Buffalo, SUNY; ³University of Warwick

InN is a narrow-gap (~0.65 eV) semiconductor which has recently generated considerable interest for its potential in applications ranging from photovoltaics to terahertz detectors to high-speed transistors. The realization of p-type InN through in-situ Mg doping has recently been reported by a number of different groups.¹⁻³ Two distinct and unrelated phenomena initially interfered with attempts to determine whether doping experiments yielded p-type conductivity:

a high density surface electron accumulation layer,⁴ and unexpected quenching of the photoluminescence.^{1,2} Verification of p-type material has since been performed using a variety of techniques including electrochemical capacitance-voltage, valence band x-ray photoelectron spectroscopy, and variable magnetic field Hall effect. The origin of the apparent photoluminescence quenching, however, has remained an open question. We have investigated recombination dynamics of Mg-doped InN epilayers grown by plasma-assisted molecular beam epitaxy using a combination of photoluminescence and time-resolved differential transmission (TRDT) measurements. The Mg concentration was determined by secondary ion mass spectrometry using an ion-implanted standard, and found to be in the range of 3×10^{17} to 1×10^{20} cm⁻³. Photoluminescence was performed using an argon ion laser and either an InSb or InGaAs detector, resulting in detectable signals from all samples. TRDT was performed at room temperature using a pump-probe technique on three separate samples, with doping densities of 6.2×10^{17} cm⁻³ (SL), 3.6×10^{19} cm⁻³ (SM) and 1.0×10^{20} cm⁻³ (SH), respectively. As has been reported by others, the photoluminescence of the films generally consisted of a single peak, with lightly doped films typically exhibiting a single feature near the bandedge. Quantum efficiency decreased markedly with increased Mg content, and many of the moderately doped films were characterized by a lower energy peak near 0.6 eV. For TRDT sample SL, the decay was single-exponential, as expected from a combination of radiative and Shockley-Read-Hall recombination. Samples SM and SH, however, were characterized by a bi-exponential decay, which is commonly attributed to Auger recombination. Sample SL, which in many respects has the same characteristics of undoped (n-type) InN, does not exhibit bi-exponential decay until higher excitation, and its extracted Auger coefficient agrees well with recent measurements of n-type InN and Ga-rich InGaN.⁵ Thus, Mg doping leads to a dramatic shift in the dominant recombination pathway, which has profound implications for devices. ¹R. E. Jones, et al., Phys. Rev. Lett. 96, 125505, 2006. ²P.A. Anderson et al., Appl. Phys. Lett. 89, 2006, 184104. ³X. Wang, et al., Appl. Phys. Lett. 91, 2007, 242111. ⁴I. Mahboob, et al., Phys. Rev. Lett. 92, 2004, 036804. ⁵D.-J. Jang, et al., Appl. Phys. Lett. 92, 2008, 042101; Y.C. Shen, Appl. Phys. Lett. 91, 2007, 141101.

2:10 PM Student

JJ3, Adducts Formation in MOCVD Growth of InAlN: Growth Pressure Dependence: *Mikiyasu Tanaka*¹; Masatomo Yamamoto¹; Ting-Ting Kang¹; Akihiro Hashimoto¹; Akio Yamamoto¹; ¹University of Fukui

InAlN has a potential application to a variety of optical and electron devices, because its band-gap energy can be changed from 0.7 to 6.2 eV. Especially, In-rich InAlN is a promising material for multi-junction tandem solar cells. We have previously reported that a single-crystalline InAlN film with an In content 1- 0.55 is successfully grown by employing atmospheric pressure MOCVD growth. However, the MOCVD growth behavior of InAlN has not yet been fully understood. For example, In composition in grown InAlN is increased with increasing growth temperature. This is in contrast to the result for MOCVD InGaIn growth where In composition is decreased with increasing growth temperature. In this paper, we report the adduct formation due to the parasitic reaction between TMA and NH₃ in the MOCVD growth of InAlN at a different pressure and its effects on the InAlN growth. Using an MOCVD system with a horizontal reactor, InAlN growth is performed with a (0001) sapphire substrates at 600°C at a pressure in the range of 76 to 730 Torr. As sources TMI, TMA and NH₃ are used and TMI/(TMI+TMA) molar ratio is fixed to 0.5. Sapphire substrates are placed at a different position (-23 ~ +23 mm) along the gas flow direction on the susceptor. Thick deposits with a rough surface are formed on the substrate at a pressure in the range of 300-600 Torr. Such deposits are adducts due to the parasitic reaction between TMA and NH₃, because they scarcely contain InAlN component. The position of the adduct formation on the susceptor is moved from the upstream side to the downstream side with decreasing growth pressure. No single-crystalline InAlN are obtained in the pressure range of 300-600 Torr due to the severe adduct formation. The Al composition in grown InAlN is found to increase with reducing growth pressure. The reduced pressure growth at around 76 Torr is effective to reduce compositional gradient along the gas flow direction, although the growth rate becomes very small (~100 nm/h). Thus, Al composition in InAlN film and

its distribution are found to be controlled by optimizing growth pressure and substrate position.

2:30 PM Student

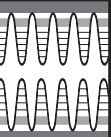
JJ4, Selective Area Growth of InN Nano-Crystals on Pt-Mask Patterned Sapphire (0001) Substrate by RF-MBE: *Jumpei Kamimura*¹; Katsumi Kishino¹; Akihiko Kikuchi¹; ¹Sophia University

InN is an attractive material for various devices such as light emitters and super high efficiency solar cells because of its narrow bandgap of 0.6-0.8 eV. Recently InN one-dimensional nanostructures, such as nanocolumns, nanowire and nanobelt, have been reported and most of them showed good optical property due to its dislocation free nature and the advantage of light extraction efficiency. Controlling the size, shape and position of high-quality InN nano-crystals is essential for employing them as building blocks of functional nanodevices. In this study, we present a novel selective area growth (SAG) technique of InN nano-crystals, in which the crystals were grown on Pt-mask patterned sapphire (0001) substrate by RF plasma-assisted molecular beam epitaxy (RF-MBE); then the SAG of InN nanocolumns was successfully performed without any buffer layers and catalysts. Prior to the SAG of the InN nanocolumns, 10-nm-thick Pt film was deposited on c-plane sapphire substrates by electron beam evaporation. Subsequently nanohole patterns, in which hexagonally shaped nanoholes were arranged in triangular lattice, were formed through electron beam lithography and dry etching. In this experiment various nanohole patterns with the different lattice period of 350-4300 nm were prepared, individually changing the nanohole diameter from 250 to 2000 nm. In addition to the period and the diameter, angular orientations of hexagonal nanoholes against the underlying sapphire were changed in two ways, that is, controlling the hexagonal side wall in parallel to (1-100) and (11-20) planes of sapphire. After initial nitridation of the substrate surface at 550°C, the InN were grown at 580°C for 1 hour under a nitrogen rich condition by RF-MBE. The grown crystals were evaluated with scanning electron microscopy (SEM) and photoluminescence (PL) spectroscopy. The PL signal was detected at 4.1K through reflective objective lens (x40) under YAG laser light excitation (532 nm) of 4.2 μP/W light power. The SEM observation confirmed that the position of InN nanocolumns was well controlled at nanoholes and the nanocolumn diameter was in the range from 400 to 3600 nm. Then the side of hexagonal InN nanocolumns tended to be aligned in parallel to (11-20) plane of sapphire, for both angular orientations of the nanoholes, which is because the crystal orientation might be determined with initial nitridation of c-plane sapphire as reported by Nanishi, et al.¹ A single-peak PL emission was observed from all the InN nanocolumns. By way of example, InN nanocolumns with diameter of about 900 nm, height of 1.0 μm and pitch of 1.0 μm showed the PL peak at 0.678 eV and the linewidth of 20 meV. Acknowledgement: This study was supported by Grants-in-Aid for Scientific Research on Priority Areas No.1806910 from the Ministry of Education, Culture, Sports, Science and Technology, Japan.

2:50 PM Student

JJ5, Pt Catalyst-Assisted Metalorganic Vapor Phase Epitaxy of InN: *Kohei Sasamoto*¹; Ken-ich Sugita¹; Akihiro Hashimoto¹; Akio Yamamoto¹; ¹University of Fukui

Indium nitride (InN) has attracted much attention as an important III-nitride semiconductor because a high electron mobility and a high saturated electron velocity are expected. Intensive studies have been made to grow high quality InN by using MOVPE or MBE method. In spite of the considerable efforts, the quality of MOVPE InN has been inferior compared with that of MBE films. Recently, we have made a systematic study on the crystallographic and electrical/optical characterization of MOVPE InN and elucidated factors that restrict the quality of MOVPE InN. The most important finding is that the growth temperature should be restricted to less than 600°C because of the deterioration of grown InN near the substrate interface. On the other hand, a higher growth temperature is required to increase NH₃ cracking rate, and as a result, to increase effective N/In ratio. To solve this dilemma, it is essential to develop a method to enhance NH₃ cracking rate at a low temperature. It is known that Pt group metals such as Pt or Ru heated at 500-1000 K can decompose NH₃ effectively. In this paper, we propose and demonstrate the first catalyst-assisted MOVPE (CA-MOVPE) of InN. In order to enhance ammonia decomposition



rate, platinum (Pt) is used as a catalyst. InN film is grown on (0001) sapphire substrates and GaN/sapphire templates using the atmosphere pressure MOVPE with a horizontal reactor. The NH₃ supply tube in the reactor, containing Pt wires, is placed on the susceptor to be heated. It is found that the electrical properties of InN films grown at 525-575°C are largely improved by using Pt catalyst with a low NH₃ flow rate (3 SLM) and an InN film with a carrier concentration in the order of 10¹⁸ cm⁻³ and a Hall mobility higher than 1300 cm²/Vs is reproducibly grown at 550-575°C. With increasing film thickness, electron mobility is increased and FWHM of (0002) X-ray rocking curve is decreased, indicating that the deterioration of grown InN is suppressed. The results obtained in this study show that intermediate species, such as NH₂, NH and N, in the NH₃ decomposition process play important roles in the InN growth process. Further improvement of InN quality will be achieved by optimizing growth conditions including the selection of catalyst metal and its operating conditions.

3:10 PM Break

Session KK: III-Nitride: Nanostructures

Thursday PM
June 25, 2009

Room: 207
Location: Pennsylvania State University

Session Chair: Huili (Grace) Xing, University of Notre Dame

3:30 PM

KK1, Nanoribbon AlN/GaN HFETs: Towards Enhancement Mode Devices: *Tom Zimmermann*¹; Yu Cao¹; Xiangning Luo¹; Guang Zhou¹; Tom Kosel¹; Debdeep Jena¹; Huili (Grace) Xing¹; ¹University of Notre Dame

We report on the design, fabrication and measurement of monolithic integrated enhancement- and depletion mode ultrathin AlN-barrier AlN/GaN nanoribbonFETs designed by a new developed method of ebeam-lithography defined nano-ribbons between source and drain contact areas. The control of ribbon-depth and -width as well as the control of the gate-length and semiconductor surface and sidewalls by dielectric materials and metal workfunctions offers a wide spectrum of the adjustment of the enhancement- and depletion-performance of the nanoribbonFETs. Also, due to the 3 nm thin AlN barrier on top of GaN substrate an ultra-shallow 2DEG with high charge density > 10¹³ cm⁻² and high electron mobility in excess of 1400 cm²/Vs is formed – thus, the depletion mode HFET owns a pinch-off voltage as low as -3 V suitable for digital integrated circuits. This reported method of threshold voltage control by using nanoribbons is a novel method amongst the methods of barrier thickness control, gate-recess techniques, C-doped GaN buffer layers, surface control by SiN passivation layer and Fluoride plasma treatment. First GaN-based digital logic was successfully demonstrated and tested under harsh environmental conditions. Low-power RIE-CL₂-plasma-etching of 70 nm wide nano-ribbons defined by ebeam-patterned HSQ-resist is used to isolate the ribbons by a 50 nm deep mesa-etch. ALD-Al₂O₃ dielectrics and Ti/Au gate-metal is wrapped around the ribbons and cover surface as well as side-walls of the ribbons. DC output characteristics of depletion- and nearly enhancement-mode devices with gate-lengths of 2 μm are demonstrated. The depletion-mode AlN/GaN HFET owns a pinch-off voltage of just -3 V with a maximum output current density of > 1 A/mm for 2 μm gates and the nanoribbonFET owns a threshold voltage of ~ -0.3 V. A threshold voltage shift towards the positive voltage side was observed by increasing of the gate-length to 3 μm basically explained by an increased gate-capacitance and short-channel effects. The for the first time demonstrated enhancement-mode AlN/GaN nanoribbonFET with a gate-length of 3 μm has a threshold-voltage of about +0.3 V and shows a maximum output current density of ~ 500 mA/mm. With the further development of high-speed normally-off AlN/GaN HFET devices fast digital GaN-based E/D-mode circuits can be designed.

3:50 PM Student

KK2, OMVPE Growth and Characterization of III-Nitride Nanorod LEDs: *Isaac Wildeson*¹; David Ewoldt¹; Robert Colby¹; Zhiwen Liang¹; Dmitri Zakharov¹; R. Edwin Garcia¹; Eric Stach¹; Timothy Sands¹; ¹Purdue University

Nano-heteroepitaxy is currently investigated as an approach towards achieving highly efficient light emitting diodes (LEDs). Specifically, nanorods and nanowires are prime LED candidates due to their high extraction efficiencies and ability to be grown without extended defects. Another benefit of nano-heteroepitaxy is strain relaxation. This is of particular importance in III-nitride LEDs as it allows higher InN content in the InGaN quantum wells without dislocation generation or phase separation. Electroluminescence results from III-nitride nanorod LEDs indicate that these structures do indeed have far superior light extraction compared to planar LEDs,¹ and can be tuned to emit at any color across the visible.² Though these results are very encouraging, much of the work on III-nitride nanorod LEDs has been done by use of MBE or HVPE; two systems not commonly used for production scale LED fabrication. Instead, the majority of industry uses organometallic vapor phase epitaxy (OMVPE) for heterostructure growth. We present a novel approach for OMVPE growth of III-nitride nanorod LEDs that utilizes similar growth conditions as conventional planar heterostructures. Our particular focus is a solution to the so called “green gap” – the current inability of producing high efficiency green LEDs. In our design, porous anodic alumina is used to template a dielectric mask from which dislocation-free, n-type GaN nanorods are grown.³ Upon completion of n-type nanorod growth, an InGaN quantum well and a subsequent p-type layer are grown to complete the LED structure within a hexagonal pyramid that sits atop the nanorod. Following growth, nanorod LEDs were subject to typical inductively coupled plasma etching/metallization required for electrical measurements. We will discuss in detail the growth as well as electrical and optical characterization of our nanorod LED devices. Electroluminescence results with a peak emission at 606nm indicate high InN content as expected within our structures. STEM and EDS cross-section analysis confirm the location of InGaN quantum well within nanopillars, as well as indicate an increase in InN content towards the apex of nanopillar. TEM confirmation on the effectiveness of our templated dislocation filter will also be shared. To put results in context, similar processing and characterization will be performed on planar LEDs grown with nanorod samples. This material is based on work supported by the Department of Energy under Award No. DE-FC26-06NT42862. ¹H.-M. Kim, et. al., Nano Lett. 4, 1059(2004). ²A. Kikuchi, et. al., Proc. SPIE 6129, 612905(2006). ³P. Deb, et. al., Nano Lett. 5, 1847(2005).

4:10 PM

KK3, Position Dependent, above and below Band Gap Photoconductivity in GaN Nanowire Photo-Gated FETs: *Aric Sanders*¹; Norman Sanford¹; Paul Blanchard¹; John Schlager¹; Kris Bertness¹; Lorelle Mansfield¹; Christopher Dodson¹; ¹National Institute of Standards and Technology

Gallium Nitride nanowires can be sensitive solar-blind UV detectors. The surface of Gallium Nitride undergoes Fermi pinning, thereby creating a large (~.5eV) band-bending. This surface band-bending effectively traps free carriers, producing a depletion zone. In nanowires this depletion effect is especially significant due to the increased surface-to-volume ratio. Photogenerated holes can change the occupancy of surface states and relax the band bending. This relaxation modulates the depletion zone and can create a large change in channel current. The nanowire acts as a photo-gated field effect transistor by transducing the change in surface band-bending caused by the photogenerated holes. This leads to a situation where a single photogenerated hole can cause up to 10⁶ electrons to flow through the channel. The ultimate sensitivity of this photo-gated FET is determined by several factors including the read-out rate, local defects, the initial surface band-bending, the background carrier concentration, and the intensity of light falling on the wire. In order to create practical sensors these parameters have to be explored. This experiment focuses on the local excitation of the nanowire, read-out rates of ~ 200Hz, and intensities at the ~1nW range for above- bandgap (325nm) excitation and ~2μW range for below-gap (442nm) excitation. We measured wires that are highly n-doped (Si) and wires with very low intrinsic doping. A wire was excited using either a

THURSDAY
PM

442nm line or 325nm line from a HeCd laser. The laser was chopped at ~200Hz, coupled to a fiber, and then magnified through a 100x UV objective creating a spot 1-2µm in diameter. The focused laser beam was used to excite the wire at different locations. The current flowing through the wire was measured using a picoammeter, and the resulting AC photocurrent was measured using a lock-in with the picoammeter acting as a current to voltage amplifier. A wire with high carrier concentration (~1x10¹⁸cm³) showed direct current at .1 V bias of ~1µA, and a photocurrent of ~20 pA under <1nW of 325nm illumination. This corresponds to a reponsivity of ~20 A/W or the production of 76 electrons/s in current for every photon/s incident on the wire. A clear position dependence of this current was seen, as exciting a point 4 µm away produced a photocurrent ~50% larger. Excitation of the wire with 442nm radiation (.2µW, wire is 10x smaller than the spot) creates a photocurrent of roughly 5 pA. This corresponds to a responsivity of .025 A/W or the production of 1 electron/s of current for every 14 photons incident on the wire. The response of nanowires with low carrier concentration (5x10¹⁴cm³), will also be presented.

4:30 PM

KK4, Control of the Growth Kinetics of GaN(11-22) for the Synthesis of GaN/AlN Nanostructures with Reduced Internal Electric Field: Lise Lahourcade¹; Julien Renard¹; Prem Kandaswamy¹; Marie-Pierre Chauvat²; Pierre Ruterana²; Bruno Gayral¹; *Eva Monroy*¹; ¹CEA-Grenoble; ²CNRS-ENSICAEN

III-nitride semiconductors deposited along the [0001] c-axis present spontaneous polarization in addition to any polarization due to their piezoelectric properties. Semipolar nitrides, with the c-axis forming an angle different from 0° or 90° with the growth direction, are a promising approach to attenuate polarization effects, while avoiding the growth difficulties of nonpolar materials that are due to their strong surface anisotropy. In this work, we analyze the plasma-assisted MBE growth of (11-22)-oriented AlN and GaN layers, as well as GaN/AlN nanostructures. We define the growth parameters leading to 3D and 2D growth modes in order to achieve semipolar quantum dots (QDs) and quantum wells (QWs) respectively, and demonstrate the strong reduction of the quantum confined stark effect (QCSE) in these structures. In a first stage, we have optimized the deposition of AlN(11-22) and GaN(11-22) planar thin films. AlN grown on m-sapphire settles into two main crystalline orientations: the nonpolar (1-100) m-plane and the semipolar (11-22) plane. Under slightly N-rich conditions (Al/N~0.95), only the AlN(11-22) crystallographic phase is detected, and the growth is two-dimensional. Regarding GaN, an AlN(11-22) buffer layer is necessary to isolate the (11-22) orientation. We present an analysis of the GaN(11-22) growth mechanisms, with the identification of the growth diagram as a function of III/V ratio and temperature. GaN deposited on AlN(11-22) can follow the Frank-Van der Merwe or the Stranski-Krastanow growth mode by the proper tuning of the growth parameters. The 2D growth of GaN(11-22) requires Ga-rich conditions with a stabilized Ga adlayer on the growing surface. Under these precise growth conditions, it is possible to decrease the rms surface roughness of GaN(11-22) layers to the range of 1 nm. These conditions were applied to the growth of multiple-quantum-well (MQW) structures. PL measurements of a series of GaN/AlN MQWs with 3 nm AlN barriers and different QW sizes attest a strong attenuation of the Stark-shift and a shorter decay time in semipolar structures in comparison to their polar counterparts. These results indicate a strong reduction of the QCSE, in agreement with theoretical calculations that predict an electric field in the semipolar QWs lower than 0.5 MV/cm, to be compared with ~10 MV/cm in similar polar heterostructures. On the other hand, after deposition of few monolayers of GaN(11-22) on AlN under slightly Ga-rich, a growth interruption under vacuum modifies the surface energy and induces GaN islanding. Applying this growth procedure, we have synthesized (11-22)-oriented GaN/AlN QD superlattices which exhibit intense room-temperature photoluminescence. The enhanced confinement in the QD structures in comparison with semipolar QWs is confirmed by the improved thermal stability of the photoluminescence.

4:50 PM **KK5, Late News**

5:10 PM **KK6, Late News**

Session LL: III-Nitride: Optical Devices II

Thursday PM
June 25, 2009

Room: 208
Location: Pennsylvania State University

Session Chairs: Russell Dupuis, Georgia Institute of Technology; Andrew Allerman, Sandia National Laboratories

1:30 PM Student

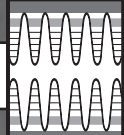
LL1, Efficiency Limitations of Green GaInN/GaN Light Emitting Devices under High Excitation: *Wei Zhao*¹; Yong Xia¹; Mingwei Zhu¹; Yufeng Li¹; Theeradetch Detchprohm¹; Christian Wetzel¹; ¹Rensselaer Polytechnic Institute

Remarkable progress in group III-nitride semiconductor technology has led to applications of high-brightness multiple quantum well (MQW)-based laser diodes (LD) and light-emitting diodes (LED). However, at the targeted operation conditions for power devices, the quantum efficiency drops to only a fraction of its maximum value at low current density. To explore the reason, a detailed spectroscopic analysis was performed to our green emitting structures under both high photon excitation and high electrical excitation. Green emitting GaInN/GaN MQW and GaN epilayers were prepared by metal organic vapor phase epitaxy. Continuous wave (cw) laser light at different wavelengths was used to provide excitation conditions comparable to and above high-power LED and LD operation. By moving the sample around the beam waist of a focused laser beam, optical excitation intensities were varied up to 1 MW/cm². The total light transmittance through the sample then was measured in the far field. Here, depending on the wavelength, we either find a strong nonlinear enhanced absorption or an enhanced transmission. At 408 nm, the transmittance through the MQW structure increased by 6% which indicates a saturable absorption. In contrast, at 514 nm, the same sample has a transmittance reduction starting at 1.7 kW/cm² and reaching 38% at the highest excitation density. This strong absorption enhancement implies that a new recombination process takes effect and may be evidence of higher order effects such as Auger processes. On the other hand, excitation up to 10 kW/cm² was achieved by electrical injection in full green emitting GaInN/GaN LED structures. The electroluminescence spectrum was measured under cw and pulsed (50 µs pulse width, 1% duty cycle) operation. Under cw operation, a saturation of the light output power was observed at electrical excitation of 2.4 kW/cm² but none was observed in pulsed operation up to 6.2 kW/cm². Also, under pulsed operation, the quantum efficiency shows only little variation under high excitation and is significantly higher than that under cw operation. According to thermal modeling results, the junction temperature rise should be limited to 180 K in cw operation but negligible under pulsed operation. An analysis of the high-energy slope of the luminescence spectra reveals that the carrier temperatures increased fast from 2 kW/cm² and reached 880 K and 601K at 3.3 kW/cm², respectively. Comparing results under both, photon excitation and electrical excitation, we can see that the nonlinear absorption, emission power saturation, and strong carrier heating all start around an excitation density of 2 kW/cm². Concluding on the efficiency droop, we so find evidence that all observations may have a common cause that seems relevant to the performance of green LEDs and LDs. This work was supported by a DARPA VIGIL program through the United States Air Force AFRL/SNH under FA8718-08-C-0004.

1:50 PM

LL2, Barrier Effect on Hole Transport and Carrier Distribution in InGaN/GaN Multiple Quantum Well Visible Light-Emitting Diodes: Zachary Lochner¹; *Jianping Liu*¹; Jae-Hyun Ryou¹; P. Doug Yoder¹; Russell Dupuis¹; ¹Georgia Institute of Technology

The quantum efficiency of InGaN/GaN MQW LEDs decreases with increasing drive current, commonly referred to as efficiency droop. It is clear that this is a fundamental problem related to the AlInGaN materials and their epitaxial structures, not a thermal issue induced by Joule heating. This phenomenon is not completely understood, although recently published works have suggested several possible causes including the escape of carriers from localized states in the quantum wells (QW); a decrease in the carrier injection efficiency due



to strain induced piezoelectric fields; Auger recombination; and the leakage of injected electrons into the p-type GaN cladding layer. Most of the discussions on the origin of efficiency droop in III-nitride LEDs point out the carrier injection into the active region and the distribution and densities of carriers in the QWs but are primarily focused on electron transport, and its related leakage current. However, an LED is a bipolar device relying on the efficient injection of both holes and electrons, and each must be distributed optimally in the active region for the effective operation of LEDs. We investigated the carrier distribution related to hole transport in InGaN/GaN MQW LEDs using conventional blue and dual-wavelength (DW) blue-green LEDs. The effects of the quantum-well barrier (QWB) on hole transport and EL characteristics were also studied by varying thickness, height, and doping of the QWB. It was found that holes were dominantly distributed in the QW close to the p-GaN layer in LEDs with conventional MQW active regions at a current of 20 mA. A decrease in the thickness or the height of the QWB enhanced hole injection into the QW located near the n-GaN layer. Silicon doping in the active region QWBs is commonly employed to yield improved electrical and optical properties of blue and violet LEDs. We have studied the effects of Si doping on the operation of green LEDs to determine whether or not the same enhancements occur in longer wavelength devices. We discovered that while Si doping lowers the potential barrier for electron carrier transport throughout the MQW, it raises the barrier for holes, inhibiting uniform distribution. Non-uniform carrier densities are also revealed by simulation of long wavelength MQWs. The model shows a strain-induced piezoelectric polarization associated with interface between the electron blocking layer (EBL) and QWB right below it resulting in the formation of a parasitic inversion layer. This electronic inversion layer charge is screened by bound holes in the MQW, yielding a non-uniform distribution of holes throughout the active region. To counter this effect, we propose a tapered EBL to spatially distribute the piezoelectric interface charge and reduce or eliminate the parasitic inversion layer. Simulations of this design show improved carrier distribution uniformity.

2:10 PM

LL3, Effect of MOCVD Growth Temperature on the Optical and Structural Properties of InGaN Quantum Well Structures: *Mary Crawford*¹; Daniel Koleske¹; Stephen Lee¹; Andrew Armstrong¹; Karl Westlake¹; Nancy Missert¹; Mary Miller¹; Karen Cross¹; ¹Sandia National Laboratories

A major challenge for solid-state lighting is the development of highly efficient InGaN LEDs at green and longer wavelengths. Understanding the low efficiency at these wavelengths requires deconvolving the impact of both materials properties (strain, polarization, compositional inhomogeneities) and growth conditions of higher-indium-composition InGaN alloys. In particular, higher-In alloys require a lower growth temperature that may, in itself, lead to reduced optical efficiency through structural degradation and increased incorporation of impurities and defects. The focus of this work is to clarify the impact of quantum-well (QW) growth temperature (T_{QW}) on the efficiency of InGaN LEDs. Given the more limited T_{QW} range for green alloys, our approach targets blue InGaN QWs of fairly high indium concentration (In~0.17) and employs a wide range of trimethylindium flows to reproduce the same QW structure over an 80°C T_{QW} span. Thus, we maintain nearly constant QW indium composition and examine the effect of T_{QW} on microstructural and luminescence properties. Such an approach has been employed by Hoffmann *et al.*¹ at higher temperatures relevant to near-UV InGaN lasers and here we explore lower temperatures relevant to blue and green InGaN devices. Our study involves InGaN multi-QW samples grown by MOCVD at different T_{QW} ranging from 680 to 760°C. Sample structural parameters were determined using high-resolution x-ray diffraction (XRD) and dynamical diffraction modeling software employing a genetic algorithm that automates nonlinear fitting of complex heterostructures (Bede RADS). All samples had QW indium compositions and thicknesses within the range of 0.169 +/- 0.008 and 2.2 +/- 0.3 nm, respectively. Automated fitting of the XRD data enabled application of more detailed structural models that included compositional grading at heterointerfaces and lateral variations in heterolayer thicknesses. The resulting fits reveal similar QW-barrier interface widths for all samples, confirming maintenance of interfacial quality at low T_{QW} . Nonetheless, photoluminescence data revealed a strong drop in internal quantum efficiency, from 62% to 17%, with decreasing T_{QW} . Photoluminescence images showed a similar spatial variation of

luminescence for all samples and confirmed lower spatially integrated intensities for lower- T_{QW} samples. The lack of structural degradation seen by XRD and the lack of a clear spatial dependence of the decrease in CL intensity with decreasing T_{QW} together suggest formation of a point-defect-mediated non-radiative pathway at low T_{QW} . To further explore this hypothesis, we will present depth-resolved deep-level optical spectroscopy data showing the evolution of deep-level states with lower T_{QW} . Implications of these results for the growth of high-efficiency LEDs will be presented. ¹Hoffmann *et al.*, J. Cryst. Growth 310, 4525 (2008). Sandia is a multi-program laboratory operated by Sandia Corporation, a Lockheed Martin Company, for the United States Department of Energy's National Nuclear Security Administration under Contract No. DE-AC04-94AL85000.

2:30 PM Student

LL4, Device Performance of Fabricated Yellow Emitting GaInN/GaN LED on C-Plane Bulk GaN Substrate: *Wenting Hou*¹; Wei Zhao¹; Mingwei Zhu¹; Theeradetch Detchprohm¹; Christian Wetzel¹; ¹Rensselaer Polytechnic Institute

GaN-based materials have gained high interest for the fabrication of green, blue and UV light emitting diodes (LEDs) and laser diodes (LDs). However, as the InN fraction in the GaInN/GaN quantum well (QW) region is increased to generate deep green or yellow light emission, the external quantum efficiency drops dramatically. Here we analyze performance of fabricated high power yellow LEDs grown in homoepitaxy on c-plane bulk GaN Epi structures were grown in metal organic vapor phase epitaxy with an active region of 10 GaInN/GaN quantum wells. With an InN-fraction as low as 8%, we obtain yellow LED performance. Mesas of size area of 300 μm by 300 μm (350 μm small die) and 600 μm by 600 μm (700 μm large die) were partially etched into the epi surface. Ti/Al/Ti/Au is evaporated as the n-type contact layers and GaN, Ni/Au is used as the p-type electrode. Ti/Au was used as the bonding metal. Under continuous wave (CW) excitation, we measure the light output power (LOP), wavelength, and forward voltage as a function of current. At 100 mA, the LOP reaches 0.67 mW (small die) and 0.84 mW (large die). We obtain a peak wavelength of 585 nm at 20 mA, and 570 nm at 100 mA (large die). With a full width at half max value of 66 nm we achieve chromaticity coordinates of $x = 0.466$ and $y = 0.517$ at 100 mA -- square in the yellow spectral region. However, LOP decreases over time, especially at high current. At 200 mA the LOP drops to about 60% after 1 minute. This is unexpected since there is a high thermal capacity of the 10 mm by 10 mm bulk GaN substrate with high thermal conductivity. In pulsed operation mode with variable low duty cycles we achieve higher LOP at up to 200 mA. There is only minor variation in the emitted spectra when compared to the CW operation mode. The most likely reason for the drop in LOP is a rise in junction temperature despite the anticipated good cooling properties of the bulk substrate. We compare our results with thermal modeling of the junction temperature variations. This work was supported by a DOE/NETL Solid-State Lighting Contract of Directed Research under DE-FC26-06NT42860.

2:50 PM Student

LL5, Well Width Study of InGaN Multiple Quantum Well Structures for Blue-Green Laser Diodes: *Veit Hoffmann*¹; Arne Knauer¹; Casten Netzel¹; Ute Zeimer¹; Hans Wenzel¹; Sven Einfeldt¹; Markus Weyers¹; Günther Tränkle¹; Jan Robert van Look²; Michael Kneissl²; ¹Ferdinand-Braun-Institut für Höchstfrequenztechnik; ²Technische Universität Berlin

The emission characteristics and laser thresholds of InGaN multiple quantum well (MQW) heterostructures in the blue-green spectral range are strongly influenced by the design and the structural properties of the active region. The high indium mole fractions that are required for QWs emitting in this wavelength range strongly affect the optical properties. For devices grown on the polar (0001) orientations the strong piezoelectric fields in the QWs result in reduced dipole matrix elements and a significant red-shift in the transition energies. In order to optimize the light output at longer emission wavelengths, InGaN MQW structures with varying well width (d_{well}) were grown by metal organic vapor phase epitaxy (MOVPE) and investigated with photoluminescence (PL), high-resolution cathodoluminescence ($\mu\text{-CL}$), and high resolution X-Ray diffraction (HRXRD). Thin wells exhibit high photoluminescence (PL) efficiencies due to a reduced quantum-confined Stark effect (QCSE). On the other hand the indium incorporation efficiency into the solid decreases because of the large indium segregation length ($L_s > d_{\text{well}}$). The delayed indium incorporation at the barrier/well interface and the segregation of indium from the QW into the barrier material at the well/barrier interface results in

an indium composition profile with gradual slopes and a reduced average indium content. In order to understand the influence of the well thickness and hence the indium concentration profile on the device characteristics 1D self-consistent laser simulations have been carried out and compared with experimental results. Furthermore, the MQW structures with different well thicknesses were embedded into optically pumped as well as current-injection laser diode structures. The lowest optical threshold power density (I_{th}) was observed for LD structures with the widest QWs of about 2.2 nm whereas I_{th} increases when d_{well} is reduced to about 1.5 nm. This behavior is reproduced by the laser simulation. Finally, we will discuss the effect of the MQW barrier composition on the light output characteristics and the threshold current density of LDs.

3:10 PM Break

Session MM:

III-Nitride: MOCVD Growth and Pseudo-Substrates

Thursday PM
June 25, 2009

Room: 208
Location: Pennsylvania State University

Session Chair: Russell Dupuis, Georgia Institute of Technology

3:30 PM

MM1, Dislocation Reduction in GaN Epilayers on Sapphire and Silicon Using a Self-Assembled Monolayer of Silica Microspheres: *Qiming Li¹; Jeffrey Figiel¹; George Wang¹; ¹Sandia National Laboratories*

We demonstrate an inexpensive and novel technique for the growth of low-dislocation-density GaN epilayers on mismatched substrates, including c-sapphire and Si(111). This technique employs self-assembled silica microspheres as a selective growth mask for dislocation reduction in GaN heteroepitaxy. Using a Langmuir-Blodgett method, silica microspheres are self-assembled into a close-packed monolayer on the surface of GaN/sapphire or GaN/Si(111) pseudo substrates. In a subsequent GaN regrowth, the silica spheres effectively terminate the propagation of threading dislocations from the underlying GaN layer. As a result, the threading dislocation density in the overgrown layer, as measured by large area AFM and cathodoluminescence (CL) scans, is reduced from the underlying GaN layer by approximately two orders of magnitude, from $3.3 \times 10^9 \text{ cm}^{-2}$ to $4.0 \times 10^7 \text{ cm}^{-2}$ on GaN/sapphire substrates and from $\sim 10^{10} \text{ cm}^{-2}$ to $6.0 \times 10^7 \text{ cm}^{-2}$ on GaN/Si substrates. This significant dislocation density reduction is attributed to a dislocation blocking and bending by the spherical GaN/silica interfaces, as confirmed by a cross-sectional TEM study. Based on a finite element analysis of the strain distribution, the GaN regrowth epilayer is free of high-intensity shear strain due to the elimination of large-curvature regions at the spherical GaN/silica interface. The absence of high-intensity shear strain is believed to minimize dislocation regeneration upon GaN coalescence over the growth mask, leading to the low dislocation density. This strain reduction is also evidenced by the large reduction in the density of cracks present in the GaN on Si layer when grown using the sphere template. Sandia is a multiprogram laboratory operated by Sandia Corporation, a Lockheed Martin Company, for the United States Department of Energy under contract DE-AC04-94AL85000.

3:50 PM Student

MM2, High Pressure MOVPE Having High-Speed Switching Valves for the Realization of High Quality AlGaIn/GaN at Low Temperature: *Kentaro Nagamatsu¹; Daisuke Iida¹; Kenichiro Takeda¹; Kensuke Nagata¹; Toshiaki Asai¹; Yoshinori Oshimura¹; Motoaki Iwaya¹; Satoshi Kamiyama¹; Hiroshi Amano¹; Isamu Akasaki¹; ¹Meijo University*

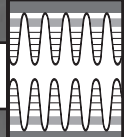
Nitride-based field effect transistor (FET) is promising for application to power switching devices such as high power inverter. High power operations have been already reported by AlGaIn/GaN-based FETs. AlGaIn/GaN-based FET should be superior to conventional AlGaIn/GaN-based FET due to much large band offset between AlGaIn and GaInN and expected higher electron mobility in GaInN. However, it is difficult to realize high quality AlGaIn/GaN heterostructure with atomically abrupt interface due to the difference of the optimum growth temperature

of AlGaIn and GaInN. To realize high quality AlGaIn/GaN heterostructure, we developed a new MOVPE system. New MOVPE system can be operated at high pressure to reduce decomposition of GaInN at high temperature. In addition, this new system contains high-speed gas switching valves with an on-off transition time less than 10 msec. to reduce decomposition of GaInN during gas evacuation and injection. As a first step, we tried to grow AlGaIn/GaN heterostructure. The reactor pressure was maintained at 150 KPa during growth. Nitrogen was used as the carrier gas. The nitrogen source was ammonia. Aluminum and gallium sources were trimethylaluminum and trimethylgallium, respectively. Underlying GaN layers with a thickness of 2 μm were grown on a c-plane sapphire substrate via the low-temperature buffer layer at 1100°C. Then we grew GaN by using high speed valve switching method with a thickness of approximately 150 nm at 650 °C. High speed valve switching method means that group III metalorganic compounds (MOs) and ammonia were supplied alternation by valve switching. In this study, we alternatively supplied the MOs and ammonia with a switching speed of 0.1sec. without interruption. Finally, Al_{0.24}Ga_{0.76}N 200 nm in thickness was grown with the same condition. The surface was mirror like from the naked eye. X-ray rocking curve full width at half maximum of (0002) diffraction from Al_{0.24}Ga_{0.76}N layer was 160 arcsec. Root mean square (RMS) surface roughness of Al_{0.24}Ga_{0.76}N layer for $\mu\text{m} \times 10\mu\text{m}$ scan and $1\mu\text{m} \times 1\mu\text{m}$ scan of atomic force microscopy (AFM) are 0.7 and 0.15 nm, respectively. On the contrary, Al_{0.24}Ga_{0.76}N/GaN heterostructure grown the conventional simultaneous gases supply method shows frosted surface. RMS surface roughness was 140 nm and 23 nm for $10\mu\text{m} \times 10\mu\text{m}$ scan and $1\mu\text{m} \times 1\mu\text{m}$ scan of AFM, respectively. We also grew GaInN using this new MOVPE system. In content in GaInN increases with increase of reactor pressure during growth. Details of the growth condition and properties of AlGaIn/GaN heterostructure will be discussed.

4:10 PM

MM3, Device Applications of GaN Lateral Polarity Junctions: *Ramón Collazo¹; Jinqiao Xie²; Anthony Rice¹; James Tweedie¹; Rafael Dalmau²; Zlatko Sitar¹; ¹North Carolina State University; ²HexaTech, Inc.*

As a consequence of the difference in surface energy between the +c, or Ga-polar, orientation and the -c, or N-polar, orientation of GaN, a difference in chemical reactivity and surface kinetics between the two different surfaces is observed. This translates into a completely different behavior for the incorporation of intentional and unintentional impurities and other point defects as a response to a given process supersaturation for each orientation, allowing for polar doping selectivity. Oxygen is found to be an impurity with higher concentration in N-polar domains than in Ga-polar domains. Acting as a shallow donor, it is the cause for the high carrier concentration observed in N-polar films. The adsorption energy for oxygen under low surface coverage is estimated to be 1.3 eV/atom lower for the N-polar surface than that for the Ga-polar surface for the corresponding expected reconstructions during growth. Utilizing the doping selectivity of the two different polar domains, we fabricated two types of devices: a lateral p/n junction in GaN by the simultaneous growth of p- and n-type regions, and a depletion-mode metal-semiconductor field effect transistor (MESFET) with n-type N-polar domains as source and drain. For the lateral p/n junction, the expected depletion region occurring at or around the inversion domain boundary (IDB) is perpendicular to the growth direction, in contrast to the traditional vertical configuration in which the depletion region opens parallel to the growth direction. It is important to note that the IDB should play a role in carrier recombination since IDBs have been recognized as optically active traps that can function as bright emission centers. The different oxygen and magnesium impurity levels in the N- and Ga-polar domains yielded an n-type carrier concentration of $1.7 \times 10^{19} \text{ cm}^{-3}$ in the N-polar domains, and a p-type carrier concentration of $1.1 \times 10^{17} \text{ cm}^{-3}$ in the Ga-polar domains. We identified in these junctions the characteristics that define a p/n junction: current rectification, electroluminescence, and the photo-effect. Details about fabrication and performance will be discussed. For the MESFET, the difference in the electronic properties of the different type of domains, i.e. as grown N-polar domains are n-type conductive and Ga-polar domains are insulating, allows for laterally selective doped areas that can be realized for improving contact resistance to the n-type conduction channel. Basically, the N-polar domains will act as the ohmic contacts to the channel that is localized in a Ga-polar domain. A MESFET with a 50 nm n-type doped layer as



the channel and Schottky contacts as the gate, with a width of 80 μm and a length of 1 μm was fabricated as an example of implementation of this novel structure. Figures of merit describing the performance will be presented including dc transconductance and specific contact resistivity.

4:30 PM Student

MM4, Realization of Full Wafer Low Dislocation Density Al_{0.25}Ga_{0.75}N on AlN/Sapphire Using Facet-Controlled Epitaxial Lateral Overgrowth: Kenichiroh Takeda¹; Fumiaki Mori¹; Motoaki Iwaya¹; Satoshi Kamiyama¹; Hiroshi Amano¹; Isamu Akasaki¹; ¹Meijo University

Group-III nitride semiconductors are promising candidates for UV-light-emitting devices such as UV-light emitting diodes (LEDs). To realize high-performance UV LEDs, thick, crack-free and high-crystalline-quality AlGa_N underlying layer with a low threading dislocation density and a device structure without any absorbing layer are essential. We demonstrated high efficiency UV LEDs on high crystalline quality AlGa_N layer on grooved AlGa_N/AlN/sapphire template with an output power of 12 mW at a DC current of 50 mA, which external quantum efficiency corresponded to the approximately 6.7 %. In this structure, high efficiency region is limited in the groove. Therefore, effective area is only half. To realize further improvement of the UV LEDs, the AlGa_N underlying layer with a low dislocation density in entire area of the wafer is essential. In this study, we attempted to grow AlGa_N using facet-controlled epitaxial lateral overgrowth on AlN coated sapphire. First, the AlGa_N layer with thickness of 2 μm on AlN/sapphire template was grown by metal-organic vapor phase epitaxy. Using the conventional photolithography and dry etching process, a periodic groove structure was formed along the m-axis direction with the 3 μm wide terrace, 3 μm wide grooves and 1 μm depth. Second, facet-controlled AlGa_N was grown on the periodic groove structure at 930°C. Third, the Al_{0.25}Ga_{0.75}N was grown on the facet-controlled AlGa_N at 1130°C. We succeeded in growing the Al_{0.25}Ga_{0.75}N with entire flat and crack free surface. Finally, the multi quantum well (MQW) structure was grown on the AlGa_N layer. We observed that the dislocation bent horizontally in the Al_{0.25}Ga_{0.75}N layer on the facet-controlled AlGa_N by the cross-sectional transmission electron microscope image. We measured the cathodoluminescence mapping of MQW on facet-controlled AlGa_N and the epitaxial lateral overgrown AlGa_N on the grooved AlGa_N template. The dark spot density of MQW on facet-controlled AlGa_N was 1~2 x 10⁸ cm⁻² at entire area. In comparison, dark spot density in CL mapping of epitaxial lateral overgrowth AlGa_N was 1x10⁸ cm⁻² in grooved region and over 1x10⁹ cm⁻² in terrace region. The comparison of PL intensity of MQWs grown on planar AlGa_N/AlN/sapphire, epitaxial lateral overgrown AlGa_N and facet-controlled epitaxial lateral overgrown AlGa_N was performed. The PL intensity of MQW on epitaxial lateral overgrown AlGa_N is 7.5 times stronger than that of flat AlGa_N, and intensity of MQW on facet-controlled epitaxial lateral overgrowth AlGa_N was further 1.5 times stronger than that of epitaxial lateral overgrown AlGa_N. In conclusion, we succeed in growing low dislocation density Al_{0.25}Ga_{0.75}N in entire area with facet-controlled epitaxial lateral overgrowth technique. It is very useful for the high efficiency short wavelength UV-LEDs and UV-LD because of the non-absorbing structure.

4:50 PM

MM5, Growth of GaN through Confined Epitaxy: Improving Materials, Enabling Devices: Jennifer Hite¹; M. Mastro¹; C. Eddy¹; M. Twigg¹; Y. Picard¹; O. Glembocki¹; ¹Naval Research Laboratory

III-N materials continue to play a significant and growing role in a range of advanced device technologies from RF electronics to visible and UV emitters and detectors. This is despite the heavy population of extended defects (dislocations) in the active regions of most of these devices which diminish the full potential performance of the device. One approach to improve this situation involves the use of confined epitaxy to reduce strain in selectively grown epitaxial material and encourage dislocation annihilation early in the growth and near the interface between the continuous epitaxial layer and the confined epitaxy region, thus reducing their concentration in device active regions. This approach is similar to lateral epitaxial overgrowth, as it uses a patterned substrate, but in order to enable vertical devices, does not involve lateral growth. Using this technique, we have developed materials with dislocation densities reduced by a factor of 10 and stress reductions of 50% compared to continuous layers. These improvements are theorized to be the result of the ability of the confined epitaxy columns to

twist and flex to accommodate strain without a need for extended defects.¹ These improved materials have been employed to make UV imaging arrays, including unique two-color UV imagers.² Although these initial results show great promise, a detailed study of the fundamental mechanisms involved in confined epitaxy is lacking. Such a study is essential to optimizing the process for the full range of the III-N quaternary materials system. This work is an initial effort toward a better understanding of the fundamentals of confined epitaxy of Al_xGa_{1-x}N (x = 0 – 0.20) regions on GaN substrates, while examining the effects of key growth parameters, such as temperature, pressure, and V/III ratio, on the confined epitaxy columns in regard to the resulting sidewall angle, dislocation density, and impurity/dopant incorporation. The effects of varying the mask dimensions, namely opening size and spacing, will also be presented. Column sidewall angle and overall morphological characterization are performed by scanning electron microscopy. Dislocation density is characterized by electron channeling contrast imaging.³ Impurity and dopant incorporation is characterized by a combination of energy dispersive x-ray spectroscopy and secondary ion mass spectrometry. Overall, the growth process is robust, resulting in smooth column surfaces (0.4nm rms roughness) and sidewalls (60-70°) for most growth conditions. As expected, the growth rate is dependent on feature size, with the rates of smaller features higher than that of larger ones. In extending the process to ternary materials (AlGa_N), cation incorporation diverges from gas phase values, with the Al content lower than expected based on molar flow fractions. Further work extending this method to growth on SiC substrates will also be discussed.

5:10 PM

MM6, Growth Mechanism of AlN/Sapphire Grown by Vapor Phase Epitaxy Using Al and Li₃N: Yoshihiro Kangawa¹; Toshihiko Nagano²; Tetsuya Ezaki²; Noriyuki Kuwano²; Koichi Kakimoto²; ¹Kyushu University, JST PRESTO; ²Kyushu University

Deep UV-LEDs are expected to have applications in many fields, such as white light illumination and high-density optical storage. However, the external quantum efficiencies of the AlGa_N UV-LEDs are quite low compared with those of InGa_N blue-LEDs which have been already commercialized. This is because a large numbers of threading dislocations are remaining in AlGa_N active layers. It is known that the threading dislocation density has a much greater influence on external quantum efficiency of LEDs composed of AlGa_N materials than of InGa_N materials. Therefore, suppressing the threading-dislocation-formation is thought to be a key factor to improve external quantum efficiency of AlGa_N UV-LEDs. Related to the suppression of threading-dislocation-formation, homoepitaxial growth might give us a solution because lattice mismatch between epi-layer and substrate causes threading-dislocation-formation. The present authors devote to grow bulk AlN which make enable to perform homoepitaxial like growth of Al-rich AlGa_N. First, we estimated about the suitable nitrogen source for bulk AlN growth. Followings are viewpoints of the estimation; (1) melting point of the source material, and (2) probability of nitrogen transfer from nitrogen source to aluminum source. From our estimation, Li₃N (melting point: 813°C) is a candidate material for bulk AlN growth. Next, we examined the chemical reaction of Al+Li₃N=AlN+3Li by vapor phase epitaxy on sapphire (a-Al₂O₃) substrate. By Raman spectroscopy and XRD analyses, it is confirmed that AlN was surely grown on the a-Al₂O₃ substrate. In the present study, we carried out cross-sectional TEM observation of the grown films to investigate the microstructures and growth mechanisms of films. TEM bright-field image reveals that AlON was formed at the early stage of growth and then AlN was grown out. This implies that the surface of a-Al₂O₃ substrate is etched by Li in the nitrogen source, Li₃N, to generate oxygen atoms that were, in turn, incorporated into grown films. After the covering of substrate surface with AlON layer, AlN was grown on it. TEM dark-field images and selected-area-diffraction patterns show that the AlN layer was composed of two types of domains: One of those has a columnar shape and the other has a hillock shape. Former type domains cover the later one. Therefore, growth rate of columnar domains might be larger than of hillock domains. The results suggest that [0001]AlN was tilted from [0001]a-Al₂O₃, though there is an epitaxial relationship along AlON and a-Al₂O₃ as [111]AlON // [0001]a-Al₂O₃. The results also show that tilting angle of [0001] of hillock-shaped AlN is smaller than of columnar one. Since the volume fraction of hillock-shaped AlN increases with the decrease of growth rate, the crystalline quality of AlN is expected to be improved by lowering the growth rate.

Session NN:

Contacts to Semiconductor Epilayers and Nanowires

Friday AM
June 26, 2009

Room: 106
Location: Pennsylvania State University

Session Chairs: Suzanne Mohney, Pennsylvania State University; Lisa Porter, Carnegie Mellon University

8:20 AM Student

NN1, Size Dependence of Nanowires (NWs) on the Formation of Silicide Contacts to Silicon Nanowire Field-Effect Transistors (SiNW FETs): *Seung-Yong Lee¹; Dong-Joo Kim¹; Tae-Hong Kim¹; Duk-Won Suh¹; Sang-Kwon Lee¹; ¹Chonbuk National University*

Semiconductor nanowires have remarkable attentions for applications in both electronics and photonics.^{1,2} In particular, SiNWs are promising as the channel material for high-performance transistors because of their electronic properties can be controlled during synthesis in a predictable manner.³ And, reducing the diameter of SiNWs was also very important for forming silicide ohmic contacts on Si NW-based field-effect transistors.⁴ At present, the size of SiNWs is controlled by a thickness of a metal thin-film deposited on the substrate prior to the NW growth as well as a size of metallic nanoparticles dispersed on substrate, where both thin-film and metallic nanoparticle are acted as a catalyst in vapor-liquid-solid growth process. It is highly important to control the size of SiNWs for fabricating well-controllable FET and other electronic devices. To control of the size of Si NWs, we used wet etching process using KOH/IPA solution.⁵ We also discuss that the electrical performance and the formation of metal silicide are highly depending on the size of SiNWs. The SiNWs were grown by a VLS method in a chemical vapor deposition system with a SiH₄ as a silicon precursor and gold as the catalyst on Si (111) substrate. The Si nanowires had diameters in the range of 150-200 nm and lengths of 5-10 μ m. To reduce the diameters of SiNWs, SiNWs were first etched with BOE for 5 s for removing the native oxide on Si substrate and then immersed in a 60°C KOH/IPA solution (20 wt % KOH in DI water ; 3:1 vol/vol). We found that the etching rate was determined to be ~ 5 nm / 1 s by the observation of FE-SEM. The SiNW FETs were fabricated by conventional e-beam lithography with a back-gated three-probe structure. Evaporated Ni electrodes were used as ohmic contacts to SiNWs. And then, to get low resistivity ohmic contacts, the SiNW FETs were annealed at a temperature of 400°C for 30 s in ambient N₂. The electrical characteristics studies were performed on several SiNW FETs with different diameters at room temperature using an HP4156C semiconductor parameter analyzer in the range of 20 fA-100 mA. ¹T. Kuykendall, P. Pauzauskis, S.-K. Lee, Y. Zhang, J. Goldberger, and P. Yang, *Nano Lett.* 3, 1063 (2003). ²S.-K. Lee, T.-H. Kim, S.-Y. Lee, K. -C. Choi, and P. Yang, *Phil. Mag.* 87, 2105 (2007). ³Y. Wu, Y. Cui, L. Huynh, C. J. Barrelet, D. C. Bell, and C. M. Lieber, *Nano Lett.* 4, 433 (2004). ⁴J. Appenzeller, J. Knoch, E. Tutuc, M. Reuter, and S. Guha, *Electron Devices Meeting* (2006). ⁵T. J. Kempa, B. Tian, D. R. Kim, J. Hu, X. Zheng, and C. M. Lieber, *Nano Lett.* 8, 3456 (2008).

8:40 AM Student

NN2, Method for Extracting Schottky Barrier Heights of Contacts to Semiconductor Nanowires: *Nicholas Dellas¹; Karthik Sarpatwari¹; Sharis Minassian¹; Joan Redwing¹; Theresa Mayer¹; Suzanne Mohney¹; ¹Pennsylvania State University*

Conventional methods for measuring Schottky barrier heights of electrical contacts to semiconductors can yield inaccurate results for contacts to semiconductor nanowires. Band bending at the surface of the nanowire adjacent to an axial metal/semiconductor contact can cause the depletion width of the Schottky barrier to vary radially. In this case, analysis of a single current-voltage (I-V) curve will yield an effective Schottky barrier height and not the actual barrier height. In order to better understand the effect of nanowire size on Schottky barrier contacts, the true Schottky barrier height needs to be extracted. To address this problem, we have employed a surround gate architecture wherein an aluminum gate is wrapped around an oxidized silicon nanowire that contains

an axial silicide/silicon contact. The advantage of this test structure is that the silicide/silicon nanowire contact and adjacent nanowire can be gated. By changing the gate voltage, we can then effectively control and modify the band bending at the oxide/silicon interface. The structure has been simulated using Sentaurus TCAD tools, and the forward bias I-V characteristics were obtained for different gate biases. The simulations show that the barrier heights extracted using the ordinary equation for thermionic emission at a Schottky barrier contact do not generally match the exact Schottky barrier height input into the simulation. Under an appropriate range of gate biases, however, the ideality factor vs. the effective Schottky barrier height can be plotted as a straight line, and the actual Schottky barrier height can be obtained by extrapolating a plot of the ideality factor vs. barrier height to $n = 1$. Additionally, simulations have explored the effects of interface states at the oxide/silicon interface, doping, and image force lowering. Finally, fabrication of wrap-around gate Schottky diodes was completed. Preliminary measurements yield a Schottky barrier height of 0.57 eV for axial θ -Ni₂Si contacts to n-type silicon nanowires with 40 nm diameters.

9:00 AM Student

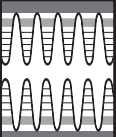
NN3, Numerical Simulation of Reduced Contact Resistance via Nanoscale Topography at the Metal/Semiconductor Interface: *Brian Downey¹; Suman Datta¹; Suzanne Mohney¹; ¹Pennsylvania State University*

The reduction in the parasitic resistance from ohmic contacts in devices is of great significance due to the continued scaling of Si-based transistors and the desire to shift to high mobility, compound semiconductors for logic applications. The ITRS roadmap predicts that the maximum allowable contact resistivity in 2015 must be less than half that used in the current technology. While the choice of materials and processing steps used to fabricate the contacts is important in minimizing contact resistance, it is essential to explore other means of reduction. High semiconductor doping at the contact is used to increase the contribution of tunneling through the Schottky barrier to the overall current; however, there is a limit to how much active dopant that can be incorporated. One possibility to reduce the contact resistance is through the use of topographical features at the metal/semiconductor interface. It has been shown that at small dimensions the tunneling component of current in Schottky diodes is increased for appropriate geometries.¹ This approach has also been exploited when nanopatterned features were employed to decrease the contact resistance to moderately doped n-GaN.² In order to predict the improvement that nanoscale features might have on different semiconductors of interest, two dimensional numerical modeling has been used prior to experimental investigation. In this study, TCAD software by Synopsys, Inc., was employed to examine the effect of various sizes, shapes, and spacings of features on contact resistance. A simple 2D structure utilizing lateral current flow in a semiconductor between two contacts was used as a basis for the study. The simulation provided the opportunity to observe how tunneling, contact area, and depletion width were affected by the addition of nanoscale features. The decrease in resistance was found to vary greatly depending on the size, shape, and spacing of the features as well as the barrier height, doping density, and semiconductor properties. While it is known that protrusions with a smaller radius of curvature will increase tunneling, especially at lower doping densities, the spacing of these features is important due to the overlap of depletion regions from adjacent features. For instance, for 2 nm radii features, the same approximate reduction in resistance could be achieved by spacing the features 6 nm apart or directly next to each other for a 100 nm length contact. The possibility of at least a 20% increase in current at a given voltage for Si ($n = 10^{20}$ cm⁻³) and 50% for InGaAs ($n = 3 \times 10^{19}$ cm⁻³) appears to be obtainable. ¹G.D.J. Smit, S. Rogge, and T.M. Klapwijk, *Appl. Phys. Lett.* 81 (20), 3852 (2002). ²H.G. Kim, P. Deb, and T. Sands, *J. Electron. Mater.* 36, 359 (2007).

9:20 AM Student

NN4, High Doping Effects on the In-Situ and Ex-Situ Ohmic Contacts to n-InGaAs: *Ashish Baraskar¹; Mark Wistey¹; Vibhor Jain¹; Uttam Singiseti¹; Greg Burek¹; Brian Thibeault¹; Yong Lee²; Arthur Gossard¹; Mark Rodwell¹; ¹University of California, Santa Barbara; ²Intel Corporation*

With the continued scaling of transistors for high-speed performance, achieving very low resistance metal-semiconductor contacts becomes crucial.



The base and emitter contact resistivities in heterojunction bipolar transistors (HBTs) must decrease in proportion to the inverse square of the transistor cutoff frequency^{1,2}. A contact resistivity of less than $1 \times 10^{-8} \Omega\text{-cm}^2$ is required for III-V HBTs and FETs for having simultaneous 1.5 THz f_t and f_{\max} ^{1,2}. High electron velocities in InGaAs enable wide-bandwidth electron devices^{3,4}, but lower-resistance ohmic contacts to InGaAs are needed. Here we report the effect of high doping on the contact resistance of in-situ and ex-situ ohmic contacts to n-type $\text{In}_{0.53}\text{Ga}_{0.47}\text{As}$, lattice matched to InP. A 150 nm $\text{In}_{0.52}\text{Al}_{0.48}\text{As}$ layer was grown by solid source molecular beam epitaxy (MBE) on semi-insulating InP (100), followed by 100 nm of silicon doped $\text{In}_{0.53}\text{Ga}_{0.47}\text{As}$. Without breaking vacuum, 20 nm of Mo was deposited on half of each sample using a shadow mask. Hall measurements were done on the bare InGaAs surfaces. All the samples were then processed into transmission line model (TLM) structures for contact resistance measurement. Ti/Au/Ni contact pads were patterned on the samples coated with Mo, whereas Ti/TiW/Ti/Au/Ni contact pads were patterned on the samples with bare InGaAs surface using i-line optical photolithography and lift-off. Mo and Ti/TiW were then dry etched in SF_6/Ar plasma using Ni as etch mask. A four-point probe technique was used to measure resistances using an Agilent 4155C semiconductor parameter analyzer. Experimental results show that the contact resistance of in-situ Mo and ex-situ Ti/TiW ohmic contacts on n-InGaAs get better if the total number of dopants is increased, even though the number of active carriers remains constant. This is evident from the lowest contact resistance achieved for in-situ Mo contacts ($(4.7 \pm 2.5) \times 10^{-9} \Omega\text{-cm}^2$) and ex-situ Ti/TiW contacts ($(7.6 \pm 3.5) \times 10^{-9} \Omega\text{-cm}^2$) for samples with $1.5 \times 10^{20} \text{cm}^{-3}$ total Si dopants but with $5 \times 10^{19} \text{cm}^{-3}$ active carriers. This contact resistance is lower than that obtained with samples with lower total Si dopants ($1 \times 10^{20} \text{cm}^{-3}$) but with similar ($5 \times 10^{19} \text{cm}^{-3}$) active carrier concentrations. We speculate that the reduction in contact resistivity is due to filling of additional surface states that are below the level of the donor band, by dopants which do not donate electrons in bulk material but do donate to lower energy surface states. Additional ionized donors reduce the Schottky barrier to electrons. Although we observe a decrease in active carrier concentration as Si atomic concentration is increased above $1 \times 10^{20} \text{cm}^{-3}$, the contact resistivity continues to decrease, as would be expected from decreased surface depletion depth from an increased ionized carrier concentration. This data strongly suggests that Si may not be amphoteric at Si concentrations below $1.5 \times 10^{20} \text{cm}^{-3}$.

9:40 AM

NN5, Nanofabrication of Niobium Electrodes for Superconducting Light Emitting Diodes: *Jae-Hoon Huh*¹; Yujiro Hayashi¹; Yasuhiro Idutsu¹; Ikuo Suemune¹; ¹Hokkaido University

Solid-state photon sources generating on-demand entangled single photon pairs are highly desired for quantum information processing and communication. Semiconductor quantum dots (QDs) are one of the most promising candidates for such solid-state sources. Electrically driven single photon sources using exciton emission in semiconductor QDs have been successfully demonstrated.¹ Entangled photon pair generation from QDs is also expected by using biexciton-exciton cascade emission. However, it has been difficult to achieve the quantum entanglement of biexciton and exciton photon pairs despite tremendous worldwide efforts mainly due to energy splitting of intermediate exciton states caused by crystallographic anisotropy of semiconductor surfaces. Time intervals and different lifetimes of biexciton and exciton photons will prevent the application to more sophisticated quantum information processing. We have proposed a new scheme to realize solid-state entangled photon pair sources using superconductors,² where Cooper pairs recombine simultaneously bypassing intermediate exciton states in semiconductor QDs. This was named as superconductor-based quantum dot light emitting diodes (SQ-LED), and Cooper pair injection into semiconductors was demonstrated using Nb/n-InGaAs/Nb vertical Josephson junction. In this paper, nano-fabrication of superconducting Nb electrodes and demonstration of superconducting LED will be presented. Nb is the superconductor with the critical temperature of 9.3K and good ohmic contacts to InGaAs have been reported.² However it is the metal with the high melting temperature of 2468°C and nano-patterning without degrading the superconductivity is not necessarily easy. We have developed a method to prepare electron-beam (EB) patterned resists without conventional

prebaking. It is demonstrated that cold-temperature development (CTD) of ZEP resist patterns drastically improves the pattern resolution compared with conventional room-temperature development. With the subsequent dry etching with CF_4 , nano-patterning up to 20 nm was accurately transferred from the CAD design. Highly selective etching of Nb against GaAs was possible with the higher CF_4 gas pressure. We have prepared a junction field-effect transistor (JFET) having a Nb (source) / n-InGaAs / Nb (drain) lateral Josephson junction on a p-InP substrate (gate), which will have the capability to control Josephson current between the source and drain by applying reverse bias to the gate. The forward bias of the gate will inject normal holes and will induce recombinations with electron Cooper pairs injected into the n-InGaAs layers from the Nb electrodes by the proximity effect. The role of Nb superconducting electrodes was studied with optical characteristics observed from the gap between the nano-patterned Nb source and drain electrodes and drastic enhancement of electroluminescence was observed below superconducting critical temperature. ¹Z. Yuan et al., *Science* 295, 102 (2002). ²I. Suemune et al., *Jpn. J. Appl. Phys.* 45, 9264 (2006).

10:00 AM Break

10:20 AM Student

NN6, The Role of Interfacial Oxidation on the Long-Term Stability of Ni-Based Ohmic Contacts to n-Type SiC: *Ariel Virshup*¹; Dorothy Lukco²; Kristina Buchholtz³; Anita Lloyd Spetz²; Lisa Porter¹; ¹Carnegie Mellon University; ²ASRC Aerospace Corporation; ³Linköping University

Silicon carbide is a prime candidate for use in high-temperature chemical sensors for applications such as cylinder-specific monitoring of hydrocarbons from automobile engines and monitoring of flue gases such as CO emitted from power plants. One of the critical limitations in high-temperature SiC gas sensors, however, is the degradation of the metal-SiC contacts over time. Nickel is widely employed as an ohmic contact to n-type SiC. In this study, we investigated the high-temperature stability of Pt/TaSi_x/Ni/SiC ohmic contacts, which have been implemented in SiC-based gas sensors developed for applications in diesel engines and power plants. In our previous studies, the specific contact resistance was characterized as a function of time in air at 300, 500, and 600°C. It was found that the contacts exhibited sufficient electrical stability for operation at 300°C; the contacts remained ohmic for over 1000 hrs in air. In contrast, the contacts heated at 500 and 600°C showed larger increases in specific contact resistance followed by non-ohmic behavior after 240 and 36 hours, respectively. In our recent studies we have focused on chemical changes within the contact layers as a function of time. Depth profiles from Auger electron spectroscopy (AES), as well as electron energy loss spectroscopy, showed complete oxidation of the tantalum-silicide layer in contacts that failed at 500 and 600°C. The high resistivity ($4.8 \times 10^{13} \Omega\text{-cm}$)¹ of the Ta₂O₅ phase, identified in failed contacts, would justify failure of these contacts. In contrast, depth profiles obtained from contacts prior to failure exhibit oxidation that is primarily confined to the metallic-layer interfaces. To understand the process of contact degradation and/or failure, the mechanism, or pathway, for oxidation was investigated. The data consistently shows higher oxygen and lower carbon concentrations near the edges of the contacts relative to the center regions, indicating that oxygen is being transported from the edges along the interfaces. A combination of Auger surface analysis and cross-section TEM analysis indicates that carbon and voids, which are products of the reaction between Ni and SiC to form Ni₃Si, combine to produce a weak interface that facilitates diffusion. We are also investigating the possibility that oxygen diffuses through the Pt cap layer into the underlying contact. TEM images reveal that the Pt layer consists of columnar grains, which also can facilitate oxygen diffusion through Pt to the underlying TaSi_x layer. Secondary ion mass spectrometry is being conducted on samples and will be used to quantify the amount of oxygen in layers. In this presentation, the elemental profiles and oxidation products as a function of heating time/temperature will be discussed, as will the possible oxidation pathways in the Ni-based contacts. ¹B.K. Moon, C. Isobe, J. Aoyama. *J. Appl. Phys.* 85, 1731 (1999).

10:40 AM Student

NN7, Ohmic Contacts to Implanted (0001)4H-SiC: *Mingyu Li*¹; Z. Chen¹; X. Zhu¹; A. Ahyi¹; T. Isaacs-Smith¹; J. Crofton¹; J. Williams¹; ¹Auburn University

The fabrication of low resistance ohmic contacts is a key technology issue for the development of SiC power diodes and transistors. In many cases, contacts are made to implanted regions due to the difficulty of doping SiC by diffusion. In this work, linear transmission line measurements (LTLM) were performed to investigate the relationships between specific contact resistance (r_c) and implanted doping concentration (N_D) for both N- and Al-implanted samples. Carbon caps were used for all samples during the post-implant thermal activation annealing process. The N- and Al-implanted samples were activated at 1550°C/30min/Ar. and 1650°C/30min/Ar., respectively. The alloy NiV7% were used for contacts to N-implanted samples with an anneal at 1100°C for 1 min. at 10⁻⁷Torr. The alloy Al70%Ti30% was used for Al-implanted samples with an anneal at 1000°C for 1 min. at 10⁻⁷Torr. The specific contact resistance for a fixed implant concentration was also studied as a function of activation annealing temperature. A second goal of this work has been to determine the activation percentage as a function of the implant concentration for the various activation annealing temperatures. Hall samples have been prepared for these measurements which await the installation and testing of a new Hall system during the next several months. Results for the implanted samples have been compared to the results reported previously for 4H epitaxial layers. Generally, the data show that the specific contact resistances are higher than predicted theoretically at high implant concentrations. This result is consistent with a lower activation percentage due to implant damage. Furthermore, the data also show that the specific contact resistance to Al-implanted samples is more sensitive to the activation anneal temperature than that to N-implanted samples.

11:00 AM

NN8, Improved n-Type 4H-SiC Schottky Barrier Diodes Using Metal Boride Contacts: *Rani Kummari*¹; Tom Oder¹; ¹Youngstown State University

We fabricated Schottky barrier diodes using Schottky contacts of different refractory metal borides deposited at room temperature (~20°C) and high temperature (600°C) on 4H n-type SiC. The borides investigated included W₂B, W₂B₅, WB, CrB₂, TiB₂, HfB₂ and ZrB₂. The thermal stability of the diodes was tested by annealing using rapid thermal processor (RTP) at 600°C for 20 minutes in nitrogen. The electrical properties of the diodes were characterized by using current-voltage (I-V) and capacitance-voltage (C-V) measurements before and after the annealing. The physical property of the boride/SiC contact was investigated using Rutherford backscattering spectroscopy (RBS). The diodes with the contacts deposited at 600°C had ideality factors around 1.04 – 1.17, while the diodes with the contacts deposited at room temperature had much larger ideality factors. The Schottky barrier heights of the diodes with the contacts deposited at 600°C and at room temperature were comparable and had an average value ~ 0.92 – 1.28 eV. The ideality factor and Schottky barrier heights of the diodes with the contacts deposited at 600°C remained unchanged even after the RTP annealing. The ideality of the diodes which were deposited at room temperature improved after annealing, with no substantial change in the barrier heights. The current density of these diodes measured at -20 V was approximately ~ 5 x 10⁻⁷ A/cm². The improved electrical property and thermal stability of the diodes with contacts deposited at 600°C is related to the removal of O₂ from the boride/SiC interface, as revealed by the RBS analyses. These results indicate improved electrical and thermal properties of boride/SiC Schottky contacts, making them attractive for high temperature applications.

11:20 AM Student

NN9, Reduction of the Specific Contact Resistance in p-Type GaN-Based Devices via Polarization Doping: *Jacob Melby*¹; Li Huang¹; Jason Gu¹; Fang Liu¹; Robert Davis¹; Lisa Porter¹; ¹Carnegie Mellon University

The power efficiency of GaN-based devices is sensitive to energy loss at the p-type contacts. Low resistance contacts to p-type GaN are difficult to achieve due to limitations in acceptor doping. These limitations may be avoided via 'polarization doping'. E. g., increased band bending induced by polarization at a coherent InGaN/GaN interface should result in a reduced barrier width and, at a minimum critical capping layer thickness, result in a two-dimensional hole gas (2DHG) in the In_xGa_{1-x}N layer¹. Au/Ni contacts deposited on 2nm-thick strained

In_xGa_{1-x}N (x = 0.20) layers on p-type GaN films were photolithographically defined into circular TLM patterns for specific contact resistance measurements. The contacts were ohmic in the as-deposited condition, in contrast to contacts without the InGaN layer. During annealing at 500°C for 2 minutes in air, the contacts without the InGaN became ohmic, but the specific contact resistance (6 x 10⁻¹ cm²) was more than three orders of magnitude higher than the specific contact resistance with the InGaN layer (1 x 10⁻⁴ cm²). Cross-sectional TEM showed that the composition and thickness of the InGaN layer were within the limits to remain coherent with the underlying GaN layer. The effects of the composition and thickness of the InGaN layer on the specific contact resistance and the hole concentration in a 2DHG have been determined using self-consistent solutions to the Schrödinger and Poisson equations. Our preliminary data from electrical measurements of actual Au/Ni/In_xGa_{1-x}N/GaN heterostructures show good agreement with the simulations.

11:40 AM

NN10, Electrical Characteristics of Ti/Al Contacts to N-Polar n-Type GaN for Vertical LEDs: *Joon-Woo Jeon*¹; *Tae-Yeon Seong*¹; Hyunsoo Kim²; Jae-Hyun Ryou²; Russell D. Dupuis²; ¹Korea University; ²Georgia Institute of Technology

Recently, high-power III-nitride-based LEDs are of technological importance for their applications in solid-state lighting. However, the external quantum efficiency of conventional top-emission LEDs is not sufficiently high enough to realize solid-state lighting. This is in part because top-emission LEDs suffer from serious problems, such as current crowding, high forward voltage drop, and poor heat dissipation, when operated under high current. To enhance the external quantum efficiency, thus, vertical-structure LEDs have been introduced. However, for n-type side-up vertical LEDs, poor n-type ohmic properties was one of the major barriers to the attainment of high-external quantum efficiency. For example, unlike ohmic contacts to Ga-face GaN, ohmic contacts to N-face n-GaN are difficult to form. In addition, unlike top-emission LEDs, the fabrication of vertical LEDs requires relatively low processing temperatures not to damage host substrates formed by wafer bonding or electroplating. In this work, to form low-temperature n-ohmic contacts for high-performance vertical LEDs, we investigate the effect of laser-irradiation on the electrical characteristics of contacts to thin-film N-face n-GaN. It is shown that the laser irradiation results in a significant increase in the electron concentration and a decrease in the Schottky barrier height as estimated from Pt-based Schottky diodes. Ti/Al contacts to the laser-irradiated N-polar sample exhibit excellent Ohmic behavior with thermal stability up to 600°C. In addition, we investigate TiN/Al contacts to N-face n-GaN. It is shown that the contacts produce better electrical properties than Ti/Al contacts. However, both the TiN/Al and Ti/Al contacts undergo degradation in the electrical properties upon annealing at 300°C, although the former shows the better characteristics. Based on the x-ray photoemission spectroscopy and secondary ion mass spectrometry results, ohmic formation and degradation mechanisms are briefly described and discussed.

12:00 PM Student

NN11, Characterization of Contact Resistance of Al, Ti, and Ni on High-Quality InN Films Grown by RF-MBE: *Shogo Kikuchi*¹; Narihiko Maeda²; Tomohiro Yamaguchi¹; Yasushi Nanishi¹; ¹Ritsumeikan University; ²NTT Photonics Laboratories

InN is a promising material for future high-speed electron device applications, since InN has outstanding material properties such as the smallest effective mass, highest saturation velocity, and largest mobility in nitride semiconductors. In this study, to exploit attractive material properties and ultimately develop InN-based electron devices, we examined the contact resistance of Al, Ti, and Ni on high-quality InN films. All the contact metals including Ni were revealed to exhibit ohmic characteristics with low contact resistances close to one another, indicating that the contact resistance in this experiment is not determined by the work function of each metal. InN films were grown on GaN templates by RF-MBE, where a novel growth method was employed that largely improved the crystal quality. GaN templates were grown on sapphire substrates by MOVPE. The sample structure was as follows: 0.7 μm InN/1.7 μm GaN/buffer layer/sapphire (0001) substrates. Both InN and GaN were undoped, and InN film had

the In-polar surface. The electron concentration and mobility of a 0.7 μm -thick InN film was $3.0 \times 10^{18} \text{ cm}^{-3}$ and $1260 \text{ cm}^2/\text{Vs}$, respectively. We characterized the contact resistance of Al, Ti, and Ni on InN films by using circular transmission line model (CTLM) method. The diameter of the inner circular electrode was 400 μm , and the spacing between inner and outer electrodes was varied from 5 to 40 μm , i.e., 5, 10, 15, 20, 30, and 40 μm . As the contact metals, Al(80 nm)/Au(90 nm), Ti(50 nm)/Au(90 nm), and Ni(50 nm)/Au(90 nm) electrodes were formed by electron beam evaporator and successive lift-off process. All the contact metals were used as the non-alloy contact. In the I-V measurements, all the contact metals exhibited almost the same ohmic characteristics including Ni, although Ni is a typical Schottky metal for (In)GaN. The contact resistance and specific contact resistance for Al, Ti, and Ni estimated from the CTLM measurements were 0.077 (Ω), 0.103 (Ω), and 0.073 (Ωmm) (Ni), and 2.0×10^{-6} (Ω), 3.9×10^{-6} (Ti), and 2.0×10^{-6} (Ωcm^2) (Ni), respectively. The specific contact resistances were thus as low as in the order of $10^{-6} \Omega\text{cm}^2$, and interestingly, their differences were found to be small considering the significant difference in the work function of each metal (4.28 (Al), 4.33 (Ti), and 5.15 eV (Ni)). The surface electron accumulation layer that generally exists in InN films, could be responsible for the result, although further investigation is required. From the viewpoint of electron device applications, non-alloy contact of Al, Ti, and Ni are thus promising as the ohmic contact. On the other hand, developing Schottky contacts to InN-based structures is among essential challenges that need to be addressed in the future.

Session OO: Nanoscale Characterization

Friday AM
June 26, 2009

Room: 108
Location: Pennsylvania State University

Session Chair: Edward Yu, University of California, San Diego

8:20 AM Student

OO1, Influence of InGaAs Well on the Size and Distribution of InAs/GaAs Quantum Dots: *Vaishno Dasika*¹; Rachel Goldman¹; Jin Dong Song²; W. J. Choi²; N. K. Cho²; J. I. Lee²; ¹University of Michigan; ²Korea Institute of Science and Technology

In the past decade, strain-induced self-assembled quantum dots (QDs) have enabled enormous advances in optoelectronics, including high-efficiency light-emitters and detectors. Further advances in light-emitters and detectors will require an understanding of the influence of variations in QD shape, composition, and strain on QD electronic states. It has been suggested that the QD size, shape and density are influenced by the presence of alloy buffer and/or capping layers. For example, it has been reported that InAs/GaAs QDs grown on InGaAs buffers have higher densities than those grown directly on GaAs. Furthermore, growth of InAs/GaAs QDs with InGaAs in lieu of GaAs capping layers apparently reduces the tendency for QD "collapse" (i.e. reduction in QD height) during overgrowth. Here, we investigate the nanometer-scale effects of InGaAs quantum wells as both a substrate, and as a cap layer, on the size, shape, and density of InAs QDs and surrounding wetting layer (WL). Using cross-sectional scanning tunneling microscopy (XSTM), we have mapped out the spatial distribution of the QDs, as well as the dimensions of the capped structures. The samples were grown by molecular beam epitaxy on (001) n+ GaAs substrates via an alternate supply of constituent atoms often termed migration enhanced epitaxy (MEE). The heterostructures consisted of 3 ML InAs QDs in an InGaAs well (QDWELL) and 3ML InAs QDs in a GaAs matrix, separated by at least 50 nm of GaAs to prevent QD stacking and coupling. For the QDWELL layer, the dots were grown on 1.25 nm of $\text{In}_{0.2}\text{Ga}_{0.8}\text{As}$, and capped with 7.5 nm of $\text{In}_{0.2}\text{Ga}_{0.8}\text{As}$. XSTM images reveal uncoupled ellipse-shaped QDs with major and minor axes of $18 \pm 5 \text{ nm}$ and $9 \pm 3 \text{ nm}$ respectively. In addition, the WL for the QD layer shows significant In clustering, which has been attributed to the enhanced diffusion length of In in the absence of As flux during MEE growth. The QDWELLS were also ellipse-shaped, but were

$\sim 16\%$ larger in diameter and $\sim 33\%$ larger in height. Furthermore, the WL for the QDWELLS appears continuous, presumably due to intermixing with the $\text{In}_{0.2}\text{Ga}_{0.8}\text{As}$ layers above and below the QDWELL layer. The QDWELL density was also higher than the QD density. This increase in QD size, density, and WL thickness in the presence of an InGaAs well are consistent with increased intermixing in QDWELLS during growth. We propose a mechanism for QD formation and collapse in the absence and presence of InGaAs wells, based upon lattice mismatch strain. During dot growth on InGaAs layers, the built in strain in the alloyed buffer leads to a reduction in the QD nucleation barrier and the reduced mismatch between the InAs QDs and the InGaAs cap layer leads to a reduction in QD dissolution upon capping.

8:40 AM Student

OO2, Using Scanned Probe Microscopy to Measure Local Electric Field Gradient Fluctuations in Polymers: Showkat Yazdani¹; *Nikolas Hoepker*¹; Seppe Kuehn¹; Roger Loring¹; John Marohn¹; ¹Cornell University

The development of sensors and devices requires increasingly sensitive technology for mapping the properties of thin films. We have shown in a previous study that the dissipation, or non-contact friction, experienced by an ultrasensitive cantilever near a surface can be used to quantify local electric field fluctuations over polymer films in the vicinity of the cantilever resonance frequency.¹ Here we use custom-fabricated attonewton-sensitivity cantilevers to show that cantilever frequency fluctuations ("jitter") can be used to probe electric field gradient fluctuations over a much broader frequency window. We present measurements of weak thermally induced dielectric fluctuations over thin films of three different polymers: polymethyl(methacrylate) (PMMA), polyvinyl(acetate) (PVAc) and polystyrene in tandem with a linear-response, zero-free parameter theory that quantitatively predicts the dependence of the effect on tip-sample distance, film thickness and polymer composition.² The agreement between theory and experiment is excellent. This result suggests using an ultrasensitive cantilever to test microscopic models of other fluctuations, such as charge fluctuations in heterogeneous electronic materials. We also present a surprising new finding that may invite contemplation of the origins of scanned probe microscopy community's current understanding of the origins of cantilever frequency shift. It is well-known that a plot of tip-sample voltage versus cantilever frequency yields a parabola centered at the contact potential. We find that jitter and friction are also parabolic in tip-sample voltage, but that the resulting contact potentials differ dramatically from those obtained via frequency parabolas. "Dielectric Fluctuations and the Origins of Non-Contact Friction," Seppe Kuehn, Roger F. Loring, and John A. Marohn, *Phys. Rev. Lett.* 96, 156103 (2006). "Dielectric Fluctuations in Force Microscopy: Noncontact Friction and Frequency Jitter," Showkat Yazdani, Seppe Kuehn, John A. Marohn, and Roger F. Loring, *J. Chem. Phys.* 128, 224706 (2008).

9:00 AM

OO3, Effects of Embedded Dipoles on the Electrical Response of Self-Assembled Monolayers: *Pengpeng Zhang*¹; Orlando Cabarcos¹; Tad Daniel¹; Paul Weiss¹; David Allara¹; ¹The Pennsylvania State University

Self assembled monolayers (SAMs) are ordered molecular assemblies formed upon adsorption of surfactants on top of a solid surface. SAMs have been widely applied in many fields including, molecular electronics, advanced lithography, and nanofabrication. Recently, interest has grown in the use of polar molecules assembled at electrodes to tune work functions as a way to engineer charge injection barriers in organic electronic devices. With this in mind, we have investigated the electrostatic properties of simple model systems prepared from self-assembled alkanethiolate monolayers on Au{111} which contain a large static dipole group embedded within the molecular backbone. The incorporation of an embedded ester moiety $[-(\text{CO}_2)_m - \text{E}]$, with an intrinsic static dipole moment of ~ 1.8 Debye magnitude, leads to the formation of a strong, highly organized, planar electric dipole layer in the SAM. X-Ray photoelectron spectroscopy data reveals a consistent shift of the C 1s photoelectron kinetic energies between the top and bottom alkyl segments, defined as $-(\text{CH}_2)_m - \text{E} - (\text{CH}_2)_n \text{CH}_3$, regardless of the relative lengths m and n . This shift correlates well with the value of the electrostatic potential across the E layer, as determined from density functional theory (DFT) calculations, quantitative infrared vibrational spectroscopy, and near edge x-ray absorption fine structure (NEXAFS) data.

Recent Kelvin probe force microscopy (KPFM) measurements, however, reveal an apparently anomalous strong dependence of surface potential on the sizes and ratios of m and n , in contrast to the constant electrostatic potential observed in XPS measurements. By grafting molecules with the embedded dipoles onto a metal surface, we have been able to tune its work function over a wide range, which can lead to potential applications in charge injection in organic electronic devices, such as organic field effect transistors, organic light emitting diodes and organic solar cells. Mechanisms underlying these effects will be discussed in terms of dipole-dipole and molecule-substrate interactions with the aid of finite element simulations.

9:20 AM

OO4, Spatially-Resolved Cathodoluminescence Study of III-Nitride Nanowires: *George Wang*¹; Qiming Li¹; A. Alec Talin¹; Andrew Armstrong¹; M. Eugenia Toimil Molares¹; ¹Sandia National Laboratories

GaN, GaN/AlGaIn, and GaN/InGaIn core-shell nanowires grown by Ni-catalyzed metal-organic chemical vapor deposition were studied by spatially-resolved cathodoluminescence (CL). For GaN nanowires, band-to-band luminescence at 362 nm and defect-related yellow luminescence at 550 nm are observed. Point defects, which lead to the yellow luminescence, possibly deplete free carriers near the nanowire surface. This depletion is evidenced by the existence of a critical GaN nanowire radius, below which yellow luminescence dominates. The thickness of the surface depletion layer is estimated to be ~15 nm based on an analysis of the 362 and 550 nm luminescence intensities as a function of nanowire diameter. GaN/AlGaIn and GaN/AlIn core-shell nanowires are observed to exhibit stronger band-to-band emission at 362 nm as compared with GaN nanowire without an AlGaIn shell. The enhanced band-to-band emission is attributed to the passivation of the surface states of GaN nanowires. Electrical measurements further suggest an improvement in the conductivity related to the presence of an AlGaIn or AlIn shell layer. GaN/InGaIn multi-quantum well core/shell nanowires were also investigated by spatially resolved CL, the results of which reveal a strong dependence of shell layer growth rate on the GaN nanowire facet orientation. The morphology revealed by the spatially resolved CL results is confirmed by cross-sectional scanning TEM studies. Sandia is a multiprogram laboratory operated by Sandia Corporation, a Lockheed Martin Company, for the United States Department of Energy under contract DE-AC04-94AL85000.

9:40 AM

OO5, Combination of Optical Characterization and In Situ Electron Microscopy: *Min Gao*¹; Wenliang Li¹; Chengyao Li¹; Qing Chen¹; Lian-Mao Peng¹; ¹Peking University

The developments of optoelectronic nano-devices demand comprehensive characterization of optical, electrical and structural properties with resolution and sensitivity of individual nanostructures. As complementary techniques to electron microscopy, luminescence and Raman spectroscopy can provide rich additional information on semiconductor properties, e.g., band structure, phonon structure, and confinements. In this paper, we present our initial efforts to combine submicron optical techniques and in situ electron microscopy, which yield insights on the physics governing the optical and electrical properties of nanomaterials and nanodevices. We have developed two approaches to enable comprehensive characterization of the same individual nanostructure. In the first approach, individual suspended semiconductor nanowires are attached to nanometer sized metal tips, which allows the same nanostructure to be probed by different instruments, such as scanning electron microscope (SEM), transmission electron microscope (TEM) and micro-photoluminescence (PL). Thus optical (PL), microstructural (SEM and TEM) and electrical (nanoprobe technique inside SEM) characterization can be carried out on the same one-dimensional nanostructure. Our results on in situ "burnt-out" ZnO nanowires show conclusive correlations among defect-related green emission, redshift of the near band edge emission, carrier density and oxygen deficiency. The suspended "nanostructure-on-a-tip" configuration can effectively avoid the complex influences of the substrate and the often used sonication process in solutions. In addition, the flexibility of above technique enables angular micro-PL measurements on individual nanostructures, yielding a quantitative technique in characterizing the waveguiding property of one-dimensional nanostructures.

In the second approach, we have integrated an optical fiber probe in the SEM nanoprobe technique to achieve comprehensive in situ optical, electrical and structural characterization inside a single chamber. The nanoprobe technique, employing sharp metal tips, is used for electrical measurement, contact, and in situ nano-manipulation. The fiber probe, controlled by a nano-manipulator, is coupled to a spectrometer or a laser, which allows local optical detection or excitation. We show in situ assembly of light emitter and photodetector based on individual nanostructures, demonstrating the potential application of above technique in building prototype optoelectronic devices and selecting suitable nanostructures for device purposes. In addition, the angular resolving power of the fiber probe detection is demonstrated to be useful for studying nanoscale waveguides.

10:00 AM Break

Session PP: Non-Destructive Testing and In-Situ Control

Friday AM
June 26, 2009

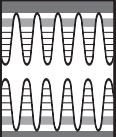
Room: 108
Location: Pennsylvania State University

Session Chair: Kurt Eyink, U.S. Air Force Research Laboratory

10:20 AM

PP1, Characterization of Planar InAs Thin Films by Transmission Electron Microscopy and Spectroscopic Ellipsometry: *Krishnamurthy Mahalingam*¹; *Kurt Eyink*¹; Marlon Twymann¹; Larry Grazulis¹; Jodi Shoaf¹; ¹Air Force Research Laboratory

InAs growth on GaAs has been studied extensively due to the potential of this system to form self-assembled quantum dots SAQDs as well as the high mobility of the InAs layer. SAQD growth is carried out under As-rich conditions, which produce either a (c4x4) or a (2x4) reconstruction. Under these conditions, the InAs growth forms several different structures: two-dimensional 2D, quasi-2D, and three-dimensional 3D clusters that change in concentration as the InAs surface coverage increased. The 3D nuclei associated with the SAQDs structure do not begin to form until the surface coverage of InAs reaches 1.65 ML. Beyond this critical coverage there is a dramatic increase in the density of SAQDs. However, several studies^{1,2} have shown that growth performed in the In-rich (4x2) surface reconstruction regime leads to a suppression of 3D-nuclei formation, maintaining a planar morphology well beyond the 1.65 ML limit. These studies have also shown that strain relaxation in this growth mode occurs predominantly via formation of Lomer dislocations. In this work, we have performed a systematic study of the influence of growth conditions on the structure of planar InAs thin films. Specifically, we conducted several growth experiments wherein the substrate temperature was varied from 623K – 693K, under As flux conditions such that the metal rich (4x2) reconstruction was maintained. The samples so grown were investigated by plan-view and cross-sectional transmission electron microscopy (TEM) and spectroscopic ellipsometry (SE). The plan-view TEM examination of all films examined revealed a well developed periodic array of Lomer dislocations (Fig. 1). Depending on growth temperature, the average dislocation spacing determined from these images was in the range 65Å – 88Å. A systematic dependence between the dislocation spacing and film thickness (measured by cross-sectional TEM) was also observed. An analysis of the SE results showed well defined changes in the critical point structures signifying changes in the dislocation spacing determined by TEM. A detailed discussion on correlations between SE results and TEM observations will be presented. ¹A. Trampert et al. Appl. Phys. Lett. 66, 2265 (1995). ²W. J. Schaffer et al. J. Vac. Sci. Tech B1, 688 (1983).



10:40 AM Student

PP2, Characterization of Near-Surface Electrical Properties of Multi-Crystalline Silicon Wafers: Patrick Drummond¹; Jerzy Ruzyllo¹; ¹Pennsylvania State University

A large portion of the current worldwide solar cell production is based on multi-crystalline silicon (mc-Si). Cast mc-Si wafers with large grain sizes offer a good compromise between cost and efficiency. Anti-reflection properties are enhanced by surface texturing, however, the near-surface electrical properties are often degraded by such processes due to crystallographic irregularities at the surface¹. In contrast to homogeneous single crystalline Si wafers, mc-Si wafers can have large variations in surface properties across the wafer. This presents a challenge for evaluating the impact of various surface treatments on mc-Si substrates. In this study we investigate Hall (bulk) and near-surface carrier mobility, as well as near-surface minority carrier recombination lifetime of mc-Si wafers as a function of location (grain), and as a function of surface treatment. The mc-Si wafer samples used in this study are p-type, with an average resistivity of 1.3 ohm-cm. The hole mobility in the bulk was measured by the Hall method, using temporary contact to the surface, with probes placed within a single grain. Near-surface properties of mc-Si wafers were characterized by photoconductive decay (PCD), again with temporary contact to the surface, utilizing tungsten probes. Photons from illumination with a monochromatic 658 nm laser source are strongly absorbed near the surface of Si. The absorption depth is approximately 4 μm . Because the carriers are generated in a shallow sub-surface region, surface characteristics will have a significant contribution to the effective measurements of mobility and recombination lifetime. The experimental results indicate that bulk mobility is, within limits, reproducible (173 - 223 $\text{cm}^2/\text{V}\cdot\text{s}$) from grain to grain, as well as from chemically polished to unpolished wafers. However, near-surface mobility measurements show a clear distinction between chemically polished and unpolished wafer surfaces, with the mobility of the former being approximately 4 times higher than that of the latter. Similarly, the near-surface minority carrier lifetime measurements show a distinct difference between wafer surface conditions, with an average of 17 μs for polished wafers compared to 5 μs for the unpolished wafers. Near-surface mobility and lifetime were found to be uniform within a given grain region, however variation was observed from grain to grain. This phenomenon was found in both wafer surface types, chemically polished and unpolished. Sensitivity to surface treatment was shown by monitoring the change in near-surface minority carrier lifetime of a polished mc-Si wafer that was processed with a 1% HF solution for 30 seconds, resulting in a reduction of lifetime from 17.4 μs to 5.2 μs . Based on the results obtained, only part of which is discussed in this abstract, it is concluded that the characterization methodology employed in this study can be useful in the monitoring of the solar cell manufacturing process using mc-Si substrates.

11:00 AM Student

PP3, 1/f Noise Characterization of Si:H Thin Films for Microbolometers: Myung-Yoon Lee¹; Hang-Beum Shin¹; David John¹; Nikolas Podraza¹; Thomas Jackson¹; ¹Pennsylvania State University

Arrays of resistors of a-Si:H, VOx, or materials possessing comparably high temperature coefficient of resistance are used in uncooled infrared microbolometer imagers. The performance of such imaging systems can be limited by the noise characteristics of the temperature sensing elements. 1/f noise in particular is problematic and can be influenced by both material characteristics and the device structure. To study 1/f noise in a-Si:H resistive elements, we have constructed a digitizing noise characterization system. In contrast to noise systems that use a low-noise amplifier followed by a dynamic signal analyzer (DSA) or similar Fourier transform tool, this system uses a low-noise amplifier (Stanford Research 570) followed by a low-noise op amp stage and a 16-bit digitizer. The digitized noise signal is then Fourier transformed or otherwise analyzed using MATLAB routines. This approach allows us to use all of the noise data collected during the sample test and provides both lower noise (by increased signal averaging) and a wider frequency range than typical DSA systems. This collection technique allows us to easily measure 1/f noise from 10^{-2} to 10^3 Hz in a single sample test. System operation is controlled using LABVIEW and allows convenient data collection, analysis, and

error evaluation. The noise system is being used to understand the roles which hydrogen dilution during deposition and alloy composition play in contributing to 1/f noise. Samples for noise measurement are prepared in a load-locked plasma enhanced chemical vapor deposition (PECVD) system with integrated real time spectroscopic ellipsometer. Hydrogenated silicon thin films or alloys with Ge or C are prepared by PECVD ($f = 13.56$ MHz) where variable deposition parameters include hydrogen dilution, substrate temperature, and plasma power. These deposition parameters control the microstructure of the material, resulting in either amorphous, microcrystalline, or mixed-phase material compositions as determined by spectroscopic ellipsometry measurements. Noise characteristics of these films are then measured and correlated with film microstructure.

11:20 AM Student

PP4, Piezoelectric Thin Films for Low Voltage, High Frequency MEMS Transducer Array: Hyunsoo Kim¹; Flavio Griggio¹; Insoo Kim¹; Kyusun Choi¹; Richard Tutwiler¹; Susan Trolier-McKinstry¹; Thomas Jackson¹; ¹Pennsylvania State University

High-frequency ultrasound array transducers using piezoelectric thin films are being developed for a high-resolution imaging system. Diagnostic ultrasonic imaging systems for medical applications such as dermatology, ophthalmology and intravascular imaging require very high resolution. This can be achieved by increasing operating frequency (30MHz~100MHz) and close coupling of the transducer and electronic circuitry. The object of this research is to explore piezoelectric thin films to fabricate high frequency array transducers by micromachining and thin film processing techniques. The resulting linear array is compatible with low-voltage CMOS, and we have designed and fabricated a fully integrated CMOS transceiver chip to interface with the transducer array. Lead zirconate titanate (PZT) was chosen as the active material for ultrasound transducer due to its high sensitivity and wide achievable bandwidth. In addition the solid solution lead nickel niobate - PZT has also been investigated. Chemical solution deposition was used to prepare PZT ($\text{PbZr}_{0.52}\text{Ti}_{0.48}\text{O}_3$) and PNN-PZT ($\text{PbNi}_{1-x}\text{Nb}_{2x}\text{O}_3 - \text{PbZr}_{1-x}\text{Ti}_x\text{O}_3$) films. A method to obtain highly {001} oriented PZT and PNN-PZT thin film was developed. It was found that dense and pyrochlore free PNN-PZT thin films show a dielectric constant as high as 1500, a remnant polarization of 20 $\mu\text{C}/\text{cm}^2$ and $\epsilon_{31,f}$ coefficient equal to -10.2 C/m^2 for thickness less than 300 nm. The geometry used for 1-D transducer arrays is a xylophone-bar type with a length:width aspect ratio of > 5:1 in order to isolate the resonance modes. The fabrication process is based on surface micromachining techniques. For the linear array transducer, a layered structure of a dielectric (SiO_2), sputtered Ti/Pt bottom electrodes, PZT, and a Pt top electrode was employed. The structure was partially released by etching the underlying silicon substrate in XeF2. Following fabrication, the transducer array was coated with parylene as a protective layer. The fabricated device is packaged into a 16-pin ceramic package and tested. Pulse-echo measurement in water demonstrates functionality of both transmit and receive operations. The center frequency of single element transducer shows ~60MHz with a 6 dB bandwidth of 30% even with no front matching layer.

11:40 AM

PP5, Effect of Applied Pressure on the Electrical Properties of Nano-Deformed Materials: David Vodnick¹; Ryan Major¹; Hysitron, Inc.

As materials and devices continue to proceed toward ever-decreasing length scales, successful integration of these materials and devices depends heavily on the ability to quantitatively assess and tailor their electrical and mechanical properties. While mechanical property testing at the nanoscale has become common practice, little research has been focused on the applied pressure-electrical response relationships of nano-deformed volumes of material. A newly developed conductive nanoindentation technique provides concurrent nanomechanical and electrical measurement capabilities and has been proven to be highly sensitive to changing probe/sample contact conditions as well as material deformation behavior. In this study, we investigate the electrical behavior of several classes of materials as a function of applied loading conditions. Baseline experimental results taken on bulk, polycrystalline gold are presented and show good agreement with theoretical results predicted using classical contact resistance calculations. However, substantial deviations from the gold baseline experiments are observed during the deformation of n and

p-type Silicon, (100) aluminum, bulk metallic glass alloys, and a PZT film. For silicon, pressure induced phase transformation pathways are investigated during high pressure loading and on subsequent pressure release. Upon loading, a transformation from crystalline Si-I transforms to a conducting metallic phase (Si-II) at a pressure of ~11 GPa. During unloading the metallic phase becomes unstable below a pressure of ~8 GPa and transforms into either amorphous (a-Si) or high-pressure polycrystalline phases (Si-III and Si-XII), depending on the rate of pressure release. Of considerable fundamental interest in regard to aluminum and other metals is the occurrence of discontinuous yielding, due to bursts in dislocation activity resolvable during the early stages of plasticity. In the case of an electropolished Al (100) single crystal, the measured current vs. applied pressure raises in a discontinuous manner owing to the dislocation activity in the nano-deformed region surrounding the indenter probe. The electrical behavior of several bulk metallic glasses (BMG) was found to be highly influenced by the applied stress state. During initial unloading the measured current through the probe/sample contact increases, despite a decrease in the probe/sample contact area. The measured current was also found to increase immediately before and during shear band formation in the BMG. The direct and indirect piezoelectric effect was investigated by applying stress to a 500nm thick PZT film while monitoring the generated voltage and applying a voltage to the film and measuring the resulting film dilation. A film dilation voltage of 40V in combination with a 4mN applied load was found to be the critical set of parameters to produce catastrophic failure of the device. Conductive nanoindentation is proving to be a versatile technique that can be used to gain a greater understanding of material deformation/ electrical response relationships.

12:00 PM Student

PP6, Electronic Properties of Nanostructured PbTe(In) Films: *Alexandr Dobrovolsky*¹; Ivan Belogorokhov¹; Zinovi Dashevsky²; Vladimir Kasiyan²; Ludmila Ryabova¹; Dmitry Khokhlov¹; ¹M.V.Lomonosov Moscow State University; ²Ben-Gurion University

Narrow gap semiconductors based on PbTe represent a group of materials that are extensively used in microelectronics and infrared optoelectronics. Doping with In induces in lead telluride the Fermi level pinning at 70 meV above the conduction band edge resulting in high mobility ($10^5 \text{ cm}^2 \text{ V}^{-1} \text{ s}^{-1}$ at $T=4.2\text{K}$) and stable electron concentration (about 10^{18} cm^{-3} at $T=4.2\text{K}$) independently on native defect content in a sample. For nanostructured materials, the Fermi level pinning should provide high homogeneity of electrical properties of grains. PbTe(In) films have been grown by deposition to a cooled glass substrate. Changing the substrate temperature allowed to obtain films with the grain size varying from 60 to 170 nm. Microstructure of the films was studied with use of XRD, AFM and SEM techniques. All films had a column-like structure with nearly equal orientation of the columns perpendicular to the substrate plane. The column diameter we determine as the grain size. Phonon modes were studied by micro-Raman scattering. Transport properties in the dc and ac modes were investigated in temperature interval 4.2-300 K. The Hall and the Seebeck coefficients were positive for all the films, though the bulk of the grains should be of the n-type due to In-doping. It means that conductivity of the films in the dc mode is related to the transport along the inversion channels at the grain surface. These channels appear due to broken bonds at the surface of the grains. Frequency dependence of the impedance components was studied in the frequency f range from 20 Hz up to 1 MHz. The impedance modulus and phase were measured and recalculated into the real Z' and imaginary Z'' parts of the impedance $Z^* = Z' - jZ''$. Measurements in the ac modes revealed that the conductivity of the films is determined by two mechanisms: charge transport along the inversion channels at the grain surface and activation through barriers at the grain boundary. Persistent photoconductivity appears in the films below $T=150\text{K}$. Frequency dependence of the relative photoresponse is non-monotonous and has a pronounced maximum. The amplitude and the position of the maximum are found to be dependent on the grain size of the films. It is demonstrated that the photoresponse in the ac mode may be by more than two orders of magnitude higher than in the dc measurements. Influence of grain size variation and film oxidation on the electronic properties is discussed.

Session QQ: Solar Cells - Organic, Hybrid and Inorganic

Friday AM
June 26, 2009

Room: Deans Hall II
Location: Pennsylvania State University

Session Chairs: Christian Wetzel, Rensselaer Polytechnic Institute; Mayank Bulsara, Massachusetts Institute of Technology

8:20 AM

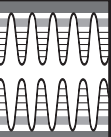
QQ1, Toward Metamorphic Multijunction GaAsP/Si Photovoltaics Grown on Optimized GaP/Si Virtual Substrates Using Anion-Graded GaAs_yP_{1-y} Buffers: *Tyler Grassman*¹; Mark Brenner¹; Andrew Carlin¹; Jeongho Park¹; Srinivasa Rajagopalan¹; Raymond Uncio¹; Ryan Dehoff¹; Michael Mills¹; Hamish Fraser¹; Steven Ringel¹; ¹The Ohio State University

The monolithic integration of high-efficiency III-V compound solar cell materials and devices with low-cost, robust, and scalable Si substrates has been a driving force in fundamental photovoltaics materials research for decades. Recent years have seen high-quality GaAs and InGaP solar cells successfully integrated with Si via Ge virtual substrates on SiGe step-graded buffers. Another route that has seen comparatively less attention exists through the growth of GaP directly on Si, followed by lattice and bandgap engineering with III-V step-graded buffers. Nonetheless, due to the extreme difficulty of high-quality polar/non-polar heteroepitaxial integration of GaP on Si, progress in this direction has been hindered by detrimental nucleation-induced defects, such as antiphase domains (APDs), stacking faults (SFs), and microtwins (MTs). Here we present growth, materials, and device results for GaP/Si and GaAs_yP_{1-y}/GaP/Si virtual substrates and subsequent GaAs_{0.7}P_{0.3} solar cells grown on GaAs_yP_{1-y}/Si, in which the presence of SFs, MTs, and APDs are successfully and simultaneously eliminated. GaP virtual substrates were produced by direct GaP growth on Si substrates using a combination of migration-enhanced epitaxy (MEE) and molecular beam epitaxy (MBE). Si(001) substrates offset 6° toward [110], which produce a double atomic stepped surface upon annealing, were used to prevent the formation of APDs in the GaP epilayers. MEE nucleation on pristine Si(001) prior to MBE bulk growth was found to be of paramount importance for achieving 2D GaP growth, preventing the formation of SF and MT planar defects, as well as APDs related to surface imperfections. With this process we have produced GaP/Si heteroepitaxial films possessing simultaneous control and elimination of SFs, MTs and APDs, creating a GaP-on-Si virtual substrate suitable for photovoltaic and other III-V/Si device applications. First-generation, unoptimized anion-graded GaAs_yP_{1-y} buffers, with aggressive net grading rates of ~3% misfit per micron, were grown on GaP/Si virtual substrates to produce final layer compositions lattice matched to GaAsP solar cells with band gaps of 1.7–1.8eV. Full lattice relaxation, as measured by high-resolution triple-axis x-ray diffraction, was achieved in the GaAs_yP_{1-y} buffers. Preliminary ~1.7eV GaAsP p-n solar cells, with no attempt to optimize the doping profiles, device structure, or back/front surface field layers, and without anti-reflection coatings, were produced in order to obtain an early assessment of the potential of this new materials system. While these cells were grown on early-generation GaP/Si virtual substrates known to possess a high density of interfacial APDs, and utilized structure designs that introduced extra series resistances, very promising I-V characteristics were measured, with $V_{oc} > 1.0\text{V}$ and $J_{sc} > 13\text{mA/cm}^2$ under in-house AM0 illumination. Next-generation cells grown on the defect-free GaP/Si virtual substrates and optimized GaAs_yP_{1-y} step-graded buffers should yield significant improvements beyond the already promising initial device results.

8:40 AM

QQ2, Growth and Characterization of BaSi₂/Si Heterostructure toward Si-Based High-Efficiency Solar Cells: *Yuta Matsumoto*¹; Dai Tsukada¹; Ryo Sasaki¹; Michitoshi Takeishi¹; Takanobu Saito¹; Takashi Suemasu¹; ¹Institute of Applied Physics, University of Tsukuba (Suemasu Lab)

Semiconducting BaSi₂ has potential interest for high-efficiency solar cells because the band gap of BaSi₂ can be increased up to approximately 1.4 eV



by replacing half of Ba atoms with isoelectric Sr atoms, which is considered suitable for solar cells. In addition, both experimental and theoretical studies have revealed that BaSi_2 has a very large optical absorption coefficient α , of over 10^5 cm^{-1} at 1.5 eV, which is more than 100 times larger than that of Si. BaSi_2 can be also grown epitaxially on Si. Thus, combination of Si with BaSi_2 will significantly improve the efficiency in solar cells. However, there have been no reports on the photoresponse properties of BaSi_2 . In this study, we have investigated the photoresponse properties of BaSi_2 epitaxial films for the first time. 900-nm-thick n-type ($\sim 10^{16} \text{ cm}^{-3}$) BaSi_2 epitaxial layers on Si(111) grown by molecular beam epitaxy were used in this investigation. Cr and Au were evaporated on the surface to form 1.5-mm-spacing striped electrodes. The same striped electrodes were also formed with Al on a 500- μm -thick n-type FZ-Si substrate for comparison. Both samples were not covered with an antireflection coating. Light absorption produces electron-hole pairs that are separated by the electric field between the electrodes, leading to current flow in the external circuit as the photoexcited carriers drift before recombination. The photocurrent was observed for photon energies greater than 1.25 and 1.05 eV for the BaSi_2/Si and FZ-Si, respectively, increasing sharply with increasing photon energy to reach maximums at approximately 1.70 and 1.25 eV, respectively. The contribution of photoexcited carriers originating from the Si substrate to the measured photoresponse spectra can be excluded. The α value of BaSi_2 exceeds 10^5 cm^{-1} at 1.70 eV; therefore, almost all the photons at 1.70 eV are absorbed within the BaSi_2 film. The external quantum efficiency at 1.70 eV increased with bias voltage and reached 7% at 7 V. This value is higher than the highest values ever reported for other semiconducting silicides by more than two orders of magnitude. In this work, photoexcited carriers drifted in the lateral direction, and therefore they were likely to experience grain boundaries. In the case of the BaSi_2 pn junction, an enhanced external quantum efficiency can be safely expected, because a much larger built-in electric field ($\sim 10^4 \text{ V/cm}$) exists around the junction, and also the distance that the carriers must travel is much shorter ($\sim 1 \mu\text{m}$) than that in the present case (1.5 mm).

9:00 AM

QQ3, Etched Silicon Pillar Array Solar Cells: *Heayoung Yoon*¹; Yu Yuwen¹; Chito Kendrick¹; Greg Barber¹; Thomas Mallouk¹; Joan Redwing¹; Theresa Mayer¹; ¹Pennsylvania State University

High efficiency planar silicon solar cells use thick, high-purity single-crystal Si (c-Si) substrates to maximize the absorption of the incident solar radiation and the collection of light-generated carriers. The use of less expensive materials with higher impurity levels and crystalline defects leads to a reduction in the minority carrier diffusion length and thus planar cell efficiency. For such materials, an alternative geometry comprised of an array of radial p-n junction pillars can be used to decouple light absorption from carrier collection and improve solar cell efficiencies. This talk will discuss the design, fabrication, and characterization of densely-packed c-Si pillar array solar cells, where the pillar radius and height is approximately equal to the diffusion length and optical thickness of the c-Si material, respectively. The high-aspect-ratio radial p-n junctions were formed by gas phase diffusion of an n-type dopant (POCl_3) into deep reactive ion etched (DRIE) p-type Si pillars, followed by Al contact metal deposition and annealing. The electrical and optical properties of a $0.125 \times 0.125 \text{ cm}^2$ c-Si pillar array that contained $\sim 10^5$ pillars each having a $3 \mu\text{m}$ diameter p-type core (10^{19} cm^{-3}) and a 300 nm thick n-type shell (10^{20} cm^{-3}) were compared to a planar control sample processed under identical conditions. The minority carrier diffusion lengths for the heavily-doped p- and n-type silicon core and shell layers are only $4 \mu\text{m}$ and $0.2 \mu\text{m}$, respectively. The pillar array showed clear rectifying properties with an ideality factor ~ 1.5 . This device had slightly lower current density ($\sim 15 \text{ mA/cm}^2$ at 1V) and higher reverse saturation current ($6 \times 10^{-6} \text{ A/cm}^2$ at -1 V) than the planar control sample. However, the photovoltaic properties of the c-Si pillar array showed a considerably higher efficiency ($\sim 11\%$) than the planar sample ($<1\%$) under 1-sun illumination. This study confirms that the high-aspect-ratio geometry is effective at improving solar cell efficiency for materials with short minority carrier diffusion lengths.

9:20 AM

QQ4, Epitaxial Film Silicon Solar Cells Fabricated by Low-Temperature Hot Wire Chemical Vapor Deposition: *David Young*¹; Kirstin Alberi¹; Ina Martin¹; Charles Teplin¹; Eugene Iwaniczko¹; Yueqin Xu¹; Anna Duda¹; Paul Stradins¹; Steve Johnston¹; Howard Branz²; ¹NREL

Film silicon solar cells grown epitaxially on inexpensive seed-layers on foreign substrates are candidates to replace Si wafer-based photovoltaics due to energy and material savings. Device-quality epitaxial silicon layers have been grown on wafers and silicon seeds on foreign substrates at temperatures well below those used in conventional c-Si epitaxy with several chemical vapor deposition (CVD) techniques. We use hot wire CVD (HWCVD) to achieve high crystalline quality epitaxial Si at low growth temperatures (620-750°C). Here we report the first epitaxial thin film Si solar cells with efficiencies $>4\%$ grown on silicon wafer templates by HWCVD at temperatures $\leq 750^\circ\text{C}$. We have characterized and modeled these devices to extract both epitaxial Si material quality and device physics to guide further improvements. The cells under investigation consisted of a $2 \mu\text{m}$ epitaxial n-type Si:P (10^{16} cm^{-3}) base layer grown on a heavily-doped Si:As ($2 \times 10^{19} \text{ cm}^{-3}$) n^+n^+ wafer. A heterojunction is formed on the epitaxial layer with hydrogenated amorphous silicon (intrinsic-a-Si:H and p-type a-Si:H) grown by HWCVD. Aluminum metal forms the back contact to the substrate wafer and heavily doped indium tin oxide provides the transparent front contact. These devices exhibit efficiencies up to 4.35% with J_{sc} near 13.7 mA/cm^2 and open circuit voltages above 500 mV. These results are competitive with other epitaxial technologies. Internal quantum efficiency (IQE) and microwave photoconductive decay measurements, coupled with PC1D simulations, suggest that device performance is primarily limited by incomplete conversion of photons at blue to ultraviolet wavelengths and an average minority carrier lifetime of $\approx 10 \text{ ns}$ in the epitaxial layer. The low blue response appears to be due (IQE modeling, cross-sectional Electron Beam Induced Current (EBIC), and scanning Kelvin probe) to surface defects in the epitaxial layer or a defective heterojunction interface. Despite the low blue response our J_{sc} is nearly ideal for a $2 \mu\text{m}$ device due to unintentional light trapping. The relatively high open circuit voltages indicate both high quality epitaxy and good junction formation. Further gains in the crystalline quality through post-growth hydrogenation and annealing steps, as well as improvement upon the simple device design utilized in this preliminary investigation, should substantially enhance the performance of these cells. While we have made significant progress in the fabrication and device physics understanding of these low-temperature epitaxial materials and devices on single crystalline substrates, the transfer of an optimized HWCVD growth routine to the deposition of epitaxial Si on a foreign substrate seed layer is the true test of this technological approach. To this end, we will present our latest results in fabricating epitaxial Si cells on Si seed-on-glass substrates. david_young@nrel.gov, 303-384-6621, 1617 Cole Blvd., M.S. 3219, Golden, CO 80401

9:40 AM

QQ5, Microstructural and Electronic Properties of Thin Film Si:H and Ge:H for Uncooled Microbolometer Applications: *Nikolas Podraza*¹; David Saint John¹; Myung-Yoon Lee¹; Hang-Beum Shin¹; Thomas Jackson¹; Robert Collins²; ¹The Pennsylvania State University; ²University of Toledo

Thin film hydrogenated silicon (Si:H) and germanium (Ge:H) are of growing interest for infrared sensing uncooled microbolometers. The electrical properties of interest for this application are a high temperature coefficient of resistance (TCR), controllable resistivity (ρ), low electrical noise and process compatibility with standard IC fabrication. In this work, Si:H thin films have been prepared by plasma enhanced chemical vapor deposition (PECVD) with resulting resistivities ranging from 1.5 to $2000 \Omega \text{ cm}$ and TCR ranging from -0.8 to $-4.0 \text{ \%}/\text{K}$. Si:H and Ge:H films prepared by PECVD have been shown to exhibit changes in microstructure as functions of processing conditions. For example, films prepared at low hydrogen dilution may remain amorphous (a-Si:H) throughout growth, while films prepared at higher dilution may initially grow as amorphous until a bulk layer thickness where microcrystallites nucleate and eventually coalesce into a single-phase microcrystalline layer ($\mu\text{-Si:H}$). In situ real time spectroscopic ellipsometry has been used in order to study variations in the growth evolution and microstructure as functions of deposition parameters

such as hydrogen dilution, R, and doping ratio, D. These types of growth evolution studies have guided optimization principles for the intrinsic and p-type layers in Si:H based thin film photovoltaic devices. Specifically, improved electronic quality a-Si:H is obtained at the maximum hydrogen dilution prior to the nucleation of microcrystallites for a specified layer thickness for photovoltaic devices. Corresponding growth evolution diagrams are being developed for materials used in uncooled microbolometers and are being evaluated in order to discern similar optimization principles by studying differences in the electrical properties (ρ , TCR) resulting from deposition parameter variations. A series of a-Si:H films has been deposited on silicon nitride (Si_3N_4) coated crystalline silicon (c-Si) substrates as functions of hydrogen dilution, $R = [\text{H}_2]/[\text{SiH}_4]$, and p-type doping ratio, using trimethylboron $D = [\text{B}(\text{CH}_3)_3]/[\text{SiH}_4]$ ranging from $D = 0$ to 0.2 . Initial studies have shown that both TCR and r increase with hydrogen dilution for fixed doping gas ratio, which indicates that the optimum TCR for a given resistivity may be obtained by varying both the hydrogen and doping gas dilutions. A growth evolution diagram has been developed for undoped Ge:H films as a function of hydrogen dilution, $R = [\text{H}_2]/[\text{GeH}_4]$, depicting transitions from amorphous to microcrystalline material under high R. a-Ge:H films exhibit relatively high TCR ranging from -2.2 to -3.6 %/K with increasing R. Additionally, amorphous and mixed-phase (amorphous+microcrystalline) n-type Si:H films have been prepared using PH_3 as the doping agent, $D = [\text{PH}_3]/[\text{SiH}_4] = 0.01$. These films were evaluated in order to quantify changes in TCR and r resulting from microstructure (a-Si:H: $\rho = 250$ Ω cm, TCR = -3.8 %/K; a+ μ c-Si:H: $\rho = 1.5$ Ω cm, TCR = -0.8 %/K).

10:00 AM Break

10:20 AM

QQ6, Characterizing the Interfacial Composition of Organic Bulk Heterojunction Solar Cells Using Organic Thin-Film Transistor Analogues: Calvin Chan¹; David Germack¹; Behrang Hamadani¹; Lee Richter¹; Dean DeLongchamp¹; David Gundlach¹; ¹National Institute of Standards and Technology

Organic photovoltaic (OPV) cells are promising candidates for solution processable, flexible, and large-area solar energy conversion. Solar cells employing blended polymer materials have been increasingly investigated because of the modest performance improvements that result from the formation of bulk heterojunctions (BHJ), which increase interfacial areas and position the active area closer to the region of exciton generation. Nevertheless, power conversion efficiencies of BHJ OPVs are still relatively low (<5%), and the factors that contribute to this limitation are still not well understood. In particular, precise characterization of the BHJ film morphology has been difficult, but is important given that the film composition at the buried hole and electron interfaces is crucial to determining the collection efficiencies at the electrodes. In this work, organic thin-film transistors (OTFTs) consisting of poly(3-hexylthiophene):[6,6]-phenyl-C₆₁-butyric-acid-methyl-ester (P3HT:PCBM) blends were studied to elucidate the compositional structure present at the bottom electrode-organic interface. Since the interfacial structure may depend on the surface energy (γ) of the substrate, gate dielectrics consisting of high- γ SiO_2 and low- γ octyltrichlorosilane-modified SiO_2 (OTS- SiO_2) were chosen because their surface energies are representative of the range used in OPV bottom contacts. BHJ OTFTs fabricated on OTS- SiO_2 dielectrics demonstrated hole-only transport that suggest P3HT-dominated transport channels, whereas devices prepared on bare SiO_2 showed ambipolar behavior that indicate the presence of a mixed P3HT/PCBM phase at the oxide-organic interface. Annealing of the P3HT:PCBM films to 140°C typical for OPV processing eliminated the surface energy-dependent compositional variation and produced P3HT-rich bottom interfaces on both high- and low- γ surfaces. These observations were directly reflected in higher short-circuit currents (I_{sc}) and fill-factors (FF) for annealed OPV devices using poly(3,4-ethylene dioxy thiophene):poly(styrene-4-sulfonate) (PEDOT:PSS) bottom contacts that have a surface energy analogous to that of bare SiO_2 . Examination of delaminated bottom interfaces using near-edge x-ray absorption fine structure (NEXAFS) spectroscopy quantitatively confirmed the changes in interfacial polymer composition that were observed in OTFT characterization. Furthermore, analysis of the top polymer-air interface with NEXAFS showed a P3HT-rich

layer that suggests a vertical composition gradient varying from the bottom interface to the top interface. The presence of a hole-transporting layer at the typically top electron harvesting contact likely contributes detrimentally to OPV device efficiencies, which could be overcome by engineering of the interaction energies at the top polymer-electrode interface. Since the surface energy-dependant composition at the dielectric-organic interface does not necessarily represent the BHJ composition in the bulk or at the top interface, the common use of OTFTs for insights into the bulk transport properties of OPVs must be applied cautiously. Nevertheless, this work demonstrates that OTFTs can still be employed to study the interfacial composition of organic films on chemically-tailored gate dielectrics that have surface energies representative of select electrodes used in OPVs.

10:40 AM

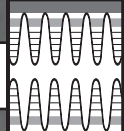
QQ7, Material and Device Requirements for Intermediate-Band Solar Cells: Albert Lin¹; Weiming Wang¹; Jamie Phillips¹; ¹University of Michigan

Intermediate band solar cells present an alternative technology to multi-junction cells in order to exceed the Shockley-Queisser limit for single-junction cells. In this approach, energy states within the bandgap extend solar cell response to longer wavelengths via excitation by multiple photons, where an increase in short circuit current is predicted without sacrificing open circuit voltage. Thus far, experimental data has failed to clearly demonstrate an advantage for intermediate band solar cells over a single-junction devices. In this work, material and device requirements to achieve high-performance intermediate band solar cells will be discussed and presented. A 1-D drift-diffusion model incorporating intermediate band optical transitions will be presented to guide the design of intermediate band devices. This model self-consistently determines the space charge distribution and drift-diffusion current in junction devices, providing a means of calculating the spatial dependence of intermediate-band state filling and optical generation and recombination rates. The model overcomes limitations of 0-D models which do not incorporate spatial dependence, and overcomes challenges associated with conventional 1-D numerical device models where carrier dependent optical transition rates and solution convergence are problematic. The optimal material parameters and device structure (absorber width for a given carrier lifetime, for example) will be presented and compared to prior results for 0-D models. Simulation results suggest that optimal solar cell conversion efficiency may be achieved when the intermediate band absorber region is doped at a concentration of one-half of the density of intermediate band states to clamp the occupation of these states at 50%. The 1-D device model will be compared to experimental data on ZnTe:O junction devices, where oxygen doping of ZnTe is found to result in an increase in short circuit current density. The requirements and outlook for ZnTeO and other intermediate band solar cells will be discussed.

11:00 AM

QQ8, Newly Developed Acene-Based Organic Semiconductors for Solar Cell Applications: Zhong Li¹; John Anthony¹; Karthik Shankar²; Craig Grimes²; Stephanie Lee³; Lynn Loo³; ¹University of Kentucky; ²Pennsylvania State University; ³Princeton University

In the architectures of next-generation solar cells, organic materials play very important functional roles, such as the light-harvesting component in a Dye-Sensitized Solar Cell (DSSC); and key components involved in the energy transformation process in an Organic Photovoltaic Cell (OPV). The enhancement of device performance therefore largely depends on the development of new organic semiconductors for such applications. Acene derivatives, pentacenes for instance, have been extensively studied for the development of better performing organic solar cells. In this study, we have prepared two series of acenes, 6,13-bis(triisopropylethynyl) pentacene carboxylic acids (TIPSPn-COOH) and 5,12-disubstituted tetracene/fullerene adducts (TetFu). The solar cells made of these new materials show encouraging results. Most importantly, this systematic study develops general molecular structure-property relationship that will point us the direction to further molecular optimization. The first class of acenes, TIPSPn-COOH, was designed to be the dyes used in DSSCs. This type of solar cell relies on efficient charge transfer between photoexcited organic dye and the metal oxide semiconductor template. In our work, the DSSCs were built using TiO₂ nanowires sensitized by pentacene derivatives via carboxylate covalent



bonds. Although for the TIPSPn-COOHs we have developed, the DSSCs all demonstrate energy conversion ability, it is noticed that the efficiency clearly depends on the nature of the linker between pentacene core and the anchor group COOH. For example, when COOH directly attaches to TIPS pentacene, the corresponding DSSC shows better performance than the case that a p-conjugated ethynylphenyl group spaces TIPS pentacene and COOH. We thus explored the effect of different linker on the charge transfer efficiency. Once the most optimized linker is determined, we will shift gear to maximizing the absorption of the corresponding pentacene for the purpose of capturing a broader cross-section of the solar spectrum. Structural tailoring at the molecular level offers us the opportunity to push the absorption beyond visible into the NIR area. TetFu, the second class of acenes, however, was designed as a n-type semiconductor used in thin-film OPV. These adducts are prepared by [4+2] Diels-Alder reaction between substituted tetracenes and C60. Their sufficient solubility in organic solvent and variable crystallization abilities in different film-forming conditions offer engineers the opportunity to modulate the solar cell performance by optimizing device fabrication. To gain an insight into the relationship between molecular/solid state structure and n-type properties of TetFu, substituents with different size and electronic features were examined. The OPV parameters obtained from the cell in which P3HT works as electron donor and TetFu works as acceptor were compared to those when [6,6]-phenyl C61 butyric acid methyl ester (PCBM) was the acceptor. Combined with the crystal structures of these TetFu adducts, we are attempting to find the solution to molecular optimization for these new n-type organic semiconductors.

11:20 AM

QQ9, Investigation of the Photo Response in Blended Organic Photovoltaic Films Using Conductive-Tip Atomic Force Microscopy: *Behrang Hamadani*¹; *Suyong Jung*¹; *Nikolai Zhitenev*¹; ¹National Institute of Standards and Technology

Organic solar cells, which have attracted considerable interest over the last few years as low-cost, simply-processed alternatives for harvesting the solar energy, have interesting nanoscale properties; a thorough understanding of which is currently lacking. Although there has been a lot of work focused on improving the overall device performance, important issues related to influence of nanoscale morphology on exciton dissociation and charge transport, effect of grain boundaries and interfaces, and contact related phenomena are mostly unexplored. Photoconductive-tip atomic force microscopy (pc-AFM) is a powerful technique that can be utilized to simultaneously gain some understanding of the local optoelectronic response of blended n-and p-type molecules and their surface morphology when prepared on transparent conducting electrodes. Here, we present transport data and local photocurrent maps and images of polythiophene/PCBM organic films collected with our pc-AFM in an inert atmosphere and vacuum, in dark and in the presence of excitation with monochromatic light. We have also used a streamlined technique for fabrication of stencil masks with sub-micron features on a suspended SiN membrane to be used as a shadow mask for evaporating small top contacts onto the organic layer. These top contacts can then be imaged and analyzed locally by the AFM tip, and the current voltage or impedance measurements can be performed on the length scales dictated by the size of the contacts. We compare the results of these measurements on nano-contacts and the pc-AFM data with those obtained with larger mm-sized devices.

11:40 AM QQ10, Late News

12:00 PM QQ11, Late News

Session RR: Silicon Carbide

Friday AM
June 26, 2009

Room: 206
Location: Pennsylvania State University

Session Chairs: Robert Stahlbush, Naval Research Laboratory; Michael Dudley, State University of New York at Stony Brook

8:20 AM Student

RR1, MOS Characteristics of (000-1) 4H-SiC: *Zengjun Chen*¹; *Xingguang Zhu*¹; *Mingyu Li*¹; *A.C. Ahyi*¹; *John Williams*¹; ¹Auburn University

The 4H polytype of silicon carbide has been studied widely for characteristics such as wide band gap and high thermal conductivity that make the polytype attractive for power electronics applications. The carbon face or (000-1) 4H-SiC has a higher oxidation rate compared to the Si-face, and high (000-1) inversion channel mobility has been reported recently [1]. In the present work, MOS capacitors and MOSFETs fabricated on the 4H carbon face SiC are investigated to provide a comprehensive view of the material. Both implanted and epitaxial layers are used to build MOSFETs. The oxide layer is grown thermally in furnace at 1150°C, followed by post-oxidation annealing. High-purity Mo is sputtered as the gate metal, and silver paste is used as a broad area back contact for all measurements. The source and drain ohmic contacts of the lateral test MOSFETs are produced by sputtering Ni on heavily doped implanted regions ($6 \times 10^{19}/\text{cm}^3$), followed by an anneal at 860°C for 4min. Hi-lo capacitance-voltage measurements at both 23°C and 300°C are used to obtain the interface trap density (D_{it}). Current-voltage measurements at room temperature are used to collect information about oxide leakage and breakdown field (E_{bd}). A three-probe I-V system is employed to determine the I_d - V_g characteristics of the MOSFETs at room temperature, and the inversion channel mobility (μ) is extracted from these characteristics. Results are compared for different post-oxidation interface passivation anneals. As shown in Fig.1, the combination of NO and H₂ annealing gives the best D_{it} ($8773 \times 10^{-11} \text{cm}^{-2} \text{eV}^{-1}$ at E_c -E=0.2eV). Direct growth in NO produces the most reliable oxide, but the measured breakdown field of 8773 MV/cm is still approximately 2 MV/cm lower than the average field measured for the Si-face (Fig. 2). The highest inversion channel mobility we obtain from the carbon face 4H-SiC with epitaxial doping concentration of $1 \times 10^{16} \text{ cm}^{-3}$ is $35 \text{ cm}^2/\text{V-s}$. Compared with the value reported by Fukuda, *et al.*, our low field mobility value is not remarkable. However, the high field mobilities are similar. We observe that the presence of mobile ions can increase our low field channel mobility. However after negative bias stress at temperatures as high as 250°C, the mobility peak value drops from $65 \text{ cm}^2/\text{V-s}$ to $35 \text{ cm}^2/\text{V-s}$. These results suggest that the effective mobility for carbon face may not be significantly higher compared to the Si face.

8:40 AM

RR2, Study of 4H-SiC/SiO₂ Interface Traps in n-Type Nitrided MOS Capacitors Using Thermally Stimulated Current and Capacitance Voltage Methods: *Peter Muzykov*¹; *Sarit Dhar*²; *Sei-Hyung Ryu*²; *Anant Agarwal*²; *Tangali Sudarshan*¹; ¹University of South Carolina; ²Cree, Inc.

In SiC power MOSFETs the low inversion channel mobility is a major drawback. This has been reported to be caused by high density of carrier trap centers at the SiC/SiO₂ interface (D_{it}). Therefore the technology of oxide formation, minimizing the D_{it}, must be developed to realize the full potential offered by the unique properties of silicon carbide to power MOSFETs. In this work, as a part of our effort in the establishment of oxidation process for high channel mobility MOSFETs, nitrided oxides on n-type 4H-SiC obtained using two different nitridation methods, namely post oxidation annealing (POA) in nitric oxide (NO) atmosphere and oxidation of the epitaxial surface layer with ion implanted nitrogen, as well as the as-oxidized (AO) 4H-SiC/SiO₂ interface (i.e. without N implants or NO annealing) were investigated. Thermally stimulated current (TSC) and Capacitance-Voltage (CV) techniques were used to characterize charge trapping in MOS capacitors fabricated using these oxide/SiC structures. Results of our TSC measurements indicate that both NO annealed

and N implanted MOS capacitors have significantly lower D_{it} than that at the AO interface. The density of traps in NO annealed samples was found to be lower than that in the N implanted samples, implying that the nitrogen implantation method might not be as effective as NO POA in D_{it} reduction, or requires optimization to further lower the density of interface states. Also, results of TSC measurements indicate that, in contrast to NO annealed samples, interface states at about 0.27 eV below conduction band edge are present in N implanted samples with a density of 10^{12} cm^{-2} in the order of magnitude. The origin of these states is not clear at this time and is under investigation. In contrast, D_{it} profile obtained from conductance measurements suggest that the N implanted samples have lower D_{it} compared to the NO samples. This result strongly indicates that the pre-oxidation N implantation process introduces significant amount of electron traps in the oxide. Capacitance-Voltage characteristics obtained at room temperature reveal significant amount of positive fixed charge (QF) in the N implanted MOS capacitors. Nitrogen implanted capacitors with lower QF had higher density of traps. It is also interesting to note that the C-V curves for the N implanted samples do not saturate properly in accumulation, most likely due to near-conduction band charge trapping in the oxide. In summary, the pre-oxidation N implantation process has been evaluated as an alternative to thermal nitridation for SiO₂/SiC. The results indicate trap densities lower than as-oxidized interfaces in agreement with previous reports. In comparison to thermally nitrided interfaces, higher amount of oxide charge trapping has been observed in these samples. Transport studies using MOSFETs are currently underway for further investigations.

9:00 AM Student

RR3, Nucleation Mechanism of Polytype Transformation in 6H and 15R SiC Crystals: *Yu Zhang*¹; Hui Chen¹; Ning Zhang¹; Michael Dudley¹; James Edgar²; K. Graszka³; Emil Tymicki³; Yimei Zhu⁴; ¹Stony Brook University; ²Kansas State University; ³Institute of Electronic Materials Technology; ⁴Brookhaven National Laboratory

A model is presented for the nucleation mechanism of 6H-SiC polytype inclusions in Physical Vapor Transport (PVT) grown 15R-SiC boules. According to this model, inhomogeneous densities of screw dislocations replicated from the 15R-SiC seed lead to uneven growth rates resulting in a quasi-vicinal growth surface. Subsequent interference between advancing vicinal growth steps and screw dislocation spiral growth steps lead to complex step overgrowth processes which can suppress all or part of the 15R 1c screw dislocation Burgers vector through the creation of Frank faults and Frank partial dislocations on the basal plane. Combined with stacking shifts induced by the passage of basal plane partial dislocations (observed to be in plentiful supply in the boule) it is shown that suppression of 9/15 of the 15R 1c dislocation Burgers vector by such step overgrowth can leave behind a residual Burgers vector corresponding to a 1c dislocation in 6H-SiC. This residual dislocation then acts as a nucleus for reproduction of the 6H SiC structure at the surface of the 15R crystal. Competition between the 6H nucleus and the surrounding 15R matrix eventually leads to lenticular shaped 6H inclusions approximately parallel to the 15R basal plane. In this paper we will present evidence in support of our model mainly comprising synchrotron white beam and monochromatic topography images recorded in transmission from thin wafers cut parallel to the [0001] growth axis of the 15R. Images recorded from 3 different a-plane wafers show uneven densities of screw dislocations with an excess occurring on one side of the wafer. 6H nucleation is believed to have occurred in close to these screw dislocations due to overgrowth by the vicinal steps. Evidence for the nucleation of Frank faults and Frank partial dislocations in these regions is also presented on these topographs. Supporting evidence for the presence of the Frank faults and partial dislocations is provided by HRTEM images recorded from regions close to the interface between the 15R substrate and the 6H inclusion. It is also noted that the 6H inclusions can act as barriers to other screw dislocations in the 15R crystal. However, once the inclusion is eventually fully enclosed by 15R crystal, the net Burgers vector eliminated from the 15R at the lower side of the inclusion must be equal to that emerging from the upper side. In some cases this can lead to accumulation of screw dislocation Burgers vector into micropipes. Occasionally, a screw dislocation from the 15R is admitted into the 6H inclusion and either is terminated on the upper side of the inclusion or

emerges from the other side back into the 15R. Rules governing such processes are discussed. A similar model is discussed for the nucleation of 15R inclusions in 6H-SiC boules.

9:20 AM Student

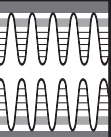
RR4, The Physical Distribution of Defects in 4H SiC MOS Structures: *Brad Bittel*¹; Corey Cochrane¹; Patrick Lenahan¹; Jody Fronheiser²; Kevin Matocha²; Aivars Lelis³; ¹Pennsylvania State University; ²GE Global Research; ³US Army Research Laboratory

We combine conventional electron paramagnetic resonance (EPR) and spin dependent recombination (SDR) to investigate the distribution of defects in 4H SiC MOS structures. EPR studies utilize MOS structures with various thickness epi-layers highly enriched with ¹³C nuclei. The naturally occurring abundance of ¹³C is 1.1%. The enriched epi-layer enrichment is 30%. The ¹³C nuclei are a sensitive "marker" in EPR because the ¹³C nucleus possesses a magnetic moment which interacts strongly with unpaired electrons in the defects, strongly altering the EPR spectrum in the ¹³C region of the samples. Comparing various thicknesses of ¹³C epi-layers (~1micron to ~400Å) we can, for example, obtain information on the depth of the oxidation induced defects. Our observations have also included effects of various anneals (NO and N₂) and "control" samples. All oxidized samples have a 500 Å SiO₂ layer. Of particular interest, we have compared conventional EPR traces of otherwise identical post oxidation structures with (a) 10,000Å ¹³C epi-layers, (b) 400Å ¹³C epi-layers and (c) only ¹²C epi-layers. The 10,000Å epi-layer ¹³C epi sample exhibits EPR structure not observed in the post oxidation ¹²C samples, clearly due to defects in the 10,000Å ¹³C epi layer. This structure is essentially below the detection limit in the unoxidized 10,000Å ¹³C epi control samples. The additional ¹³C structure is also far weaker in the 400Å ¹³C oxidized samples. These results demonstrate that (a) oxidation creates defects within the SiC and more importantly (b) that these oxidation defects extend deeply into the SiC, far deeper than 400Å. Our conventional EPR measurements are complimented by ongoing SDR results on fully processed 4H SiC MOSFETs. SDR is not well suited to study processing steps such as oxidation because it typically requires a fully processed device. However SDR is particularly well suited to study interface/ near interface defects, where as EPR is sensitive to all paramagnetic centers within the sample. SDR results on very low quality device ($\mu_n \sim 1 \text{ cm}^2/\text{Vsec}$) show interface/near interface dominating defects distributions [1,2]. However, especially in high quality devices ($\mu_n \sim 20 \text{ cm}^2/\text{Vsec}$), the SDR amplitude is not peaked when the gate is biased so as to yield equal numbers of electrons and holes at the semiconductor dielectric boundary. If most of the deep level defects are that boundary, a peak in the SDR amplitude would occur under those circumstances. Since it does not, the result indicates that these defects extend significantly into the SiC. Our results indicate that electrically active defects extend into the SiC and that OXIDATION induced defects are generated quite deeply into the SiC. [1] M. Dautrich et al., Appl. Phys. Lett. 89, 223502, (2006).[2] D. Meyer et al., Mat. Sci. Form. 483, pp. 593-596, (2005).

9:40 AM

RR5, MOCVD HfO₂/SiO₂ Gate Stacks for Improved Reliability in SiC MOSFET's: *Nick Sbrockey*¹; Mvs Chandrashekar²; Elane Coleman¹; Michael Spencer²; Gary Tompa¹; ¹Structured Materials Industries, Inc.; ²Cornell University

Silicon Carbide is a very attractive semiconductor material, due to its wide bandgap, high carrier saturation velocity and high thermal conductivity. The development of SiC MOSFET's will enable advanced devices for extreme conditions (high power, high voltage and high frequency) and extreme environments (high temperature and high radiation flux). One of the main limitations to SiC MOSFET development is the gate oxide. This presentation will describe work to develop gate oxide technology for SiC MOSFET's, based on the high-k dielectric material hafnium oxide. HfO₂ films were deposited by Metal Organic Chemical Vapor Deposition (MOCVD). The substrates used included silicon wafers, for basic characterization of the HfO₂ film material and electrical properties, and 4H-SiC substrates for device characterization and verification. The HfO₂ films were deposited in a rotating disc MOCVD reactor, using hafnium tetrakis ethylmethylamide, argon and oxygen, in the substrate temperature range of 300 C to 450 C, and a nominal chamber pressure



of 10 Torr. Details of the effects of the MOCVD process parameters on the resulting film properties will be presented. Films with high dielectric constant (ranging up to $k = 20$) were readily obtained on all substrates. However, films deposited directly on the semiconductor substrate showed significant hysteresis in capacitance/voltage behavior. For HfO_2 films deposited on substrates with a nominal 10 nm SiO_2 dielectric interlayer, reduced C/V hysteresis is observed, as well as better control of the transistor turn-on voltage, as indicated by a smooth dependence of flatband voltage on film thickness. HfO_2 films deposited in the temperature range of 300 C to 450 C were amorphous, as evidenced by the lack of observed x-ray diffraction peaks. However, these films could be readily crystallized by subsequent annealing. Crystallization of the films caused the flatband voltage to vary in an unpredictable manner, and increased the C/V hysteresis. This has negative implications for fabrication of SiC MOS devices, since subsequent processing could cause crystallization of the gate dielectric and degradation of device performance. An approach to suppress this tendency for crystallization by adding small amounts of silicon precursor during MOCVD growth of the HfO_2 films will also be discussed.

10:00 AM Break

10:20 AM

RR6, On the Driving Force for Shockley Stacking Fault Motion in Hexagonal SiC: *Joshua Caldwell*¹; Mario Ancona¹; Robert Stahlbush¹; Orest Glembocki¹; Karl Hobart¹; Kendrick Liu¹; ¹Naval Research Laboratory

Single Shockley stacking faults (SSFs) in hexagonal silicon carbide (SiC) are defects that nucleate and expand within low-doped epitaxial material, as in the drift layer of a pin diode, due to the recombination of injected electron-hole pairs (ehps). This in turn induces an increase in the forward voltage drop (V_f) in bipolar devices, as well as in unipolar devices where minority carrier injection can be initiated. Over the past decade, a significant effort has been put into determining the primary driving force for SSF nucleation and expansion. A more complete understanding of the driving force mechanism governing SSF expansion and contraction would assist in developing models for limiting their influence and/or limiting their nucleation in the epilayers. Up until recently, the reported models were all based on the hypothesis that SSFs were thermodynamically stable with respect to the 4H-SiC host lattice, and therefore these models tended to focus on determining the reason for this improved stability. However, recent annealing and high temperature device operation experiments have clearly shown that SSFs are not the preferred state of the material. Here, we introduce and discuss a possible mechanism describing the primary driving force governing SSF expansion and contraction that is consistent with the previously reported experimental observations. Further, we also will present further experimental observations and simulation results that strengthen the support for this model. The model is based on the relative energy associated with the filling of the two-dimensional density of states associated with the SSFs under forward bias conditions in comparison to the quasi-electronic Fermi energy under the same conditions. According to our model, if the latter is higher in energy relative to the filling of the SSF density of states, further filling of the SSFs will occur leading to further SSF expansion. However, if the reverse is true, then depopulation of the SSF states would occur, thereby inducing SSF contraction. We will illustrate how this model can be used to describe various phenomenological SSF dynamics, such as SSF annealing, V_f drift saturation, high temperature and low current stressing effects and the current-induced recovery effect. Silvaco simulations of such conditions will also be used for supporting evidence.

10:40 AM Student

RR7, Nucleation Mechanism of Dislocation Half-Loop Arrays in 4H-Silicon Carbide Homo-Epitaxy: *Ning Zhang*¹; Yu Zhang¹; Michael Dudley¹; Robert Stahlbush²; ¹The State University of New York at Stony Brook; ²Naval Research Laboratory

Defect-related issues in silicon carbide (SiC) have posed significant barriers to the broader implementation of SiC-based devices. A case in point is that basal plane dislocations (BPDs) are observed to dissociate in the epilayer regions of p-i-n devices under forward bias and lead to lifetime limiting forward voltage drops. Half loop arrays (HLAs) provide new sources of BPDs and have been the

subject of much study although the details of their formation mechanism have remained elusive. In this study, we have investigated HLAs using ultraviolet photoluminescence (UVPL) imaging and we present a model for their formation mechanism. HLAs were investigated in a 100 μm thick epilayer, grown on an 8° off-cut 4H-SiC substrate. UVPL images shows that HLAs are connected to the near surface end of the mobile threading segment of a BPD and to the trailing segment of BPD deposited near the substrate epilayer interface i.e., the interfacial dislocation (ID) segment. When the sample is subsequently subjected to extended UV exposure, the BPD segments in the HLA expand in opposite directions with same Si-core partials and form rhombic shaped Shockley faults, while the ID does not experience stacking fault expansion along most of its length. Based on our study, a BPD close to edge orientation is expected to dissociate into partials of the same sign, with either Si or C-core depending on the sign of the original dislocation. Due to the faulting behavior of HLA and ID, we can conclude that the BPD segments in the HLA have large edge component and the ID has large C-core edge character. This reveals the fact that the BPD segments of the HLA and the ID originate from the same gliding BPD but have opposite sense. As expansion continues further, the partials emanating from adjacent HLA basal segments merge and annihilate indicating that they are all on the same basal plane. Based on the observed features above, a model is proposed for the nucleation mechanism of dislocation HLAs in 4H-SiC homo-epilayer. During the sideways glide of threading segments of screw oriented BPDs during epitaxial growth, the surface intersections of the screw oriented BPDs adopt more edge character making them susceptible to conversion into sessile TEDs, which subsequently pin the motion of the BPD. Continued glide during further growth enables part of the mobile BPD to escape through the surface leaving two additional large edge component surface intersections which can again be converted into TEDs. The process repeats leaving arrays of half loops comprising two TEDs and a short BPD segment with significant edge component.

11:00 AM Student

RR8, Characterization of 4H-SiC Schottky and p-n Diodes Using Thermally Stimulated Current: *Marko Tadjer*¹; Robert Stahlbush²; Karl Hobart²; Fritz Kub³; Akin Akturk¹; Sarah Haney³; Brett Hull³; ¹University of Maryland; ²Naval Research Laboratory; ³CREE, Inc.

Thermally stimulated current (TSC) techniques have been used in the past to identify defects in Si and 4H-SiC MOS capacitors and transistors [1, 2]. In this paper, we explored the properties of epitaxial and implanted 4H-SiC by applying the TSC technique to devices without oxide, such as 4H-SiC Schottky and p-n diodes. The diodes characterized in this work were fabricated on three types of 4H-SiC: p-type epitaxial 4H-SiC with Al acceptor doping of $N_A = 1 \times 10^{16} \text{ cm}^{-3}$ or $5 \times 10^{17} \text{ cm}^{-3}$, and p-type Al-implanted 4H-SiC with $N_A = 5 \times 10^{17} \text{ cm}^{-3}$. Room temperature carrier concentrations were confirmed using C-V analysis. The TSC current was measured using a Keithley 6517 electrometer. When cooled to 250 K, a forward bias of 3 V was applied, filling carrier traps. The device was cooled down to 16 K while maintaining the bias, and subsequently warmed back to 250 K with reverse bias applied. TSC spectra using a constant forward bias during cooldown ($V_{\text{fwd}} = -3 \text{ V}$) and a variable reverse bias during warmup ($V_{\text{rev}} = 0$ to 25 V) revealed peaks around 55 K and 75 K. The observed TSC peaks around 55 K were due either to residual nitrogen donors or defects in the field oxide separating the Schottky and overlay metals. The peaks in the 72-82 K range have been shown to be caused partially by hole traps and ionization of Al acceptor levels. However, using Fermi-Dirac statistics, it was shown that ionization of Al continues well beyond cryogenic temperatures [3]. While the TSC peaks subside around 90 K, the measured TSC current remained positive up to 250 K. It should be noted that the current decreased to fA levels if the temperature was kept constant, thus proving the current beyond the peaks was not due to DC leakage. The signal dependence on the applied reverse bias resulted from the change in device band bending, which was the combined result of the change in surface and bulk potentials as the temperature increased. The n-p source-body junction of an epitaxial 4H-SiC LDMOSFET was characterized using TSC as well. Three peak groups could be distinguished, belonging to Al acceptor activation (near 80 K), substrate defects or possible implantation damage (90-100 K), and defect states in the space charge region

(peaking at 160 K). TSC measurements up to 150 °C and DLTS data on the Schottky diodes will also be presented at the meeting. [1] T. E. Rudenko et al., *Microelectronic Engineering* 72 (2004) 213-217. [2] J. G. Simmons and G. W. Taylor, *Solid State Electronics*, 1974, v. 17, pp. 125-130 and 131-135. [3] A. Akturk, J. Allnut, Z. Dilli, N. Goldsman, and M. Peckerar, *IEEE Trans. Electr. Dev.*, v. 54, no. 11, pp. 2984, 2007.

11:20 AM Student

RR9, Generation of Dislocations and Precipitates in Heavily Al-Doped 4H-SiC Epitaxial Layers Grown by the Low-Temperature Halo-Carbon Method: *Hrishikesh Das*¹; Bharat Krishnan¹; Siva Kotamraju¹; Yaroslav Koshka¹; ¹Mississippi State University

In our previous work, the possibility to achieve good quality homoepitaxial growth at temperatures below 1300°C was demonstrated using halo-carbon growth precursor. This method was shown to be suitable for selective epitaxial growth of 4H-SiC using SiO₂ mask [1]. A possibility of achieving high values of doping by the low-temperature halo-carbon growth was also demonstrated and applied to forming ohmic contacts to p-type SiC [2]. The solubility limit is the biggest obstacle when trying to incorporate dopant species at very high concentrations. Precipitate formation takes place if the solubility limit is exceeded. Even at moderately high values of doping below the solubility limit, stress build-up in the lattice and enhanced dislocation formation may be a problem. While dislocations and precipitate formation have been investigated in epitaxial SiC grown at traditionally high growth temperatures (above 1500°C), very little is known about defect generation and precipitate formation in heavily doped epitaxial layers grown at low temperatures (<1400°C). In this paper, we investigate the generation of defects and precipitates in p-type epitaxial layers heavily doped with Al in-situ during the halo-carbon low-temperature epitaxial process. The samples were subjected to Molten Potassium Hydroxide (KOH) etching to reveal dislocations in epitaxial layers and the substrates. For relatively thin epitaxial layers, we developed a convenient technique to expose the underlying substrate defects based on removal of epitaxial layers by KOH. By excluding the substrate dislocations from the consideration, only the defects generated during the epitaxial growth were evaluated. The number of defects generated during the epitaxial growth with in-situ Al doping was found to monotonically increase when the Al doping was increased. In addition to the regular dislocation etch pits, smaller etch pits appeared in the higher doped samples. The concentration of the small etch pits increased exponentially with Al doping. At the highest Al doping used in this study, the number of the small etch pits dominate over the regular dislocation-related etch pits. The small etch pits behave during KOH as defects that are localized at certain (and apparently different) depths in the epitaxial layer. This allowed us to suggest that the small etch pits could be due to precipitates caused by the excessive Al incorporation. SEM pictures of the small etch pits show a unique dual core structure. Additional characterization is conducted to evaluate the size and structure of these defects and their depth distribution. The onset of the precipitation and its relationship to the total Al concentration (which is expected to be different at low growth temperatures used in this study compared to the much higher temperatures used in the previous studies) is quantitatively evaluated.

11:40 AM RR10, Late News

12:00 PM

RR11, Surface Related Defect in 4H SiC Substrates: *Mary Ellen Zvanut*¹; Sarah Thomas¹; ¹University of Alabama at Birmingham

Oxidation of SiC and Si has long been one of the many benefits of using SiC in electronic devices. Unfortunately, many problems associated with surface and/or interface defects remain to be solved. In particular, it is now thought that oxidation induces defects in the substrate. For this reason, we have begun a series of studies to investigate a defect detected by electron paramagnetic resonance (EPR) that is thought to be associated with the surface, and perhaps oxidation. Earlier studies have not clarified the structure of the defect nor have they concretely determined the location. The goal of our present work is to address the latter through a series of oxidation and reactive ion etching studies. The initial findings demonstrate the unique effects of oxygen on an EPR detected center. Three types of 4H SiC substrates are being studied: 3 ohm-cm

single-sided polished p-type, 5-10 ohm-cm double-sided polished n-type, and vanadium-doped double sided polished high resistivity. All samples were cut on a diamond wheel and cleaned in a series of solvents in preparation for EPR measurements. X-band EPR was performed at room temperature throughout a series of anneals in either N₂ or O₂ with less than 1 ppm H₂O present or at 1150 °C in steam. The spectra of all of the as-cut samples were dominated by the presence of an 8 G wide isotropic signal with g=2.0024, typical of carbon dangling bonds. A recent study using our p-type substrates showed that the signal was due to cutting, and therefore is associated with the edges. A 600 °C dry N₂ anneal reduces the cut-induced signal and reveals that a second isotropic, 3 G wide spectrum with g=2.0022 is also present in the as-cut samples. The second spectrum remains unaltered by 30 min N₂ heat treatments at temperatures as high as 900 °C, but the intensity decreases by a 25% during a 30 min dry O₂ anneal at this temperature. A 6 h oxidation in steam produced the same g=2.0022 signal but the intensity was 40% less than that remaining after the 1000 °C O₂ treatment. The decreased intensity during the O₂ anneal suggests that the defect is either being altered by reaction with oxygen or removed by oxidation-induced etching of the substrate. Either mechanism suggests that the defect lies near the surface since oxidation is known to take place at the surface and the oxidizing species do not diffuse far in SiC at these temperatures. To clarify the location, we are performing RIE and oxidation-etching studies, the results of which will be presented at the meeting. The work is supported by Dr. Paul Maki, ONR Grant N0014-09-1-0082. The p-type substrates were supplied by Dr. J. Williams, Auburn University.

Session SS:

III-Nitride: Characterization of Defects

Friday AM
June 26, 2009

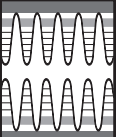
Room: 207
Location: Pennsylvania State University

Session Chair: Joan Redwing, Pennsylvania State University

8:20 AM

SS1, Quantitative and Depth-Resolved Defect Spectroscopy in InGaN/GaN Heterostructures: *Andrew Armstrong*¹; Mary Crawford¹; Daniel Koleske¹; ¹Sandia National Laboratories

Internal quantum efficiency (IQE) of In_xGa_{1-x}N-based quantum wells (QWs) decreases as x increases to extend the emission wavelength. The quantum-confined Stark effect seems an unavoidable contributor to this diminishment for polar nitride films. Defects can also degrade IQE, but understanding defect properties could help to mitigate their impact. Presently, the role of defects, their physical origin, and dependence on growth parameters are incompletely understood for InGaN films. Therefore, a quantitative method to study defects in InGaN/GaN QWs is desired that can discriminate between InGaN- and GaN-related defects. While luminescence techniques can resolve InGaN- versus GaN-related defects within QWs, it is difficult to study non-radiative defects or extract quantitative information such as defect density (D) or absolute deep level energy (E_d) with these methods. We have implemented depth-resolved deep level optical spectroscopy (DLOS) to investigate defects in InGaN/GaN heterostructure Schottky diodes that are grown under conditions optimized for a typical InGaN QW. A 200 nm thick UID-In_{0.02}Ga_{0.98}N underlayer (UL) was re-grown via MOCVD at 880°C upon a p-GaN:Mg buffer, followed by a 12.5 nm UID-In_{0.17}Ga_{0.83}N cap grown at 760°C. The UID-In_{0.17}Ga_{0.83}N cap mimics the well region of a QW. Diodes were formed by evaporating ~8 nm thick semi-transparent Ni Schottky contacts, and side contacts were formed by pressing In into a scribe alley. In_xGa_{1-x}N (x=0.17, 0.02) defects were studied using DLOS to determine E_d and lighted capacitance-voltage (LCV) to determine D_r. Depth-resolved DLOS was achieved by tailoring the Mg doping profile and exploiting the piezoelectric fields such that an applied bias selectively distributes the DLOS sensitivity among the In_{0.17}Ga_{0.83}N "well", the In_{0.02}Ga_{0.98}N UL, or the heterointerface region between them. The location of the defects corresponding to the observed deep levels was ascertained from the differential DLOS spectra



for different biases. At 0 V, $\text{In}_{0.17}\text{Ga}_{0.83}\text{N}$ “well” defects dominated the DLOS spectra, revealing deep levels at $E_v + 1.60$ eV and $E_v + 2.59$ eV, where E_v is the valence band maximum. Weak $\text{In}_{0.02}\text{Ga}_{0.98}\text{N}$ UL near-band edge absorption was observed at 0 V. At -3 V bias, $\text{In}_{0.02}\text{Ga}_{0.98}\text{N}$ near-band edge absorption intensified, confirming enhanced sensitivity to the UL. DLOS at -3 V indicated additional deep levels at $E_v + 2.15$ eV and $E_v + 3.30$ eV, which are attributed to defects in the UL. At an intermediate bias, another distinct DLOS spectrum emerged due to defects located near the heterointerface. A net D_i of $1.9 \times 10^{12} \text{ cm}^{-2}$ was measured using LCV. Having determined the spatial location of the observed defects, their possible physical origin and influence on QW IQE will be discussed. Sandia is a multi-program laboratory operated by Sandia Corporation, a Lockheed Martin Company, for the United States Department of Energy’s National Nuclear Security Administration under Contract No. DE-AC04-94AL85000.

8:40 AM Student

SS2, Characterization of Traps in N-Face AlGaIn/GaN Materials and Devices Using Deep Level Optical Spectroscopy: *Tony Homan*¹; Aaron Arehart¹; Andrew Malonis¹; Man Hoi Wong²; Yi Pei²; Christy Poblentz²; Andrea Corrión²; Rongming Chu²; Umesh Mishra²; James Speck²; Steven Ringel¹; ¹The Ohio State University; ²University of California, Santa Barbara

AlGaIn/GaN materials and devices grown on the N-face of the III-N crystal, i.e. the (000-1) orientation, as opposed to the more common Ga-face (0001) orientation are of great promise in the GaN electronics community [Rajan et al. *Jpn.J.Appl.Phys.*, 44, L1478 (2005)]. The fundamental effect of this is to reverse the net direction of polarization within the III-N device structure, allowing formation of a two-dimensional electron gas (2DEG) within the upper GaN layer of a GaN/AlGaIn/GaN heterostructure above the GaN/AlGaIn interface, as opposed to the conventional structure wherein the 2DEG lies in the GaN layer just beneath an AlGaIn barrier layer. This reversal generates several immediate consequences of great impact on GaN HEMT devices, including the creation of an AlGaIn back barrier that increases 2DEG confinement. Other advantages compared to Ga-face structures are a reduction in surface electric field magnitude, lower contact resistance, reduced gate-channel distance, and lower gate leakage and reduced dispersion than Ga-face devices [Rajan et al. *J.Appl.Phys.* 102, 044501 (2007)]. To date, the question of electronic defects in N-face nitrides has been relatively unexplored, and since the impact of traps on GaN electronic devices is substantial, exploration of traps introduced by virtue of growth in the (000-1) orientation and by the more complex growth structure used in N-face devices is necessary. In this study, we apply deep level optical spectroscopy (DLOS) using both capacitance based (C-DLOS) and current based (I-DLOS) methods as well as conventional DLTS to N-face GaN layers and N-face GaN/AlIn/GaN HEMT structures to investigate traps and their properties in these newly emerging class of III-N materials. The N-face bulk layers and device structures were grown by plasma-assisted molecular beam epitaxy PAMBE on free standing N-face GaN and SiC substrates, respectively. GaN layers were processed into semi-transparent, 80 Å thick Ni Schottky structures to facilitate C-DLOS and DLTS measurements, whereas the GaN/AlIn/GaN structures were processed into full HEMT devices. Measurements made on the bulk N-face GaN materials revealed traps whose energy levels and concentrations matched those observed earlier for Ga-face material [Arehart et al. *Appl.Phys.Lett.* 93, 112101 (2008)], with dominant DLOS-detected levels present at $E_c - 2.62$ eV and $E_c - 3.28$ eV, which were earlier ascribed to V_{Ga} -related and C_{N} acceptors, respectively. The primary difference in trap introduction between N-face and Ga-face GaN was a $\sim 10\times$ increase in the concentration of the nitrogen vacancy-related trap at $E_c - 0.25$ eV. N-face HEMT devices revealed a very complex trapping spectrum, in which a state clearly existing within an N-face AlIn layer is observed at $E_c - 3.44$ eV as well as states that match those found in the bulk N-face GaN layer. We are currently performing depth-resolved DLOS measurements applied to special AlGaIn/GaN N-face test heterostructures so that unambiguous trapping properties within N-face AlIn and AlGaIn layers, and N-face GaN layers within N-face HEMT structures can be discerned.

9:00 AM Student

SS3, Evidence of a Donor Trap at the Negative Polarization Interface of a Ga-Face GaN / InGaIn / GaN Quantum Well: *Christopher Schaake*¹; Brian Swenson¹; David Brown¹; Stacia Keller¹; James Speck¹; Umesh Mishra¹; ¹University of California, Santa Barbara

Nitride-based light emitting diodes (LEDs) have seen large improvements in output powers and quantum efficiency over the past fifteen years, but still suffer from efficiency “droop” at high injection currents. Rajan *et al* found a donor-like hole trap 60 meV above the valence band in a N-polar HEMT that was located at the AlGaIn / GaN interface with net negative polarization. We believe a similar trap may exist at the InGaIn / GaN interface with net negative polarization in Ga-face GaN which may play a role in reducing an LED’s quantum efficiency at high injection. In this work, we used a technique combining ultraviolet light exposure and capacitance-voltage (CV) measurements to evaluate the trap density at the net negative polarization interface between InGaIn and GaN. Three p-i-n diodes were grown by MOCVD with 5, 10, and 15 nm thick $\text{In}_{0.14}\text{Ga}_{0.86}\text{N}$ active regions. A 45 nm thick “spacer” was grown on top of the active region to keep the trap level below the Fermi level to ensure the traps began filled with electrons. The p-type GaN was doped with $N_A \sim 2 \times 10^{19} \text{ cm}^{-3}$, and the n-type GaN was doped with $N_D \sim 3 \times 10^{17}$. The n-type doping was kept low to ensure a change in capacitance was due to a change in the n-type depletion width. All three diodes were held at reverse bias and exposed to broad spectrum UV lamp while capacitance was monitored with a 1 MHz sampling frequency. When the UV lamp was turned on, capacitance immediately increased in all 3 samples due to free electrons and holes screening the polarization charges. The capacitance gradually increased during the 8 minutes the UV lamp was left on. The increase was not as large or immediate as when the lamp was turned on because free electrons in the active region could repopulate the trap. When the UV lamp was switched off, capacitance immediately dropped, but it was still larger than before UV radiation. The capacitance then decayed slowly for 20 minutes, but never returned to its original value. The slow decay was attributed to the limited availability of electrons to repopulate the trap. The ionized trap density was calculated from charge neutrality and the condition that the built-in voltage remains the same. We found the trap density to be at least $3 \times 10^{11} \text{ cm}^{-2}$ for the sample with a 5 nm active region, and at least $6 \times 10^{11} \text{ cm}^{-2}$ for the samples with 10 nm and 15 nm active regions.

9:20 AM Student

SS4, Photo-Assisted High-Frequency Capacitance-Voltage Characterization of Interface States Density in $\text{Si}_3\text{N}_4/\text{GaN}$ Metal-Insulator-Semiconductor Interfaces: *Brian Swenson*¹; Umesh Mishra¹; ¹University of California at Santa Barbara

A revised method to measure the interface state density of $\text{Si}_3\text{N}_4/\text{GaN}$ metal-insulator-semiconductor diodes is reported. The wide band gap of GaN suppresses hole generation at room temperature and consequently allows measurements in deep depletion. Using the method outlined in this paper the total interface state density can be measured throughout the bandgap above the bias in deep-depletion utilizing an above bandgap light source and a high-frequency (1MHz) Capacitance-Voltage measurement instrument. We report a peak interface state density of $5.0 \times 10^{12} \text{ cm}^{-2} \text{ eV}^{-1}$ at ~ 0.3 eV using this procedure while the Terman method reports a peak of $< 2 \times 10^{11} \text{ cm}^{-2} \text{ eV}^{-1}$ for the same $\text{Si}_3\text{N}_4/\text{GaN}$ MIS diode without illumination.

9:40 AM Student

SS5, Elastic Buckling of AlN Ribbons on Elastomeric Substrate: *Huichan Seo*¹; Ivan Petrov¹; Hyejin Jeong¹; Patrick Chapman¹; Kyekyoon Kim¹; ¹University of Illinois at Urbana-Champaign

Recently considerable attention was given to flexible forms of materials comprising both organic and inorganic materials. Various materials have been used such as polythiophenes for organic materials, and silicon, nanowires, nanotubes and graphene sheets for inorganic materials. As for work on inorganic materials, silicon has been the main focus of the research. Wide bandgap materials, especially III-V nitrides, have also proved to be very suitable for optical as well as electronic devices due to their high thermal stability and high breakdown fields. These nitride semiconductors are good candidates for flexible electronics. Growth of high-quality films of nitride semiconductors is, however,

nontrivial due to the lack of proper substrates and so are the difficulties of fabricating flexible films, such as underlying layer etching, which explains why there have been minimal research activities relating to flexible nitrides. In this study, we report on high-quality AlN films grown on Si (111) substrate and describe the procedures for forming flexible AlN ribbons. The wavelengths of the wavy ribbons were shown to vary with the film thickness and the tensile and compressive strains were applied to test the mechanical stability of the ribbons. We have fabricated a flexible form of single crystalline AlN ribbons with periodic and wavelike structures on an elastomeric substrate. Single crystalline AlN films were grown on Si (111) substrate using high vacuum unbalanced magnetron sputtering. Crystallinity of the AlN films was confirmed with x-ray diffraction and pole figure. The AlN ribbons were transferred to a prestrained (3.1%) elastomeric substrate and the resulting 'wavy' ribbons on the substrate were flexible up to 30% strain without any crack formation on the surface. When tension was applied, AlN ribbons became flat with a 3.2 % lengthening, which equaled the prestrain. As the film thickness changed from 300 to 900 nm, the periods of the waves varied from 95 to 277 μm which were within a 10% error of the calculated values. When PDMS substrate was stretched by more than 3.2 % lengthening, ribbon length did not change appreciably. By contrast, when compression was applied, the projected length of wavy ribbons decreased giving rise to a shortening of 27.8 % ($e = -0.3$). Beyond the 27.8 % shortening cracks began to appear on the surface of the ribbons giving rise to a failure in which the cracks on the surface and some ribbons merged due to unstable adhesion sites. These mechanical instabilities may result from accumulated stress of AlN ribbons due to the compression.

10:00 AM Break

Session TT: III-Nitride: Growth and Characterization of Optical Devices

Friday AM
June 26, 2009

Room: 207
Location: Pennsylvania State University

Session Chair: Joan Redwing, Pennsylvania State University

10:20 AM

TT1, Characterization of Recessed-Gate AlGaIn/GaN HEMTs as a Function of Etch Depth: *Travis Anderson*¹; *Marko Tadjer*²; *Michael Mastro*¹; *Karl Hobart*¹; *Fritz Kub*¹; ¹Naval Research Laboratory; ²University of Maryland

There is currently significant interest in developing AlGaIn/GaN High Electron Mobility Transistors (HEMTs) for both microwave and power switching applications due to their high electron mobility relative to Si, and higher sheet carrier density and higher breakdown voltage than GaAs. This device typically operates in depletion mode, but enhancement mode operation is highly desirable particularly for power switching applications. It has been reported that normally off operation can be achieved by implementing an ultra thin AlGaIn layer formed by ICP etching, but few detailed studies of the etch process and device performance as a function of depth have been reported. We have fabricated recessed-gate HEMTs using a low-damage Cl_2 -based ICP etch to study the performance improvements and degradation as a function of recess depth. Using material from the same wafer and an etch recipe with a rate of ~ 3 A/s, devices were fabricated with recess depths varying from 0 to 25 nm on a structure that consisted of 25 nm $\text{Al}_{0.25}\text{GaIn}$ and 2 μm GaIn with an AlN buffer layer on a sapphire substrate. Using a recessed van der Pauw pattern, we were able to measure mobility, sheet resistance and sheet carrier density changes as a function of recess depth, and we were able to extract threshold voltage shifts using the HEMT devices. It was found that the threshold voltage approached zero as the recess approaches the AlGaIn/GaN heterojunction, shifting from -1.5 V to -0.0024 V, but did not become positive. At the same time, mobility decreased an order of magnitude over the etch range studied, from 1350 to 100 $\text{cm}^2/\text{V}\cdot\text{s}$ and sheet resistance increased orders of magnitude, from 1200 to 6.3×10^6 ohm/sq . This is thought to be due to plasma damage,

which can be recovered by annealing. Sheet carrier density also decreased slightly from 5×10^{12} to 1×10^{12} cm^{-2} . The results were compared to non-recessed van der Pauw patterns on the same reticle, which served as reference points to verify the uniformity of the relevant parameters. As an alternative to plasma etching, wet etching using heated AZ400K developer was also investigated. Etch rates were nearly an order of magnitude lower than low power ICP etching, but concerns about plasma damage were eliminated. This etch was found to be selective to AlN over GaN, so a capped epi-structure was implemented incorporating a thin AlGaIn layer for a near-zero threshold voltage and an AlN cap to maintain high 2DEG density and low source and drain resistance. Using a SiN_x mask, it was possible to wet etch a gate opening through the AlN and stop selectively on the AlGaIn layer. In addition to DC I-V and Hall measurements, electroluminescence was also used to characterize these devices for comparison to standard and SiN_x-passivated HEMTs.

10:40 AM Student

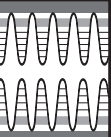
TT2, AlGaIn/GaN HFET Structures Grown on Vicinal Bulk GaN: *Judith Grenko*¹; *T. Paskova*²; *A. Hanser*²; *E. Preble*²; *K. Evans*²; *C. Ebert*³; *C. L. Reynolds, Jr.*¹; *M. A. L. Johnson*¹; ¹NCSU; ²Kyma Technologies, Inc.; ³Veeco Turbodisc

We report on the characterization of AlGaIn/GaN heterostructure field effect transistor (HFET) structures grown by organometallic vapor phase epitaxy on vicinal bulk c-axis GaN substrates with the intent of discerning the effect of substrate offcut angle on structural properties. HFET structures consisted of 0.5 μm GaN capped with 15 nm of $\text{Al}_{0.19}\text{Ga}_{0.81}\text{N}$ grown on vicinal bulk GaN substrates. The offcut angles range from 0.3°-1.7° off the c-axis toward the M-plane and 1.8° toward the A-plane. Atomic force microscopy measurements reveal a minimum in root-mean-square (RMS) roughness at an offcut angle of 0.7° off the c-axis toward the M-plane. The RMS roughnesses for substrates with offcuts ranging from 0.5° to 1.7° were all below 1.5 nm. This is consistent with the presence of more steps and ledges for adatom attachment with increasing offcut angle. High resolution double crystal x-ray diffraction (DCXRD) rocking curves around the symmetric (002) peak of c-GaN reveal a minimum in the out-of-plane compressive strain of the AlGaIn layer at 1.4° offcut, and this out-of-plane strain increases on either side of this minimum. Reciprocal space maps around the asymmetric (105) peak were also investigated to further understand the microstructure and in-plane strain. Two-axes, continuous 2θ - ω scans at stepped ω intervals reveal an elongation of the GaN in the ω -direction as the offcut angle increases. The dispersion in the 2θ - ω direction and the tilt from 0° in the AlGaIn film also correlate with the measured offcut. It is well known that dopant incorporation and activation in III-V semiconductors are dependent on substrate orientation, which is related to the atomic species and bonding in the lattice. Since these heterostructures included a magnesium-doped GaN layer in addition to an unintentionally doped GaN layer, the room temperature cathodoluminescence (CL) and photoluminescence (PL) data track the magnesium incorporation as it depends on the vicinal offcut, which is consistent with these earlier studies on traditional III-Vs. Room and liquid nitrogen temperature Van der Pauw Hall mobility and carrier concentration data will also be presented.

11:00 AM Student

TT3, Study of Growth Kinetics and Characterization of AlGaIn Grown by Ammonia-Based Metal-Organic Molecular Beam Epitaxy: *Daniel Billingsley*¹; *Walter Henderson*¹; *David Pritchett*¹; *William Doolittle*¹; ¹Georgia Institute of Technology

The characteristics of Al_xGa_{1-x}N grown by ammonia-based metal-organic molecular beam epitaxy (NH₃-MOMBE) on GaN templates were investigated as a function of growth regime. Recent increased interest in ammonia as the nitrogen source for the growth of III-Nitrides by MBE has arisen due to larger stable growth ranges [1], increased growth temperatures [2], increased growth rates [3] and ease of scalability. When NH₃ is employed in a MOMBE environment, highly C-doped GaN layers can be produced [4], which would lead to reduced leakage currents in AlGaIn/GaN high electron mobility transistors (HEMTs). However, to date, no one has produced a HEMT grown by NH₃-MOMBE. This study is intended to determine the feasibility of using NH₃-MOMBE for the production of high-carbon containing HEMTs. For the



fabrication of HEMTs grown by NH₃-MOMBE, proper understanding of the reactions that occur during the growth of AlGa_xN is essential, especially how these reactions effect surface smoothness needed for abrupt interfaces. In this study, growth rates were determined via optical interferometry, as shown in Figure 1, and used to define the growth regimes for GaN and AlGa_xN grown at 770 and 860°C. By defining the stoichiometric growth conditions, the efficiency at which NH₃ is utilized was calculated for both GaN and AlGa_xN. The NH₃ utilization efficiency was found to increase by a factor of 2-2.5 for the growth of AlGa_xN, due to the catalytic effect of Al on the cracking of NH₃ [5-7]. As seen in Figure 2, increasing the Al gas phase composition leads to a further increase in the NH₃ utilization efficiency as a result of increased catalyzation. The solid Al composition was dependent on growth regime, with higher Al incorporation in films grown with lower V/III ratios, as seen in Figure 3, due to increased Al reactivity compared to Ga when growing in N-limited growth environments [5, 8]. Based on this improved understanding of growth kinetics, Al_xGa_{1-x}N (0 < x < 1) films were grown at 870°C. Growth rate, shown in Figure 4, varied with Al composition in a “U-shape” fashion resulting from the competition between increased ammonia cracking and increased Al sticking coefficient compared to Ga. Atomically smooth AlGa_xN was achievable for films grown to ~850 Å, as seen in Figure 5. AlGa_xN surface pitting, attributed to threading dislocations [9], was found to be dependent on V/III ratio, with pit density decreasing with increased V/III ratios. These surface pits ultimately decreased to a value equivalent to the GaN template for Al_xGa_{1-x}N (0.5 < x < 0.9). Full-widths at half-maximum (FWHMs) of AlGa_xN (002) mimicked the values of the GaN templates, indicating that the grown AlGa_xN films were of high quality.

11:20 AM Student

TT4, Interface Analysis of Ti/Al/Ti/Au Ohmic Contacts with Regrown n+-Ga_xN Layers Using Molecular Beam Epitaxy: *Huichan Seo*¹; Shankar Sivaramakrishnan¹; Jian-Min Zuo¹; Patrick Chapman¹; Kyekyoon Kim¹; ¹University of Illinois at Urbana-Champaign

GaN-based materials, such as AlGa_xN, InGa_xN and AlInGa_xN, have been extensively studied for applications involving optoelectronic and electronic devices. Development of low-resistance and thermally-stable ohmic contacts for GaN has great importance for high-performance devices. We previously reported on the metal-semiconductor field-effect transistors (MESFETs) fabricated by the regrowth process using plasma-assisted molecular beam epitaxy (PAMBE), which showed high peak drain current and transconductance. We extended the technique to high electron mobility transistors (HEMTs) with alloyed and nonalloyed ohmic contacts producing very low resistance and high peak current. In this study, we examined the interface between metals and GaN layers after the annealing process using transmission electron microscopy (TEM). Samples used in this study consisted of a 200-nm-thick n-type GaN grown by PAMBE on an MOCVD-grown semi-insulating GaN-template. The electron concentration and mobility were 3.8 * 10¹⁷ cm⁻³ and 300 cm²/Vs, respectively. A 100-nm-thick patterned SiO₂ mask was formed on the n-GaN to facilitate the PAMBE-regrowth process. After a 60-nm-thick n+-Ga_xN layer was grown on SiO₂, poly-GaN and SiO₂ mask were removed by a molten KOH solution after which alloyed ohmic metals of Ti/Al/Ti/Au were deposited on n+-Ga_xN. Energy dispersive x-ray spectra (EDX) and scanning transmission electron microscopy (STEM) showed that TiN layers formed between metal alloys and n+-Ga_xN layers and that nitrogen atoms diffused from the GaN layers. Al atoms penetrated into the highly doped layer and formed Al-rich AlGa_xN layers. Al contents were calculated to be 60 % from high resolution transmission electron microscopy (HR-TEM). Si confinement in the n+-Ga_xN layers was confirmed by electron energy loss spectra (EELS) line scan. From the nano-beam diffraction (NBD) analysis, the directional relationship between GaN and TiN was [1 0 0]Ga_xN // [-1 1 0]TiN and TiN twins were also observed from the patterns. From the TEM analysis one may conclude that TiN formation and Si dopant confinement can be the reason for low ohmic contacts with regrown n+-Ga_xN.

11:40 AM Student

TT5, Growth and Characterization of Gallium Nitride on Magnesium Calcium Oxide: *Andrew Gerger*¹; Brent Gilal¹; Cammy Abernathy¹; ¹University of Florida

As the interest for Gallium Nitride based materials and devices expand, focus on controlling the quality of material is becoming a priority. One of main prerequisites of high quality film growth is closely lattice-matched substrates. In this study, the focus of GaN growth upon a lattice tunable oxide is investigated. The oxide utilized is MgCaO. This oxide has the unique feature of maintaining single phase as the metal ratios are varied. Lattice parameter of the oxide is therefore able to be changed and matched to that of GaN. With a matched substrate, the subsequent GaN growth has less strain which results in decreased level of defects in the film. GaN films are typically grown on sapphire or silicon carbide substrates with lattice mismatch of 17% and 3%, respectively. This requires growing a buffer layer on top of the substrate, typically a micron thick, then subsequent growth of the device structure. If a suitable lattice matched substrate can be used, then the need for the buffer layer can be reduced or even eliminated. Magnesium oxide (MgO) is a cubic rocksalt material with a lattice spacing of 4.20Å. The atom spacing on the (111) plane that has the same symmetry to the (0001) plane of the III-Nitride materials is 2.98Å. This means that the interface of MgO and GaN, for example, will have a lattice mismatch of -6.5%, MgO (111)//GaN (0001). Calcium oxide (CaO) has the same rocksalt structure as MgO and has a lattice parameter of 4.799Å. The (111) of CaO and the (0001) of GaN have a lattice mismatch of approximately +6.5%. Calcium and magnesium have the same valence and this allows for calcium to replace magnesium in the MgO lattice (calcium is too large to fit into an interstitial site) to create a ternary alloy of MgO and CaO, or MgXCa_{1-X}O, depending on stoichiometry. Therefore, a ternary of Mg_{0.5}Ca_{0.5}O should be lattice matched to GaN. An additional advantage to this system is the oxide's application as a dislocation blocking layer when grown upon a GaN substrate. TEM images show termination of threading dislocations at the GaN/oxide interface. Since the slip systems between the two materials are different, defects do not propagate in the growth direction. Normally dislocations in GaN traverse vertically through the growing surface. The MgCaO ternary has a slip plane that is parallel with the growth surface, resulting in termination of the defects from the substrate. This result shows ability to greatly enhance the GaN quality during the subsequent growth on the oxide.

12:00 PM TT6, Late News

A

Abell, J	26
Abernathy, C	105
Acord, J	53, 62
Adamo, C	71
Adur, R	74
Agarwal, A	99
Ahyi, A	92, 99
Aissa, B	35
Aivazian, G	68
Aizpurua, J	15
Akasaka, T	64
Akasaki, I	65, 88, 89
Akturk, A	101
Alanis-Camacho, F	56
Alberi, K	97
Alden, J	82
Allara, D	57, 71, 93
Allredge, L	92
Allen, M	72
Allerman, A	44, 86
Amano, H	65, 88, 89
Amsharov, K	21
Ancona, M	24, 101
Anderson, T	41, 104
Anderson, W	75
Ante, F	21
Anthony, J	6, 48, 49, 76, 77, 78, 98
Apostolopoulos, G	52
Arehart, A	103
Arias, A	6, 20, 48
Ariyawansa, G	27
Armstrong, A	87, 94, 102
Arulkumaran, S	42
Aruta, C	71
Asai, T	88
Asano, T	29
Ashkenov, N	56
Ashley, T	24
Avasthi, S	17
Awadelkarim, O	72
Awschalom, D	80

B

Babcock, S	47
Bae, J	17
Bahir, G	62
Bahuguna, A	56
Balakrishnan, G	23, 26
Balandin, A	81
Balliet, C	77
Balocchi, A	78
Banerjee, S	14
Bangert, U	29
Bank, S	13, 25
Bao, W	81
Baraskar, A	23, 90
Barber, G	97
Barton, R	82
Baumgart, H	17, 55
Belogorokhov, I	96
Ben-Yaacov, T	53
Bennndorf, G	74
Bennett, B	24, 25
Bertness, K	66, 67, 68, 69, 85
Bewley, W	26

Bhat, I	45, 47
Bhattacharya, P	27
Biedermann, B	59
Biedermann, L	61
Biehne, G	30, 74
Billingsley, D	104
Bisogno, V	71
Biswas, K	32
Bittel, B	100
Blanchard, P	67, 68, 85
Boles, M	59, 60, 61
Boos, J	24
Borca-Tasciuc, T	32, 33
Borchers, J	79
Bougerol, C	62
Brachwitz, K	75
Brandt, M	6, 56, 73, 74
Branz, H	14, 97
Brenner, M	96
Brillson, L	22, 52, 72, 73, 74
Brinkley, S	38
Brookes, N	71
Brooks, C	51, 70
Brown, D	22, 103
Brubaker, M	69
Bryant, G	15, 26
Buchholt, K	91
Buckle, L	24
Buckle, P	24
Bulsara, M	32, 96
Burek, G	23, 90
Burke, R	54
Burmistrova, P	34
Buyanova, I	73, 78
Byeon, K	66
Byun, K	19

C

Cabarcos, O	57, 71, 93
Caldwell, J	101
Calizo, I	81
Calley, W	70
Campbell, J	72
Campbell, P	82
Canedy, C	26
Cao, W	6, 49, 50
Cao, Y	21, 41, 83, 85
Capano, M	59, 60, 61
Carlin, A	96
Carpenter, P	57
Carroll, M	45
Cartwright, A	75, 83
Carver, A	70
Castillo, E	32, 33
Caviglia, A	70
Cavlero, R	82
Cederberg, J	45
Cezar, J	71
Cha, S	32
Chabal, Y	18
Chabinyk, M	20, 48, 76
Chai, J	54
Chakraborty, A	38
Champlain, J	24
Chan, C	98
Chandrashekhar, M	59, 82, 83, 100
Chang, L	54

Chang, W	29, 52
Chang, Y	16
Chapman, P	63, 103, 105
Chauvat, M	86
Chen, H	70, 100
Chen, P	69
Chen, Q	94
Chen, R	55
Chen, W	73, 78
Chen, Y	50
Chen, Z	92, 99
Cherenack, K	50
Cherng, T	24
Cheung, M	83
Chicoine, M	18
Cho, H	39
Cho, N	93
Cho, Y	79
Choi, K	95
Choi, S	43
Choi, W	93
Chow, T	41
Chowdhury, S	23
Chu, R	22, 103
Chu, X	55
Chu, Y	26
Chung, J	79
Chung, K	14
Chung, M	34
Chung, S	79
Cochrane, C	100
Coh, S	71, 72
Cohen, L	24
Colby, R	85
Coleman, E	100
Coleman, P	29
Colinge, C	18, 19
Collazo, R	42, 88
Collins, R	97
Colombo, L	14
Coomber, S	24
Cooper, J	77
Corrion, A	103
Craighead, H	82
Crawford, M	44, 87, 102
Creighton, J	48
Crofton, J	92
Crook, A	25
Cross, K	87
Crowe, I	29
Cutler, P	34

D

Dalmau, R	42, 88
Daniel, T	93
Das, H	102
Dasgupta, S	22, 62
Dashevsky, Z	96
Dasika, V	93
Datta, S	90
Davidson, J	58
Davis, R	40, 92
Davydov, A	66, 68
Dawson, L	45
Dehoff, R	96
del Alamo, J	22
Delker, C	69

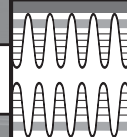
Dellas, N.....	16, 90	Ferdousi, F.....	14	Hader, J.....	26
DeLongchamp, D.....	98	Feric, M.....	76, 77, 78	Hähnel, A.....	18
DenBaars, S.....	22, 38, 53	Figiel, J.....	88	Halsall, M.....	29
Denbaars, S.....	62	First, P.....	60	Hamadani, B.....	98, 99
Denidni, T.....	35	Fisher, P.....	59, 60	Hamwi, S.....	76
Derenge, M.....	14	Fitting Kourkoutis, L.....	51, 70	Han, J.....	32, 37, 38, 39, 40, 49
Detchprohm, T.....	37, 38, 86, 87	Frantz, E.....	82	Han, M.....	49
Dhar, S.....	99	Fraser, H.....	96	Han, S.....	45
Dickey, E.....	71	Freitas, J.....	64	Haney, S.....	101
Dietrich, C.....	74, 75	Frenzel, H.....	6, 30, 56	Hang, Q.....	41
Dimoulas, A.....	52	Fritz, R.....	46	Hanser, A.....	104
DiNezza, M.....	75	Fronheiser, J.....	100	Hanser, D.....	38
Dion, J.....	43	Fujii, K.....	74	Hapenciuc, C.....	32
Dixon, F.....	25	Fujita, S.....	54	Harmand, J.....	78
Dobrovolsky, A.....	96	Furdyna, J.....	79	Harris, J.....	28
Dobrowolska, M.....	79	Furukawa, Y.....	13, 45	Harrison, S.....	60
Dobrowolska-Furdyna, M.....	83			Harvey, T.....	69
Dodson, C.....	67, 68, 85	G		Hashimoto, A.....	84
Dong, Y.....	74	Galata, S.....	52	Haungs, A.....	75
Donnelly, J.....	14	Gao, M.....	94	Hayashi, S.....	18, 19
Doolittle, A.....	42, 64	Gao, S.....	27, 28, 58	Hayashi, Y.....	91
Doolittle, W.....	70, 104	Gao, W.....	55	He, Y.....	26
Douglas, E.....	29	Garcia, R.....	85	Heeg, T.....	51, 70, 72
Doutt, D.....	22, 52, 73, 74	Gariglio, S.....	70	Heeney, M.....	77
Downey, B.....	58, 90	Garrett, G.....	42	Hemesath, E.....	36
Doyle, K.....	54	Gaskill, D.....	82	Henderson, W.....	64, 70, 104
Drummond, P.....	95	Gauntt, B.....	71	Herman, L.....	82
Duda, A.....	97	Gautam, N.....	24	Hetzer, M.....	22, 74
Dudley, M.....	99, 100, 101	Gayral, B.....	86	Hirai, A.....	39
Dupuis, R.....	25, 43, 86, 88, 92	Ge, Z.....	83	Hiroki, H.....	82
Durbin, S.....	54, 72, 83	Gerger, A.....	105	Hite, J.....	89
E		Germack, D.....	98	Ho, X.....	35
Ebert, C.....	104	Ghiringhelli, G.....	71	Ho, Y.....	54
Eckstein, J.....	70	Ghosh, A.....	56	Hobart, K.....	41, 101, 104
Eddy, C.....	82, 89	Ghosh, S.....	81	Hochmuth, H.....	6, 30, 56, 74
Eddy, Jr., C.....	41	Gibb, S.....	42	Hoepker, N.....	93
Edgar, J.....	100	Gila, B.....	105	Hoffmann, V.....	87
Edmunds, C.....	61	Gilbertson, A.....	24	Hofmann, T.....	56
Egawa, T.....	42	Glembocki, O.....	89, 101	Holmes, A.....	13
Eichfeld, S.....	16	Goerrn, P.....	31	Holonyak, N.....	25
Einfeldt, S.....	87	Goesele, U.....	18	Homan, T.....	46, 103
El Khakani, M.....	35	Goldman, R.....	93	Hong, E.....	66
Ellguth, M.....	75	Goodman, K.....	16, 67	Hong, J.....	6, 48
Elmatbouly, H.....	32	Goorsky, M.....	13, 18, 19	Horita, M.....	40
Emeny, M.....	24	Gossard, A.....	23, 25, 90	Horn, M.....	71
Engel-Herbert, R.....	51	Goto, H.....	74	Hou, W.....	38, 87
Erfurth, W.....	18	Grandusky, J.....	42	Hu, E.....	65
Evans, K.....	104	Grassman, T.....	46, 96	Hu, S.....	18
Ewoldt, D.....	85	Grasza, K.....	100	Hu, W.....	16
Eyink, K.....	94	Graudejus, O.....	6, 49, 50	Huang, G.....	27
Ezaki, T.....	89	Grazulis, L.....	94	Huang, L.....	92
F		Grenko, J.....	104	Huang, Y.....	25
Facchetti, A.....	20, 78	Griggio, F.....	95	Huffaker, D.....	26, 28, 68
Fang, T.....	81	Grimes, C.....	98	Huh, J.....	91
Fang, Z.....	29, 74	Grundmann, M.....	6, 30, 54, 56, 73, 74, 75	Hull, B.....	101
Fanton, M.....	53, 62, 82	Gu, D.....	17, 55	Huo, Y.....	28
Fareed, Q.....	43	Gu, J.....	40, 92	Hwang, C.....	75
Fatehi, A.....	16, 46	Gu, Q.....	46	Hwang, J.....	66
Fay, P.....	17	Guest, J.....	35	Hyeon, T.....	79
Fearn, M.....	24	Guillemette, J.....	16	Hyung, J.....	31
Feenstra, R.....	42, 59, 60, 81	Gundlach, D.....	6, 49, 76, 77, 78, 98	I	
Feng, M.....	25	Guo, W.....	27	Ida, S.....	15
Fennie, C.....	70	Gwilliam, R.....	29	Idutsu, Y.....	15, 91
Ferain, I.....	19	H		Iida, D.....	65, 88
		Habib, M.....	35	Im, S.....	31, 32, 75
				Ing, N.....	42

Inoue, K.....	35	Kato, D.....	15	Kummari, R.....	92
Isaacs-Smith, T.....	92	Kawai, T.....	45	Kunert, B.....	13, 46
Ito, S.....	15	Ke, X.....	70, 71	Kuno, K.....	67
Ive, T.....	53	Kedzierski, J.....	59, 60	Kuo, H.....	38
Iwaniczko, E.....	97	Keisuke, Y.....	45	Kuwano, N.....	89
Iwasaki, S.....	35	Keita, K.....	82		
Iwaya, M.....	65, 88, 89	Kelchner, K.....	37, 38	L	
J		Keller, S.....	22, 23, 103	Laberge, L.....	35
Jackson, M.....	19	Kendrick, C.....	83, 97	Lackner, D.....	24
Jackson, T.....	6, 29, 30, 48, 49, 76, 77, 95, 97	Kennedy, J.....	54	Lagarde, D.....	78
Jacobs, R.....	47	Kern, K.....	21	Lahourcade, L.....	62, 86
Jacquith, M.....	78	Khan, A.....	43	Lajin, A.....	30, 73, 74
Jae-Hoon, H.....	15	Khandelwal, M.....	40	Lalonde, A.....	34
Jafferis, N.....	6, 49	Khokhlov, D.....	96	Lantratov, V.....	26
Jain, V.....	90	Khoshakhlagh, A.....	24	Larsson, M.....	52
Jalan, B.....	51	Kikuchi, A.....	84	Lau, C.....	81
Jamil, M.....	14	Kikuchi, S.....	92	Lau, K.....	66
Janes, D.....	57, 66, 68, 69	Kim, C.....	26	Lauhon, L.....	36
Jang, J.....	29	Kim, D.....	31, 36, 90	Law, J.....	63
Jansen, M.....	21	Kim, H.....	17, 38, 43, 92, 95	Lee, B.....	31, 32
Jaquith, M.....	76	Kim, I.....	95	Lee, C.....	20, 51
Jaskolski, W.....	15	Kim, J.....	65	Lee, D.....	79
Jean, R.....	57	Kim, K.....	63, 103, 105	Lee, G.....	75
Jena, D.....	16, 21, 41, 43, 67, 80, 81, 82, 83, 85	Kim, M.....	26, 65	Lee, H.....	66
Jeon, J.....	92	Kim, S.....	29, 69, 75	Lee, I.....	38, 39, 40
Jeong, H.....	103	Kim, T.....	36, 90	Lee, J.....	17, 50, 70, 93
Jernigan, G.....	82	Kim, Y.....	32, 49, 79	Lee, K.....	31, 32, 75
Jha, S.....	47	Kimoto, T.....	40	Lee, M.....	95, 97
Jiang, W.....	32, 33	King, P.....	83	Lee, S.....	6, 31, 36, 44, 48, 79, 87, 90, 98
Jimison, L.....	77, 78	King, R.....	13	Lee, W.....	65
Joh, J.....	22	Kinkeldei, T.....	50	Lee, Y.....	90
John, D.....	95	Kirby, B.....	79	Lelis, A.....	100
Johnson, M.....	104	Kirchner, K.....	14	Lenahan, P.....	50, 69, 72, 100
Johnston, S.....	97	Kirchoefer, S.....	52	Leonhardt, D.....	45
Jones, A.....	78	Kishimoto, T.....	35	Leung, B.....	38, 40
Jones, J.....	6, 49, 50	Kishino, K.....	84	Li, C.....	94
Jones, K.....	14	Kist, R.....	20	Li, F.....	46
Joo, J.....	79	Klauek, H.....	21	Li, J.....	43
Joshi, M.....	18	Klaue-Rehberg, R.....	18	Li, M.....	92, 99
Ju, S.....	69	Klein, B.....	67	Li, Q.....	48, 88, 94
Julien, F.....	62	Knauer, A.....	87	Li, W.....	94
Jung, S.....	99	Kneissl, M.....	87	Li, X.....	55
Jurchescu, O.....	6, 49, 76, 77, 78	Knights, A.....	29	Li, Y.....	6, 37, 38, 48, 86
K		Ko, T.....	38, 39, 40	Li, Z.....	98
Kahn, A.....	17, 76	Kobayashi, Y.....	64	Lian, C.....	22, 43
Kakimoto, K.....	89	Koblmueller, G.....	63	Liang, B.....	68
Kalilikashtiban, R.....	29	Kodambaka, S.....	35, 36, 80	Liang, M.....	54
Kalyuzhnyy, N.....	26	Koleske, D.....	87, 102	Liang, Z.....	85
Kamada, Y.....	54	Konar, A.....	81	Liebich, S.....	13, 46
Kamella, C.....	21	Kong, B.....	39	Lim, W.....	29
Kameyama, N.....	54	Kosel, T.....	16, 67, 85	Lin, A.....	98
Kamimura, J.....	84	Koshka, Y.....	102	Lin, C.....	22
Kamins, T.....	28	Kotamraju, S.....	102	Lin, H.....	28
Kamiyama, S.....	65, 88, 89	Kowalewski, T.....	20, 77	Lin, Y.....	38, 48
Kandaswamy, P.....	62, 86	Kowalsky, W.....	31, 76	Lindle, J.....	26
Kaneko, K.....	54	Kraft, U.....	21	Liu, B.....	16
Kang, H.....	17	Krishna, L.....	34, 51	Liu, C.....	33
Kang, T.....	84	Krishna, S.....	24	Liu, E.....	14
Kang, W.....	58	Krishnan, A.....	72	Liu, F.....	92
Kangawa, Y.....	10, 89	Krishnan, B.....	102	Liu, G.....	33
Kanji, Y.....	82	Krishnan, S.....	72	Liu, J.....	86
Karthik, C.....	32, 33	Kroeger, M.....	76	Liu, K.....	101
Kasiyan, V.....	96	Kshirsagar, A.....	28	Liu, X.....	78, 79
Kasu, M.....	64	Kub, F.....	41, 101, 104	Liu, Y.....	55
		Kuech, T.....	17, 47	Liu, Z.....	66, 69
		Kuehn, S.....	93	Lloyd Spetz, A.....	91
		Kumano, H.....	15	Lochner, Z.....	86

Loo, L	98	Mintairov, S.....	26	Park, M	17
Look, D	74	Mishra, U	22, 23, 53, 62, 63, 103	Park, S	32, 49, 75, 77
Lopez, F	36	Miskovsky, N	34	Parkin, S	76
Lorenz, M.....	6, 30, 56, 73, 74, 75	Missert, N.....	87	Parpia, J	82
Loring, R	93	Mita, S	42	Paskova, T	38, 104
Los, A	79	Mitsuyoshi, S	13	Pearton, S	29, 73
Los, V	79	Mohney, S	16, 28, 58, 72, 90	Pei, Y	63, 103
Loth, M	6, 49, 76	Molnar, R	61	Peng, L	94
Lu, P	57	Moloney, J.....	26	Penot, J	19
Lu, S	18	Monroy, E	62, 86	Perea, D	36
Lu, Y	53	Monteyed, A	68	Perera, A.....	27
Lujan, R.....	20, 37	Moran, P.....	34, 51, 69, 70	Petrov, I	103
Lukco, D	91	Mori, F	89	Petzold, M	17, 18
Luo, X	81, 85	Mourey, D	6, 30, 48, 49	Phillips, J	53, 98
Luria, J	76, 78	Moutanabbir, O	18, 28	Picard, Y	41, 89
Luxmi, L.....	59, 60, 81	Mulcahy, B	70	Pitts, O	24
M					
Machhadani, H.....	62	Muller, D	51, 70	Plis, E	24
Madhukar, A	29	Müller, S.....	73, 75	Poblenz, C	103
Maeda, N	92	Muzykov, P	99	Podraza, N.....	30, 51, 71, 95, 97
Maehashi, K	35, 58	Myers, R.....	80	Pokatilov, E	81
Mahalingam, K	94	Myers, S	24	Pooley, O	24
Maitani, M	57	Myers, T	54, 61, 63	Porter, L	20, 90, 91, 92
Major, R	95	Myers-Ward, R	82	Prakash, G	59, 61
Malis, O.....	61	N			
Malkova, N	15	Nagamatsu, K.....	88	Preble, E.....	38, 104
Mallouk, T	97	Nagano, T.....	89	Pritchett, D	104
Malonis, A	103	Nagata, K	88	Protasenko, V.....	16, 43, 67
Manfra, M	21, 40, 61	Nair, H	25	Purushothaman, B.....	77
Mannhart, J	70	Nakamura, S.....	38	Q	
Mansfield, L	67, 68, 69, 85	Namkoong, G	64	Qi, Y	17
Marie, X	78	Nanishi, Y.....	92	R	
Maritato, L	71	Narayanan Kutty, M.....	24	Radu, I	19
Marohn, J	76, 78, 93	Naumann, F	17, 18	Raina, S	58
Martin, I	14, 97	Neméth, I	46	Rajagopalan, S	96
Mastro, M.....	41, 89, 104	Netzel, C	87	Ramanath, G	32, 33
Masui, H	62	Newman, C	20	Ramani, S	28
Matioli, E	65	Ng, T	20, 37	Randall, C	69
Matocha, K.....	100	Nidhi, N.....	22	Rangaraju, N	80
Matsubara, T	65	Nika, D	81	Rangel, E.....	65
Matsumoto, K	35, 58	Nimmatoori, P	16	Rao, S	45, 47
Matsumoto, Y.....	96	Nishinaka, H	54	Ravishankar, N.....	33
Mavrou, G	52	Noemaun, A.....	65	Rearick, D	53, 62
Mawst, L	47	Norton, D	29	Redwing, J.....	16, 62, 90, 97, 102, 104
Maximov, I	52	Nurmikko, A.....	38	Reedy, R.....	14
Mayer, A	34	O			
Mayer, T	16, 57, 90, 97	Oder, T	92	Reeves, R	54, 83
McConville, C	83	Oh, M	31, 32, 75	Reiche, M.....	18
McCulloch, I	77	Ohlmann, J.....	46	Reifenberger, R	59, 61
McCullough, R	20, 77	Ohno, Y	35, 74	Ren, F	29
McEuen, P	82	Okada, H	13, 45	Ren, T	57
Mehta, R	32, 33	Orgiani, P	71	Renard, J	86
Mei, Z	69	Orloff, N.....	51	Reynolds, Jr., C.....	104
Melby, J	40, 92	Oshimura, Y	88	Reyren, N	70
Melville, A	53	Ou-Yang, J.....	19	Rice, A	42, 88
Mendelsberg, R	54	P			
Merz, J	15, 26	Panayiotatos, Y.....	52	Richter, C	6, 49
Merz, T	22, 73	Pang, L	63	Richter, L.....	98
Metcalfé, G	39	Papanicolaou, N	24	Riedl, T	31, 76
Meyer, J.....	26, 76	Parashar, N	80	Rieutord, F	19
Mi, Z	16, 46	Park, C	31, 75	Ringel, S.....	46, 96, 103
Miao, F	81	Park, H	66	Rivnay, J.....	78
Miller, M	44, 87	Park, J	79, 82, 96	Robinson, J	53, 62, 82
Mills, M.....	96	Q			
Minassian, S	90	Qi, Y			
Mintairov, A	26	R			

Roshko, A.....	66	Shu, Y	77	Thibeault, B.....	90
Rotter, T	26	Shub, M.....	14	Thiel, S	70
Ruterana, P.....	86	Simon, J.....	43, 67	Thomas, S.....	102
Rutkowski, M.....	52	Sims, J	15	Thompson, R.....	67
Ruzyllo, J.....	28, 95	Singh, A.....	67	Tian, W	51
Ryabova, L.....	96	Singh, B.....	33	Timoshevskii, A.....	79
Ryan, J	72	Singh, K.....	20	Tivakornsasithorn, K.....	79
Ryou, J	25, 43, 86, 92	Singiseti, U.....	22, 23, 90	Toimil Molares, M.....	94
Ryu, S	99	Sitar, Z.....	42, 88	Toledo, N.....	62
S					
Sahmuganathan, V.....	46	Sivaramakrishnan, S.....	105	Tomasulo, S.....	38
Saint John, D.....	30, 97	Sivco, D.....	61	Tompa, G.....	31, 54, 100
Saito, T	96	Snyder, D.....	62, 82	Toney, M.....	77, 78
Sakr, S	62	Snyder, M.....	53	Tränkle, G.....	87
Salleo, A.....	20, 76, 77, 78	Son, J	79	Triscone, J.....	70
Samarth, N.....	80	Song, J.....	93	Troester, G.....	50
Sambandan, S.....	6, 20, 48	Song, K.....	17	Trolier-McKinstry, S.....	95
Sanders, A.....	66, 67, 68, 85	Song, Y.....	83	Trybus, E.....	64
Sandhu, R.....	59	Speck, J.....	22, 38, 39, 53, 62, 63, 65, 103	Tsai, C	64
Sands, T.....	32, 34, 85	Spencer, M.....	59, 82, 83, 100	Tsetkov, D.....	66
Sanford, N.....	66, 67, 68, 69, 85	Sridhara, K.....	28	Tsoutsou, D.....	52
Sarpawatari, K.....	72, 90	Srivastava, N.....	59, 60	Tsujita, Y.....	58
Sasaki, R.....	96	Stach, E.....	85	Tsukada, D.....	96
Sasakura, H.....	15	Stahlbush, R.....	99, 101	Tsvetkov, D.....	68
Sasamoto, K.....	84	Steger, M.....	24	Tu, C	78
Sato, H	15	Stemmer, S.....	50, 51	Turner, K.....	18
Sbrockey, N.....	100	Stolz, W.....	13, 46	Tutuc, E.....	14
Schaaake, C.....	103	Stradins, P.....	14, 97	Tutwiler, R.....	95
Schiffer, P.....	70, 71, 80	Street, R.....	6, 20, 48	Tweedie, J.....	42, 88
Schlager, J.....	66, 67, 68, 85	Sturm, J.....	6, 14, 17, 49	Twigg, M.....	89
Schlom, D.....	51, 70, 71, 72	Subramanian, S.....	6, 48, 77	Twymann, M.....	94
Schmidt, F.....	73, 75	Suda, J	40	Tymicki, E.....	100
Schmidt, M.....	73, 75	Sudarshan, T.....	99	U	
Scholz, R.....	18	Suemasu, T.....	96	Umeno, K.....	13
Schowalter, L.....	42	Suemune, I.....	15, 91	Unocic, R.....	96
Schroeder, J.....	34	Sugita, K.....	84	Urakami, N.....	13
Schubert, E.....	65	Suh, D	31, 90	V	
Schubert, J.....	51, 70	Sun, J	6, 49, 52	Vanderbilt, D.....	71, 72
Schubert, M.....	56	Sun, Q.....	38, 39, 40	Van de Walle, C.....	53
Schwartz, J.....	17	Sun, S	31, 54	van Look, J.....	87
Scott, A	57	Sun, Y.....	59, 60	Van Mill, B.....	82
Seitz, O	18	Sunder, M.....	51, 70	Vardi, A.....	62
Selvamanickam, V.....	47	Sung, M.....	31, 32	Veal, T.....	83
Selvaraj, S.....	42	Swami, N.....	56	Vijayraghavan, K.....	25
Senda, R.....	65	Swaminathan, K.....	46	Vincent, S.....	19
Senz, S	18	Swanson, M.....	70	Virshup, A.....	91
Seo, H	63, 103, 105	Swenson, B.....	23, 103	Vispute, R.....	14
Seong, T.....	92	Szkopek, T.....	16	Vlasenko, L.....	73
Shanabrook, B.....	28	T		Vodnick, D.....	95
Shang, S	69	Tadger, M.....	41, 101, 104	Volz, K.....	13, 46
Shankar, K.....	98	Tahy, K	81, 82	von Wenckstern, H.....	30, 73, 74, 75
Shanmugasundaram, K.....	28	Taishi, T.....	74	Voora, V.....	56
Shao, C	55	Takada, M.....	15	Vurgafman, I.....	26
Shen, H	29, 42	Takeda, K.....	88, 89	W	
Shen, P.....	39	Takeishi, M.....	96	Wagner, S.....	6, 49, 50
Shen, S.....	79, 83	Talin, A.....	94	Wakahara, A.....	13, 45
Sheng, J.....	45	Tanaka, M.....	84	Walker, A.....	57
Shenoy, V.....	80	Tang, C.....	66	Wang, C.....	46, 55
Shields, V.....	59, 83	Tang, K.....	41	Wang, G.....	48, 83, 88, 94
Shih, Y	54	Tangtrakarn, N.....	70	Wang, K.....	83
Shilling, D.....	81	Tapily, K.....	55	Wang, W.....	54, 98
Shin, H.....	95, 97	Tchernycheva, M.....	62	Wang, X.....	73, 78
Shintri, S.....	45, 47	Tedesco, J.....	82	Wang, Y.....	50, 69
Shivaraman, S.....	59, 82, 83	Teplin, C.....	14, 97		
Shoaf, J.....	94	Teweldebrhan, D.....	81		
Shrestha, P.....	55	Therriault, D.....	35		
		Thewalt, M.....	24		

Warusawithana, M	70	Young, D	97
Watkins, S	24	Young, E	39
Weber, E	21	Young, T	20, 77
Wei, L	58	Yu, E	63, 93
Weisbuch, C	65	Yu, J	79
Weiss, B	34	Yu, X	82
Weiss, P	93	Yum, J	50
Wenckstern, H	54	Yuwen, Y	97
Weng, X	53, 62		
Wenzel, H	87	Z	
Wessels, B	78, 80	Zakharov, D	85
Westlake, K	87	Zakharov, N	18
Wetherington, M	82	Zaumseil, J	35
Wetzel, C	37, 38, 65, 86, 87, 96	Zeimer, U	87
Weyers, M	87	Zemlianov, D	57
Wiedenmann, K	72	Zemlyanov, D	61
Wiederrecht, G	35	Zhang, B	43
Wijewarnasuriya, P	45	Zhang, C	27, 58
Wildeson, I	85	Zhang, F	58
Williams, J	92, 99	Zhang, J	52
Willner, B	31, 54	Zhang, N	100, 101
Wilson, M	80	Zhang, P	93
Wirthmüller, A	62	Zhang, Q	28
Wistey, M	22, 23, 25, 90	Zhang, R	77
Wong, K	66	Zhang, S	36
Wong, M	22, 63, 103	Zhang, Y	32, 33, 38, 39, 100, 101
Wong, P	15, 68	Zhao, D	6, 30, 49
Wong, W	6, 37, 48	Zhao, F	78
Woodall, J	45	Zhao, H	50
Wortman, R	34	Zhao, L	38
Wraback, M	39, 42	Zhao, W	38, 86, 87
Wu, F	63	Zheleva, T	14
Wu, Y	40, 59	Zheng, M	70
		Zhitenev, N	99
X		Zhou, C	69
Xi, B	57	Zhou, G	85
Xi, X	51	Zhu, D	65
Xia, Y	37, 38, 86	Zhu, M	17, 38, 80, 86, 87
Xie, J	88	Zhu, T	27, 28, 58
Xie, Y	35, 36	Zhu, X	92, 99
Xing, H	16, 21, 22, 41, 43, 67, 81, 82, 85	Zhu, Y	100
Xiong, H	6, 49	Zide, J	25
Xu, H	52	Zielinski, M	15
Xu, J	27, 28, 58	Zimmerman, J	25
Xu, Y	97	Zimmermann, T	41, 85
		Zimprich, M	13
Y		Zinnkann, S	13, 46
Yamaguchi, T	92	Zippel, J	75
Yamamoto, A	84	Zscheschang, U	21
Yamamoto, M	84	Zuo, J	105
Yan, H	20	Zvanut, M	102
Yang, C	17		
Yang, G	55		
Yao, T	74		
Yao, Y	55		
Yarborough, M	26		
Yazdanian, S	93		
Ye, P	59		
Yen, T	75		
Yerino, C	38, 39, 40		
Yoder, P	86		
Yonenaga, I	74		
Yonezu, H	13, 45		
Yoon, H	57, 97		
Yoon, Y	29		
You, S	37, 38		



WEDNESDAY		THURSDAY		FRIDAY	ROOM
AM	PM	AM	PM	AM	
REGISTRATION in Penn Stater Conference Center, 1st Level 3:00-5:00 PM, Tuesday, June 23 7:30 AM-5:00 PM, Wednesday, June 24			EXHIBITS in Presidents Hall I & II 9:30 AM-4:00 PM; 6:00-8:00 PM, Wednesday, June 24 10:00 AM-4:00 PM, Thursday, June 25		
EMC Plenary Lecture/Student Awards	Session L: Thermoelectrics and Thermionics				Presidents Hall III & IV
Session A: Epitaxy	Session G: Narrow Bandgap Materials Session H: Epitaxy for Devices	Session S: Epitaxy on Si Session T: Metamorphic and Templated Growth	Session HH: Spin-Dependent (or Spintronic) Electronic Materials		
Session B: Low Dimensional Structures: Wires and Dots; Dots in Wires	Session I: Quantum Dot Optical Characterizations and Photonic Devices Session J: Quantum Dot Materials Characterization and Epitaxy	Session U: Flexible and Printed Thin-film Electronics	Session CC: III-V NW - Characterization Session DD: III-V NW - Growth and Processing	Session NN: Contacts to Semiconductor Epilayers and Nanowires	106
Session C: Semiconductor Processing	Session K: ZnO Thin Film Transistors	Session V: Oxide Thin Film Integration I	Session EE: Oxide Thin Film Integration II	Session OO: Nanoscale Characterization Session PP: Non-Destructive Testing and In-Situ Control	108
Session D: Materials Integration: Wafer Bonding and Engineered Substrates	Session M: Carbon Based Nanowires and Tubes Session N: Group IV Nanowires	Session Y: Graphene I	Session II: Graphene II	Session RR: Silicon Carbide	206
Session E: Organic Thin Film and Crystalline Transistors: Devices, Materials and Processing I	Session O: III-Nitride: Optical Devices on Non-Polar Substrates Session P: III-Nitride: Growth and Characterization of Non-Polar Materials	Session Z: III-Nitride: MBE Growth and Intersubband Structures Session AA: III-Nitride: MBE Growth	Session JJ: III-Nitride: Indium Nitride Session KK: III-Nitride: Nanostructures	Session SS: III-Nitride: Characterization of Defects Session TT: III-Nitride: Growth and Characterization of Optical Devices	207
Session F: III-Nitride: Growth of Electronic Devices	Session Q: III-Nitride: Processing of Electronic Devices Session R: III-Nitride: AlGaIn Materials and Devices	Session BB: III-Nitride: Optical Devices I	Session LL: III-Nitride: Optical Devices II Session MM: III-Nitride: MOCVD Growth and Pseudo-Substrates		208
		Session W: ZnO Growth	Session FF: ZnO Characterization		Deans Hall I
		Session X: Molecular Electronics: Devices, Materials, and Molecular Electronics and Chem/Bio Sensors	Session GG: Organic Thin Film and Crystalline Transistors: Devices, Materials and Processing II	Session QQ: Solar Cells - Organic, Hybrid and Inorganic	Deans Hall II